BULGARIAN CHEMICAL COMMUNICATIONS

Journal of the Chemical Institutes
of the Bulgarian Academy of Sciences
and of the Union of Chemists in Bulgaria

A facile synthesis of 3-chloro-2-phenyl-4*H*-chromen-4-ones using grinding technique at room temperature

D.K. Sharma[*1], S. Kumar[2]

[1]Department of Chemistry, Kishan Lal Public (P. G.) College, Rewari, Haryana, 123401, India
[2]Department of Chemistry, Technological Institute of Textile and Sciences, Bhiwani, Haryana, 127021, India

An efficient procedure for the synthesis of 3-chloro-2-phenyl-4*H*-chromen-4-ones by selective chlorination of 1-(2-hydroxyphenyl)-3-phenylpropane-1,3-diones with potassium chloride and ammonium persulfate gave 2-chloro-1-(2-hydroxyphenyl)-3-phenylpropane-1,3-diones which on cyclisation with phosphorus pentoxide yielded 3-chloro-2-phenyl-4*H*-chromen-4-ones under grinding conditions.

Keywords: 1-(2-hydroxyphenyl)-3-phenylpropane-1,3-diones; 3-chloro-2-phenyl-4*H*-chromen-4-ones; grinding technique; chlorination.

INTRODUCTION

3-Chloro-2-phenyl-4*H*-chromen-4-ones constitute an important class of compounds in flavanoid chemistry due to their significant biological properties [1-4] and also act as important intermediates for the synthesis of 2-aroylcoumaranones [5]. These compounds are generally obtained by direct chlorination of 2-phenyl-4*H*-chromen-4-ones [6,7] or by selective chlorination of 1-(2-hydroxyphenyl)-3-phenylpropane-1,3-diones followed by cyclisation of α-chloro derivatives [5,8]. However, selective chlorination of 1-(2-hydroxyphenyl)-3-phenylpropane-1,3-diones followed by cyclisation remains the most practical method for their preparation. Chlorination of 1-(2-hydroxyphenyl)-3-phenylpropane-1,3-diones has generally been carried out using sulfuryl chloride [5] or by oxidative chlorination using phase transfer catalysis [8].

But all the existing methods make use of highly toxic chemicals and organic solvents causing extreme damage to our environment.

The grinding technique has been considered to be an important tool to carry out reactions under solvent-free conditions, with maximum yield and minimum cost, and it also got much attention due to its operational simplicity [9,10]. In continuation of our work to develop efficient and ecological procedures for the synthesis of organic compounds avoiding hazardous chemicals and organic solvents [11] at any stage of the reaction, we report an efficient procedure for the synthesis of 3-chloro-2-phenyl-4*H*-chromen-4-ones using aqueous grinding technique which avoids the use of hazardous chemicals and organic solvents during work-up.

EXPERIMENTAL

All the chemicals were obtained from commercial sources. Melting points were determined in open capillary tubes. IR (KBr) spectra were recorded on a Perkin-Elmer spectrum BX series FT-IR spectrophotometer; ^{1}H NMR and ^{13}C NMR spectra were recorded on a Bruker 400 MHz and 100 MHz spectrometer, respectively, using TMS as the internal standard. The elemental analyses were performed on a Perkin Elmer 2400 elemental analyzer. Silica gel (100-200 mesh) was used for column chromatography. 1-(2-Hydroxyphenyl)-3-phenylpropane-1,3-diones 1a-1f, required for the present study, were prepared by Baker-Venkataraman rearrangement using grinding technique as reported previously [12].

General procedure for the synthesis of 3-chloro-2-phenyl-4H-chromen-4-ones (3a-3f)

A mixture of 1-(2-hydroxyphenyl)-3-phenylpropane-1,3-diones 1a-1f (1 mmol), potassium chloride (2 mmol) and ammonium persulfate (2.5 mmol) moistened with 10 drops of water was ground in a mortar by a pestle at room temperature for 10 min. The reaction mixture was diluted with ice-cold water and the separated solid was filtered, washed with water and dried in vacuum over anhydrous calcium chloride. The mixture of the dry solid and phosphorous pentoxide (1 mmol) was ground together in a mortar by pestle for 10-15 min, when formation of a single product was observed by thin layer chromatography. The reaction mixture was diluted with ice-cold water; the solid that separated out was filtered, washed

---
* To whom all correspondence should be sent:
E-mail: dksharma_84@rediffmail.com

with water and crystallized from ethanol to afford 3-chloro-2-phenyl-4*H*-chromen-4-ones 3a-3f.

3-Chloro-2-phenyl-4H-chromen-4-one (3a). IR (KBr, ν_{max}/cm^{-1}): 1667, 752; ^{1}H NMR (400 MHz, CDCl$_3$, δ/ppm): 8.35-8.37 (dd, 1H, *J*=8.0 Hz & *J*=2.0 Hz), 7.72-8.05 (m, 3H), 7.25-7.65 (m, 5H); ^{13}C NMR (100 MHz, CDCl$_3$, δ/ppm): 179.8, 157.1, 155.5, 134.5, 131.6, 129.8, 129.8, 129.5, 127.2, 127.1, 127.1, 124.8, 121.1, 119.7, 104.8; Anal. calcd for C$_{15}$H$_9$ClO$_2$: C, 70.59; H, 3.53; Cl, 13.84. Found: C, 70.47; H, 3.53; Cl, 13.75.

3-Chloro-2-(4-methoxyphenyl)-4H-chromen-4-one (3b). IR (KBr, ν_{max}/cm^{-1}): 1660, 750; ^{1}H NMR (400 MHz, CDCl$_3$, δ/ppm): 8.35-8.37 (dd, 1H, *J*=8.0 Hz & *J*=2.0 Hz), 8.05 (d, 2H, *J*=8.0 Hz), 7.71-7.85 (m, 1H), 7.30-7.60 (m, 2H), 7.10 (d, 2H, *J*=8.0Hz), 3.92 (s, 3H); ^{13}C NMR (100 MHz, CDCl$_3$, δ/ppm): 179.9, 163.2, 157.1, 155.5, 134.6, 127.7, 127.7, 127.2, 124.8, 123.3, 121.2, 119.8, 115.9, 115.9, 104.8, 56.1; Anal. calcd for C$_{16}$H$_{11}$ClO$_3$: C, 67.03; H, 3.87; Cl, 13.39. Found: C, 67.12; H, 3.75; Cl, 13.26.

3-Chloro-6-methyl-2-phenyl-4H-chromen-4-one (3c). IR (KBr, ν_{max}/cm^{-1}): 1665, 740; ^{1}H NMR (400 MHz, CDCl$_3$, δ/ppm): 8.20 (d, 1H, *J*=8.0 Hz), 8.0-8.10 (m, 2H), 7.50-7.85 (m, 5H), 2.40 (s, 3H, CH$_3$); ^{13}C NMR (100 MHz, CDCl$_3$, δ/ppm): 180.1, 157.2, 152.8, 136.5, 135.5, 131.7, 129.9, 129.9, 129.5, 127.1, 127.1, 125.6, 119.1, 118.6, 104.8, 20.7; Anal. calcd for C$_{16}$H$_{11}$ClO$_2$: C, 70.99; H, 4.10; Cl, 13.12. Found: C, 67.12; H, 4.18; Cl, 13.03.

3-Chloro-2-(4-methoxyphenyl)-6-methyl-4H-chromen-4-one (3d). IR (KBr, ν_{max}/cm^{-1}): 1660, 745; ^{1}H NMR (400 MHz, CDCl$_3$, δ/ppm): 8.15 (d, 1H, *J*=8.0 Hz), 7.98 (d, 2H, *J*=8.0 Hz), 7.90-7.95 (m, 2H), 6.85 (d, 2H, *J*=8.0 Hz), 3.90 (s, 3H, OCH$_3$), 2.25 (s, 3H, CH$_3$); ^{13}C NMR (100 MHz, CDCl$_3$, δ/ppm): 180.1, 163.2, 157.2, 152.8, 136.5, 135.5, 127.7, 127.7, 125.6, 123.3, 119.1, 118.6, 116.0, 116.0, 104.9, 55.8, 20.7; Anal. calcd for C$_{17}$H$_{13}$ClO$_3$: C, 67.91; H, 4.36; Cl, 11.81. Found: C, 67.80; H, 4.39; Cl, 11.71.

3-Chloro-7-methyl-2-phenyl-4H-chromen-4-one (3e). IR (KBr, ν_{max}/cm^{-1}): 1664, 725; ^{1}H NMR (400 MHz, CDCl$_3$, δ/ppm): 8.30 (d, 1H, *J*=8.0 Hz), 7.50-8.10 (m, 5H), 7.30 (dd, 1H, *J*=8.0 Hz & *J*=2.0 Hz), 6.92 (s, 1H), 2.40 (s, 3H); ^{13}C NMR (100 MHz, CDCl$_3$, δ/ppm): 179.9, 157.1, 155.1, 146.9, 131.7, 129.8, 129.8, 129.7, 128.5, 127.1, 127.1, 123.6, 121.0, 114.5, 104.8, 21.4; Anal. calcd for C$_{16}$H$_{11}$ClO$_2$: C, 70.99; H, 4.10; Cl, 13.12. Found: C, 70.85; H, 4.15; Cl, 13.03.

3-Chloro-2-(4-methoxyphenyl)-7-methyl-4H-chromen-4-one (3f). IR (KBr, ν_{max}/cm^{-1}): 1680, 750; ^{1}H NMR (400 MHz, CDCl$_3$, δ/ppm): 8.05 (d, 1H, *J*=8.0 Hz), 7.35-7.85 (m, 4H), 7.28 (dd, 1H, *J*=8.0 Hz & *J*=2.0 Hz), 7.05 (s, 1H), 3.85 (s, 3H), 2.20 (s, 3H); ^{13}C NMR (100 MHz, CDCl$_3$, δ/ppm): 179.8, 163.2, 157.2, 155.1, 146.9, 128.5, 127.7, 127.7, 123.6, 123.5, 121.0, 116.0, 116.0, 114.5, 104.8, 55.6, 21.4; Anal. calcd for C$_{17}$H$_{13}$ClO$_3$: C, 67.89; H, 4.36; Cl, 11.81 Found: C, 67.80; H, 4.41; Cl, 11.71.

RESULTS AND DISCUSSION

1-(2-Hydroxyphenyl)-3-phenylpropane-1,3-dione 1a was ground with potassium chloride and ammonium persulfate in a mortar using a pestle under slightly moist conditions. Formation of two compounds was observed by thin layer chromatography, which were separated by column chromatography and were identified as 2-chloro-1-(2-hydroxyphenyl)-3-phenylpropane-1,3-dione (2a) and 3-chloro-2-phenyl-4*H*-chromen-4-one (3a) (Scheme 1).
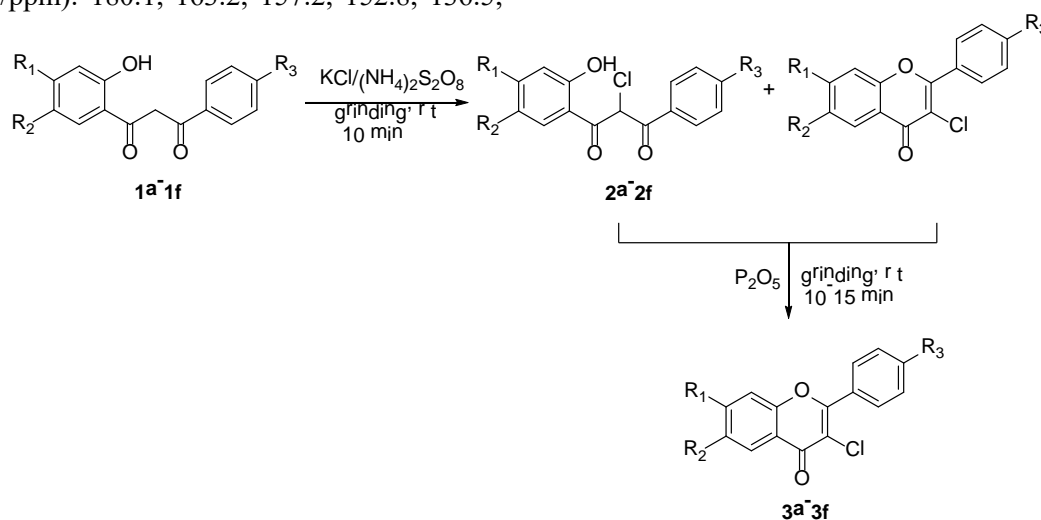
Scheme 1. Synthesis of 3-chloro-2-phenyl-4*H*-chromen-4-ones using grinding technique

Table 1. Physical data of 3-chloro-2-phenyl-4*H*-chromen-4-ones.

Compound	R_1	R_2	R_3	Time (min) (a+b)	Mp (°C)	Mp. (°C) ref. [5]	Yield (%)[c]
3 a	H	H	H	10+10	124-25	125	85
3 b	H	H	OCH_3	10+10	131-33	135	95
3 c	H	CH_3	H	10+10	137-39	139	85
3 d	H	CH_3	OCH_3	10+15	133	135	90
3 e	CH_3	H	H	10+15	122-24	122	80
3 f	CH_3	H	OCH_3	10+15	150	152	92

a - time for grinding with KCl and $(NH_4)_2S_2O_8$
b- time for grinding with P_2O_5
c- Purified isolated yields

It appears that 2-chloro-1-(2-hydroxyphenyl)-3-phenylpropane-1,3-dione **2a** formed at the initial stage undergoes cyclisation to some extent under these conditions to give 3-chloro-2-phenyl-4*H*-chromen-4-one **3a**. The mixture of the two products obtained in the above reaction on grinding with phosphorus pentoxide without any further purification gave only 3-chloro-2-phenyl-4*H*-chromen-4-one, involving the cyclisation of the remaining uncycled 2-chloro-1-(2-hydroxyphenyl)-3-phenylpropane-1,3-dione. The reaction mixture on dilution with ice-cold water gave the product directly, thus avoiding the use of any organic solvent for extraction. Optimum conditions for the reaction were achieved by using varying amounts of potassium chloride and ammonium persulfate and best results were obtained with 2 mmol of potassium chloride and 2.5 mmol of ammonium persulfate. The presence of moisture was found essential, in the absence of which no reaction was found to take place. This was attributed to the fact that the formation of chloride and persulfate ions is being facilitated and the oxidation of the chloride ion produces chlorine *in situ* which is consumed there and then in the reaction. The HCl produced during the reaction is absorbed in the medium by the water present and does not spoil the atmosphere.

The validity of the reaction was established by converting differently substituted 1-(2-hydroxyphenyl)-3-phenylpropane-1,3-diones **1a-1f** into 3-chloro-2-phenyl-4*H*-chromen-4-ones **3a-3f** (Scheme 1, Table 1) in high yield.

CONCLUSIONS

In conclusion it can be said that the present method developed for the selective chlorination of 1-(2-hydroxyphenyl)-3-phenylpropane-1,3-diones and synthesis of 3-chloro-2-phenyl-4*H*-chromen-4-ones under solvent-free conditions using grinding technique is simple, clean, mild, highly efficient and ecological.

REFERENCES

1. G.P. Ellis, Chromenes, Chromanones and Chromones: The Chemistry of Heterocyclic Compounds, John Wiley & Sons, New York, USA, 1973.
2. M.P. De Meo, C. Beudot, D. Dauzonne, R. Elias, M. Laget, H. Guiraud, G. Balansard, G. Dumenil, *Mutat. Res.,* **417**, 141 (1998).
3. K.A. Jacobson, Y. Karton, J.L. Jiang, X.D. Ji, N. Melman, M.E. Olah, G.L. Stiles, *J. Med. Chem.,* **39**, 2293 (1996).
4. K.A. Jacobson, K.S. Park, J.L. Jiang, Y.C. Kim, M.E. Olah, G.L. Stiles, X.D. Ji, *Neuropharmacology,* **36**, 1157 (1997).
5. H.L. Gaggad, K.N. Wadodkar, *Indian J. Chem.,* **17B**, 641 (1979).
6. S.Y. Dike, M. Mahalingam, *Synth. Commun.,* **19**, 3443 (1989).
7. H.S. Rho, B.S. Ko, Y.S. Ju, *Synth. Commun.,* **31**, 2101 (2001).
8. J.K. Makrandi, Sashi, S. Kumar, *Indian J. Chem.,* **43B**, 895 (2004).
9. D. Sharma, S. Kumar, J.K. Makrandi, *Chem. Sc. Trans.,* **2**, 403 (2013).
10. C.B. Aakeroy, A.S. Sinha, K.N. Epa, C.L. Spartz, J. Desper, *Chem. Commun.,* **48**, 11289 (2012).
11. D. Sharma, J.K. Makrandi, S. Kumar, *Green. Chem. Lett. Rev.,* **4**, 127 (2011).
12. D. Sharma, J.K. Makrandi, S. Kumar, *Green. Chem. Lett. Rev.,* **2**, 53 (2009).

ПРОСТА СИНТЕЗА НА 3-ХЛОРО-2-ФЕНИЛ-4*H*-ХРОМЕН-4-ОНИ С ИЗПОЛЗВАНЕТО НА СМИЛАНЕ ПРИ СТАЙНА ТЕМПЕРАТУРА

Д.К. Шарма[*1], С. Кумар[2]

[1]Департамент по химия, Публичен колеж „Кишан Лал", Реуардж, Харияна 123401, Индия
[2] Департамент по химия,, Технологичен институт за наука и текстил, Бхвуани, Харияна 127021, Индия

(Резюме)

Постигната е ефективна процедура за синтезата на 3-хлоро-2-фенил-4*H*-хромен-4-они чрез селективното хлориране на 1-(2-хидроксифенил)-3-фенилпропан-1,3-диони с калиев хлорид и амониев персулфат. Получени са 2-хлоро-1-(2-хидроксифенил)-3-фенилпропан-1,3-диони които след циклизация с дифосфорен пентоксид дава 3-хлоро-2-фенил-4*H*-хромен-4-они след смилане.

Composition and structure of Ni-Co coating depending on the ratio of Ni and Co in a citrate electrolyte

K. Ignatova[1]*, Y. Marcheva[2]

[1]University of Chemical Technology and Metallurgy – Sofia, 8 blvd. Kl. Ohridsky, Sofia 1000, Bulgaria
[2]Technical Univerity - Sofia, 8 bul. Kl. Ohridsky, Sofia 1000, Bulgaria

This paper reports the effect of the Ni/Co ratio in a citrate electrolyte (with an optimum content of Na_3 citrate) on the deposition kinetics, chemical and phase composition of the Ni-Co alloy coating, current cathodic efficiency of the electrodeposition, and morphology of the coating. It was established that by increasing the Co content in the solution, the deposition potentials of the Ni-Co alloy were shifted towards the values where Co reaches a plateau of limited diffusion current. When the Co content in the solution increases and the applied cathodic potential gets more positive values, the Co content in the alloy increases (up to max 85%), and so does the cathodic current efficiency (in respect to electrodeposition of the alloy). The Co content in the alloys deposited in all studied electrolytes was over 60 mass % and the phenomenon of "anomalous" co-deposition of Ni and Co in the alloys was identified.

The SEM images of the alloy coatings deposited at potentiostatic conditions show that when the Co content in the alloy increases, the dimension of the crystals increases from about 100 nm up to about 300 nm. The alloy coatings have mixed structure of face-centered cubic (fcc) and hexagonal closed packed (hcp) lattice, which was proven by the XRD results.

Key words: kinetics of deposition, morphology, chemical composition, Ni-Co alloys, phase structure

INTRODUCTION

Recently, there is an increasing interest to nanostructured Co alloys which are mostly applied in magnetic sensor technologies and magnetic electronics [1-5]. The metals from the iron group and their alloys, including Ni-Co, exhibit high hardness, wear resistance and anti-corrosion protection. Ni-Co alloys are widely used in medicine, nuclear power systems, chemical and oil industry [6-8]. In addition to their excellent ferromagnetic and super hydrophobic properties, the nanostructured Co, Ni, and Ni-Co coatings also exhibit valuable catalytic properties [9-11]. The studies of electrodeposited Ni-Co alloys have shown that their microstructure and properties strongly depend on the Co content which can be controlled by the experimental parameters, such as bath composition, temperature, pH value, current density, etc. [2, 12-20].

According to the binary phase diagram of Ni and Co [26] and their similar atomic diameters, the Ni-Co alloy forms a substitution solid solution. Myung and Nobe [20] and Golodnitsky et al. [13] found three different crystal structures of Ni-Co alloy controlled by the Co-content. At low cobalt content (<40-50%) pure face-centered cubic (fcc) lattice (which would exist for pure nickel) was identified. As the content of cobalt increased, both fcc and hexagonal close packed lattice (hcp) appeared, and for Co-rich alloy (>80%), pure hcp was observed.

Similar conclusions were proposed by Tury [19] and El-Feky Hesham [16] in the case of pulse deposition of Ni-Co alloys. The differences in the results about the phase composition of the Ni-Co alloys [15-20] are not very significant and are related to differences in the electrolyte composition and deposition conditions.

In previous works [27, 28] the effect of $Na_3C_6H_5O_7.2H_2O$ (Na_3 citrate) and H_3BO_3 concentrations on the electrolyte stability and deposition kinetics of Ni-Co alloys [27] as well as on the chemical composition, morphology and the phase composition [28] was studied. It was established that with increasing the concentration of Na_3 citrate in the solution (0.2-0.6 M), the deposition of Ni-Co alloy took place with lower cathodic current efficiency and bigger crystal dimensions; the Ni deposition was more difficult. As an optimum Na_3 citrate concentration in the electrolyte the lowest one (0.2M) was assumed.

The object of this paper is to study the effect of the ratio of the main components Ni and Co in a low-acidic citrate electrolyte (optimized in respect to Na_3 citrate concentration) on the deposition kinetics of Ni-Co alloys, chemical composition, current efficiency of the electrodeposition, morphology and phase composition of the Ni-Co coatings.

EXPERIMENTAL

The study was carried out in three electrolytes with compositions given in Table 1. All solutions were freshly prepared with distilled water and

---

* To whom all correspondence should be sent:
E-mail: katya59ignatova@gmail.com

analytical grade chemicals. The pH was adjusted through addition of H_2SO_4 and NaOH.

The electrolyte compositions differ in the Ni/Co ratio within the range 1-3 through a change in the Co concentration at constant content of Ni (0.3M) and of the other electrolyte components (Table 1).

Table 1. Electrolyte compositions

Electrolyte (pH = 5.5)	Co [mol.dm^{-3}]	Ni [mol.dm^{-3}]	H_3BO_3 [mol.dm^{-3}]	Na_3citrate [mol.dm^{-3}]	Ni/Co ratio in the electrolyte
I	0.1	0.3	0.485	0.2	3
II	0.2	0.3	0.485	0.2	1.5
III	0.3	0.3	0.485	0.2	1

The deposition of the Ni-Co alloy coatings was examined using the method of potentiodynamic polarization curves with a scan rate of 30 mV.s^{-1} at room temperature using the Wenking Electrochemical Analysis System (Germany). A conventional three-electrode cell (total volume of 150 dm^3) equipped with a platinum foil counter electrode and saturated calomel electrode (SCE) as reference electrode was used. The working electrode was a disk-shaped copper electrode with surface area of 1 cm^2. All potentials are quoted with respect to the SCE.

The coatings intended for analysis were deposited for 6 min on rectangular copper plates with dimensions of 1.5×4 cm at constant potentials, determined from the polarization curves in the studied electrolytes. After electrodeposition the coatings were dissolved in 3.0 M HNO_3 and analyzed.

Prior to electrodeposition, the surface of the copper cathodes was rinsed with distilled water, cleaned in an etching solution $(H_2SO_4 : HNO_3 = 1:1; + 10\% \ HCl)$, rinsed several times with distilled water and dried.

Elemental analyses of the coatings (in mass %) were performed by means of atomic emission spectral analysis, ICP-OES (high-dispersion ICP) using a Prodigy equipment (Teledyne Leeman Labs). Based on the data for the chemical content, the corresponding values for the cathodic current efficiency (CCE) of electrodeposition of the Ni-Co alloy were calculated following the law of Faraday:

$$CCE = \frac{\Delta m_{pr}}{\Delta m_{th}}.100,\%$$ where: Δm_{pr} is the practical mass of the Ni-Co coating, [g]; $\Delta m_{th} = q_{Ni-Co}I.t$ is the theoretically determined mass of the Ni-Co alloy [g]; **I** is the current during deposition [A]; t - the time of deposition [s];

$$q_{Ni-Co} = \frac{q_{Ni}.q_{Co}}{N_{Co}q_{Ni} + N_{Ni}q_{Co}} [eq.C^{-1}]$$ is the electrochemical equivalent of the alloy, calculated using the data about the chemical content of the alloy (N_{Ni} and N_{Co} are the molar parts of Ni and Co in the alloy).

The morphology of the coatings was examined through scanning electron microscopy (SEM) using the JSM-6390 Jeol equipment (Oxford Instruments). The phase composition of the coatings was identified using X-ray analysis with a powder diffractometer Philips PW 1050, CuKα radiation and operating voltage of 20.0 kV.

RESULTS AND DISCUSSION

Kinetics of deposition of the Ni-Co alloy

Comparisons between the potentiodynamic curves of deposition of Ni, Co and Ni-Co alloy coatings in the studied electrolytes are shown in Fig.1 (a-c).

As can be seen, the curves for the Ni deposition (curves 1) in all studied electrolytes have no plateau of limited diffusion current. An activation nature of the polarization was established [29, 30]. In the deposition curves of Co (curves 2), as well as the curves for the Ni-Co alloy deposition sharply expressed plateaus can be seen, which can be related to diffusion limitations. When the concentration of Co in the solution increases, the plateau of the limited current density in the curves of Co and CoNi deposition is shifted to more negative potentials, while the potentials for Ni deposition (-1.1V to -1.3V) stay the same. This phenomenon shows that the potentials for the Ni-Co alloy deposition (-1.0V to -1.3V) in the electrolytes with compositions II and III will correspond to conditions, where Co deposition will take place with diffusion limitations, which would worsen the structural characteristics of the alloy.

For all studied Ni/Co ratios in the solution co-deposition of Ni and Co in the Ni-Co alloy is possible. The kinetic peculiarity of the deposition of each metal will affect the structure of the alloy coatings.

Chemical composition of the Ni-Co alloy and current efficiency

The data about the percent content of the coating depending on the deposition potential (in the range of -1.1V to -1.3V) and on the Ni/Co ratio in the electrolyte are shown in Fig. 2.
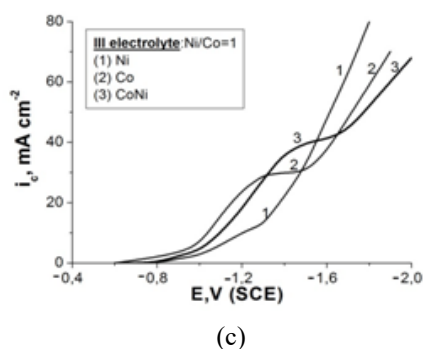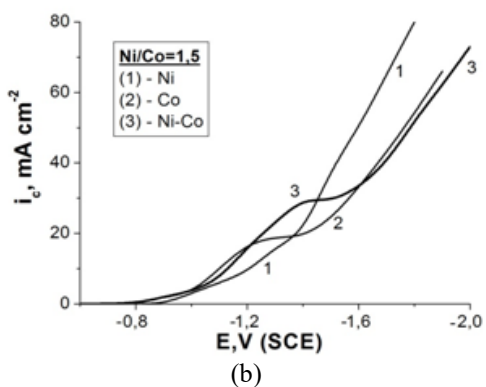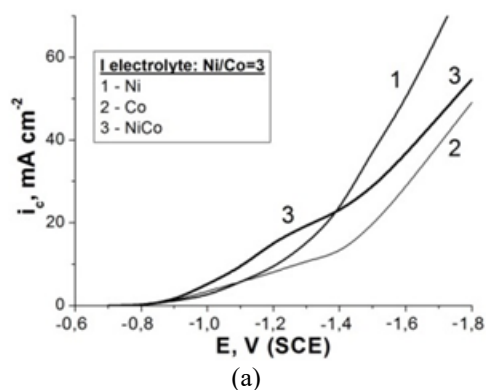
(a)

(b)

(c)

Fig. 1. Comparison of the polarization curves of deposition of Ni (1), Co (2) and the Ni-Co alloy (3) in electrolytes with composition I (a); II (b) and III (c).
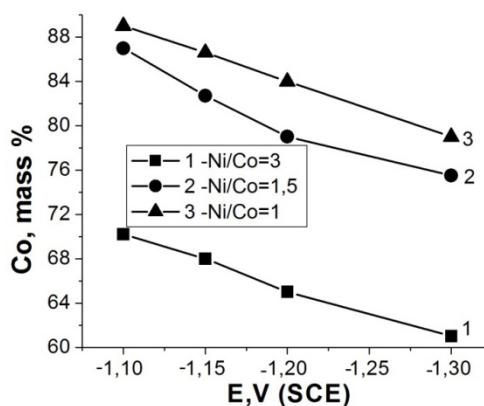

Fig. 2. Chemical content (in mass % of Co) of Ni-Co alloys depending on the cathodic potential and on the Ni/Co ratio in the electrolytes with composition I (1); II (2) and III(3).

For all studied Ni/Co ratios in the solution, the Co content in the alloy coatings is over 60% even though the Co content in the electrolytes is 50 and under 50% (Table 1). This result proves that Co is deposited preferentially in the Ni-Co alloy and for all electrolyte compositions the phenomenon "anomalous deposition" exists.

This phenomenon was also established by other authors [6-8, 21, 22]. According to Brenner [22], it consists in preferential deposition of the less noble metal in the alloy at comparable conditions for both metals. There are attempts to explain this phenomenon with formation of solid solutions [6], inclusion of oxides of metals with higher extent of oxidation associated with the presence of oxygen in the solution [23, 24] or formation of complexes [25].

Data presented on Fig. 2 show that the Co content in the coatings of Ni-Co alloy increases when the Ni/Co ratio in the solution increases and when the cathodic potential has positive values. In electrolyte I (with the lowest Co concentration) the Co content in the alloys increases from 62% at -1.3 V to 70% at −1.1V (respectively Ni decreases from 43% to 30%). In the case of electrolyte III the Co content is about 79-90% depending on the deposition potential value.

The cathodic current efficiency, CCE (in mass %) decreases when the deposition potential goes in negative direction for all Ni/Co ratios in the solution (Fig.3). This result can be explained with the increasing part of the reaction of hydrogen evolution at more negative potentials.
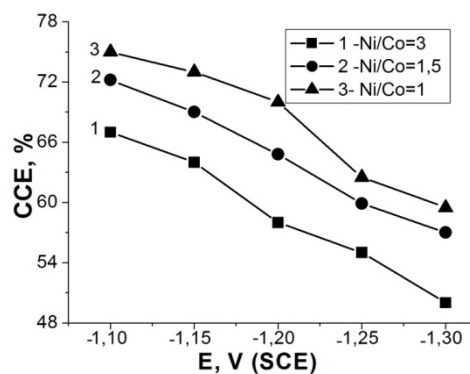

Fig. 3. Cathodic current efficiency (CCE, %) during Ni-Co alloy deposition depending on the deposition potential E, V (SCE) and on the Ni/Co ratio in electrolytes with composition I (1); II (2) and III (3).

At a given potential, as the Co concentration in the solution increases (composition III), the cathodic efficiency of the current also increases (Fig.3, 3).This effect can be related to the coating morphology. During hydrogen evolution, the electrolyte in the cathodic space is getting alkaline and complexes $Ni(OH)^+$ and $Co(OH)^+$are formed [19]. Because of higher adsorption ability, $Co(OH)^+$

315

are accumulated on the peaks of the rising crystals to a higher extent, which is a reason for the increase in Co content in the alloy and also for the growing dimensions of the crystals (Fig. 6). When the Ni content in the alloy increases (resp. the Co content decreases) the cathodic current efficiency decreases, which can be explained by the increase in the electrocatalytic activity of the coatings in respect to the reaction of hydrogen evolution because of the higher Ni content and finer crystal structure.

Effects of depolarization and overpolarization during deposition of Ni-Co alloys

The effects of depolarization and overpolarization during the deposition of Ni and Co in the Ni-Co alloy in electrolyte III were investigated. The results for the electrolytes with compositions I and II were similar.
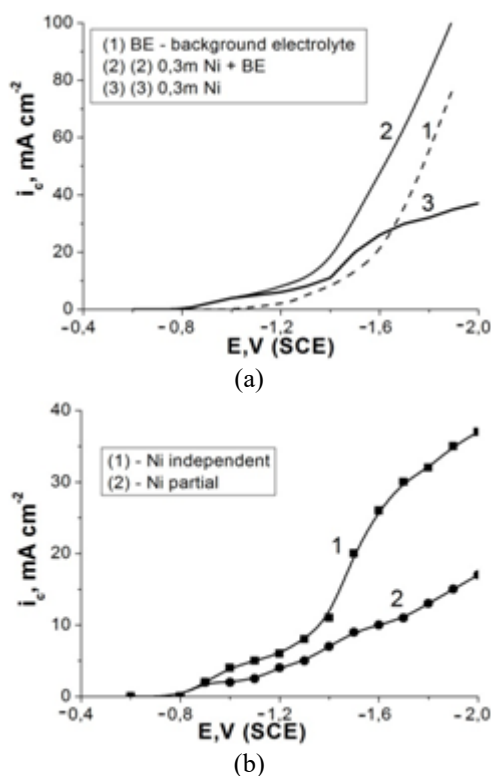

(a)

(b)

Fig. 4. (a) Partial curve of Ni deposition in alloy (3) obtained from the curves of Ni deposition in an electrolyte with composition 0.3M Ni+0.485M H_3BO_3 and 0.2M Na_3 citrate (2) and the curve in the background electrolyte (BE) (1); (b) Comparison of the curve of individual deposition of Ni (1) with the partial curve of deposition of Ni in the Ni-Co alloy (2).

In Figs. 4 (a,b) and 5 (a,b) the curves for individual deposition of Ni and Co are compared to the curves, obtained in a solution containing boric acid and Na_3 citrate (in concentrations given in Table 1), serving as a background to the electrolyte for deposition. This comparison was made with the aim to extract from the total current corresponding to

each cathodic potential, the current due to the reactions related to background electrolyte and mainly to the reaction of cathodic evolution of hydrogen. The partial curves for deposition of metals in the alloy are obtained by decomposition of the deposition curves of Ni and Co in the alloy. The decomposition was performed by subtracting the current for the pursuing reactions (using data for the cathodic efficiency of current, Fig. 3) and the current for deposition of the second metal from the total current corresponding to each cathodic potential.

The comparison of the curves on Figs. 4 and 5 shows that the polarization during Ni and Co co-deposition in the alloy is higher than those of their individual deposition, i.e. Ni and Co are deposited in the alloy with overpolarization. This result shows difficulties in the co-deposition of the two metals, which are often related to thermodynamic difficulties during electrocrystallization [31, 32].
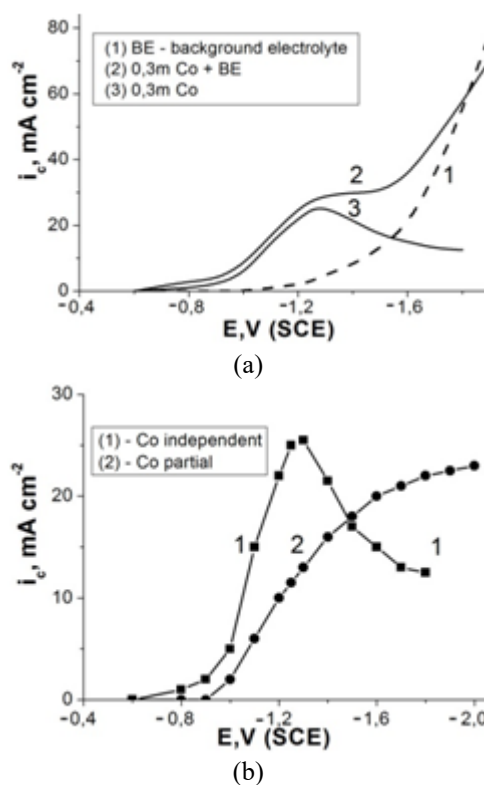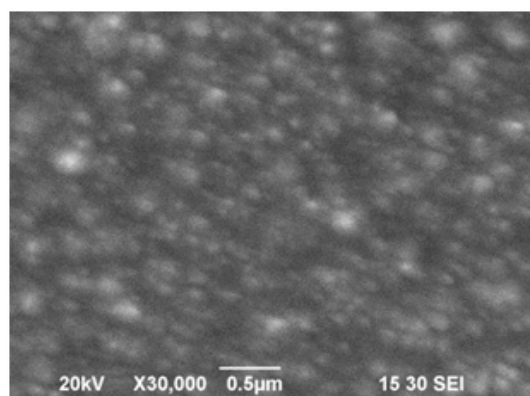

(a)

(b)

Fig. 5. (a) Partial curve of Co deposition in alloy (3) obtained from the curves of Co deposition in an electrolyte with composition 0.3M Ni+0.485M H_3BO_3 and 0.2M Na_3 citrate (2) and the curve in the background electrolyte (BE) (1); (b) Comparison of the curve of individual deposition of Co (1) with the partial curve of deposition of Co in the Ni-Co alloy (2).
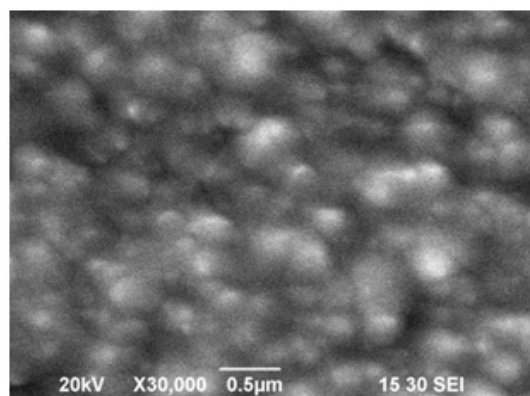
Morphology and phase composition of Ni-Co alloys.

Fig. 6 presents SEM images of the Ni-Co coating deposited in electrolytes with composition I (Fig. 6,a), II (Fig. 6,b) and III (Fig. 6,c) at a deposition
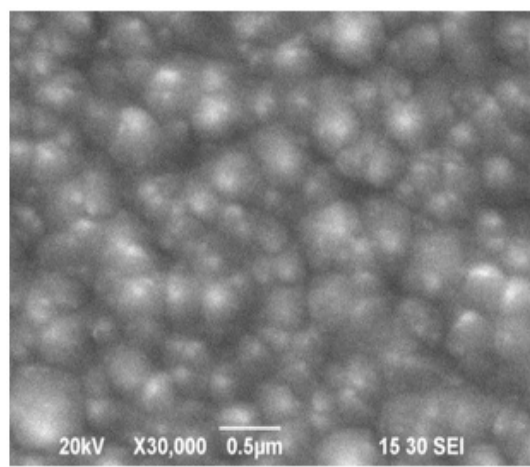
potential E= - 1.2 V (SCE). As can be seen, in the Ni-Co alloy coatings with higher Ni content deposited from electrolyte I (Fig. 6,a), the crystal dimensions are less than 100 nm, while by increasing the Co content, the dimensions gradually increase to about 150-250 nm in electrolyte II (Fig. 6,b) and to 300 nm in electrolyte III (Fig. 6,c). In the latter case the alloy coatings are characterized with formation of spheroidal crystals with uniform distribution by form and dimensions.

Fig.7 shows the XRD patterns of Ni-Co alloy electrodeposited from the three studied solutions at the deposition conditions for coatings used in SEM analysis. Ni-Co alloy coatings deposited from the three electrolytes are characterized by polycrystal structure. In the XRD patterns 4 peaks can be seen at 2θ values 44.4°, 51°, 76.5° and 92.5°, corresponding to reflexes by (111), (200), (220) and (311) faces for a face-centered cubic (fcc) lattice of a nickel-rich phase. The XRD patterns contain also 2θ values of 41.3°, 47.5° and 75° corresponding to reflexes by (100), hcp (101), hcp (110) from a hexagonal close packed (hcp) lattice of a Co-rich phase.
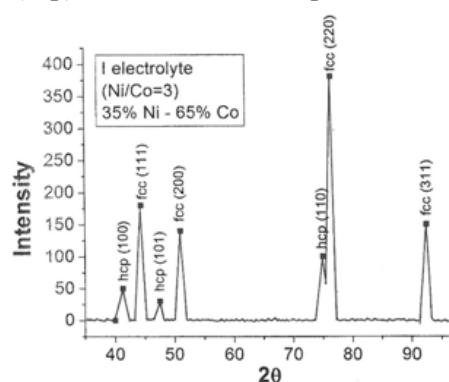

(a)   65% Co-35% Ni (electrolyte I)

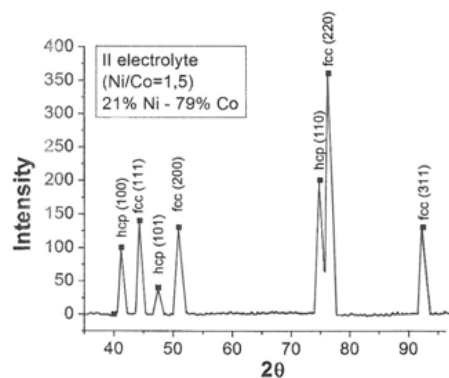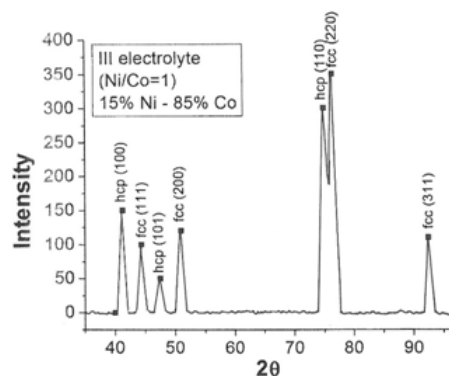(b)   79% Co- 21% Ni (electrolyte II)

(c) 85% Co-15% Ni (electrolyte III)

Fig. 6. SEM images of Ni-Co alloys deposited at a potential E = -1.2V (SCE) in electrolytes with compositions I (a) II (b) and III (c).

(a)

(b)

(c)

Fig. 7. XRD patterns of Ni-Co alloys deposited in electrolytes with composition I (a); II (b) and III (c) at E= -1.2V(SCE).

317

By rising the Co content in the alloys from 65% to 85% (Fig.7) the intensity of the peaks related to the hcp phase increases compared to those of the fcc phase. It can be concluded that the alloys deposited in the studied electrolytes are a mixture of fcc and hcp phases.

The obtained results support the conclusions made in [15,16,19]. In the case of nanostructured materials, the crystallographic structure may differ from the geometric structure of micro- or macro-structured materials. Based on this statement the formation of mixed structure is possible [33] in which either hexagonal Co contains cubic structured Ni or hexagonal Co is built in the cubic structured Ni. A theoretical model of the described crystal structure is given in [19].

CONCLUSIONS

The co-deposition of Ni and Co in Ni-Co alloy coatings in electrolytes with different Ni/Co ratio is possible in all electrolytes studied. Increasing the Co concentration in the solution, the potentials for Ni-Co alloy deposition are displaced towards conditions, at which Co is deposited with diffusion limitations, which could worsen the quality of the alloys, especially at more negative potentials.

At all investigated Ni/Co ratios in the solution, the Co content in the alloy coatings (in mass %) is over 60% and a conclusion was made about the phenomenon of "anomalous deposition" of Ni and Co**.**

The deposited Ni-Co alloys are with nano-dimensioned structure. When the Co content in the alloy decreases, the dimensions of the crystals decrease from about 300 nm to about and less than 100 nm.

The Ni-Co alloys are characterized with a mixed structure of face-centered cubic (fcc) and hexagonal closed packed (hcp) lattice, i.e. either hexagonal Co contains cubic structured Ni or hexagonal Co is built in the cubic structured Ni.

REFERENCES

1. C.P. Singh, R.K. Shukia, S.C .Srivastava, *Surface Technology*, **16**, 219 (1982).
2. L. Wang, Y. Gao, Q. Xue, H. Liu, T. Xu, *Applied Surface Science*, **242**, 326 (2005).
3. B.Y.C. Wu, C.A. Schuh, P.J. Ferreira, *Metallurgical and Materials Transactions A*, **36A**, 1927 (2005).
4. Q. Huang, D. Davis, E.J. Podlaha, *J. Appl. Electrochem.*, **36**, 871 (2006).
5. S.M.S.I. Dulal, E.A. Charles, S. Roy, *Electrochimica Acta*, **49**, 1927 (2004).
6. K.Y. Sasaki, J.B. Talbot, *J. Elecrochem. Soc.*, **145**, 981 (1998).
7. W.Betteridge, Nickel and its Alloys, John Wiley&Sons, Inc., New York, 1984.
8. W. Betteridge, Cobalt and its Alloys, John Wiley&Sons, Inc., New York, 1982.
9. H. Li, J. Liao, Y. Du, T. You, W. Liao, L. Wen, *Chem. Commun.*, **49**, 1768 (2013).
10. V. Pashova, L. Mirkova, M. Monev, *Electrochemical Soc. Transactions*, 25(35), 395 (2010).
11. M. Rojas, C.L. an, H.J. Miao, D.L. Piron, *J. Applied Electrochem*, **22**, 1135 (1992).
12. A.N.Correira, S.A.S. Machado, *Electrochimica Acta*, **45**, 1733 (2000).
13. D. Golodnitsky, Yu. Rosenberg, A. Ulus, *Electrochimica Acta*, **47**, 2707 (2002).
14. E. Gomez, J. Ramirez E. Valles, *J. Appl. Electrochem.*, **28**, 71 (1998).
15. T. Mahalingam, K. Sundaram, S. Velumani, M. Raja, S. Thanikaikarasan, Y.D. Kim, R. Asomoza, *Advanced Materials Research*, **68**, 52 (2009).
16. El-Feky Hesham, A.N. Mosaad, R. Sudipta, H. Nadia, A. Baraka, *Science China Chemistry,* **56**, 1446 (2013).
17. A. Karpuz, H. Kockar, M. Alper, O. Karaagac, M. Haciismailoglu, *Applied Surface Science*, **258**, 4005 (2012).
18. L. Tian, J. Xu, S. Xiao, *Vacuum*, **86,** 27 (2011).
19. B. Tury, G.Z. Radnoczi, G. Radnoczi, M.L. Vasanyi, *Surface and Coatings Technology*, **202**, 331 (2007).
20. N.V. Myung, K.Nobe, *J. Electrochem. Soc.*, **147**, 4156 (2000)
21. S.S. Belevskii, S.P. Yushchenko, A.I. Dikusar, *Surface Engineering and Applied Electrochemistry*, **48**, 97 (2012).
22. A. Brenner, *Electrodeposition of Alloy*, vol. 1 and 2, Academic Press, New York, 1963.
23. J. Horkans, *J. Electrochem. Soc.*, **126**, 861 (1979)
24. K.M. Yin, J.-H. Wei, J.-R. Fu, B.N. Popov, S.N. Popova, R.E. White, *J. Appl. Electrochem.*, **25**, 543 (1995).
25. J. Horkans, *J. Electrochem. Soc.*, **128**, 45 (1981).
26. Constitution of Binary Alloys, M. Hansen (Ed.), *Metallurgy and Metallurgical Engineering Series,* 2nd edition, McGraw-Hill, USA, 1958, p. 485.
27. K. Ignatova, *Bulg. Chem. Commun.*, **47**, 776 (2015).
28. K. Ignatova, I. Piroeva, S. Vladimitova-Atanassova, *Journal of Chemical Technologyand Metallurgy*, **51**, 199 (2016).
29. K. Ignatova, D. Lilova, *Journal of Chemical Technology and Metallurgy*, **50**, 199(2015)
30. K. Ignatova, D. Lilova, *Journal of Chemical Technology and Metallurgy*, **50**, 207 (2015).
31. D. Manova, J. Lutz, S. Mändl, H. Neumann, in: Workshop "Oberflächentechnologie mit Plasma- und Ionenstrahlprozessen", 10-12 März, (2009), Leibniz-Institut für Oberflächenmodifizierung, e.V. Leipzig und Institut für Physik der Ernst-Moritz-Arndt-Universität Greifswald, 2009.
32. Tz. Uzunov, Physics of metals, Technical University-Sofia, 2004.
33. Introduction to Nanotechnology, C.P. Poole, F.J. Owens Jr (Eds), Wiley and Sons Inc., Hoboken, New Jersey, 2002, p.78.

СЪСТАВ И СТРУКТУРА НА Ni-Co ПОКРИТИЯ В ЗАВИСИМОСТ ОТ СЪОТНОШЕНИЕТО НА Ni И Co В ЦИТРАТЕН ЕЛЕКТРОЛИТ

К. Игнатова[1] , Й. Марчева[2]

[1]*Химико-Технологичен и Металургичен Университет - София, бул. Кл.Охридски 8, София 1000, България*
[2]*Технически Университет - София, бул. Кл.Охридски 8, София 1000, България*

(Резюме)

В статията се докладва влиянието на съотношението Ni/Co в цитратен електролит (с оптимално съдържание на Na₃ citrat от 0,2M) върху кинетиката на отлагане, химичния и фазов състав на сплавното Ni-Co покритие, токовата използваемост за електроотлагане и морфологията на покритията. Установено е, че с нарастване на съдържанието на Co в разтвора, потенциалите на отлагане на Ni-Co сплав се изместват към стойности, при които кобалтът достига до плато на граничен дифузионен ток. При нарастване на съдържанието на Co в разтвора, катодният потенциал на отлагане на сплавта се измества в по-положителна посока, като при това съдържанието на кобалт в сплавта нараства (до максимум 85%), както и катодната използваемост на тока по отношение на отлагане на сплавта. Съдържанието на Co в сплавите, отложени във всички изследвани електролити, беше над 60 мас.% като беше установен ефект на „аномално" съотлагане на Ni и Co в сплавите.
Резултатите от SEM анализа на сплавните покрития, отложени в потенциостатичен режим, показаха, че когато съдържанието на Co в сплавите нараства, размерът на кристалите също нараства от около 100 nm до около 300 nm. Сплавните покрития представляват смес от фази със стенно-центрирана (fcc) и с хесагонална опаковка (hcp), доказано от резултатите на XRD анализа.

Analytical and numerical study of the diffusion of chemically reactive species in an Eyring-Powell fluid over an oscillatory stretching surface

S.U. Khan[1*], N. Ali[2], T. Hayat[3, 4]

[1]Department of Mathematics, COMSATS Institute of Information Technology, Sahiwal 57000, Pakistan
[2]Department of Mathematics and Statistics, International Islamic University, Islamabad 44000, Pakistan
[3]Department of Mathematics, Quaid-i-Azam University 45320, Islamabad 44000, Pakistan
[4]Nonlinear Analysis and Applied Mathematics (NAAM) Research Group, Department of Mathematics, Faculty of Science, King Abdulaziz University, Jeddah 21598, Saudi Arabia

This study deals with the unsteady flow of an Eyring-Powell fluid induced by an oscillatory stretching surface in presence of chemical reaction. The elastic sheet is stretched periodically back and forth in its own plane. The equations governing the flow are derived employing fundamental law of mass, momentum and diffusion. The independent variables in the governing equations are reduced by using dimensionless variables which are solved by using two different techniques, namely, homotopy analysis method and an implicit finite difference scheme. Solutions obtained by both methods are compared and found in excellent agreement. The physical variables such as longitudinal velocity component and mass concentration are examined in detail for various values of the parameters of interest.

Keywords: Eyring-Powell fluid, chemical effects, oscillatory stretching sheet, Homotopy analysis method, finite difference scheme.

INTRODUCTION

The study of convective flow under the influence of magnetic field and chemical reaction has practical applications in many areas of science and engineering. This phenomenon plays a vital role in chemical industry, petroleum industry, cooling of nuclear reactors, packed-bed catalytic reactors, etc. In view of all these applications many researchers studied the effects of chemical reaction on the flow of different fluids. The specialized literature on this topic is discussed in the following paragraphs. Chambre and Young [1] discussed the diffusion of a chemically reactive species in a laminar boundary layer flow over a flat plate. Andersson et al. [2] studied the laminar boundary layer flow induced by a stretching sheet in the presence of chemical reaction effects. Takhar et al. [3] discussed the diffusion of chemically reactive species in a second-order fluid over a stretching sheet. Akyildiz et al. [4] studied the diffusion of chemically reactive species in a second-grade fluid over a porous stretching surface. Hayat and Abbas [5] used homotopy analysis to analyze the effects of chemical reaction in a Maxwell fluid. In another paper, Hayat et al. [6] examined the effects of mass transfer in a unsteady flow of Maxwell fluid over a stretching sheet. The effect of chemical reaction and variable viscosity with heat and mass transfer for a Hiemenz flow through a Darcian porous

medium was investigated by Seddeek et al. [7]. Aziz [8] used a numerical technique to discuss the effects of chemical reaction and heat mass transfer in a viscous fluid.

Ferdows and Qasem [9] investigated the effects of the order of chemical reaction on a boundary layer flow with heat mass transfer over a linearly stretching surface. Krishnendu [10] discussed the effects of mass transfer in presence of chemical reaction over a porous flat plate. Mukhopadhyay and Bhattacharyya [11] used a shooting method to analyze the first-order constructive/destructive chemical reaction in a flow of Maxwell fluid over a stretching sheet. The chemically reactive hydromagnetic flow of a second-grade fluid in a semi-porous channel was discussed by Abbas et al. [12]. Apart of these, some recent attempts regarding flows of different fluids in presence of chemically reactive species can be found in refs. [13-17].

Motivated by the studies mentioned above, the aim of this paper is to analyze the unsteady flow and mass transfer of chemically reactive species. The rheological behavior of the fluid is captured by the constitutive equation of the Eyring-Powell model. This model has already been used by several authors to discuss non-Newtonian flows [18-21]. Unlike typical studies, the stretching sheet is assumed to be oscillatory. The idea of flow over an oscillatory stretching sheet was introduced by Wang [22]. The work of Wang [22] was extended by few authors including Siddapa et al. [23], Abbas et al. [24, 25], Zheng et al. [26] and Ali et al. [27].

* To whom all correspondence should be sent:
E-mail: sk_iiu@yahoo.com

The proposed study extends the analysis of Wang [22] by considering an Eyring-Powell fluid model in the presence of chemically reactive species. The solution of the governing problem is obtained by a homotopy analysis method (HAM) and a finite difference scheme. A comparison of both solutions is made. Based on the numerical solution a parametric study is carried out to quantify the effects of various emerging parameters on the flow and concentration characteristics inside the boundary layer.

FLOW ANALYSIS

Let us consider an unsteady, two-dimensional and magnetohydrodynamic (MHD) flow of an incompressible Eyring-Powell fluid past over an oscillatory stretching sheet coinciding with plane $\overline{y} = 0$ (see Fig. 1).
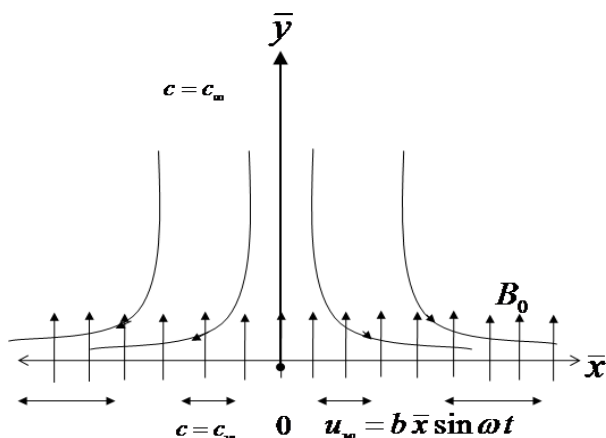

Fig. 1. Geometry of the problem.

The elastic sheet is periodically stretched back and forth with a velocity $u_w = b\overline{x}\sin\omega t$ ($\overline{x}$ is the coordinate along the sheet, b is the maximum stretching rate and ω represents the frequency). A magnetic field of magnitude B_0 is applied in the direction perpendicular to the sheet. Let c_w denotes the concentration at the surface while the concentration far away from the surface is c_∞. The continuity, momentum and concentration equations for an Eyring-Powell fluid can be expressed as [21]

$$\frac{\partial u}{\partial x} + \frac{\partial v}{\partial y} = 0, \tag{1}$$

$$\frac{\partial u}{\partial t} + u\frac{\partial u}{\partial x} + v\frac{\partial u}{\partial y} = \left(\nu + \frac{1}{\rho\beta^*C}\right)\frac{\partial^2 u}{\partial y^2}$$
$$-\frac{1}{2\rho\beta^*C^3}\left[\left(\frac{\partial u}{\partial y}\right)^2\frac{\partial^2 u}{\partial y^2}\right] - \frac{\sigma B_0^2}{\rho}u, \tag{2}$$

$$\frac{\partial c}{\partial t} + u\frac{\partial c}{\partial x} + v\frac{\partial c}{\partial y} =$$
$$D\frac{\partial^2 c}{\partial y^2} - k(c - c_\infty), \tag{3}$$

where u and v are velocity components along $\overline{x}$ and $\overline{y}$ directions, respectively, ν represents the kinematic viscosity, ρ is the density, β^* and C denote the material parameters of the Eyring-Powell model, c is the concentration field, D is the concentration expansion coefficient, k is the chemical reaction rate.

Eqs. (1)-(3) are subjected to the conditions

$$u = u_\omega = b\overline{x}\sin\omega t, \quad v = 0, \quad c = c_w \text{ at } \overline{y} = 0, \quad t > 0, \tag{4}$$

$$u \to 0, \quad c \to c_\infty \qquad \text{at} \qquad \overline{y} \to \infty, \tag{5}$$

Let us introduce appropriate variables [22, 24]

$$y = \sqrt{\frac{b}{\nu}}\,\overline{y}, \qquad \tau = t\omega, \tag{6}$$

$$u = b\overline{x}f_y(y,\tau), \quad v = -\sqrt{\nu b}f(y,\tau),$$

$$\phi(y,\tau) = \frac{c - c_\infty}{c_w - c_\infty}. \tag{7}$$

Utilizing Eqs. (6) and (7), Eq.(1) is identically satisfied and Eqs. (2) and (3) become

$$(1+K)f_{yyy} - Sf_{y\tau} - f_y^2 + ff_{yy} - M^2 f_y - \lambda K f_{yy}^2 f_{yyy} = 0, \tag{8}$$

$$\phi_{yy} + Sc\left(f\phi_y - S\phi_\tau\right) - Sc\beta\phi = 0, \tag{9}$$

with boundary conditions

$$f_y(0,\tau) = \sin\tau, \quad f(0,\tau) = 0, \quad \phi(0,\tau) = 1, \tag{10}$$

$$f_y(\infty,\tau) = 0, \qquad \phi(\infty,\tau) = 0. \tag{11}$$

In the above equations $K = 1/\mu\beta^*C$ and $\lambda = \overline{x}^2 b^3 / 2\nu C^2$ are dimensionless material fluid parameters, $S \equiv \omega/b$ is the ratio of the oscillation frequency of the sheet to its stretching rate, $M = \sqrt{\sigma B_0^2 / \rho b}$ is the Hartmann number, $Sc = \upsilon/D$ is the Schmidt number and $\beta = k/b$ denotes the chemical reaction parameter. According to Javed et al. [18], Eq. (2) is subject to the constraint $\lambda K \ll 1$.

The skin-friction coefficient C_f is defined as

$$C_f = \frac{\tau_w}{\rho u_w^2}, \qquad (12)$$

where τ_w denotes the shear stress at the wall. In view of (6) and (7), Eq. (12) takes the following form [19]

$$\text{Re}_x^{1/2} C_f = \left[(1+K) f_{yy} - \frac{K}{3} \beta f_{yy}{}^3 \right]_{y=0}, \qquad (13)$$

where $\text{Re}_x = u_w \overline{x} / \nu$ is the local Reynold number.

HOMOTOPY ANALYSIS METHOD

Homotopy analysis method is one of the powerfull analytic approaches to solve nonlinear partial and ordinary differential equations. This method was proposed by Liao [28] and then used by many authors for solution of different nonlinear problems [29-34]. Now we briefly describe the application of this method to the boundary value problem developed in the previous section. The boundary conditions lead to the following initial guesses for $f(y,\tau)$ and $\phi(y)$

$$f_0(y,\tau) = \sin\tau (1 - \exp(-y)),$$
$$\phi_0(y) = \exp(-y). \qquad (14)$$

Introducing linear operators

$$\pounds_f(f) = \frac{\partial^3 f}{\partial y^3} - \frac{\partial f}{\partial y}, \quad \pounds_\phi(f) = \frac{\partial^2 f}{\partial y^2} - f, \qquad (15)$$

satisfying

$$\pounds_f \left[C_1 + C_2 \exp(-y) + C_3 \exp(y) \right] = 0, \qquad (16)$$

$$\pounds_\phi \left[C_4 \exp(-y) + C_5 \exp(y) \right] = 0, \qquad (17)$$

where $C_i \quad (i = 1, 2, ...5)$ are constants. The zero$^{\text{th}}$-order deformation problems defined

$$(1-p) \pounds_f \left[\hat{f}(y,\tau;p) - f_0(y,\tau) \right] =$$
$$p \hbar_f N_f \left[\hat{f}(y,\tau;p) \right], \qquad (18)$$

$$(1-p) \pounds_\phi \left[\hat{\phi}(y,\tau;p) - \hat{\phi}_0(y,\tau) \right] =$$
$$p \hbar_\phi N_\phi \left[\hat{f}(y,\tau;p), \hat{\phi}(y,\tau;p) \right], \qquad (19)$$

$$\hat{f}(0,\tau;p) = 0, \quad \frac{\partial \hat{f}(y,\tau;p)}{\partial y} \bigg|_{y=0} =$$
$$\sin\tau, \quad \frac{\partial \hat{f}(y,\tau;p)}{\partial y} \bigg|_{y\to\infty} = 0. \qquad (20)$$

$$\hat{\phi}(0,\tau;p) = 1, \quad \hat{\phi}(\infty,\tau;p) = 0, \qquad (21)$$

where $p \in [0,1]$ is an embedding parameter. The associated nonlinear operators N_f and N_ϕ are

$$N_f \left[\hat{f}(y,\tau;p) \right] = (1+K) \frac{\partial^3 \hat{f}(y,\tau;p)}{\partial y^3} - S \frac{\partial^2 \hat{f}(y,\tau;p)}{\partial y \partial \tau} -$$
$$M^2 \frac{\partial \hat{f}(y,\tau;p)}{\partial y} - \left(\frac{\partial \hat{f}(y,\tau;p)}{\partial y} \right)^2 + \hat{f}(y,\tau;p) \left(\frac{\partial^2 \hat{f}(y,\tau;p)}{\partial y^2} \right)$$
$$-\lambda K \left(\frac{\partial^2 \hat{f}(y,\tau;p)}{\partial y^2} \right)^2 \left(\frac{\partial^3 \hat{f}(y,\tau;p)}{\partial y^3} \right), \qquad (22)$$

$$N_\phi \left[\hat{\phi}(y,\tau;p), \hat{f}(y,\tau;p) \right] = \frac{\partial^2 \hat{\phi}(y,\tau;p)}{\partial y^2} +$$
$$Sc \left(\hat{f}(y,\tau;p) \frac{\partial \hat{\phi}(y,\tau;p)}{\partial y} - S \frac{\partial \hat{\phi}(y,\tau;p)}{\partial \tau} \right) - \beta Sc\phi \qquad (23)$$

The zero$^{\text{th}}$-order deformation problems defined above have the following solutions corresponding to $p = 0$ and $p = 1$

$$\hat{f}(y,\tau;0) = f_0(y,\tau), \hat{f}(y,\tau;1) = f(y,\tau), \qquad (24)$$

$$\hat{\phi}(y,\tau;0) = \phi_0(y,\tau), \hat{\phi}(y,\tau;1) = \phi(y,\tau). \qquad (25)$$

Using Taylor's series expansion, we can write

$$\hat{f}(y,\tau;p) = f_0(y,\tau) + \sum_{m=1}^{\infty} f_m(y,\tau) p^m,$$
$$f_m(y,\tau) = \frac{1}{m!} \frac{\partial^m \hat{f}(y,\tau;p)}{\partial p^m} \bigg|_{p=0}, \qquad (26)$$

$$\hat{\phi}(y,\tau;p) = \phi_0(y,\tau) + \sum_{m=1}^{\infty} \phi_m(y,\tau) p^m,$$
$$\phi_m(y,\tau) = \frac{1}{m!} \frac{\partial^m \hat{\phi}(y,\tau;p)}{\partial p^m} \bigg|_{p=0}. \qquad (27)$$

The convergence of the above series solution depends upon $\hbar_f$ and $\hbar_\phi$. We assume that $\hbar_f$ and $\hbar_\phi$ are selected so that Eqs. (25) to (26) converges at $p = 1$. Therefore

$$f(y,\tau) = f_0(y,\tau) + \sum_{m=1}^{\infty} f_m(y,\tau), \qquad (28)$$

$$\phi(y,\tau) = \phi_0(y,\tau) + \sum_{m=1}^{\infty} \phi_m(y,\tau), \qquad (29)$$

The mth-order of the deformation problem is

$$\pounds_f\left[f_m(y,\tau)-\chi_m f_{m-1}(y,\tau)\right]=h_f R_m^f(y,\tau), \quad (30)$$

$$\pounds_\phi\left[\phi_m(y,\tau)-\chi_m \phi_{m-1}(y,\tau)\right]=h_\phi R_m^\phi(y,\tau), \quad (31)$$

$$f_m(0,\tau)=0, \quad \frac{\partial f_m(0,\tau)}{\partial y}=0, \quad \frac{\partial f_m(\infty,\tau)}{\partial y}=0, \quad (32)$$

$$\phi_m(0,\tau)=\phi_m(\infty,\tau)=0, \quad (33)$$

$$R_m^f(y,\tau)=(1+K)\frac{\partial^3 f_{m-1}}{\partial y^3}-S\frac{\partial^2 f_{m-1}}{\partial y\partial \tau}-M^2\frac{\partial f_{m-1}}{\partial y}$$

$$+\sum_{k=0}^{m-1}\left(\begin{array}{c}f_{m-1-k}\dfrac{\partial^2 f_k}{\partial y^2}-\dfrac{\partial f_{m-1-k}}{\partial y}\dfrac{\partial f_k}{\partial y}-\\[2mm]\lambda K\dfrac{\partial^2 f_{m-1-k}}{\partial y^2}\displaystyle\sum_{l=0}^{k}\dfrac{\partial^2 f_{k-1}}{\partial y^2}\dfrac{\partial^3 f_{1}}{\partial y^3}\end{array}\right), \quad (34)$$

$$R_m^\phi(y,\tau)=\frac{\partial^2 \phi_{m-1}}{\partial y^2}-S(Sc)\frac{\partial \phi_{m-1}}{\partial \tau}-\beta Sc\phi_{m-1}+$$

$$Sc\sum_{k=0}^{m-1}\left(f_{m-1-k}\frac{\partial \phi_k}{\partial y}\right). \quad (35)$$

$$\chi_m=\begin{cases}0, & m\leq 1,\\ 1, & m>1.\end{cases} \quad (36)$$

The general solution at m^{th}-order can be expressed as

$$f_m(y,\tau)=f_m^*(y,\tau)+C_1+C_2\exp(-y)+C_3\exp(y), \quad (37)$$

$$\phi_m(y,\tau)=\phi_m^*(y,\tau)+C_4\exp(-y)+C_5\exp(y). \quad (38)$$

where $f_m^*(y,\tau)$ and $\phi_m^*(y,\tau)$ indicate the particular solutions. The constants C_i $(i=1,2...,5)$ using conditions (20) and (21) get values

$$C_3=C_5=0, \quad C_2=\frac{\partial f_m^*(0,\tau)}{\partial y}, \quad (39)$$

$$C_1=-C_2-f_m^*(0,\tau), \quad C_4=-\phi_m^*(0,\tau).$$

DIRECT NUMERICAL SOLUTION OF THE PROBLEM

The system of nonlinear partial differential equations (8)–(9) with the boundary conditions (10) and (11) are solved numerically using a finite difference scheme with Fortran software. We use coordinate transformation $\eta=1/(y+1)$ to transform the semi-infinite physical domain $y\in[0,\infty)$ to finite calculation domain $\eta\in[0,1]$, i.e.:

$$y=\frac{1}{\eta}-1, \quad \frac{\partial}{\partial y}=-\eta^2\frac{\partial}{\partial \eta},$$

$$\frac{\partial^2}{\partial y^2}=\eta^4\frac{\partial^2}{\partial \eta^2}+2\eta^3\frac{\partial}{\partial \eta}, \quad \frac{\partial^2}{\partial y\partial \tau}=-\eta^2\frac{\partial^2}{\partial \eta\partial \tau},$$

$$\frac{\partial^3}{\partial y^3}=-\eta^6\frac{\partial^3}{\partial \eta^3}-6\eta^5\frac{\partial^2}{\partial \eta^2}-6\eta^4\frac{\partial}{\partial \eta}.$$

Using the above transformations in Eqs. (8) and (9)

$$S\frac{\partial^2 f}{\partial \eta\partial \tau}=\eta^2\left(\frac{\partial f}{\partial \eta}\right)^2+\left[6(1+K)\eta^2-2\eta f\right]\left(\frac{\partial f}{\partial \eta}\right)+$$

$$\left[6(1+K)\eta^3-\eta^2 f\right]\left(\frac{\partial^2 f}{\partial \eta^2}\right)+(1+K)\eta^4\left(\frac{\partial^3 f}{\partial \eta^3}\right)$$

$$-M^2\left(\frac{\partial f}{\partial \eta}\right)-\lambda K\eta^{12}\left(\frac{\partial^2 f}{\partial \eta^2}\right)^2\left(\frac{\partial^3 f}{\partial \eta^3}\right)-$$

$$6\lambda K\eta^{11}\left(\frac{\partial^2 f}{\partial \eta^2}\right)^3-6\lambda K\eta^{10}\left(\frac{\partial f}{\partial \eta}\right)\left(\frac{\partial^2 f}{\partial \eta^2}\right)^2$$

$$-4\lambda K\eta^{10}\left(\frac{\partial f}{\partial \eta}\right)^2\left(\frac{\partial^3 f}{\partial \eta^3}\right)-$$

$$24\lambda K\eta^9\left(\frac{\partial f}{\partial \eta}\right)^2\left(\frac{\partial^2 f}{\partial \eta^2}\right)-24\lambda K\eta^8\left(\frac{\partial f}{\partial \eta}\right)^3$$

$$-4\lambda K\eta^{11}\left(\frac{\partial f}{\partial \eta}\right)\left(\frac{\partial^2 f}{\partial \eta^2}\right)\left(\frac{\partial^3 f}{\partial \eta^3}\right)-$$

$$24\lambda K\eta^{10}\left(\frac{\partial f}{\partial \eta}\right)\left(\frac{\partial^2 f}{\partial \eta^2}\right)^2-24\lambda K\eta^9\left(\frac{\partial f}{\partial \eta}\right)^2\left(\frac{\partial^2 f}{\partial \eta^2}\right) \quad (40)$$

$$\eta^4\frac{\partial^2 \phi}{\partial \eta^2}+2\eta^3\frac{\partial \phi}{\partial \eta}-Sc\left(f\eta^2\frac{\partial \phi}{\partial \eta}+S\frac{\partial \phi}{\partial \tau}\right)- \quad (41)$$

$$\beta Sc\phi=0,$$

$$f_\eta=0, \quad \phi=0 \quad \text{at} \quad \eta=0, \quad (42)$$

$$f=0, \quad f_\eta=-\sin\tau, \quad \phi=1 \quad \text{at} \quad \eta=1, \quad (43)$$

In the second step, we discretize Eqs. (18) and (19) for L equally spaced points $\eta=(\eta_0,\eta_1,\eta_2,...\eta_{L+1})\in[0,1]$ with a step size of $\Delta\eta=1/(L+1)$ at time instants $\tau=(\tau^1,\tau^2,...)$, where $\tau^i=\tau^1+i\Delta\tau$. The numerical values of $\left(f_1^n,f_2^n,...,f_L^n\right)$ and $\left(\phi_1^n,\phi_2^n,.....,\phi_L^n\right)$ are sought at these points at each time level provided that the boundary conditions at $\eta=\eta_0=0$ and $\eta=\eta_{L+1}=1$ are known. The initial conditions for velocity field are:

$$f(\eta,\tau=0)=0 \quad \text{and} \quad \phi(\eta,\tau=0)=0. \quad (44)$$

We construct the semi-implicit time difference scheme for f and ϕ as follows:

$$S \frac{1}{\Delta \tau}\left(\frac{\partial f^{(n+1)}}{\partial \eta} - \frac{\partial f^{(n)}}{\partial \eta}\right) = \eta^2 \left(\frac{\partial f^{(n)}}{\partial \eta}\right)^2 +$$

$$\left[6(1+K)\eta^2\right]\left(\frac{\partial f^{(n+1)}}{\partial \eta}\right) - 2\eta f^{(n)}\left(\frac{\partial f^{(n)}}{\partial \eta}\right) +$$

$$6(1+K)\eta^3 \left(\frac{\partial^2 f^{(n+1)}}{\partial \eta^2}\right) - 2\eta f^{(n)}\left(\frac{\partial f^{(n)}}{\partial \eta}\right) -$$

$$\eta^2 f^{(n)}\left(\frac{\partial^2 f^{(n)}}{\partial \eta^2}\right) + (1+K)\eta^4\left(\frac{\partial^3 f^{(n+1)}}{\partial \eta^3}\right) -$$

$$M^2\left(\frac{\partial f^{(n+1)}}{\partial \eta}\right) - \lambda K \eta^{12}\left(\frac{\partial^2 f^{(n)}}{\partial \eta^2}\right)^2\left(\frac{\partial^3 f^{(n)}}{\partial \eta^3}\right) -$$

$$6\lambda K \eta^{11}\left(\frac{\partial^2 f^{(n)}}{\partial \eta^2}\right)^3 - 6\lambda K \eta^{10}\left(\frac{\partial f^{(n)}}{\partial \eta}\right)\left(\frac{\partial^2 f^{(n)}}{\partial \eta^2}\right)^2 -$$

$$4\lambda K \eta^{10}\left(\frac{\partial f^{(n)}}{\partial \eta}\right)^2\left(\frac{\partial^3 f^{(n)}}{\partial \eta^3}\right) -$$

$$24\lambda K \eta^9\left(\frac{\partial f^{(n)}}{\partial \eta}\right)^2\left(\frac{\partial^2 f^{(n)}}{\partial \eta^2}\right) - 24\lambda K \eta^8\left(\frac{\partial f^{(n)}}{\partial \eta}\right)^3 -$$

$$4\lambda K \eta^{11}\left(\frac{\partial f^{(n)}}{\partial \eta}\right)\left(\frac{\partial^2 f^{(n)}}{\partial \eta^2}\right)\left(\frac{\partial^3 f^{(n)}}{\partial \eta^3}\right) - \qquad (45)$$

$$24\lambda K \eta^{10}\left(\frac{\partial f^{(n)}}{\partial \eta}\right)\left(\frac{\partial^2 f^{(n)}}{\partial \eta^2}\right)^2 -$$

$$24\lambda K \eta^9\left(\frac{\partial f^{(n)}}{\partial \eta}\right)^2\left(\frac{\partial^2 f^{(n)}}{\partial \eta^2}\right),$$

$$S(Sc)\frac{\left(\phi^{(n+1)} - \phi^{(n)}\right)}{\Delta \tau} = \left(\eta^4 \frac{\partial^2 \phi^{(n+1)}}{\partial \eta^2} + 2\eta^3 \frac{\partial \phi^{(n+1)}}{\partial \eta}\right) - \qquad (46)$$

$$Scf^{(n)}\eta^2 \frac{\partial \phi^{(n+1)}}{\partial \eta} - Sc\beta\phi.$$

The advantage of the scheme is that only linear equations for each new time step $(n+1)$ are to be solved. Two systems of linear equations for $f_i^{(n+1)}$ and $\phi_i^{(n+1)}$ at the time step $(n+1)$ can be solved by using Guassian elimination.

CONVERGENCE OF HAM SOLUTION AND ITS COMPARISON WITH A NUMERICAL SOLUTION

The convergence of HAM solution depends upon the suitable choice of auxiliary parameters $\hbar_f$ and $\hbar_\phi$. The *h*-curves are plotted in Fig. 2(a-b) to show the convergence region of the HAM solution for a particular set of involved parameters. From these figures it is clear that for this choice of parameter value a convergent solution can be obtained when $-1.4 \leq \hbar_f < 0$ and $-2 \leq \hbar_\phi < 0$.

To check the accuracy of HAM solution, the numerical values of $f''(0,\tau)$ at different order of approximations are shown in Table 1. The convergent values of $f''(0,\tau)$ can be obtained by increasing order of approximation. Figs. 3 and 4 show the comparison of HAM solution with a numerical solution at two different orders of approximation. An excellent agreement between HAM solution and numerical solution can be achieved at 15th order of approximation.

Table 1. The convergence of the HAM solution of $f''(0,\tau)$ for different order of approximation with $S = 0.1$, $M = 1.2$, $K = 0.5$, $\lambda = 0.4$ and $\tau = 0$, $\tau = 0.5\pi$ and $\tau = 1.5\pi$, respectively.

Order of approximation	$\tau = 0$	$\tau = 0.5\pi$	$\tau = 1.5\pi$
1	-0.02500	-1.26000	0.66400
3	-0.03363	-1.33995	0.563498
10	-0.03475	-1.36026	0.55218
12	-0.03475	-1.36048	0.55210
15	-0.03476	-1.36050	0.55210
25	-0.03476	-1.36050	0.55210
30	-0.03476	-1.36050	0.55210

RESULTS AND DISCUSSION

In this section graphical results obtained *via* a finite difference method are displayed in order to examine the effects of involved parameter on velocity component f' and concentration field ϕ. Fig. 5(a-c) demonstrates the effects of the relative amplitude of frequency to the stretching rate S, fluid parameters λ and Hartmann number M on the evolution series of the velocity component f' at a fixed distance $y = 0.25$ from the sheet, respectively. Fig. 5(a) shows that the amplitude of the flow motion at this location decreases by increasing S. However, this decrease is marginal and it is anticipated that such a trend is prevalent even for larger values of S. Fig. 5(b) depicts that the amplitude of the flow increases by increasing fluid parameter λ. This increase in the amplitude of flow motion is attributable to the increased effective viscosity induced by larger values of λ. The influence of Hartmann number M on time evolution of the velocity component f' is shown in Fig. 5(c). The figure reveals that the amplitude of the velocity component f' decreases by increasing Hartmann number.

The velocity profile f' for various values of S at four different distances $\tau = 8.5\pi$, $\tau = 9\pi$, $\tau = 9.5\pi$ and $\tau = 10\pi$ are shown in Fig. 6(a-d). Fig. 6(a) shows that at time instant $\tau = 8.5\pi$ the velocity decreases by increasing S. The back flow occurs near the surface where f' gets negative. The effects of S at time interval $\tau = 9\pi$ are depicted in Fig. 6(b). The velocity f' at this time instant oscillates near the surface and finally approaches zero. The amplitude of oscillation is found to increase with an increase in S. Fig. 6(c) elucidates that at time instant $\tau = 9.5\pi$, the velocity f' gets the value -1 at the wall and becomes zero far away from the surface without performing oscillation. A decrease in the amplitude of velocity is observed at this time instant. Fig. 6(d) reveals that at time instant $\tau = 10\pi$, the velocity f' is zero both at the surface and far away from the surface. It is also observed that at this time the amplitude of back flow increases by increasing S.

Fig. 7(a) shows the variation of f' for different values of λ at $\tau = 8.5\pi$. Here it is observed that the velocity approaches from 1 at the surface to zero far away from the surface. The occurrence of back flow near the surface is also observed at this time instant that is found to increase by increasing λ. Fig. 7(b) indicates that at this time instant

$\tau = 9\pi$, the velocity oscillates near the surface before approaching zero far away from the surface. Moreover, the amplitude of the back flow is found to increase with λ. The variation of f' with λ at time instant $\tau = 9.5\pi$ is shown in Fig. 7(c). Here, the magnitude of velocity decreases by increasing λ. Occurrence of back flow at $\tau = 10\pi$ with its strengthening for larger values of λ is observed in Fig. 7(d).

Fig. 8(a-d) illustrates the effects of Sc, β, λ and S on the concentration profile ϕ. Fig. 8(a) is plotted to observe the effects of Smith number Sc on the concentration profile ϕ. From this figure we observe that mass concentration decreases for large values of Sc. Moreover, it is also seen from this figure that the concentration boundary layer thickness decreases by increasing Schmidt number Sc. These effects may be attributable to the increase in the rate of solute transfer from the surface by increasing the Schmidt number. The effect of chemical reaction parameter β on concentration is shown in Fig. 8(b). Here, we again observe that the mass concentration decreases by increasing β. Fig. 8(c) illustrates the effects of fluid parameter λ on the concentration profile ϕ. From this figure it is clear that the concentration increases by increasing fluid parameter λ. Fig. 8(d) shows opposite effects, i.e. mass concentration decreases by increasing the relative amplitude of frequency to the stretching rate parameter S. Fig. 9(a-d) describes the effects of relative amplitude of frequency to the stretching rate S, Hartmann number M and fluid parameters K and λ on the time-series of shear stress at the wall for the first five periods $\tau \in [0, 10\pi]$. Fig. 9(a) shows the influence of the relative amplitude of frequency to the stretching rate S on the skin-friction coefficient $\mathrm{Re}_x^{1/2} C_f$ by keeping other parameters fixed. It is clear from this figure that the amplitude of oscillation of the skin-friction coefficient increases by increasing the relative amplitude of frequency to the stretching rate S. From Figure 9(b) it is clear that the skin friction coefficient oscillates with time and the amplitude of oscillation increases for large values of Hartmann M. The effects of fluid parameter λ and K are illustrated in Figs. 9(c) and (d), respectively. These figures show an opposite trend, i.e. the skin friction coefficient $\mathrm{Re}_x^{1/2} C_f$ decreases monotonically by increasing these fluid parameters.

CONCLUSIONS

In the present study, we have investigated the mass transfer in a unsteady flow of an Eyring-Powell fluid model over an oscillatory stretching sheet. The non-similar solution of the governing nonlinear partial differential equations is obtained analytically by a homotopy analysis method and numerically by a finite difference scheme. The flow and mass transfer characteristics are explained graphically for the several values of the involved parameters. The main findings can be summarized as:

•   The convergence of the HAM solution is largely dependent on the choice of auxiliary parameters and the order of approximation.

•   The amplitude of the flow velocity at a fixed distance from the sheet decreases with increasing ratio of oscillating frequency to stretching rate S and Hartmann number M while a converse Eyring-Powell fluid parameter λ trend is computed with increasing λ.

•   The concentration profile increases for large values of Eyring-Powell fluid parameter λ while it decreases for large values of Schmidt number Sc, ratio of oscillating frequency to stretching rate S and chemical reaction parameter β.

•   The concentration boundary layer thickness decreases with increasing Schmidt number Sc, ratio of oscillating frequency to stretching rate S and chemical reaction parameter β. In contrast, an increasing Eyring-Powell fluid parameter λ increases the concentration boundary layer thickness.

•   The amplitude of the skin friction coefficient increases with increasing the Hartmann number M, and the ratio of oscillation frequency of the sheet to its stretching rate S, while it is suppressed with increasing the Eyring-Powell fluid parameters λ and K.

•   In the limiting case when $\lambda, K \to 0$, our results reduce to the corresponding results of Wang [22].
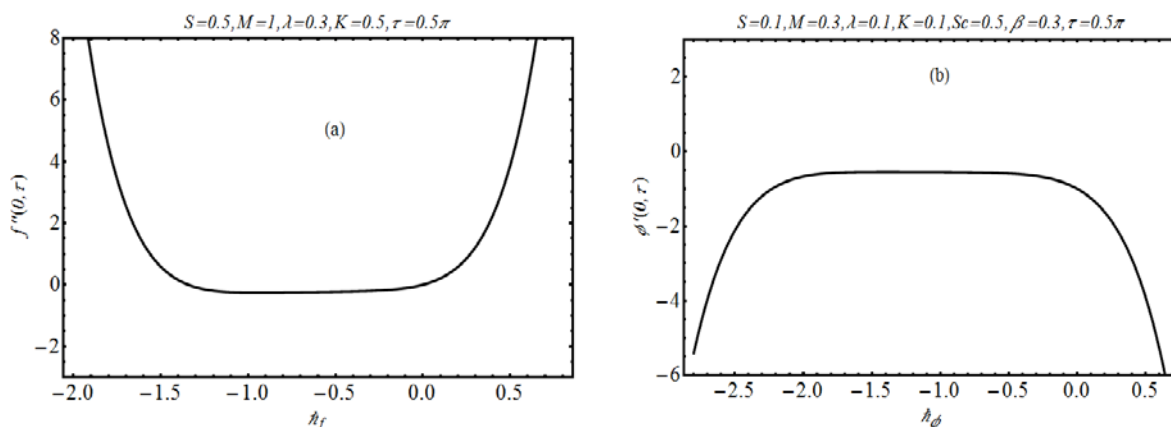

Fig. 2. The $\hbar -$ curves at 6th order of approximation: (a) for velocity; (b) for concentration profile.
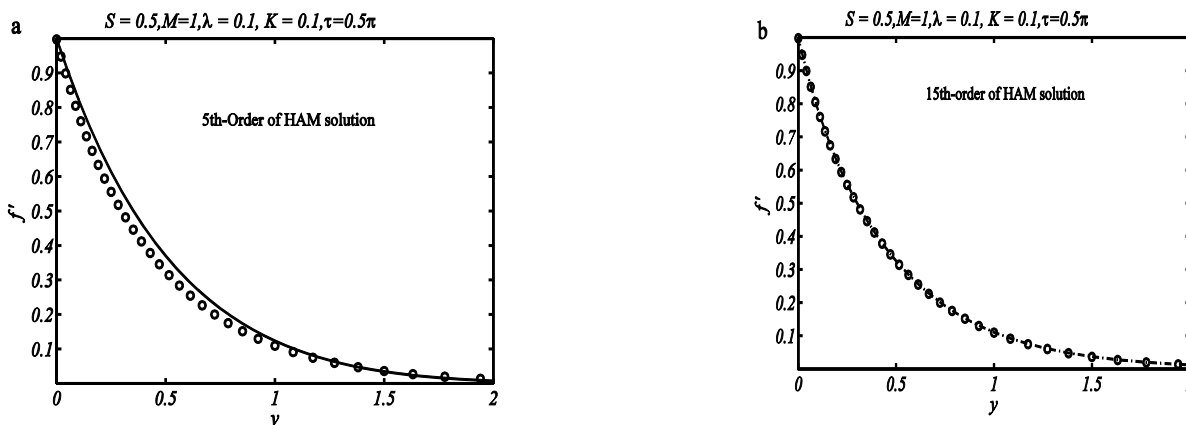

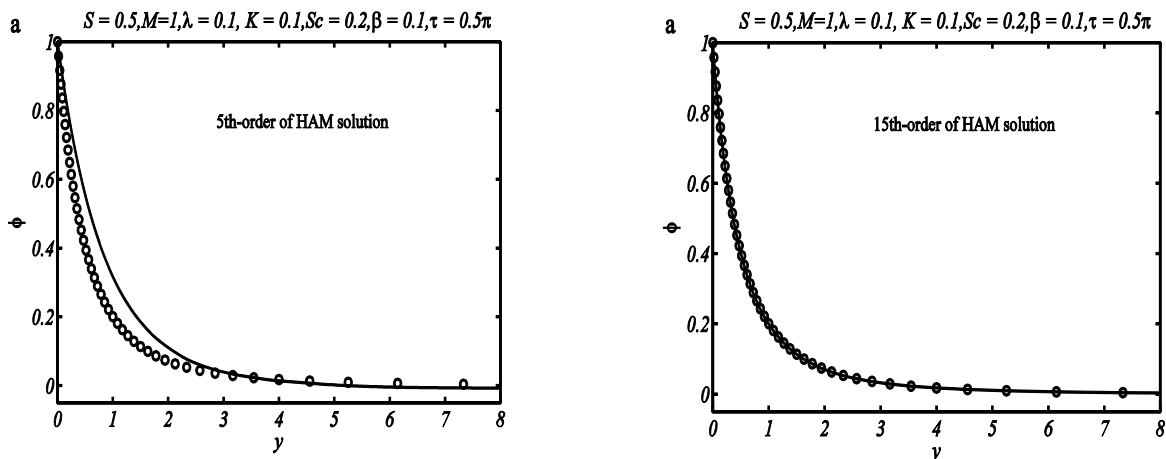**Fig. 3.** Comparison of $f'(y,\tau)$ obtained from HAM solution (solid lines) and the numerical solution (open circles).

Fig. 4. Comparison of concentration field $\phi(y, \tau)$ obtained from HAM solution (solid lines) and the numerical solution (open circles).
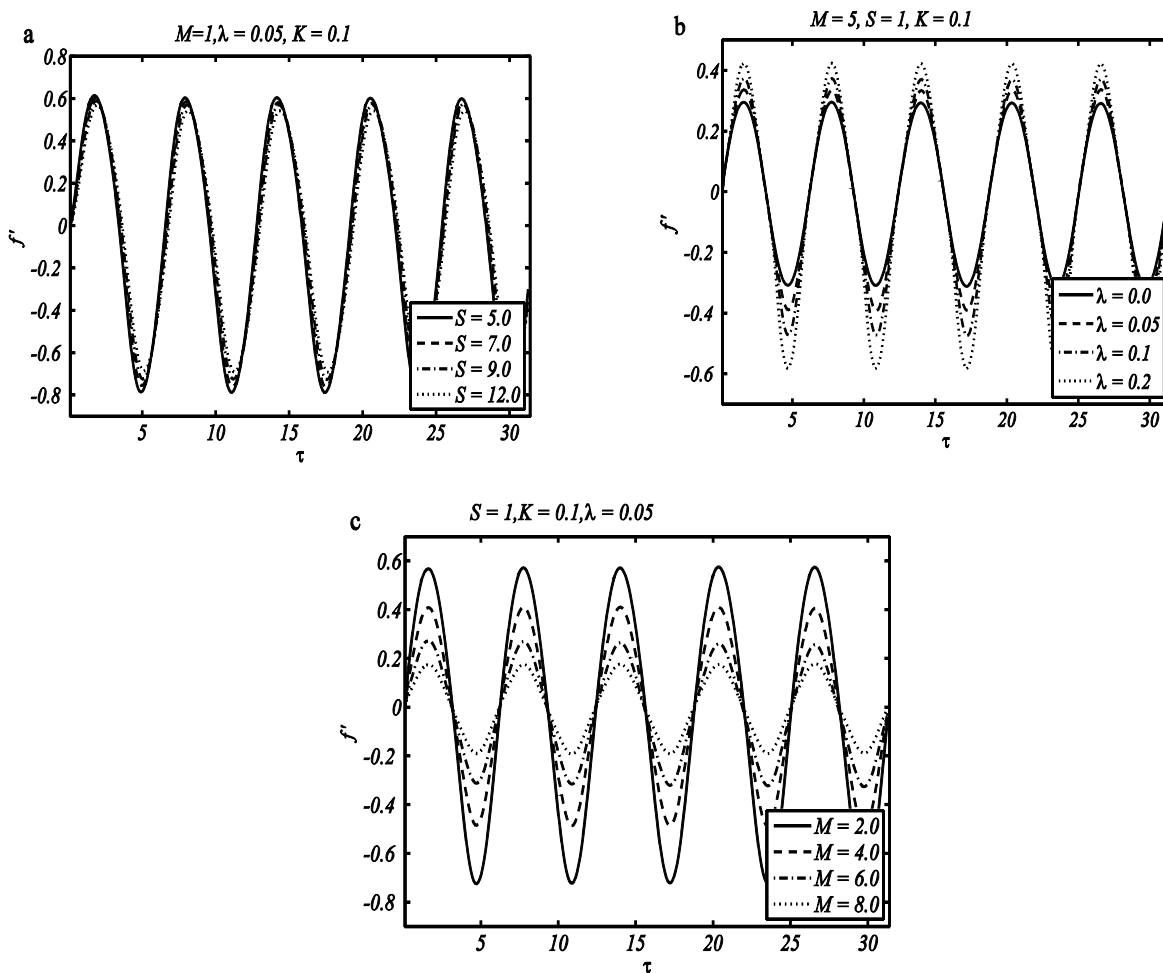

Fig. 5. Velocity profile as a function of time: (a) effects of S; (b) effects of λ; (c) effects of M.
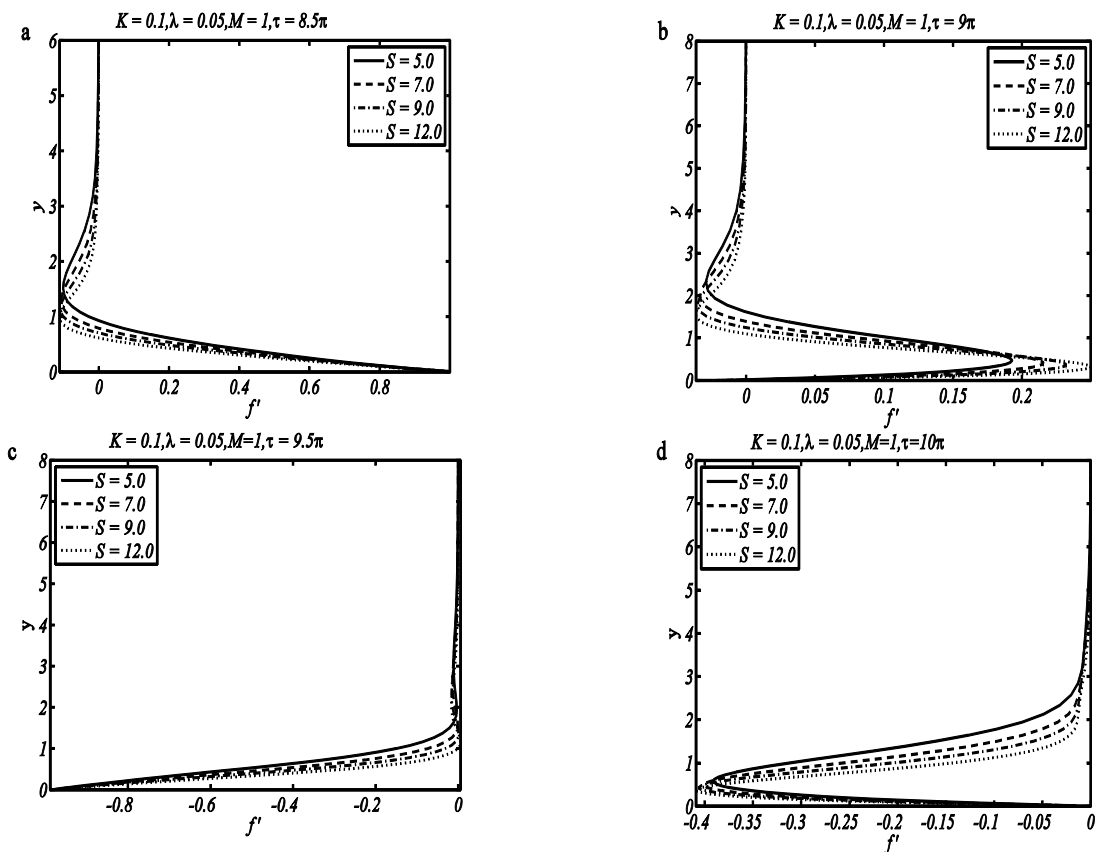
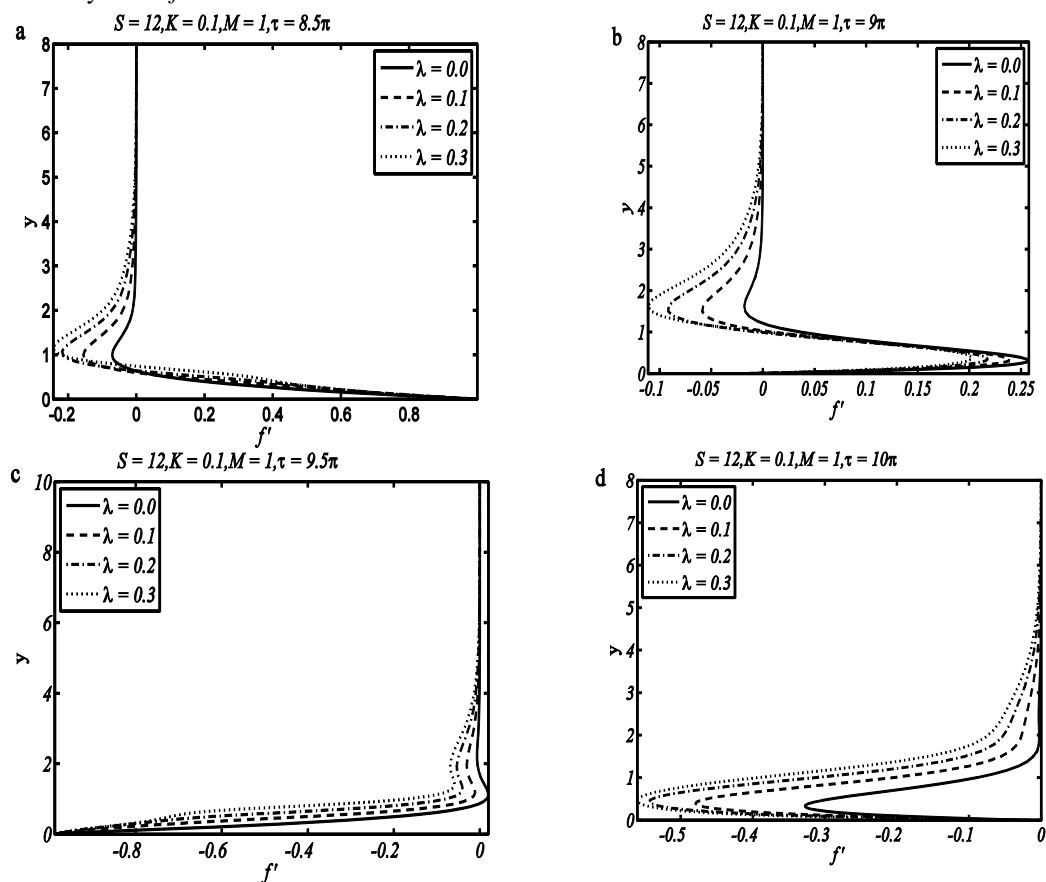**Fig. 6.** Velocity field f' for different values of S.

Fig. 7. Velocity field f' for different values of λ.
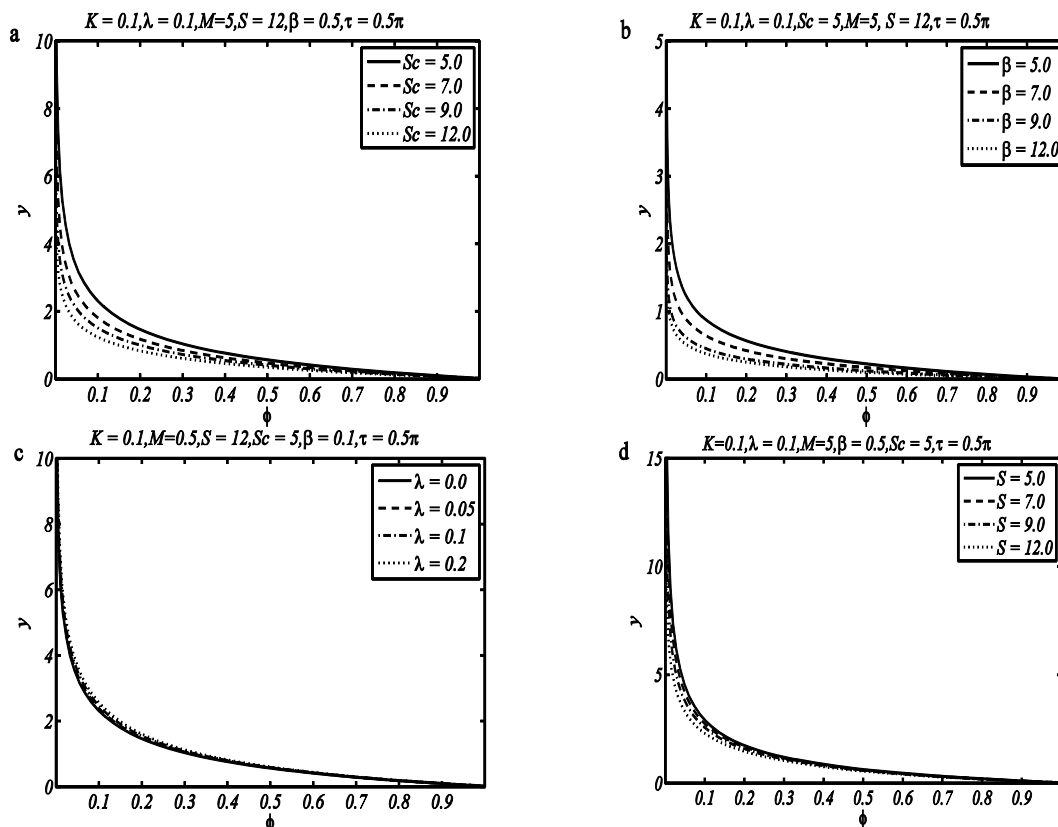
Fig. 8. Concentration field ϕ (a) effects of ; Sc (b) effects of β ; (c) effects of λ ; (d) effects of S.
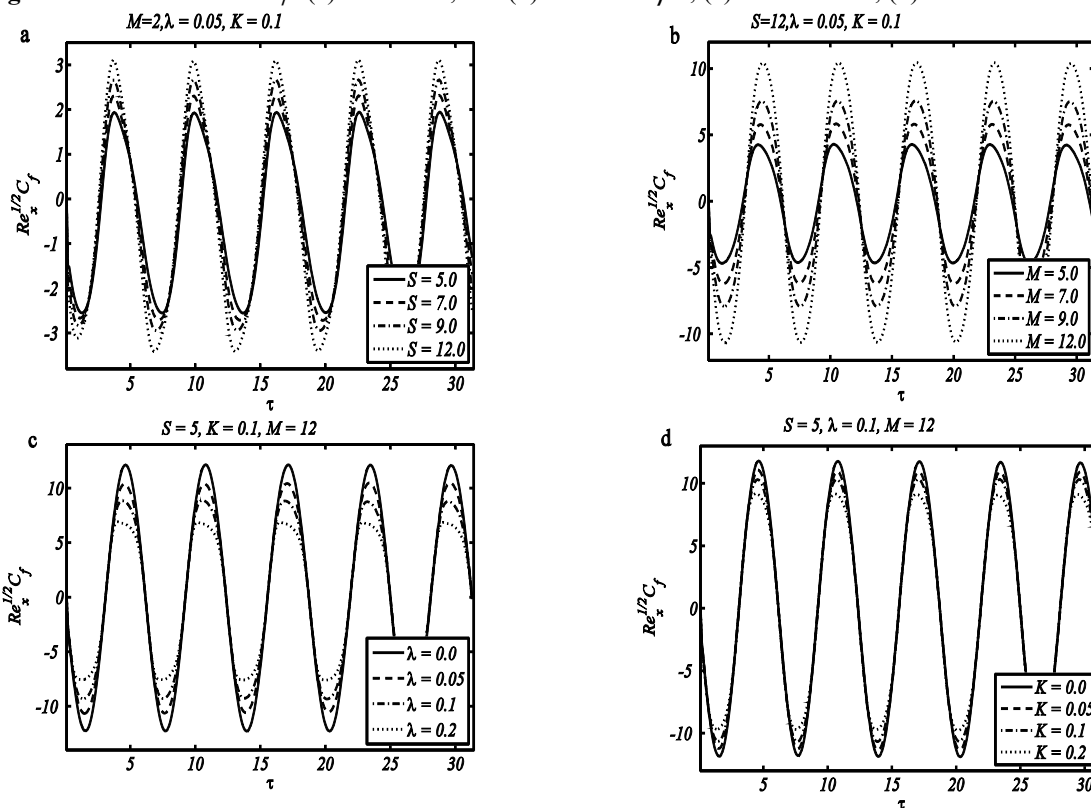

Fig. 9. The skin friction coefficient $\mathrm{Re}_x^{1/2} C_f$ as a function of time: (a) effects of S ; (b) effects of M ; (c) effects of λ ; (d) effects of K.

REFERENCES

1. P. L. Chambre, J. D. Young *J, Phys. Fluids*, **1**, 48 (1958).
2. H. I. Andersson, O. R. Hansen, B. Holmedal, *Int. J. Heat Mass Tran.*, **37**, 659 (1994).
3. H.S. Takhar, A.J. Chamkha, G. Nath, *Int. J. Eng. Sci.*, **38**, 1303 (2000).
4. F.T. Akyildiz, H. Bellout, K. Vajravelu, *J. Math. Anal. Appl.* 320, 322 (2006).
5. T. Hayat and Z. Abbas, *Z. angew. Math. Phys.*, **59**, 124 (2008).
6. T. Hayat, M. Awais, M. Sajid, *Int J. Mod. Phys. B*, **25**(21) 2863 (2011).
7. M. A. Seddeek, A. A. Darwish, M. S. Abdelmeguid, *Comm. Nonlinear Sci. Num. Simulation,* **12**, 213(2007).
8. M.A. El-Aziz, *Chem. Eng. Commun.*, **197**, 1261, (2010).
9. M. Ferdows, M. Qasem, , *Am. J. Fluid Dynamics,* **2**(6), 89, (2012).
10. K. Bhattacharyya, *Chem. Eng. Bulletin.*, **15**, 6, (2011).
11. S. Mukhopadhyay, K. Bhattacharyya, *J. Egyp. Math. Society*, **20**, 229 (2012).
12. Z. Abbas, B. Ahmad, S. Ali, *J. Appl. Mech. Tech. Physics,* **56**(5), *878 (2015).*
13. T. Hayat, M. Mustafa, S. Asghar, *Nonlinear Analysis: Real World Applications,* **11**(4), 3186 (2010).
14. Z. Ziabakhsh, G. Domairry, H. Bararnia, H. Babazadeh, *J. Taiwan Inst. Chem. Engineers*, **41**, 22 (2010).
15. S. A. Kechil, *J. Porous Media*, **12**(1), 1053 (2009).
16. T. Hayat, M. Awais, Ambreen Safdar, Awatif A. Hendi, *Nonlinear Analysis: Modelling and Control*, **17** (1), 47 (2012).
17. S. A. Shehzad, T. Hayat, M. Qasim, S. Asghar, *Braz. J. Chem. Eng.*, **30,** 187 (2013).
18. V. Sirohi, M. G. Timol, N.L. Kalathia, *Reg. J. Energy Heat Mass Transfer,* **6**, 219 (1984).
19. T. Javed, N. Ali,Z. Abbas, M. Sajid, *Chem. Eng. Commun.*, **200**, 327 (2012).
20. T. Hayat , Z. Iqbal, M. Qasim, S. Obaidat, *Int. J. Heat Mass Tran.*, **55**, 1817 (2012).
21. T. Hayat, S. Asad, M. Mustafa, A. Alsaedi, *Plos One,* **9**(7), e103214 (2014)..
22. C. Y. Wang, *Acta Mech..* **72,** 261 (1988).
23. B. Siddappa, S. Abel, V. Hongunti., *ll Nuovo Cimento* D, **17**, 53 (1995).
24. Z. Abbas, Y. Wang, T. Hayat, M. Oberlack, *Int. J. Nonlinear Mech.*, **43**,783 (2008).
25. Z. Abbas, Y. Wang , T. Hayat, M. Oberlack *Int. J. Numer. Meth*. Fl., **59**, 443 (2009).
26. L.C. Zheng, X.Jin, X. X. Zhang and J. H. Zhang, *Acta Mech. Sinica*, **29**(5), 667 (2013).
27. N. Ali, S. U. Khan, Z. Abbas, *Z. Naturforsch.*, **70**(7)a, 567 (2015).
28. S. J. Liao, *J. Ship Res.* **36**, 30 (1992).
29. S. J. Liao, *Commun. Non-linear Sci. Numer. Simulation,* **11**, 326 (2006).
30. S. J. Liao, *Int. J. Non-Linear Mechanics*, **34**(4), 759 (1999).
31. S. J. Liao, *J. Fluid Mech.*, **488,** 189 (2003).
32. M. Turkyilmazoglu, *Int. J. Thermal Sciences*, **50**(5), 831 (2011).
33. M. Turkyilmazoglu, *Math. Comp. Modelling*, **53,** 1929 (2011).
34. S. Abbasbandy, A. Shirzadi, *Stud. Nonlinear Sci.,* **1**(4), 127 (2010).

АНАЛИТИЧНО И ЧИСЛЕНО ИЗСЛЕДВАНЕ НА ДИФУЗИЯТА НА ХИМИЧЕСКИ АКТИВНИ ВЕЩЕСТВА ВЪВ ФЛУИД НА EYRING-POWELL НАД НАДЛЪЖНО ОСЦИЛИРАЩА ПОВЪРХНОСТ

С.У. Хан[1*], Н. Али[2], Т. Хаят[3,4]

[1]Департамент по математика, Институт по информационни технологии COMSATS, Сахиуал, Пакистан
[2]Департамент по математика и статистика, Международен ислямски университет, Исламабад, Пакистан
[3]Департамент по математика, Университет Куаид-и-Азам, Исламабад, Пакистан
[4]Изследователска група по нелинеен анализ и приложна математика,Департамент по математика, Научен факултет, Университет „Крал Абдулазиз" Джеда, Саудитска Арабия

(Резюме)

Това изследване засяга нестационарния поток на флуид на Eyring-Powell породен от надлъжно осцилираща повърхност в присъствие на химична реакция. Еластичният лист се разтяга периодично напред-назад в собствената си равнина. Изведени са уравненията на движението прилагайки основните закони за запазване на масата, на количеството движение и на дифузията. Намалени са независимите променливи чрез въвеждането на безизмерни променливи, а уравненията се решават по два метода: хомотопен анализ и неявна диференчна схема. Сравнението на резултатите по двата метода показва отлично съгласие. Физичните променливи (надлъжната скорост и масовата концентрация са подробно изследвани за различни параметри.

Clean, simple and efficient synthesis of spiro-2-amino-4*H*-pyran-3-carbonitrile *via* HBF$_4$–SiO$_2$ nanoparticles: a green protocol

B. Sadeghi[1]*, F. Baharestan[1], A. Kafi[1], A. Hassanabadi[2]

[1]Department of Chemistry, Yazd Branch, Islamic Azad University, PO Box 89195-155, Yazd, Iran
[2]Department of Chemistry, Zahedan Branch, Islamic Azad University, PO Box 98135-978, Zahedan, Iran

We have reported that fluoroboric acid adsorbed on nano silica-gel (HBF$_4$–SiO$_2$ NPs) catalyzed the one-pot synthesis of spiropyrans by condensation of ninhydrin, malononitrile and enolizable systems in good to excellent yields. This new protocol employing HBF$_4$–SiO$_2$ NPs, which are a solid acidic, green and inexpensive catalyst, offers advantages such as mild reaction conditions, short reaction times and easy work-up. The catalyst is recyclable with reproducible results without any loss of its activity.

Keywords: HBF$_4$–SiO$_2$ NPs, solid acid, ninhydrin, malononitrile, enolizable systems, green chemistry

INTRODUCTION

Multi-component one-pot syntheses have emerged as powerful tools owing to their ability to give products in a single operation step from three or more reactants with high atom economy. These reactions are widely applied in biological and pharmaceutical chemistry for producing different structures and combinatorial libraries for drug discovery[1]. Spiro compounds are an important class of structural motifs of numerous natural products with biological properties [2,3]. On the other hand, the pyran ring is important from pharmaceutical point-of-view and exhibits promising biological activities such as antiviral [4], anticancer [5,6], anti-HIV [7], antimicrobial [8] and calcium channel antagonist activity [9].

Spiropyrans in particular, have attracted strong interest owing to their potential activity as hypertensive, analgesic agents and their applications in industrial fields such as photochromic materials in data recording [10]. In recent years, a variety of synthetic procedures for spiro-2-amino-4H-pyran-3-carbonitriles synthesis have been reported [11,12]. Each of these methods has merits but the development of facile, green and economical synthetic methodologies is still essential. There are many limitations, such as the use of expensive and excess amounts of catalysts, elevated temperatures, long reaction times, and low yields. Hence, we have developed an efficient procedure for the one-pot three-component synthesis of biologically active spiro-2-amino-4*H*-pyran-3-carbonitrile derivatives in the presence of HBF$_4$–SiO$_2$ nanoparticles as a solid-phase acidic catalyst. The application of environmentally benign water and solid acid catalyst represents a powerful green procedure.
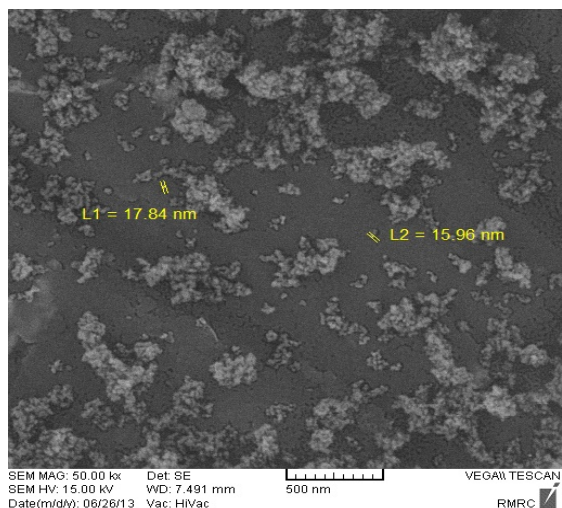
EXPERIMENTAL

Instruments

Melting points were determined with an Electrothermal 9100 apparatus. Elemental analyses were performed using a Costech ECS 4010 CHNS-O analyser. Mass spectra were recorded on a FINNIGAN-MAT 8430 mass spectrometer operating at an ionization potential of 70 eV. IR spectra were recorded on a Shimadzu IR-470 spectrometer. ^{1}H and ^{13}C NMR spectra were recorded on a Bruker DRX-500 Avance spectrometer for solutions in d$_6$-DMSO using TMS as an internal standard. The morphologies of the products were observed using SEM with a Holland Philips XL30 microscope at an accelerating voltage of 25 kV. The chemicals for this work were purchased from Fluka (Buchs, Switzerland) and were used without further purification. Stable silica nanoparticles were obtained according to [17] and used for preparation of the catalyst HBF$_4$–SiO$_2$ NPs.

Synthesis of HBF$_4$–SiO$_2$ nanocrystals

A magnetically stirred suspension of nano silica-gel (2.67 g) in diethyl ether (50 mL) was treated with 40% aq HBF$_4$ (0.3 g) for 3 h. The mixture was concentrated and the residue dried under vacuum at 100 ºC for 72 h to afford HBF$_4$–SiO$_2$ NPs. The dimensions of the nanoparticles were observed by SEM (Scheme 1). The catalyst resembles a net, which is considered as an advantage, since the reactants are situated in the mesh vents and reactions are performed with certain regularity.

---

* To whom all correspondence should be sent:
E-mail: sadeghi@iauyazd.ac.ir

Scheme 1. SEM image of HBF$_4$–SiO$_2$ NPs

General experimental procedure

A mixture of ninhydrin (1 mmol), malononitrile (1.2 mmol), enolizable system (**3a-f**, 1 mmol), HBF$_4$–SiO$_2$ NPs as a catalyst (0.02 g) and H$_2$O (5 mL) was placed in a round-bottom flask. The materials were magnetically stirred at ambient temperature for the appropriate time, as given in Table 2. After completion of the reaction and evaporation of the solvent, the crude product was recrystallized from hot ethanol to obtain the pure compound.

RESULTS AND DISCUSSION

In continuation of our investigations of the application of solid acids in organic synthesis [13-16] we investigated a novel and efficient method for the synthesis of spiro-2-amino-4*H*-pyran-3-carbonitrile derivatives by three-component condensation of ninhydrin **1**, malononitrile **2** and an enolizable system (**3a-f**), in the presence of HBF$_4$–SiO$_2$ NPs as a catalyst (Scheme 2).

The study was initiated by using ninhydrin, malononitrile and dimedone (**3b**) as model substrates for the preparation of **4b**. There was no reaction without HBF$_4$–SiO$_2$ NPs in H$_2$O at room temperature (Table 1, entry 1). The transformation of ninhydrin with malononitrile and dimedone proceeded smoothly with HBF$_4$–SiO$_2$ NPs (0.02 g), and at the end of the reaction (about 8 min later), the product was collected by filtration and recrystallized from ethanol, affording the nicely crystalline **4b** in good yield (94%, Table 1, entry 2). Different solvents (CH$_2$Cl$_2$, EtOH and CH$_3$CN) were screened in the model reaction in the presence of HBF$_4$–SiO$_2$ NPs as a catalyst, but they resulted in low yields (Table 1, entries 6-8). Decreasing the catalyst loading from 0.02 to 0.01 g, significantly lowered the yield of the reaction product (Table 1, entries 9, 10). The yields of **4b** were not further improved with increased amount of the catalyst (Table 1, entry 11). Thus, it is clear from the experiments that the best condition for **4b** could be entry 2, employing HBF$_4$–SiO$_2$ NPs (0.02 g) as a solid acid in aqueous medium at room temperature. An interesting feature of this method is that the catalyst can be regenerated at the end of the reaction and can be used several times without losing its activity. To recover the catalyst, after completion of the reaction, the mixture was filtered and the catalyst was washed with CHCl$_3$ and then dried. This process was repeated for two cycles and the yield of the product did not change significantly (Table 1, entries 12, 13).
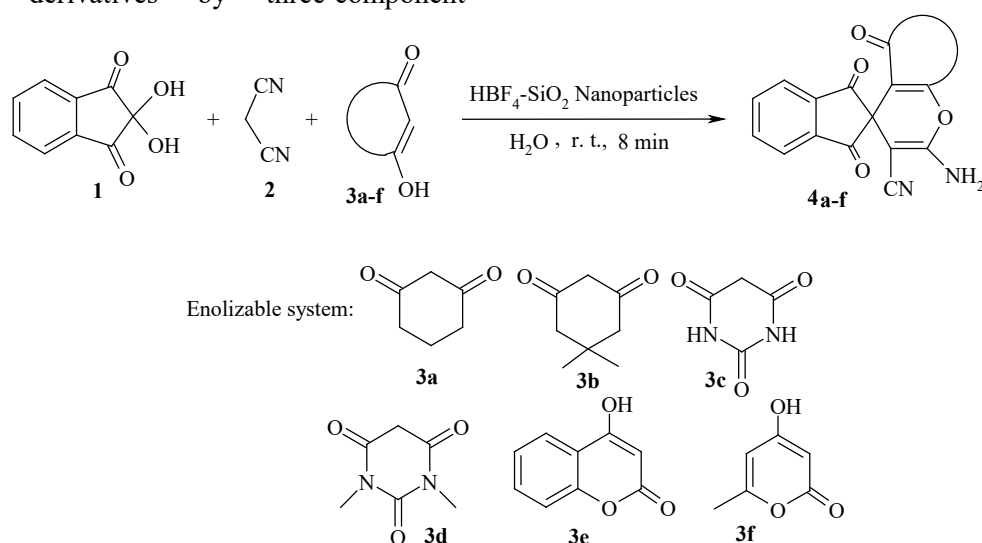
Scheme 2. Synthesis of spiro-2-amino-4*H*-pyran-3-carbonitrile derivatives catalyzed by HBF$_4$–SiO$_2$ NPs.

Table 1. Optimization of the reaction conditions for the synthesis of **4b**[a].

Entry	Catalyst (amount)	Solvent/ Cond.	Time (min)	Yield (%) [Ref.]
1	HBF$_4$–SiO$_2$ NPs (0)	H$_2$O/ r.t.	60	0
2	HBF$_4$–SiO$_2$ NPs (0.02 g)	H$_2$O/ r.t.	8	94
3	NaHCO$_3$ (0.2 mmol)	EtOH/ Reflux	20	92 [11]
4	DBU (10 mol%)	H$_2$O/ r.t.	10	85 [12]
5	SiO$_2$-HBF$_4$ (0.02 g)	H$_2$O/ r.t.	8	Trace
6	HBF$_4$–SiO$_2$ NPs (0.02 g)	EtOH/ r.t.	8	64
7	HBF$_4$–SiO$_2$ NPs (0.02 g)	CH$_3$CN/ r.t.	8	57
8	HBF$_4$–SiO$_2$ NPs (0.02 g)	CH$_2$Cl$_2$/ r.t.	8	40
9	HBF$_4$–SiO$_2$ NPs (0.015 g)	H$_2$O/ r.t.	8	90
10	HBF$_4$–SiO$_2$ NPs (0.01 g)	H$_2$O/ r.t.	8	84
11	HBF$_4$–SiO$_2$ NPs (0.03 g)	H$_2$O/ r.t.	8	94
12	HBF$_4$–SiO$_2$ NPs (0.02 g)2nd	H$_2$O/ r.t.	8	90
13	HBF$_4$–SiO$_2$ NPs (0.02 g)3rd	H$_2$O/ r.t.	8	87

[a] Reaction conditions: 1 mmol of ninhydrin, 1 mmol of malononitrile, 1 mmol of dimedone.

Table 2. Synthesis of spiro-2-amino-4*H*-pyran-3-carbonitrile derivatives[a].

Entry	Enolizable system	Product	Time (min)	Yield (%)[b]	M.p. (°C)	
					Found	Reported [Ref.]
1	**3a**	**4a**	10	90	284-285	> 300 [11]
2	**3b**	**4b**	8	94	289-291	> 300 [11]
3	**3c**	**4c**	12	88	273-275	> 300 [11]
4	**3d**	**4d**	10	89	260-262	> 300 [11]
5	**3e**	**4e**	7	90	> 300	> 300 [11]
6	**3f**	**4f**	10	91	290-295	288-292 [12]

[a] Reaction conditions: 1 mmol of ninhydrin, 1.2 mmol of malononitrile, 1 mmol of enolizable system, in aqueous medium at room temperature.

[b] Isolated yields.

After optimizing the reaction conditions, a series of enolizable systems were employed under similar circumstances to evaluate the substrate scope of this reaction. The results are summarized in Table 2. In all cases, the enolizable systems underwent the reaction smoothly and gave products in excellent yields.

The compounds **4a-f** were characterized by ^{1}HNMR and IR spectroscopy and elemental analysis [11,12].

In conclusion, we have successfully developed an efficient, atom-economical and simple methodology for the synthesis of spiro-2-amino-4*H*-pyran-3-carbonitrile derivatives by a three-component reaction in aqueous medium at room temperature. Prominent among the advantages of this method are: operational simplicity, mild reaction conditions, short reaction times, high yields, environmental safety and cheapness of the catalyst. The present method does not involve any hazardous organic solvents and liquid acid catalysts. Therefore, this procedure could be classified as green chemistry.

REFERENCES

1. N. K. Terret, M. Gardner, D. W. Gordon, R. J. Kobylecki, J. Steel, *Tetrahedron*, **51**, 8135 (1995)
2. K. A. Parker, A. Dermatakis, *J. Org. Chem.,* **62,** 4164 (1997)
3. M. J. Kukla, H. J. Breslin, C. J. Diamond, P. P. Gtous, C. Y. Ho, M. Miranda, J. D. Rodgers, R. G. Sherrill, E. D. Clercq, *J. Med. Chem.,* **34**, 3187 (1991)
4. S. Wang, G. W. Milne, X. Yan, I. J. Posey, M. C. Nicklaus, L. Graham, W. G. Rice, *J. Med. Chem.,* **39**, 2047 (1996)
5. D. R. da Rocha, A. C. G. de Souza, J. A. L. C. Resende, W. C. Santos, E. A. dos Santos, C. Pessoa, M. O. de Moraes, L. V. Costa-Lotufo, R. C. Montenegro, V. F. Ferreira, *Org. Biomol. Chem.,* **9**, 4315 (2011)
6. Y. Dong, Q. Shi, K. Nakagawa-Goto, P.-C. Wu, S. L. Morris-Natschke, A. Brossi, K. F. Bastow, J.-Y. Lang, M.-C. Hung, K.-H. Lee, *Org. Biomol. Chem.,* **18**, 803 (2010)
7. M-z. He, N. Yang, X-J. Yao, C-l. Sun, M. Yang, *Med. Chem. Res.,* **20**, 200 (2010)
8. H. Hussain, S. Aziz, B. Schulz, K. Krohn, *Nat. Prod. Commun.,* **6**, 841 (2011).
9. A. Shahrisa, M. Zirak, A. R. Mehdipour, R. Miri, *Chem. Heterocycl. Compd.,* **46**, 1354 (2011).
10. C. P. McCoy, L. Donnelly, D. S. Jones, S. P. Gorman, *Tetrahedron Lett.,* **28**, 657 (2007).
11. Y. He, H. G, J. Tian, *J. Chem. Res.,* **35**, 528 (2011)
12. P. Saluja, K. Aggarwal, J. M. Khurana, *Synth. Commun.,* **43**, 3239 (2013).
13. B. Sadeghi, B. F. Mirjalili, M. M. Hashemi, *Tetrahedron Lett.,* **49**, 2575 (2008).

14. B. Sadeghi, A. Hassanabadi and M, Kamali, *J. Chem. Res.*, **36**, 9 (2012).
15. B. Sadeghi, S. Zavar and A. Hassanabadi, *J. Chem. Res.*, **36**, 343 (2012).
16. B. Sadeghi, Z. Nasirian and A. Hassanabadi, *J. Chem. Res.*, **36**, 391 (2012).
17. K. Lee, A. N. Sathyagal, A. V. McCormick, *Colloids Surfaces A*, **144**, 115 (1998).

ЧИСТ, ПРОСТ И ЕФЕКТИВЕН СИНТЕЗ НА СПИРО-2-АМИНО-4*H*-ПИРАН-3-КАРБОНИТРИЛ ЧРЕЗ НАНОЧАСТИЦИ HBF$_4$-SiO$_2$: ЗЕЛЕН ПРОТОКОЛ

Б. Садеги[1]*, Ф. Бахарестан[1], А. Кафи[1], А. Хасанабади[2]

[1]*Катедра по химия, клон Яздад, Ислямски университет Азад, ПК 89195-155, Язд, Иран*
[2]*Катедра "Химия", клон "Захадън", Ислямски университет "Азад", ПК 98135-978, Захадън, Иран*

(Резюме)

Съобщава се, че флуороводородната киселина, адсорбирана върху нано силикагел (HBF4-SiO$_2$ NPs), катализира едностъпален синтез на спиропирани чрез кондензация на нинхидрин, малононитрил и енолизируеми системи при добри до отлични добиви. Този нов протокол, използващ HBF$_4$-SiO$_2$ NPs, който е твърд, киселинен, зелен и евтин катализатор, предлага предимства като меки реакционни условия, кратки реакционни времена и лесна обработка. Катализаторът се рециклира с възпроизводими резултати без загуба на неговата активност.

Sorption capacity of the oil sorbents for removing of thin films of oil

D.A.Baiseitov, M.I.Tulepov, L.R.Sassykova*, Sh.E.Gabdrashova, G.A.Essen, K.K.Kudaibergenov, Z.A.Mansurov

Al-Farabi Kazakh National University, 71, al-Farabi, 050040, Almaty, Kazakhstan

Object of research are different sorbents of thin films of oil. The dependence of the sorption capacity of the sorbents on the amount of sorbent, sorption duration, the thickness of the oil film, as well as on the number of cycles of use of the sorbent was investigated. The maximum sorption for each type of oil took happened on the sorbents with the definite values of bulk density. It follows from the obtained results that the synthesized sorbents may be used as adsorbents for the removal of thin oil films.

Keywords: oil sorbent, sorption capacity, thin film of oil.

INTRODUCTION

Currently, the pollution of surface water objects by petroleum hydrocarbons happens not only under accident oil spills, but also during routine maintenance. The process of timely removal of oil pollution from the water surface is topical because of the increasing technogenic influence on the ecosystem. It is therefore particularly important to find ways to solving this problem. There is a search of materials suitable for collecting oil from the surface of water and sewage industrial water.

Cleaning of the surface of water bodies from contamination involves the removal of the oil film by mechanical and/or physical and chemical methods. The most perspective and environmentally expedient is the method of removing oil films with the help of oil sorbents [1]. The materials used for the collection of oil and petroleum products from water, are commonly called oil sorbents, collectors of oil and oil absorbers. One of the main problems during cleaning surface of water bodies from pollution is the removal of a thin oil film having the ability to spread over vast distances in the shortest terms, violating the oxygen exchange [2-3].

For the obtaining oil sorbents various raw materials are used [4]. By the mechanism of oil removal the sorbents are distinguished, which act through physical surface adsorption. Here, the collection of oil occurs due to adhesion to the surface of the sorbent particles. In this case, the amount of oil absorbed is determined by the value of the specific surface of the material and its properties (hydrophobic and oleophilic). Literature and patent data show that such a mechanism for collecting oil and petroleum products is realized for oleophilic powders and granular materials with closed porous structure and materials in which no appropriately sized pores are available for the molecules of the removable substances [5].

EXPERIMENTAL

All researches experiments were carried out using the methods described in [6-8]. A Petri dish was filled with water and weighed, and then an oil slick was applied to the water surface without touching the walls of the dish, followed by cup reweighing. Then, on the oil slick a sample of sorbent was applied in order to absorb it and the dish was reweighed. Gain of oil weight to the sorbent weight gave the value of the absorption capacity of the sorbent in water.

The weight of dry dish was 134.15 g and with water - 178.93 g. The weight of the oil slick was 0.4 g and the weight of the dish became 179.33 g. After the total absorption of the oil slick modified by carbon sorbent with weight of 0.04 g, the weight of the cup amounted to 179.37 g, and the sorption capacity was 10.0 g/g.

The weight of dish with water was 173.44 g and with the oil spill - 173.90, after applying of the sample of carbon sorbent of vegetable origin with weight of 0.22 g, the oil spill was absorbed by the sorbent. The sorption capacity of the sorbent was 5.0 g/g, i.e. 1 g of sorbent could adsorb 5 g of oil.

After repeating the experiment under mixing of oil and sorbent, the total absorption of the oil slick has been achieved with 0.05 g of modified carbon sorbent, i.e. the sorption capacity increased to 10.9 g /g.

For creation of oil film in a Petri dish about 40 ml of water with a salt concentration of 17-20 g/l (seawater) was poured and a few drops of oil were dropped. The diameter and thickness of the formed oil slick film were determined.

* To whom all correspondence should be sent:
E-mail: larissa.rav@mail.ru

RESULTS AND DISCUSSION

For the laboratory tests the medium viscous oil of Karazhanbas field (Kazakhstan) was used (Figure 1). The dependence of the sorption capacity of the obtained carbonized sorbents based on rice husks (CRH) on the amount of sorbent, the sorption time, the thickness of the oil film, as well as on the number of cycles of use of the sorbent was studied.
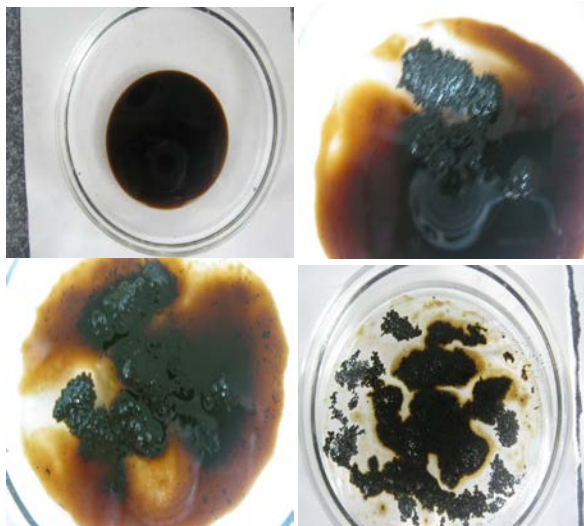

Fig.1. Sorption of Karazhanbas oil

Figure 2 shows the sorption capacity of the sorbents as a function of the sorption time. As can be seen from the presented data, the maximum sorption of oil is in the first ~ 3-4 min, after which the sorbent based on foam rubber and sunflower husk carbonizate (FRCSH- 300) was able to retain the sorbed oil for two days, whereas the sorbents on the basis of polystyrene foam and carbonizate of rice husk PFCRH-400 and modified foam rubber (MFR-300) gradually began to release it after 4 h of active sorption.

Such behavior of the sorbents may be due to the lower level of hydrophobicity and oleophilicity of sorbents based on PFCRH-400 and MFR-300, and to the different structure of the sorbents.

The sorption capacity of vegetable materials without polymers was studied. With the increase in mass of the taken sorbent the amount of sorbed oil gradually increased. After reaching the optimal sorption time (4 h), the speed of the active sorption markedly decreased, which may be explained on the one hand by the oil saturation of the sorbents, and on the other, by the process of desorption (in the case of CRH-400 and -300).

The dependence of the sorption capacity of the sorbents on the thickness of the oil film was also studied (Fig.3).
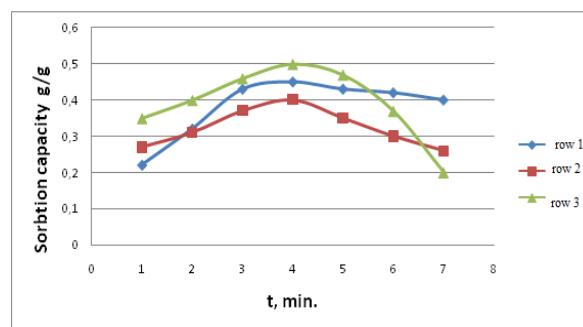

Fig.2. Dependence of the sorption capacity of the sorbents on the sorption duration: 1 - rubber foam + carbonizate of sunflower husk (FRCSH- 300) ; 2 - polystyrene foam + carbonizate of rice husk (FPCRH-400) ; 3 - modified rubber foam (MFR -300)
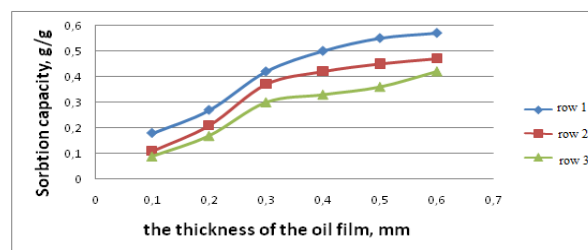

Fig.3. Dependence of the sorption capacity of the sorbent on the thickness of the oil film: 1 - rubber foam + carbonizate of sunflower husk (FRCRH- 300); 2- polystyrene foam + carbonizate of rice husk (FPCRH - 400); 3- modified rubber foam (MFR-300)

It is known that the maximum absorption capacity of the sorbent is exhibited with excess amount of absorbed oil [9,10]. As seen in Fig. 3, an increase of the thickness of the oil film increases the oil absorption capacity of the sorbents.

The results of the study of the dependence of the sorption capacity of the sorbents on the number of used cycles are presented in Table 1.

The regenerability of the sorbents is one of their basic characteristics. The obtained results show a good regenerability of the sorbents and a possibility of their repeated use.

Regeneration of the sorbents was carried out by centrifugation and washing with a hydrocarbon solvent followed by air drying.

The data in Table 1 demonstrate the suitability of the sorbents synthesized by us as adsorbents for the removal of thin oil films.

We have also studied the maximum oil absorption by CKP-400 depending on the viscosity and the physical state of aggregation, i.e. the sorbed oil product was petroleum oil, oil, gasoline and diesel fuel.

In those cases, when the thickness of the oil spill layer was less than the thickness of the sorbent, the collection of oil from the water surface also occurred. Table 2 shows that the sorbent absorbs the

oil «Mobil» to a higher degree than gasoline and diesel. This is possibly because of the increased affinity of the sorbent to the sorbed oil.

On increasing the film thickness, the oil sorption capacity of the sorbent increases.

From the data in Table 2 it is clear that the collection of products of relatively low viscosity (gasoline and diesel) depends on their excess and the real-absorbing properties of the sorbent are characterized by amount of oil absorption at the level of 30-40 g/g.

This sorbent is easily regenerated by simplest squeezing of the absorbed oil. Despite the high oil absorption of sorbent "CRH- 400", its application in dispersed form is time consuming and not technological due to significant technical difficulties that arise on spraying the sorbent on the surface of the oil spills and subsequent collecting of the spent sorbent.

As the performance of the sorbent strongly depends on the ambient temperature, for example, in winter conditions, in this work was also investigated the influence of temperature and volume weight of sorbents on the basis of apricot stone CAS-400 and rice husk CRH-400.

Table 3 shows the temperature dependence of the sorption capacity of sorbents (with weight by volume of 50 g/cm^3 of CAS-400 and 150 g/cm^3 of CRH-400) on oil and petroleum products in the temperature interval from 10 to 50°C. After analyses of the data of Table 3, it is possible to claim the following regularities: in the case of oil and fuel oil, the temperature increase leads to a constant growth of the sorption capacity of sorbents from CAS-400 with weight by volume of 50 g/cm^3.

In this case, the established temperature limit for the sorbents is not the limit of saturation by oil and fuel oil. The maximum adsorption capacities of these sorbents are 22.5 and 24.2 g/g, respectively. In the case of gasoline and diesel fuel in the sorbent CAS-400 with weight by volume of 50 g/m^3 the maximum sorption of diesel fuel increased with temperature and at 30 ^{0}C was equal to 3.5 g/g.

Table 1. Dependence of the sorption capacity of the sorbents on the number of used cycles.

Cycles used	Sorption capacity, g/g		
	FRCRH-300	FPCRH-400	MFR -300
1	0.45	0.49	0.42
2	0.44	0.40	0.40
3	0.35	0.38	0.40
4	0.33	0.35	0.32

Table 2. Effect of the thickness of oil and oil products on the sorption capacity of the sorbent CRH-400, g/g

Collected oil product	Layer thickness, cm	Amount (g/g of of the sorbent) on the collected oil product		Degree of squeezing, %
		absorbed	squeezed	
Oil field "Kumkol"	4.1	38-40	28	86
Oil "Mobil"	1.1	53-60	43	87
Motor car gasoline	3	32-33	25	78
Diesel fuel	4	24-30	19	77

Table 3. Influence of temperature of the medium and bulk density of sorbents on the sorption capacity for oil and petroleum products (g/g)

Weight by volume, g/cm^3	Temperature of medium, ^{0}C	Sorption capacity of sorbents, g/g			
		Oil	Fuel oil	Diesel fuel	Gasoline
CAS-400 50 g/cm^3	10	9.3	7.4	1.6	1.4
	15	12.4	11.5	2.4	2.1
	25	15.6	16.2	3.5	3.0
	30	17.4	17.3	3.5	2.4
	35	20.4	21.4	2.4	-
	40	22.5	24.2	1.0	-
CRH-400 150 g/cm^3	10	4.0	2.2	8.3	7.2
	15	5.3	2.5	9.2	8.1
	20	5.4	2.6	10.3	9.1
	25	6.2	3.4	11.4	12.1
	30	8.1	5.2	12.5	12.1
	35	8.8	6.3	12.4	-
	40	10.2	7.2	12.0	-

A further increase in temperature of the medium caused a decrease in the sorption capacity of the sorbent for diesel fuel. This is due to the fact that the sorbents AS-400 are of sufficiently large mesh size ensuring that the forces of attraction between sorbate molecules are higher than those between sorbate and sorbent molecules, resulting in a liquid phase portion flowing from the cells of a solid sorbent during weighing [11].

In Table 3 the regularities of changes of the sorption capacity of sorbents CRH-400 with a bulk density of 150 g/m^3 on temperature are presented. By analogy, in this case, regardless of the type of the sorbate, a regular increase of the temperature of sorption capacity was observed. This is due to the fact that with increasing temperature, the viscosity of oil and petroleum products is reduced and thereby accelerates the migration of sorbate to a diffusion region of fine-mesh macrostructure of the sorbents. However, here the opposite picture is observed, the sorption capacity for diesel fuel and gasoline is higher than that of oil and fuel oil. In this case, we are confronted with the specifics of selective sorption of sorbents and their ability to selectively sorb oil and petroleum products depending on the size of the cells and bulk density. The studies showed the potential application of the sorbents synthesized by us as adsorbents for the removal of thin oil films. On the basis of experimental data it was revealed that the maximum absorption of crude oil is reached when the film thickness of dispersed sorbent is of equal proportions as the thickness of the oil spill layer, i.e. in the case of oil «Mobil» with a layer thickness of 1.1 cm the maximum quantity of oil products - 53-60 g is adsorbed.

CONCLUSION

It was shown that irrespective of the type of oil and volume weight of the sorbent, with an increase in the thickness of the oil layer from 1.0 to 7.0 mm there was a general tendency to increase the sorption capacity. It should be note that the maximum sorption for each type of oil occurred on the sorbents with the definite values of bulk density.

REFERENCES

1. G.Deschamps, H.Caruel, M.-E.Borredon, Ch.Bonnin, Ch.Vignoles, *J.Environmental Science & Technology*, **5**, 1013-1015(2003).
2. V.E. Ryabchikov, Modern methods of water preparing for industrial and domestic use, M., De Le print, 2004, p. 300.
3. F.A. Kamenshikov, E.I. Bogomolniy, Removal of oil products from the water surface and ground, M., Izhevsk, Institute of computer science, 2006, p.528.
4. G.I. Gorozhankina, L.I. Pinchukova, *Pipeline Transport of Oil*, **4**, 12 (2000) .
5. V.V. Bordunov, E.O. Koval, I.A. Sobolev, *Oil and gas technologies*, **6**, 30 (2000).
6. D. A. Baiseitov, M.I. Tulepov, L.R. Sassykova, Sh.E. Gabdrashova, E. Gul'dana, D.A.Zhumabai, K.K.Kudaibergenov, Z. A.Mansurov, *Int.J.Chem.Sci.*, **13(2),** 1027-1033(2015).
7. D.Baiseitov, M. Tulepov, L.Sassykova, Sh.Gabdrashova, K.Kudaibergenov, Z.Mansurov, *Rev. Roum.Chim*, **62(3)**,249-253*(*2017).
8. K. Kudaibergenov, Y. Ongarbayev, M. Tulepov, Z. Mansurov, *Advanced Materials Research*, **893**, 478 (2014).
9. H. Luik, I. Johannes, V. Palu, L. Luik, K. Krwusement, *J. Anal. Appl. Pyrolysis*, **79**, 121 (2004).
10. R.-Q. Sun, L.-B. Sun, Y. Chun, Q.-H. Xu, *Carbon*, **46**, 1757 (2008)
11. Y.N. Kahramanly, *Refining and Petrochemistry*, **12**, p.42, (2010).

СОРБЦИОНЕН КАПАЦИТЕТ НА СОРБЕНТ ЗА ОТСТРАНЯВАНЕТО НА ТЪНКИ СЛОЕВЕ ОТ ПЕТРОЛ

Д.А. Байсейтов, М.И. Тулепов. Л.Р. Сасикова*, Ш.Е. Габдрашова, Г.А. Есен, К.К. Кудайбергенов, З.А. Мансуров

Национален университет Ал-Фараби, Алмати, Казахстан

(Резюме)

Изследвани са зависимостта на сорбционния капацитет от количеството на сорбента, времето на сорбция дебелината на филма от петрол, както и броя на циклите на използване. В резултат е установено, че може да се използват изследваните синтетични сорбенти за отстраняването на тънки филми от петрол.

Caffeine release from selected pharmaceutical preparations

M. Szymański[1*], E.W.-Banaszczak[1], R. Siwek[1], M. Frankowska[2], A. Szymański[2]

[1] Department of Pharmacognosy, Poznań University of Medical Sciences, Święcickiego 4, 60-781 Poznań, Poland
[2] Faculty of Chemistry, Adam Mickiewicz University, Umultowska 89b, 61-614 Poznań, Poland

Reference drugs that are available on the Polish market were subjected to qualitative, quantitative and caffeine release analyses. The HPLC technique was used in all assays.

Determination of the pharmaceutical availability of caffeine showed the following values of release for the respective preparations: Apap Extra 97.2±2.4%; Guaranax 66.8±1.3%; Guarana (Herbapol) 94.1±1.1%; Guarana (Walmark) 99.9±5.0%, Panadol 86.9±0.2%, Diabolo Guarana 73.5±5.0%, Magne B-6 Active 55.4±13.6%, Drive Max 88.2±1.6%. For Guarana Caps, pharmaceutical availability was not determined because the substance was not released from the capsule in the acceptor fluid (HCl, pH=2).

The results of the analysis of the selected dietary supplements for their caffeine content confirmed earlier reports on instances of divergence between the actual concentration of a given active substance and the declared value. The analysis of caffeine release profiles for the selected pharmaceuticals shows significant differences between them. The analyses did not indicate the presence of a caffeine-tannins complex. No extended or retarded release of caffeine from preparations containing a guarana seed extract, which might otherwise be indicative of a gradual release of caffeine from such complex, was observed. Differences in the profiles of caffeine release from the test preparations are attributable to the properties of the respective drug forms, such as the presence of a coating or gelatin capsule. The test results are not indicative of the presence of a caffeine-tannins complex which, otherwise, might cause caffeine to be gradually released.

Keywords: caffeine, pharmaceutical preparations, release of active substance, caffeine-tannins complex, high-performance liquid chromatography

INTRODUCTION

The structure of derivatives of xanthines, such as caffeine (Fig. 1), was identified in the 19th century. The discovery is deemed to have been made by Hermann Emil Fischer (1852–1919), who demonstrated (in 1897) that caffeine and uric acid had similar structures before proving that the compound was trimethylxanthine. On the other hand, Fischer's research merely confirmed the structure proposed earlier by Ludwig Medicus (1847–1915) [1].
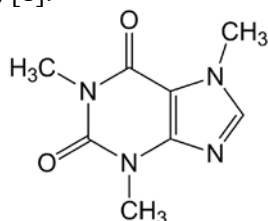

Fig. 1. Caffeine.

The effect of caffeine is observed in the cerebral cortex, the autonomous nervous system, and the cardiac muscles [2]. Nevertheless, a number of studies on the effect of caffeine fail to give an unambiguous answer about the effect itself and its intensity. This is explained by the occurrence of individual and environmental differences, affecting the metabolism of the compound [3]. Reasonable doses of caffeine (100–300 mg/day) stimulate the activity of the cerebral cortex by enhancing both intellectual and physical efficiency and helping fight drowsiness and fatigue. Different opinions are expressed on the effect of caffeine on the ability to concentrate [2]. Among purine group alkaloids, when compared with theobromine and theophylline (Fig. 2 and Fig. 3), caffeine has the strongest stimulating effect on the central nervous system [4].
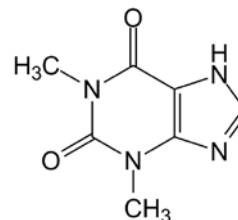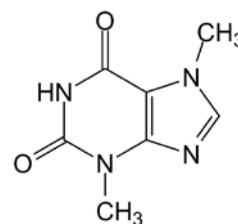

Fig. 2. Theobromine.

Fig. 3. Theophylline.

* To whom all correspondence should be sent:
E-mail: mszymanski@ump.edu.pl

The daily consumption of caffeine in Europe is in the range of 280–490 mg [5]. Caffeine is quickly and almost completely (99%) absorbed after oral administration. Its maximum blood concentration is observed after 50 to 75 min. Its pharmacokinetics after intravenous administration is comparable to that after oral administration [6]. Between 25–40% of the drug is bound with plasma protein, and its distribution volume is 0.52–1.05 l/kg. The compound readily passes through the placenta barrier, the blood-brain barrier, and into the milk of breast-feeding mothers [7].

Caffeine is considered to be the most frequently used psychoactive substance. According to the American Psychiatric Association (APA), a substance is regarded as having an addictive effect if at least three of the seven proposed criteria are satisfied. Caffeine satisfies four of the seven criteria: tolerance to the effect of the compound is observed, withdrawal symptoms are shown, patients have problems in reducing its consumption, and the substance is used even though it is known to have undesirable effects and being harmful to the body [8].

MATERIALS AND METHODS

Test material

The test material included dietary supplements and drugs with caffeine, available in Poland. Their compositions and forms are shown in Table 1.

Reagents

- methanol for HPLC (from Merck)
- caffeine (from Sigma-Aldrich)
- water for HPLC (from J. T. Baker)

Equipment

The analyses were performed using the following equipment:
- Liquid chromatograph HP 1050 from Hewlett Packard, with UV detector;
- Paddle apparatus for analysis of active substance release from solid drug forms, set up as described in the Polish Pharmacopoeia IX – Apparatus 2.

Chromatographic conditions

- analytical wave length: 280 nm.
- stationary phase – Waters Symmetry column C-18, 5 μm (4.6 × 250 mm).
- mobile phase – methanol : water 40:60.

Table 1. Composition of test preparations with caffeine.

| Preparation	Composition, as declared by manufacturer	Form of preparation
	Dietary supplements	
Diabolo Guarana	Guarana seed extract 380 mg (45 mg caffeine)	capsules
Magne – B6 Active	Guarana seed extract 232 mg (min. 51 mg caffeine)	coated tablets
Drive Max	Guarana seed extract 10% (30 mg caffeine)	capsules
Guaranax	Guarana extract 400 mg (20% caffeine)	capsules
Guarana	Guarana seed extract (min. 27 mg caffeine)	capsules
Guarana	Guarana 800 mg, (10.5 mg caffeine)	tablets
Guarana Caps	Guarana extract 450 mg (100 mg caffeine)	capsules
	Drugs	
Etopiryna	Acetylsalicylic acid 300 mg Etenzamid 100 mg Caffeine 50 mg	tablets
Coffepirine	Acetylsalicylic acid 450 mg Caffeine 50 mg	tablets
Panadol Extra	Paracetamol 500 mg Caffeine 65 mg	coated tablets
Apap Extra	Paracetamol (500mg), Caffeine (65mg)	coated tablets

Table 2. Statistical parameters for the calibration curve y = ax + b.

Statistical parameters	Peak height curve	Peak area curve
a (gradient)	1.8589	0.5561
b (abscissa)	0.3023	-0.6191
R	0.9989	0.9991
R^2	0.9978	0.9983
S	1.8120	0.4721
av. Y	99.26	28.98
RSD [%]	1.8	1.6

R – regression coefficient; S – deviation of curve; RSD – relative standard deviation

Preparation of calibration curve for caffeine solutions

The calibration curve for caffeine was prepared by consecutive dilutions using a stock solution of concentration of 1 mg/ml. Solutions with concentrations of 5, 10, 25, 50, 100, 200 μg/ml were prepared using the mobile phase. Three injections were made for the standard solution. The calibration curve is shown in Fig. 4 and its parameters are shown in Table 2.
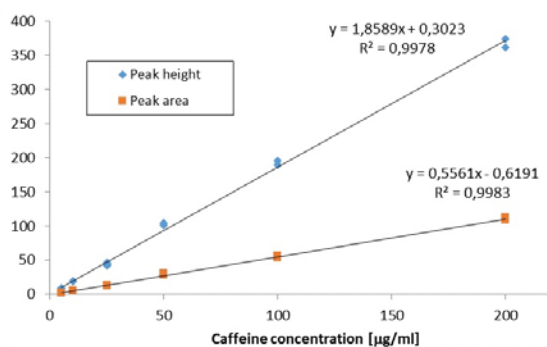
Fig. 4. Calibration curves for caffeine

Preparation of the pharmaceuticals to testing

The selected pharmaceutical preparations with caffeine were in the form of tablets or capsules. The tablets were dissolved in 50 ml measuring flasks filled with a 40% methanolic solution. The content of the capsules was quantitatively transferred into 50 ml measuring flasks and then dissolved in a 40% methanolic solution.

Determination of caffeine release profiles for selected preparations

The rate of release of caffeine from the selected preparations was found by the method described in the Polish Pharmacopoeia IX. The rate of release of a medicinal substance, also termed pharmaceutical availability, was found for *in vitro* conditions, using a paddle apparatus.

The samples, drawn from the apparatus, were analyzed by HPLC.

Test conditions for determination of the rate of caffeine release

The test apparatus was a 1000 ml thermostated three-necked flask. A hydrochloric acid solution (pH = 2) was used as the acceptor fluid. The volume of the acceptor fluid was 500 ml. The material in the flask was continuously stirred during the test using a mechanical paddle stirrer. The acceptor fluid was maintained at a constant temperature of 37.0±0.5ºC.

The test procedure and drawing samples for analysis

The volume and the temperature of the acceptor fluid were controlled before starting the test. As soon as the temperature was stable at 37.0±0.5ºC, a single form of the selected preparation was introduced, while commencing time measurement. Samples (1ml) of the acceptor fluid were drawn using an automatic pipette at specified intervals, selected depending on the drug form. Every time after drawing a sample, the volume of the acceptor fluid was supplemented by adding 1ml of the hydrochloric acid solution at pH=2. The fluid volume drawn for testing was transferred to Eppendorf test tubes. The samples for testing were drawn until the results of chromatographic analysis indicated no increment in the caffeine contents in three consecutive portions of the test solution. Three independent release rate tests were performed for each test preparation.

METHOD VALIDATION

Precision

The precision of the method was assessed with repeatability and intermediate precision (intra-day and inter-day).

The repeatability of the method to assay caffeine was found by injecting a 10 μg/ml caffeine standard solution in the chromatographic column 10 times. From the obtained analyte retention times, the mean value of retention was found to be 4.653±0.008

min. The resulting peaks were characterized by symmetry, good repeatability and very good precision, as indicated by their low RSD of 0.178%.

The resulting peak areas were used to determine their corresponding concentrations. The results, as well as the values of standard deviations and RSD, are shown in Table 3.

Intra-day precision was determined by injecting three different concentrations (10, 25 and 50 μg/ml) for six times on the same day. Peak areas were measured; their corresponding analyte concentrations, standard deviations and % RSD's were calculated.

Inter-day precision was determined by injecting three different concentrations (10, 25 and 50 μg/ml) six times for three days in a week. Peak areas were measured; their corresponding analyte concentrations, standard deviations and % RSD's were calculated.

The interday and intraday precisions of caffeine are presented in Table 4. The low % RSD values of repeatability (0.189%), intra-day (0.21% - 0.27%) and inter-day (0.21% – 0.39%) variations indicate that the precision of the proposed method is good.

Limit of detection and limit of quantification

The limit of detection (LOD) under the present chromatographic conditions is defined by the concentration of analyte giving a signal to noise ratio of 3:1. The limit of quantification (LOQ) is defined as the lowest value of the analyte concentration that is determinable with the appropriate precision and accuracy. From 6 parallel results, obtained for the respective concentrations of the standard solution, the values of the relative standard deviation were calculated and the value of RSD vs. caffeine concentration was used for finding LOQ for RSD = 10%.

For the test caffeine: LOD = 3 μg/ml and LOQ = 9 μg/ml.

Accuracy

Accuracy was found by determining the amount of the caffeine standard added to the previously analyzed product. The analyte standard was added at three different concentrations (50, 100 and 150%) of caffeine in the preparations. The analysis was carried out three times for the selected products having different declared concentrations of caffeine (Table 5).

For the test preparations, mean recovery for three different analyzed amounts of the standard added was in the range from 100.04 to 100.41%.

RESULTS AND DISCUSSION

Assay of caffeine in the selected preparations

The test samples were analyzed by HPLC to find the actual content of caffeine in the test preparations. The results are shown in Table 6.

Analysis of test samples and obtaining of release profiles

The test samples were analyzed one by one, using HPLC. Increments in the caffeine peak heights were referred to the time after which a sample was collected. The percentages of caffeine release from the respective preparations were calculated from the peak heights, using values for standard solutions of caffeine. Using the above information, the caffeine release profiles were plotted for the test preparations (Fig. 5A-H).

Release profiles, showing the percentage release of an active substance from a given drug form vs. time, are an important source of information about the properties of pharmaceutical preparations and their quality. The pharmaceutical availability tests of the selected preparations with caffeine, performed by the present authors, were intended to verify the theory that the release of caffeine from drugs containing guarana extract was extended in time. In the literature, the phenomenon is accounted for by the gradual decomposition of guaranine complexes in the presence of gastric juice. Information on the mild, long-lasting effect of caffeine originating from guarana seeds is habitually provided in leaflets for drugs having a stimulating effect.

Table 3. Results of repeatability (n=10).

	Retention time (min)	Assay of caffeine (μg/ml)
	4.655; 4.649; 4.666; 4.649; 4.659; 4.667; 4.646; 4.651; 4.648; 4.643	10.02; 9.98; 10.01; 10.03; 10.04; 9.99; 10.02; 10.03; 10.03; 10.02
Mean	4.653	10.02
SD	0.008	0.02
RSD [%]	0.178	0.189

n – number of repetitions, SD – standard deviation, RSD – relative standard deviation

Table 4. Intermediate precision (n=6).

Concentration of caffeine (μg/ml)		Precision	
		Intra-day	Inter-day
		10.02; 10.00; 10.05; 10.01; 10.00; 10.04	Day 1. 10.02; 10.00; 10.05; 10.01; 10.00; 10.04
	Mean	10.02	10.02
	S.D.	0.02	0.02
	RSD	0.21	0.21
			Day 2. 10.02; 9.99; 10.04; 9.98; 10.03; 10.04
10	Mean		10.02
	S.D.		0.03
	RSD		0.26
			Day 3. 10.04; 10.01; 10.05; 9.97; 10.04; 10.03
	Mean		10.02
	S.D.		0.03
	RSD		0.29
		25.09; 25.10; 24.95; 24.96; 25.05; 25.06	Day 1. 25.09; 25.10; 24.95; 24.96; 25.05; 25.06
	Mean	25.04	25.04
	S.D.	0.06	0.06
	RSD	0.26	0.26
			Day 2. 25.12; 24.91; 24.97; 25.06; 25.07; 25.12
25	Mean		25.04
	S.D.		0.08
	RSD		0.34
			Day 3. 25.16; 24.90; 24.99; 25.12; 25.09; 25.12
	Mean		26.06
	S.D.		0.10
	RSD		0.39
		50.22; 49.90; 50.14; 49.92; 50.05; 50.18	Day 1. 50.22; 49.90; 50.14; 49.92; 50.05; 50.18
	Mean	50.07	50.07
	S.D.	0.14	0.14
	RSD	0.27	0.27
			Day 2. 50.21; 50.00; 49.85; 50.18; 50.10; 50.20
50	Mean		50.09
	S.D.		0.14
	RSD		0.28
			Day 3. 50.25; 50.12; 49.90; 49.92; 50.05; 50.22
	Mean		50.08
	S.D.		0.15
	RSD		0.29

Table 5. Results of recovery study (n=3).

Drug name	Amount added mg/tablet	Amount recovered mg/tablet	Recovery% ± SD	Mean recovery% ± SD
Apap Extra	32	32.3	100.94 ± 0.03	100.35 ± 0.77
	65	65.4	100.62 ± 0.02	
	97	96.5	99.48 ± 0.03	
Coffepirine	25	25.1	100.40 ± 0.04	100.04 ± 0.62
	50	50.2	100.40 ± 0.05	
	75	74.5	99.33 ± 0.04	
Guarana Caps	50	50.3	100.60 ± 0.05	100.41 ± 0.25
	100	100.5	100.50 ± 0.06	
	150	150.2	100.13 ± 0.07	
Guarana	5	4.95	99.00 ± 0.05	100.28 ± 1.93
	10	10.25	102.5 ± 0.06	
	15	14.90	99.33 ± 0.05	

Table 6. Content of caffeine in the selected preparations.

| Preparation	Declared content of caffeine [mg]	Assay of caffeine [mg]	SD
Diabolo Guarana	45	64.1	6.9
Magne – B6 Active	min. 51	92.2	1.8
Drive Max	30	39.3	1.6
Guaranax	80	107	5
Guarana	min. 27	54.7	5.2
Guarana	10.5	11.0	0.7
Guarana Caps	100	105	5
Etopiryna	50	51.4	3.0
Coffepirine	50	50.6	2.5
Panadol Extra	65	64.4	3.1
Apap Extra	65	65.7	2.5

For drugs with a non-modified release, the duration of pharmaceutical availability tests is preferably 30, 45 or 60 minutes. After that time, a minimum of 80% of their active substance will have been released [9].

In the case of dietary supplements with caffeine originating from guarana, the drug forms are not ones with modified release. The process may be extended because the caffeine-tannins complex is decomposed. Moreover, differences in the active substance release for different forms of pharmaceutical preparations must be taken into account. The test preparations in question were in the form of tablets and capsules.

The pharmaceutical availability tests indicate that the release of caffeine from the preparations was as follows: Apap Extra 97.2±2.4% (release time 25.0±0.0 min); Guaranax 66.8±1.3% (101.7±1.3 min); Guarana (Herbapol) 94.1±1.1% (20.0±0.0 min); Guarana (Walmark) 99.9±5.0% (release time 20.0±0.0 min), Panadol 86.9±0.2% (20.0±0.0 min), Diabolo Guarana 73.5±5.0%

(release time 38.3±2.9 min), Magne B-6 Active 55.4±13.6% (43.3±5.8 min), Drive Max 88.2±1.6% (23.3±2.9 min). For Guarana Caps, pharmaceutical availability was not determined because the dietary supplement failed to decompose in the acceptor fluid (HCl, pH=2).

The test results did not indicate the presence of a caffeine-tannins complex in the dietary supplements containing a guarana seed extract, or any extended or retarded release of caffeine from preparations with a guarana seed extract, which might otherwise be indicative of a gradual release of caffeine from the complex. Differences in the caffeine release profiles for the test preparations are attributable to the properties of the respective drug forms, such as the presence of a coating or gelatin capsule. A research model for *in vitro* conditions does not encompass all the processes taking place in the living body. Therefore, the potential effect of other chemical compounds existing in the guarana seeds on the absorption processes taking place *in vivo* should be considered.
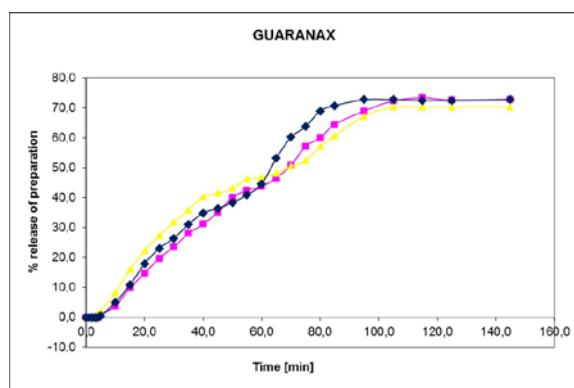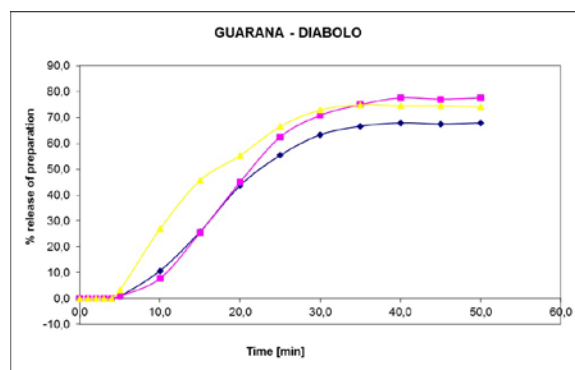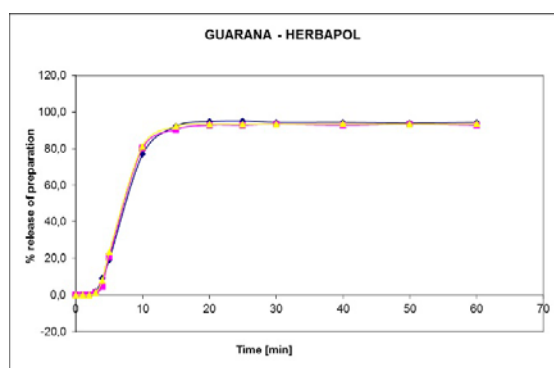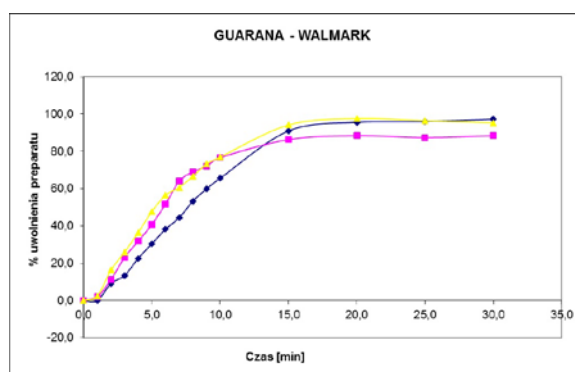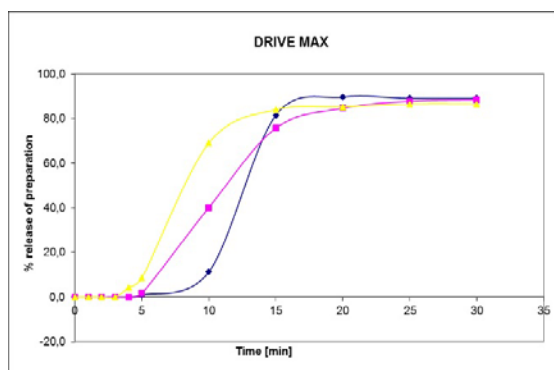
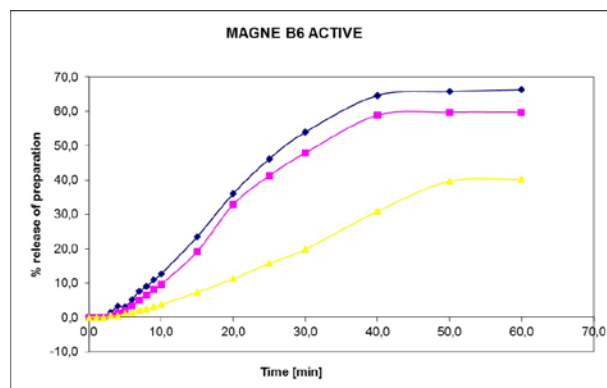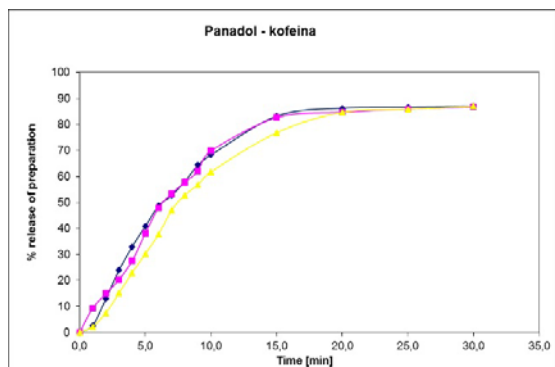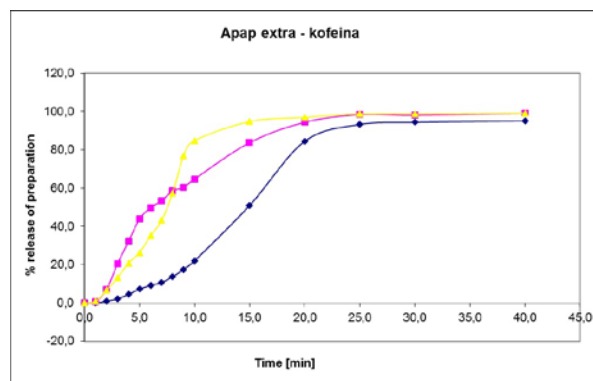**Fig. 5A-H.** Caffeine release profiles for the test preparations.

CONCLUSIONS

The HPLC method for determination of caffeine is characterized by very good precision and accuracy, as well as very good repeatability. The limits of detection and quantification are 3 and 9 μg/ml, respectively.

The pharmaceutical availability test results indicated that caffeine release from the test preparations was from 99.9±5.0% for Guarana (Walmark) (release time 20.0±0.0 min) to 55.4±13.6% for Magne B-6 Active (43.3±5.8 min). For Guarana Caps, pharmaceutical availability was not determined because it failed to decompose in the acceptor fluid (HCl, pH=2).

Findings for the test dietary supplements with a guarana seed extract do not indicate the presence of a caffeine-tannins complex, or any extended or retarded release of caffeine from such preparations, which might otherwise be indicative of the gradual release of caffeine from the complex.

REFERENCES

1. B. Bertil, Notes on the History of Caffeine Use, Methylxanthines, Handbook of Experimental Pharmacology 200, Springer-Verlag Berlin Heidelberg, 2011.
2. M. Zając, E. Pawełczyk, A. Jelińska, Chemia leków, Poznan University of Medical Sciences, Poznań, 2006.
3. A. Smith, *Food Chem. Toxicol.,* **40**, 1243 (2002).
4. E. Mutschler, Farmakologia i Toksykologia, Wydawnictwo Medyczne Urban & Partner, Wrocław, 2004.
5. R. Wierzejska, *Rocznik Państwowego Zakładu Higieny*, **63**, 141 (2012).
6. M.J. Arnaud, Metabolism of caffeine. Garattini S (Editor), Caffeine, coffee and health. New York: Raven Press, 1993, p. 43.
7. http://www.urpl.gov.pl/[12 June 2013]
8. A. Nehlig, *Neurosci. Biobehav. Rev.,* **23**, 563 (1999).
9. S. Janicki, A. Fiebig and M. Sznitowska, Farmacja stosowana. Wydawnictwo Lekarskie PZWL, Warszawa, 2008.

ОСВОБОЖДАВАНЕ НА КОФЕИН ОТ ИЗБРАНИ ФАРМАЦЕВТИЧНИ ПРЕПАРАТИ

М. Шимански[1*], Е.В. Банашчак[1], Р. Сивек[1], М. Франковска[2], А. Шимански[2]

[1] *Департамент по фармакогнозия, Медицински универсритет в Познан, 60-781 Познан, Полша*
[2] *Химически факултет, Faculty of Chemistry, Adam Mickiewicz University, Umultowska 89b, 61-614 Poznań, Poland*

(Резюме)

Референтните лекарства на полския пазар са обект на качествен и количествен анализ, както и на анализ по отношение отделянето на кофеин. За тези анализи са използва високоефективна течна хроматография.

Определянето на фармацевтичната достъпност на кофеина показва следните стойности на освобождаване за различните препарати: Apap Extra 97.2±2.4%; Guaranax 66.8±1.3%; Guarana (Herbapol) 94.1±1.1%; Guarana (Walmark) 99.9±5.0%, Panadol 86.9±0.2%, Diabolo Guarana 73.5±5.0%, Magne B-6 Active 55.4±13.6%, Drive Max 88.2±1.6%. For Guarana Caps фармацевтичната достъпност не е определена поради факта, че субстанцията не се освобождава от капсулите в приемния флуид (HCl, pH=2).

Резултатите от анализите на тези хранителни добавки за кофеиновото им съдържание потвърждават предишни съобщения за различия между реалната концентрация на дадена активна субстанция и декларираната стойност. Анализите на кофеиновите профили на освобождаване показват значителни различия. Анализите не показват наличие на кофеин-танинов комплекс. Не се наблюдава ускорено или забавено освобождаване от препарата, съдържащ екстракт от семена на guarana, което може да е показателно за постепенното освобождаване от такъв комплекс. Разликите в профилите на освобождаване на кофеина от тестовите препарати са показателни за свойствата на лекарствените форми, като филм-таблетки или капсули. Тестовите резултати не са показателни за наличието на кофеин-танинови комплекси, които иначе могат да причинят постепенното освобождаване на кофеина.

Stability studies on solution equilibria of Zn(II) pyrimidine nucleus bases

S. Shobana[1], P. Subramaniam[1,*], J. Dharmaraja[2], S. Arvind Narayan[3], L. Mitu[4]

[1]*Department of Chemistry and Research Centre, Aditanar College of Arts and Science, Virapandianpatnam, Tiruchendur–628 216, Thoothukudi District, Tamilnadu, India*
[2]*Department of Chemistry, Faculty of Science and Humanities, Sree Sowdambika College of Engineering, Chettikurichi, Aruppukottai–626 134, Tamilnadu, India*
[3]*Department of Science and Humanities, Rohini College of Engineering & Technology, Anjugramam, Kanyakumari–629 851, Tamilnadu, India*
[4]*Department of Physics and Chemistry, University of Pitesti, Pitesti–110040, Romania*

pH-metric titrations were carried out to determine the activity and stability of metal chelates of a substituted pyrimidine nucleus base namely 5-Fluorouracil(5-FU: A) and some essential peptide constituents *ie*., amino acids *viz.* glycine(gly; B), L-alanine(ala; B), L-valine(val; B), L-phenylalanine(phe; B). From the titration data, we have obtained satisfactory stability constant values for the metal chelates and the stability decreased with increasing temperature. At different temperatures (300, 310, 320 and 330 ± 0.1 K), the thermodynamic parameters $(\Delta^{\ddagger}G, \Delta^{\ddagger}H$ and $\Delta^{\ddagger}S)$ of the formed species were calculated from the stability constants.

Keywords: pH-Metric titrations, Metal chelates, Stability constant, Thermodynamic parameters.
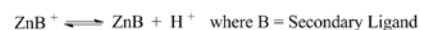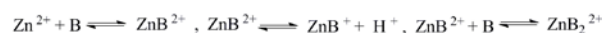
INTRODUCTION

The transition metal(II) ions play a vital role in complexation with nucleus bases and peptides since metal(II) ions which act as cofactors in the enzymatic regulation reactions [1] and as models for transition metal–based chemical nucleases in Nucleic acid and Medicinal chemistry [2, 3]. The chelates derived from nitrogen and oxygen donor atoms with transition metal (II) ions take a crucial place in biological, analytical, industrial and therapeutic applications [4]. The interactions of substituted pyrimidine nucleus bases and peptides with transition metal (II) ions are of considerable biological interest since such mixed chelation in biological fluids of living systems shows a sturdy relation between chelation therapy and pH-metry [5]. Thus, classical coordination and bioinorganic chemistry reaches to modern organometallic and bioorganometallic chemistry [6]. The interaction of a substituted pyrimidine nucleus base (A) with Zn(II) metal ion can be interpreted satisfactorily in terms of the equilibria for the 1:5 stoichiometry;

$$Zn^{2+} + A^- \rightleftharpoons ZnA^+ \; , \quad ZnA^+ + A^- \rightleftharpoons ZnA_2$$
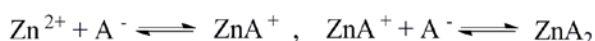
where A = Primary Ligand

The Zn(II)–amino acids (1:5) systems indicate the following equilibria, for which the constants have been measured.

$$Zn^{2+} + B \rightleftharpoons ZnB^{2+} \; , \quad ZnB^{2+} \rightleftharpoons ZnB^+ + H^+ \; , \quad ZnB^{2+} + B \rightleftharpoons ZnB_2{}^{2+}$$

$$Zn^{2+} + B^* \rightleftharpoons ZnB^{2+} \; , \quad ZnB^{2+} \rightleftharpoons ZnB^+ + H^+ \; , \quad Zn^{2+} + B^- \rightleftharpoons ZnB^+$$

$$ZnB^+ \rightleftharpoons ZnB + H^+ \quad \text{where B = Secondary Ligand}$$

The metal transport is possible in biofluids due to the extra stability of the formed mixed chelates [5]. The strong affinity of the metal (II) ions to ligands with nitrogen donor atoms makes peptides interesting targets for chelate formation research [7–9]. In view of this, the present work explores the stability constant and thermodynamic parameters $(\Delta^{\ddagger}G, \Delta^{\ddagger}H$ and $\Delta^{\ddagger}S)$ at 300, 310, 320 and 330 K studies on Zn(II)–5-FU(A)–gly/ala/val/phe(B) metal chelates.

EXPERIMENTAL

Materials

All the chemicals were of extra pure Sigma Aldrich and Fluka (Puriss) products. The solvents used for the physical measurements are of AR grade and are purified by standard methods [10]. Carbonate free sodium hydroxide (NaOH) solution (0.3 M) was prepared from a Titrisol solution (ClNa) (Merck) and its concentration was standardized against standard potassium hydrogen phthalate $(KC_8H_5O_4)$ solution [11]. Zinc (II) perchlorate: $Zn(ClO_4)_2$ solution was prepared and estimated. Doubly distilled CO_2 free water (H_2O) with a specific conductance equal to $(1.81 ± 0.1 \; \Lambda^{-1} \; cm^{-1})$ was used for the preparation of the solution.

---

* To whom all correspondence should be sent:
E-mail: psubramaniam.ac@gmail.com

Multiple pH-metric titrations were carried out for each system as per the previously reported procedure [12–14] and the measurements were restricted within the pH range 2.5–9.0. Above these pH values, the systems undergo hydroxylation to form a precipitate of [Zn(OH)$_2$] which interferes with the measurements. The pH-metric titration curves are shown in Fig. (1).
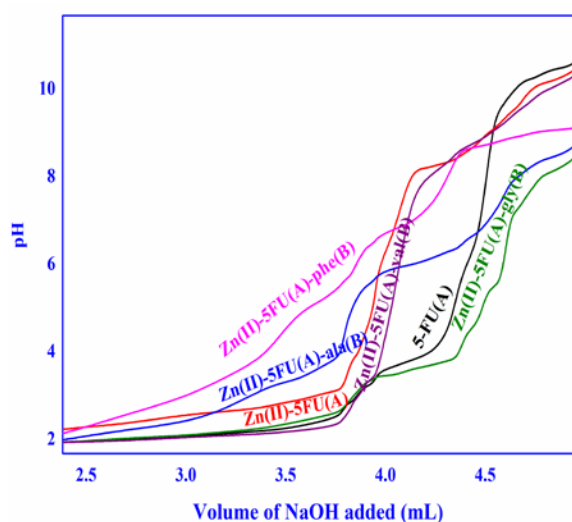

Fig. 1. pH-metric titration curves of 5-FU (0.15 M), Zn(II)–5-FU(A) (1:5), Zn(II)–5- FU(A)amino acids(B) (1:1:1) systems at 310 K and I = 0.15 M (where I = Ionic strength).

These pH-metric data were analysed with the aid of SCOGS (Stability Constants of Generalized Species) computer program [11–14]. The present experimental pH readings were corrected by the Van Uitert and Hass relation [15]. The concentration distribution curves of various metal speciations in solution were analysed by HySS (Hyperquad Simulation and Speciation) program using the calculated stability constant values [16].

RESULTS AND DISCUSSION

pH-metric and mixed equilibria studies

The binary chelate formation of Zn(II) with 5-FU(A) in 1:5 stoichiometry and calculated stability constant values for the binary systems have been reported [12, 13]. In addition to various binary species HA(5-FU–H), ZnA(Zn–5-FU), ZnA$_2$(Zn–5-FU$_2$), HB(gly/ala/val/phe–H), H$_2$B(H–gly/ala/val/phe–H), ZnB (Zn–gly/ala/val/phe) and ZnB$_2$(Zn–gly$_2$/ala$_2$/val$_2$/phe$_2$), the formation of metal chelates of stoichiometry MAB(Zn–5-FU–gly/ala/val/phe) and MAB$_2$ (Zn–5-FU–gly$_2$/ala$_2$/val$_2$/phe$_2$) have also been detected pH-metrically. Above pH > 9.0, the systems undergo hydroxylation, forming hydroxo species [Zn(OH)$_2$].

348

The $\log K \frac{Zn}{ZnAB}$ / $\log K \frac{Zn}{ZnAB_2}$ values obtained at different temperatures in Zn(II)–5-FU(A)–gly/ala/val/phe(B) systems are given in Table (1) and are compared favourably with $\log K \frac{Zn}{ZnA}$ value in Zn(II)–5-FU(A) binary systems. This shows that, the ligand 5-FU(A) in mixed ligand system binds with a Zn(II) ion in a manner similar to its binding in their binary ZnA system *i.e.,* the ligand 5-FU(A) acts as bidentate and binds through deprotonated N$_3$ and C$_4$ carbonyl oxygen atoms. Again, $\log K \frac{Zn}{ZnB}$ / $\log K \frac{Zn}{ZnB_2}$ values in ZnAB/ZnAB$_2$ systems compare favourably with $\log K \frac{Zn}{ZnB}$ / $\log K \frac{Zn}{ZnB_2}$ values in Zn(II)–amino acid systems and this shows that the binding mode of secondary amino acid ligands(B) in mixed chelate ZnAB/ZnAB$_2$ species is similar to its bidentate binding mode in the corresponding binary systems. Thus, the four coordinating positions in Zn (II)–5-FU(A)–gly/ala/val/phe(B) systems would be occupied by the bidentate binding of 5-FU(A) and amino acids(B) respectively. The remaining positions in ZnAB systems would be occupied by two water molecules to form a stable hexa coordinated environment Fig. (2).
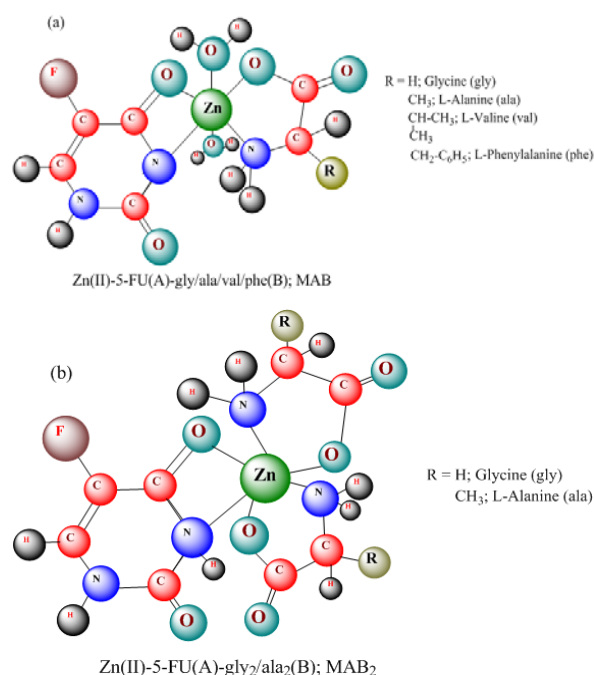

Fig. 2. The proposed structures of (a) MAB and (b) MAB$_2$ species as solution states.

The binding of amino acid(B) ligands in ZnAB species in the presence of 5-FU(A) ligand involves a stable chelate ring. This is also confirmed from the plot of $\log K \frac{Zn}{ZnA}$ / $\log K \frac{ZnB}{ZnAB}$ *vs. pKa* values of 5-FU(A) from which it is evident that all the points due to the binary species fit on a straight line [17]. Also, the points corresponding to the ZnAB metal chelates form a straight line parallel to those of the binary species which is shown in Fig. (3).
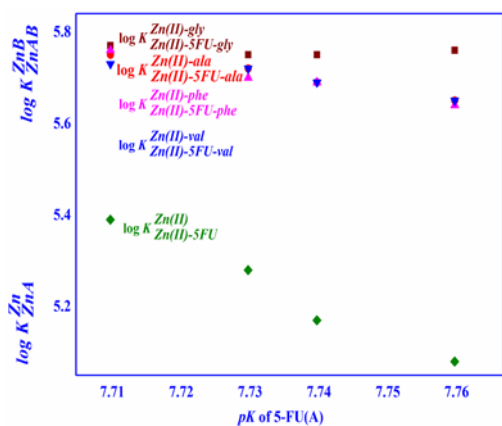

Fig. 3. The plot between $\log K \frac{M}{MA}$ / $\log K \frac{MB}{MAB}$ *vs. pK* values of primary ligand 5-FU(A) at different temperatures

From Table (1), the overall stability of ZnAB metal chelates follows the stability order as: Zn (II)–5-FU–gly > Zn(II)– 5-FU–ala > Zn(II)–5-FU–val > Zn(II)–5-FU–phe. From Table (1), the calculated $\Delta \log K_{ZnAB}$ values for all these systems are more positive compared to the statistically expected value [18] which indicates that the marked stabilities of metal chelates as compared to their binary analogues.

The calculated disproportionation parameter ($\log X$) values for all the species are higher than 2.28 (statistically expected value = + 0.6) which suggest that the preference for the formation of ZnAB metal chelates when compared to the formation of corresponding binary ZnA_2/ZnB_2 species *i.e.*, the inter–ligand and electronic interactions are present in the metal chelates [19].

The $\log X$ values can only indicate the coordination tendency of the secondary ligand towards binary ZnA species, but it fails to explain the stabilizing order of metal–ligand bonds after the species formation. Hence, a new parameter $\log X'$ is considered and the observed $\log X'$ values are greater than 0.3. It suggests that ZnA and ZnB bonds

in mixed chelate systems are stronger than those of binary systems. Also, the percentage relative stabilization *% R.S.* parameter indicates a noticeable stabilization is present in the ZnAB metal chelates than the corresponding binary species [20].

Stability and structure of MAB₂ species

The ZnAB₂ species for the Zn(II)–5-FU(A)– gly/ala(B) systems, the solvent water molecules of ZnAB species would be replaced by a second molecule of glycine/alanine ligands(B). The obtained $\log K \frac{ZnB_2}{ZnAB_2}$ / $\log K \frac{ZnA}{ZnAB_2}$ values in Zn(II)–5-FU–gly/ala systems are comparable with $\log K \frac{Zn}{ZnA}$ and $\log K \frac{ZnA}{ZnB_2}$ values in the binary systems. The ZnAB₂ species in the Zn(II)–5-FU(A)– gly/ala(B) systems would be six coordinated due to the bidentate binding nature of one molecule of 5-FU(A) and two molecules of gly/ala(B) ligands respectively. The calculated $\Delta \log K_{ZnAB_2}$ values are more positive while compared to the statistically expected values indicating the enhanced stabilities for ZnAB₂ systems [19, 20].

Species distribution diagram

The speciation diagram for Zn(II) metal chelate systems, taken as a representative pyrimidine amino acid, is given in Fig. (4). The deprotonated Zn(II)–5-FU(A)–gly(B) species (M:A:B = 1:1:1) attains a maximum concentration of 61 % at pH 6.3. The log β value of this species is 10.50 at 310 K with a *% R.S.* value of 9.89. The species Zn(II)–5-FU(A)– ala(B) starts to form at pH ~3.4 and with increasing pH, its concentration increases reaching the maximum of 66% at a pH ~ 6.4. The MAB species of Zn(II)–5-FU(A)–val(B) and Zn(II)–5-FU(A)– phe(B) metal chelate systems were found with maximums of 63 % and 64 % at pH 7.1 and 6.4 respectively.

In addition, the ZnAB₂ species is formed with gly/ala(B) and the formation starts above a pH of 7.2. It has been found that their percentage of formation increases with the pH in the range 7.2–8.4 and reaches saturation values at only *ca.* 17.12–18.31 % of the total of Zn(II) ions.

Effect of temperature and thermodynamic parameters

Determination of the thermodynamic parameters ($\Delta^{\ddagger}G$, $\Delta^{\ddagger}H$ and $\Delta^{\ddagger}S$) relative to the formation of metal chelates for binary Zn(II) systems are given in Table (2) and are shown in Fig. (5).

Table 1. Stability constant and stabilization effects of the metal chelates for Zn(II)–5-FU(A)–gly, ala, val and phe(B) systems in an aqueous medium at different temperatures in $I = 0.15$ M (NaClO$_4$)

Parameters	Stability constant values at different temperature															
	300 K				310 K				320 K				330 K			
	gly	ala	val	phe	gly	ala	val	phe	gly	ala	val	phe	gly	ala	val	phe
$\log\beta_{ZnAB}$	10.63(4)	10.46(3)	10.16(7)	10.02(7)	10.50(3)	10.36(3)	10.06(3)	9.93(6)	10.38(4)	10.27(5)	9.97(7)	9.84(8)	10.29(6)	10.19(7)	9.87(4)	9.75(5)
$\log\beta_{ZnAB_2}$	14.91(5)	14.65(7)	--	--	14.71(6)	14.54(7)	--	--	14.56(5)	14.44(6)	--	--	14.40(6)	14.34(5)	--	--
$\log K^{ZnA}_{ZnAB}$	5.24	5.07	4.77	4.63	5.22	5.08	4.78	4.65	5.21	5.10	4.80	4.67	5.21	5.11	4.79	4.67
$\log K^{ZnB}_{ZnAB}$	5.76	5.65	5.64	5.65	5.75	5.69	5.69	5.69	5.75	5.72	5.70	5.72	5.77	5.75	5.76	5.73
$\log K^{ZnA}_{ZnAB_2}$	9.52	9.26	--	--	9.43	9.26	--	--	9.39	9.27	--	--	9.32	9.26	--	--
$\log K^{ZnB_2}_{ZnAB_2}$	5.93	5.82	--	--	5.85	5.80	--	--	5.84	5.78	--	--	5.80	5.75	--	--
$\log K^{ZnAB}_{ZnAB_2}$	4.28	4.19	--	--	4.21	4.18	--	--	4.18	4.17	--	--	4.11	4.15	--	--
$\Delta\log K_{ZnAB}$	0.37	0.26	0.25	0.26	0.47	0.41	0.41	0.41	0.58	0.55	0.53	0.55	0.69	0.67	0.68	0.65
$\Delta\log K_{ZnAB_2}$	0.54	0.43	--	--	0.57	0.52	--	--	0.67	0.61	--	--	0.72	0.67	--	--
$\log X_{Zn}$	2.59	2.40	2.32	2.28	2.60	2.44	2.41	2.38	2.63	2.47	2.48	2.44	2.70	2.51	2.54	2.49
$\log X'_{Zn}$	1.46	1.35	1.34	1.35	1.49	1.43	1.43	1.43	1.51	1.48	1.46	1.48	1.57	1.55	1.56	1.53
%RS	7.60	5.41	5.53	5.95	9.89	8.71	9.38	9.67	12.53	12.09	12.41	13.35	15.27	15.09	16.55	16.17

Standard deviations are given in parentheses   [Error limit: $\pm (0.02 - 0.08)$
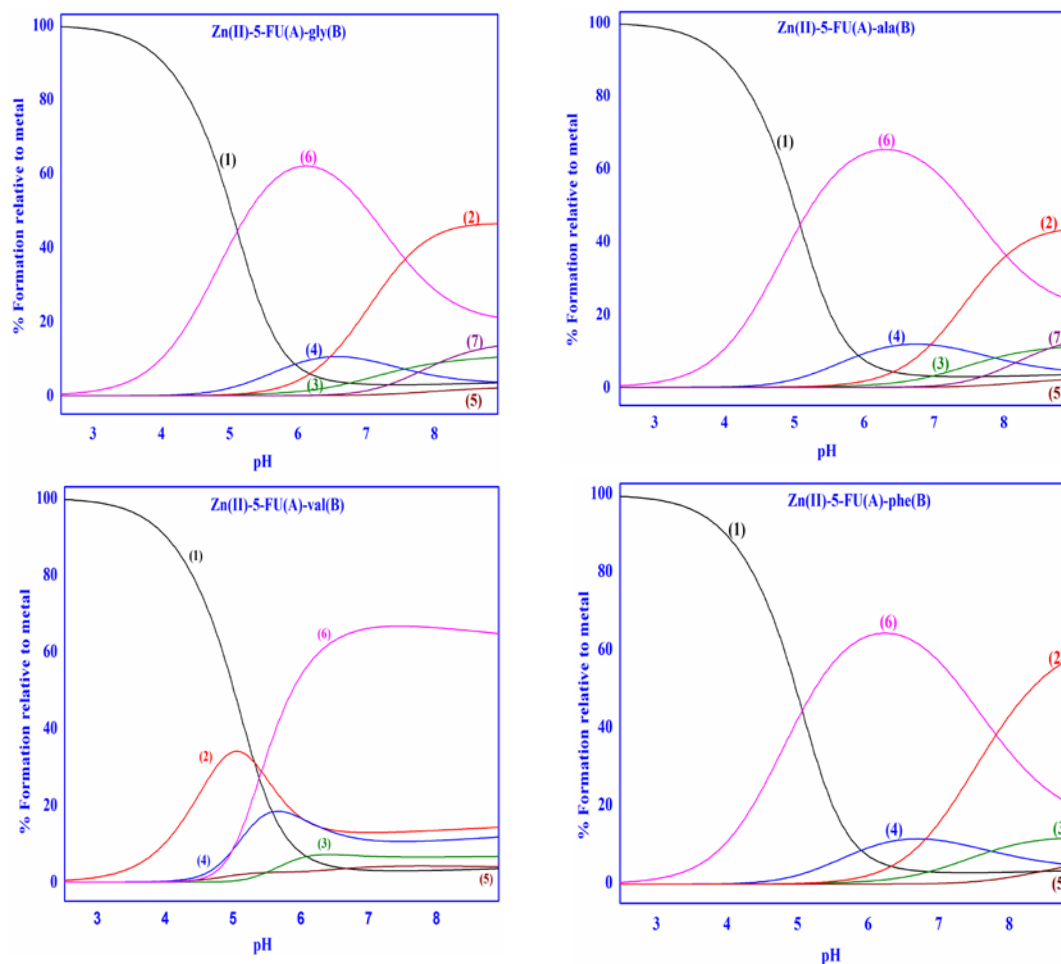

Fig. 4. Species distribution diagrams of Zn(II)–5-FU(A)–gly/ala/val/phe(B) chelates(1:1:1) at 300 K in aqueous medium (1) free Zn(II) ion, (2) Zn(II)–A, (3) Zn(II)–A$_2$, (4) Zn(II)–B, (5) Zn(II)–B$_2$, (6) Zn(II)–AB and (7) Zn(II)–AB$_2$ species.

Table 2. Thermodynamic parameters for binary systems of Zn(II)–5-FU(A) and Zn(II)–gly/ala/val/phe(B) and Zn(II)–5-FU(A)– gly/ala/val/phe(B) metal chelates.

System	Species	$-\Delta^{\ddagger}G$ (kJ mol^{-1}) Temperature (K)				$-\Delta^{\ddagger}H$ (kJ mol^{-1})	$\Delta^{\ddagger}S$ (J K^{-1} mol^{-1}) Temperature (K)			
		300	310	320	330		300	310	320	330
Zn(II)–5-FU(A)	HA	44.58	45.94	47.36	48.72	38.16	21.38	25.10	28.76	31.99
	H$_2$A	–	–	–	–	–	–	–	–	–
	ZnA	30.96	31.34	31.68	32.10	19.72	37.46	37.48	37.36	37.51
	ZnA$_2$	55.66	56.63	57.66	58.64	25.77	99.63	99.53	99.64	99.51
Zn(II)–gly(B)	HB	56.12	56.86	56.86	56.68	50.82	17.68	19.51	18.88	17.76
	H$_2$B	69.22	69.68	70.83	70.83	52.71	55.02	54.75	55.08	54.91
	ZnB	27.97	28.19	28.37	28.56	22.17	19.34	19.43	19.36	19.36
	ZnB$_2$	51.58	52.59	53.43	54.34	24.24	91.14	91.45	91.21	91.21
Zn(II)–ala(B)	HB	57.67	57.69	58.12	58.83	48.51	30.53	29.62	30.10	31.25
	H$_2$B	71.11	72.12	73.04	73.80	44.13	89.95	90.29	90.33	89.92
	ZnB	27.63	27.72	27.88	28.05	23.32	14.36	14.11	14.24	14.34
	ZnB$_2$	50.72	51.88	53.06	54.28	15.18	118.46	118.37	118.37	118.46
Zn(II)–val(B)	HB	58.07	58.41	59.13	59.58	42.86	50.70	50.14	50.82	50.67
	H$_2$B	72.72	73.90	74.57	75.57	45.09	92.12	92.94	92.13	92.38
	ZnB	25.76	25.94	26.16	25.97	25.77	0.64	0.54	1.22	0.60
	ZnB$_2$	47.73	48.49	49.32	50.04	24.45	77.61	77.56	77.72	77.55
Zn(II)–phe(B)	HB	54.51	54.73	54.90	55.48	45.38	30.42	30.14	29.73	30.58
	H$_2$B	68.70	69.27	70.34	71.21	42.51	87.30	86.32	86.97	86.97
	ZnB	25.10	25.17	25.24	25.40	22.19	9.70	9.60	9.54	9.72
	ZnB$_2$	46.36	47.13	47.98	48.84	19.51	89.48	89.09	88.95	88.88
Zn(II)–5-FU(A)–gly(B)	ZnAB	61.06	60.08	58.56	57.56	21.64	131.41	143.35	133.92	135.03
	ZnAB$_2$	85.65	84.15	83.11	75.07	31.86	179.28	245.47	169.11	174.74
Zn(II)–5-FU(A)–ala(B)	ZnAB	62.32	61.49	59.71	58.94	17.08	131.25	143.27	133.96	135.14
	ZnAB$_2$	87.31	86.30	87.73	82.01	19.51	178.88	215.46	173.11	162.11
Zn(II)–5-FU(A)–val(B)	ZnAB	63.60	62.93	61.08	60.29	18.19	131.13	243.27	134.87	135.02
Zn(II)–5-FU(A)–phe(B)	ZnAB	89.21	88.48	82.36	72.60	17.05	179.22	215.51	178.90	188.44

The calculated $\Delta^{\ddagger}H$ and $\Delta^{\ddagger}S$ values can be considered as the sum of two contributions such as the release of solvent (H$_2$O) molecules and metal–ligand bond formation. From Table (2), the abnormal high positive $\Delta^{\ddagger}S$ values of the binary systems are consistent with the hypothesis that a large number of water molecules are released upon complexation [19, 20].

The thermodynamic parameters for all the mixed ligand ZnAB and ZnAB$_2$ systems are given in Table (2). A negative $\Delta^{\ddagger}G$ values for all these complexes suggest the complexation process is spontaneous [17–20]. The negative $\Delta^{\ddagger}H$ values show that the chelation process is exothermic and the complexation process favorable at very low temperature. All the species show positive $\Delta^{\ddagger}S$ values which suggest that the complexation of the 5-FU(A) ligand with a Zn(II) ion in the presence of amino acid(B) ligands is entropically favorable.
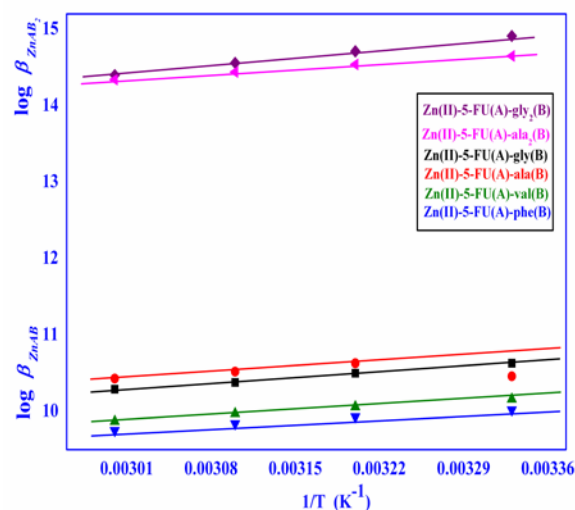

Fig. 5. The Van't Hoff plot of $\log \beta_{MAB}$ values of Zn(II)–5-FU–gly/ala/val/phe(B) and $\log \beta_{MAB_2}$ values of Zn(II)–5-FU(A)–gly$_2$/ala$_2$ systems *vs.* 1/T for MAB and MAB$_2$ mixed chelates.

351

Electronic absorption spectra

The diamagnetic nature of the Zn(II) ion does not show any d–d transition in the visible region. However, the Zn(II)–5-FU(A)–gly, ala, val and phe(B) metal chelates show only one band at 26381 (379 nm), 26246 (381 nm), 26455 (378 nm) and 26372 cm^{-1} (379 nm) respectively in the UV region due to L→M charge transfer (LMCT) transition, which corresponds to a six–coordinated distorted octahedral environment around the Zn(II) ion with two water molecules present in the *z*–axes of the cartesian coordinate [21].

CONCLUSION

The solution equilibria studies of Zn(II)–5-FU(A)–gly/ala/val/phe(B) metal chelates in an aqueous medium at different temperatures (300, 310, 320 and 330 ± 0.1 K) have been studied at a constant ionic strength (I = 0.15 M). The percentage distribution of various binary and metal chelate species in the solution state on the basis of various equilibrium data have shown that ZnAB metal chelates have a higher stability than other species formed. Moreover, the amino acids gly(B) and ala(B) have found to form moderately stable ZnAB$_2$ species in addition to the most stable ZnAB species. The thermodynamic factors such as $\Delta^{\ddagger}G$, $\Delta^{\ddagger}H$ and $\Delta^{\ddagger}S$, and the binding nature of ligands in terms of $\Delta \log K$ have also been determined along with the $\log X$ statistical parameter.

REFERENCES

1. S. A. Rahim, S. Hussain, M. Farooqui, *Chem. Science Trans.,* **4**, 176 (2015).
2. J. Mosquera, M. I. Sanchez, J. L. Mascaren aS, M. Eugenio Vazquez, *Chem. Commun.*, **51**, 5501 (2015).
3. A.T. Abdelkarim, *International Journal of Pharma Sciences.,* **5**, 839 (2015).
4. M. M. Mahrouka, A. T. Abdelkarim, A. A. El-Sherif, M. M. Shoukry, *Int. J. Electrochem. Sci.*, **10**, 456 (2015).
5. V. Shalini, S. Dharmveer, K. Rajendra, S. Brajesh Kumar, V. Krishna, *Res. J. Chem. Sci.,* **5**, 42 (2015).
6. W. Beck, *Z. Naturforsch., B: Chem. Sci.*, **64b**, 1221 (2009).
7. M. S. Aljahdali, A. T. Abdelkarim, A. A. El-Sherif, M. M. Ahmed, *J. Coord. Chem.*, **67**, 870 (2014).
8. A.T. Abdelkarim, A. A. El-Sherif, *Eur. J. Chem.*, **5**, 328 (2014).
9. M. S. Aljahdali, A. T. Abdelkarim, A. A. El-Sherif, *J. Solution Chem.*, **42**, 2240 (2013).
10. D. D. Perrin, W. L. F. Armarego, D. R. Perrin, Purification of Laboratory Chemicals, Pergamo Press, Oxford, 1980.
11. G. Gran, *Analyst*, **77**, 661 (1952).
12. S. Shobana, J. Dharmaraja, S. Selvaraj, *Spectrochim. Acta*, **107**, 117 (2013).
13. S. Shobana, P. Subramaniam, J. Dharmaraja, S. Arvindnarayan, *Inorg. Chim. Acta,* **435**, 244 (2015).
14. J. Dharmaraja, P. Subbaraj, T. Esakkidurai, S. Shobana, S. Raji, *Acta Chim. Slov.*, **61**, 803 (2014).
15. L. G. Van Uitert, C. G. Haas, *J. Am. Chem. Soc.*, **75**, 451 (1953).
16. L. Alderighi, P. Gans, A. Ienco, D. Peters, A. Sabatini, A. Vacca, A., *Coord. Chem. Rev.*, **184**, 311 (1999).
17. H. Sigel, *Chem. Soc. Rev.*, **22**, 255 (1993).
18. H. Sigel, *Angew. Chem. Int. Ed.*, **14**, 394 (1975).
19. H. Sigel, IUPAC Coordination Chemistry–20, D. Banerjea (Ed.), Pergamon Press, Oxford, New York, 27 1980.
20. R. Thanavelan, G. Ramalingam, G. Manikandan, V. Thanikachalam, *J. Saudi Chem. Soc.*, **18**, 227 (2014).
21. M. Zaky, M. Y. El-Sayed, S. M. El-Megharbel, S. A. Taleb, M. S. Refat, *Bulgarian Chem. Commun.*, **47**, 105 (2015).

ИЗСЛЕДВАНИЯ НА СТАБИЛНОСТТА НА РАВНОВЕСИЕТО В РАЗТВОРИ НА Zn(II)-КОМПЛЕКСИ С ПИРИМИДИНОВИ БАЗИ

С. Шобана[1], П. Субраманиам[1,*], Дж. Дхармараджа[2], С. Арвинд Нараян[3], Л. Миту[4]

[1]*Департамент по химия с Изследователски център, Колеж „Адинатар" за изкуство и наука, Вирапандианпатнам, Тиручендур–628 216, Тамил Наду, Индия*

[2]*Департамент по химия, Факултет за наука и хуманитарни дейности, Колеж „Сри Саудамбика" по инженерство, Четикуричи, Арупукотай – 626 134, Тамул Наду, Индия*

[2]*Департамент по наука и хуманитарни дейности, Колеж „Рохини" по инженерство и технологии, Анджуграман, Канякумари–629 851, Тамул Наду, Индия*

[4]*Департамент по физика и химия, Университет в Питещ, Питещ –110040, Румъния*

(Резюме)

Използвано е pH-метрично титруване за определяне на активността и стабилността на метални хелати на заместени пиримидинови бази т.е. 5-флуороацил(5-FU: A) и някои есенциални пептидни компоненти, т.е. аминокиселини: глицин (gly; B), L-аланин (ala; B), L-валин (val; B), L-фенилаланин (phe; B). От данните от титруването ние получихме задоволителни стойности за стабилитетните константи на метални хелати, като стабилността намаляваше с повишаването на температурата. От тези стабилитетни константи са изчислени термодинамичните параметри на изследваните съединения $(\Delta^{\ddagger}G, \Delta^{\ddagger}H$ и $\Delta^{\ddagger}S)$ при различни температури (300, 310, 320 и 330 ± 0.1 K).

Liquid chromatography-electrospray ionization-tandem mass spectrometry (LC-ESI-MS/MS) analysis of *Russelia equisetiformis* extract

M. Riaz[1]*, N. Rasool[2]*, M. Iqbal[3], A. Tawab[3], F. E-Habib[3], A. Khan[4], M. Farman[5]

[1]*Department of Chemistry, University of Sargodha, Women Campus, Faisalabad, Pakistan*
[2]*Department of Chemistry, Government College University, Faisalabad-38000, Pakistan*
[3]*Health Biotechnology Division, National Institute for Biotechnology and Genetic Engineering, P. O. Box 577, Jhang Road, Faisalabad 38000, Pakistan*
[4]*Department of Chemistry, COMSATS Institute of Information Technology, Abbottabad 22060, Pakistan*
[5]*Department of Chemistry, Quaid-I-Azam University, Islamabad 45320, Pakistan*

Plants produce phytochemicals to defend themselves from attacks of microorganisms. The presence of phytochemicals in *Russelia equisetiformis* was established by liquid chromatography-electrospray ionization-tandem mass spectrometry (LC-ESI-MS/MS). The plant material was extracted with methanol and analyzed by LC-ESI-MS/MS. This analysis revealed the presence of mostly antioxidant phenolic phytochemicals such as chlorogenic acid (1), methyl protocatechuate (2), *p*-coumaric acid (3), 4-hydroxybenzoic acid (4), gallic acid (5), caffeic acid (6), caftaric acid (7), syringic acid (8), and catechin (9). These results illustrate that the methanolic extract of *Russelia equisetiformis* can be used as a nutraceutical against oxidative stress inducing ailments.

Keywords: *Russelia equisetiformis,* ESI-MS/MS, methyl protocatechuate, caffeic acid, syringic acid, catechin

INTRODUCTION

Plants have been known to be the richest source of natural antioxidants and antimicrobial compounds [1,2]. In view of the importance of the plants as remedy for diseases, there is a need of proper evaluation of plants for their biological and phytochemical properties [3]. In medicinal plants, phenolic compounds are a large and diverse group of molecules, which include various families of phytochemicals. Phenolics are the most abundant secondary metabolites such as phenolic acids, condensed tannins, flavonoids, and lignins. All these phytoconstituents are involved in many processes in plants and animals. Among other phytoconstituents the phenolics and flavonoids are most interesting because of their various roles in plants protection, as well as in human health [4]. In plants, phenolics and flavonoids play several functions in flowers, seed pigmentation, fertility, reproduction, and in different reactions to defend against abiotic stresses like ultra violet light or biotic stresses such as pathogen attacks [5]. The phytochemicals found in plants are organic biomolecules known as naturally occurring antibiotics [6]. The synthetic antioxidants like butylated hydroxyanisol, butylated hydroxytoluene, and propyl gallate are used as food antioxidants but these antioxidants have adverse effects on health causing degenerative diseases and cancer [7].

Scrophulariaceae is a family of flowering plants and consists mostly of herbs or small shrubs, and rarely trees. The plants are annual herbs with flowers having bilateral, or rarely, radial symmetry [8]. This family also includes medicinal plants [9].

Russelia equisetiformis (Firecracker) is an evergreen, perennial shrub with an attractive look. Under optimum cultivation conditions, firecracker plants produce distinguished blossoms. *Russelia equisetiformis* is easily propagated from rooted cuttings. It grows up to four feet with red flowers, and much reduced leaves. *Russelia equisetiformis* is traditionally used as a medicinal plant and is considered to have analgesic, anti-inflammatory and membrane stabilizing ability [10]. We already analyzed plant extracts for antioxidant and antimicrobial properties [11]. In order to further extend the study, in this work the presence of secondary metabolites was evaluated by LC-ESI-MS/MS. The latter was carried out to analyze the extract of *Russelia equisetiformis* in order to ascertain the chemistry of secondary metabolites. This analysis may highlight the potential of *Russelia equisetiformis extracts*.

MATERIALS AND METHODS

The research work presented in this paper was conducted at the Department of Chemistry, Government College University, Faisalabad, Pakistan and the liquid chromatography-electrospray ionization-tandem mass spectrometry (LC-ESI-MS/MS) assay was carried out at the

* To whom all correspondence should be sent:
E-mail: riaz_453@yahoo.com; nasirhej@yahoo.co.uk

Health Biotechnology Division, National Institute for Biotechnology and Genetic Engineering, Jhang Road, Faisalabad, Pakistan.

General Procedure

Collection of Plant Material

The whole plants of *Russelia equisetiformis* belonging to the family *Scrophulariaceae* were collected by a team from the University of Agriculture, Faisalabad, Pakistan. The plant was identified by Dr. Mansoor Hameed (Taxonomist), Department of Botany, University of Agriculture, Faisalabad, Pakistan. A voucher specimen (No. 420) was deposited in the herbarium of the above department.

Extraction of phenolic compounds from Russelia equisetiformis for liquid chromatography-electrospray ionization-tandem mass spectrometry (LC-ESI-MS/MS) analysis

Phenolic compounds in *Russelia equisetiformis* sample were extracted according to the already reported method [12] with minor modifications. 1.0 g of plant sample was mixed with 20 mL of absolute methanol for 10 min. After centrifugation at $2500 \times g$ for 10 min, the supernatant was removed. The extraction was repeated thrice. Supernatants were combined, evaporated at 45°C to dryness using a rotary evaporator. The extract was stored at 4°C until use.

Analysis by liquid chromatography-electrospray ionization-tandem mass spectrometry (LC-ESI-MS/MS)

The phenolics in *Russelia equisetiformis* were analyzed by liquid chromatography combined with electrospray ionization mass spectrometry (LC-ESI-MS). The plant extract was filtered through a 0.45 µm membrane before analysis. Separation of phenolic compounds was performed on a Surveyor Plus HPLC system equipped with Surveyor Auto (Thermo Scientific, San Jose, CA, USA). The pump was equipped with a Luna RP C-18 analytical column (4.6×150 mm, 3.0 µm particle size) (Phenomenex, USA). Elution solvent consisted of LC-MS grade methanol and acidified water (0.5% formic acid v/v) as the mobile phases A and B, respectively. Solvent elution was performed in a gradient system running at a flow rate of 0.3 mL/min. The gradient elution was programmed as follows: from 10% to 30% A & 90 to 70% B from 0 to 10 min followed by 30 to 50% A & 70 to 50% B in the next 20 min. This flow was maintained till

the end of analysis. 20 min re-equilibration time was used after each analysis. The column was maintained at 25°C and the injection volume was 5.0 µL. The effluent from the HPLC column was directed to the electron spray ionization mass spectrometer (LTQXL[TM] linear ion trap Thermo Scientific, River Oaks Parkway, USA). The mass spectrometer was equipped with an ESI ionization source. Parameters for analysis were set using negative ion mode with spectra acquired over a mass range from *m/z* 260 to 800. The optimum values of the ESI-MS parameters were: spray voltage, +4.0 kV; sheath gas and auxiliary gas 45 and 5 units/min, respectively; capillary temperature 320°C; capillary voltage, -20.0 V, and tube lens voltage -66.51 V. The accurate mass spectral data of the molecular ions were processed through the Xcalibur Software (Thermo Fisher Scientific Inc, Waltham, MA, USA).

RESULTS AND DISCUSSION

Plants are being used throughout the history in conventional medicine. At present, about two-thirds to three-quarters of the world population is dependent on plant-based medicines for the treatment of many diseases. Therefore, there is an increasing interest to study the phytochemical and biological properties of plants. Phytochemical contituents found in plants have prominent pharmacological properties. In the present work, *Russelia equisetiformis* was analysed for phenolic compounds by LC-ESI-MS/MS.
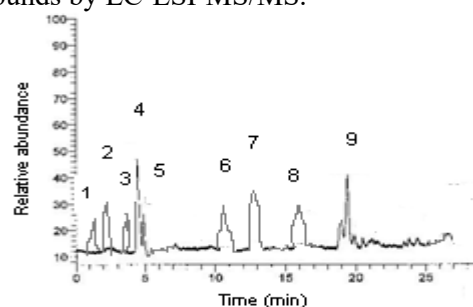

Fig. 1. The chromatogram of *Russelia equisetiformis* sample analyzed by liquid chromatography

The LC-ESI-MS/MS analysis (Figures 1-6) of *Russelia equisetiformis* sample showed the presence of phytochemicals such as chlorogenic acid (1), methyl protocatechuate (2), *p*-coumaric acid(3), 4-hydroxybenzoic acid (4), gallic acid (5), caffeic acid (6), caftaric acid (7), syringic acid (8), and catechin (9) (Table 1). The structures of the compounds identified are shown in Figure 2.

Table 1. Chemical compounds in *Russelia equisetiformis* extract determined by liquid chromatography-electrospray ionization-tandem mass spectrometry (LC-ESI-MS/MS)

Retention time (min)	Major MS/MS m/z (intensity)	Molar mass	Name of identified compound
2.14	353.1 (45), 191.1(42), 179(62), 173(100)	354.31	Chlorogenic acid (1)
3.10	167.1 (30), (152.1 (100), 108.0 (11)	168.12	Methyl protocatechuate (2)
3.66	163.05 (45), 119(100)	164.16	*p*-Coumaric acid (3)
4.60	137.25 (20), 121(60), 93(90)	138.12	4-Hydroxybenzoic acid (4)
4.70	169.15 (40), 125(100)	170.12	Gallic acid (5)
10.40	179.3 (100) 161.1 (10), 135.1 (27)	180.16	Caffeic acid (6)
11.80	311.15 (25), 178 (45), 148 (90)	312.22	Caftaric acid (7)
16.20	197.10 (35), 179.10 (60), 135.10 (100)	198.17	Syringic acid (8)
19.81	289.15 (35), 271.2 (15), 245.1 (45)	290.27	Catechin (9)
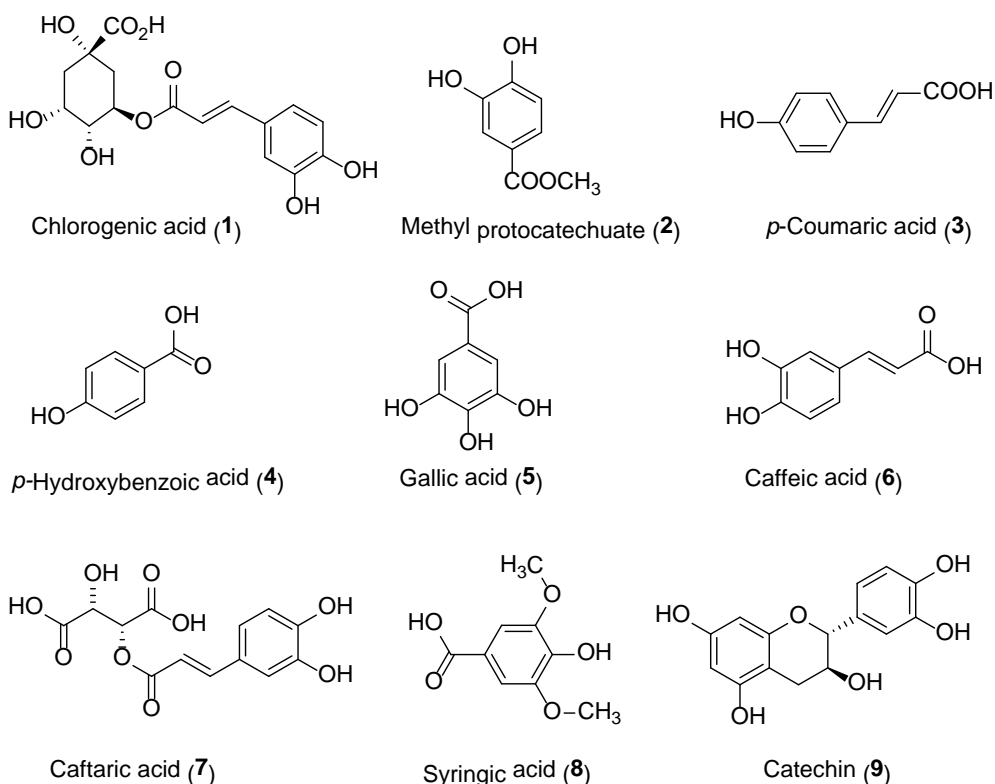
Fig. 2. Structures of the compounds in *Russelia equisetiformis* sample extract analysed by liquid chromatography-electrospray ionization-tandem mass spectrometry (LC-ESI-MS/MS)
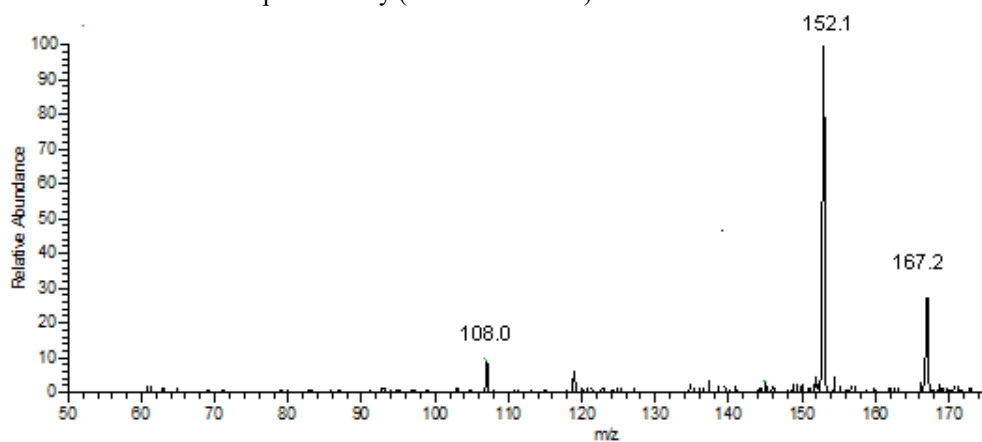

Fig. 3. A representative mass spectrum of methyl protocatechuate (2) in *Russelia equisetiformis* extract analysed by liquid chromatography-electrospray ionization-tandem mass spectrometry (LC-ESI-MS/MS).
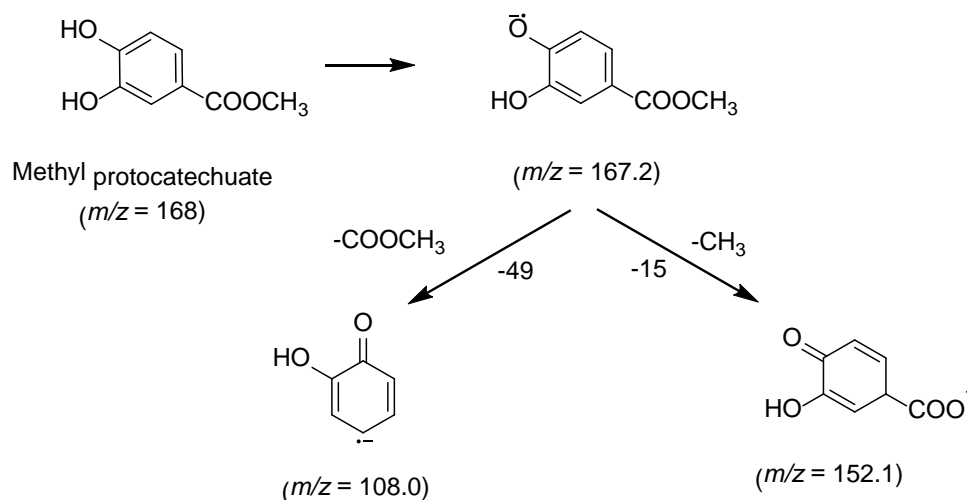
Fig. 4. Fragmentation pattern of the structure of methyl protocatechuate (2) in *Russelia equisetiformis* extract analysed by liquid chromatography-electrospray ionization-tandem mass spectrometry (LC-ESI-MS/MS)

The identification of compounds was made by comparison of retention times with the known standards analysed with the same solvent system and conditions. The ESI-MS/MS spectra of the analysed samples were also compared with the standards and data in the literature.

The presence of methyl protocatechuate (2) was confirmed by comparing the retention time with standards and ESI-MS/MS pattern in the chromatogram (Figure 3). The presence of a peak in the negative mode at *m/z* 167.2 corresponded to the molecular formula $C_8H_8O_4$.

The fragment ion peaks at *m/z* = 152.1 due to loss of CH_3 (–15) and at *m/z* = 108.0 due to loss of $COOCH_3$ (–49) confirmed the presence of methyl protocatechuate (2) (Figure 3).

Compound 6 has a molecular ion peak in negative ion mode at *m/z* = 179.3 which corresponds to the molecular formula of caffeic acid $C_9H_8O_4$, as evident from its mass spectrum

(Figure 5). The fragment ion peak at *m/z* 135.1 was due to the loss of CO_2 (–44). The other fragment ion at *m/z* 161.1 was due to the loss of water molecule (–18). These fragments confirmed the presence of caffeic acid (6) (Figure 6). The use of mass spectrometry coupled to liquid chromatography is ideal for the assay of phenolics found in the plants. The advantage of LC-MS/MS is that separation and structural elucidation of compounds can be obtained in a continuous manner [13]. Ionization by electrospray is one of the extensively used methods for LC-ESI-MS/MS studies [14]. In the ESI negative ion mode, analysis of small molecules containing free carboxyl groups, yields mainly the ion [M-H]⁻, relating to their carboxylate anion [15]. The identification of phenolic compounds in *Russelia equisetiformis* extract was based on chromatograms obtained by HPLC and ESI-MS/MS and comparison with literature data [16].
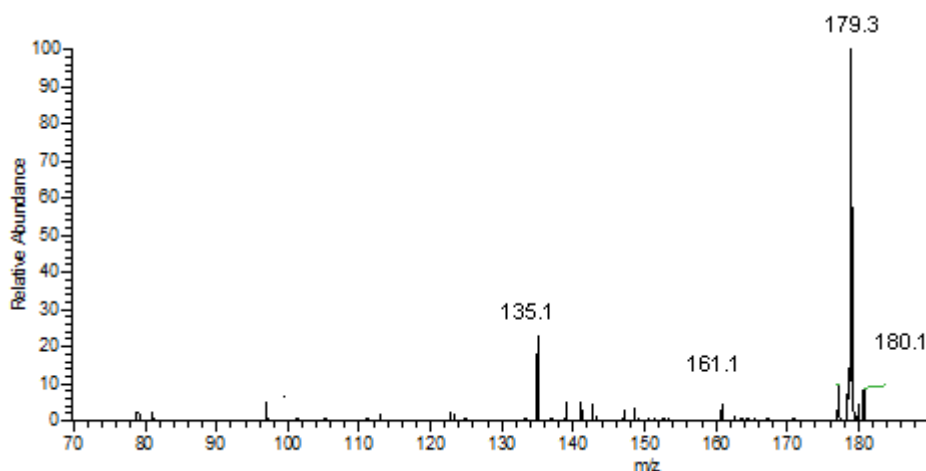

Fig. 5. Mass spectrum of caffeic acid (6) in *Russelia equisetiformis* extract analysed by liquid chromatography-electrospray ionization-tandem mass spectrometry (LC-ESI-MS/MS).
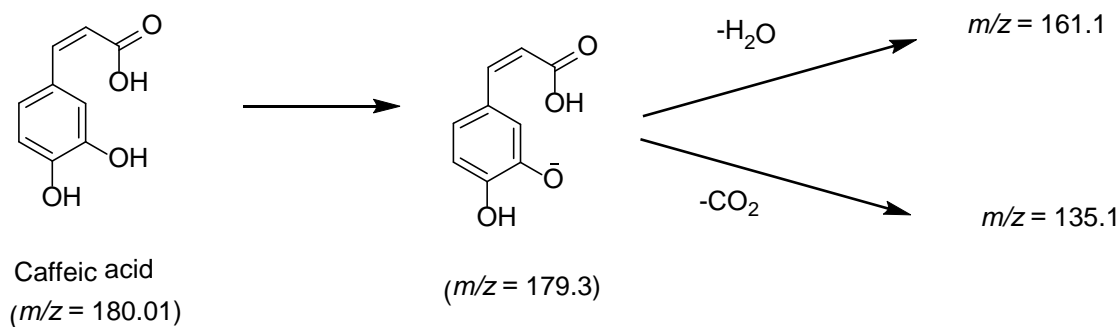
Fig. 6. Representative fragmentation pattern of caffeic acid (6) in *Russelia equisetiformis* extract analysed by liquid chromatography-electrospray ionization-tandem mass spectrometry (LC-ESI-MS/MS)

CONCLUSIONS

The liquid chromatography-mass spectrometry analysis of *Russelia equisetiformis* sample revealed the presence of phytochemicals such as chlorogenic acid (1), methyl protocatechuate (2), *p*-coumaric acid (3), 4-hydroxybenzoic acid (4), gallic acid (5), caffeic acid (6), caftaric acid (7), syringic acid (8), and catechin (9). This analysis may highlight the potential of *Russelia equisetiformis* extracts.

REFERENCES

1. S. Albayrak, A. Aksoy, O. Sagdic, E. Hamzaoglu, *Food Chem.,* **119**, 114 (2010).
2. E. O. Farombi, *Afr. J. Biotechnol.*, **2**, 662 (2003).
3. FAO, Trade in medicinal plants, 1st ed. Food and Agriculture Organization (FAO), United Nations, Rome, Italy, 2004.
4. J.B. Harborne, C.A. Williams, *Phytochem.,* **55**, 481 (1992).
5. G. Forkmann, S. Martens, *Curr. Opin. Biotechnol.,* **12**, 155 (2001).
6. P.R. Seidil, *Annals of the Brazilian Academy of Sciences,* **74**, 145 (2000).
7. S. Iqbal, M.I. Bhanger, F. Anwar, *LWT-Food Science and Technology,* **40**, 361 (2007).
8. R.G. Olmstead, C.W. De-Pamphilis, A.D. Wolfe, N.D. Young, W.J. Elisons, R. P.A., *Am. J. Bot.*, **88**, 348 (2001).
9. S. Ahmad, Flora of the Punjab: Key to genera and species, 1st ed. Published by the Society at Biological Laboratories, Lahore, Pakistan, 1980.
10. E.O. Awe, M. J.M., O.A. Adeloye, S.O. Banjoko, *J. Nat. Prod.,* **2**, 3 (2009).
11. M. Riaz, N. Rasool, I. Bukhari, M. Shahid, F. Zahoor, M. Gilani, M. Zubair, *Afri. J. Microbiol. Res.,* **6**, 5700 (2012).
12. K. K. Adom, R. H. Liu, *J. Agri. Food Chem.,* **50**, 6182 (2002).
13. M. Kallenbach, I.T. Baldwin, G. Bonaventure, *Plant Methods,* **5**, 1 (2009).
14. D.W. Johnson, *Clin. Biochem.,* **38**, 351 (2005).
15. T. Nishikaze, M. Takayama, *International Journal of Mass Spectrometry,* **268**, 47 (2007).
16. G. Dinelli, A.S. Carretero, R.D. Silvestro, I. Marotti, S. Fu, S. Benedettelli, L. Ghiselli, A. F. Gutierrez, *J. Chromatogr. A,* **1216**, 7229 (2009).

АНАЛИЗ НА ЕКСТРАКТ ОТ *Russelia equisetiformis* ЧРЕЗ ТЕЧНА ХРОМАТОГРАФИЯ, СЪЧЕТАНА С ЕЛЕКТРОСПРЕЙ-ЙОНИЗАЦИЯ И МАС-СПЕКТРОМЕТРИЯ (LC-ESI-MS/MS)

М. Риаз[1]*, Н. Расуул[2], М. Икбал[3], А. Тауаб[4], Ф. Е. Хабиб[3], А. Хан[4], М. Фарман[5]

[1]*Департамент по химия, Университет в Саргодха, Дамски кампус, Файсалабад, Пакистан*
[2]*Департамент по химия, Правителствен университет, Файсалабад -38000, Пакистан*
[3]*Отделение по здравна биотехнология, Нацинален институт по биотехнология и генно инженерство, Файсалабад-38000, Пакистан*

[4]*Департамент по химия, Институт по информационни технологии COMSATS, Аботабад 22060, Пакистан*
[5]*1Департамент по химия, Университет Куаид-и-Азам, Исламабад 45320, Пакистан*

(Резюме)

Растенията произвеждат фито-химикали за собствена защита срещу микроорганизмите. Наличието на фито-химикали в *Russelia equisetiformis* е анализирано с помощта на течна хроматография, съчетана с електро-спрей йонизация и мас-спектрометрия. (LC-ESI-MS/MS). Растителната суровина се екстрахира с метанол и се анализира чрез LC-ESI-MS/MS. Анализът разкрива наличието главно на антиоксидантни фенолни фито-химикали, като хлорогенна киселина (1), метул-протокатехат (2), *p*-кумаринова киселина (3), 4-хидроксибензоена киселина (4), галова киселина (5), кафеена киселина (6), кафтарова киселина (7), сирингова киселина (8) и катехин (9). Тези резултати показват, че екстрактите от *Russelia equisetiformis* с метанол може да се използват за неутрализиране на окислителни стресове, причиняващи болести.

Quantification of DEHP into PVC components of intravenous infusion containers and peritoneal dialysis set before and after UV-A treatment

I. Kostić[1*], T. Anđelković[1], D. Anđelković[1], A. Bojić[1], T. Cvetković[2], D. Pavlović[2]

[1]*University of Niš, Faculty of Sciences and Mathematics, Višegradska 33, 18000 Niš, Serbia*
[2]*University of Niš, Faculty of Medicine, Zoran Đinđić Boulevard 80, 18000 Niš, Serbia*

The presence of di-(2-ethylhexyl) phthalate (DEHP) in 8 different parts of plastic medical devices that are used in two important medical procedures was determined and influence of UV radiation on DEHP leaching was investigated. DEHP determination was carried out by gas chromatography – mass spectrometry (GC-MS). The results showed that set for peritoneal dialysis contains DEHP approx. 35% by weight of bag and approx. 37% by weight of tubing. Results obtained for samples from transfusion set showed that Quadruple blood bag and transfer bag contain almost the same amount of DEHP (25.63% and 26.92% by weight, respectively) while SAG-M transfer bag contains lower amount of DEHP (16.07%). All samples of tubing material showed the higher concentration level of DEHP than coupled bags. Very low amount was leached by Peritoneal Dialysis Solution from PVC dialysis bag (3.72 µg L^{-1}), despite the fact that dialysis bag contains DEHP in high concentration level. Obtained concentration of DEHP in CPD solution from Quadruple blood bag is higher than concentration in Peritoneal Dialysis Solution about 10 times (37.04 µg L^{-1}). DEHP was not detected in solution from SAG-M transfer bag. Obtained values are under estimated upper-bound dose of DEHP received by adult patients undergoing procedures of peritoneal dialysis 0.01 mg/kg/day (for adult with average body weight 70 kg) and transfusion as part of surgical procedures 8.5 mg/kg/day. Results obtained after UV treatment showed that UV radiation has a certain influence on leaching of DEHP from samples of PVC medical devices. All investigated samples contained smaller amount of DEHP after UV-A treatment than samples which were not treated by UV radiation.

Keywords: di-(2-ethylhexyl) phthalate (DEHP); medical devices; polyvinyl chloride (PVC); UV radiation

INTRODUCTION

Phthalate diesters (phthalates) may be found in a broad range of industrial products because they are widely used as plasticizers. They are added to plastic polymers (e.g. polyvinyl chloride – PVC) to increase flexibility and softness [1-3]. PVC is used in the production of toys, floors tiles, building materials, clothing, automobiles, cleaning materials, cosmetics and food packaging, industrial tubing, medical devices, *etc.* [4-5]. Due to their widespread use, relatively large amounts of these compounds are released into the environment [6].

In general, PVC medical devices contain up to 40% of plasticizers by weight [7-9]. Di-(2-ethylhexyl) phthalate (DEHP) is the most abundant plasticizer, but other phthalates such as diethyl phthalate (DEP), di-*n*-butyl phthalate (DnBP) and benzylbutyl phthalate (BzBP) can be found in PVC materials [10]. Patients undergoing medical procedures, such as parenteral nutrition support, blood transfusion, hemodialysis, peritoneal dialysis, cardiopulmonary bypass (CPB), are in contact with PVC medical devices which contain DEHP [11]. A various types of medical devices are made from

PVC, such as enteral and parenteral nutritional tubing, infusion and transfusion tubings, blood bags and tube systems for blood cell separation, bags and tubing for peritoneal dialysis [12]. In humans, phthalates are rapidly hydrolyzed to the monoesters and then further metabolized and they can be detected in urine, breast milk, faeces, *etc*. [13]. DBP, BzBP and DEHP are introduced in the list of potentially endocrine disruptors [14]. Some of these health outcomes may be the result of phthalate-induced increases in oxidative stress or inflammation, which have been demonstrated in animal studies [15].

Phthalates are not bound to plastic material therefore phthalates can migrate to the medium that is in contact [14, 16]. Various conditions may enhance the migration of phthalates from PVC medical devices into the surrounding media. It is possible that the content and transfer properties of phthalates may be influenced by optical radiation and temperature change during storage [7, 17].

Estimated upper-bound dose of DEHP received by adult patients can be various for different medical procedures. Relatively high doses of DEHP can be received by patients who are transfused with large volumes of blood and blood products over a short period. A patient undergoing a routine, elective surgical procedure typically receives about

two units of packed red blood cells. Transfusion of this volume of blood will result in a DEHP dose equivalent to the TI value, approximately 0.5 mg/kg/day. The highest estimated daily exposure levels for blood transfusion is 8.5 mg/kg for adult trauma patients. Long-term use of some procedures can result in significant total DEHP exposure [18]. Assuming a patient undergoing continuous ambulatory peritoneal dialysis (CAPD) is dialyzed with 8 L of fluid/day, the upper-bound estimate of the daily dose of DEHP infused into the peritoneum would be on the order of 1 mg/day (0.13 g/ml× 8,000 ml/day × 0.001 mg/g) [19].

Various analytical methods can be used for quantitative determination of DEHP, including HPLC, LC-MS, GC-MS, *etc*. [20] Also, numerous preconcentration methods can be applied, such as solid-phase extraction (SPE), solid-phase microextraction (SPME), headspace solid-phase microextraction (HS-SPME), liquid-phase microextraction (LPME) and dispersive liquid-liquid microextraction (DLLME) [6, 21, 22]. The most conventional liquid-liquid extraction method (LLE) performed with hexane, dichloromethane, ethyl acetate or acetone has recovery values in the range between 70 and 100% and is relatively short and easily performed. Because of that, LLE method for extraction followed with GC-MS seems to be the best choice for sample preparation and detection of phthalates. In this study, a GC-MS method was used for determination of DEHP [12, 23-25].

The aim of this work was DEHP determination in medical devices – dialysis set and transfusion set – based on polyvinyl chloride (PVC), and investigation of UV-A (ultraviolet radiation) effects on DEHP leaching. Quantitative determination of DEHP was performed by total dissolution of plastic material. Determination of DEHP was done by GC-EI-MS as the one of the most common methods for phthalate quantification, due to specificity, sensitivity and availability of instrumental technique.

EXPERIMENTAL

Materials and chemicals

Medical devices were taken from the local Clinical Center Niš, Serbia. Samples consisted of filled plastic bag and tubing from peritoneal dialysis set (Baxter, USA) and bags and tubing from transfusion set (TIANHE Pharmaceutical, China).

DEHP, DBA, hexane and tetrahydrofurane (THF) were purchased from Sigma Aldrich, USA.

Solvents were HPLC grade and screened to determine the DEHP background. Hexane was used as a solvent for stock solutions and working standards.

Preparation of standards

Amount of DEHP standard was accurately weighted out by analytical balance with precision at ±0.00001 g (Kern, Germany) and diluted with *n*-hexane to 5 ml. This solution was labeled as stock solution and was stored in the fridge. Working standard solutions were obtained by diluting of stock solution, obtaining the series of the concentration range from 0.25 to 10 µg ml^{-1}.

All sample manipulation was done avoiding any contact with plastic equipment. Special care was taken to avoid the contamination of solvents with plastic laboratory materials during standards and sample preparation. All glassware was washed with hot water and sodium lauryl sulfate, rinsed with ultrapure deionized water and subsequently thoroughly rinsed with dichloromethane. After cleaning, glassware was sealed with aluminum foil and stored in a clean environment to avoid adsorption of phthalates from the air.

Instrumental analysis

Analysis was carried out by gas chromatography coupled to mass spectrometer (Hewlett Packard 6890 series GC System with autosampler connected with Agilent 5973 Mass Selective Detector (Electron Ionization MSD-EI, single quadrupole). The separation was achieved with 30 m × 0.25 mm × 0.25 µm a non-polar AGILENT DB-5MS column coated with 5% phenyl, 95% dimethylpolysiloxane. The oven temperature was programmed from 65 °C (holding time 1 min) to 220 °C (1 min) at rate of 20 °C min^{-1}, then to 280 °C at rate of 5 °C min^{-1} (4 min). Volume of 1 µL was injected in the splitless mode. Helium was the carrier gas (1.0 ml min^{-1}) and the inlet temperature was 250 °C. The operating temperature of the MSD was 280°C with the emission energy of 70 eV. The MSD was used in the single ion-monitoring (SIM) mode at *m/z* 149. The identification of target compounds was based on the relative retention time, the presence of target ions and their relative abundance. The most abundant ion *m/z* 149 was chosen for quantification of DEHP, with no qualifier ions, due to the simplicity of the matrix. The dwell time was 100 ms. DEHP fragmentation pathways are given in Fig. 1 [26]. Ion *m/z* 185 was chosen as representative ion of DBA internal standard.
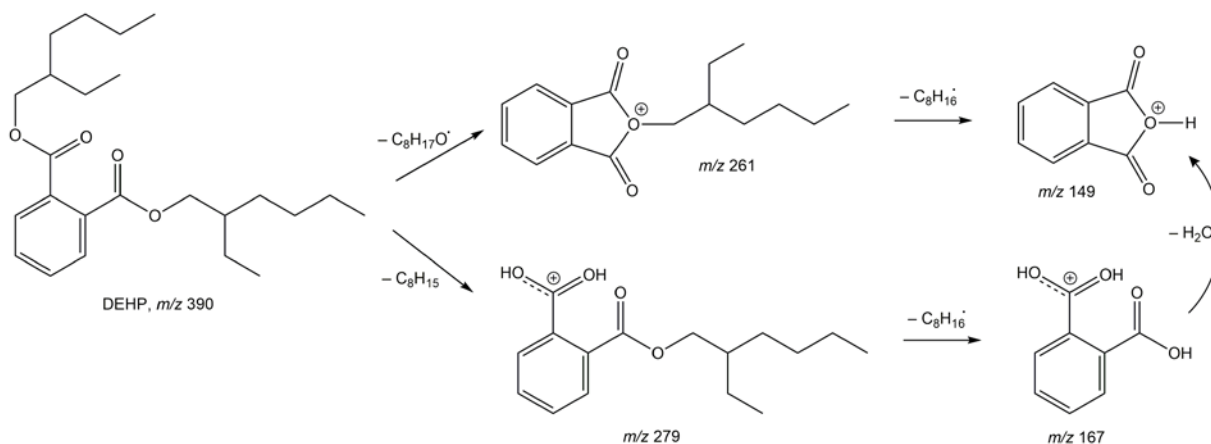
Fig. 1. DEHP fragmentation pathways.

Treatment of solid samples from PVC medical devices

PVC medical devices were kept up in the shade and at room temperature. Some PVC samples were irradiated with UV-A light, using UV-A lamps at 365 nm (PHILIPS, 18w/10 BL, 25 W, G 13), at the distance of 10 cm for 12 hours. After radiation treatment, the samples were stored in shade.

Determination of DEHP in solid samples from PVC medical devices

A PVC sample (0.01 g) was dissolved in 10 ml of THF by soaking overnight at room temperature. Totally dissolved plastic polymer was precipitated by addition of 10 ml of hexane. Obtained solutions showed high level of turbidity and they had to be filtered through the 0.45 μm PTFE filter. After filtering, samples still had a certain level of turbidity and they were centrifuged at 6000 rpm for 3 min to remove it. Then, sample solutions were put into 2 ml vials and DBA was added as internal standard commonly used in phthalate determination. Samples were analyzed by GC-MS.

Determination of DEHP in liquid samples

Individual solutions from investigated bags, usually present in formulations for peritoneal dialysis and blood transfusion were stored in PVC bags at room temperature. The analyzed samples were: 2000 ml solution for peritoneal dialysis (Dianeal® Low Calcium Peritoneal Dialysis Solution with 1.5% dextrose, 538 mg sodium chloride; 448 mg sodium lactate; 18.3 mg calcium chloride; 5.08 mg magnesium chloride; pH 5.2), 63 ml CPD solution from Quadruple blood bag 450 ml (0.299 g citric acid (anhydrous); 2.63 g sodium citrate (dihydrate); 0.222 g monobasic sodium phosphate (monohydrate); 2.55 g dextrose (monohydrate); 100 ml water for injection) and 100 ml solution from SAG-M transfer bag (0.877 g

sodium chloride; 0.0169 g adenine; 0.900 g dextrose (monohydrate); 0.525 g mannitol; 100 ml water for injection). Liquid samples were collected in glass flasks and stored at 4 ºC until analysis. Since the usual shelf-life of investigated solutions is three years, migration rates of DEHP from plastic containers were measured after a period of 36 months in order to determine the maximum possible leached concentration of DEHP before expiration period of the medical product. Each sample with 5 ml of hexane was mixing for 24 hours. The organic layers were transferred to glass vials, internal standard was added and aliquots were injected into GC-MS directly with no clean up stage.

RESULTS AND DISCUSSION

The chromatogram in Fig. 2 shows the separation of DEHP and DBA, as internal standard. Retention times for DBA and DEHP were 9.94 and 18.27 min, respectively.
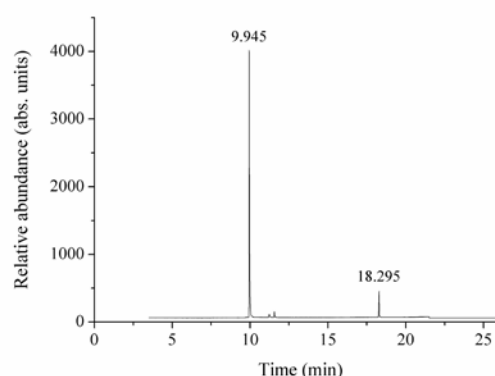

Fig. 2. GC-MS chromatogram of a standard solution containing DEHP (conc. 0.25 μg/ml) and DBA (conc. 1.0 μg/ml); abundance in arbitrary units is given for TIC.
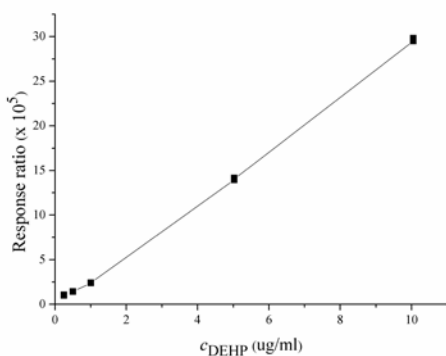
Fig. 3. Analytical curve for DEHP for concentration range 0.25 – 10 µg/ml.

The analytical curve obtained for DEHP within concentration range 0.25 – 10 µg/ml is linear with coefficient of determination of $R^2 = 0.99853$ and linear equation $y = (2.94352\pm0.03017)x - 0.18073\pm0.15241$ (Fig. 3). Limit of quantitation (LOQ) was determined using signal to noise ratio of 10 to 1, for repeated measurements with RSD less than 20%. The obtained LOQ value was 0.05 µg/ml.

The determined DEHP concentration levels, approx. 35% by weight of bag and approx. 37% by weight of tubing from peritoneal dialysis set, are high but expected, bearing in mind that the PVC type of plastic material is used for medical device production. Obtained results are given in Table 1.

Results obtained for samples from transfusion set are given in Table 2 and showed that Quadruple blood bag and transfer bag contain almost the same amount of DEHP by weight (25.63% and 26.92%, respectively) while SAG-M transfer bag contains lower amount of DEHP (16.07%). The determined DEHP concentration levels in tubing material from transfusion set showed that all samples contain more than 30% DEHP by weight. All samples of tubing material from transfusion set showed the higher concentration of DEHP than coupled bags. The most significance difference was found between SAG-M transfer bag and coupled tubing.

Results obtained after UV treatment showed that UV radiation has a certain influence on leaching of DEHP from samples of PVC medical devices. All investigated samples contained smaller amount of DEHP after UV-A treatment than samples which were not treated by UV radiation. Obtained results are given in Table 3.

Table 1. Percentage of DEHP in solid PVC samples of dialysis set before and after UV treatment.

Dialysis set (Baxter)	Total content of DEHP (%)	Total content of DEHP after UV-A treatment (%)
Dialysis bag	35.81±1.55	15.89±0.12
Tubing from dialysis set	37.58±0.78	14.01±0.33

Table 2. Percentage of DEHP in solid PVC samples of transfusion set before and after UV treatment

Transfusion set (Tianhe Pharmaceutical)	Total content of DEHP (%)	Total content of DEHP after UV-A treatment (%)
Quadruple blood bag	25.63±1.34	18.91±0.77
Tubing coupled to Quadruple blood bag	31.27±1.59	17.12±0.55
SAG-M transfer bag	16.07±0.98	4.02±0.15
Tubing coupled to SAG-M transfer bag	31.64±1.33	22.29±0.82
Transfer bag	26.92±0.85	18.72±0.24
Tubing coupled to transfer bag	35.66±1.87	13.27±0.14

Table 3. Amount of leached DEHP from solid samples after UV treatment (%)

Sample	Amount of leached DEHP after UV treatment (%)
Dialysis bag	55.63
Tubing from dialysis set	62.72
Quadruple blood bag	26.22
Tubing coupled to Quadruple blood bag	45.25
SAG-M transfer bag	74.98
Tubing coupled to SAG-M transfer bag	29.55
Transfer bag	30.46
Tubing coupled to transfer bag	62.79

Samples from dialysis set showed that UV radiation caused greater leaching of DEHP from samples of tubing than samples of bag. Transfusion set showed that UV-A radiation had greater influence on DEHP leaching from samples of SAG-M transfer bag (> 74%) than from samples of Quadruple blood bag and transfer bag (< 27% and 31%, respectively). Also, UV-A radiation has greater influence on DEHP leaching from samples of tubing coupled to transfer bag (62%), than tubing coupled to Quadruple blood bag (45%) and the lowest influence on DEHP leaching from samples of tubing coupled to SAG-M transfer bag.

The results obtained for DEHP from Peritoneal Dialysis Solution, CPD solution from Quadruple blood bag and solution from Transfer bag are given in Table 4. Very low amount was leached by Peritoneal Dialysis Solution from PVC dialysis bag, despite the fact that dialysis bag contains DEHP in high concentration level. Concentration of DEHP in CPD solution is higher than concentration in Peritoneal Dialysis Solution about 10 times. DEHP was not detected in solution from SAG-M transfer bag.

Table 4. DEHP concentrations (μg L^{-1}) in Peritoneal Dialysis Solution, CPD solution from Quadruple blood bag and solution from transfer bag stored in PVC bags.

Sample	DEHP concentration (μg L^{-1})
Dialysis solution	3.72±0.21
CPD solution from Quadruple blood bag	37.04±0.25
Solution from Transfer bag	n.d.

On average, patient under peritoneal dialysis procedure receives about 8 L of Peritoneal Dialysis Solution a day and from this obtained result it means that human body receives about 30 μg DEHP in total. Obtained value is under estimated upper-bound dose of DEHP received by adult patients undergoing procedures of peritoneal dialysis 0.01 mg/kg/day (for adult with average body weight 70 kg).

Patient undergoing a routine, elective surgical procedure typically receives about two units of packed red blood cells, volume of 450 ml. Bearing in the mind that volume of CPD solution in Quadruple blood bag is 63 ml, it means that total amount of DEHP in each units of packed red blood cells is 2.33 μg. Obtained value is under estimated upper-bound dose of DEHP received by adult patients undergoing surgical procedures (8.5 mg/kg/day).

CONCLUSION

The presence of DEHP in 8 different parts of plastic medical devices, such as dialysis set (bags and tubing) and transfusion set (bags and tubing) were determined and UV-A effect on DEHP leaching was investigated. Obtained results showed that majority of investigated samples of medical devices contains DEHP > 30% by weight. All investigated tubing material contain DEHP in higher amount than coupled bags. Results obtained after UV-A treatment showed that UV-A radiation has a huge influence on leaching level of DEHP from PVC materials. UV-A radiation showed the biggest influence on DEHP leaching from samples of SAG-M transfer bag.

DEHP was determined in Peritoneal Dialysis Solution and CPD solution from Quadruple blood bag, while solution from SAG-M transfer bag did not contain DEHP. Concentration of DEHP in CPD solution is higher than concentration in Peritoneal Dialysis Solution about 10 times. Obtained values are under estimated upper-bound dose of DEHP received by adult patients undergoing procedures of peritoneal dialysis 0.01 mg/kg/day (for adult with average body weight 70 kg) and transfusion as part of surgical procedures 8.5 mg/kg/day.

REFERENCES

1. T. Fierens, M. Van Holderbeke, H. Willems, S. De Henauw, I. Sioen, *Environment International*, **51**, 1 (2013).
2. P. Prapatpong, W. Kanchanamayoon, *Journal of Applied Sciences*, **10**, 1987 (2010).
3. Z. Guo, S. Wang, D. Wei, M. Wang, H. Zhang, P. Gai, J. Duan, *Meat Sci.*, **84**, 484, (2010).
4. I. Al-Saleh, N. Shinwari, A. Alsabbaheen, *J. Toxicol. Sci.*, **36**, 469 (2011).
5. C. Perez, M.C.B. Alonso, P. Barmejo-Barera, *J. Chromatogr. B: Anal. Technol. Biomed. Life Sci.*, **879**, 231 (2011).
6. H.-Y. Shen, *Talanta*, **66**, 734 (2005).
7. R. Ito, F. Seshimo, Y. Haishima, C. Hasegawa, K. Isama, T. Yagami, K. Nakahashi, H. Yamazaki, K. Inoue, Y. Yoshimura, K. Saito, T. Tsuchiya, H. Nakazawa, *Int. J. Pharm.*, **303**, 104 (2005).
8. K. Inoue, M. Kawaguchi, R. Yamanaka, T. Higuchi, R. Ito, K. Saito, H. Nakazawa, *Clin. Chim. Acta*, **358**, 159 (2005).
9. G. Latini, M.Ferri, F. Chiellini, *Curr. Med. Chem.*, **17**, 2979 (2010).

10. M. Veiga, D. Bohrer, P. C. Nascimento, A. G. Ramirez, L. M. Carvalho, R. Binotto, *J. Braz. Chem. Soc.*, **23**, 72 (2012).
11. G. Latini, *Clin. Chim. Acta*, **361**, 20 (2005).
12. H. Luo, G. Sun, Y, Shen, K. Xu, *SpringerPlus*, **3**, 58 (2014).
13. M.J. Silva, E. Samandar, J.L.Jr. Preau, L.L. Needham, A.M. Calafat, *Toxicology*, **219**, 22 (2006).
14. E. Fasano, F. Bono-Blay, T. Cirillo, P. Monzuori, S. Lacorte, *Food Control*, **27**, 132 (2012).
15. K. K. Ferguson, R. Loch-Caruso, J. D. Meeker *Environ Res.*, **111**, 718 (2011).
16. D. Zhang, H. Lui, Y. Liang, C. Wang, H. Liang, H. Cai, *Front Earth Sci.*, **3**, 73 (2009).
17. P. D. Zygoura, E. K. Paleologos, M. G. Kontominas, *Food Chem.*, **128**, 106 (2011).
18. Di(2-ethylhexyl) phthalate, National Toxicology Program, US Department of Health and Human Services, Report on Carcinogens, Twelfth Edition, 2011, p.156.
19. FDA, Safety Assessment of Di(2-ethylhexyl)phthalate (DEHP) Released from PVC Medical Devices, U.S. Food and Drug Administration, 2001, p.10.
20. S. Keresztes, E. Tatar, Z. Czegeny, G. Zaray, V. G. Mihucz, *Sci. Total Environ.*, **458-460**, 451 (2013).
21. P. Liang, J. Xu, Q. Li, *Anal. Chim. Acta*, **609**, 53 (2008).
22. R.Y. Su, X.W. Zhao, Z.Y. Li, Q. Jia, P. Liu, J.B. Jia, *Anal. Chim. Acta*, **676**, 103 (2010).
23. P. Kueseng, P. Thavarungkul, P. Kanatharana, *J. Environ. Sci. Health. Part B*, **42**, 569 (2007).
24. L. K. Sorensen, *Rapid Commun. Mass Spectrom.*, **20**, 1135 (2006).
25. E. Fasano, T. Cirillo, F. Esposito, S. Lacorte, *LWT – Food Sci. Technol.*, **64**, 1015 (2015).
26. M. C. Pietrogrande, D. Rossi, *Anal. Chim. Acta*, **1**, 480 (2003).

КОЛИЧЕСТВЕНО ОПРЕДЕЛЯНЕ НА DEHP В КОМПОНЕНТИ ОТ ИНТРАВЕНОЗНИ СИСТЕМИ И ПРИБОРИ ЗА ПЕРИТОНИАЛНА ДИАЛИЗА ОТ PVC ПРЕДИ И СЛЕД ТРЕТИРАНЕ С УЛТРАВИОЛЕТОВИ ЛЪЧИ

И. Костич[1*], Т. Андьелкович[1], Д. Андьелкович[1], А. Божич[1], Т. Цветкович[2], Д. Павлович[2]

[1]*Университет в Ниш, Научно-математически факултет, 18000 Ниш, Сърбия*
[2] *Университет в Ниш, Медицински факултет, 18000 Ниш, Сърбия*

(Резюме)

Изследвано е наличиието на ди-(2-етил-хексил) фталат (DEHP) в 8 различни части на пластмасови медицински съоръжения, използвани в два много важни процеса, както и влиянието на облъчването с ултравиолетови лъчи. Определянето на DEHP е извършвано с газ-хроматография/мас-спектрометрия (GC-MS). Резултатите показват, че уредите за перитониална диализа съдържат приблизително 35% тегл. от торбичката и около 37% от тръбите. Резултатите, получени за проби от системи за кръвопреливане показват, че квадруполните торбички за кръв и за пренасяне съдържат почти еднакво количество DEHP (съответно 25.63% и 26.92% тегл.), докато торбичките за пренос SAG-M съдържат по-малко от DEHP (16.07%). Всички проби от тръбичките показват по-висока концентрация отколкото при свързаните торбички. Извлечени са много малки количества във физиологичния разтвор за перитониална диализа (Peritoneal Dialysis Solution) от торбичките за диализа от PVC (3.72 µg L^{-1}), въпреки че самите торбички за диализа съдържат по-големи количества от DEHP. Получената концентрация на DEHP в разтвора на CPD от квадруполна кръвна торбичка е по-висока от концентрацията в разтвора за перитонеална диализа около 10 пъти (37,04 µg L^{-1}). DEHP не е открит в разтвор от SAG-M трансферна торбичкаа. Получените стойности са под пресметната горна доза DEHP, получена от възрастни пациенти, подложени на процедури на перитонеална диализа 0,01 mg / kg / ден (за възрастни със средно телесно тегло 70 kg) и трансфузия като част от хирургични процедури 8,5 mg / kg / ден. Резултатите, получени след UV обработка, показват, че ултравиолетовото лъчение оказва известно влияние върху излугването на DEHP от проби на медицинските изделия от PVC. Всички изследвани проби съдържат по-малко количество от DEHP след третиране с UV-A, отколкото проби, които не са третирани с ултравиолетова радиация.

Preparation of chromium doped LiAlSiO$_4$ glass-ceramics

I.I. Koseva[1]*, P.T. Tzvetkov[1], A.S. Yordanova[1], M.O. Marychev[2], O.S. Dimitrov[3], V.S. Nikolov[1]

[1]Institute of General and Inorganic Chemistry, Bulgarian Academy of Sciences, 1113 Sofia, Bulgaria.
[2]N.I. Lobachevsky State University of Nizhni Novgorod, Nizhni Novgorod 603950, Russia
[3]Institute of Electrochemistry and Energy Systems, Bulgarian Academy of Sciences, 1113 Sofia, Bulgaria

Pure and chromium doped homogeneous glasses from the system Li$_2$O-Al$_2$O$_3$-SiO$_2$-LiBO$_2$=8.26:28.09:33.05:30.6 wt% are prepared after heating at 1130ºC for 24 h. Glass-ceramics with various transparencies are obtained after thermal treatment of the parent glass at different temperatures for different times. The crystallizing phases, the degree of crystallinity and the particle size are determined. Absorption and emission spectra are presented for the glass-ceramic sample with crystallizing phases LiAlSiO$_4$ and LiBO$_2$, treated at 500ºC during 6 h. The spectra show the co-existence of Cr^{3+} and Cr^{4+} ions.

Keywords: LiAlSiO$_4$, chromium doped glass-ceramics, X-ray diffraction, absorption and emission spectra

INTRODUCTION

Chromium (Cr^{4+}) doped laser single crystals and glass-ceramics are attractive and important for optical communications, remote sensing and biomedical applications. These lasers operate in the near infrared range, so-called eye-safe wavelength range, which includes wavelengths between 1.1 and 1.6 μm.

It is known that the laser active ion emitting in this range (Cr^{4+}) has to be in tetrahedral position. Therefore, a suitable laser matrix is particularly important. Different matrices are reported in the literature: Cr^{4+}:Mg$_2$SiO$_4$ [1-3], Cr^{4+}:Ca$_2$SiO$_4$ [4,5], Cr^{4+}:Ca$_2$GeO$_4$ [6,7], Cr^{4+}:CaMgSiO$_4$ [8], Cr^{4+}:Li$_2$MgSiO$_4$ [9], Cr^{4+}:YAG [10, 11].

Another possible material suitable as a matrix for Cr^{4+} doping is LiAlSiO$_4$. This compound is also known as eucryptite.

LiAlSiO$_4$ is a technologically relevant ceramic, owing to its near to zero thermal expansion coefficient, great thermal and chemical shock resistance, exceptional thermal stability. Up to now, this material is used not only in the field of domestic cookware, but also for various specific applications like heat exchangers, ring laser gyroscopes, precision optical devices and radiation dosimetry purposes. [12] To our knowledge, obtaining of this glass-ceramic doped by chromium is not published so far, probably due to the difficulties to produce homogeneous glasses, since they display both high melting point and high viscosity.

The LiAlSiO$_4$ structure has been studied by Winkler and has been confirmed by Roy [13, 14]. High eucryptite, LiAlSiO$_4$, is isomorphous with high

quartz, where half of the Si atoms are replaced by Al forming the three-dimensional network of corner-sharing AlO$_4$ and SiO$_4$ tetrahedra. The Li$^+$ ions are placed in void channels within the spirals of (Si,Al)O$_4$ tetrahedra. According to Schulz, the unit cell is with hexagonal symmetry (P6$_2$22) [15, 16]. The high eucryptite form is stable on cooling even with prolonged heating at low temperatures [17]. Roy also established the reconstructive inversion of the high eucryptite to the rhombohedral phenacite type of low eucryptite (α-eucryptite) at 972º ± 10ºC. At about 650°C γ-eucryptite is formed, and its structure is monoclinic with space group *Pa*. At 900–1000°C γ-eucryptite transforms into the final high-temperature polymorph β-eucryptite [18, 19].

Although the compound appears to be in different structural forms, the presence only of LiO$_4$, SiO$_4$ and AlO$_4$ tetrahedra in the eucryptite structure is favorable for doping with chromium ion in 4+ state of oxidation.

In this paper we report our attempt to prepare chromium doped LiAlSiO$_4$ glass-ceramics.

EXPERIMENTAL

Li$_2$CO$_3$ (p.a.), Al$_2$O$_3$ (p.a.), SiO$_2$ (p.a.), H$_3$BO$_3$ (p.a.) and Cr$_2$O$_3$ (p.a.) were used as raw materials. Glass synthesis was carried out in a resistive furnace with Kanthal heating wire permitting maximum working temperature of 1200ºC and in a chamber furnace with MoSi$_2$ heating elements permitting maximum working temperature of 1550ºC. The temperature was controlled using a Pt/Pt–10%Rh thermocouple connected to a Eurotherm controller. Glasses of the desired compositions about 30 grams in weight were melted in platinum crucibles. First the mixture was heated at 700ºC for decomposition of the carbonates and boric acid and then the melt

---

* To whom all correspondence should be sent:
E-mail: ikosseva@svr.igic.bas.bg

was heated at the proper temperature for homogenization. The obtained glass was cooled to room temperature by quick removal from the furnace. Some of the glasses were quenched by pouring onto a steel plate and pressing with another steel plate. The prepared glasses were thermally treated for establishing the crystallizing phases.

Structural characterization was carried out by powder X-ray diffraction (XRD) using a Bruker D8 Advance powder diffractometer with Cu Ka radiation and SolX detector. X-ray diffractograms were recorded at room temperature. Data were collected in the 2θ range from 10 to 80∘ with a step of 0.04∘ and 1 s step^{-1} counting time. X-ray diffractograms were identified using the Diffractplus EVA program. The mean crystallite size and the unit cell parameters were calculated from the integral breadth of all peaks (Pawley fit) using Scherrer equation and the TOPAS 3 program.3 – General profile and structure analysis software for powder diffraction data, 2005, Bruker AXS, Karlsruhe, Germany. The area of the amorphous phase was determined by using a straight line for description of the background and a single line for fitting the amorphous component.

The particle morphology of the glass and glass-ceramic samples was determined using a transmission electron microscope JEOL model JEM 200 CX equipped with EM-ASID3D scanning attachment, working in secondary electron detection mode. Specimens were covered with a carbon-gold film.

The UV–Vis spectra were taken with a Thermo Evolution 300 UV-Vis spectrophotometer equipped with a Praying Mantis device.

The emission spectra in the 1000-1600 nm range where measured with 813.4 nm excitation by the laser diode ATC-C1000-100-TMF-808-10. The rating monochromator SP-150 (Acton Research Corporation) with 32×32 ruled diffraction grating and 300 grooves/mm and 1 μm blaze wavelength was used for the spectra. InGaAs ID-441-C was the detector in the near infrared. The emissions from a black body specimen at determined temperature were utilized for standardization of the data. All spectra were recorded at room temperature.

RESULTS AND DISCUSSION

Glass compositions

As a first step two different compositions from the system $Li_2O-Al_2O_3-SiO_2$ were selected for preparing the glasses: $Li_2O.Al_2O_3.2SiO_2-Li_2O.SiO_2=$ 60:40 (C1) and $Li_2O.Al_2O_3.2SiO_2-Li_2O.SiO_2 =$ 65:35 (C2). According to M.K.Murthy and F.A.

Hummel, the first composition is eutectic with melting point 1070ºC and the second composition is with melting point about 1150ºC [20, 21]. For these two compositions the powders was heated at 700ºC for 30 min for decomposition of the carbonates. Then the samples were treated at temperatures between 1300 and 1500ºC and time between 30 min and 4 h.

It was found that a major factor in obtaining a homogeneous glass in this temperature range is not the temperature, but the treatment time. So in both C1 and C2 compositions treated at 1400 and 1500°C for 30 min inhomogeneous glass with bubbles was obtained, and the temperature treatment at 1350ºC for 4 h resulted homogeneous glass, especially for composition C2. The preparation of homogeneous glass during cooling to room temperature proved to be problematic due to the rapid crystallization of the glass during the cooling. An additional problem using these two compositions is the fact that in the glass not only the desired phase, $LiAlSiO_4$, crystallized, but also two other phases Li_2SiO_3 and $Li_{2.5}Al_{0.5}SiO_4$ (Fig. 1).
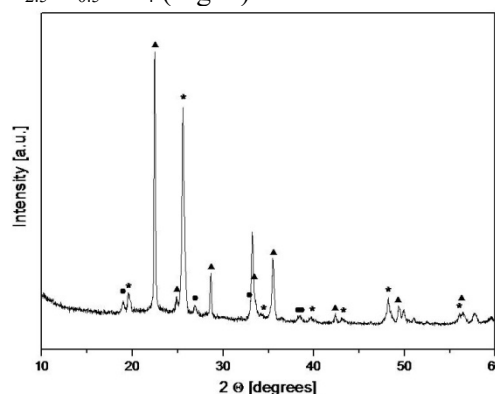

Fig. 1. XRD patterns of the phases crystallized in the glass with composition C2 after thermal treatment at 1350ºC for 4 h and cooling to room temperature (*- $LiAlSiO_4$, ●-Li_2SiO_3, ▲ - $Li_{2.5}Al_{0.5}SiO_4$).

Inability to obtain a homogeneous glass at room temperature was the reason to try obtaining glass with the addition of B_2O_3. It is known from the literature that boron oxide is a good glass former. For the preparation of the glass the composition $LiAlSiO_4-LiBO_2$=69.4:30.6 wt% ($Li_2O-Al_2O_3-SiO_2-LiBO_2$=8.26:28.09:33.05:30.6 wt%) (C3) was selected. The glass with this composition, pure or doped by 2 at% Cr, was successfully homogenized after heating at 1130ºC during 24 h and transparent glass was obtained after rapid cooling to room temperature. XRD analyses acknowledged obtaining of glass mass without phases crystallized.

Thermal treatment of the glass

The glass with composition C3 was thermally treated at different temperatures for different times. The results for the crystallizing phases obtained in the glass are presented in Table 1.

The table shows that after thermal treatment of the glass below 500°C, samples with small peaks of the desired phase are obtained. In all other regimes of thermal treatment addition of different phases to the desired phase occurred. For example, after thermal treatment at 500°C $LiBO_2$ crystalized as a second phase. After thermal treatment above this temperature Li_4SiO_4, $Li_4B_{10}O_7$ and $Li_4B_2O_5$ occurred (Fig. 2).

For further investigations samples with a second phase of $LiBO_2$ were chosen. The presence of more than one non-desired phase implies obtaining the desired phase in a lower concentration which reduces the optical properties of the glass-ceramic.

Transparency and degree of crystallization of the glass-ceramics after thermal treatment:

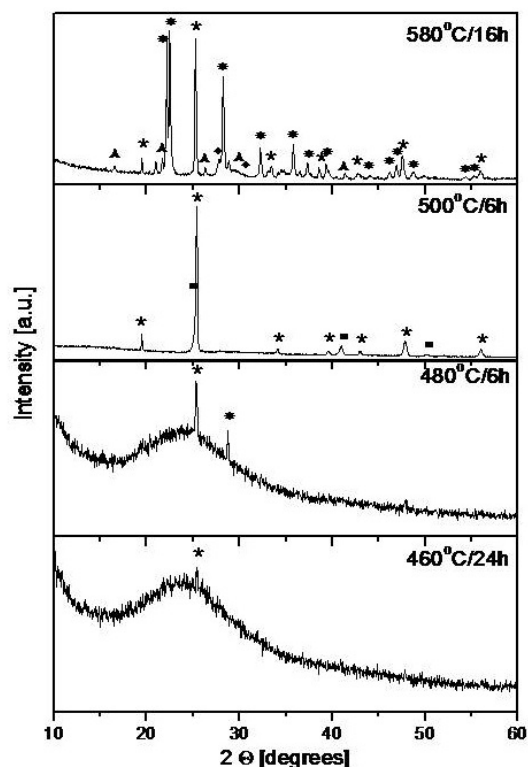Transparency of the glass-ceramics and the degree of crystallization are presented in Table 2.

Fig.2. XRD patterns of the glass-ceramics after thermal treatment at different temperatures for different times (★-LiAlSiO₄ hexagonal, ✳-LiAlSiO₄ monoclinic, ■-LiBO₂, ▲-Li₄B₁₀O₁₇, ◆-Li₄B₂O₅).

Table 1. Crystallizing phases obtained in the glass with composition C3 after thermal treatment at different temperatures for different times.

Time [h] °C	2	4	6	16	24
460	Glass		Glass		Glass
480	Glass Small peaks of LiAlSiO₄	Glass Small peaks of LiAlSiO₄	Glass Small peaks of LiAlSiO₄ and SiO₂		
500	LiAlSiO₄ LiBO₂	LiAlSiO₄ LiBO₂	LiAlSiO₄ LiBO₂	LiAlSiO₄ LiBO₂	
530	LiAlSiO₄ LiBO₂	LiAlSiO₄ LiBO₂ Li₄SiO₄		LiAlSiO₄ LiBO₂ Li₄SiO₄	
580				LiAlSiO₄ Li₄B₁₀O₇ Li₄B₂O₅	

Table 2. Transparency of the glass-ceramics and degree of crystallization [%]:

Time [h] °C	2	4	6	16	24
500	Transparent 29	Transparent 80	Transparent 85	Translucent 87	Opaque
530	Transparent 81				

As can be seen from the table, the glass-ceramics are transparent up to the crystallization degree of about 85%. At higher degrees of crystallization the glass-ceramics becomes translucent or opaque. The crystallization degree slightly depends on the thermal treatment time and more on the thermal treatment temperature.

Particle size:

Particle size of the glass-ceramics depending on the thermal treatment conditions is presented in Table 3.

The particle size is about 50 nm and slightly depends on the thermal treatment time, but depends on the treatment temperature. This result is in agreement with the crystallization degree values.

Table 3. Particle size of the glass-ceramics [nm]:

Time[h] °C	2	4	6	16
500	22	53	48	51
530	52			

According to the results obtained, after the beginning of the crystallization, the increased time of treatment probably does not lead to expanding of the nucleated seeds, but to arising of new seeds. This can be seen also from the patterns of the glass-ceramics treated at 500°C for 2, 4, 6 and 16 h and of glass-ceramics treated at 500 and 530°C for 2 h (Fig. 3). No significant difference can be seen between XRD patterns of the samples treated for 6 and 16 h at 500°C, but there is a significant difference in the XRD patterns for the samples treated at 500 and 530°C for 2 h.
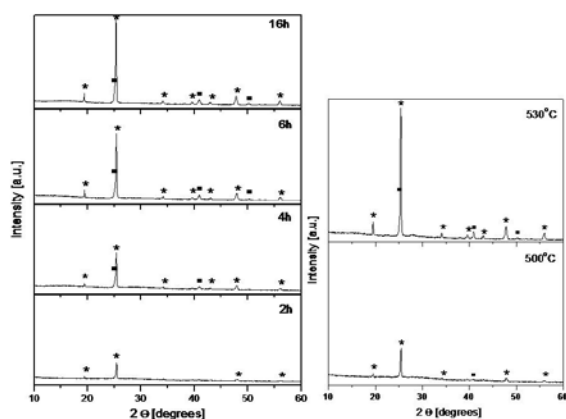

Fig. 3. XRD patterns of the glass-ceramics treated at different conditions ($\star$-LiAlSiO₄, ■-LiBO₂).

Fig.4 presents the SEM micrographs of the initial glass and glass-ceramics. As can be seen, the particle size is from 30 to 50 nm. This result is in accordance with the particle size calculated by the Scherrer equation.
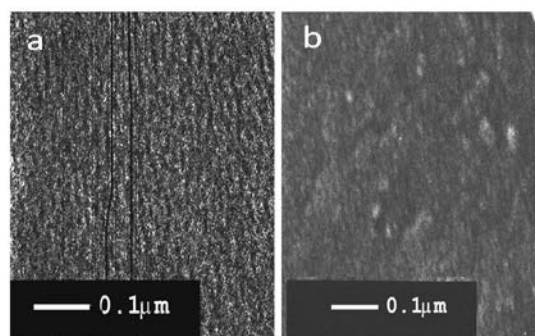

Fig. 4. SEM micrographs of the initial glass (a) and the glass-ceramic (b).

Absorption and emission

Fig.5 presents the absorption and the emission spectra of the glass-ceramics treated at 500°C for 6 h.
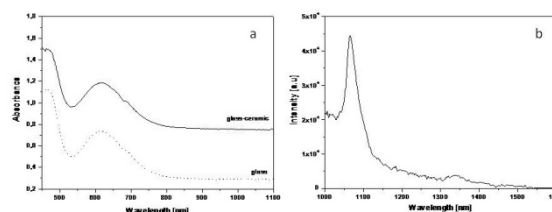

Fig. 5. Absorption (a) and emission (b) spectra of the glass-ceramic treated at 500°C for 6 h.

Absorption spectra of the glass and glass-ceramic samples show similar Cr ions absorption bands assigned to different types of chromium ions. The absorption spectra consist of strong absorption bands between 520 and 800 nm and a weak one near infrared absorption between 800 and 1100 nm. According to the literature [7], in the region 520-800 nm a strong band exists ascribed to the transition of $^4A_2 \rightarrow {}^4T_2$ of Cr^{3+}. A maximum at 615 nm in our glass and glass-ceramic is observed. Multiplet bands at 680 nm may be ascribed to the transition of $^3A_2 \rightarrow {}^3T_1$ of Cr^{4+} with energy-level splitting in a distorted tetrahedron. The $^3A_2 \rightarrow {}^3T_1$ absorption band of the tetrahedral Cr^{4+} centers overlap with the $^4A_2 \rightarrow {}^4T_2$ absorption band of octahedral Cr^{3+} centers. Since there are both Cr^{3+} and Cr^{4+} ions, these absorption bands are not pure Cr^{4+} bands. Another band from 800 to 1100 nm is ascribed to $^3A_2 \rightarrow {}^3T_2$ of Cr^{4+}. There is more intense absorbance in the glass-ceramic sample compared with the initial glass.

The emission spectra overlap from 1000 to 1550 nm. There is a strong peak at 1065 nm and a weak, broad one at 1340 nm. The absorption spectra show different oxidation states of the chromium ions in the glass-ceramic samples. In accordance to the absorption spectra the first emission peak could be attributed to $^4T_2 \rightarrow {}^4A_2$ of Cr^{3+} ions and the second peak is attributed to $^3T_2 \rightarrow {}^3A_2$ of Cr^{4+} in tetrahedral

occupation. Such emission spectrum is expected [22], taking into account the existence of three matrices (residual glass, LiAlSiO₄ and LiBO₂), where the chromium ion could be incorporated.

CONCLUSION

Pure and chromium doped homogeneous glasses from the system Li₂O-Al₂O₃-SiO₂-LiBO₂=8.26:28.09:33.05:30.6 wt% are prepared after 24 h heating at 1130ºC. Glass-ceramics with various transparencies are obtained after thermal treatment of the parent glass at different temperatures and times. The crystallizing phases, the degree of crystallinity and the particle size are determined. In all thermal regimes LiAlSiO₄ appears. Except LiAlSiO₄, different crystallizing phases crystallize depending on the treatment conditions. The glass-ceramics are transparent to the crystallization degree of about 85%. The particle size is about 50 nm and slightly depends on the thermal treatment time, but depends on the treatment temperature. Absorption and emission spectra are presented for the sample with crystallizing phases LiAlSiO₄ and LiBO₂ treated at 500ºC for 6 h. The spectra show the co-existence of the Cr^{3+} and Cr^{4+} ions.

REFERENCES

1. V. Petričević, S.K. Gayen, R.R. Alfano, K. Yamagishi, H. Anzai, Y. Yamaguchi, *Appl. Phys. Lett.*, **52**, 1040 (1988).
2. H.R. Verdun, L.M. Thomas, D.M. Andrauskas, T. McCollum, A. Pinto, *Appl. Phys. Lett.*, **53**, 2593 (1988).
3. A.M. Ulyashenko, N.V. Nikonorov, A.K. Przhevuskii, *B .Russ. Acad. Sci.: Physics*, **71**, 159 (2007).
4. L. Yang, V. Petricevic, R. R. Alfano, In Novel laser sources and applications (Proceedings of a workshop November 12-13, 1993, San Jose, California), USA, 1993, p. 103.
5. R.R. Alfano, A. Bykov, V. Petricevic, *US Patent* 7,440, 480 (2008).
6. A.B Bykov, V Petricevic, J Steiner, Di Yao, L.L Isaacs, M.R Kokta, R.R Alfano, *J. Cryst. Growth*, **211**, 295 (2000)
7. M.Yu. Sharonov, A.B. Bykov, T. Myint, V. Petricevic, R.R. Alfano, *Opt. Commun.*, **275**, 123 (2007)
8. K.A. Subbotin, L.D. Iskhakova, E.V. Zharikov, S.V. Lavrishchev, *Crystallogr. Rep.,* **53**, 1107 (2008).
9. C. Anino; J. Thery, D. Vivien, In: Tunable Solid State Lasers, International Society for Optics and Photonics. 1997, p. 38.
10. A.G. Okhrimchuk, A.V. Shestakov, *Opt. Mater.,* **3**, 1 (1994).
11. J. Dong, K. Ueda, A. Shirakawa, H. Yagi, T. Yanagitani, A.A. Kaminskii, *Opt. Express,* **15**, 14516 (2007).
12. V. Correcher, L. Sanchez-Munoz, J. Garcia-Guinea, J.M. Gomez-Ros, A. Delgado, *Nuc. Instrum. Meth. A,* **562**, 456 (2006).
13. H.G.F. Winkler, *Acta Cryst.*, **1**, 27 (1948)
14. R. Roy, D.M. Roy, E.F. Osborn, *J. Am. Ceram. Soc.,* **33**, 152 (1950).
15. H. Schulz, V. Tscherry, *Acta Cryst. B*, **28**, 2174 (1972).
16. W.I. Abdel-Fatah, M.S. Fayed, S.R. Gooda, W.F.F. Mekky, *J. Sol–Gel Sci. Techn.*, **13**, 981 (1998).
17. J.H. Westbrook, *J. Am. Ceram. Soc.,* **41**, 433 (1958).
18. P. Norby, *Zeolites*, **10**, 193 (1990).
19. B.E. Douglas, S.M. Ho, in: Structure and Chemistry of Crystalline Solids Springer, ISBN-10: 0-387-26147-8; ISBN-13: 978-0387-26147-8, 2006, p. 253.
20. M.K. Murthy, F.A. Hummel, *J. Am. Ceram. Soc.,* **37**, 14 (1954).
21. E.M. Levin, Phase Diagrams for Ceramists, Columbus, Ohio: American Ceramic Society, 1956, p. 87.
22. S. Morimoto, *J. Ceram. Soc. Jpn,* **112**, 486 (2004).

ПОЛУЧАВАНЕ НА ДОТИРАНА С ХРОМ СТЪКЛОКЕРАМИКА СЪДЪРЖАЩА LiAlSiO₄

Й. И. Косева[1]*, П. Ц. Цветков[1], А. С. Йорданова[1], М. О. Маричев[2], О. С. Димитров[3], В. С. Николов[1]

¹Институт по обща и неорганична химия, Българска академия на науките, 1113 София, България
²Нижни Новгородски университет „Н.И. Лобачевски", Нижни новгород 603950, Русия
³Институт по електрохимия и енергийни системи, Българска академия на науките, 1113 София, България

(Резюме)

Синтезирани са чисти и дотирани с хром хомогенни стъкла от системата Li₂O-Al₂O₃-SiO₂-LiBO₂= 8.26:28.09:33.05:30.6 wt% след 24 часово нагряване при 1130ºC. Прозрачни стъклокерамики са получени след термично третиране на стъклата при различни температури и с различна продължителност. Определени са кристализиращите фази, степента на кристализация и размерът на частиците. Представени са спектри на абсорбция и емисия за стъклокерамични образци с кристализиращи фази LiAlSiO₄ и LiBO₂ термично третирани при 500ºC за 6h. Спектрите показват едновременното присъствие на йони Cr^{3+} и Cr^{4+}.

Biocompatibility of aluminium alloys and anodic Al$_2$O$_3$

R.D. Mantcheva[1], D.D. Kiradzhiyska [1*], Y.N. Feodorova[2], K.I. Draganova[3]

[1]*Department of Chemical Sciences, Faculty of Pharmacy, Medical University - Plovdiv, 15A V. Aprilov blvd, 4000 Plovdiv, Bulgaria*
[2]*Department of Medical Biology, Medical Faculty, Medical University - Plovdiv, 15A V. Aprilov blvd, 4000 Plovdiv, Bulgaria*
[3]*Department of Microbiology and Immunology, Faculty of Pharmacy, Medical University - Plovdiv, 15A V. Aprilov blvd, 4000 Plovdiv, Bulgaria*

The purpose of this study is to investigate the biocompatibility, viability and cytotoxicity of ternary aluminium alloys Al-Si-Zr and anodized aluminium EN AW 1050A. There is a wide variety of metals used in different medical devices. For this reason, methods of improving their technical properties and enhancing their biocompatibility are increasingly looked for. Ternary alloys with different contents of the constituents were examined under conditions of co-cultivation with immortalized PDL and serum-freeMcCoy Plovdiv cell cultures. Zirconium was used in the process of casting of the alloys due to its good biological qualities and corrosion resistance. In comparison, the properties of anodized technical aluminium with different oxide film thickness were examined. The process of anodization was carried out in 15% H$_2$SO$_4$ for defined periods of time. The results showed that 10 and 20 μm thick oxide films provide better development of the cells compared to the ternary system. Metal surfaces with 10 μm thick oxide film showed the best properties in terms of cells vitality, proliferation and growth.

Keywords: Al-Si-Zr, biocompatibility, cell cultures, anodized aluminium.

INTRODUCTION

Metallic biomaterials are often used to reinforce or replace components of the skeleton, e.g. artificial joints, bone plates, screws, intramedullary nails, spinal fixation, external fixators, valves, stents, dental implants, etc. They should have high tensile strength and fatigue, greater resistance to fracture compared to ceramic materials, etc. The choice of materials for medical implants is also based on properties such as corrosion resistance, biocompatibility, bioadhesion, biofunctionality, genotoxicity, carcinogenicity, cytotoxicity, etc. [1, 2].

There is an enormous variety of materials and alloys used for the manufacture of implants. Some examples are Ti-6Al-4V; Ti-6Al-7Nb; Ti-15Mo; Ti-3Al-2,5V; NiTi; Co-Ni-Cr-Mo-Fe; Ni-Cr; Co-Cr; L-605; zirconium, Al$_2$O$_3$ and others. Their production technologies are based on methods of materials science, metallurgy, chemistry and electrochemistry.

Aluminium has good mechanical properties such as lightness, workability, high heat conductivity and electrical conductivity, high corrosion ressistance, etc. However, its low strength necessitates the development of alloys through alloying with other elements. In some cases, the alloying element is zirconium due to its high strengthening effect on the aluminium matrix and its good biological properties [3]. It also facilitates the growth of the inert Al$_2$O$_3$ onto the aluminium padding, which defines the corrosion resistance of the native metal. For this reason, the mechanical indicators and the operation of Al-Si-Zr alloys in biological environment were examined.

The use of conventional aluminium as a construction material in medical devices is continuously expanding. There are various methods of treatment to improve its corrosion resistance and biocompatibility. Besides making changes in the chemical composition there are also various surface modification techniques including ion implantation, or deposition of ceramic layers (TiN, DLC, Al$_2$O$_3$, ZrO$_2$), plasma spraying, chemical vapor deposition, physical vapor deposition, etc. Surface modification is the major current area of research in biomaterials [4].

A well-known technique is the obtaining of a protective oxide film on the surface of the metal matrix. Surface oxide film formed on metallic materials plays an important role as an inhibitor of the release of metallic ions, to improve corrosion resistance and tissue compatibility [5]. Al$_2$O$_3$ is an inert material with a well-known application mostly in dentistry. The protective effect of Al$_2$O$_3$ helps with corrosia and at the same time is capable of reducing the friction on articular surfaces [6]. Aluminium oxide obtained through the process of anodization has the qualities needed for it to be

* To whom all correspondence should be sent:
E-mail: denica.kiradjiiska@gmail.com

more and more widely used in the production of biomaterials. Its porous structure allows it to be filled with a bioactive material, which enhances the compatibility and the antibacterial action of the metal pad [7, 8]

The purpose of this study was to investigate the biocompatibility, viability and cytotoxicity of metal samples of ternary Al-Si-Zr alloys with different amounts of zirconium additions and aluminium (EN AW 1050A) which have been subjected to electrochemical anodization and on which Al_2O_3 layers of various thickness were formed.

EXPERIMENTAL CONDITIONS

The electrochemical experiment was performed in accordance with [9]. It is well known that porous films on the aluminium surface with high pore concentration can be produced by anodic oxidation in electrolytes which dissolve Al_2O_3 (phosphoric acid, oxalic acid, sulfuric acid, etc.). Samples of technical aluminium (EN AW 1050A) with a surface area of 0.02 dm^2 were anodized galvanostatically (15 $mA.dm^{-2}$) at constant temeperature (20ºC) in 15% (w/w) H_2SO_4. The time of Al_2O_3 formation was calculated depending on the desired film thickness [9]. It is also found that the oxides obtained under these conditions exhibit different thickness and the same porosity $\alpha = 0.15$ [10].

Ternary Al–Si–Zr ribbons were prepared from the respective master alloys by flat–flow casting and rapid solidification, as previously described [11, 12]. Samples with a surface area of 0.02 dm^2 were cut and subjected to several biotests.

Cell cultures

PDL cell line of immortalized precursor cells from periodontal ligament.

Cells were cultured in the DMEM/Ham's F-12 1:1 medium with 10 % FCS, 100 I. U. penicillin and 100 µg/ml streptomycin. The procedures for cell culturing and storing were performed according to [13].

Serum-free cell line McCoy-Plovdiv.

Cells were cultured in the DMEM/Ham's F-12 1:1 medium with 15 mM HEPES, 100 I. U. penicillin and 100 µg/ml streptomycin. The procedures for cell culturing and storing were performed according to [14].

Experimental design

Biocompatibility testing

Metal lamellas were placed in 8-well slides with coverslip for cell with a lid for cell cultures. Cells with different innitial seeding density were added and incubated for 96 and 198 h . The state of the cell monolayer and cell morphology cultures was inspected every 24 h using an inverted light microscope (Nikon Eclipse TS100). Assessment of changes in the cell layer was made at the border delineated by the edge of lamella and the slide. Direct visualization of cultured cells was not possible because of the opaque nature of metallic lamellas. Microscopic images were captured using a Nikon camera and a photo documentation system. At the end of the incubation period, the cultures were examined for vitality with the reactant WST-1. The state of the cultured cells onto the metal surfaces was also visualised by a LIVE/DEAD test.

Cytotoxicity testing

In this test McCoy Plovdiv cells were treated with the DMEM/Ham's F-12 1:1 medium pre-incubated with the Al-Si-Zr ribbons for 24, 48, 72 and 96 h . After 24-h of treatment the cytotoxic effect was determined microscopically and by a vitality test using the reagent WST-1. The results were statistically analyzed.

Viability testing

In our measurements we used the reagent WST-1 (Roche Diagnostics, Mannheim, Germany), which was reduced from cellular enzymes (mitochondrial dehydrogenases) to a water-soluble product. Accumulation of formazan product formed correlates directly with the count of metabolically active cells in the culture. The cells were incubated for 4 h with the reagent WST-1 at 37°C, after which the absorbance of the resulting colored product was measured at 450 nm wavelength using the ELISA reader *Sunrise* (Tecan, Maennedorf, Switzerland).

Immunofluorescense

The samples were washed twice with PBS tempered at 37ºC. Cells were fixed with 4% paraformaldehyde/PBS for 10 min and permeabilized with ice-cold acetone for 5 min. Incubation in 3% FCS/PBS for 30 min was performed to block non-specific binding. FITC-conjugated phalloidin (1:40 in PBS) (Invitrogen) was used to stain actin and Hoechst 33342 (3 µg/ml) (Sigma) was used for nuclear staining.

The microscopic examination was conducted by the use of epifluorescence microscope Nikon Eclipse TS100.

EXPERIMENTAL RESULTS AND DISCUSSION

The metal plates subjected to bio testing had dimensions of $1 \times 1 \times 0.5$ mm. They were numbered from 1 to 6, and had the following characteristics of surface treatment:

Table 1. Characteristics of surface treatment

Sample number	Type of treatment
1	untreated aluminum
2	anodized aluminum, oxide film thickness d = 10 μm
3	anodized aluminum, oxide film thickness d = 20 μm
4	anodized aluminum, oxide film thickness d = 30 μm
5	Al-Si-Zr ribbon (w_{Zr} = 0.27 %)
6	Al-Si-Zr ribbon (w_{Zr} = 1.09 %)

Ternary alloy Al-Si-Zr

With a view to studying the application of the new ternary alloys in biological environment, a series of experiments with serum-free McCoy Plovdiv and PDL cell lines of immortalized cells, precursors of periodontal ligament were conducted. 24 h after the start of incubation of McCoy-Plovdiv cells with metal lamellas, in the samples, dead cells, rounded and clustered cells, without well-formed monolayer, were seen near the edges of lamellas. By increasing the time the amount of dead cells was much greater (Fig. 1)
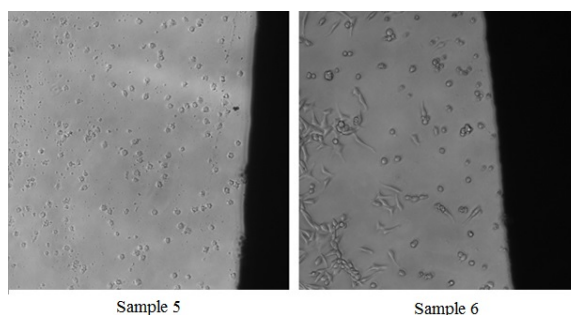

Sample 5   Sample 6

Fig. 1. McCoy-Plovdiv cells cultured with samples 5 and 6 for 96 h

In the cytotoxicity testing in sample 5, reduction in cell count by more than 50% under the influence of the medium in which the lamella stayed for only 24 h was recorded. In sample 6, reduction in cell count by about 30% was recorded.

By increasing the time for which the lamellas stayed in the medium, a trend for increase in the toxicity of these media was established. This was convincingly confirmed by the very low levels of surviving cells in sample 5 (6.5%) and 6 (13.7%), which coincides with our visual microscopic observations. Consequently, four times higher zirconium content in the aluminium alloy increases twice the percentage of surviving cells.

Impairment of cell monolayer, rounded and dead cells near the edge of the lamella were found in samples 5 and 6. The state of the cell layer was assessed at the border delineated by the edge of lamella and the slide using an optical microscope. It was not possible to observe the cells directly in the individual stages of the experiment because of the dense nature of the metal lamellas.

For assessment of the biocompatibility with PDL cells of the different lamellas, at the end of the incubation period they were fixed and stained with fluorescent dyes that allow visualizing the cells adhered to metallic surface. Data from these observations are presented in Fig. 2.

No viable cells connected to the surface could be seen on sample 5. There were fragments of cells and cell nuclei debris. In sample 6, there were few connected cells which were not well spread as a layer or were clustered. The two samples, 5 and 6, had a markedly negative effect on cell growth in *in vitro* conditions. Cell adhesion, spreading of cells, cell proliferation and formation of a monolayer on these lamellas was impeded. Besides the influence of the direct contact with the metal surfaces, an indirect cytotoxic activity of molecules or compounds released/produced in the medium was observed. This toxic activity increases with the time in which metal plates 5 and 6 were incubated in a medium without cells.

Aluminium EN AW 1050A

To examine the effect of different surface modifications on cell growth and biocompatibility, PDL cells were placed with a low initial seeding density. This made it possible to assess the development of the culture and the increase in the number of cells, cell proliferation, adaptation of cells and their colonization on the respective substrate.

Two initial seeding density levels were chosen, for which previous information shows that they reach subconfluent and confluent state, when they are grown onto a glass (the bottom of the axilla) for 4 and 7 days respectively. This could be seen clearly on Fig. 3 (A-1; A-2) and Fig. 4.

Fig. 5 presents the results obtained for the number of PDL cells cultured for 96 and 168 h together with samples 1, 2, 3 and 4. It can be seen that for sample 2 (oxide film thickness of 10 μm) and sample 3 (oxide film thickness of 20 μm) the values are higher (sample 2 - 68.3% at 96 h and 72.6% at 168 h; sample 3 - 52.6% at 96 h and 59.4% at 168 h) compared to those for sample 1 - untreated aluminium (42.8% - 96 h, 45.9% - 168 h).

The absence of toxic effect was evaluated by microscopic observation of native cultures (Fig. 3).

Outside the metal lamellas, the formation of the cell layer consisting of cells with normal morphology and splitting cells can easily be seen. Fluorescent-microscopic images showing the development of cells on the surface of the different samples are shown on Fig. 6.

The best cell development (more living cells adhered to the surface) is seen with samples 2 and 3, and it is weaker (with less living cells on the surface) with sample 4 (thickness of the oxide film 30 μm).
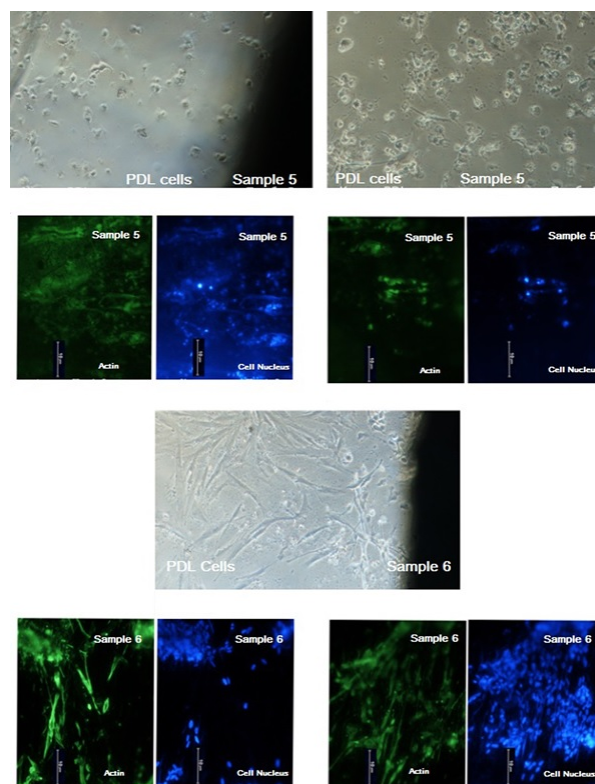
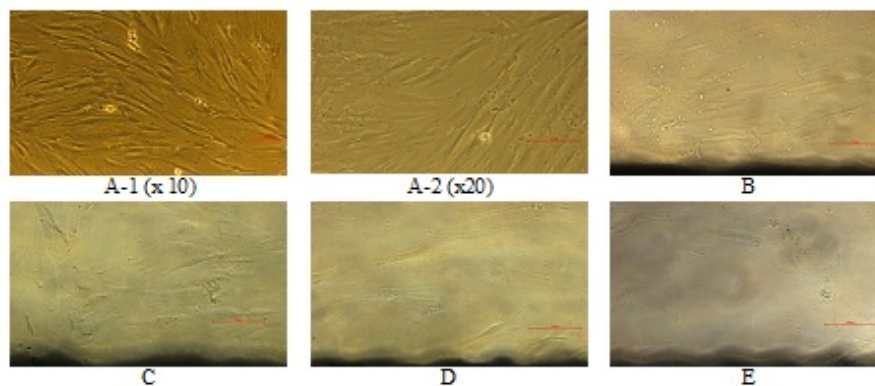**Fig. 2.** PDL cells cultured with samples 5 and 6 for 96 h.

Fig. 3. Human PDL cells, co-cultivated with sample 1(B), sample 2(C), sample 3(D), sample 4(E) for 24h. Control (A) - cells, cultivated on glass (A-1, magnification ×10; A-2, magnification ×20). Inverted light microscope. Magnification ×20.

Fig. 4. Human PDL cells, cultivated on glass for 24h. Visualisation with a reactant LIVE/DEAD and Hoechst 33342. Fluorescence microscope. Magnification ×10.
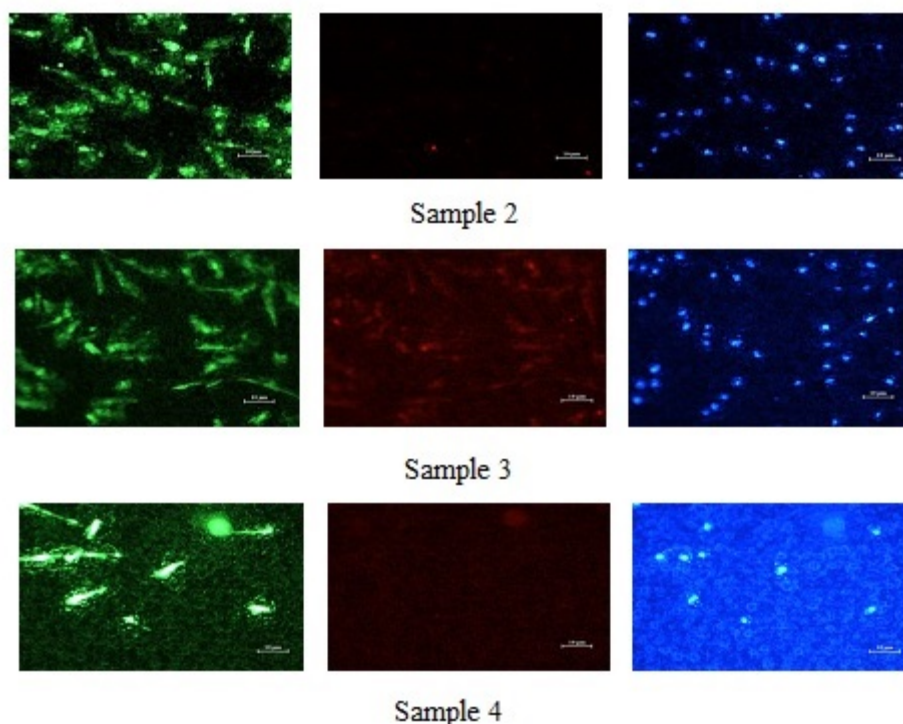
Fig 6. Human PDL cells, cultivated with sample 2, 3, 4 for 24h. Visualisation with reactant LIVE/DEAD and Hoechst 33342. Fluorescence microscope. Magnification ×10.
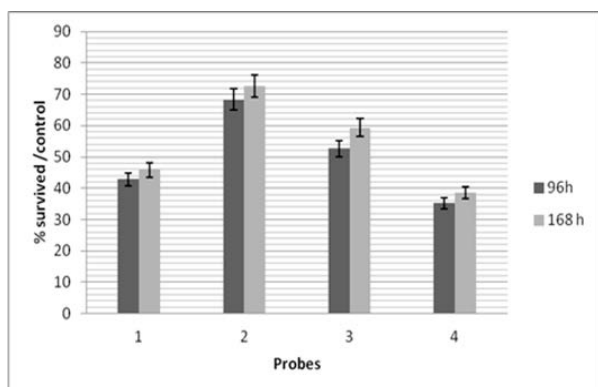

Fig. 5. Viability of PDL cells co-cultured with samples 1, 2, 3 and 4 for 96 h (black bars) and 168 h (grey bars).

CONCLUSIONS

From the experiments and analysis of the obtained results we can make several conclusions.

Al-Si-Zr ribbons - samples 5 (w_{Zr} = 0.27 %) and 6 (w_{Zr} = 1.09 %) impede cell adhesion and cell growth of McCoy-Plovdiv and PDL cell lines. They have a negative impact on the development of McCoy-Plovdiv and PDL cells in conditions of co-culture, initiating changes in cell morphology and cell monolayer and causing cell death. Samples 5 and 6 generate cytotoxic activity in the culture medium, causing cell death of McCoy-Plovdiv cells. The higher content of zirconium in the ternary alloy increases the percentage of surviving cells and improves the biocompatibility of the material.

The experiments with human PDL cells for assessment of the viability and biocompatibility of the investigated samples confirm that the anodic Al₂O₃ films provide better conditions for development of PDL cells compared to untreated aluminium and ternary Al-Si-Zr alloys. Metal surfaces with 10 μm thick oxide film (sample 2) show the best properties in terms of cells vitality, proliferation and growth compared to sample 3 (20 μm thick oxide film) and sample 4 (30 μm thick oxide film).

REFERENCES:

1. H. Alexander, J. Brunski, S. Cooper., L. Hench, R. Hergenrother, A. Hoffman, J. Kohn, R. Langer, N. Peppas, B. Ratner, S. Shalaby, S. Visser, I. Yannas, in: Biomaterials Science: An Introduction to Materials in Medicine, B. Ratner, A. Homan, F. Schoen, J. Lemons (eds), Academic Press, San Diego, CA, 1996, p. 37.
2. M. Balazic, M. Brojan, D. Bombac, R. Jr. Caram, F. Kosel, J. Kopac, in: Surface Engineered Surgical Toolsand Medical Devices, J. Jackson, W. Ahmed (eds), Springer, 2007, p. 533.
3. M. Fujita, *Kokubyo Gakkai Zasshi*, **60** (1), 54 (1993).

375

4. K. de Groot, Bioceramics of Calcium Phosphate, CRC Press, Boca Raton, 1983.
5. G. Manivasagam, D. Dhinasekaran, A. Rajamanickam, *Recent Patents on Corrosion Science*, **2**, 40 (2010).
6. E. Briggs, M. Karlsson, A. Walpole, E. Palsgard, P. Wilshaw, *Journal of Material Science: Materials in Medicine*, **15**, 1 (2004).
7. A. Walpole, E. Briggs, M. Karlsson, E. Palsgard, P. Wilshaw, *Mat.-wiss. u. Werkstofftech.*, **34**, 1064 (2003).
8. G. J. Chi, S. W. Yao, J. Fan, W. G. Zhang, H. Z. Wang, *Surface and Coatings Technology*, **157**, 162 (2002).
9. G. Patermarakis, P. Lenas, Ch. Karavassilis, G. Papayiannis, *Electrochimica Acta*, **36**, 709 (1991).
10. Ch. Girginov, I. Kanazirski, A. Zahariev, P. Stefchev, *J. Univ. Chem. Tech. Met.*, **47**, 187 (2012)
11. G. Tong, L. Dakuia, W. Zuoshanb, L. Xiangfaa, *Materials Science and Engineering A.*, **552**, 523 (2012).
12. O. Schob, H. Nowotny, F. Benesovsky, *Planseeber. Pulvermetall.*, **10**, 65 (1962).
13. D. Docheva, D. Padula, C. Popov, *European Cells and Materials*, **19**, 228 (2010).
14. M. Draganov, M. Murdjeva, V. Sarafian, *Cytotechnology*, **42** (3), 163 (2003).

БИОСЪВМЕСТИМОСТ НА АЛУМИНИЕВИ СПЛАВИ И АНОДЕН Al₂O₃

Р. Д. Манчева[1], Д. Д. Кираджийска[1*], Я. Н. Феодорова[2], К. И. Драганова[3]

[1]*Катедра „Химични науки", Фармацевтичен Факултет, Медицински Университет – Пловдив, бул. Васил Априлов 15А, 4000 Пловдив, България*
[2]*Катедра „Медицинска биология", Медицински Факултет, Медицински Университет – Пловдив, бул. Васил Априлов 15А, 4000 Пловдив, България*
[3]*Катедра „Микробиология и имунология", Фармацевтичен Факултет, Медицински Университет – Пловдив, бул. Васил Априлов 15А, 4000 Пловдив, България*

(Резюме)

Целта на настоящата работа е да се изследват биосъвместимост, виталност и цитотоксичност на тройни алуминиеви сплави Al-Si-Zr и анодиран технически алуминий EN AW 1050A. Съществува голямо разнообразие от метали, използвани в различни медицински устройства. Поради това все по-често се търсят методи за оптимизиране на техните механични свойства, а също и за повишаване на биосъвместимостта им. Тройни сплави с различно съдържание на легиращ елемент цирконий са изследвани в условия на съвместно култивиране с клетъчни линии PDL и McCoy-Plovdiv. Цирконият е влаган в процеса на леене на сплавите поради добрите му биологични качества и корозионна устойчивост. За сравнение са разгледани свойствата на образци от получен по електрохимичен път оксиден филм с различна дебелина върху технически алуминий. Анодирането е проведено в разтвор на 15% H₂SO₄ за определени интервали от време. Резултатите показват, че оксидни филми с дебелина 10 и 20 μm осигуряват по-добро клетъчно развитие в сравнение с тройната система Al-Si-Zr. Оксиден филм с дебелина 10 μm демонстрира най-добри качества по отношение на клетъчна виталност, пролиферация и растеж.

Evaluation of the separation of steroids in combined forms by RP HPLC with UV-detection and gas chromatography

D. Tsvetkova[1*], D. Obreshkova[1,2], S. Ivanova[1,2], B. Hadjieva[3]

[1]Department of Pharmaceutical Chemistry,Medical University-Sofia, Faculty of Pharmacy, 2 Dunav Str., Sofia 1000, BULGARIA

[2]Department of Pharmacognosy and Pharmaceutical Chemistry, Medical University-Plovdiv, Faculty of Pharmacy, 15A Vasil Aprilov Str., Plovdiv 4002, BULGARIA

[3]Medical University-Plovdiv, Medical College,15A Vasil Aprilov Str., Plovdiv 4002, BULGARIA

The aim of the current study is the evaluation of the separation of steroids from accompanying substances in drug products as follows: estradiol hemihydrate from didrogesterone (in Femoston tabl.) and estradiol valerate from levonorgestrel (in Climonorm tabl.) and ciproterone acetate (in Climen tabl.). Reversed phase (RP) HPLC with UV-detection and gas chromatography were applied. For the RP HPLC method with UV-detection the following conditions were used: a) column: Nova Pack C_{18}; isocratic elution with mobile phase: acetonitrile : methanol : water = 40 : 5 : 55 v/v/v; flow rate: 1 ml/min; UV-detection at λ = 204 nm; b) column Nova Pack C_{18}; gradient elution with: 0-10 min: acetonitrile : methanol : water = 35 : 5 : 60 v/v/v; 10-20 min; acetonitrile : methanol : water = 70 : 5 : 25 v/v/v, flow rate: 1 ml/min, UV-detection at λ = 230 nm.

Although RP-HPLC separation at isocratic conditions allows determination of estradiol hemihydrate with high reproducibility with the highest sensitivity at λ = 204 nm, the analysis in medicinal products requires additional time for elution of components more non-polar than estradiol hemihydrate, which are present in the sample: in Femoston tabl.: t_R = 13.42 min for didrogesterone; t_R = 4.85 min for estradiol hemihydrate. The experimental results showed that RP HPLC separation with gradient elution is characterized by higher selectivity. It is found that the detection wavelength λ = 230 nm is optimal for the achievement of high sensitivity and it is universal for the identification of other active principles and for obtaning of a stable base line with gradient elution.

For the GC method: a column HP-35 (30 m × 0.25 mm × 0.25 µm), temperature program from 100 ºC to 330 °C and mass detection were used. Degradation of analytes at high temperature, their different degree of ionization and the different sensitivity of their detection lead to uncertainty in the GC/MS analysis, therefore, HPLC is the more suitable method for analysis of steroid components.

Keywords: Estradiol, RP HPLC, UV-detection, GC, combined forms.

INTRODUCTION

Osteoporosis is a skeletal disease which is more common in women than men: 50 % of women [1] and 25 % of men aged over 50 have fractures [2]. Osteoporosis in postmenopausal women is caused by the reduced estrogen levels [3, 4] leading to an imbalance between the activity of osteoblasts and osteoclasts [5]. The imbalance between bone resorption and formation is due to the extension of the life cycle of osteoclasts and shortening the cycle of osteoblasts [6]. In postmenopause, bone resorption rate sharply increases. Estrogens bind to estrogen receptors in the cells. Estrogens inhibit the degradation of bone tissue and suppress bone resorption by regulating the expression of RANK-receptor activator of nuclear factor kB (NFkB) and osteoprotegrin in osteoblasts [7].

Hormones reduce the production of interleukin 1, interleukin 6, tumor necrosis factor α [8] and macrophage colony stimulating factor, which mediate osteoclastogenesis [9]. Hormone therapy reduces the estrogen deficiency [10], decreases the risk of osteoporotic fractures, suppresses biochemical markers of bone resorption, improves bone mineral density [11] and reduces bone loss [12]. Estrone stimulates the development of osteoblasts in women and testosterone is the hormone responsible for bone health in men [13]. Hormone therapy includes: estradiol (Climara); danazol (Danocrine); medroxy-progesterone acetate (Provera); nandrolone (Retabolil); noresthisterone acetate (Primolut); oxandrolone (Anavar); testosterone; tibolone (Livial); stanozolol (Winstrol). Combination of estrogens and bisphophonates alendronate [14], risedronate [15] and zoledronate [16], has additive effects on the reduction of bone resorption markers. In postmenopausal women the combination estrogen/alendronate increases bone mineral density [17].

In combined drug products for the treatment of menopausal symptoms in postmenopause are

---

* To whom all correspondence should be sent:
E-mail: dobrinka30@mail.bg; dobrinka30@abv.bg

applied: 1) estradiol hemihydrate with didrogesterone 10 mg (Femoston tabl.) and norethisterone acetate 1 mg (Trisequense tabl.); 2) estradiol valerate with: ciproterone acetate 1 mg (Climen tabl.) [18]; dienogest 2 mg (Climodien tabl.) [19] and Levonorgestrel 0.15 mg (Climonorm tabl.) [20].

For the determination of 17β-estradiol and estradiol valerate in combination with other components in the tablets the following methods have been developed: I) RP HPLC with UV-detection: 1) 17β-estradiol/estriol/estrone: column C_{18} micro Bondapak (250 mm × 4.6 mm × 10 μm) in isocratic mode, mobile phase: acetonitrile : water = 50 : 50 v/v, flow rate: 1 ml/min, column temperature: 30 °C, λ = 205 nm [21]; 2) 17β-estradiol/drospirenone: column Waters Symmetry C_{18} (250 mm × 4.6 mm × 5 μm), mobile phase: acetonitrile : water = 70 : 30 v/v, λ = 279 nm [22]; 3) estradiol valerate/dienogest: column ACE C_8 (250 mm × 4.6 mm × 5 μm), mobile phase: ammonium nitrate : acetonitrile = 30 : 70 v/v, flow rate: 2 ml/min, λ = 280 nm, internal standard cyproterone acetate [23]; II) gas chromatography with mass detection (GC/MS): 17β-estradiol [24] and estradiol valerate/medroxyprogesterone acetate [25].

The advantage of these methods is good selectivity, obtained by using columns with length 250 mm and diameter size of particles 5-10 μm.

The aim of the current study is the estimation of the influence of lower column length (150 mm) and lower diameter size of particles (3.5-4 μm) on the isocratic and gradient RP-HPLC separation of steroids from accompaning substances in drug products.

MATERIALS AND METHODS

Materials

1) Reference substances:

Estradiol hemihydrate N: D00 166 536, purity > 99 %

Estradiol valerate, purity > 99 %

Didrogesterone, purity > 99 %

Levonorgestrel, purity > 99 %

Ciproterone acetate, purity > 99 %

2) Solvents with pharmacopoeial purity: acetonitrile for HPLC (Sigma Aldrich, N: SZBD 150 SV UN 1648); methanol (Sigma Aldrich, N: SZBD 063 AV UN 1230); ultra pure water.

3) drug products: Femoston tabl. (estradiol hemihydrate 2 mg/didrogesterone 10 mg) (N: 341141 Abbott, Netherland); Climonorm tabl. estradiol valerate 2 mg/levonorgestrel 0.15 mg (N: WEKSBH Bayer (Germany); Climen tabl.: estradiol valerate 2 mg/ciproterone acetate 1 mg (N: 344418, Bayer (Germany).

Methods

I. Instrumentation.

1) HPLC 200 chromatograph (Perkin Elmer, USA) with: spectrophotometric detector LC-785A (Bioanalytical systems, USA); autosampler 200 series; thermostat (Perkin Elmer, Waltham, MA, USA); columns: Nova Pack C_{18} (150 mm × 4.6 mm × 4 μm) (Waters USA,WAT 044375); Li Chrospher C_{18} (125 mm × 4 mm × 4 μm) (Phenomenex, USA, 00E-3043-D0); Zorbax Eclipse XDB C_8 (150 mm × 4.6 mm × 3.5 μm) (Agilent, USA, 993967-906).

2) Gas chromatograph "Trace" with mass spectral detector TSQ ("Thermo Fisher Scientific", Waltham, MA, USA); "split/splitless" injector; capillary column HP-35 (30 m × 0.25 mm × 0.25 μm) ("Agilent", Santa Clara, CA, USA).

3) Ultrasonic bath (Branson Wilmington, NC, USA).

4) Apparatus for ultra pure water "Milli-Q", "Millipore" (Bedford, MA, USA) and "Elga" (VWR International, Randor, PA, USA).

II. Chromatographic conditions.

1) RP HPLC – columns: Nova Pack C_{18}, Li Chrospher C_{18}, Zorbax Eclipse XDB C_8, isocratic elution with mobile phase: acetonitrile : methanol : water = 40 : 5 : 55 v/v/v, flow rate: 1 ml/min, UV-detection at an analytical wavelength λ = 204 nm.

2) RP HPLC – columns: Nova Pack C_{18}, Li Chrospher C_{18}, Zorbax Eclipse XDB C_8, gradient elution with: 0-10 min: acetonitrile : methanol : water = 35 : 5 : 60 v/v/v; 10-20 min: acetonitrile : methanol : water = 70 : 5 : 25 v/v/v, flow rate: 1 ml/min, UV-detection at λ = 230 nm.

3) GC: column HP-35 (30 m × 0.25 mm × 0.25 μm), split/splitless injection at 260 °C, temperature program from 100 ºC to 330 °C and mass detection by electron impact ionisation mode and monitoring of positive ions.

III. Preparation of stock standard solution of estradiol hemihydrate and estradiol valerate.

Accurately weighed quantities (0.05 g) of the reference substances estradiol hemihydrate and estradiol valerate were separately dissolved in 15 ml acetonitrile under sonication in ultrasonic bath. After dilution with acetonitrile in a volumetric flask of 50.0 ml solutions with a concentration of steroids 1.0 mg/ml were obtained.

IV. Preparation of standard solution of estradiol hemihydrate for RP HPLC.

Standard solution was prepared by dilution of 200 μl of the stock standard solution of estradiol

hemihydrate (1.0 mg/ml) in a volumetric flask of 10.0 ml with acetonitrile. The resulting solution was with concentration of estradiol hemihydrate 2.10^{-5} g/ml (20 µg/ml). The solution was filtered through a membrane filter 0.45 µm and analyzed by the described RP HPLC method.

V. Preparation of standard solution of estradiol hemihydrate for GC/MS.

The standard solution was prepared by dilution of 1 ml of the stock standard solution of estradiol hemihydrate (1.0 mg/ml) in a volumetric flask of 10.0 ml with acetonitrile. The resulting solution was with concentration of estradiol hemihydrate: 1.10^{-4} g/ml (100 µg/ml). The solution was filtered through a membrane filter 0.45 µm and analyzed by the described RP HPLC method.

VI. Preparation of solutions from tablets.

From the stirred tablet mass an amount equivalent to 2 mg estradiol hemihydrate was weighed, 10 ml of acetonitrile were added and samples were sonicated for 5 min in an ultrasonic bath with periodical stirring. The resulting suspension was diluted in a volumetric flask of 100.0 ml with acetonitrile, sonicated for 10 min in an ultrasonic bath, and placed for 30 min in the dark place for precipitation. An aliquot part was filtered through a membrane filter 0.45 µm and analyzed by the described RP HPLC method.

RESULTS AND DISCUSSION

I, Analysis of estradiol hemihydrate and estradiol valerate by RP-HPLC with UV-detection.

HPLC with UV-detection was carried out in order to find out the more suitable stationary phase for separation of estradiol hemihydrate and estradiol valerate from potential related ingredients in: Femoston tabl. (esteradiol hemihydrate/didrogesterone), Climonorm tabl. (estradiol valerate/levonorgestrel) and Climen tabl. (estradiol valerate/ciproterone acetate).

Columms Nova Pack C_{18} (150 mm × 4.6 mm × 4 µm), Li Chrospher C_{18} (125 mm × 4 mm × 4 µm) and Zorbax HDB C_8 (150 mm × 4.6 mm × 3.6 µm) were investigated. The evaluation of the various columns operating in reversed mode shows that Nova Pack C_{18} (150 mm × 4.6 mm × 4 µm) displays the highest parameters (efficiency and selectivity) for estradiol hemihydrate and estradiol valerate and accompanying substances in Femoston tabl., Climonorm tabl. and Climen tabl. In isocratic RP-HPLC with columm Nova Pack C_{18} in Femoston tabl. for didrogesterone t_R = 13.42 min was obtained in comparison with didrogesterone t_R = 8.5 min obtained with Li Chrospher C_{18}.

On Fig. 1. are illustrated: chromatogram of standard solution of estradiol hemihydrate and chromatogram of 10 µl of solution of Femoston tabl. in 100 ml of acetonitrile.

The chromatograms are obtained under conditions of the isocratic mode, column Nova Pack C_{18}, mobile phase: acetonitrile : methanol : water = 40 : 5 : 55 v/v/v, flow rate: 1 ml/min and UV-detection at λ = 204 nm.
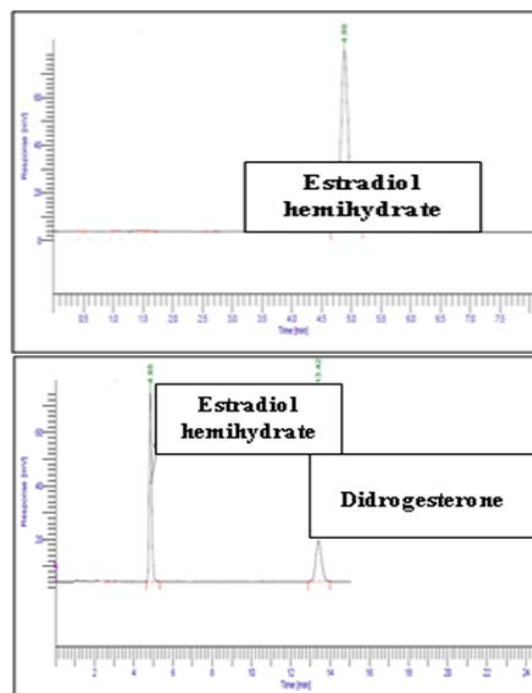

Fig. 1. Chromatograms of 20 µl of 20 µg/ml standard solution of estradiol hemihydrate and of Femoston tabl: isocratic RP-HPLC, flow rate: 1 ml/min, λ = 204 nm.

Identification of estradiol hemihydrate in Femoston tabl. is proven by the equal data for the chromatographic parameter retention time (t_R = 4.86 min) in the tablets and in the standard of estradiol hemihydrate. The equal results for t_R = 13.42 min in the tabl. and in the standard confirm the identification of didrogesterone in Femoston tabl.

RP HPLC separation in isocratic conditions allows determination of estradiol hemihydrate with high reproducibility. Sensitivity is highest at λ = 204 nm. Inspite of this benefit, the disadvantage is that the determination under isocratic conditions in medicinal products requires additional time for elution of components more non-polar than estradiol hemihydrate present in the sample: in Femoston tabl.: t_R = 13.42 min for didrogesterone; t_R = 4.85 min for estradiol hemihydrate.

In order to optimize the conditions for RP HPLC analysis of estradiol hemihydrate in the presence of related components the RP HPLC with gradient elution was applied for analysis in tablets in the

379

column: Nova Pack C_{18}. After isocratic elution the time for cleaning of the column take more time (1.5 h) than after gradient elution (1 h), which is the reason for using the gradient mode of analysis.

Chromatograms are illustrated on Fig. 2. (Femoston tabl.), Fig. 3. (Climonorm tabl.) and Fig. 4. (Climen tabl.).

The equal data for $t_R = 4.86$ min in the tabl. and in the standard of estradiol hemihydrate prove the identification of estradiol hemihydrate in Femoston tabl. Identification of didrogesterone in Femoston tabl. is confirmed by the equal results for $t_R = 8.5$ min in the tablets and in the standard of didrogesterone.

Identification of estradiol valerate in Climonorm tabl. and Climen tabl. is proven by the equal values of $t_R = 11.46$ min in tabl. and in standard of estradiol valerate. The equal results for $t_R = 8$ min in Climonorm tabl. and in the respective standard confirm the identification of levonorgestrel in tabl. In Climen tabl. ciproterone acetate is identified by the equal data for $t_R = 8.29$ min in the tablets and in the standard of ciproterone acetate.

In gradient RP-HPLC analysis of estradiol hemihydrate in the presence of related components, the gradient elution with detection at $\lambda = 230$ nm is optimal for the achievement of high sensitivity and is universal for the identification of other active principles and for obtaining of stable base line. From Figs. 2, 3 and 4 it is obvious that in RP gradient elution the active principles of the examined products were separated for 10 min, but the presence of other non-polar ingredients requires additional 10 min for elution and this leads to increasing of the time of analysis to about 20 min. The methods can be used for the routine analysis of estradiol hemihydrate and estradiol valerate in combined pharmaceutical products.

II. Identification of estradiol hemihydrate and estradiol valerate by gas chromatography with mass spectral detection.

On Fig. 5. a chromatogram of the standard solution of estradiol hemihydrate with concentration of 100 μg/ml and the mass spectrum of the peak with a retention time of $t_R = 6.2$ min, obtained by electron impact ionisation mode and monitoring of positive ions are illustrated.
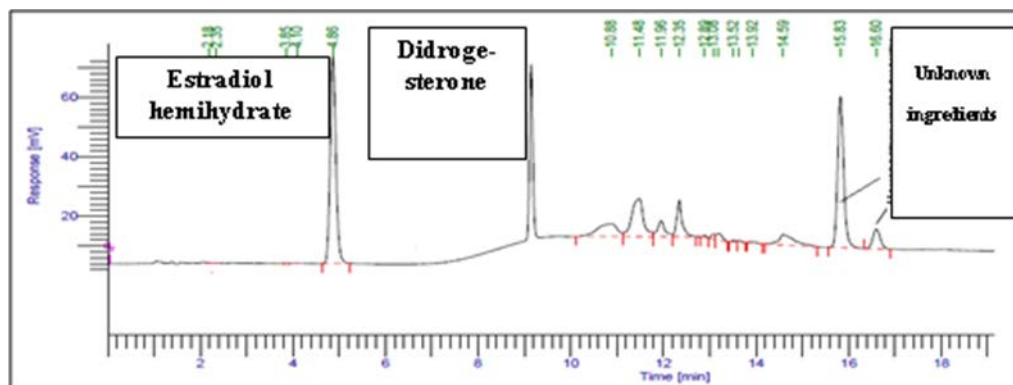

Fig. 2. Chromatogram of Femoston tabl. obtained by gradient RP-HPLC with UV-detection at $\lambda = 230$ nm.
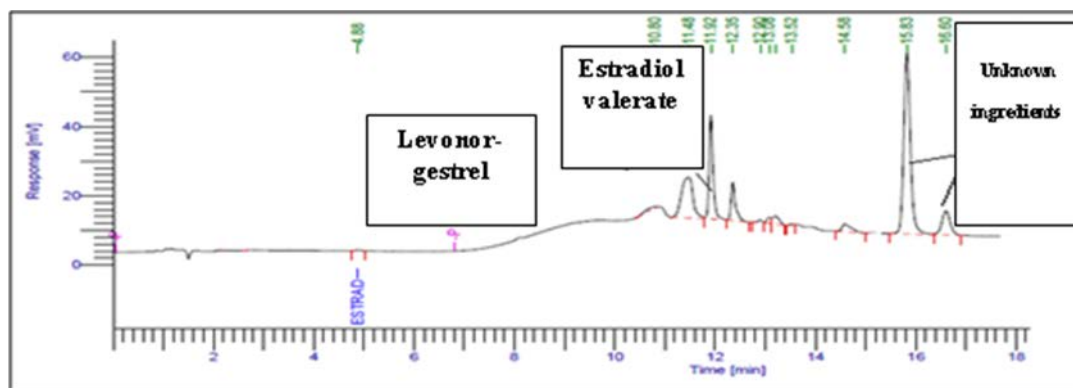

Fig. 3. Chromatogram of Climonorm tabl. obtained by gradient RP-HPLC with UV-detection at $\lambda = 230$ nm.
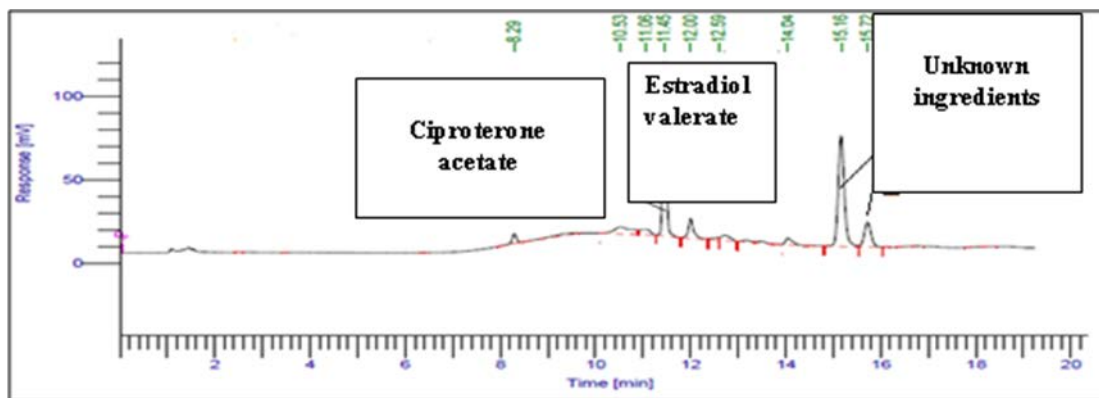
Fig. 4. Chromatogram of Climen tabl. obtained by gradient RP-HPLC with UV-detection at λ = 230 nm.
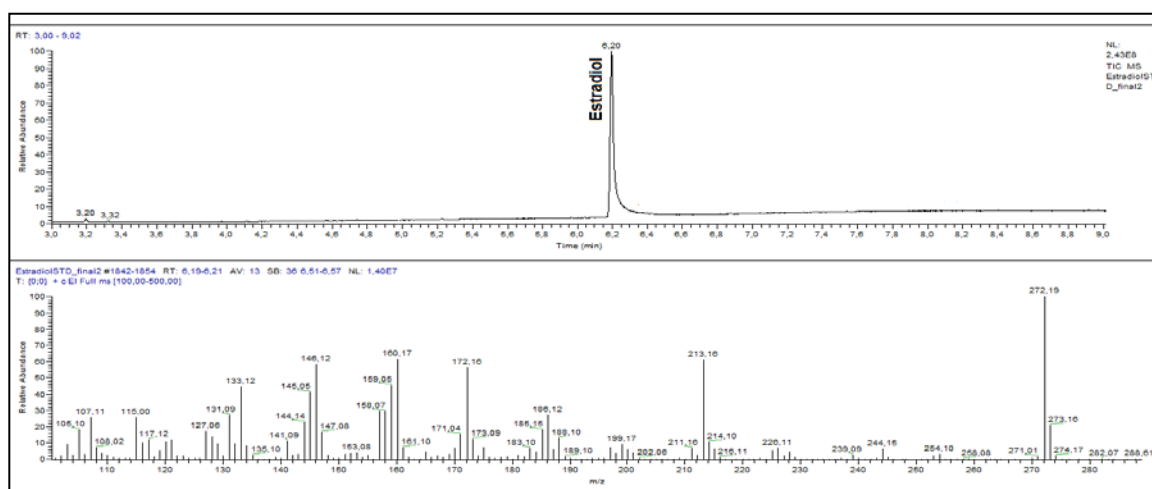

Fig. 5. Chromatogram of a standard solution of estradiol hemihydrate and mass spectrum of the peak at t_R = 6.2 min.
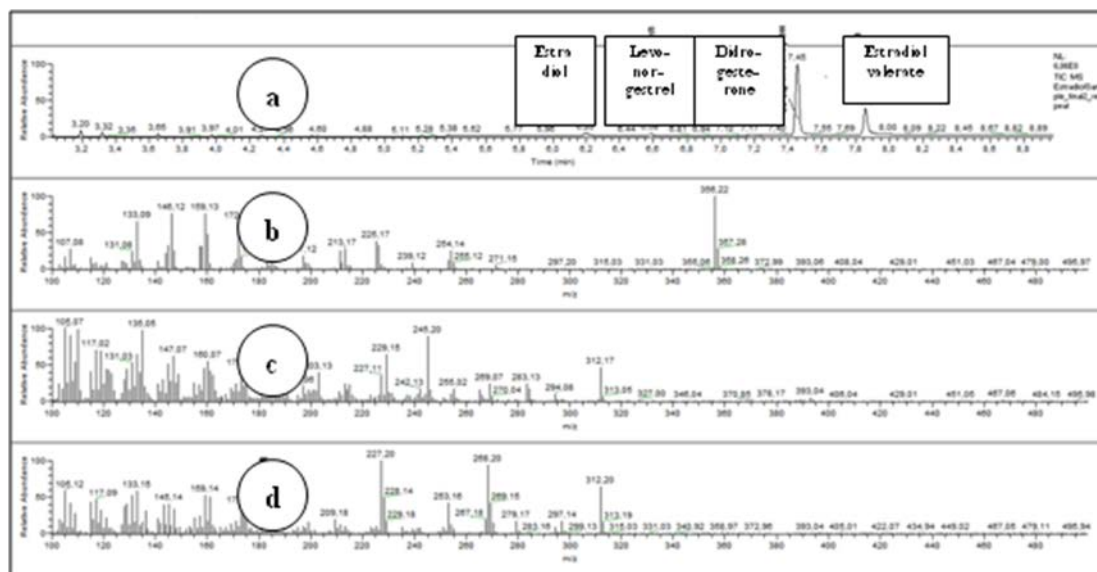

Fig. 6. Total ion chromatogram of a mixed acetonitrile solution of Femoston tabl., Climonorm tabl. and Climen tabl.

A mixed solution of Femoston tabl., Climonorm tabl. and Climen tabl. was filtered and analysed by gas chromatography. Fig. 6. shows: a) chromatogram of a mixed solution of Femoston tabl., Climonorm tabl. and Climen tabl. in acetonitrile and mass spectra of: b) estradiol valerate: t_R = 7.86 min; c) levonorgestrel: t_R = 6.58 min; d) didrogesterone: with t_R = 7.45 min.

From Fig. 6. it is obvious that the use of gas chromatography allows to analyze Femoston tabl., Climonorm tabl. and Climen tabl. and to identify their active principles. Mass spectral identification using specific mass spectral libraries is particularly convenient in the qualitative analysis. Steroids are very sensitive to contamination of the liner in the injector when introducing the sample at high temperature, which leads to degradation of the analytes. The electronic ionization with positive ion monitoring is the most popular variant of mass spectral detection in gas chromatography, but leads to a very different degree of ionization of the various analytes, and thus achieves a different sensitivity for detection thereof. For this reason, as shown in Fig. 7., although the concentrations of estradiol hemihydrate and didrogesterone are equal, the magnitude of their signals is clearly different and cyproterone acetate in Climen tabl. is not registered on the chromatogram. For quantitative analysis of the active ingredients in the tablets GC/MS requires the use of clean liners and a suitable internal standard.

CONCLUSION

Insipite of the fact, that RP HPLC separation with isocratic elution and UV-detection is characterized with the highest sensitivity at λ = 204 nm, the disadvantage for analysis of estradiol hemihydrate in medicinal products is that it requires additional time for elution of the more non-polar components. On the other hand, the degradation of analytes at a high temperature, their different degree of ionization and the different sensitivity of the detection lead to uncertainty of the GC/MS analysis. Due to this two reasons and because of higher selectivity, the RP HPLC method with gradient elution and UV-detection at λ = 230 nm is the most appropriate option for analysis of steroid components such as estradiol hemihydrate and estradiol valerate in dosage combined preparations.

REFERENCES

1. L. A. Cummings-Vaughn, J. K. Grammack, *Med. Clin. North Amer.*, **95**(3), 495 (2011).

2. E. Seeman, G. Bianchi, S. Khosla, J. A. Kanis, E. Orwoll, *Osteoporos. Int.*, **17**(11), 1577 (2006).

3. A. R. Genazzani, M. Gambacciani, H. P. Schneider, C. Christiansen, *Climacteric.*, **8**(2), 99 (2005).

4. S. Ejiri, M. Tanaka, N. Watanabe, R. B. Anwar, E. Yamashita, K. Yamada, M. Ikegame, *J. Bone Miner. Res.*, **26**(5), 409 (2008).

5. L. G. Raisz, *J. Clin. Invest.*, **115**(12), 3318 (2005).

6. J. C. Gallagher, *Maturitas*, **60**(1), 65 (2008).

7. B. L. Riggs, *J. Clin. Invest.*, **106**(10), 1203 (2000).

8. G. E. Krassas, P. Papadopoulou, *J. Musculoskelet. Neuronal. Interact.*, **2**(2), 143 (2001).

9. F. A. Tremollieres, C. A. Ribot, *Maturitas*, **65**(4), 348 (2010).

10. V. B. Popat, K. A. Calis, V. H. Vanderhoof, G. Cizza, J. C. Reynolds, N. Sebring, J. F. Troendle, L. M. Nelson, *J. Clin. Endocrinol. Metab.*, **94**(7), 2277 (2009).

11. J. A. Cauley, J. Robbins, Z. Chen, S. R. Cummings, R. D. Jackson, A. Z. LaCroix, M. LeBoff, C. E. Lewis, J. McGowan, J. Neuner, M. Pettinger, M. L. Stefanick, J. Wactawski-Wende, N. B. Watts, *JAMA*, **290**(13), 1729 (2003).

12. Y. Z. Bagger, L. B. Tanko, P. Alexandersen, H. B. Hansen, A. Mollgaard, P. Ravn, P. Qvist, J. A. Kanis, C. Christiansen, *Bone*, **34**(4), 728 (2004).

13. P. R. Ebeling, *N. Engl. J. Med.*, **358**(14), 1474 (2008).

14. A. V. Jaroma, T. A. Soininvaara, H. Kröger, *Bone Joint J.*, **97-B**(3), 337 (2015).

15. J. Reginster, H. W. Minne, O. H. Sorensen, M. Hooper, C. Roux, M. L. Brandi, B. Lund, D. Ethgen, S. Pack, I. Roumagnac, R. Eastell, *Osteoporos. Int.*, **11**(1), 83 (2000).

16. D. M. Black, P. D. Delmas, R. Eastell, I. R. Reid, S. Boonen, J. A. Cauley, F. Cosman, P. Lakatos, P. C. Leung, Z. Man, C. Mautalen, P. Mesenbrink, H. Hu, J. Caminis, K. Tong, T. Rosario-Jansen, J. Krasnow, T. F. Hue, D. Sellmeyer, E. F. Eriksen, S. R. Cummings, *N. Engl. J. Med.*, **356**(18), 1809 (2007).

17. H. G. Bone, S. L. Greenspan, C. McKeever, N. Bell, M. Davidson, R. W. Downs, R. Emkey, P. J. Meunier, S. S. Miller, A. L. Mulloy, R. R. Recker, S. R. Weiss, N. Heyden, T. Musliner, S. Suryawanshi, A. J. Yates, A. Lombardi, *J. Clin. Endocrinol. Metabolism*, **85**(2), 720 (2000).

18. J. T. Jensen, J. Bitzer, M. Serrani, *J. Contracept.*, **4**(1), 39 (2013).

19. A. Graziottin, *Minerva Ginecol.*, **66**(5), 479 (2014).

20. D. B. Georgiev, S. Golbs, A. Goudev, *Methods Find. Exp. Clin. Pharmacol.*, **23**(4), 197 (2001).

21. P. Wilson, *J. AOAC Int.*, **92**(3), 846 (2009).

22. Z. Aydoğmuş, E. M. Yılmaz, S. Yörüsün, S. Akpınar, *Int. School. Res. Not.*, **2015**, Article ID 534065, (2015).

23. M. G. Cağlayan, I. M. Palabiyik, F. Onur, *J. AOAC Int.*, **93**(3), 862 (2010).

24. B. Yilmaz, Y. Kadioglu, *Int. J. Pharm. Sci. Rev. Res.*, **2**(2), 44 (2010).

25. B. Yilmaz, *Anal. Sci.*, **26**(3), 391 (2010).

ОЦЕНКА НА РАЗДЕЛЯНЕТО НА СТЕРОИДИ В КОМБИНИРАНИ ФОРМИ ЧРЕЗ RP HPLC С UV-ДЕТЕКЦИЯ И ГАЗОВА ХРОМАТОГРАФИЯ

Д. Цветкова[1]*, Д. Обрешкова[1,2], С. Иванова[1,2], Б. Хаджиева[3]

[1]*Катедра "Фармацевтична химия",Медицински университет-София, Фармацевтичен факултет, ул. Дунав N : 2, София 1000, БЪЛГАРИЯ*

[2]*Катедра "Фармакогнозия и фармацевтична химия"Медицински университет-Пловдив, Факултет по фармация, ул. Васил Априлов N: 15А, Пловдив 4002, БЪЛГАРИЯ*

[3]*Медицински университет-Пловдив, Медицински колеж, ул. Васил Априлов N: 15А, Пловдив 4002, БЪЛГАРИЯ*

(Резюме)

Целта на настоящото изследване е оценката на разделянето на стероиди от придружаващи вещества в лекарствени продукти: Естрадиол хемихидрат от Дидрогестерон във Femoston табл. и Естрадиол валерат от Левоноргестрел (в Climonorm табл.) и Ципротерон ацетат (в Climen табл.). Приложени са HPLC метод с обърнати физи и УВ-детекция и газова хроматография. HPLC с УВ-детекция е проведен при следните условия: а) колона: Nova Pack C_{18}, изократично елуиране с подвижна фаза: ацетонитрил : метанол : вода = 40 : 5 : 55 об/об/об, скорост на потока: 1 мл/мин, УВ-детекция при аналитична дължина на вълната $\lambda = 204$ nm; б) колона Nova Pack C_{18}, градиентно елуиране: 0-10 мин: ацетонитрил : метанол : вода = 35 : 5: 60 об/об/об; 10-20 мин: ацетонитрил : метанол : вода = 70 : 5 : 25 об/об/об, скорост на потока: 1 мл/мин, УВ-детекция при $\lambda = 230$ mn.

Въпреки че, RP-HPLC разделянето при изократични условия позволява определяне на Естрадиол хемихидрат с висока възпроизводимост с най-висока чувствителност при $\lambda = 204$ nm, анализът на лекарствени продукти изисква допълнително време за елуиране на по-неполярни от Естрадиол хемихидрат компоненти, които присъстват в пробата: във Femoston табл.: $t_R = 13.42$ мин за Дидрогестерон и $t_R = 4.85$ мин за Естрадиол хемихидрат. Експерименталните резултати показват, че HPLC методът с градиентно елуиране се характеризира с по-висока селективност и, че дължината на вълната $\lambda = 230$ nm е оптимална за постигането на висока чувствителност и е универсална за идентифицирането на други активни съставки и за получаване на стабилна базова линия при градиентно елуиране.

При газовата хроматография са използвани: колона HP-35 (30 m x 0.25 mm x 0.25 μm), температурна програма от 100 °C до 330 °C и мас-детекция. Разграждането на аналитите при висока температура, тяхната различна степен на йонизация и различната чувствителността при детекцията им са причина за несигурност при газ-хроматографския анализ, поради което, HPLC е по-подходящ метод за анализ на стероидни компоненти.

Estimation of linearity and precision of the HPLC-HILIC method for analysis of estradiol hemihydrate

D. D. Tsvetkova[1]*, St. A. Ivanova[1,2], L. Saso[3], D. Obreshkova[1,2], M. Dimitrov[4]

[1]*Department of Pharmaceutical Chemistry, Faculty of Pharmacy, Medical University-Sofia, Dunav Str. 2, Sofia 1000, Bulgaria*

[2]*Department of Pharmacognosy and Pharmaceutical Chemistry Faculty of Pharmacy, Medical University-Plovdiv, Plovdiv 4002, Vasil Aprilov Str. 15A, Bulgaria*

[3]*Department of Physiology and Pharmacology ”Vittorio Erspamer”Sapienza University of Rome, Rome, Italy*

[4]*Department of Pharmaceutical Technology and Biopharmaceutics, Faculty of Pharmacy, Medical University-Sofia, Dunav Str. 2, Sofia 1000, Bulgaria*

The aim of the present study was the estimation of linearity and precision of an isocratic HPLC-HILIC method with UV-detection for identification and determination of estradiol hemihydrate in pharmaceutical dosage forms. Linear regression analysis was performed. The reg ression calib ration curve was built. Linearity accordance between concentration and peak area in the range: 3.10^{-6} g/ml ÷ 4.10^{-5} g/ml was proved by the regression equation: y = 2698.99 x – 2307.98. The least squares regression yielded a correlation coefficient R^2 = 0.999. LOD = 8.10^{-7} g/ml, LOQ = 8.10^{-6} g/ml. The results for the accuracy at P = 99 % (t = 4.03) were presented by the percent recovery R [%] within the confidence interval: RC: 97.16 % ÷ 101.84 % (RSD = 1.42).

Precision was estimated by standard deviation, relative standard deviation and confidence interval. All data for the obtained quantity of estradiol hemihydrate correspond to the confidence interval: 1.96 mg/100 ml ÷ 2.02 mg/100 ml (SD = 0.03; RSD = 1.51).

The high selectivity and efficiency of separation by HPLC-HILIC with UV-detection at λ = 230 nm in an Amino-column and the elution of non-polar analytes before the polar ones (estradiol) shortens the time for analysis and leads to high repeatability.

Keywords: HPLC-HILIC, estradiol hemihydrate, linearity, precision.

INTRODUCTION

Osteoporosis is a widespread disease throughout the world and is considered as a major risk factor for public health [1]. In osteoporosis, the imbalance between bone resorption and formation is due to the increased life cycle of osteoclasts and shortened cycle of osteoblasts [2].

Estrogens bound to the estrogen receptors in the cells suppress the degradation of bone tissue and inhibit bone resorption by regulation of the expression of RANK-receptor activator of nuclear factor kB and osteoprotegrin in osteoblasts [3].

In postmenopausal women bone resorption rate is sharply increased. The low levels of estrogen at menopause reduce the ability for absorption and utilization of calcium in the bones, stimulate osteoclasts and inhibit the function of osteoblasts [4].

Stimulators of apoptosis of osteoclasts are bisphosphonates and calcitonin [5]. The mechanism of action of bisphosphonates on bone is complex and involves a decrease in the production and activity of osteoclasts, increase of osteoclast apoptosis, resulting in specific inhibition of farnesyl pyrophosphate synthetase – an enzyme that regulates biosynthesis of malonate, cholesterol and regulatory proteins (rab, rho, rac), which mediate the osteoclast activity. By affecting the osteoclasts, bisphosphonates inhibit bone resorption and decrease vertebral and non-vertebral fracture risk [6].

Adverse effects of bisphosphonates are esophageal cancer, nausea, vomiting [7] and atrial fibrillation (zoledronate) [8].

The molecular mechanism of action of selective estrogen receptor modulators (SERM) like raloxifene [9] include selective binding to α and β estrogen receptors.

Strontium ranelate inhibits osteoclastogenesis by suppression of the differentiation and activity of osteoclasts [10].

Hormonal therapy with estradiol [11] suppresses bone resorption and reduces the loss of bone mass [12]. Combined therapy leads to a greater reduction of fractures than single agent. The administration of bisphosphonate with raloxifene shows greater improvement in body mass density [13].

Hydrophilic interaction chromatography (HILIC-HPLC) has been described by Andrew Alpert in 1990 [14] as HPLC with hydrophilic

---

stationary phase and reversed-phase type eluents [15]. The HILIC mode of separation currently has been successfully applied for separation of some organic compounds and biomolecules [16]. It is suitable for analysis of carbohydrates, peptides and polar pharmaceuticals [17] and for quality assurance of glycoproteins in biological products [18].

Through HPLC with hydrophilic interaction a 10-fold increase in sensitivity in comparison with RP-HPLC is achieved [15].

Literature review reveals that for the determination of 17β-estradiol alone or in combinations with other drugs the most often applied methods are UV-spectrophotometry [19], derivative spectrophotometry [20], HPLC with normal phases [21] and HPLC with reversed phases and UV-detection [19], whereas for 17β-estradiol and drospirenone: a C_{18} column, mobile phase: acetonitrile : water = 70 : 30 v/v, λ = 279 nm [20].

The aim of the present study was the validation of the isocratic HPLC-HILIC method with UV-detection in accordance with the International Conference on Harmonization Guidelines [22] for the analytical parameters: limearity, LOD, LOQ. precision (repeatability) and accuracy for identification and determination of estradiol hemihydrate in dosage preparation.

MATERIALS AND METHODS

Materials

I) Reference standard: estradiol hemihydrate: D00 166536 with purity > 99 %.

II) Reagents with analytical grade quality: acetonitrile for HPLC (Sigma Aldrich, N: SZBD 150 SV UN 1648), distilled water.

III) Tablets

Trisequens tabl. (2 mg estradiol hemihydrate/1 mg norethisterone acetate) (DF 70298 Novo Nordisk, Netherlands)

Climonorm tabl. (2 mg estradiol valerate/0.15 mg levonorgestrel) (WEKSBH Bayer, Germany)

Climen tabl. (2 mg estradiol valerate/10 mg ciproterone acetate) (344418, Bayer, Germany).

Methods: HPLC-HILIC method

Instrumentation

HPLC 200 (Perkin Elmer, USA) with: spectrophotometric detector LC-785A (Bioanalytical systems, USA); thermostat (Perkin Elmer, Waltham, MA, USA); ultrasonic bath (Branson Wilmington, NC, USA); apparatus for ultra pure water: "Milli-Q", "Milipore" (Bedford,

MA, USA) and " Elga" (VWR International, Randor, PA, USA).

Chromatographic conditions: isocratic HPLC-HILIC elution with: stationary phase: column Spherisorb Amino (250 mm × 4.6 mm × 5 μm), mobile phase: acetonitrile : water = 55 : 45 v/v, flow rate: 2 ml/min and UV-detection at λ = 230 nm.

Preparation of solutions of the reference substance estradiol hemihydrate for validation of the HPLC-HILIC-method for analytical parameter linearity.

Preparation of stock standard solution of estradiol hemihydrate

An accurately weighed quantity (0.05 g) of the reference substance estradiol hemihydrate was dissolved in 15 ml of acetonitrile under sonication in a ultrasonic bath. After dilution with acetonitrile in a volumetric flask of 50.0 ml a solution with a concentration of estradiol hemihydrate of 1.0 mg/ml was obtained.

Preparation of standard solutions of estradiol hemihydrate

For the calibration curve for HPLC-HILIC-method a series of standard solutions were prepared by dilution of 30 μl, 50 μl, 100 μl, 200 μl, 300 μl and 400 μl of the stock standard solution of estradiol hemihydrate (1.0 mg/ml) in volumetric flasks of 10.0 ml with the mobile phase acetonitrile : water = 55 : 45 v/v. The resulting solutions were with concentrations of estradiol hemihydrate: 3.10^{-6} g/ml, 5.10^{-6} g/ml, 1.10^{-5} g/ml, 2.10^{-5} g/ml, 3.10^{-5} g/ml and 4.10^{-5} g/ml, respectively. The solutions were filtered through a membrane filter 0.45 μm and analyzed by the described HPLC-HILIC-method.

Preparation of solutions from tablets

From the stirred tablet mass an amount equivalent to 2 mg estradiol hemihydrate was weighed, 10 ml of acetonitrile were added and the samples were sonicated for 5 min in an ultrasonic bath under periodical stirring. The resulting suspension was diluted in a volumetric flask of 100.0 ml with acetonitrile, sonicated for 10 min in an ultrasonic bath, and placed in the dark place for 30 min for precipitation. An aliquot was filtered through a membrane filter 0.45 μm and analyzed by the described HPLC-HILIC-method.

RESULTS AND DISCUSSION

In order to search for opportunities to shorten the time of analysis, other options for chromatographic separation were used. Due to the

presence in the analyzed compounds of mainly less polar components than estradiol hemihydrate and estradiol valerate, the possibilities for their elution in reversed order by HPLC-HILIC distribution mechanism were tested.

The chromatograms from the isocratic HPLC-HILIC elution of the components of tablets are illustrated for: trisequens tabl. (estradiol hemihydrate/norethisterone acetate) (Fig. 1.); climonorm tabl. (estradiol valerate/levonorgestrel) (Fig. 2.) and climen tabl. (estradiol valerate/ciproterone acetate) (Fig. 3.). The optimized conditions were: column Spherisorb Amino (250 mm × 4.6 mm × 5 μm), mobile phase: acetonitrile : water = 55 : 45: v/v, flow rate: 2 ml/min, UV-detection at λ = 230 nm.
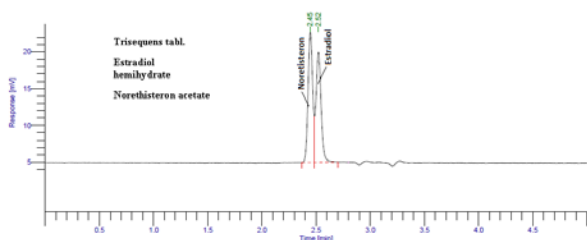

Fig. 1. Chromatogram of trisequens tabl. (estradiol hemihydrate/norethisterone acetate) at isocratic HPLC-HILIC, flow rate: 2 ml/min, UV-detection at λ = 230 nm.
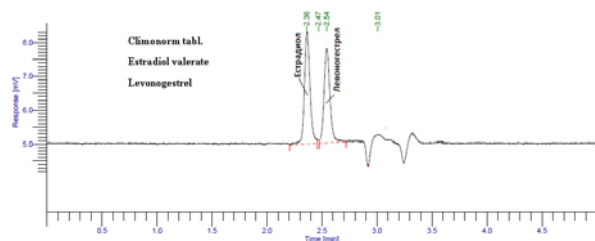

Fig. 2. Chromatogram of climonorm tabl. (estradiol valerate/levonorgestrel) at isocratic HPLC-HILIC, flow rate: 2 ml/min, UV-detection at λ = 230 nm.
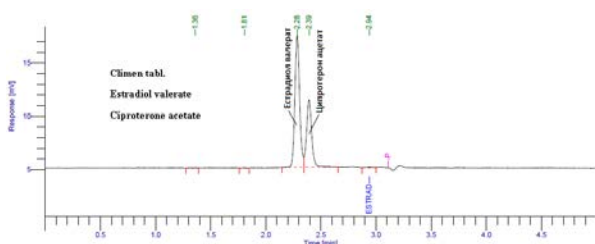

Fig. 3. Chromatogram of climen tabl. (estradiol valerate/ciproterone acetate) at isocratic HPLC-HILIC, flow rate: 2 ml/min, UV-detection at λ = 230 nm.

From Fig. 1, Fig. 2 and Fig. 3. it is obvious that the components of trisequens tabl., climonorm tabl. and climen tabl. are separated by HPLC-HILIC mechanism using Amino column in less than 4 min.

Validation of the isocratic HPLC-HILIC-method with UV-detection for analysis of estradiol hemihydrate

HPLC-HILIC-analytical method for estradiol hemihydrate was validated in terms of the analytical parameters: selectivity, linearity, limit of detection (LOD), limit of quantification (LOQ), precision (repeatability) and accuracy.

Selectivity

Placebo solution, containing starch as a supplement, without the active substance estradiol hemihydrate was prepared. The selectivity of the applied method was confirmed by the fact that on the chromatogram with placebo preparation there was no peak with t_R, corresponding to t_R of estradiol hemihydrate (t_R = 2.87) in standard solution. This fact confirms the lack of interference from the excipient starch commonly present in tablets [22].

Study of the analytical parameter linearity

For estimation of the linearity, the HPLC-HILIC-method was applied under chromatographic conditions: column Spherisorb Amino (250 mm × 4.6 mm × 5 μm), mobile phase acetonitrile : water = 55 : 45 v/v, flow rate: 2 ml min, UV-detection at λ = 230 nm.

Data for the concentration (C) and the peak area (A) for solutions with estradiol hemihydrate are presented in Table 1.

Table 1. Concentration (C) and peak area (A) for linearity for estradiol hemihydrate.

N:	C [g/ml]	A
1.	3.10^{-6}	5904.8
2.	5.10^{-6}	9872.6
3.	1.10^{-5}	22932.9
4.	2.10^{-5}	51561.5
5.	3.10^{-5}	79069.4
6.	4.10^{-5}	105994.0

The dependence of chromatographic peak area on the concentration of estradiol hemihydrate was evaluated by obtaining the chromatograms of standard solutions with concentrations: 3.10^{-6} g/ml, 5.10^{-6} g/ml, 1.10^{-5} g/ml, 2.10^{-5} g/ml, 3.10^{-5} g/ml, 4.10^{-5} g/ml. The experimental results for the peak areas obtained for solutions with increasing concentration, were subjected to linear regression analysis to obtain the regression equation: y = ax + b (a – slope, b – interept).

Linearity accordance between concentration and peak area in the range: 3.10^{-6} g/ml ÷ 4.10^{-5} g/ml was proved by the regression equation: y = 2698.99.x – 2307.98, with calculated correlation coefficient R^2

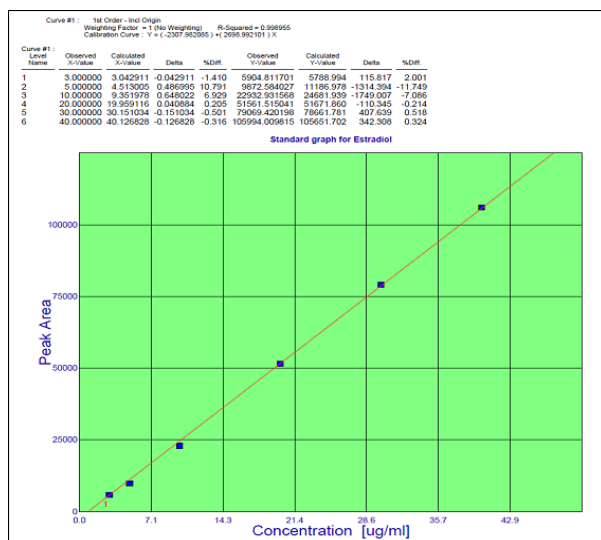= 0.9999. The linear relationship between peak area (A) and concentration (C) [g/ml] is shown in Fig. 4.

Fig. 4. Linearity for estradiol hemihydrate of the HPLC-HILIC-method with UV-detection at $\lambda = 230$ nm and flow rate 2 ml/min

Study of the analytical parameters LOD and LOQ.

The sensitivity of the HPLC-HILIC-method using chromatographic conditions was defined as LOD (concentration, at which the obtained ratio of signal to noise is 3:1) and LOQ (concentration, at which the obtained ratio of signal to noise is 10:1). From the chromatogram of 10 μl standard estradiol hemihydrate solution (C = 3.10^{-6} g/ml) were calculated: LOD = 8.10^{-7} g/ml; LOQ = 8.10^{-6} g/ml.

Estimation of the analytical parameters accuracy and precision (repeatability) of the HPLC-HILIC-method.

For the estimation of analytical parameters accuracy and precision (repeatability), the descibed HPLC-HILIC-method was applied to 6 standard solutions containing known amounts of estradiol hemihydrate: 100 % (2 mg/100 ml).

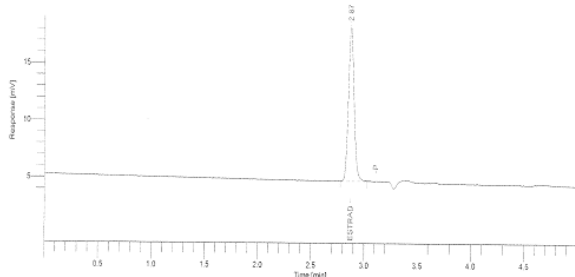On Fig. 5. the chromatogram of a standard solution of estradiol hemihydrate is presented.

The quantity of drug was calculated by the method of calibration curve using the regression equation. In Table 2. are summarized data for: N – number of individual measurements (N = 6); A – peak area; UA – Chauvenet criterion for peak area; C – quantity of estradiol hemihydrate obtained by the method of calibration curve; UC – Chauvenet criterion for obtained content; RC – degree of recovery [%]; $\overline{X}$ – arithmetical mean; SD – standard deviation; RSD [%] – relative standard deviation; $S\,\overline{X}$ – mean quadratic error; P – confidence possibility [%]; t – coefficient of Student; $\overline{X} \div t.S\,\overline{X}$ – confidence interval; E – relative error [%].

Table 2. Validation of the HPLC-HILIC method for accuracy and precision (repeatability) of estradiol hemihydrate.

N:	A	U A	C [mg/100 ml]	UC	RC [%]
1.	50287	1.38	1.95	1.33	97.5
2.	50522	1.09	1.96	1.0	98
3.	51688	0.36	2.00	0.33	100
4.	51697	0.37	2.00	0.33	100
5.	51899	0.62	2.01	0.67	100.5
6.	52312	1.13	2.02	1.0	101
$\overline{X} \pm$ SD	51401 ± 808		1.99 ± 0.03		
$\overline{R}$ [%] ± RSD [%]					99.5 ± 1.42
SD	808		0.03		1.41
RSD [%]	1.57		1.51		1.42
$S\,\overline{X}$			0.01		0.58
P [%]			95.0		99.0
t			2.57		4.03
t. $S\,\overline{X}$			0.03		2.34
$\overline{X} \pm$ t.$S\,\overline{X}$			1.96 ÷ 2.02		97.16 ÷ 101.84
E [%]			0.5		0.58

Fig. 5. Chromatogram of a standard solution of estradiol hemihydrate: HPLC-HILIC-method with UV-detection at $\lambda = 230$ nm and flow rate 2 ml/min.

For the assessment of accuracy and precision the sample standard deviation (SD) was calculated by applying Bessel's correction, in which the denominator $N - 1$ (degrees of freedom) is used instead of N and in this case $(S)^2$ is an unbiased estimator for (SD) [22].

For the estimation of precision (repeatability) the uncertainty of the result was used, which is determined by: standard deviation (SD), relative standard deviation (RSD) and confidence range. Repeatability is expressed by SD and RSD for 6 standard solutions with added content of estradiol hemihydrate: 2 mg/100 ml. All data for the obtained concentration of estradiol hemihydrate correspond to the confidence interval: 1.96 mg/100 ml ÷ 2.02 mg/100 ml (SD = 0.03; RSD = 1.51).

The results for the accuracy at P = 99 % (t = 4.03), expressed by the percent recovery R [%] ± RSD [%] are within the respective confidence interval RC: 97.16 ÷ 101.84 % (RSD = 1.42).

CONCLUSIONS

The HPLC-HILIC-method is validated in terms of the analytical parameters specificity, linearity: y = 2698.99 x - 2307.98, LOD = 8.10^{-7} g/ml, LOQ = 8.10^{-6} g/ml, repeatability. The higher selectivity and efficiency of separation by HPLC-HILIC with UV-detection at $\lambda = 230$ nm in an Amino-column and elution of the less polar analytes before the more polar ones (estradiol) shortens the time for analysis and leads to better repeatability.

REFERENCES

1. C. Holroyd, C. Cooper, E. Dennison, *Best Pract. Res. Clin. Endocrinol. Metab.*, **22**(5), 671 (2008).
2. J. C. Gallagher, *Maturitas*, **60**(1), 65 (2008).
3. B. L. Riggs, *J. Clin. Invest.*, **106**(10), 1203 (2000).
4. C. J. Rosen, *N. Engl. J. Med.*, **353**(6), 595 (2005).
5. J. A. Knopp, B. M. Diner, M. Blitz, G. P. Lyritis, B. H. Rowe, *Osteoporos. Int.*, **16**(10), 1281 (2005).
6. D. B. Kimmel, *J. Dent. Res.,* **86**(11), 1022 (2007).
7. B. Abrahamsen, P. Eiken, R. Eastell, *N. Engl. J. Med.*, **360**(17), 1789 (2009).
8. A. Mak, M. W. Cheung, R. C. Ho, A. A Cheak, C. S. Lau, *BMC Musculoskelet. Disord.*, **10**(1), 113 (2009).
9. K. E. Ensrud, J. L. Stock, E. Barrett-Connor, D. Grady, L. Mosca, K. T. Khaw, Q. Zhao, D. Agnusdei, J.A. Cauley, *J. Bone Miner. Res.*, **23**(1), 112 (2008).
10. G. M. Blake, J. E. Compston, I. Fogelman, *J. Bone Miner. Res.*, **24**(8), 1354 (2009).
11. B. Ascott-Evans, E. W. W. Sonnendecker, T. De Villiers, *JEMDSA*, **13**(1), 8 (2008).
12. Y. Z. Bagger, L. B. Tanko, P. Alexandersen, H. B. Hansen, A. Mollgaard, P. Ravn, P. Qvist, J. A. Kanis, C. Christiansen, *Bone*, **34**(4), 728 (2004).
13. O. Johnell, W. H. Scheele, Y. Lu, J.-Y. Reginster, A. G. Need, E. Seeman, *J. Clin. Endocrinol. Metab.*, **87**(3), 985 (2002).
14. A. J. Alpert, *Anal. Chem.*, **80**(1), 62 (2008).
15. P. Hemström, K. Irgum, *J. Sep. Sci.*, **29**(12), 1784 (2006).
16. E. S. Grumbach, D. M. Wagrowski-Diehl, J. R. Mazzeo, B. Alden, P.C. Iraneta, *LC-GC North America*, **23**(Suppl. 1), 89 (2005).
17. B. Buszewski, S. Noga, *Anal. Bioanal. Chem.*, **402**(1), 231 (2012).
18. W. Ding, H. Nothaft, C. M. Szymanski, J. Kelly, *Mol. Cell. Proteomics*, **8**(9), 2170 (2009).
19. B. Yilmaz, Y. Kadioglu, *Arab. J. Chem.*, **2**(1), 1 (2013).
20. Z. Aydoğmuş, E. M. Yılmaz, S. Yörüsün, S. Akpınar, *Int. School. Res. Not.*, **2015**(1), 1 (2015).
21. R. D. Josephs, A. Daireaux, T. Choteau, S. Westwood, R. I. Wielgosz, *Anal. Bioanal. Chem.*, **407**(11), 3147 (2015).
22. International Conference on Harmonization Guidelines. Validation of analytical procedures: text and methodology Q2 (R1): FDA. Fed. Regist., **60**(1), 11260 (1995).

ОЦЕНКА НА ЛИНЕЙНОСТТА И ТОЧНОСТТА НА HPLC-HILIC-МЕТОД ЗА АНАЛИЗ НА ЕСТРАДИОЛ ХЕМИХИДРАТ

Д. Цветкова[1]*, Ст. А. Иванова[1,2], Л. Сасо[3], Д. Обрешкова[1,2], М. Димитров[4]

[1]*Катедра "Фармацевтична химия", Медицински университет-София, Фармацевтичен факултет, ул. Дунав N : 2, София 1000, България*

[2]*Катедра "Фармакогнозия и фармацевтична химия"Медицински университет-Пловдив, Факултет по фармация, ул. Васил Априлов N: 15А, Пловдив 4002, България*

[3]*Катедра по Физиология и фармакология "Vittorio Erspamer", Университет Сапиенца-Рим, Рим, Италия*

[4]*Катедра по Технология на лекарствата и биофармация, Медицински университет - София, Фармацевтичен факултет, ул. Дунав N : 2, София 1000, България*

(Резюме)

Целта на настоящото изследване е оценката на линейността и прецизността на изократичен HPLC-HILIC метод с УВ-детекция за идентифициране и определяне на естрадиол хемихидрат във фармацевтични дозирани форми. Извършен е линеен регресионен анализ. Построена е калибрационна права. Линейната зависимост между концентрацията и площта на пиковете в диапазона: 3.10-6 g/ml ÷ 4.10-5 g/ml се доказва от регресионното уравнение: y = 2698.99 x - 2307.98. Регресията на най-малките квадрати дава коефициент на корелация $R^2 = 0.999$. LOD = 8.10^{-7} g/ml, LOQ = 8.10^{-6} g/ml. Резултатите за точността при P = 99 % (t = 4.03) са представени чрез аналитичния добив R [%] и отговарят на доверителния интервал: RC: 97.16 ÷ 101.84% (RSD = 1.42).

Прецизността е представена чрез стандартно отклонение, относително стандартно отклонение и доверителен интервал. Всички данни за полученото количество естрадиол хемихидрат съответстват на доверителния интервал: 1.96 mg/100 ml ÷ 2.02 mg/100 ml (SD = 0.03, RSD = 1.51).

Високата селективност и ефективност на разделянето чрез HPLC-HILIC-метода с UV-детекция при λ = 230 nm при използване на Амино-колона и елуирането на неполярните аналити преди полярните (естрадиол), съкращава времето за анализ и води до висока повторяемост.

Comparative study of some biochemical parameters of the fungi *Mucor plumbeus*, *Aspergillus niger* and *Trichoderma harzianum*

I. Matović-Purić[1], D. Pecarski[2], Z. Jugović[3], D. Jovičić[4], D. Đorđević[5], P. Mašković[6]

[1]*Medical School, Episkopa Nikifora Maksimovića no. 8, Čačak, Serbia*
[2]*Higher Education School of Professional Health Studies, Cara Dusana 254, Belgrade, Serbia*
[3]*High-sanitarian Health School of Professional Studies "Visan", Tošin bunar 7a, Belgrade, Serbia*
[4]*Singidunum University, Faculty of Applied Ecology – Futura, Požeška 83, Belgrade, Serbia*
[5]*University of Niš, Faculty of Sciences and Mathematics, Višegradska 33, Niš, Serbia*
[6]*University of Kragujevac, Faculty of Agronomy, Čačak, Serbia*

The aim of this study was to examine the effect of high concentrations of the commercial detergent "Merix" (Henkel, Kruševac) on the growth, development and biochemical characteristics of the tested fungi isolated from sewage and industrial wastewater. Metabolic activity of *Mucor plumbeus, Aspergillus niger* and *Trichoderma harzianum* grown in such liquid nutrient medium and control medium is monitored over following biochemical parameters: amounts of free and total organic acids, pH values, redox potential and biomass. Depending on the fungus species, there was a biomass inhibition at various concentrations under the influence of the detergent in the period from the third to the sixth day. Detergent concentration of 0.3% was decomposed in all tested fungus - detergent mixtures.

Key words: *Aspergillus niger*, *Mucor plumbeus*, *Trichoderma harzianum*, detergent, ethoxyl-oleyl-cetyl alcohol, sodium tripolyphosphate

INTRODUCTION

Many researchers stated that microorganisms, particularly some kinds of fungi, can act as potential degraders of detergents [1,2]. Among the fungi which have such ability, filamentous fungi (*Deuteromicotina)* are especially distinguished due to their physiological and biochemical characteristics [5]. Specificity in apical growth of these fungi enables penetration in solid substrates and excretion of extracellular enzymes from vesicles on the top of hyphae to environment. Under the influence of these enzymes complex organic compounds are decomposed to simpler ones, thus the fungi can be used for growth and development of mycelia and biomass accumulation [3,4,6]. Filamentous fungi are attractive microorganisms for the study of biodegradation of organic matter due to their well-developed defense mechanisms and structure of the cell wall. Fungi are recognized for their superior capability to produce a large variety of extracellular proteins, organic acids and other metabolites, as a result of adaptation to severe environmental constraints [7]. *Mucor racemosus Fresenius* is a dimorphic fungus (genus Mucor) whose growth is induced by carbon dioxide and hexose sugar in the direction of creating a multipolar bud as in yeast or in the

direction of branched aerial hyphens [8]. When grown on synthetic and organic substrates *M. racemosus* produces various enzymes such as invertase, alkaline phosphatase, protease, lipase, which have applications in biotechnology and bioremediation.

The *Aspergillus* fungus was first recognized as an organism in 1729 by Micheli [9]. The genus *Aspergillus* is found worldwide and consists of more than 180 officially recognized species, and comprises a particularly important group of filamentous ascomycete species [10]. Although it includes the major filamentous fungal pathogen of humans, *Aspergillus fumigatus* [11], most of the members are useful microorganisms in nature for degradation of plant polysaccharides [12], and they are important industrial microorganisms for the large-scale production of both homologous and heterologous enzymes [13-17]. Among them, *Aspergillus oryzae* and *Aspergillus niger* are on the Generally Recognized as Safe List of Food and Drug Administration in the United States [18]. *Aspergillus niger* is one of the most important microorganisms used in biotechnology [19,20] which produces many extracellular enzymes.

Trichoderma spp. are common saprophytic fungi that are interactive in soil, root and foliar environments. They are well-known biocontrol agents and also have considerable metabolic diversity [11]. They are recognizable for degradation of chitin, glucans, lignin and cellulose

---

* To whom all correspondence should be sent:
E-mail: agrofarmzorka@gmail.com

[12]. *Trichoderma harzianum* can degrade various organic compounds such as DDT (dichlorodiphenyltrichloroethane), dieldrin, endosulfan, PCNB (pentachlororonitrobenzene) and PCP (pentachlorophenol) [13]. Therefore, *Trichoderma* strains play an important role in the bioremediation of soil contaminated with pesticides, herbicides and insecticides. Data about the proteolytic enzyme profiles of *Trichoderma* strains revealed that the protease system of *Trichoderma* is complex containing a large set of enzymes. Some of these proteases are involved in mycoparasitic action, nematicidal activity and plant colonization. However, only a few *Trichoderma* proteases have been examined until now for their potential applicability for commercial purposes.

On inoculated fungi species grown under *in vitro* conditions, in the presence of the mentioned pollutants, the metabolic changes of bioproduction of different organic compounds in various aging steps of fungi, have been investigated. The aim of this study was to find out, among the great variety of fungal species from wastewater, these which are resistant to effects of detergent and its components. Metabolic activity of *Mucor plumbeus, Aspergillus niger* and *Trichoderma harzianum* grown in such liquid nutrient medium and control medium was monitored over following biochemical parameters: amounts of free and total organic acids, pH values, redox potential and biomass.

MATERIALS AND METHODS

Isolation of Mucor racemosus Fresenius and cultivation

The fungus species was isolated from wastewater samples of the Rasina River, downstream where the industrial wastewaters of the factory Henkel, Serbia, discharge into river. Sample of wastewater was taken in late May 2010. Sample was taken in a sterile container and transferred to the microbiology laboratory where it was disposed of in a refrigerator at 4°C. Within 24h, different dilutions of the sample were transferred on Petri plates with malt agar and streptomycin to prevent bacterial growth. The plates were then maintained at room temperature for 5 days. Positive cultures were subcultured on malt agar and potato dextrose agar for the isolation of a pure, single colony for identification. The identification of the fungus *M. racemosus Fresenius* (1976) was based primarily on the macroscopic and microscopic morphology and was carried out by systematic keys. The fungus was maintained on potato-dextrose-agar (PDA) slant grown at 30°C, stored at 4±0.5°C, and

subcultured monthly in sterile conditions. During the experiment, the fungus was cultivated in the sterile modified Czapek Dox liquid medium of the following composition (g L^{-1}): $NaNO_3$ – 3, K_2HPO_4 – 1, $MgSO_4 \times 7H_2O$ – 0.25, $FeSO_4 \times 7H_2O$ – 0.01, sucrose – 30, distilled water up to 1000 mL (control-K) and the same medium with additional 5 g of detergent to obtain a concentration of 0.5% (medium D5).

Erlenmeyer flasks with liquid growth medium were sterilized at 121°C for 20 min (autoclave pressure, 0.14 MPa). The pH was adjusted before sterilization at about 4.70 with 1 mol dm^{-3} HCl.

Inoculation and sampling

The liquid growth media were stored in Erlenmeyer flasks (200 mL of medium in 250 mL flask). One positive control without detergent with spores, one test flask with detergent and with spores and one negative control with detergent but without spores were used in this experiment. Inoculation of media occurred with 2 mL of spore suspension (5×106 conidia mL^{-1}). Erlenmeyer flasks in three replicates were placed on an electric shaker (Kinetor, Ljubljana, Slovenia) thus enabling uniform and constant mixing.

All experiments were carried out at room temperature, under alternate light and dark for 16 days. Sampling was started three days after inoculation and repeated every third day until the end of the experiment. Mycelium as removed by filtration through Whatman filter paper No.1 and mycelia dry weight was determined. Filtrate was harvested by centrifugation at 10,000g for 10 min (4°C) and the supernatant was used as crude enzyme extract.

Measurement of pH and redox potential

pH and redox potential were measured by digital electric pH meter (PHS-3BW Microprocessor pH/mV/temperature meter) type of Bante with a glass electrode model 65-1.

Determination of dry weight biomass

The mycelia previously removed from the fermentation broth were washed with sterile distilled deionized water several times. Both filter paper and mycelia were then dried in an oven at 80°C to a constant weight of the dry of mycelia and filter paper.

The experiments were performed using monosporial culture of the fungi *Aspergillus niger* van Tiegheme isolated from the river Lepenica (Serbia) on a wastewater outpouring site. Identification of the culture was done at the Faculty

of Biology, Belgrade, Laboratory for algae, fungi and lichens. Monosporial culture of the fungi was obtained by the method of exhaustion on poor potato-dextrose agar [24].

The method can be summarized as follows: fungi were inoculated into a flask that contained a chemically-defined microbial growth medium and the surfactant to be tested. The fungi were grown in the sterile liquid nutrient medium according to Czapek consistING of: 3g $NaNO_3$, 1g K_2HPO_4, 1g $MgSO_4$, 0.25g $MgSO_4 \times 7H_2O$, 0.01g $FeSO_4 \times 7H_2O$ and 30g saccharose, dissolved in 1000 ml of distilled water. Detergent designated D, ethoxyl-oleylcetyl alcohol (AOC) and sodium tripolyphosphate (TPP) were added (1%) and the flasks were incubated for 4-8 days. The flasks containing 200ml of medium were uniformly and constantly shaken on a Kinetor shaker at room temperature under conditions of alternate light-dark cycles [25]. The sterility of the nutrient medium was tested using mesopeptone agar.

For the determination of free organic acids 10ml of medium was taken and mixed with 50ml of ethanol. After incubation at 70°C in a water bath for 1-1.5 h, the mixture was filtered through a special filter. The filtrate was concentrated at 50°C - 60°C under reduced pressure to 40ml, transferred to a volumetric flask and made up to 100ml after addition of a teaspoon of active charcoal. After standing in a water bath for 30-45 min at 70°C, 10ml aliquots of filtrate were taken for the determination of the free organic acids by titration with 0.1 M NaOH in the presence of phenolphthalein as indicator [26-28].

Isolation and identification of Trichoderma harzianum Rifai

The selected fungus species originated from wastewater samples of the Rasina River, downstream where the industrial wastewaters of the factory Henkel (Kruševac, Serbia) discharge into river. Sample of wastewater was taken in late May 2010.

The identification of the fungus *T. harzianum Rifai* was based primarily on the macroscopic and microscopic morphology and was carried out by systematic key. The fungus was maintained on potato-dextrose-agar (PDA) slant grown at 30°C, stored at 4±0.5°C, and subcultured monthly in sterile conditions.

Fermentation conditions

During the experiment, the fungus was cultivated in a sterile modified Czapek Dox liquid medium of the following composition (g L^{-1}): $NaNO_3$-3, K_2HPO_4-1, $MgSO_4 \times 7H_2O$-0.25, $FeSO_4 \times 7H_2O$-0.01, sucrose-30, distilled water up to1000mL (control-C) and the same medium with additional 3g of detergent to obtain a concentration of 0.3% (medium D3). Erlenmeyer flasks with liquid growth medium (200mL of medium in 250mL flask) were sterilized at 121°C for 20 min (autoclave pressure, 0.14 MPa). The pH was adjusted before sterilization at about 4.70 with 1 mol L^{-1} HCl. After addition of detergent to the liquid growth medium the pH value of the medium was measured again.

Inoculation and sampling

One positive control without detergent with spores, one test flask with detergent and with spores and one negative control with detergent but without spores were used in this experiment. Inoculation of media occurred with 2mL spore suspension (5×10^6 conidia mL^{-1}). Erlenmeyer flasks in three replicates were placed on an electric shaker thus enabling uniform and constant mixing. All experiments were carried out at room temperature, under alternate light and dark for 16 days. Sampling was started three days after inoculation and repeated every third day until the end of the experiment. Mycelium was removed by filtration through Whatman filter paper No.1. Filtrate was harvested by centrifugation at 10000g for 10 min (4°C) and the supernatant was used as crude enzyme extract.

Measurement of pH and redox potential

pH and redox potential were measured on a digital electric pH meter (PHS-3BW Microprocessor pH/mV/temperature meter) type Bante with a glass electrode model 65-1.

Determination of biomass dry weight

The biomass dry weight of the mycelia was determined according to the procedure described in Jakovljevic *et al.* (2014) [9].

Statistical analysis

All experiments were performed in triplicate and results were expressed as means ± standard deviation. For statistical analysis, the following tests were used: Mann-Whitney, Kruskal-Wallis and test for correlation coefficient by SPSS (Chicago, IL) statistical software package (SPSS for Windows, ver. XIII, 2004). Coefficient of correlation was determined at the levels of significance 0.05 and 0.01.

RESULTS AND DISCUSSIONS

The influence of the detergent Merix (Merima, Kruševac, Serbia) and its components (ethoxyl-oleyl-cetyl alcohol and sodium tripolyphosphate) on the metabolic activity of the fungi *Mucor plumbeus, Aspergillus niger* and *Trichoderma harzianum* was studied. The metabolic changes of bioproduction of different organic compounds in various aging steps of the fungi in the presence of pollutant was investigated. These fungi were isolated from the river Lepenica (Serbia) on the wastewater outpouring site and were chosen because they were the most abundant there. The fungi were then grown in a liquid nutrient medium according to Czapek, where 1% of detergent or its component was added, during the incubation period of 4-8 days after inoculation.

Metabolic activity of *Mucor plumbeus, Aspergillus niger* and *Trichoderma harzianum* grown in such liquid nutrient medium and control medium was monitored over the following biochemical parameters: amounts of free and total organic acids, pH values, redox potential and biomass.

Organic acids play a key role in alkali tolerance, especially for intracellular ionic homeostasis. Organic acids produced by fungi into the medium can exist in free (FOA) and in bound form. The sum of the amounts of both free and bound organic acids represents the amount of total organic acids (TOA). Figures 1 and 2 show the concentrations of free organic acids (FOA) and of total organic acids (TOA) in the fermentation broth measured during the fungal growth. Production of free and total organic acids increased in all cases (for all three fungi) at the end of the experimental period (Table 1, Figure 1).
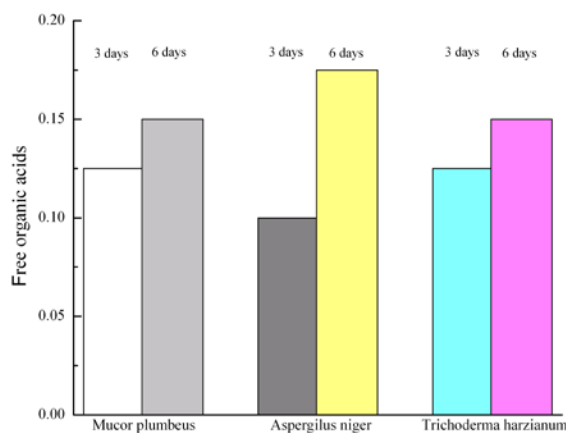

Fig. 1. Change in the concentration of free organic acids (expressed as %) in a nutrient medium with detergent.

After three days of observation, the lowest concentration of free acid was measured for the fungus *Aspergillus niger*, and its value is 0.100%. For the same period, *Mucor plumbeus* and *Trichoderma harzianum*, showed a higher content of free acid, 0.125%. On the sixth day of observation, for *Mucor plumbeus* and *Trichoderma harzianum*, the content of free organic acids was 0.150%, and the highest concentration of free acid was displayed b+y *Aspergillus niger*. Based on the measured values of the concentration of free organic acids, we can see that *Aspergillus niger*, after three days had the lowest value and after six days the highest value.

Similar values for the examined fungi have been found by other authors. The concentration of free organic acids in *Aspergillus niger* at an early growth stage (day 3) was lower than 0.100% and at the sixth day - less than 0.150%. The lowest value was recorded during the autolysis (day 9) and amounted to 0.380%, the highest being at the 16th day - 1.200%. For *Trihoderma harzianum* the concentration of free acids at the third day was the lowest (0.03%) and at the 16th day – the highest, 0.12%. In the same research the concentration of free organic acids in *Mucor racemosus* was determined which was the highest - 0.14%, recorded during the exponential growth phase [30].

In other studies, for *Aspergillus niger* higher concentrations of free organic acids in the substrate with detergent were recorded and their value after 4 and 7 days amounted to 1.80% and 2.50%, respectively. In the same research, the concentration of free organic acids in *Trichoderma viride* was determined after 4 days - 1.00%, and after 7 days - 1.20%, which were higher than those recorded for *Trichoderma harzianum* [27].

In Table 2 and on Figure 2 the total free acids for all 3 fungi *Mucor plumbeus, Aspergillus niger* and *Trichoderma harzianum* are shown.

In studies by other authors slightly lower values of the content of total organic acids have been noticed. The concentration of total organic acids for *Aspergillus niger* after the third day was below 0.6%, while after the sixth day the concentration was about 0.70%. For *Trihoderma harzianum* the highest value recorded during exponential growth was 0.69% to 1.06% after the sixth day. For *Mucor racemosus* the largest concentration was observed at the sixth day - 13.01% [30]. In a similar study, the total content of organic acids in the substrate with a detergent, for *Aspergillus niger* after the 4th day amounted to 2.60%, while at the 7th day it was slightly lower, 2.30%. For *Trichoderma viride*, the total content of organic acids in the medium with

detergent after the 4th day was 1.50% and after the 7th day - 2.00% [27].

Chemical compositions of growth media and experimental conditions have influence on fungal development and total biomass. Many investigations showed that the Czapek Dox liquid medium has good properties for fungal cultivation and high biomass production [14].
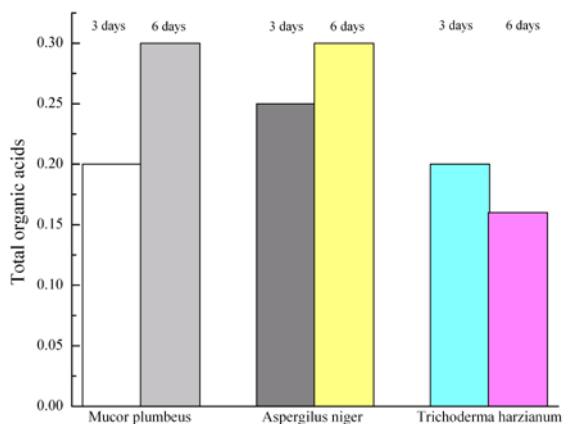

Fig.2. Total organic acids for *Mucor plumbeus, Aspergillus niger* and *Trichoderma harzianum*

The fungus cultivated in a medium without detergent (K medium) showed similar biomass amount. But after the influence of detergent (D), the biomass amount rapidly decreased (Table 3, Figure 3).
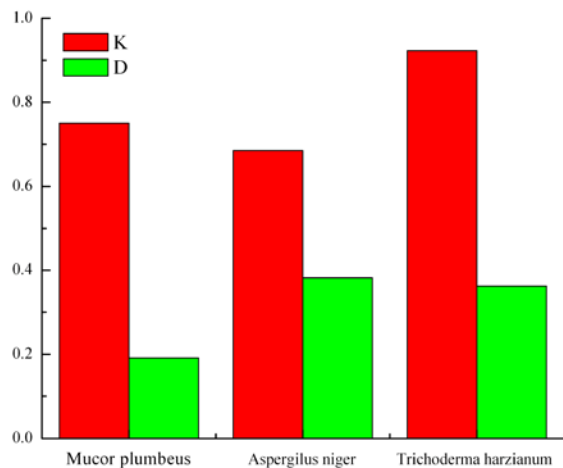

Fig.3. Biomass (g) *Mucor plumbeus, Aspergillus niger* and *Trichoderma harzianum*

In this study the changes in pH and redox potential during fungal growth were estimated because these parameters are very important for regular growth and development and affect the morph-physiological characteristics and biochemical properties of the microorganisms.

The optimum external pH for fungal growth was under acidic conditions from 4.5 to 5. Fungi generally alter the pH of the medium in which they grow, due to uptake of anions or cations from the

394

medium [25,26]. Therefore, the various changes witnessed in the pH values of the culture media are a result of the utilization of nutrients from the growth media [27]. Based on literature data, the fungi do not develop at pH above 9. This study provides evidence that *M. Racemosus Fresenius* could tolerate a wide range of environmental pH, from 4.75 to 9.80. Figure 4 shows that the pH values of the fermentation broth changed during the fungus growth from inoculation until the 16th day. The initial pH values of the media were 4.75 in K medium and 9.80 in D5 medium before inoculation. Also, one negative control (nkD5) with detergent but without spores was tested. The pH values of inoculated growth media changed in relation to their composition and growth phases of fungus. pH value of K medium increasing from inoculation until the 6th day. During stationary and autolysis phases, the pH value slightly decreased but these changes were not statistically significant. In contrast, the pH value of the D5 medium decreased in the exponential growth phase. The largest decrease in the pH value was observed in the medium D5 between the 3rd and 6th day (from 9.36 to 6.46 units) which corresponds to primary exponential growth phase. These changes of pH were less expressed in the secondary exponential growth phase. Interestingly, the final pH values of the different media were very similar although the differences between the initial pH values were very significant.

In the papers of other authors it was observed that the pH value of the substrate K for *Aspergillus niger* gradually decreased during the growth and development of the fungus, with the largest reduction recorded in the period up to the 9th day of inoculation, ranging from pH 4.80 to pH 2.53, while the least pH change was observed from the 9th to the 16th day. In the medium D3, the biggest decrease in pH was in the primary exponential phase from the 3rd to the 6th day, with pH in the range from 9.13 to pH 6.49. For *Trichoderma harzianum* in the substrate K the largest pH increase was during the first three days from 4.80 to 5.40 and the largest reduction from the 3rd to the 6th day from 5.40 to 4.82 while the pH changes during the stationary phase and autolysis were much lower. In the medium D3, the pH value displayed the least changes in the initial stage of development fungi from inoculation to the 6th day. In the phase of exponential growth, from 6th to 9th day, there was the largest change in pH from 6.07 to 9.05, and the stationary phase pH changes were minimal. For *Mucor racemosus* the pH value of the control substrate K gradually increased to the 6th day, while

during the stationary phase and autolysis it decreased. The largest decrease in pH in the substrate D3 was during the inoculation period to the 3rd day with pH changing from 9.35 to 6.24, and in the substrate D5 it was from the 3rd to the 6th day with pH changing from 9.36 to 6.46. In the secondary exponential growth phase, the pH changes were significantly lower [30].

Table 1. Changes in concentration of free organic acids (expressed as %) in the nutrient medium with detergent.

Fungus in nutrient medium with detergent	*Mucor plumbeus*		*Aspergillus niger*		*Trichoderma harzianum*	
Incubation period	day 3	day 6	day 3	day 6	day 3	day 6
Concentration of free organic acids (%)	0.125	0.150	0.100	0.175	0.125	0.150

Table 2. Total organic acids for *Mucor plumbeus*, *Aspergillus niger* and *Trichoderma harzianum*.

Fungus in nutrient medium with detergent	*Mucor plumbeus*		*Aspergillus niger*		*Trichoderma harzianum*	
Incubation period	day 3	day 6	day 3	day 6	day 3	day 6
Concentration of free organic acids (%)	0.200	0.300	0.250	0.300	0.200	0.160

Table 3. Biomass (g) of *Mucor plumbeus*, *Aspergillus niger* and *Trichoderma harzianum*

	Mucor plumbeus		*Aspergillus niger*		*Trichoderma harzianum*	
Incubation period	Biomass content in the control medium (g)	Biomass content medium with detergent (g)	Biomass content in the control medium (g)	Biomass content medium with detergent (g)	Biomass content in the control medium (g)	Biomass content medium with detergent (g)
16th day	0.7501	0.1915	0.6852	0.3823	0.9226	0.3627

Table 4. pH values of *Mucor plumbeus*, *Aspergillus niger* and *Trichoderma harzianum*

	Mucor plumbeus		*Aspergillus niger*		*Trichoderma harzianum*	
Incubation period	pH value in the control medium	pH value in medium with detergent	pH value in the control medium	pH value in medium with detergent	pH value in the control medium	pH value in medium with detergent
3rd day	4.76	9.19	6.13	9.10	3.71	9.00
6th day	3.95	6.20	6.70	6.93	3.58	8.92
9th day	3.41	6.33	6.89	6.22	2.62	5.86
12th day	3.43	6.15	7.17	6.20	2.42	5.97
16th day	3.19	5.88	7.39	6.25	2.36	5.19

Table 5. Redox potential of *Mucor plumbeus*, *Aspergillus niger* and *Trichoderma harzianum*.

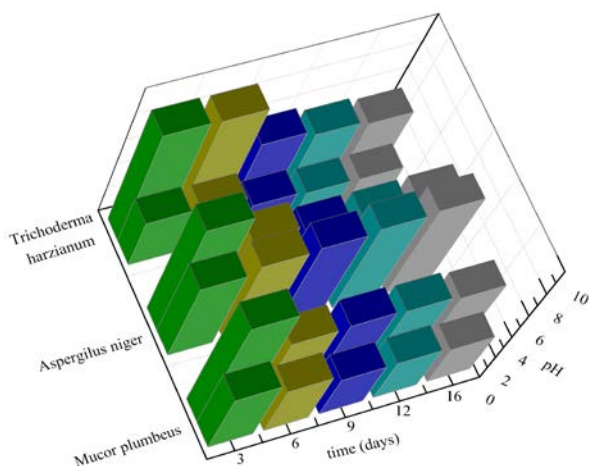|	*Mucor plumbeus*		*Aspergillus niger*		*Trichoderma harzianum*	
Incubation period	Redox potential in the control medium (mV)	Redox potential in medium with detergent (mV)	Redox potential in the control medium (mV)	Redox potential in medium with detergent (mV)	Redox potential in the control medium (mV)	Redox potential in medium with detergent (mV)
3rd day	131	123	51	118	191	112
6th day	176	44	18	4	197	106
9th day	194	37	4	43	236	63
12th day	193	56	11	53	243	66
16th day	200	66	23	46	244	104

Fig. 4. pH values of *Mucor plumbeus, Aspergillus niger* and *Trichoderma harzianum*

Table 5 and Figure 5 illustrate that the redox potential values of fermentation broth changed during the growth of fungus from inoculation until the 16th day. The initial redox potential values were 130 mV in K and–148 mV in D5 medium before inoculation. One negative control (nkD5) with detergent but without spores was also tested. The redox potential of the K medium decreased during the exponential growth phase (from inoculation until the 6th day), whereas it slightly increased throughout stationary and autolysis phases. During the biphasic exponential growth of the fungus in D5 medium, the redox potential increased more intensively in the primary than in the secondary exponential growth phase. The decrease in redox potential was measured in D5 medium on the 9th day only.
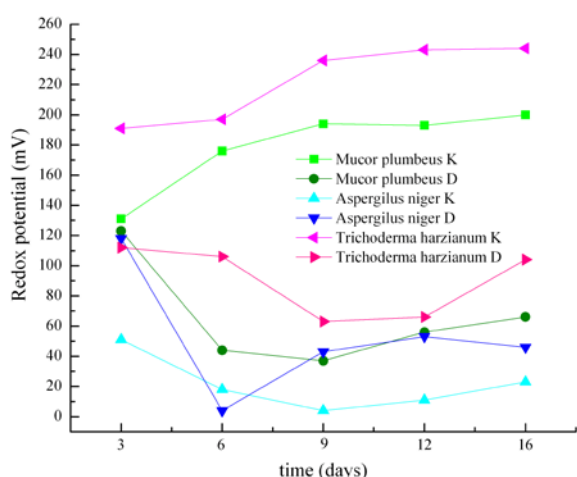
Fig. 5. Redox potential of *Mucor plumbeus, Aspergillus niger* and *Trichoderma harzianum.*

In other studies, it was observed for *Aspergillus niger* that the value of the redox potential gradually decreased from the inoculation period until the end of the experiment, except for the 3rd and 6th day. The values of the redox potential of the medium D3 have increased from the moment of inoculation to the 9th day, while the largest change in redox potential was noticed in the phase of exponential growth. For *Trichoderma harzianum*, the value of the redox potential of the control surfaces, decreased from the beginning inoculation till the end of the experiment with the exception of the 3rd and 6th day. In the medium D3, the redox potential values gradually increased during the period of cultivation and the largest changes were noticed between the 6th and 9th day. The value of the redox potential during the growth of the fungus *Mucor racemosus* was measured in the control substrates and in the media with a detergent concentration of 0.3% and 0.5%. The value of the redox potential in the control medium rapidly decreased from inoculation to the 6th day, with a slight increase during the stationary phase and autolysis. The redox potential in the substrate D3 gradually increased until the end of the experiment and the largest changes were noticed in the exponential growth phase (day 3), in addition to the 6th and 9th day. The redox potential of in the substrate D5 also gradually increased until the end of the experiment, with the exception of the 6th and 9th day, and the largest changes were from the 3rd to the 6th day and from the 9th to the 16th day [30].

In this study it was observed that for *Aspergillus niger* the redox potential in the control substrate also gradually decreased from the beginning of inoculation to the 9th day when the lowest value was recorded, then there was a gradual increase in the value of the redox potential from the 12th to the 16th day of the experiment. As opposed to the previous studies, the value of the redox potential of the medium D3 decreased with the largest decrease was recorded at the 3rd day and 6th day. For *Trihoderma harzianum*, the redox potential value in the control medium gradually increased from inoculation until the end of the experiment, in contrast to the above studies, where the value of the redox potential gradually decreased. In the medium D3, the redox potential value gradually decreased during the experiment, except from the 12th to the 16th day. For *Mucor racemosus*, the value of the redox potential in the control medium gradually decreased until the end of the experiment, while that in the substrate D3 gradually decreased with the exception the 12th and the16th day when there was a gradual increase.

CONCLUSION

The content of free organic acids for *Aspergillus niger* amounted to 0.100% on the third day and 0.175% on the sixth day. For the fungus *Mucor plumbeus* the content of free organic acids on the third day was 0.125%, while on the sixth day - 0.150%. The content of free organic acids for *Trichoderma harzianum* was 0.125% after the third day and 0.150% after the sixth day.

In the medium with the detergent the content of total organic acids in the examined fungi was determined on the third and the sixth day after the beginning of inoculation. The content of total organic acids for *Aspergillus niger* after the third day was 0.250%, and after the sixth day - 0.300%. The content of total organic acids for *Mucor plumbeus* at the third day amounted to 0.200% and on the sixth day - 0.300%. For the fungus *Trichoderma harzianum,* at the third day the content of total organic acids was 0.200%, while at the sixth day - 0.160%.

The fungi cultivated in a medium without detergent showed similar biomass. But after the influence of detergent (D), the biomass rapidly decreased. At the end of the experiment, for *Mucor plumbeus*, which grew in a medium without detergent, the biomass amounted to 0.7501g, the biomass content in the substrate with a detergent was 0.1915g. For *Aspergillus niger*, the control medium at the end of the experiment had a biomass content of 0.6852g and in the medium with detergent - 0.3823g. In the same conditions, *Trihoderma harzianum* had 0.9226g of biomass in the control medium, while in the medium with detergent - 0.3627g.

The pH value of *Mucor plumbeus* in a medium without detergent gradually decreased from the beginning of inoculation to the end of the experiment. The pH value of the medium with a detergent, was the largest on the third day - 9.19 and then decreased to pH 5.88. *Aspergillus niger* in the control medium had a minimum value of pH on the third day - 6.13, then pH increased to a value of 7.39 at the end of the 16th day. The pH value in a medium with a detergent decreased from 9.10 to 6.25. The pH value of *Trichoderma harzianum* in the control medium decreased from 3.71 to p 2.36, and in the medium containing detergent from 9.00 to 5.19.

The redox potential for *Mucor plumbeus* in the control medium decreased from 131 mV at the beginning of the inoculation to 200 mV at the end of the experiment. In a medium with detergent, for *Aspergillus niger* the redox potential at the third day was the largest one - 118 mV, then it rapidly decreased till the 6th day and increased again to 53 mV at the 12th day. The redox potential in the control medium for *Aspergillus niger* was the largest at the third day (51 mV), then it first decreased to 4 mV and then increased to 23mV. The redox potential of the control medium for *Trichoderma harzianum* was the lowest on the third day - 191mV and gradually increased to 244mV on the 16th day. The redox potential of *Trichoderma harzianum* in the medium with detergent was the largest at the third day - 112 mV, then it decreased to 66 mV (day 12), and increased to 104mV on the 16th day.

The presence of a detergent in the nutrient medium and its degradation products during the fermentation of the fungus, influenced the biochemical changes of all examined parameters. Detergent influenced the inhibition of fungal biomass at a different percentage, depending on the type of fungi. All fungi degraded a detergent concentration of 0.3%, except the *M. racemosus* degrading a detergent concentration of 0.5%. Research has indicated that the tested fungi can decompose the detergent and its products, indicating the possibility of their use for that purpose.

REFERENCES

1. J.L. Sanz, E. Culubret, J. De Ferrer, A. Moreno, J.L. Berna, *Biodegradation*, **14**, 57 (2003).
2. P. Bonin, C. Cravo-Laureau, V. Michotey, A. Hirchler-Rea, *Ophelia*, **58**, 243 (2004).
3. http://www.scielo.cl /scielo.php?pid=S0717-345819.
4. G. Saucedo-Castañeda, B.K. Lonsane, J.M. Navarro, S. Roussos, M. Raimbault, *Applied Biochemistry and Biotechnology*, **36**, 47 (1992).
5. M. Raimbault, Fermentation en milieu solide: croissance de champignons filamenteux sur substrats amylacés. Série Travaux et Documents, ORSTOM, Paris, 1981.
6. G. Saucedo-Castañeda, B.K. Lonsane, J.M. Navarro, S. Roussos, M. Raimbault, *Process Biochemistry*, **27**, 97 (1992).
7. V.G. Lilly, H.L. Barnett, Physiology of the fungi, McGraw--Hill Book Co., New York, 1951, p. 464.
8. P. Borgia, P.S. Sypherd, *J. Bacteriol.*, **130**, 812 (1977).
9. P.A. Micheli, Nova Plantarum Genera, Florentiae, 1729.
10. O.P. Ward, W.M. Qin, J. Dhanjoon, J. Ye, A. Singh, *Advances in Applied Microbiology*, **58**, 1 (2005).
11. J.L. Brookman, D.W. Denning, *Current Opinion in Biotechnology*, **3**, 468 (2000).
12. R.P. de Vries, *Applied Microbiology and Biotechnology*, **61**, 10 (2003).
13. O.B. Fawole, S.A. Odunfa, *International Biodeterioration & Biodegradation*, **52**, 223 (2003).

14. L. Wang, D. Ridgway, T. Gu, M. Moo-Young, *Biotechnology Advances*, **23**, 115 (2005).
15. N.C. Mhetras, K. Bastawde, D.V. Gokhale, *Bioresource Technology*, **100**, 1486 (2009).
16. B. Joseph, P.W. Ramtke, G. Thomas, *Biotechnology Advances*, **26**, 457 (2008).
17. F. Hasan, A.A. Shah, A. Hameed, *Enzyme and Microbial Technology*, **39**, 235 (2006).
18. M.J. Tailor, T. Richardson, *Advances in Applied Microbiology*, **25**, 7(1979).
19. F.J. Contesini, D.B. Lopes, G.A. Macedo, M. da Graca Nascimento, P. de Oliveira Carvalho, *Journal of Molecular Catalysis B: Enzymatic*, **67**, 163 (2010).
20. S. Mitidieri, A.H.S. Martinelli, A. Schrank, M.H. Vainstein, *Bioresource Technology*, **97**, 1217 (2006).
21. R. Hermosa, A. Viterbo, I. Chet, E. Monte, *Microbiology*, **158,** 17 (2012).
22. M.S.Y. Haddadin, J. Haddadin, O.I. Arabiyat, B. Hattar, *Bioresour. Technol.*, **100**, 4773 (2009).
23. A. Katayama, F. Matsumura, *Environ. Toxicol. Chem.*, **12**, 1059 (1993).
24. M.V. Gorlenko, D.V. Sokolov, Plant growing. **II**, Prosvetenije, Moscow, 1976.
25. J. Stojanović, Influence of detergent on biochemical properties of some fungi *in vitro*. Ph.D. Dissertation. Faculty of Science, Kragujevac, 1990.
26. D. Veličković, Contribution to study of aminoacidic composition dynamics of protein complex and aminoacids in apple fruits during the vegetative period and storage. Ph.D. Dissertation. University of Belgrade, Belgrade,1971.
27. J. Stojanović, M. Stojanović, A. Milovanović, *Acta Veterinaria Beograd*, **51**, 171 (2001).
28. J. Stojanović, D. Veličković, J. Vučetić, *Acta Veterinaria Beograd*, **52**, 267 (2002).
29. V.D. Jakovljević, J.M. Milićević J.D. Stojanović M.M. Vrvić, *Chem. Ind. Chem. Eng. Q.*, **20**, 587 (2014).
30. V.D. Jakovljevic, Biohemical characteristics of selected type of fungi in function biodegradation detergent. Ph.D. Dissertation. University of Kragujevac, Kragujevac, 2014.
31. J. Mehta, M. Jakhetia, S. Choudhary, J. Mirza, D. Sharma, P. Khatri, *Eur. J. Exp. Biol.*, **2**, 2061 (2012).
32. E. Moore-Landecker, Fundamentals of Fungi, Prentice Hall, Upper Saddle River, New York, 1996, p.574.
33. D.H. Griffin, Fungi Physiology, Wiley-Liss, New York, 1994, p.468.
34. M. Orlowski, *Microbiol. Rev.*, **55**, 234 (1991).

СРАВНИТЕЛНО ИЗСЛЕДВАНЕ НА НЯКОИ БИОХИМИЧНИ ПАРАМЕТРИ НА ГЪБИ
Mucor plumbeus, Aspergillus niger И *Trichoderma harzianum*

И. Матович-Пурич[1], Д. Печарски[2], З. Югович[3], Д. Йовичич[4], Д. Джорджевич[5], П. Маскович[6]

[1]*Медицинско училище, Епископ Никифор Максимович,№. 8, Чачак, Сърбия*
[2]*Висше училище за професионално здравеопазване, Кара Душана 254, Белград, Сърбия*
[3]*Висше санитарно здравно училище за професионални изследвания "Визан", Тошин бунар 7а, Белград, Сърбия*
[4]*Университет Сингидунум, Факултет за приложна екология - Футура, Пожешка 83, Белград, Сърбия*
[5]*Университет Ниш, Факултет за науки и математиката, Вишеградска 33, Ниш, Сърбия*
[6]*Университет Крагуевац, Факултет по агрономия, Чачак, Сърбия*

(Резюме)

Целта на това изследване е да се изследва ефектът от високите концентрации на търговския детергент "Merix" (Хенкел, Крушевац) върху растежа, развитието и биохимичните характеристики на тестваните гъби, изолирани от канализационни и промишлени отпадъчни води. Метаболитната активност на *Mucor plumbeus, Aspergillus niger* и *Trichoderma harzianum*, отглеждани в такава течна хранителна среда и контролна среда се следи по следните биохимични параметри: количества свободни и общи органични киселини, рН стойности, редукционен потенциал и биомаса. В зависимост от видовете гъбички има инхибиране на растежа на биомасата при различни концентрации на детергента в периода от третия до шестия ден. Концентрацията на детергента от 0,3% се разлага във всички тествани смеси гъби - детергенти.

Investigation of the mechanism and kinetics of extraction from plant materials

E. Simeonov[1*], Z. Yaneva[2], C. Chilev[1]

[1]*Department of Chemical Engineering, University of Chemical Technology and Metallurgy, 8 Kl. Ohridski Blvd., 1756 Sofia, Bulgaria,*
[2]*Chemistry Unit, Department of Pharmacology, Animal Physiology and Physiological Chemistry, Trakia University, Students Campus, 6000 Stara Zagora, Bulgaria*

A comprehensive systematic study on the mechanism of solid-liquid extraction of valuable components from plant materials was conducted. Experimental series of extraction of flavonoids from red geranium roots - *Geranium Sanguineum L.* (extractant 70% C_2H_5OH), and of tobacco concrete from tobacco leaves - *Nicotiana tabacum* L. (extractant H_2O), were done. Parametric investigations of the effect of: solid phase size ($R = 0.2 \times 10^{-3} \div 1.2 \times 10^{-3}$ m), effective diffusion coefficient ($D_{eff} = 10^{-10} \div 10^{-12}$ m²s⁻¹), partial mass transfer coefficient ($k = 10^{-5} \div 10^{-7}$ ms⁻¹), temperature ($T = 20 \div 60$ °C) and liquid/solid ratio ($\xi = 0.01 \div 0.03$ m³kg⁻¹), on the changes in the solid/liquid concentration were done. Significant correlation between the experimental data and the model values is established.

INTRODUCTION

Solid-liquid extraction is a process, the products of which are widely used in pharmaceutics, cosmetics and food industries, and also applied for environmental purposes. The description and calculation of the process faces serious difficulties both from methodological and mathematical points of view. The latter provoked numerous scientific studies focused on the process kinetics [1-7], the diffusivities [8-12], the extraction yields [6,9], or the process design [13-15]. Mathematical modeling is a powerful means for optimization of the equipment, simulation, design and control, allowing theoretical description of the process and evaluation of the mass transfer coefficients. Yet, the process description is very difficult because of the influence of a large number of parameters: variable in time solid phase pore structure, irregular particle shape, large particles size distribution, etc. The initial concentration of the active substance may also differ for the same raw material as a function of the crop area, storage conditions, operational temperature during the processing, and liquid/solid ratio. The kinetic coefficients also vary during the extraction process. To set up an experimental installation one needs to be acquainted with the diffusion type and the factors that are of main importance for the process. For that purpose, there are two different approaches, the first one is an analytical solution based on some simplifications for the three classic shapes of the solid phase. The second approach is a numerical solution combined with experimental data to obtain the necessary kinetic parameters applying the method of standard function or characteristic function [15].

The process of extraction of useful components from plant raw materials has been almost ever limited by the mass transfer inside the solid phase pores. Each experimental kinetic curve (dependence) includes indirectly all factors that influence the diffusion process velocity, as solid polydispersion and anisotropy, solid particles form, change in liquid phase concentration.

Such a kinetic curve can be represented by an equation of the type:

$$C_1 = A - B.e^{(-H.\tau)}, \qquad (1)$$

where A, B and H are constants determined numerically on the basis of the experimental data that have specific physical meaning, compared with the analytical solution of the process of solid phase extraction [10,14]. Quantitatively, these factors are reported by the effective diffusion coefficient (D_{eff}). The exact calculation of D_{eff} is of significant importance for the engineering solution of the process. In practice, there are experimental methods and such combining experimentally obtained data with analytical solutions. Chilev *et al.* (2014) suggested a new empirical model for the calculation of D_{eff} that was valid for a wide range of plant materials from which useful components were extracted with hydroalcoholic solutions [16].

The aim of the present study is to determine the mechanism and method of calculation and description of an extraction process by classical diffusion models, based on experimentally obtained

---

* To whom all correspondence should be sent:
E-mail: evgeni@uctm.edu

data. Furthermore, it establishes the effect of a number of parameters, characterizing a real system, on the extraction kinetics, in order to obtain more accurate modeling and control of the process.

EXPERIMENTAL

Plant materials

Experiments were carried out with two plant materials important to practice. The roots from *Geranium Sanguineum* L. were used as a solid phase for the extraction of flavonoids, and tobacco leaves (*Nicotiana tabacum* L.) - for obtaining tobacco concrete (extractable substances).

Extraction design

The kinetic experiments were performed in a stirred vessel. The ground raw material with suitable size was placed in the reactor and poured on with 70% C_2H_5OH/H_2O or pure H_2O. The reactor was immersed in a water bath and the temperature was maintained constant, controlled by a thermometer. The mixture was continuously stirred. To ensure limiting internal diffusion the angular velocity of the mixer was regulated. After extraction, the samples were taken and filtered through pleated filter to separate the solid from the liquid phase.

Experimental conditions

System I: Geranium Sanguineum L. - 70% C_2H_5OH

The kinetic study was carried out by periodical extraction from the roots of *Geranium Sanguineum* L. in a stirred vessel. The process temperature was $T = 20°C$. To eliminate the external mass transfer resistance the agitation rate was maintained at $n = 5$ s^{-1}. The experiments were performed with three sizes of the solid phase particles ($R = 0.2 - 0.4$ mm, $R = 0.4 - 0.8$ mm and $R = 0.8 - 1.25$ mm), at a liquid/solid ratio $\xi = 0.02$ m^3 kg^{-1} and 70% C_2H_5OH/H_2O solution as a solvent. The extracts were filtered with paper folded filter (Boeco Germany, Grade 6). The concentration of valuable compounds in the liquid phase (C_l) after the extraction was measured. Each experimental point of the kinetic curve was determined based on the average value of three independent experiments.

System II: Nicotiana tabacum L. – water

The experimental results were obtained in a batch reactor at the following conditions: extraction temperature – $T = 20°C$ and agitation rate – $n = 7$ s^{-1}, which ensured internal diffusion as a rate limiting stage (the external resistance was eliminated). The extraction experiments were conducted at three

liquid/solid values: $\xi = 0.01$ m^3 kg^{-1}, $\xi = 0.02$ m^3 kg^{-1} and $\xi = 0.03$ m^3 kg^{-1}. The initial concentration of the extractable substance (tobacco concrete) was experimentally determined - $C_o = 607.97$ kg m^{-3}.

Analytical methods for the extraction analysis
Spectrophotometric analysis for the determination of total flavonoids for system I - Geranium Sanguineum L. - 70% C_2H_5OH

The content of total flavonoids was determined by a colorimetric method with catechin. A calibration curve was obtained following the procedure: in a 10 ml volumetric flask 4 ml distilled water, 0.3 cm^3 $NaNO_2$ and 1 cm^3 of previously prepared 100 mg dm^{-3} catechin solution were added; the solution mixture was well shaken. After 5 min 0.3 cm^3 $AlCl_3$ and 2 cm^3 of NaOH were added and the solution was made up to 10 cm^3 with distilled water. Four more solutions with different catechin concentrations were prepared following the above cited procedure. The absorbances were measured on a UV/VIS spectrophotometer (BOECO – Germany S-22), at a wavelength of 510 nm *vs* a blank sample [17].

Weight analysis for the determination of extractable substances for system II - Nicotiana tabacum L. – water

A weighing method with precision of 10^{-3} g was applied for the quantitative determination of tobacco concrete. The extracts were evaporated in a drying oven at $T = 70°C$.

Kinetics study and modeling

In the absence of convective transport, the extraction from solid materials is described by the nonstationary diffusion equation ($\dfrac{\partial C_2}{\partial x} \neq const$ and $\dfrac{\partial C_2}{\partial \tau} \neq 0$). In porous solids, for the three "classical" shapes (unlimited plate, infinite cylinder and sphere) of the solid phase, the summary equation for symmetrical mass transfer has the following form [18]:

$$\frac{\partial C_2(x,\tau)}{\partial \tau} = \frac{1}{X^t}\frac{\partial}{\partial X}\left[X^t D_{eff} \frac{\partial C_2(x,\tau)}{\partial X} \right] \quad (2)$$

At $D_{eff} = const.$ it can be rearranged by solving the one-dimensional *Fick's* law for the three "classical" shapes of the solid phase – plate, sphere and cylinder:

$$\frac{\partial C_2}{\partial \tau} = D_{eff}\left(\frac{\partial^2 C_2}{\partial x^2} + \frac{t}{x}\frac{\partial C_2}{\partial x}\right) \quad (3)$$

with the following boundary conditions:

$$-D_{eff}\left(\frac{\partial C_2}{\partial x}\right)_{x=x} = k\left(\frac{C_{2_{x=x}}}{m} - C_1\right) \quad (4)$$

$$\left(\frac{\partial C_2}{\partial x}\right)_{x=0} = 0 \quad (5)$$

$$C_{2,\tau=0} = C_0 \quad (6)$$

$$\beta(C_0 - \overline{C}_2) = C_1 - C_m \quad (7)$$

The general analytical solution has the form:

$$\frac{C_0 - \overline{C}_2}{C_0 - C_m} = \frac{1}{1+\beta} - \sum_{n=1}^{\infty}\frac{4.(\upsilon+1)}{\mu_n^2 + 4(\upsilon+1)^2.\beta(1+\beta)}.\exp^{-\mu_n^2\frac{D_{eff}\tau}{R^2}}$$

$$(8)$$

where C_0 is the initial concentration in the solid phase; $C_m = C_{1i}$ by periodical processes; C_{1i} -initial concentration in the liquid phase; $\overline{C}_2$ - average concentration in the solid phase; D_{eff} – effective diffusion coefficient in the pores of the solid phase; R - size of the solid particles; τ – time; $\beta = \dfrac{C_{1eq}}{C_0 - C_{1eq}}$; C_{1eq} – equilibrium concentration in the liquid phase; μ_i – roots of the characteristic equation; υ – shape factor for the solid phase; m - distribution coefficient, $m \approx 1$ because of the low concentration range (well known fact in literature for the investigated plant material).

The boundary condition of the third kind – eqn. (4), which assumes equality of the mass flow from the solid phase to the surface towards the mass flow in the fluid phase, can be presented as follows:

$$-\left|\frac{\partial \overline{C}_2}{\partial \psi}\right|_{x=R} = Bi\left(\overline{C}_{2_{x=R}} - \overline{C}_1\right) \quad , (9)$$

where R is a characteristic particle size, $\psi = x/t$ - relative coordinate, and $Bi = kR/D_{eff}$ - *Biot* number.

The value of the partial mass transfer coefficient k depends on the hydrodynamic conditions of the porous particle wrapping, and it is a major kinetic indicator of the stage of the extraction process, which involves mass transfer from the solid surface through the boundary layer to the core of the fluid flow. The value of Bi determines the mode of the diffusion extraction.

At high wrapping velocity $k \to \infty$, $Bi \to \infty$ ($Bi > 30 \div 40$), the mode is internal diffusion, and the extraction rate is limited by solid phase diffusion. The opposite results correspond to lower values of the mass transfer coefficient k. At $k \to 0$, $C_2 \to const.$ and $Bi < 1$ the mode is external diffusion, and the process rate is limited by external diffusion – mass transfer from the solid surface.

In the boundary conditions, the concentration C_1 of the extractable component in the liquid phase is introduced. This concentration is approximately constant when the amount of the extractant is much greater than the amount of the extractable component. Such a ratio between the phases is some times artificially created in experimental conditions to facilitate the processing of the experimental data.

RESULTS AND DISCUSSION

Numerical solutions and analysis

The model described above can be used for extraction processes with various types of plant materials with different type of the internal structure and different size of the solid phase fractions, as well as when applying various extractants for the same raw material, etc. Practically, to use this model it is necessary to clarify the influence of the individual parameters on the type and accuracy of the solution and to present subsequent comparison with the experimental results for different liquid/solid systems.

Initially, a numerical study on the impact of various factors on the overall solution of the model was conducted. The programming environment MatLab 8.0 was used. The function „pdepe", which solves initial-boundary value problems for systems of parabolic and elliptic partial differential equations (PDEs) in the one space variable x and time τ with variable coefficients, was selected. The coefficients may depend on x, τ, C and $\frac{\partial C}{\partial x}$.

This function can be used for different types of symmetry - slab, cylindrical, or spherical.

The plant material may have different shapes and sizes. Usually they represent bits of herb leaves, flowers or roots. Therefore, the geometry of the system is a plate or a sphere. Thus, the numerical experiments were conducted for both types of system geometry. The solution of the differential eqn. (8) gives the distribution of

concentration in the solid phase over time. By the boundary condition eqn. (4), however, the concentration profiles in the liquid phase could be determined, and they can be compared with the experimental data. Therefore, the effect of individual factors on the distribution of concentration first in the solid phase and then in the liquid phase was initially examined. During the numerical experiments the following values of the variables, which were not changed in the course of the calculation procedure, were used: $C_{2.0}$ = 317 kg m^{-3}, $C_{1.0}$ = 0 kg m^{-3} and C_{eq} = 5.8 kg m^{-3}.

Factors influencing the concentration change in the solid phase

The parameters affecting the concentration distribution in the solid phase could be summarized as direct and indirect, or internal and external. The first group of parameters, on which the external diffusion mass transfer depends directly, includes the particle size R and the coefficient of effective diffusion D_{eff}. The latter is directly related to the structure of the solid phase. The second group includes factors associated with the external mass transfer of a substance: the partial diffusion coefficient in the boundary layer around the particle k and the concentration change in the liquid phase C_1.

Factors directly influencing the change of solid phase concentration

Effective diffusion coefficient (D_{eff})

The first parameter of this type is the effective diffusion coefficient. It is a complex function which depends on the pore diffusion coefficient and the structure of the solid phase – pore size distribution, pore curvature, etc. [14,15]. During the extraction process, the solid phase changes its structure regularly or irregularly, thus D_{eff} will generally depend on the spatial coordinates and time. To determine the effect of this parameter on the solution, numerical experiments at $D_{eff} = const$ but changing in a different order, were conducted (Fig. 1).

The obtained solutions were for a plate. In this case, the system is symmetrical with the axis of symmetry passing through half the thickness of the plate. The numerical solutions were obtained for solid particle thickness R = 0.3×10^{-3} m and this spatial coordinate was divided into 10 parts (size of the integration step). Time changed from 0 to 7200 s, and the time interval was divided into 100 parts. The partial external diffusion coefficient was k = 10^{-5} m s^{-1}. Figure 1 presents the change of the solid

phase concentration C_2 depending on the spatial coordinate x, i.e. amending half the plate thickness from zero to R = 0.3×10^{-3} m. With respect to the time coordinate, the figure depicts the concentration profiles for the initial moment "zero" (C_2 at time zero) and for the final moment (all other curves) at τ = 7200 s. Obviously, at τ = 0 s the concentration of the extractable component is C_2 = 317 kg m^{-3} and it is regularly distributed in the solid phase volume. At τ = 7200 s for all values of D_{eff} the solution displayed the highest concentration in the particle center at x = 0, which decreased to the boundary value at $x = R$.
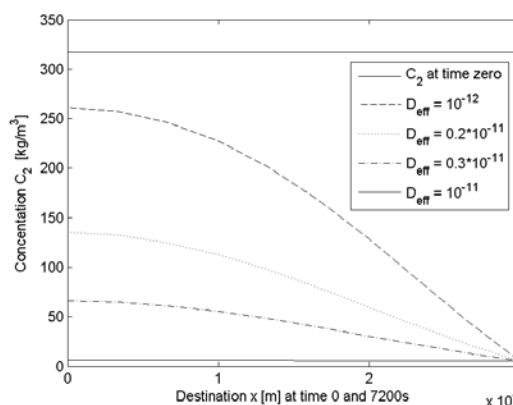

Fig. 1. Effect of D_{eff} on the change of solid phase concentration (C_2).

The figure shows that the smaller value of D_{eff}, provokes the higher concentration in the center of the particle at the final time. At D_{eff} = 10^{-11} m^2 s^{-1}, the concentration in the core was practically equal to that at the plate surface $C_2|_{x=0} \approx C_2|_{x=R}$, i.e. the total quantity of the extractable component was extracted from the solid phase. Hence, the more intense the internal diffusion, the less amount of extractable component remained in the solid phase after specific time. According to Fig. 1, a relatively small modification of D_{eff}, with only one order of magnitude, resulted in large differences in the concentration profiles in the final point of time, i.e., a strong influence of the effective diffusion coefficient on the final solution was observed. It is known that at $Bi \leq 1$ the process is limited by external mass transfer, for $1 \leq Bi \leq 30 \div 40$ a combined mass transfer mechanism is observed, and at $Bi \geq 30 \div 40$ the diffusion is internal [14,18]. In the case of the presented numerical experiments, Bi changed in the region 300 - 3000, i.e. the process was limited by internal diffusion.

Such study is essential when the target component is of high price, and it is necessary to be fully recovered from the solid phase. Thus, for a particular system at known D_{eff}, the final point of

time can be determined so that practically 100% of the extractable component can be extracted from the solid phase.

Solid phase particles size

From practice, it is known that one of the stages during the preparation of the raw material for extraction is crushing or cutting of the solid phase, i.e. the particle size influences the overall process. To investigate this dependence, numerical experiments for different particle radius (in a spherical coordinate system) and different leaves thickness (for a plate) were conducted. The obtained results at $D_{eff} = 10^{-11}$ m^2 s^{-1} are presented in Fig. 2. The other parameters are as in the numerical experiments for D_{eff} in the previous section. Figure 2 displays the solutions for spherical coordinate system at $\tau = 0$ and $\tau = 7200$ s.

Obviously, the larger the particles, the greater amount of the extractable component remained in them after 7200 s. At $R = 1.4 \times 10^{-3}$ m, the concentration in the particles center after 7200 s approximated the initial concentration. For small particles with $R \leq 0.4 \times 10^{-3}$ m, practically the entire quantity of the extractable component was extracted after 7200 s. Consequently, at a given intensity of the external diffusion, the greater the particle size, the greater amount of extractable components remained there after a certain period. In this case, Bi number varied between 200 and 1400, i.e. the rate limiting stage was internal diffusion. This study is essential when the target compound is of high price, and the optimization problem for choosing the time of extraction and particle size has to be solved, so that substantially the whole of the extractable component has to be extracted from the solid phase.
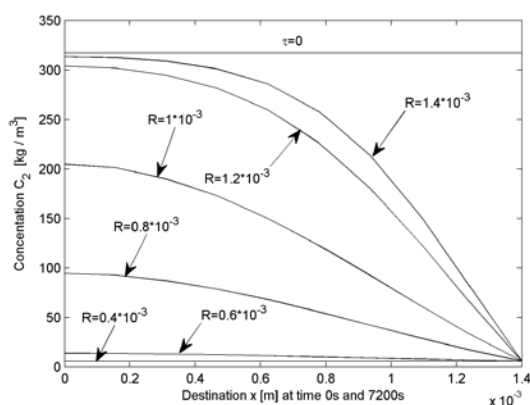

Fig. 2. Effect of the solid particles size (R) on the change of solid phase concentration (C_2).

Factors indirectly influencing the change of solid phase concentration

Partial mass transfer coefficient

This parameter is related to the external mass transfer through the boundary layer of the particle. Numerical experiments for various k values, $D_{eff} = 10^{-11}$ m^2 s^{-1} and slab symmetry – $R = 0.8 \times 10^{-3}$ m, were conducted. The other parameters were as in the previous numerical experiments for D_{eff}. Figure 3 presents the numerical solutions for the initial and final time moments.

Obviously, for $k \geq 10^{-6}$ m s^{-1}, the latter parameter actually did not influence the concentration change in the solid phase, as these values of k correspond to $Bi > 80$, which means rapid diffusion through the external boundary layer. Thus, the process was limited by internal diffusion, and the external mass transfer did not influence the derived solution. For $k \approx 10^{-7}$ m s^{-1} and $Bi \approx 8$ the external diffusion affected the overall process rate, i.e. the latter depended on both external and internal diffusion. In this case, k influenced the concentration distribution in the solid phase, which was confirmed by the numerical experiments presented in Fig. 3.
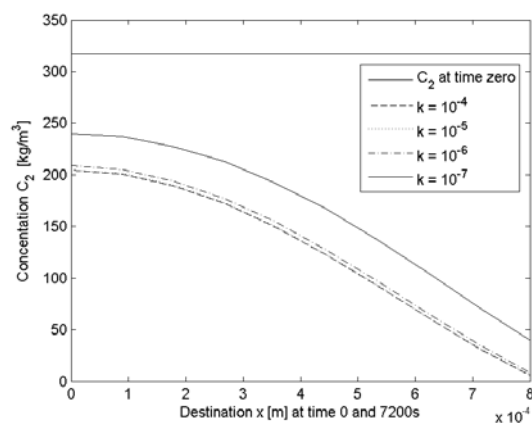

Fig. 3. Effect of k on the change of solid phase concentration (C_2).

Liquid/Solid ratio

The second parameter that indirectly affects the solution is the liquid/solid ratio ξ. It is directly related to the concentration in the liquid phase C_1. The concentrations in both phases are interconnected by the boundary condition eqn. (4). Since the concentration in the liquid phase is generally lower than that in the solid and it changes in a narrow range, very little influence of this parameter on the solution could be expected (i.e. the distribution of the concentration in the solid phase). Thus, numerical experiments at $D_{eff} = 10^{-11}$ m^2 s^{-1}, $k = 10^{-5}$ m s^{-1} and at two values of the particle sizes $R = 0.8 \times 10^{-3}$ and 1×10^{-3} m were carried out. The values of the other parameters were the same

403

as those of the numerical experiments for D_{eff} in Section 3.2.1. To ascertain the impact of C_1 on C_2, numerical solutions were obtained in which the boundary condition was set sequentially $C_1 = 0$ (at liquid/solid ratio infinity) for the entire time interval and $C_1 \neq const.$, i.e. likewise C_1 changes over time depending on the solution.
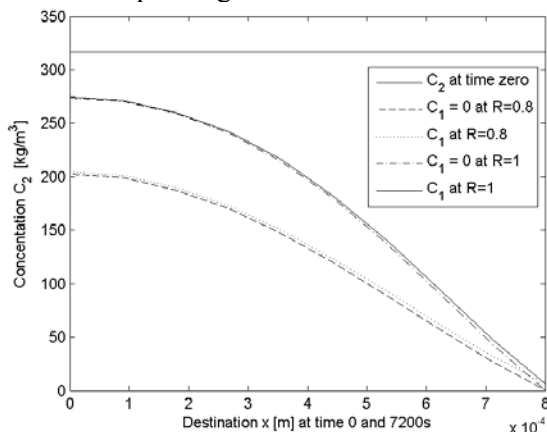

Fig. 4. Effect of the liquid/solid ratio (ξ) on the solid phase concentration (C_2).

According to Fig. 4 for both selected particle diameters, the difference between the solutions at constant and variable C_1 was very small, i.e. the influence of this parameter on the distribution of concentration in the solid phase was very weak, as already mentioned.

In conclusion, the concentration profiles in the solid phase were mainly influenced by the effective diffusion coefficient and particle size. Depending on their values for a given system, an optimum solution with regard to the necessary extraction time and the recovery rate of the target component has to be found. The influence of the other parameters was much slighter, and it probably manifests in mixed modes (with both external and internal diffusion control), which practically do not occur for extraction processes from raw plant materials.

Factors influencing the change of liquid phase concentration

Liquid phase concentration depends on the following three factors:
1. Mass transfer to the interior of the liquid phase;
2. Intensity of mass transfer through the boundary layer around the particle;
3. Concentration on the solid phase surface $C_2 \big|_{x=R}$.

The first factor is related to the mechanism of mass transfer of the extractable component in the liquid phase (molecular and convective diffusion). Typically, using suitable techniques (e.g., vigorous stirring) with a rather high accuracy the operation of the extractors approaches the ideal mixing regime. Thus, the concentration of the extractable component in the liquid phase at a given time is instantaneously equalized for the entire phase volume. Therefore, the impact of this parameter was eliminated.

Intensity of mass transfer through the boundary layer around the particle

The intensity of mass transfer through the boundary layer around the particle depends on the partial mass transfer coefficient, k. This coefficient depends mainly on the nature of the solvent and the extractable component and is in the order of 10^{-4} - 10^{-6} m s^{-1}. Rarely, for highly viscous extractable agents and for mass transfer of organic macromolecules or complexes, it may be reduced to 10^{-7} m s^{-1}. By the *Biot* number, calculated on the basis of the values of k and D_{eff}, the rate limiting mass transfer mechanism – internal or external diffusion, could be determined. For extraction from plant materials, D_{eff} is usually of the order of 10^{-11} m^2 s^{-1}, while $k \approx 10^{-5}$ m s^{-1}. The latter implies a limitation of the diffusion process in the solid phase pores, which is confirmed by numerous experimental results [10,14,18]. The effect of the mass transfer coefficient through the boundary layer around the solid particle on the liquid phase concentration was investigated. Numerical experiments (Fig. 5) were conducted for various k values at the following conditions: $D_{eff} = 10^{-11}$ m^2 s^{-1}, $R = 0.8$ m, phase equilibrium constant $m = 1$. The other parameters: initial solid/liquid concentration, etc., were the same as those in the previous numerical experiments. *Bi* number changed in the range 8 – 8000.
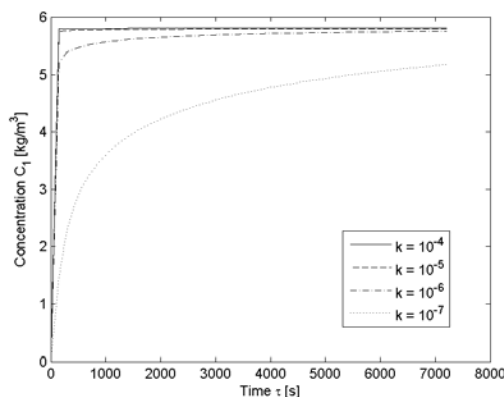

Fig. 5. Effect of k on the change of C_1.

Figure 5 displays the concentration profiles in the liquid phase, obtained by the numerical solution of the model for the time period 0 – 7200 s. Obviously, at $k = 10^{-4}$ and 10^{-5} m s^{-1} and $Bi = 8000$ and 800, respectively, the curves practically interflowed. These values corresponded to rapid mass transfer through the boundary layer around the particle, and demonstrated that further increase of Bi by k would be senseless and would not alter the rate of concentration change in the liquid phase. The effect of k became apparent at values $k < 10^{-6}$ m s^{-1}, i.e. $Bi < 80$. Then the mass transfer through the boundary layer around the particle was hindered, as for $Bi = 80$ ($k = 10^{-7}$ m s^{-1}) the rate of C_1 increase was significantly reduced.

Phase equilibrium constant

The equilibrium state of extraction represents the dependence of the equilibrium concentration in the liquid phase on the solid phase concentration for a given temperature and at various liquid/solid ratios. Usually, it is a straight line of the type: $C_1^* = m.C_2$, where m is the phase equilibrium constant. The values of this constant could be larger or smaller than unity. The equilibrium type affects the entire extraction process. The equilibrium constant is included in the boundary condition presented by eqn. (4), thus influencing the solution of the task. The effect of this parameter on the liquid phase concentration change was numerically investigated. The numerical experiments were conducted for $m = 0.5$, 1, 2 and 3, corresponding to equilibrium line slopes: 25°65``, 45°, 63°43``and 71°57``, respectively. The values of the other parameters were as follows: $k = 10^{-6}$ m s^{-1}, $D_{eff} = 10^{-11}$ m^2 s^{-1}, R = 0.3x10^{-3} m and $Bi = 30$. Figure 6 presents the strong influence of this parameter on the type of the obtained solutions. The equilibrium constant affected the nature of the curvature of the obtained solutions, and hence the accuracy of the calculation.
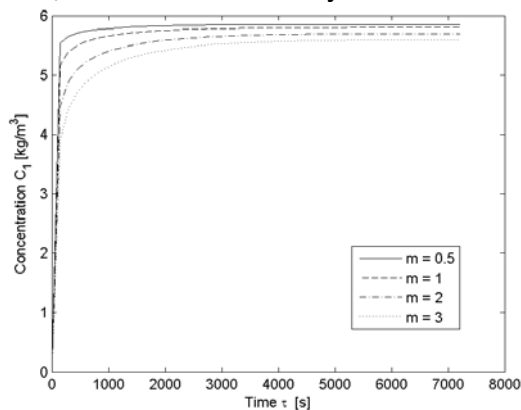

Fig. 6. . Effect of *m* on the change of C_1.

Effective diffusion coefficient in the solid phase pores

Since the concentration on the grain surface, $C_2\big|_{x=R}$, depends on the one hand on the effective diffusion coefficient of the extractable component D_{eff}, and on the other on the partial external mass transfer coefficient k in the boundary layer around the particle, the complex influence of both parameters was tested. D_{eff} and k participate in the calculation of Bi. Since C_1 is lower than the solid phase concentration C_2 (increased driving force) and if the mass transfer through the boundary layer is very intensive (at $k = 10^{-4}$, 10^{-5} m s^{-1}), the concentration $C_2\big|_{x=R}$ ceases to depend on D_{eff} and depends only on k. The change in the value of D_{eff}, in this case, influenced the distribution of the extractable component inside the particle (as depicted in Fig. 1), but did not influence the boundary concentration $C_2\big|_{x=R}$, which was approximately equal to C_1. Figure 7 presents the change of boundary concentration with time for $k = 10^{-4}$ and 10^{-7} m s^{-1}, $D_{eff} = 10^{-9}$ and 10^{-11} m^2 s^{-1}, respectively, and R = 0.3×10^{-3} m. The corresponding values of Bi are 30, 3000 and 0.03, 3, respectively.
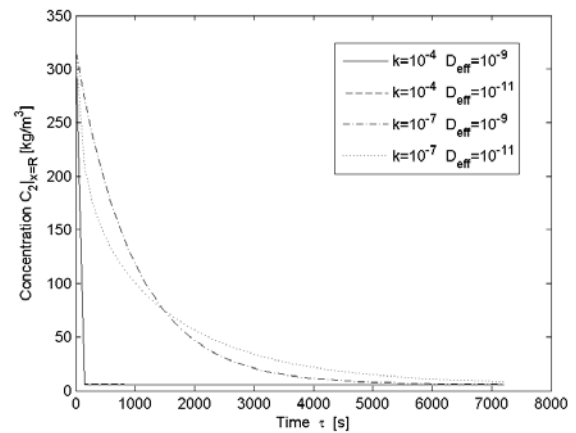

Fig. 7. Effect of k and D$_{eff}$ on the concentration $C_{2|x=R}$.

According to the data in Fig. 7 in the case of large values of $k = 10^{-4}$ m s^{-1}, i.e. rapid mass transfer through the external boundary layer, corresponding to $Bi = 30$ *and* 3000 (mixed mass transfer mode), D_{eff} did not influence the type of the obtained curves. Hence, the change of $C_2\big|_{x=R}$ depended only on k, rather than D_{eff}. For $D_{eff} = 10^{-9}$ and 10^{-11} m^2 s^{-1} the curves coincided (Fig. 7). For small values of $k = 10^{-7}$ m s^{-1}, i.e. hindered mass

transfer through the boundary layer, the curves for both D_{eff} values were well distinguished. In this case, the external and internal diffusion became commensurable ($Bi = 0.03$ and 3). For $k = 10^{-7}$ m s^{-1} and $D_{eff} = 10^{-9}$ m^2 s^{-1} ($Bi = 0.03$) there was a pronounced external diffusion mode and D_{eff} started to affect the change of the liquid phase concentration. According to the figures, the impact of D_{eff} was less pronounced than that of k. Consequently, the dependence of the change of C_2 on D_{eff} varied but only when the overall speed of the process was limited by external diffusion and this change was insignificant. D_{eff} did not affect C_2 for the cases of limiting internal diffusion or mixed mass transfer mode.

Solid particles size

Almost similar results were obtained when the impact of particle size on the change of concentration in the liquid phase was investigated (Fig. 8).

The corresponding values of Bi for the four cases displayed in Fig. 8 were 3000, 13000 and 0.3, 3. Hence, at $k = 10^{-4}$ m s^{-1} the process was controlled by internal diffusion, and at $k = 10^{-7}$ m s^{-1} the mode was mixed. Obviously, the effect of solid particles size was more significant for low k values, i.e. mixed mass transfer mode - $Bi \leq 3$. At $k \approx 10^{-4}$ m s^{-1}, the curves coincided. In that case, C_1 did not depend on the solid particles size.
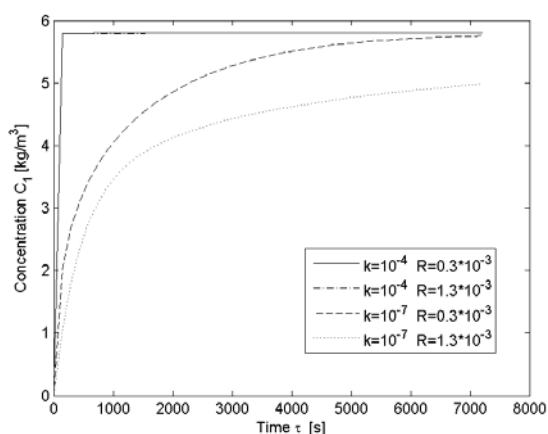

Fig. 8. Effect of the solid particles size (R) on the change of C_1.

It can be summarized that C_1 was influenced mainly by the rate limiting diffusion mechanism related to Bi, which is in direct correlation with k. At $k = 10^{-4} - 10^{-5}$ m s^{-1} ($Bi \geq 60 \div 70$), the diffusion is fast, thus C_1 and $C_2|_{x=R}$ did not depend

on D_{eff} and the solid particles size. At $k = 10^{-6} - 10^{-7}$ m^{2}s^{-1} ($Bi \approx 30 \div 0.03$), slight dependence of the concentration profiles in the liquid phase on D_{eff} and on the solid particles size was established.

The equilibrium phase constant also affected the accuracy of the solution, although less than k, but again in the regions of mixed and external diffusion control of the process. The influence of this parameter in the case of internal diffusion was insignificant. For most extraction systems, the value of the equilibrium phase constant is approximately 1, but in some cases of multi component extraction of polymers, and when mixed extracting agents (containing both polar and non-polar molecules) are applied, this value can be variable.

Numerical studies aimed to establish the influence of the size of the integration step on the spatial coordinate and time were conducted. For this purpose, solutions were obtained by dividing the spatial coordinate and the time interval into 5, 10, 100, 200, 500 and 1000 parts. The resulting solutions were identical regardless of the step of integration in space or time. This indicated greater resistance of the solution and could be accepted as a criterion for reliable results.

Experimental validation

The experimental data for target compounds extraction at different process conditions are presented in Table 1.

The experimentally obtained data for the extraction kinetics of the investigated solid-liquid systems can be described with an acceptable accuracy by eqn. (1). The values of *A*, *B* and *H* were estimated by nonlinear regression analysis of the experimental data and presented in Table 2 for different sizes of the solid phase - *System I Geranium Sanguineum* L. - 70% C_2H_5OH and different solid-liquid ratios - *System II Nicotiana tabacum* L. – H_2O.

Effect of the liquid/solid ratio

To investigate the effect of the liquid/solid ratio on the process kinetics, extraction experiments with *Nicotiana Tabacum L.* were conducted. The experimental results are presented in Table 1.They were described with sufficient accuracy by eqn. (1). The values of the constants *A, B* and *H* were determined by non-linear regression on the basis of the experimental data. The effective diffusion coefficient was calculated by the *Standard function method* [14-18]. Its values are presented in Table 2.

Numerical solutions of the model for the three liquid/solid ratios were obtained. Figure 9 displays the experimental data and the numerical solutions.

Obviously, satisfactory compliance between the experimental and model curves was achieved.
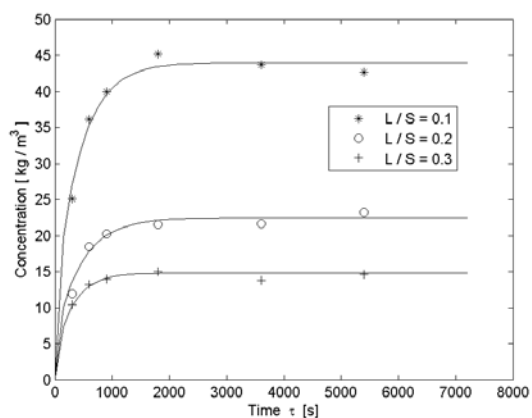

Fig. 9. Mathematical modeling of the experimental results for different liquid/solid ratios.

Effect of the particle size

To study the influence of the solid phase size on the process kinetics, extraction experiments of total flavonoids from *Geranium Sanguineum L.* were performed. The experimental data are presented in

Table 1. Solid particles with average sizes of 0.4×10^{-3}, 0.8×10^{-3} and 1.25×10^{-3} m were used for the experiments. The values of the parameters from eqn. (1) and those of D_{eff} are presented in Table 2. Figure 10 illustrates the experimental data and the numerical model solutions for the three studied cases.
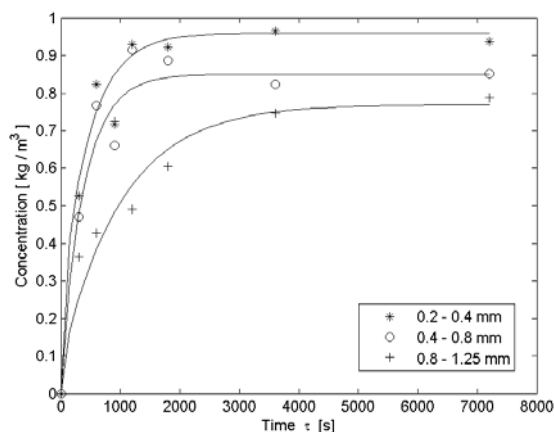

Fig. 10. Mathematical modeling of the experimental results for different particle sizes.

Table 1. Experimental data for extracted components concentration in the liquid phase C_1 (kg m^{-3}) under different process conditions

	Nicotiana Tabacum L.			*Geranium Sanguineum* L.		
τ (s)	$\xi = 0.01$ (m^3 kg^{-1})	$\xi = 0.02$ (m^3 kg^{-1})	$\xi = 0.03$ (m^3 kg^{-1})	$R=(0.2\text{-}0.4)$ $\times 10^{-3}$ (mm)	$R=(0.4\text{-}0.8)$ $\times 10^{-3}$ (m)	$R=(0.8\text{-}1.25)$ $\times 10^{-3}$ (m)
300	25.14	11.93	10.38	0.527	0.470	0.364
600	36.15	18.45	13.26	0.823	0.767	0.428
900	39.99	20.28	13.94	0.717	0.661	0.725
1200	-	-	-	0.929	0.915	0.491
1800	45.16	21.5	15.00	0.922	0.887	0.604
3600	43.7	21.68	13.77	0.965	0.823	0.746
5400	42.64	23.19	14.60	-	-	-
7200	-	-	-	0.937	0.852	0.788

Table 2. Values of the coefficients A, B, and H from eqn. (1) and of D_{eff} calculated by the standard function method.

Parameter	A	B	H	$D_{eff} \times 10^{10}$ (m^2 s^{-1})
For Liquid/Solid Ratios (*Nicotiana Tabacum*)				
$\xi = 0.01$ (m^3 kg^{-1})	43.7	43.1	0.003	0.30955
$\xi = 0.02$ (m^3 kg^{-1})	22.2	22.1	0.0026	0.28064
$\xi = 0.03$ (m^3 kg^{-1})	14.3	13.8	0.0045	0.47784
For particle size (*Geranium Sanguineum*)				
$R = 0.4 \times 10^{-3}$ (m)	0.933	0.9272	0.002713	1.2097
$R = 0.8 \times 10^{-3}$ (m)	0.8406	0.8391	0.002824	5.0567
$R = 1.25 \times 10^{-3}$ (m)	0.7532	0.6815	0.001053	4.7499

According to Fig. 10, when the particles size was reduced, the quantity of the extracted component increased and the kinetics of the process was intensified. Satisfactory correlation between the experimental and model data was observed.

Effect of temperature

To study the effect of temperature on the concentration profiles in the liquid phase, experimental data from a previous publication of the scientific team was used [16]. The obtained numerical solution for the examined system was compared to the experimental data.
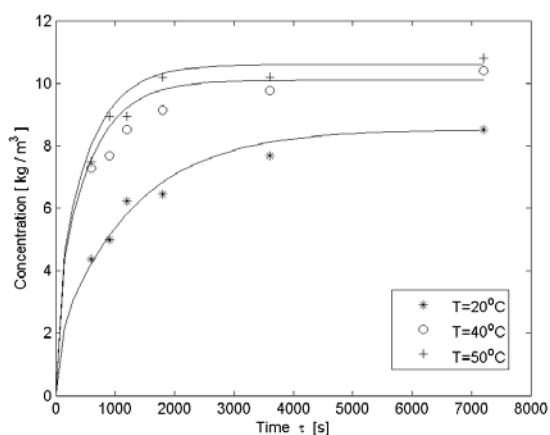
Fig. 11. Mathematical modeling of the experimental results for different temperatures.

Figure 11 presents the experimental results and numerical solutions of tannins extraction from *Cotinus coggygria*. The processing temperature was T = 20, 40, and 50°C. The experiments were performed at liquid/solid ratio ξ = 0.02 kg m^{-3}, density of the solid phase ρ_{sol} = 961 kg m^{-3}, characteristic solid particle size $R = 1.5 \times 10^{-4}$ m, and initial tannins concentration in the solid phase C_0 = 353.66 kg m^{-3}. The values of the constants A, B and H and the coefficient D_{eff} (calculated by the standard functions method) were published previously [16]. A direct relationship between temperature and the quantity of the extracted tannins was observed. There is a good agreement between experimental and modeled results.

CONCLUSIONS

A parametric study of the influence of various parameters on the concentration change in the solid and liquid phase, during the extraction of target components from plant materials, was conducted. The extraction kinetics of the systems *Geranium Sanguineum* L.–70% C$_2$H$_5$OH and *Nicotiana tabacum* L. – H$_2$O was experimentally investigated. The comparative analyses outlined that the effect of the various tested parameters on the process kinetics was complex and its magnitude was determined by the mode of the diffusion control based on Bi number values. The experimental data showed that, in all cases of extraction from plant materials, the process was controlled by internal diffusion. Thus, the main parameters influencing the kinetics of the process were the effective diffusion coefficient and the size of the solid particles.

The decrease in the solid particles size at constant other parameters lead to a decrease of the Bi value. According to the conducted numerical experiments, the extraction process was intensified at smaller particle sizes. At particles sizes smaller than $R = 0.4 \times 10^{-3}$ m, practically the entire quantity of the target component was extracted after 7200s. The latter was confirmed by the experimental data for extraction of flavonoids from *Geranium Sanguineum L.* The effective diffusion coefficient depended predominantly on the temperature and the solid phase structure, as confirmed by both the performed numerical experiments and the experimental data for tannins extraction from *Cotinus coggygria* L. Therefore, by increasing the temperature the amount of the extracted material was increased. The liquid/solid ratio was directly related to the change of the liquid phase concentration C_1. The numerical experiments displayed slighter influence of this parameter on the numerical model solution. The liquid/solid ratio affected predominantly the driving force and therefore, the intensity of the diffusion process. The latter was confirmed by the experimental data of target compounds extraction from *Nicotiana tabacum L.*

The influence of the partial mass transfer coefficient through the external boundary layer and the equilibrium phase constant was investigated numerically. These two parameters affected the model solution only in the regions of mixed and external diffusion control ($Bi < 30 \div 40$). For internal diffusion, the influence of both parameters was insignificant.

The numerical modeling of all experimental data displayed satisfactory compliance between the experimental and model results. The comparative analyses and the suggested mathematical model could be applied for the simulation and description of extraction processes from various plant materials at verified technological parameters influencing the process intensity.

NOMENCLATURE

A = coefficient defined by eqn. (1)
B = coefficient defined by eqn. (1)
Bi = Biot number ($Bi = kR/D_{eff}$)
C_1 = concentration in the liquid phase (kg m^{-3})
C_{1eq} = equilibrium concentration in the liquid phase (kg m^{-3})
C_2 = concentration in the solid phase (kg m^{-3})
C_o = initial concentration in the solid phase (kg m^{-3})

$\bar{C}_2$ = average concentration in the solid phase (kg m^{-3})

D_{eff} = effective diffusion coefficient (m^2 s^{-1})
H = coefficient defined by eqn. (1)
k = external mass transfer coefficient (m s^{-1})
m = distribution coefficient
n = agitation rate (s^{-1})
R = characteristic size of the solid particles (m)
T = temperature (ºC)
x = coordinate (m)

Greek Letters

δ = solid particles size (mm)
μ_i = roots of the characteristic equation
v = shape factor
ξ = liquid/solid ratio (m^3 kg^{-1})
ρ_{sol} = density of the solid phase (kg m^{-3})
τ = time (s)
ψ = relative coordinate ($\psi = x / t$)

REFERENCES

1. C.H. Chon, R. Yusoff, G.-C. Ngoh, *Chem. Eng. Res. Des*, **92** (6), 1169 (2014).
2. M. Cisse, P. Bohuon, F. Sambe, C. Kane, M. Sakho, M. Domier, *J. Food Eng.,* **109** (1), 16 (2012).
3. A. Stoiza, T. Dobre. M. Stoescu, A. Sturzoiu, O.C. Parvulescu, *Food Bioprod. Process.,* **94**, 218 (2015).
4. R. Wongkittipong, L. Prat, S. Damroglerd, C. Gourdon, *Sep. Purif. Technol.,* **40** (2), 147 (2004).
5. J. D. Espinoza-Péreza, A. Vargasa, V.J. Robles-Olveraa, G.C. Rodríguez-Jimenesa, M.A. García-Alvarado, *J. Food Eng.,* **81** (1), 72 (2007).
6. A. Bucić-Kojić, M. Planinića, M. Tomasa, M. Bilića, D. Velića, *J. Food Eng.,* **81** (1), 236 (2007).
7. M. Pinelo, J. Sineiro, M. J. Núñez, *J. Food Eng.,* **77**, 57 (2006).
8. T.A. Nguyena, P. Verbovena, N. Scheerlincka, S. Vandewalleb, B.M. Nicolaïa, *J. Food Eng.,* **72**(1), 63 (2006).
9. I. Seikova, E. Simeonov, E. Ivanova, *J. Food Eng.,* **61**, 165 (2004).
10. E. Simeonov, I. Tsibranska, A. Minchev, *Chem. Eng. J.,* **73**, 255 (1999).
11. I. Seikova, E. Simeonov, *Sep. Sci. Technol.,* **38** (15), 3713 (2003).
12. M. Izadifar, O.D. Baik, *Sep. Purif. Technol.*, **63** (1), 53 (2008).
13. A. Senol, A. Aydin, *J. Food Eng.*, **75** (4), 565 (2006).
14. E. Simeonov, I. Seikova, I. Penchev, A. Minchev, *Ind. Eng. Chem. Res.,* **42** (7), 1433 (2003).
15. E. Simeonov, I. Seikova, I. Pentchev, A. Mintchev, *Ind. Eng. Chem. Res.,* **43**, 4903 (2004).
16. Ch. Chilev, V. Koleva, E. Simeonov, *Ind. Eng. Chem. Res.,* **53**, 6288 (2014).
17. D. Marinova, F. Ribarova, M. Atanasova, *J. Chem. Technol. Metall.,* **40** (3), 255 (2005).
18. G.A. Axelrood, W. Lisjanski, Extraction (Solid-liquid systems); USSR, *Chimia*: St. Peterburg, 115 (1974).

ИЗСЛЕДВАНЕ НА МЕХАНИЗМА И КИНЕТИКАТА НА ЕКСТРАКЦИЯ ОТ РАСТИТЕЛНИ СУРОВИНИ

Е. Симеонов[1*], З. Янева[2], Ч. Чилев[1]

[1]*Катедра „Инженерна химия“, Химикотехнологичен и металургичен университет, бул. „Кл. Охридски“ 8, 1756 София, България*

[2]*Секция „Химия“, Катедра „Фармакология, физиология на животните и физиологична химия“, Ветеринарномедицински факултет, Тракийски университет, Студентски град, 6000 Стара Загора, България*

(Резюме)

Проведено е цялостно систематично изследване на механизма на извличане на полезни компоненти при твърдо-течна екстракция от растителни суровини. Извършени са серии от експерименти на екстракционно извличане на флавоноиди от корени на кръвен здравец - *Geranium Sanguineum L.* (екстрагент 70% C$_2$H$_5$OH), и на тютюнев конкрет от тютюневи листа - *Nicotiana tabacum* L. (екстрагент H$_2$O). За целта бе проведено параметрично изследване на влиянието на параметрите: размер на твърдата фаза ($R = 0.2 \times 10^{-3} \div 1.2 \times 10^{-3}$ m), коефициентът на ефективна дифузия ($D_{eff} = 10^{-10} \div 10^{-12}$ m^{2}s^{-1}) частен коефициент на масопренасяне ($k = 10^{-5} \div 10^{-7}$ ms^{-1}), температура ($T = 20 \div 60$ ºC) и хидромодул ($\xi = 0.01 \div 0.03$ m^{3}kg^{-1}), върху изменението на концентрацията в твърдата и течната фаза. Установена е много висока степен на корелация между експерименталните и моделни стойности.

Assessment of different PLS algorithms for quantification of three spectrally overlapping drugs

G. Gergov[1] *, A. Alin[2], M. Doychinova[3], M. De Luca [4], V. Simeonov[5], Y. Al-Degs[6]

[1]*Department of Chemistry, Faculty of Pharmacy, Medical University, Dunav St.2, Sofia 1000, Bulgaria.*
[2]*Department of Statistics, Dokuz Eylul University, Izmir, Turkey*
[3]*Institute of Chemical Engineering, Bulgarian Academy of Sciences, Acad. G. Bonchev St., bl.103, Sofia 1113, Bulgaria*
[4]*Department of Pharmacy, Health and Nutritional Sciences, University of Calabria, 87036 Rende, Italy*
[5]*Laboratory of Chemometrics and Environmetrics, Faculty of Chemistry and Pharmacy, Sofia University*
"St. Kliment Ohridski", J. Bourchier Blvd. 1, Sofia 1164, Bulgaria.
[6]*Chemistry Department, The Hashemite University, P.O. Box 150459, Zarqa 13115, Jordan*

The primary aim of the present study was to compare the prediction power of different PLS algorithms as applied to the quantification of three spectrally overlapping drugs. Four variants of PLS were chosen for multivariate calibration and prediction of the three components of the drug formulation (paracetamol, propyphenazone and caffeine). NIPALS and SIMPLS algorithms were the most commonly used algorithms. The other tested algorithms were Kernel and Bidiagonalization which have been rarely applied in pharmaceutical analysis.

First-order data were created by measuring UV-spectra of drug mixtures over the range 190-300 nm with a resolution of 2.0 nm (i.e., 56 spectral points/sample). Reduced five-level full factorial design was used and the prediction power of PLS variants was tested for drugs levels outside the ranges selected in the calibration set.

De Luka method and the confirmative bootstrap method were helpful for the quick selection of the spectral regions.

The external prediction using the PLS-Kernel calibration model showed significant advantages in the analysis of the common marketed formulation SARIDON. The three drugs in SARIDON were quantified with mean recoveries and precisions of 96.4 (1.3), 95.1 (2.5) and 96.2 (2.9) for paracetamol, propyphenazone and caffeine, respectively. This turned out to be the optimal algorithm which could be successfully applied for the routine analysis of analgesic and antipyretic tablets in the pharmaceutical industry.

Keywords: PLS1 algorithms: NIPALS, SIMPLS, KERNEL, BIDIAGONALIZATION, Spectral overlapping; De Luca method, Bootstrap method, SARIDON formulation.

INTRODUCTION

Pharmaceutical formulations, in which one dominant component is combined with other drugs, are designated to enhance the final pharmacological effects of each substance and to cover a larger medical treatment [1]. Formulations containing paracetamol PAR, propyphenazone PRO, and caffeine CAF represent a commonly prescribed combination for pain relief [2]. Paracetamol is a common antipyretic and analgesic agent used as an alternative to aspirin (acetylsalicylic acid) in some countries [1]. Propyphenazone is derived from pyrazolone with analgesic, antipyretic and anti-inflammatory effects [2]. It is a non-steroidal antiinflammatory drug incorporated together with paracetamol into many analgesic combinations [2-3]. CAF, a methylated xanthine and potent stimulant of the central nervous system, has been added to PAR and PRO in various combinations [1,3]. Caffeine is also known to synergistically increase the analgesic effect of paracetamol and

propyphenazone, providing relief from symptoms like headache, muscular aches, neuralgia, backache, joint pain, rheumatic pain, migraine, toothache and menstrual pain [2,4]. In Eastern Europe, very common marketed formulations containing PAR, PRO and CAF are known as SARIDON® and Pararemin® [3]. On the Bulgarian market the generic product SARIPHEZON® is also available.

Typical doses of the earlier preparations are 250 mg PAR, 150 mg PRO and 50 mg CAF, however, different levels are also available in the market. NeoOptalidon® is a common formulation with lower drug-doses 200 mg PAR, 125 mg PRO and 25 mg CAF, while Veramon® is available with higher PRO dosage: 200 mg PAR and 285 mg PRO [8].

The aforementioned ternary-drug formulations are of great challenge for pharmaceutical analysts to develop reliable and simple analytical procedures avoiding expensive chromatographic separation and characterized by low-consumption of organic solvents and short analysis time.

Quantification of PAR, PRO and CAF in different pharmaceutical preparations was carried

---

* To whom all correspondence should be sent:
E-mail: ggergov@abv.bg

out using liquid chromatography [3,5]. Derivative spectroscopic methods were also suitable for resolving such complex mixtures. Derivative ratio zero-crossing spectrophotometric determination of the three analytes was demonstrated by Dink *et al.* [5]. However, the applicability of derivative spectroscopic methods for handling overlapped spectra would be limited. More powerful multivariate calibration and UV spectrophotometry for accurate assaying marketed formulations has been well documented [1,8]. Among the multivariate calibration methods, classical least squares CLS, principal component regression PCR, and partial least squares regression PLS have been intensively applied [6].

Dink et al. proposed UV chemometric determination of a ternary mixture containing PAR, PRO and CAF in pharmaceutical preparations [7]. De Luca and co-workers have applied several chemometric methods using zero and derivative spectra to get better external prediction for PAR-PRO-CAF [8] .The same authors proposed a new procedure for wavelength selection based on the cumulative regression coefficients.

PLS modeling is the most important multivariate calibration method in many different fields including chemical and pharmaceutical analysis. PLS method has a very important advantage over other chemometric methods for using concentrations knowledge directly in calculations. PLS can deal with collinearity and offers an interactive diagnostic exploration of the data [9]. Modern instruments can generate a large number of data points per sample, which needs more advanced PLS-algorithms to end up with accurate results within minimum time , numerical stability and capacity [10,11]. PLS (particularly the nonlinear iterative partial least squares-NIPALS) is the most frequently adopted algorithm in chemical and pharmaceutical analysis [12,13]. Undoubtedly, the dramatic improvement in software production, modeling, and programming languages has positively reflected on the popularity of multivariate calibration. The intense applicability of PLS-NIPALS in pharmaceutical analysis is attributed to its availability in most commercial softwares like MVC1® and TOMCAT® [14,15]. For example, NIPALS is suitable for modeling many variables-**X** but it requires long computational time and more memory-storage [16]. PLS-SIMPLIS is proposed for increasing calibration speeding [17]. Along with this, there are two versions of the de Jong's algorithm (SIM-PLS and WIM-PLS), which are implemented in TOMCAT®[15]. WIM-PLS is specially designed for wide X matrices . Another

approach, although not as fast, was presented and called the Kernel PLS algorithm . PLS-Kernel is considered as an adjustable algorithm which can be adopted for systems of many variables or even many mixtures by creating condensed and small matrices [18,19]. The kernel algorithms were improved by Dayal and MacGregor [20]. PLS-Bidiagonalization is an advanced version of another algorithm which decomposes the X matrix into three smaller matrices of orthonormal vectors [11] and this algorithm deserves investigation as it has no application in pharmaceutical analysis. It is known that the mentioned algorithms are different in their mechanisms for running chemical analysis [10,11,16].

There are two main goals of this work: a) assessment of the resolving power of four common PLS algorithms (NIPALS, SIMPLS, Kernel, and Bidiagonalization) for quantification of three spectrally overlapping drugs, and b) quick quantification of the active ingredients (PAR, CAF, and PRO) in the highly consumed marketed drug SARIDON® with minimum sample clean up. The application of the newly proposed De Luca procedure and bootstrap methods for selecting informative spectral regions before multivariate calibration is evaluated.

Theoretical background

PLS is an efficient tool for developing a quantitative relationship between several predictor variables **X** (spectral measurements in this work) and a property of interest **Y** (the independent variables or drugs content in this work). Mathematically, the relationship between **X** and **Y** or **y** (for one single independent variable) is given as [16]: **y**=**Xb,** where **y, X,** and **b** are drug standard concentrations in the calibration samples arranged in a vector**,** the data matrix containing the absorbances of standard solutions that are measured at different wavelengths, and the calibration sensitivity which is necessary for estimating drug content in the extracts of SARIDON®. PLS is an efficient numerical tool to find **b** which is often accomplished using different variants of PLS [11]. In general, the dimensions of the mentioned quantities are **X** (*I* samples×*J* variables) and **Y** (*I* samples×*k* solutes), **y** (*I* samples×1), and **b** (*J* variables×1). The tested PLS-variants are NIPALS, SIMPLS, Kernel, and Bidiagonalization. In the tests of comparing algorithms only PLS1(one dependent variable) was considered. The best selection of the optimum number of PLS-factors (A) is carried out by using leave-one-out cross-validation technique [21].

A brief summary on the PLS-variants is provided in this section.

PLS-NIPALS

This classical algorithm is suitable for modeling different sizes of X matrices which containing the explanatory variables. Therefore, for matrices of $I>J$ or $J>I$ but the algorithm reported to be not suitable for many variables $\mathbf{X}$ matrices [10-11]. This algorithm decomposes $\mathbf{X}$ and $\mathbf{y}$ (or $\mathbf{Y}$) into smaller matrices and vectors to estimate calibration vector $\mathbf{b}$ to be used in the next prediction stages. The general steps of the algorithm are [10-11,16]:

$\mathbf{w}$: PLS-weight for $\mathbf{X}$: $\mathbf{w}^t = \mathbf{u}^t\mathbf{X}/(\mathbf{u}^t\mathbf{u})$

$\mathbf{t}$: PLS-score for $\mathbf{X}$: $\mathbf{t} = \mathbf{Xw}$

$\mathbf{q}$: PLS-loading for $\mathbf{y}$: $\mathbf{q} = \mathbf{t}^t\mathbf{y}/(\mathbf{t}^t\mathbf{t})$

$\mathbf{u}$: PLS-score for $\mathbf{y}$: $\mathbf{q} = \mathbf{yq}/(\mathbf{q}^t\mathbf{q})$

$\mathbf{p}$: PLS-loading for $\mathbf{X}$: $\mathbf{p} = \mathbf{t}^t\mathbf{X}/(\mathbf{t}^t\mathbf{t})$

$\mathbf{X}$ and optionally $\mathbf{y}$ are then deflated before repeating the above steps for the new PLS-variable:
$\mathbf{X}_1 = \mathbf{X} - \mathbf{t}_1\mathbf{p}_1^t$ and $\mathbf{y}_1 = \mathbf{y} - \mathbf{t}_1\mathbf{q}_1^t$

The next component is estimated using $\mathbf{X}_1$ and $\mathbf{y}_1$ and proceeding with $\mathbf{X}_2, \mathbf{y}_2 \ldots \mathbf{X}_A$, $\mathbf{y}_A$ until an adequate model is established. Once the earlier vectors are estimated using the optimum number of factors (A), then $\mathbf{b}$ is estimated as:

$\mathbf{b} = \mathbf{W}^t(\mathbf{PW}^t)^{-1}\mathbf{q}$

where $\mathbf{W}$ is the weights matrix for $\mathbf{X}$, $\mathbf{P}$ is the loadings matrix of $\mathbf{X}$, and $\mathbf{q}$ is the loading vector for $\mathbf{y}$. t and -1 stand for transpose and inverse operations, respectively. Once $\mathbf{b}$ is estimated by PLS-NIPALS, prediction of the target drug from the unknown spectrum $\mathbf{a}_{un}$ is carried out as following:

$c_{un} = \mathbf{a}_{un}\mathbf{b}$

PLS-SIMPLS

This algorithm is faster than PLS-NIPALS but it is not recommended for many variables-X matrices. To find the useful calibration vector b, the following quantities are computed [16, 17]:

$\mathbf{s} = \mathbf{X}^t\mathbf{y}$

$\mathbf{r}$: PLS-loading for $\mathbf{y}$: $\mathbf{r} = \mathbf{s}$

$\mathbf{t}$: PLS-score for $\mathbf{X}$: $\mathbf{t} = \mathbf{Xr}$

$\mathbf{p}$: PLS-loading for $\mathbf{X}$: $\mathbf{p} = \mathbf{X}^t\mathbf{t}$

$\mathbf{q}$: PLS-loading for $\mathbf{y}$: $\mathbf{q} = \mathbf{y}^t\mathbf{t}$

The quantities $\mathbf{r}$, $\mathbf{t}$, $\mathbf{p}$, and q are stored in $\mathbf{R}$, $\mathbf{T}$, $\mathbf{P}$ and $\mathbf{q}$, respectively. Before estimating the next PLS-variable s is projected on a subspace of $\mathbf{P}$. The above algorithm is stopped once all PLS-variables are estimated as outlined earlier. Regression vector is calculated as [17]:

$\mathbf{b} = \mathbf{Rq}$

Prediction of the target drug in the new sample (extract of formulation) is estimated as shown above. PLS-SIMPLS is faster than classical PLS-NIPALS as it proceeded without deflation of $\mathbf{X}$ and $\mathbf{y}$ and fewer matrices (to find $\mathbf{b}$) are used [16].

PLS-Bidiagonalization

Basically, this advanced algorithm is started by decomposing $\mathbf{X}$ into three matrices [11]:

$\mathbf{X} = \mathbf{URV}^t$

Where, $\mathbf{U}(I \times J)$ and $\mathbf{V}(I \times J)$ are matrices with orthonormal columns (i.e., $\mathbf{U}^t\mathbf{U} = \mathbf{V}^t\mathbf{V} = 1$) and $\mathbf{R}(J \times J)$ is the bidiagonal matrix. It is imprint to mention that in the earlier algorithms all columns in the generated matrices must be orthogonal (i.e., $\mathbf{W}^t\mathbf{W} = \mathbf{P}^t\mathbf{P} = 0$). Once the $\mathbf{U}$, $\mathbf{R}$ and $\mathbf{V}$ matrices are estimated with the optimum PLS-variables, the calibration vector is estimated as [11]:

$\mathbf{b} = \mathbf{VR}^{-1}\mathbf{Uy}$

PLS-Kernel

There are two common variants of Kernel algorithm so far [11, 16, 18, 19]. The first one can handle matrices of many samples, i.e. I is larger than J ($I >> J$), and the other one (which is suitable for the current drug system) was proposed for many variables $\mathbf{X}$-matrices ($J >> I$). In all kernel algorithms, condensed matrices are created from $\mathbf{X}$ and $\mathbf{Y}$ (or $\mathbf{y}$) which is an essential step. In the adopted algorithm, two condensed matrices are created $\mathbf{XX}^t$ and $\mathbf{YY}^t$ or $\mathbf{yy}^t$. Kernel matrix is then estimated as: $\mathbf{XX}^t\mathbf{YY}^t$. The main steps of the algorithm are [19]:

1. The eigenvector of the kernel matrix is taken as the first $\mathbf{X}$ score vector $\mathbf{t}_1$. The Y score vector is then estimated as: $\mathbf{u}_1 = \mathbf{YY}^t\mathbf{t}_1$

2. The next step is to update the association matrices by eliminating the explained variable as follows:

$\mathbf{G}_1 = \mathbf{I} - \mathbf{t}_1\mathbf{t}_1^t$ (I identity matrix)

$\mathbf{X}_1\mathbf{X}_1^t = \mathbf{G}_1\mathbf{XX}^t\mathbf{G}_1$

$\mathbf{Y}_1\mathbf{Y}_1^t = \mathbf{G}_1 \mathbf{YY}^t \mathbf{G}_1$

The above operations save us from going back to the original large matrices and calculation of association matrices which are necessary at the start of the algorithm. As can be seen, the matrices

involved in Kernel algorithm have lower dimensions than the original matrices.

3. The next **t** and **u** vectors are estimated as outlined above using the updated matrices. The calibration matrix (containing the calibration vectors for the target solutes) are estimated from weight and loading matrices (**W, P** and **Q**) as follows:

$$\mathbf{W} = \mathbf{X^t U}$$
$$\mathbf{P} = (\mathbf{T^t X})(\mathbf{T^t T})^{-1}$$
$$\mathbf{Q} = (\mathbf{T^t Y})(\mathbf{T^t T})^{-1}$$

Step 3 is repeated until the optimum number of PLS-variables is estimated.

It should be mentioned that all vectors in **W** should be normalized before creating the **b** vector [18, 19]:

$$\mathbf{b} = \mathbf{W}(\mathbf{P^t W})^{-1}\mathbf{Q^t}$$

The solutes could be predicted from the spectrum $\mathbf{a_{un}}$ of the sample as follows:

$$\mathbf{C_{un}} = \mathbf{a_{un} b}$$

De Luca wavelength selection method

The main steps of the De Luca method [8] are:
1. Firstly, the optimal number of factors (A) for components in the mixture is found.
2. Secondly, regression vectors for every component using A are estimated from PLS - algorithms: $\mathbf{B} = \mathbf{W}(\mathbf{P^t W})^{-1}\mathbf{Q^t}$.

The regression coefficients for every component have different values at each wavelength:

$$C = b_0 + b_1\lambda_1 + b_2\lambda_2 + \cdots + b_n\lambda_n$$

where C is the analyte concentration, b the regression coefficients and λ is the wavelengths.

3. The sum of the absolute values of regression coefficients gives a new vector called curve of cumulative coefficients (B):

$$B_{\lambda i} = \sum_{i=1}^{n} |b_i|$$

4. Finally, the mean of cumulative coefficients is estimated and so the cutoff values are obtained:

$$\bar{B} = \frac{1}{n}\sum_{i=1}^{n} B_i$$

5. The appropriate wavelength range includes the crossing points between cutoff value ($\bar{B}$) and the curve of cumulative coefficients (B).

EXPERIMENTAL

Chemicals and reagents

The drugs (Paracetamol, Propyphenazone and Caffeine) as shown in Fig 1 with maximum purity (> 99%) were purchased from Sigma–Aldrich. A 100.0 mg/L standard solution of each drug was prepared by dissolving 100 mg (±0.0001 g) from the corresponding pure materials in doubly distilled water in a 1.0 L volumetric flask. Due to the modest solubility of PAR and PRO in water, the initial solutions were mildly heated (50 °C). The calibration mixtures (22 solutions) and validation mixtures (12 solutions) were directly prepared from the stock solutions by appropriate dilution using distilled water.
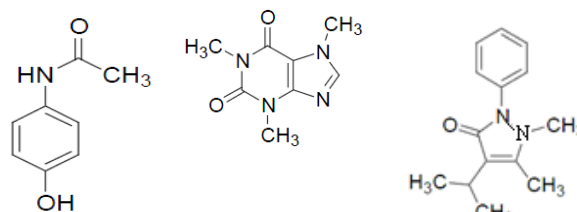
Paracetamol   Caffeine   Propyphenazone
Fig. 1. Structural formulae of the drugs

Apparatus and software

The absorbance measurements were obtained using a quartz cuvette of 1.0 cm optical path, by a HP8452A diode-array UV–Vis spectrometer. The spectra of drugs were recorded over the wavelength range of 190–300 nm and the digitalized absorbance values were exported to MATLAB® for further analysis. Numerical solutions are calculated using MatLab®2013a (The Mathworks, Natick, MA, USA). PLS-variants (NIPALS, SIMPIS, Kernel and Bidiagonalization) were runned using home-made matlab® codes based on the algorithms outlined in the former section. The matlab® codes are available upon request from the authors. Independently, mathematical calculations were carried out using MVC1® [14] and TOMCAT® [15] programs which are freely available. Cross-validation procedure was carried out using cross-validation.m function from TOMCAT®, which is modified to be applicable for SIMPLS, Kernel and Bidiagonalization algorithms.

Calibration and validation sets

There are many strategies for building a calibration set which is necessary to run the calibration model. In pharmaceutical analysis, full factorial design is often adopted to end up with accurate multivariate calibration analysis. For *n* concentration levels for *k* solutes, the number of calibration mixtures *I* that should be prepared is n^k. Finally, a large reduction in the number of mixtures is obtained by applying Brereton's table [22]. It is proposed for multilevel multifactor (multi-solute) systems. According to Brereton's design, the number of mixtures is $I = n^2$ and the maximum

number of analyzed solutes is *I*-1. In our work, five-level full factorial design was adopted. Following this design, 25 mixtures should be prepared and up to 24 solutes analyzed [22]. In this work, 22 mixtures are found representative and prepared according to the levels provided in Table 1. The levels of drugs in the calibration set were randomly selected. As can be seen from Table 1, the levels of the drugs were carefully chosen to be comparable to those present in the marketed formulation (250 mg PAR-150 mg PRO-50 mg CAF per tablet). For PAR and PRO, the selected levels are 0, 4.0, 6.0, 8.0, and 10.0 mg/L, while for CAF, the levels were 0, 1, 2, 4, and 8 mg/L. For the three drugs, the concentration levels were coded as: -2 for the lower concentration and +2 for the higher concentration. In general, the design would show that the levels of drugs are orthogonal and span a large variation in levels. The orthogonal design is necessary for building a stable and robust PLS model. A 12-mixture validation set was prepared in order to test the performance of the models. For a validation set, new concentration levels were created for the three solutes, and the prediction power of the PLS model was tested for drugs levels outside the ranges selected in the calibration set. For example, 12.0 mg/L (for PAR and PRO) and

16.0 mg/L (for CAF) were selected and these levels are out of the calibration range.

Preparation of the formulation before analysis

The drugs were safely extracted from SARIDON following a simple procedure. Pharmaceutical formulations were assayed by weighing the content of five tablets, grinding to a fine powder, and storing in a cold place. A great care was taken to ensure safe extraction of the three drugs from the complex extract of the formulation. Extraction by hot water was found useful, as will be shown later. An amount exactly corresponding to the average tablet weight was suspended in water or hot water (50 °C) and made up to a volume of 1000 ml. The final suspension was sonicated for 10 min and then filtered through a PTFE 0.45 μm membrane filter. Samples were scanned after proper dilution using a spectrophotometer over the spectral range 190-300 nm. The initial examination of the spectra indicated the existence of co-extracted components (mainly excipients) which needs application of multivariate calibration for more accurate quantification. Derivative spectroscopic methods were found of limited application for this complex system.

Table 1. Composition of calibration and validation sets

	Calibration set (mg/L)			Validation set (mg/L)		
Number	Paracetamol	Propyphenazone	Caffeine	Paracetamol	Propyphenazone	Caffeine
1	4.0 (-1)	6.0 (0)	2.0 (0)	12.0	6.0	2.0
2	6.0 (0)	6.0 (0)	2.0 (0)	10.0	12.0	2.0
3	8.0 (1)	6.0 (0)	2.0 (0)	10.0	6.0	8.0
4	4.0 (-1)	6.0 (0)	2.0 (0)	10.0	6.0	16.0
5	8.0 (1)	0 (-2)	0 (-2)	0	0	8.0
6	10.0 (2)	4.0 (-1)	0 (-2)	8.0	6.0	1.6
7	10.0 (2)	6.0 (0)	2.0 (0)	6.0	4.8	1.6
8	10.0 (2)	8.0 (1)	4.0 (1)	6.0	4.0	0.8
9	10.0 (2)	10.0 (2)	8.0 (2)	8.0	4.8	1.6
10	0 (-2)	8.0 (1)	0 (-2)	0	4.8	1.6
11	10.0 (2)	6.0 (0)	1.0 (-1)	8.0	4.8	0
12	10.0 (2)	6.0 (0)	2.0 (0)	8.0	0	1.6
13	10.0 (2)	6.0 (0)	4.0 (1)			
14	10.0 (2)	6.0 (0)	0 (-2)			
15	0 (-2)	6.0 (0)	2.0 (0)			
16	10.0 (2)	0 (-2)	2.0 (0)			
17	0 (-2)	0 (-2)	2.0 (0)			
18	10.0 (2)	6.0 (0)	1.0 (-1)			
19	10.0 (2)	6.0 (0)	2.0 (0)			
20	8.0 (-1)	0 (-2)	0 (-2)			
21	0 (-2)	8.0 (1)	0 (-2)			
22	0 (-2)	0 (-2)	8.0 (2)			

a. Five-level full factorial design according to orthogonal Brereton`s design [22]. Values in parentheses are the codes necessary for building orthogonal mixtures.

RESULTS AND DISCUSSION

Spectral overlapping

The UV absorption spectra of the three drugs along with the typical SARIDON extract are given in Fig 2.

As indicated in Fig 2, the drugs exhibited strong UV absorption over the studied range (190-300 nm). Both PAR and CAF showed their typical spectra with suitable wavelengths for detection at 244 and 274 nm, respectively. In fact, the absorption spectrum of PRO has irregular shape where the drug has stable absorption over the range 210-270 nm. The spectra of the drugs are highly overlapped over the studied range. Net analytical signal (NAS) is a suitable method to characterize the analytical figures of merit and spectral overlapping related to the multivariate calibration [23]. NAS analysis indicates that PAR, PRO and CAF would be detected down to 0.21, 0.37 and 0.15 mg/L^{-1} respectively. On the other hand, NAS calculations indicate a high degree of spectral overlap with other signals for PRO (80% spectral overlap). PAR and CAF showed lower spectral overlapping (71 and 55%). The absorption spectrum of the mixture indicated the additive nature of the individual signals of the drugs and the linearity of the current system. In fact, the experimental spectrum and the one estimated from the single-drug spectra were almost identical indicating the additive nature of the generated signals. The claimed values of the three drugs in the formulations indicated that PAR and PRO are more dominant than CAF (250 mg PAR, 150 mg PRO and 50 mg CAF per one tablet). This fact clearly reflected on the shape of the recorded spectrum (dilution factor 1:25) of drug extract where the final shape is very close to that of PAR. The similarity of the extract spectra with PAR would indicate that the extraction procedure was effective as the drugs were selectively obtained among other constituents like excipients.
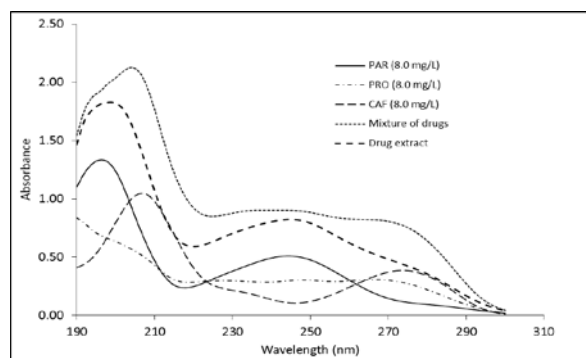
In fact, simultaneous determination of the ternary drug system is not possible by univariate calibration which is due to intense spectral overlapping. In our view, the main analytical problem in the current system is the intense spectral overlap where the influence of unexpected interference is also high, as indicated from the spectrum of the drug extract.

In this study, three matrices were created: calibration matrix (22×56), validation matrix (12×56) and matrix of drug extracts (18×56).

Selection of the optimum spectral ranges before PLS calibration

In fact, the performance of multivariate calibration would be improved if calibration is carried out over certain informative ranges instead of the entire spectrum. There are many procedures for selecting those informative regions prior to multivariate calibration, including statistical analysis related to the external validation [24], genetic algorithm [25], changeable size moving-window [26], and De Luca's procedure [8]. In the latter procedure, the absolute values of the calibration vector **b** (obtained by the PLS model) for the three solutes were numerically summed to find the cumulative coefficient B. Another important line called cutoff line is estimated. This line is necessary for the final selection of the spectral ranges of the studied drugs. The De Luca plot is given in Fig 3.

As indicated in the plot, the best spectral ranges which are included in the calibration are those located under the De Luca line and above the cutoff line. The best regions for analyzing drugs are: 202-220, 234-254, and 266-284 nm. In fact, the purpose of the cutoff line was to help the analyst to select or locate the informative spectral ranges [8].
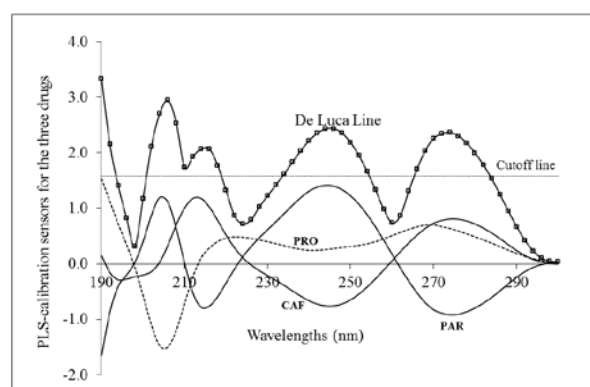

Fig. 2. Absorption spectra of the studied ternary drug system

Fig. 3. De Luca plot generated from PLS-calibration

Table 2. Prediction of drugs in the validation set before and after applying De Luca`s procedure for selecting the informative spectral regions.

	Spectral region (nm) 190-300 nm (56 points/spectrum)[a]			De Luca wavelength selection (31 points/spectrum)[a]		
	PAR	PRO	CAF	PAR	PRO	CAF
PLS-NIPALS variables	8	10	7	8	6	7
REP%[b]	5.9	14.3	12.2	4.9	7.9	6.7
RMSEP[b]	0.45	0.78	0.40	0.37	0.67	0.39
Mean Recovery[b]	98.5	90.7	96.1	99.0	90.8	96.4

a. Based on De Luca procedure, the optimum spectral regions for drugs are: 202-220, 234-254, and 266-284 nm (31 spectral points/sample).

b. Statistical analyses were applied to the non-zero concentration of the drugs. REP%: Relative error of prediction and RMSEP: root mean square error of prediction.

The regions that left over would account for the serious overlapping between drugs (220-230 nm, 258-266 nm, as shown in Fig 3). Although the first region (190-194 nm) would be included in the regression, it was excluded, as it is close to the extreme limit of the instrument. One more interesting point in the procedure is including the maximum wavelengths of absorption of drugs like 244 nm for PAR and 208/274 nm for CAF. It was interesting to notice that 196 nm (a significant wavelength for PAR) was excluded by the procedure. Now, the numerical analysis by PLS (NIPALS variant) was repeated to quantify the drugs in the validation set using selected regions. The main results are compiled in Table 2.

Application of De Luca method for selecting the informative spectral regions has improved PLS regression in certain aspects. For PRO, the number of PLS-variables was reduced from 10 to 6 which will reflect on the computation time. Moreover, the prediction power of the model was improved by applying De Luca procedure. Another important method that would be used for finding the optimum spectral ranges is the bootstrap method [16]. In this method, bootstrap sampling is used to estimate the standard errors in the PLS-calibration vectors $\mathbf{b}$ (for each drug) and from these errors an assessment of each explanatory variable on modeling $\mathbf{y}$ is carried out. Usually 1000 bootstrap samples are enough to estimate the standard error in $\mathbf{b}$. From bootstrap samples (taken from $\mathbf{X}$ and $\mathbf{y}$), the standard errors of b_j, $j = 1,…,A$ (σ_{bj}) are estimated and are used to calculate the standardized coefficients b_j/σ_{bj}. The standardized coefficient larger than 1.96 is considered important at 0.05 significant level meaning this variable is essential for modeling $\mathbf{y}$. The bootstrap procedure was repeated for each drug. Bootstrap analysis indicated that the best spectral regions for PAR are 212-220, 230-252, and 258-282 nm. For PRO: 190, 194-196, 206, 212-228, 232-242, 248-280 nm. For CAF: 190, 194-198, 204-206, 212-228, 244-272, and 282-290 nm.

For PAR, the results of De Luca were comparable to the bootstrap ranges. However, for the other two drugs, more spectral regions were obtained by bootstrap compared to De Luca. Accordingly, PLS-NIPALS calibration was repeated using the regions of bootstrap and the optimum PLS-variables were also estimated by the cross-validation technique. The overall results were comparable to those obtained by De Luca/PLS-NIPALS.

Comparison between PLS variants for drugs quantification

MVC1 and TOMCAT are the most commonly used software package in the pharmaceutical analysis [14,15]. MVC1 uses only NIPALS [14], but in TOMCAT, except for NIPALS, there are additional two variants of the SIMPLS algorithm: the WIM-PLS and SIM-PLS algorithms [15]. Nine PLS-algorithms are available for handling different kinds of data, but application of Kernel and Bidiagonalization is rather limited [11].

For the current drug system, the size of the $\mathbf{X}$ matrix is 22×56. From a practical point of view, the size of $\mathbf{X}$ is an adjustable parameter and is dependent on the system under investigation.

The current analytical system was subjected to different PLS-variants and the assessment strategy was based on two items: a) number of PLS-variants needed to build the model, and b) the prediction power of different PLS-variants. Model of lower PLS-variables with better prediction is the best choice. Other important criteria including computational time and memory-storage were not investigated [16].

For each drug, PLS-variables needed for calibration (A) were estimated by the leave-one-out method. The final PRESS-PLS-variable plots are shown in Fig 3a, 3b and 3c and the performance for drug prediction is summarized in Table 3.
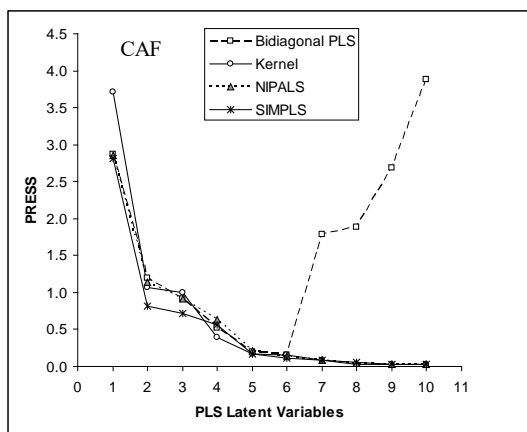
Fig 3 a). PRESS-Latent variables plots for different PLS-variants as obtained by cross-validation technique for CAF
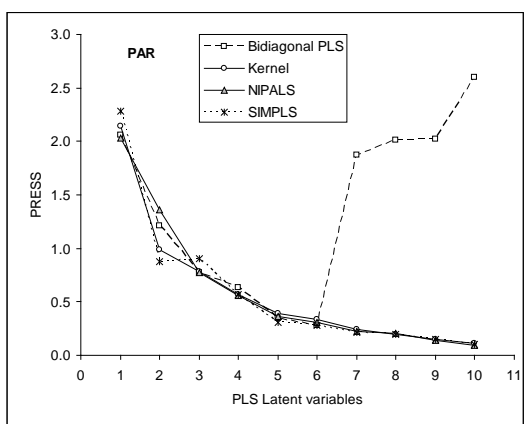

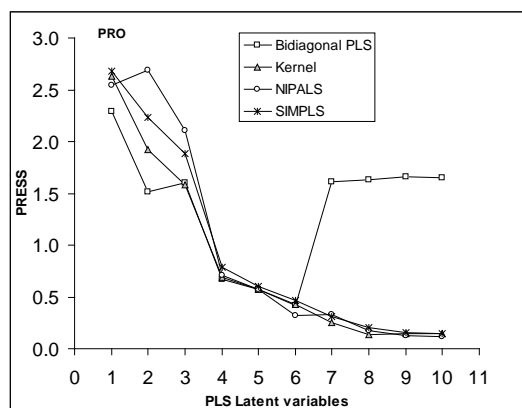**Fig 3 b).** PRESS-Latent variables plots for different PLS-variants as obtained by cross-validation technique for PAR

In fact, typical PRESS-Latent variable plots were obtained for all variants (except Bidiagonalization). In all cases, a large reduction in PRESS is observed with increasing variables. Generally speaking, from 6 to 10 variables are needed in all variants to explain the variances in the data. Except for PLS-Bidiagonal, the models exhibited a stable performance at high latent variables. The interesting point in Fig 3 is the abrupt jump in PLS-Bidiagonalization behavior

where PRESS is suddenly increased at 7 variables and this is true for the three drugs. The optimum number of factors needed for optimum prediction is shown in Table 3.

Fig 3 c). PRESS-Latent variables plots for different PLS-variants as obtained by cross-validation technique for PRO

The performance of PLS-variants was comparable for PAR prediction in the validation set with an overall recovery of 97.2-99.7 and excellent REP% 1.6-4.9. Although the NIPALS model used fewer variables (compared to SIMPLS and Kernel) for prediction, the model needs longer computation time, particularly for many variables-X matrices [16]. For all variants, poor prediction was observed for PRO and this is attributed to intense spectral overlap of this drug with other components. Due to its unstable performance and poor prediction for PRO (16.2%) and CAF(8.5%), PLS-Bidiagonalization (see Fig 3 c) was not appropriate algorithm. Kernel model, in fact, outperformed other variants for PAR, PRO and CAF prediction which is expected, as this algorithm is perfectly designed for the current analytical system. Compared to the other variants, PLS-kernel is known for its shorter computation time and less computer storage [18,19].

Table 3. Prediction of drugs in the validation set using several PLS-variants

PLS-variant[a]	A[b]	Mean recovery	REP%	RSD	A	Mean recovery	REP%	RSD	A	Mean recovery	REP%	RSD
		PAR				PRO				CAF		
NIPALS	8	99.0	4.9	3.4	6	90.8	7.9	2.9	7	96.4	6.7	4.0
SIMPLS	9	97.4	3.2	2.9	10	89.0	12.5	3.5	9	90.3	11.8	2.8
Kernel	9	97.2	3.3	2.8	8	95.5	5.4	2.5	9	96.4	5.5	2.7
Bidiagonal	6	99.7	1.6	1.1	6	82.0	16.2	6.5	6	109.8	13.7	8.5

a. See "Theoretical background" section for more details on the algorithms.
b. PLS-factors needed for optimum modeling was estimated using cross-validation technique [21].

Drugs quantification in SARIDON formulation and comparison with other methods

Although PLS-variants were workable for simultaneous analysis of PAR-CAF-PRO in their pure mixtures, the performance of the models was further tested for SARIDON® formulation. In real preparations, excipients are present along with the drug component which may negatively interfere with drugs quantification by PLS-regression. The extraction experiments indicated that distilled water is an efficient extractant for the three drugs. Accordingly, the consumption of expensive and toxic organic solvents is avoided. Moreover, hot water (50 °C) was also tested for drugs extraction. After extraction, the extracts were directly scanned by UV and the obtained spectra were analyzed by PLS calibration. As Kernel model was the optimum model for drugs prediction, the model was used for drugs quantification in real extracts. The overall results are summarized in Table 4.

The analytical performance of the Kernel-PLS method should be tested against a standard analytical procedure to asses the overall accuracy and precision. The levels of drugs in the marketed formulation were accurately measured by an independent chromatographic procedure and this was carried out by the manufacturer at earlier stages. The following main conclusions are drawn from Table 4: a) the proposed Kernel-PLS is workable for quantifying drugs with stable performance. No advanced cleaning procedures like solid phase or liquid-liquid extraction are applied in the current case and no chromatographic procedures are applied; b) extraction by hot water (50 °C) clearly ended up with better results and this is attributed to the enhanced solubility of drugs at higher temperature. Extraction at still higher temperatures is not recommended due to the unexpected influences on the chemical structure of drugs; c) the estimated recoveries ± RSD (96.4 (1.3), 95.1 (2.5) and 96.2 (3.0) for PAR, PRO and CAF, respectively) reflected the applicability of the Kernel-PLS method for drugs quantification. In fact, many analytical methods were proposed for PAR-PRO-CAF quantification in commercial pharmaceutical formulations. The reported methods extended from laborious matrix cleaning-liquid chromatography to non-separative ones including partial least squares PLS calibration.

For further assessment, the current method was compared with published methods as summarizes in Table 5.

Most of the reported methods are using either ethanol or methanol for drugs extraction, however, other aqueous solvents are also applicable. For chromatographic methods, the main steps of extract-cleaning were centrifugation and filtration. In general, all chromatographic procedures were found efficient for drugs quantification with acceptable accuracy and precision. The best detection of the ternary system was reported by Soponar and co-workers [3]. Using micellar electrokinetic capillary chromatography with DAD detection, the drugs were quantified in SARIDON® with very low detection limits of 42, 194, and 74 ng/ml for PAR, PRO and CAF, respectively [3].

Table 4. Quantification of active ingredients in marketed SARIDON® formulation by Kernel-PLS

Extraction [a]	PAR			PRO			CAF		
	Content (mg/tablet)	Rec %[b]	RSD [b]	Content (mg/tablet)	Rec %	RSD	Content (mg/tablet)	Rec %	RSD
water extraction (25 °C)									
S1	239.3			127.8			44.0		
S2	229.8	93.8	1.7	137.5	86.7	6.1	34.3	80.2	10.4
S3	233.8			120.0			42.0		
S4	235.2			135.0			40.0		
Hot water extraction (50 °C)									
S1	240.0			144.1			48.5		
S2	241.0	96.4	1.3	140.5	95.1	2.5	46.5	96.2	2.9
S3	237.5			139.0			48.5		
S4	245.0			146.8			49.3		

a. In all extractions, 5.0 g tablets of SARIDON® were grinded and a mass equivalent to one tablet was directly extracted with water. The extract was centrifuged and finally filtered through a 0.45 μm filter. Before spectral analysis, 1:25 dilution was carried out with distilled water. Four identical extractions were carried out (*n*=4).

b. The overall accuracy (mean recovery) and precision (RSD) were estimated against the actual or claimed values (250 mg PAR, 150 mg PRO and 50 mg CAF) provided by the manufacturer.

Table 5. Comparison of the analytical characteristics of Kernel-PLS with published methods for PAR-PRO-CAF quantification in commercial pharmaceutical formulations

Formulation (mg/tablet)	Extraction solvent	Matrix purification	Analytical technique	LOD (mg L^{-1})	Spike Rec. (%)	RSD (%)	Ref.
Chromatographic methods							
Not provided PAR 250 PRO 150 CAF 50	Methanol	Centrifugation	HPLC-DAD	Not provided	PAR 100.2 PRO 99.8 CAF 99.3	PAR 0.2 PRO 0.2 CAF 0.2	27
Not provided PAR 250 PRO 150 CAF 50	Methanol	Centrifugation	HPLC-DAD	Not provided	PAR 102.4 PRO 97.5 CAF 99.6	PAR 1.4 PRO 1.2 CAF 0.8	28
Not provided PAR 250 PRO 150 CAF 50	Distilled water	Centrifugation and membrane filtration	Micellar electrokinetic capillary chromatography-MECK-DAD	PAR 0.6 CAF 0.8 PRO 0.8	PAR 100.3 PRO 99.9 CAF 100.0	PAR 0.2 PRO 0.2 CAF 0.4	29
SARIDON® PAR 250 PRO 150 CAF 50	Methanol	Filtration by pore-size filter paper (no centrifugation)	HPLC-UV (other related drugs were also detected)	PAR 0.042 PRO 0.194 CAF 0.074	97.2-102.3	0.5-1.1	3
Pararemin® PAR 250 PRO 150 CAF 50	Methanol	Filtration by pore-size filter paper (no centrifugation)	HPLC-UV (other related drugs were also detected)	PAR 0.042 PRO 0.194 CAF 0.074	97.9-101.1	1.8-2.6	3
Minoset® PAR 250 PRO 150 CAF 50	Methanol	Filtration and dilution	HPLC-UV	PAR 0.30 PRO 0.25 CAF 0.36	PAR 100.0 PRO 100.0 CAF 100.0	PAR 0.4 PRO 0.6 CAF 1.8	5
Non-Chromatographic methods							
Minoset® PAR 250 PRO 150 CAF 50	0.1 M HCl	Filtration and dilution	Derivative UV-Spectrophotometry	PAR 0.29 PRO 0.35 CAF 0.10	PAR 99.8 PRO 100.1 CAF 99.0	PAR 0.3 PRO 0.5 CAF 1.6	5
Minoset plus® PAR 250 PRO 150 CAF 50	gastric juice solution	Shaking, and filtration by 0.20pm membrane filter	Multivariate calibration PLS-NIPALS	Not provided	PAR 100.0 PRO 99.9 CAF 101.6	PAR 0.7 PRO 1.2 CAF 2.7	7
NeoOptalidon® PAR 200 PRO 125 CAF 25	Ethanol	Sonication and filtration by 0.45pm membrane filter. Final extract diluted (1000 time) by distilled water	Multivariate calibration PLS-NIPALS (absorbance)	Not provided	PAR 105.1 PRO 105.5 CAF 126.9	PAR 3.75 PRO - CAF -	8
SARIDON® PAR 250 PRO 150 CAF 25	Ethanol	Sonication and filtration by 0.45pm membrane filter. Final extract diluted (1000 time) by distilled water	Multivariate calibration PLS-NIPALS (absorbance)	Not provided	PAR 103.1 PRO 106.6 CAF 129.5	PAR 3.75 PRO - CAF -	8
Veramon® PAR 200 PRO 285	Ethanol	Sonication and filtration by 0.45pm membrane filter. Final extract diluted (1000 time) by distilled water	Multivariate calibration PLS-NIPALS (absorbance)	Not provided	PAR 95.9 PRO 88.5	PAR 3.75 PRO -	8
SARIDON® PAR 250 PRO 150 CAF 50	Hot water (50 °C)	Shaking, centrifugation, and filtration by 0.45 pm membrane filter	Multivariate calibration PLS-Kernel (absorbance spectra)	PAR 0.21 PRO 0.37 CAF 0.15	PAR 96.4 PRO 95.1 CAF 96.2	PAR 1.3 PRO 2.5 CAF 2.9	This work

The drugs were quantified after separation by C$_{18}$ column with excellent recoveries 97.2-102.3 and precision 0.5-1.1 [3]. In general, the reported chromatographic methods manifested an excellent analytical performance for quantifying commercial tables containing PAR, PRO and CAF [5, 27-29].

As can be seen from table5, chromatographic procedures have shown a better precision compare to multivariate calibration methods. Interestingly and as depicted in this table , multivariate calibration methods do not apply any extra purification or preconcentration step and

419

manifested a comparable stable analytical performance to chromatographic methods. As indicated in Table 5, the proposed multivariate calibration has achieved better detection for drugs without using advanced instruments. Although derivative spectrophotometry was workable for analyzing PRO, CAF and PRO in commercial tablet (Minoset®), the overall precision seems to questionable [5]. As shown in Table 5, PLS-NIPALS is the most adopted algorithm for drugs quantification in commercial tables. Indeed, PLS-NIPALS was effective for analyzing the current ternary-drug system in different commercial formulations with optimum accuracy and precision. Dinç and co-workers showed that the results obtained by derivative spectrophotometry and liquid chromatography for PAR-CAF-PRO quantifications are statistically comparable [5]. De Luca and co-workers showed that application of PLS NIPALS on absorbance spectra gave good recovery only for PAR, but for PRO and CAF satisfactory quantifications were obtained using third derivative spectra [8]. Our results demonstrate that recovery can be improved especially for CAF using only absorbance spectra and Kernel-PLS algorithm. Besides the reported detection limits, accuracy, and precision of Kernel-PLS method is of comparable quality to laborious and time-consuming chromatographic methods. Another advantage of the proposed method is that no extensive matrix-cleaning procedures are adopted.

CONCLUSIONS

The following main conclusions are deduced from the current pharmaceutical-chemometric study:

• Modeling many variables-X matrices is less time-consuming and very safe using Kernel-PLS method.

• Selection of informative spectral regions by De Luca`s method has improved the overall regression which was also in agreement with bootstrap method.

• Extraction of the ternary drug mixture by hot water instead of using ethanol or other toxic organic solvents is a good practice.

• The reported recoveries±RSD [96.4 (1.3), 95.1 (2.5) and 96.2 (3.0) for PAR, PRO and CAF, respectively] proved the applicability of Kernel-PLS method for drugs quantification in commercial SARIDON®.

The proposed multivariate calibration procedure is applicable for other formulations and, in the same time indicated the adequacy of Kernel-PLS for pharmaceutical analysis.

420

REFERENCES

1. M.R. Khoshayand, H. Abdollahi, M. Shariatpanahi, A. Saadatfard, A. Mohammadi, *Spectrochim. Acta A,* **70**, 491 (2008).
2. H.G. Kraetsch, T. Hummel, J. Lötsch, R. Kussat, G. Kobal, *Eur. J. Clin. Pharmacol.,* **49,** 377 (1996).
3. F. Soponar, D. Staniloae, G. Moise, B. Szaniszlo, V. David, *Rev. Roum. Chim.*, **58**, 433 (2013).
4. J.R. Migliardi, J.J. Armellino, M. Friedman, D.B. Gillings, W. T. Beaver, *Clin. Pharmacol. Ther.*, **56**, 576 (1994).
5. E. Dinç, G. Kökdil, F. Onur, *J. Pharm. Biomed. Anal.*, **26**, 769 (2001).
6. Y.S. Al-Degs, A.H. El-Sheikh, A.A. Issa, M. Al-Ghouti, M. Sunjuk, *Water Sci. Technol.*, **66**, 1647 (2012).
7. E. Dinc, C. Serin, F. Tugcu-Demiroz, T. Doganay, *Int. J. Pharm.*, **250**, 339 (2003)
8. M. De Luca, F. Oliverio, G. Ioele, G. Ragno, *Chemometr. Intel. Lab.*, **96**, 14 (2009).
9. P. C. Damiani, G. M. Escandar, A. C. Olivieri, H. C. Goicoechea, *Current Pharm. Anal.*, **1**, 145 (2005).
10. J.A. Martins, R.F. Teófilo, M.M. Ferreira, *J. Chemom.*, **24**, 320 (2010).
11. M. Andersson, *J. Chemom.*, **23**, 518 (2009).
12. H.W. Darwish, I.A. Naguib, *Drug Test. Anal.,* **5**, 325 (2013)
13. H.W. Darwish, S. A. Hassan, M.Y. Salem, B. A. El-Zeany, *Spectrochim. Acta A*, **122**, 744, (2014)
14. A.C. Olivieri, H.C. Goicoechea, F.A. Iñón, *Chemom. Intell. Lab. Syst.*, **73**, 189 (2004).
15. M. Daszykowski, S. Serneels, K. Kaczmarek, P. Van Espen, C. Croux, B. Walczak, *Chemom. Intell. Lab. Syst.*, **85**, 269 (2007).
16. A. Alin, *Stat. Papers*, **50**, 711 (2009).
17. S. de Jong, *Chemom. Intell. Lab. Syst.*, **18**, 251 (1993).
18. S. Rännar, F. Lindgren, P. Geladi, S. Wold, *J. Chemom.*, **8**, 111 (1994).
19. S. Rännar, P. Geladi, F. Lindgren, S. Wold, *J. Chemom.*, **9**, 459 (1995).
20. B.Dayal, J.MacGregor. *J. Chemom.,***11**, 7 (31997).
21. D.M. Haaland, E.V. Thomas, *Anal. Chem.*, **60**, 1193 (1988).
22. R. Brereton, *Analyst,* **122**, 1521 (1997).
23. S. Yousefinejad, B. Hemmateenejad, *Drug Test. Anal.,* **4,** 507 (2012).
24. M.S. Linares, J.M.G. Fraga, A.I. Jimenez, F. Jimenez, J.J. Arias, *Anal. Lett.*, **32**, 2489 (1999).
25. J. Ghasemi, A. Niazi, R. Leardi, *Talanta*, **59**, 311 (2003).
26. Y.P. Du, Y.Z. Liang, J.H. Jiang, R.J. Berry, Y. Ozaki, *Anal. Chim. Acta*, **501**, 183 (2004).
27. M.G. Mamolo, L. Vio, V. Maurich, *J. Pharm. Biomed. Anal.*, **3**, 157 (1985)
28. A.M. Di Pietra, R. Gatti, V. Andrisano, V. Cavrini, *J. Chromatogr. A*, **729**, 355 (1996).
29. D. Emre, N. Özaltýn, *J. Chromatogr. B*, **847**, 126 (2007).

ОЦЕНКА НА РАЗЛИЧНИ PLS АЛГОРИТМИ ЗА КОЛИЧЕСТВЕНО ОПРЕДЕЛЯНЕ НА ТРИ СПЕКТРАЛНО ПРИПОКРИВАЩИ СЕ ЛЕКАРСТВА

Г. Гергов[1] *, А. Алин[2], М. Дойчинова[3], М. Де Лука [4], В. Симеонов[5] , Я. Ал-Дегс[6]

[1]*Катедра „Химия“, Фармацевтичен факултет, Медицински университет София, 1000, ул. „Дунав“2, София, България.*

[2]*Катедра „Статистика“, Университет „Девети септември“, Измир, Турция*

[3]*Институт по инженерна химия, Българска Академия на Науките, ул. „Акад. Г. Бончев“, бл. 103, София, България*

[4]*Катедра „Фармация , Здравни науки и хранене“, Калабрийски университет, 87036 Ренде, Италия*

[5]*Лаборатория „Хемометрия и екометрия“, Факултет по химия и фармация, Софийски университет "Св. Климент Охридски", 1164 София, бул. Дж. Баучър 1, София, България.*

[6]*Катедра „Химия“, Хашемитски университет, П.К. 150459, Ез-Зарка 13115, Йордания*

(Резюме)

Основната цел на настоящото изследване е да се сравни прогнозната мощ на различни PLS алгоритми, прилагани за количествено определяне на три спектрално припокриващи се лекарства. Бяха избрани четири варианта на PLS за многовариационно калибриране и предсказване на трите компонента на лекарствената форма (парацетамол, пропифеназон и кофеин). Алгоритмите NIPALS и SIMPLIS са най-често срещаните и използвани алгоритми. Другите тествани алгоритми са Kernel и Bidiagonalization, които се прилагат сравнително рядко във фармацевтичния анализ.

Данните от първи ранг бяха генерирани чрез измерване на UV-спектрите на лекарствените смеси в диапазона 190-300 nm с разделителна способност от 2,0 nm (т.е. 56 спектрални точки / проба). Използван бе редуциран пълен факториален дизайн на пет нива и прогнозната мощност на PLS вариантите беше тествана за концентрационни нива на лекарствата извън диапазоните, избрани в калибрационната матрица.

Методът на Де Лука и потвърждаващия буутстрап метод бяха избрани като удачни за оптимална селекция на спектралните региони.

Външното валидиране използвайки калибрационния модел PLS-Kernel показа значителни предимства при анализа на таблетки SARIDON. Трите лекарства в SARIDON бяха количествено определени с аналитичен добив и прецизност 96.4 (1.3), 95.1 (2.5) and 96.2 (2.9) съответно за парацетамол, пропифеназон и кофеин. Това се оказва оптималния алгоритъм, който може успешно да се приложи за рутинен анализ на аналгетични и антипиретични многокомпонентни таблетки във фармацевтичната индустрия.

Gelatinization of industrial starches studied by DSC and TG

A. Rangelov[1], L. Arnaudov[2], S. Stoyanov[2,3,4], T. Spassov[1]*

[1] University of Sofia "St. Kl. Ohridski", Faculty of Chemistry and Pharmacy, Sofia, Bulgaria
[2] Unilever Research and Development, 3133AT Vlaardingen, The Netherlands
[3] Physical Chemistry and Soft Matter, Wageningen University, 6703 HB Wageningen, The Netherlands
[4] Department of Mechanical Engineering, University College London, WC1E 7JE, UK

The microstructure and thermal behaviour of industrial starches with different origin were characterized by X-ray diffraction and thermal analyses (DSC, TG). Some of the studied starches revealed crystalline structure (type A and type B), while others were predominantly amorphous, having only about 15 % crystallinity. The moisture content of the pristine starches correlated with their microstructure: starches with a higher amount of amorphous phase showed larger water content. The thermal behaviour of the starches with different amount of additional water was also studied by DSC. In a starch-water paste at higher water content the gelatinization started earlier and gelatinization enthalpy change was greater, than what was observed at lower water content. At certain starch to water ratio two distinguished endothermic peaks denoted the gelatinization and melting processes. The determined enthalpies of gelatinization were in the range of 5-15 J/g and did not correlate with the initial crystallinity of the starches. The activation energies of gelatinization in the range 40-100 kJ/mol, obtained by the Kissinger method, were found not to depend on the initial crystallinity of the starch either. At starch concentrations of 20-35% after the gelatinization endothermic peaks a clear exothermic effect could also be observed, which could be described by the formation of internal hydrogen-bonded associations.

Keywords: gelatinization, heat-moisture treatment, starches

INTRODUCTION

Starch is a natural biopolymer, produced and stored in plants as partially crystalline granules, consisting mainly of two components: predominantly linear amylose and highly branched amylopectin [1]. It is commonly used in food, chemical, textile, papermaking, medicine and many other industries [2]. Depending on the botanical source starch granules may vary in size (from <1 to 100μm), shape (including spherical, lenticular, oval, elongated) with alternating semi-crystalline and amorphous layers (growth rings) [3, 4]. Granules may also have different type of crystallites and crystal fraction [5]. The crystallinity of the granules is often assigned to the double helix formed by the branches of amylopectin [6]. Wide-angle X-ray diffraction can be used to determine if starches have A-, B-, or C-type crystallinity, as well as the contribution of the amorphous and the crystalline regions to the overall X-ray pattern. In general, cereal starches generate A-type X-ray diffraction patterns; tuber and high amylose starches are of the B-type; and legume, root and some fruit and stem starches, are of C-type, which is a combination of A- and B-type polymorphs [7,8]. The hilum, which is the core of the granule and the starting point from which the granule grows, is usually less organized than the rest of the granule and could be situated either near the middle or towards one end of granules [9].

Starch granules are insoluble in cold water. During heat treatment of starch in presence of sufficient amount of water, starch gelatinization occurs, where amylose is leached into the outside solution, while bulk water penetrates into the granules, which leads to swelling, destabilization of the crystalline structure, resulting in granule fragmentation and a loss of birefringence. The kinetics of this process depends on the temperature and on the ratio crystalline to amorphous regions, since the latter tend to absorb water more easily. It is believed that there is a certain amount of bound water in the native starch granule, specific to different starches, which is crucial for their gelatinization behaviour and which depends on the ratio of crystalline vs. amorphous regions.

Since starch is the major source of energy in human nutrition, providing more than 50% of the caloric value, and the properties of starch foods strongly depend on the processing, obtaining a better understanding of gelatinization is essential not only from a scientific, but also from an industrial point of view, as well. Many methods have been suggested for investigating the gelatinization process of starches, including electron microscopy, optical microscopy, X-ray diffraction, differential scanning calorimetry, viscosity measurement and more. Stevens and Elton (1971) first reported the

---

* To whom all correspondence should be sent:
E-mail: nhtts@chem.uni-sofia.bg

application of DSC for measuring the heat of gelatinization of the starch/water system [10]. Two distinct endotherms can be observed during heating of starch in a low- water content system. Donovan (1979) reported that these endotherms were determined by the degree of hydration of ordered regions within the starch granules and the high-temperature transition disappears in presence of excess water [11]. In most starches these order-disorder transitions may follow two different mechanisms of melting and gelatinization. Melting usually takes place at low water contents (less than 30%) and corresponds to the high temperature endotherm, while gelatinization occurs in the presence of excess water (more than 70% for most starches) and corresponds to the low temperature endotherm on the thermogram [12]. Both processes can be observed if heating is done at an intermediate moisture content [13]. Evans and Heisman (1982) proposed the so-called "Cooperative melting theory" which explained the bi-phasic endotherm as a result of different crystallite stability within the granules [12]. Water absorption by the granules lowers the melting points of crystallites resulting in quick melting. This reduces the constraints of still remaining crystallites to lower their melting points. This process of cooperative melting happens quickly in sufficient amount of water and leads to a single DSC endotherm. When the available water is not sufficient for the cooperative melting to occur a distinct second endotherm or a "shoulder" appears on the thermogram representing melting of remaining crystallites at a higher temperature. Biliaderis et al. suggested that gelatinization process involves partial melting, recrystallization, and final melting of the crystallites, while Fukuoka et al. reported that enthalpic transitions during heat-moisture treatment represent a number of different simultaneously occurring processes [14,15]. Some authors reported that in the presence of more than 70% water in the system only one endothermic peak was visible in the DSC curve, while at 50% water content, two distinct peaks were observed [16].

Although many starch gelatinization theories have been suggested, none of them is able to thoroughly explain the mechanism of structural changes that granules undergo during heating in the presence of water, therefore further research is needed [17]. It is commonly accepted that depending on the starch nature and the conditions of the thermal experiments (amount of water, heating rate, quality of the DSC baseline, accounting of specific heat, C_p, variation) serious differences in the thermal behaviour of the examined starch can be observed. Additionally, due to the different rate of the phase transformations occurring during gelatinization, routine DSC does not always give an adequate explanation of these processes. Therefore, the present work aims at studying the gelatinization process in a series of starches of industrial interest from different sources and different pre-treatments at various experimental conditions (amount of additional water, heating rate), combining carefully performed thermal (DSC,TG) and X-ray diffraction (XRD) analyses.

MATERIALS AND METHODS

Materials

Modified starches with different origin were the objects of the present study. Information about their origin and modification treatment is presented in table 1.

Thermflo was obtained from Ingredion (UK), Merigel 100 and Merigel 340 starches were provided by Tate & Lyle (UK). Eliane 100 and Eliane SC 160 starches were supplied by AVEBE (Netherlands).

Optical and Scanning Electron Microscopy (SEM)

The morphology of the starches was characterized by optical and scanning electron microscopy (SEM-JEOL 5510). For the electron microscopy starch granules were dispersed on a holder, coated with a thin golden layer, and used for observation.

Table 1. List of the starches used in the study, their origin and modification.

Trade name	Origin and modification
Thermflo	Maize starch, with high amylopectin content (> 95%)
Merigel 100	Maize, pre-gelatinized
Merigel 340	Maize, pre-gelatinized, with high amylopectin content (>95%)
Eliane 100	Native waxy potato starch
Eliane SC 160	Waxy potato starch, pre-gelatinized, acetylated

X-Ray Diffractometry (XRD)

The structure and microstructure of the dry starch powder samples were studied by X-ray diffraction (XRD) with Cu-Ka radiation. The time per step was 5 sec, the step was 0.03°, operating voltage of 30kV and current of 15mA.

Differential Scanning Calorimetry (DSC) and Thermogravimetric Analysis (TGA)

DSC (Perkin Elmer DSC7) and DTA/TG (Perkin Elmer Pyris) were used to study the thermal behavior of the dry starches as well as of the starch-water suspensions (pastes) varying the starch concentration. The DSC experiments with the starch-water pastes were carried out in sealed sample pans at a scanning rate of 10 K/min. All samples were scanned one hour after sealing, in order to equilibrate. For the enthalpies of starch gelatinization the arithmetic average of 3 independent measurements was taken.

Kissinger analysis

DSC curves, used for Kissinger analysis were obtained by preparing three samples for each starch and scanning them with three different heating rates. Samples were prepared by placing the same amount of starch and water in sealed sample pans, so that 10% w/w was obtained. All the samples were given one hour to equilibrate before scanning. The used scanning rates (2.5 K/min, 5K/min, and 10K/min) were selected so as to ensure actual heating rates of the samples.

RESULTS AND DISCUSSION

The morphology and the microstructure of starches with different origin were characterized by electron microscopy (fig.1) and X-ray diffraction (fig.2). Typical morphology of starch granules with an irregular shape is presented in fig.1. The granule size did not differ very much for the different starches, as it ranged from about 10 to 50 μm. The granule surface was rough; pores and holes could also be observed at higher magnification. Formation of granule agglomerations was seen, as well. One of the studied starches (Thermflo) showed A-type crystalline structure with characteristic diffraction peaks at 15°, 17°, 18° and 23°, while Eliane 100 revealed diffraction peaks typical for crystal structure type B (intensive peak at 17° and less

intensive ones at 15°, 20°, 22° and 24°). Merigel 100, Merigel 340 and Eliane SC160 could be considered as mainly amorphous, which was expected because these three starches had been pre-gelatinized, fig.2. The degree of starch crystallinity, determined from the X-ray diffraction patterns, according to the method described in [18], ranged from about 15% to 75%, Table 2.
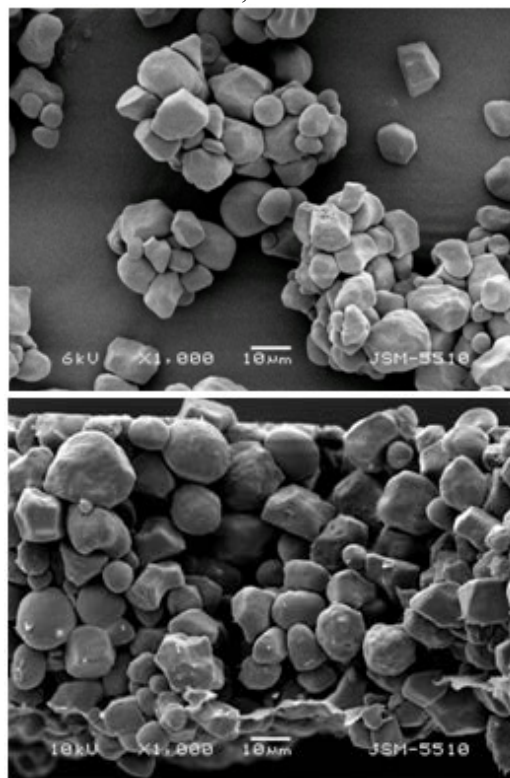
Fig. 1. SEM micrographs of Thermflo starch.
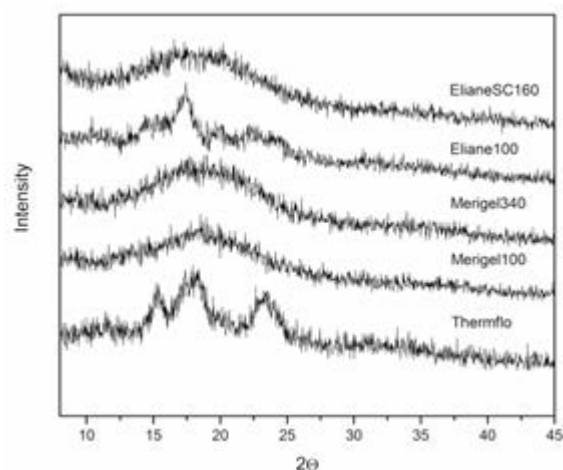
Fig. 2. XRD patterns of the untreated starch powders.

Table 2. Moisture content, relative crystallinity and heat effect, measured for the used starches.

Starch	Moisture content (%)	Relative crystallinity (%)	Heat effect (J/g)
Thermflo	11.4	74	88.5
Merigel 100	8.6	34	62.5
Merigel 340	7.2	23	51.9
Eliane 100	13.8	58	151.7
Eliane SC160	6.8	17	55.2

The native moisture content and the thermal behaviour of the initial starches were studied by TG and DSC, fig.3 and fig. 4, respectively. The thermogravimetric curves of all starches had identical shape, but differed in the height of the first step (weight decrease), fig.3. Water is the only volatile component of the dry starches (containing only native moisture) and during heating it is released in the temperature range of 60-120°C; at higher temperatures (250-300°C) starches undergo thermal degradation and lose between 60% and 80% of their weight for only few degrees.
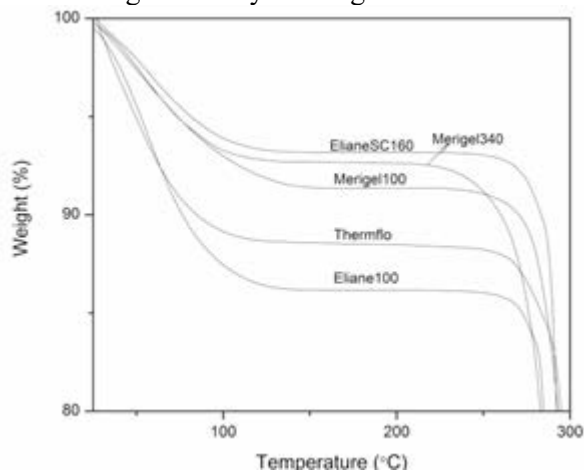
Fig. 3. TG curves of the untreated starches (containing only the native moisture).
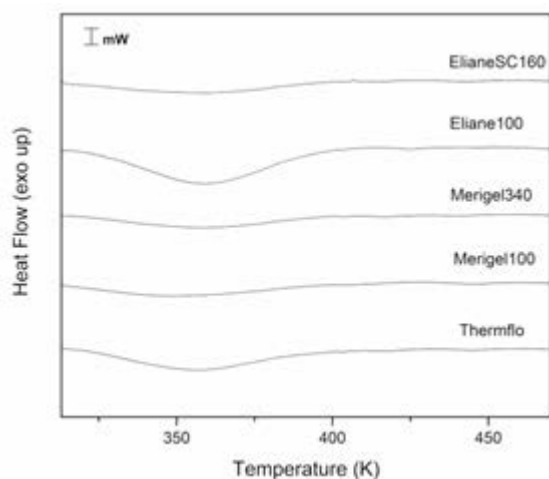
Fig. 4. DSC curves of the untreated starches (containing only the native moisture).

The observed differences in the moisture content and in the thermal stability of the studied starches were also expected due to their different origin, crystal type, relative crystallinity and different starch modification. The starches moisture content varied between 7 and 14 wt.% and for the non-pregelatinized starches showed obvious correlation with the degree of crystallinity. The starches with lower crystallinity had larger amount of included moisture, which confirmed available results for other starches [19,20].

The DSC results corresponded entirely to the TG analysis and correlated with those of the XRD. The single endothermic peaks observed by DSC in the temperature range 30-130°C (fig.4) had to be obviously related to the release of moisture from the starches, which process was also detected by the themogravimetric analysis. The temperatures and enthalpies (heat effects) of the DSC peaks, connected with the moisture release, are also presented in Table 3.

It is possible the larger heat absorbed (endothermic heat effect) observed for starches with larger crystallinity to be due not only to the water release, but also to the melting of parts of the crystalline starch granule regions. However, typical crystallite melting endotherms were not seen in the DSC curves of the dry samples, which confirmed that the presence, quantity, and type of plastisizer play significant role in the process of gelatinization [21, 22]. It is necessary to be mentioned that good quality DSC curves of dry starch samples (containing only native moisture) are not frequently seen in the literature.

Studying the starches gelatinization when using the same amount of additional water (10 wt.% starch in water suspension; heating rate 10 K/min) revealed identical DSC curves for all samples – a broad endothermic peak was observed. However, the starches thermal scans differed in the peak area, as well as in the temperature range of the gelatinization peak. DSC curves of two of the investigated starches having different structure are presented in fig.5.

Table 3. Enthalpy change and activation energy of the gelatinization process for all studied starches.

Starch	T$_{max}$ [K]	Activation energy [kJ/mol]	Gelatinization enthalpy [J/g]
Thermflo	336	62.4±16.1	5.67
Merigel100	339	105.6±23.3	36.65
Merigel340	336	74.5±4.7	4.52
Eliane100	341	58.2±4.2	12.36
ElianeSC160	341	49.1±10.6	13.05
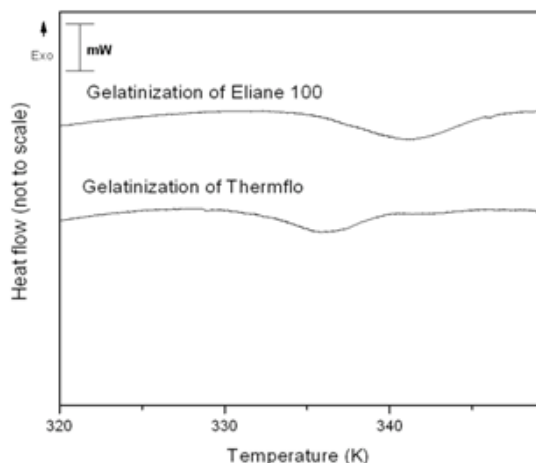
Fig. 5. DSC curves of Thermflo and Eliane 100.

a

b

Fig. 6. a) DSC data in Kissinger coordinates for the two crystalline starches given in the legend; b) DSC data in Kissinger coordinates for the three pre-gelatinized amorphous starches.

Both, the thermal effects (enthalpy change) and the activation energy of the gelatinization process were determined, Table 3, for all studied starches. For the apparent activation energy of gelatinization, E_a, Kissinger's analysis was applied [23]:

$$ln\frac{q}{T_{max}^2} = -\frac{E_a}{RT_{max}} + const. , \qquad (1)$$

where q is the heating rate, T_{max} is the temperature of the maximum of the endothermic DSC peak and E_a is the activation energy of the thermally activated process (in this case gelatinization). According to the Kissinger's method, the activation energy can be obtained by plotting $ln(q/T_{max}^2)$ vs. $1000/T_{max}$. Fig.6a shows the DSC data in Kissinger coordinates for the two crystalline starches and in fig.6b the data for the pre-gelatinized amorphous starches are presented. The values for the activation energies ranged from about 40 to 105 kJ/mol, and the highest value applied for Merigel100, which is also the starch with the highest gelatinization enthalpy. Both the activation energies and heat effects of gelatinization were close to those available in the literature for similar systems [24-28]. Furthermore, two different methods for obtaining activation energies (thermal and rheological) seem to produce consistent results, indicating, that both are suitable for investigating the gelatinization process [29].

To understand the influence of the gelatinization on the structure of the starch granules XRD analysis was applied to a sample obtained after gelatinization of Thermflo. The X-ray diffractograms of the initial starch and of the corresponding gel are shown in fig.7. Drastic reduction in the intensity of the crystalline peaks could clearly be seen, revealing that the gelatinization took place in a large degree, and resulted in an amorphous granule structure according to the XRD data.
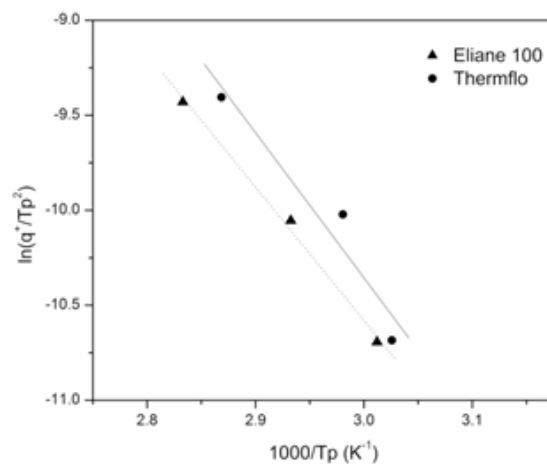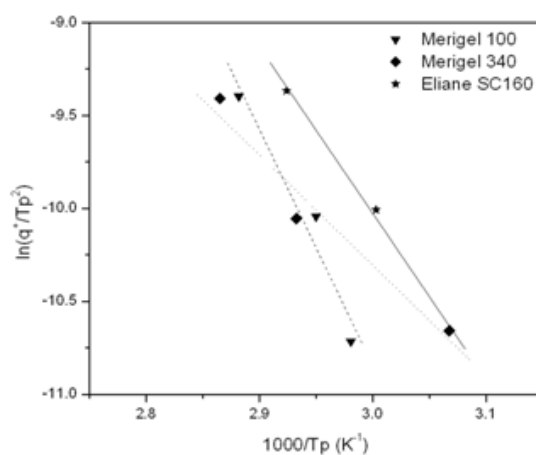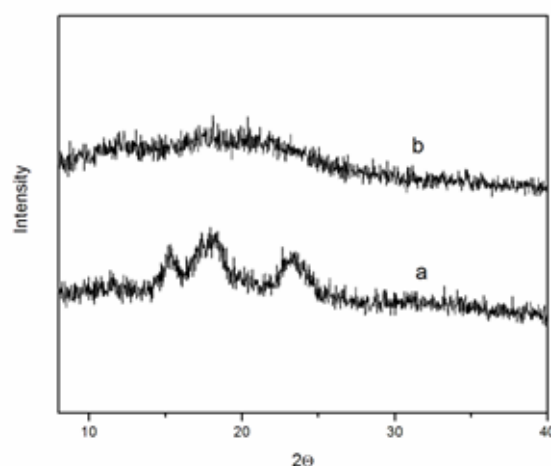
Fig. 7. XRD patterns of the untreated Thermflo, a, and of the corresponding gel, b.

It is known, however, that except gelatinization a process of melting is also possible in starch-water suspensions with insufficient amount of water.

Moreover, although carefully studied, these processes still need further understanding due to the great diversity of the results available in the literature, as well as to the big importance of the gelatinization for the cooking properties of the starches with different origin. To separate both processes (gelatinization and melting) a series of DSC measurements on a starch-water system (paste) at different concentrations were performed. DSC plots of gelatinization of Thermflo with different concentrations are shown in fig.8, as the weight percentage of the starch was varied between 5% and 90%. At large amount of water (5% starch) the gelatinization process started at lower temperatures, and a big complex endothermic peak was observed, which might be due to the fact that the peaks of gelatinization and melting were strongly overlapped. With the increase of the starch concentration the endothermic peaks became more separated and the two processes (gelatinization and melting) became distinguishable. Besides, the peaks were shifted to lower temperatures. At concentrations 20-30% two clearly separated peaks were observed, as the low temperature one corresponded to starch gelatinization and the high-temperature peak – to the melting of the non-gelatinized crystalline parts of the starch granule. Although both processes are extremely sensitive to the amount of additional water, the heat (enthalpy change) determined from the low-temperature DSC peak showed a very good correspondence to the heat effects of gelatinization determined in excess water.

This result is inconsistent with the available report in the literature [16], revealing that in the presence of more than 70% water in the system only one endothermic peak was visible in the DSC curve, while at 50% water content, two distinct peaks were observed.

Exactly in the same range of 20-35% starch concentration after the endothermic DSC peaks a clear exothermic effect (peak) could also be seen, which could be described by possible formation of hydrogen-bond associations between the free ends of the unwound helixes of amylopectin and parts of amylopectin molecules other than their original helix partner [30]. Another possible explanation of the exothermic DSC effect is based on the association of the amylose molecules extracted from the granule into the surrounding water or formation of amylose-lipid complexes [31].

As it could be expected, at insufficient amount of water in the system not all of the starch granules and crystalline parts participated in the gelatinization process and the heat effect gradually decreased with

a

b

c
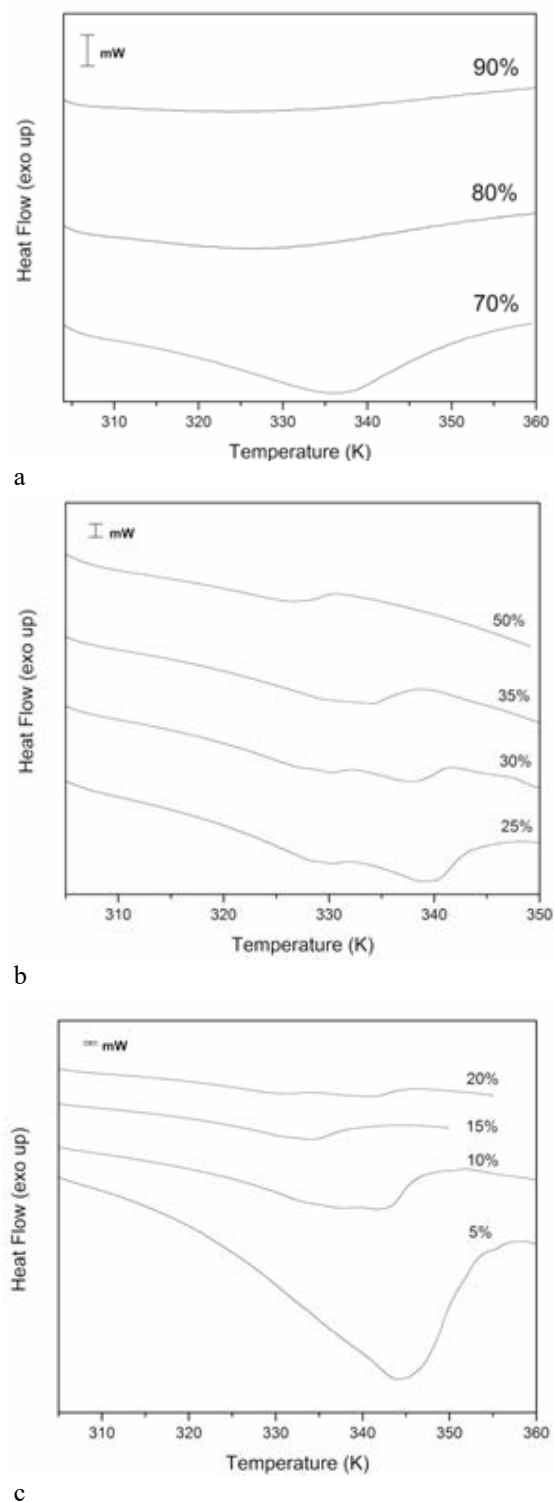
Fig. 8. DSC curves of gelatinization of Thermflo at different concentrations.

the starch concentration increase. At the same time the intensity of the high-temperature peak increased, which corresponded to the melting of larger amount of ordered starch zones. At further increase of the starch concentration the two endothermic peaks gradually transformed to a single peak. At these concentrations the water in the system was not enough for the gelatinization to take place.

427

This result shows that by precise control of these processes (gelatinization and melting) it is possible to obtain starch gelatinization preserving some of the ordered granules zones, which may result in materials and food products with interesting mechanical and digestive properties.

CONCLUSIONS

The microstructure and thermal behaviour of starches with different origin were investigated. It was found that the starches structure ranges from predominantly crystalline (type A or type B) to almost amorphous (15% crystallinity) and their moisture content correlated with their microstructure. The starches revealed different thermal behaviour when varying the amount of water added to the starch before the DSC experiments, which is consistent with the results of similar experiments available [33]. At larger water content the gelatinization started at lower temperatures and the gelatinization enthalpy change was larger as observed by other authors as well [34]. At starch concentrations in the range 20-30% two distinguished endothermic DSC peaks denoted the gelatinization and the melting processes [35]. A clear exothermic thermal peak was also seen, which could be explained by the formation of internal hydrogen bonds. Both the enthalpies and the activation energy of gelatinization were determined and it was found that they did not depend on the initial crystallinity of the starches.

Our results indicate that by adjusting the ratio of water vs. starch and gelatinisation temperature one can control granule melting and gelatinisation independently, allowing to obtain gelatinized starches where parts of the ordered granule zones are preserved, which in turn can result in materials and food products with interesting mechanical and digestive properties.

REFERENCES
1. D.J. Gallant, B. Bouchet, P.M. Baldwin, *Carbohyd. Polym.* **32**, 177 (1997).
2. R. Hoover, T. Hughes, H.J. Chung, Q. Liu, *Food Res. Int.* **43**, 399 (2010).
3. J.L. Jane, J. In BeMiller, R. Whistler (Eds.). Structural features of starch granules II. Starch: Chemistry and technology, 3rd ed., Academic Press, Amsterdam, 2009, p. 193.
4. J.L. Jane, T. Kasemsuwan, S. Leas, H. Zobel, J.F. Robyt, *StarchStärke*, **46**, 121 (1994).
5. M.G. Sajilata, R.S. Singhal, P.R. Kulkarni, *Compr. Rev. Food Sci. F.*, **5**, 1 (2006).
6. R. Hoover, *Carbohyd. Polym.* **45,** 253 (2001).
7. R.F. Tester, J. Karkalas, X. Qi, Starch, *J. Cereal Sci.,* **39,** 151 (2004).
8. A. Sarko, H.-CH. Wu, *Starch/Stärke*, **30,** 73 (1978).
9. A. Gott, H. Barton, D. Samuel, R. Torrence, in: Biology of starch. Ancient starch research, R. Torrence, H. Barton (eds.), Left Coast Press, Walnut Creek, CA, 2006, p. 35.
10. D.J. Stevens, G.A.H. Elton, *Starch/Stärke*, **23**, 8 (1971).
11. J.W. Donovan, *Biopolymers,* **18**, 263 (1979).
12. I.D. Evans, D.R. Haisman, *Starch/ Stärke,* **34**, 224 (1982).
13. A.-C. Eliasson, *Starch/Stärke*, **32**, 270 (1980).
14. C.G. Biliaderis, C.M. Page, T.J. Maurice, B.O. Juliano, *J. Agr. Food Chem.*, **34**, 6 (1986).
15. M. Fukuoka, K. Ohta, H. Watanabe, *J. Food Eng.*, **53**, 39 (2002).
16. F. Nakazawa, S. Noguchi, J. Takahashi, *Agr. Biol. Chem. Tokyo,* **48**, 2647 (1984).
17. W.S. Ratnayake, D.S. Jackson, Advances in Food and Nutrition Research, Chapter 5 Starch Gelatinization, Elsevier, 2008.
18. A. Lopez-Rubio, B.M. Flanagan, E.P. Gilbert, M.J. Gidley, *Biopolymers,* **89**, 761 (2008).
19. M. Schirmer, A. Höchstötter, M. Jekle, E. Arendt, T. Becker, *Food Hydrocolloid.*, **32**, 52 (2013).
20. H. Liu, L. Yu, F. Xie, L. Chen, *Carbohyd. Polym.*, **65**, 357 (2006).
21. H. Jacobs, J.A. Delcour, *J. Agr. Food Chem.*, **46**, 2895 (1998).
22. T.A. Waigh, K.L. Kato, A.M. Donald, M.J. Gildey, C.J. Clarke, C. Riekel, *Starch/Starke,* **52**, 450 (2000).
23. H.E. Kissinger, *Anal. Chem.* **29**, 1702 (1957).
24. W.S. Ratnayake, D.S. Jackson, *Carbohyd. Polym.* **67**, 511 (2007).
25. R.B. Campanha, C.M.L. Franco, *J. Therm. Ana.l Calorim.*, **106**, 799 (2011).
26. H. Liu, L. Yu, G. Simon, K. Dean, L. Chen, *Carbohyd. Polym.*, **77**, 662 (2009).
27. W. Jiranuntakul, C. Puttanlek, V. Rungsardthong, S. Puncha-arnon, D. Uttapap, *J. Food Eng.*, **104**, 246 (2011).
28. S.S. Sablani, S. Kasapis, Z.H. Al-Tarqe, I. Al-Marhubi, M. Al-Khuseibi, T. Al-Khabori, *J. Food Eng.*, **82**, 443 (2007).
29. F. Teyssandiera, P. Cassagnaua, J.F. Gérardb, N. Mignardc, *Carbohyd. Polym.* **83**, 400 (2011).
30. T.A. Waigh, M.J. Gidley, B.U. Komanshek, A.M. Donald, *Carbohyd. Res.,* **328**, 165 (2000).
31. P. Le Bail, H. Bizot, M. Ollivon, G. Keller, C. Bourgaux, A. Buléon, *Biopolym.,* **50**, 99 (1999).
32. D. Bajer, H. Kaczmarek, K. Bajer, *Carbohyd Polym.,* **98**, 477 (2013).
33. S. Wang, L. Copeland, *J. Agric. Food Chem.*, **60**, 6439 (2012).
34. L. Zhaofeng, L. Wenjing, G. Zhengbiao, L. Caiming, H. Yan, C. Li, *Food Hydrocolloid.,* **48**, 189 (2015).
35. Z. Fu, L. Wang, H. Zou, D. Li, B. Adhikari, *Carbohyd. Polym.*, **101**, 727 (2014)

ГЕЛИРАНЕ НА ИНДУСТРИАЛНИ НИШЕСТЕТА, ИЗСЛЕДВАНО С ДСК И ТГ

А. Рангелов[1], Л. Арнаудов[2], С. Стоянов[2,3,4], Т. Спасов[1]

[1] *Софийски Университет „Св. Климент Охридски", Факултет по Химия и Фармация*
[2] *Униливер- Изследване и Развитие, 3133АТ Влаардинген, Холандия*
[3] *Физикохимия и Меки Материали, Университет на Вагенинген, 6703 НВ Вагенинген, Холандия*
[4] *Департамент по Механично Инженерство, Университетски Колеж Лондон, WC1E 7JE, OK*

(Резюме)

Микроструктурата и термичните свойства на индустриални нишестета с различен произход бяха изследвани с помощта на рентгенова дифракция и термичен анализ (ДСК, ТГ). Някои от изследваните нишестета демонстрираха кристална структура (тип А и тип Б), а други бяха предимно аморфни, с около 15% степен на кристалност. Влагосъдържанието на чистите нишестета корелираше с тяхната микроструктура: нишестета с по-голямо количество аморфна фаза имаха по-високо влагосъдържание. Термичното поведение на нишестетата с добавено различно количество вода също беше изследвано с помощта на ДСК. В сместа нишесте-вода при по-големи количества вода гелирането започваше по-рано и енталпията на гелиране беше по-висока от наблюдаваната при по-малки количества вода. При определено съотношение нишесте-вода два отделни ендотермични пика показват процесите на гелиране и топене. Определените енталпии на гелиране бяха в рамките 5-15 Дж/г и не корелираха с първоначалната степен на кристалност на нишестетата. Не беше открита зависимост между активиращите енергии на гелиране в рамките на 40-100 КДж/мол, получени по метода на Кисинджер, и степента на кристалност. При концентрации на нишесте между 20% и 35% след ендотермичния пик на гелиране се наблюдава екзотермичен ефект, който би могъл да се обясни с формиране на вътрешни водородни връзки.

Different types of pretreatment of lignocellulosic wastes for methane production

I.S. Simeonov, D.D. Denchev, L.V. Kabaivanova*, E.Tz. Kroumova, E.Y. Chorukova,
V.N. Hubenov, S. N. Mihailova

Stephan Angeloff Institute of Microbiology - Bulgarian Academy of Sciences, Sofia 1113, „Acad. G. Bonchev" Str. 26

Biotechnological processes for anaerobic digestion of lignocellulosic substrates were performed in a laboratory bioreactor. Bioreactors used were operating at 35°C to follow the process of methane production. Cattle manure and wheat straw were involved in a ratio of 65:35 as a substrate, as well as only wheat straw as a sole substrate. We report on performing two pretreatment techniques to the substrates - chemical with ammonium hydroxide (NH_4OH) and polyethylene glycol (PEG) and biological – employing white-rot basidiomycetes (*Trametes hirsuta*) before starting the process of anaerobic digestion. The biological method of pretreatment gave the highest cumulative biogas yield for the substrate wheat straw and cattle manure. Chemical pretreatment lead to higher specific biogas yield when only wheat straw was used as a substrate. Both methods were easy to perform and lead to increased biomethane yield in comparison to that obtained with the participation of untreated substrates.

Key words: substrate pretreatment, anaerobic digestion, biomethane yield

INTRODUCTION

Anaerobic digestion of lignocellulosic biomass provides an excellent opportunity to convert abundant bioresources into renewable energy [1]. Anaerobic digestion is a process of organic matter mineralization by microorganisms into biogas (mainly methane and carbon dioxide) and digestate in the absence of oxygen [2]. The products obtained are of arising energetic and ecological significance. Biodegradation of organic wastes is a complex biotechnological process, which is performed by a specific microbial community. It combines the breakdown of wastes with opportunities to obtain the energy carrier methane. The chemical composition of the substrates used has a direct impact on the efficiency of their conversion. Microbial digestion of lignocellulose contained in the agricultural wastes is difficult to accomplish and slow because of the presence of lignin therein. This requires preliminary physical, chemical or biological treatment. To enhance the enzymatic and microbial accessibility, preliminary treatment was identified as an obligatory step before accomplishment of the whole complex biotechnological process [3]. Generally lignocelluloses have a stable structure, insoluble in water and resistant to both mechanical and enzymatic effects. Over the years, a great variety of pretreatment methods have been exploited [4]. Because of the simultaneous presence of lignin and crystalline cellulose, the water molecules can not penetrate into the lignocellulose fibers. To optimize the anaerobic digestion of wheat straw and manure and make the biogas process more profitable, several pretreatment techniques were evaluated. Pretreatment technology is a prerequisite to facilitate the release of monomers from a lignocellulosic biomass prior to enzymatic biodegradation [5]. Recently, some methods have been tried with ionic liquids, but they were still expensive and unpractical [6]. Alkaline hydrolysis results in the reduction of degree of polymerization and loosening of the intermolecular bonds connecting the lignin and hemicelluloses, thus increased porosity of the material and increased specific surface area of the lignocelluloses was realized [7]. Involving wood decaying fungi in a pretreatment process that can break down all major wood components (cellulose, hemicelluloses and lignin) more or less simultaneously, would result in substrates more accessible to biodegradation. Much efforts are aimed at developing a pre-treatment technology, which is eco-friendly and cost effective, aiming at increasing the porosity of the substrate, removing lignin or hemicellulose, and reducing the overall crystallinity in the structure to facilitate the biological conversion of biomass into bioenergy and biobased products [8]. Lignocellulosic substrates are suitable for continuous biogas production, because of their high potential methane yield [9, 10].

The aim of this study was the development of an effective technology for anaerobic digestion of lignocellulosic wastes by selecting the most effective method for pretreatment of wheat straw added to cattle manure to realize higher degree of anaerobic digestion of substrate and obtaining maximum methane yield.

* To whom all correspondence should be sent:
E-mail: lkabaivanova@yahoo.com

EXPERIMENTAL

The bioreactor working volume was 3 dm^3, equipped with a system for monitoring and control and continuous stirring. Released gas volume from both bioreactors was measured using a graduated cylinder in the gas holder working on a water displacement principle. Concentration of methane was measured with an automatic gas analyzer "Dräger" equipped with an IR-sensor for methane.

Certain parameters characterizing the process were followed during its realization:

Total solids were measured by dehydration of a certain volume of culture liquid at 105 °C; volatile solids - by burning at 575° C [11].

Cellulose concentration in the samples was measured according to the photometric method proposed by Updegraff [12].

Two types of pretreatment were performed:

1) Chemical pretreatment: 28% NH$_4$OH, polyethylene glycol-4000 (3%) and water were involved; a ratio of 1:0.5:20 was used for straw: NH$_4$OH: H$_2$O. The mixture underwent heating at 90 °C for 5h in a water bath. This was followed by rinsing till neutral pH.

2) Biological pretreatment was accomplished by white-rot basidiomycetes - *Trametes hyrsuta,* isolated from soil samples from Bulgaria. The inoculum was prepared by inoculation of 50 mL potato dextrose medium (glucose, 20.0 g/L) with 3 mycelial disks (diameter of 0. 5 cm, from a 7 day-old culture from potato dextrose agar). Incubation was without agitation at 28 °C for 7 days. The ob-tained biomass was transferred onto sterile 5 g of wheat straw and incubated statically for 10 days.

As a criterion for the effectiveness of pretreatment served the residual concentration of cellulose, the total organic matter in dry wheat straw and composition and volume of the biogas released.

RESULTS AND DISCUSSION

Several of the substrates used today for biogas production are slowly degraded and only partially digested in the process of anaerobic biodegradation. This was the reason to apply chemical and biological pretreatment of wheat straw in our experiments before introduction of the pretreated substrate into the bioreactor. Experiments were carried out for untreated and pretreated substrates for comparison and evaluation of the different pretreatment techniqies - chemical and biological (*Trametes hyrsuta*), (Fig.1).

Fig. 1. Digital image of *Trametes hyrsuta*

The results presented in Table 1 show the changes in the chemical composition of the substrate before and after the corresponding pretreatment method.

Among the biological methods for pretreatment, the use of wood degrading fungi is one of the most effective and widely applied methods (Fig. 2). The hyphae of the fungi can secrete many ligninolytic enzymes which catalyze oxidative reactions during lignin depolymerization [13]. The peroxidases produced by them weaken and/or destroy the bonds linking cellulose and lignin.

Fig. 2. Schematic presentation of biological pretreatment of wheat straw and introduction into the bioreactor.

Table 2 presents the changes in the organic solids after cultivation in an anaerobic digester for biogas production when cattle manure and wheat straw or only wheat straw were used as substrates. The degree of biodegradation of the substrate was calculated. The data obtained indicate that the biological pretreatment improves the rate of biodegradation. From the reports available, it is evident that white rot fungi can be used to remove lignin from lignocellulosic substrates and by shortening the incubation time and optimization of the delignification process better utilization of the substrate can be realized [14]. Our results clearly indicate that the biological pretreatment improves the rate of biodegradation. The percentage of biodegradation in the variant with biological pretreatment (54.2 %) is the highest one, compared with all other variants.

The daily production of biogas was followed for a period of 15 days when cattle manure and wheat straw were used as a substrate (Fig. 3 a) and 20 days when only wheat straw was involved in the

anaerobic biodegradation (Fig. 3 b). The daily production of biogas applying the two methods of pretreatment was different, as well as the lenghth of the process during which biogas was released as a result of digestion. It is seen that the amount of biogas after biological pretreatment is the greatest one in comparison to the control option, followed by the chemical treatment for both substrates tested.

The effect of pretreatment appeared to be less expressed when only wheat straw was used as a substrate, considering the rate of biodegradation. It was calculated to be 36.9% at biological

pretreatment and 16.2% when chemical pretreatment was applied.

Table 3 presents the yields of biogas and methane obtained from the consumed substrate. The most efficient synthesis of biogas was observed after biological prereatment (cumulative biogas yield). An important feature is the percentage of methane in the biogas released. The obtained results showed that both chemical or biological pretreatment techniques applied to the substrate increase the percentage of methane in the biogas.

Table 1. Chemical composition of wheat straw before and after pretreatment.

Substrate	Pretreatment		Total Solids, %	Volatile Solids, %	Cellulose, %
Wheat straw	Chemical	before	93.7	95.2	41.7
		after	91.8	90.1	36.2
	Biological	before	93.7	95.2	41.7
		after	92.1	93.5	31.8
Cattle manure	Without pretreatment		22.3	83.2	17.4

Table 2. Changes of organic matter after cultivation in a bioreactor for biogas production

Substrate	Method of pretreatment	VS, g/dm^3			Rate of biodegradation, %
		Influent	Effluent	Utilization g/dm^3	
Cattle manure+wheat straw	No pretreatment	41.3	26.6	14.7	35.6
Cattle manure+wheat straw	Chemical	32.8	16.1	16.7	50,9
Cattle manure+wheat straw	Biological	31.2	14.3	16.9	54.2
Wheat straw	No pretreatment	27,5	24.2	3.3	14.85
Wheat straw	Chemical	22.2	18.6	3.6	16.2
Wheat straw	Biological	27.3	17.2	10.1	36.9
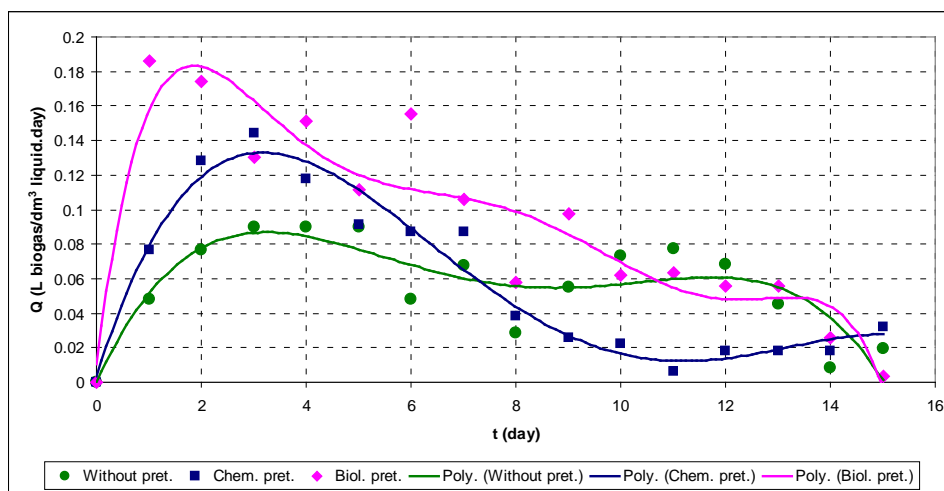
a
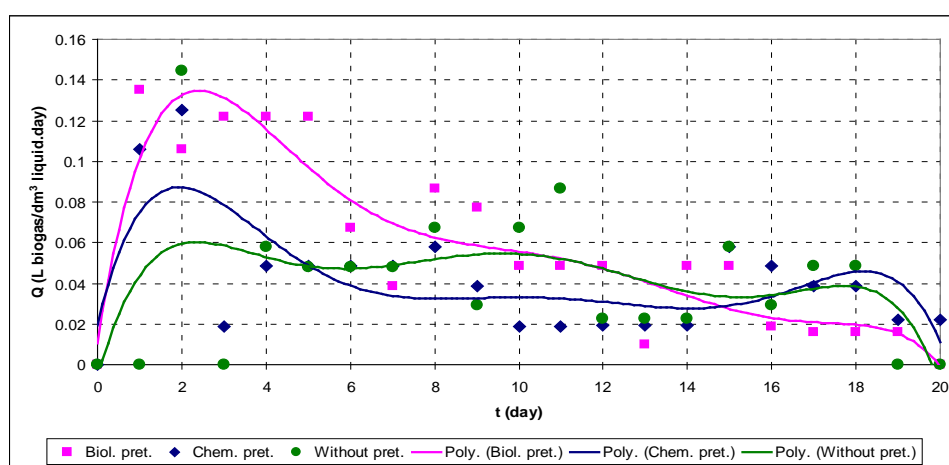
b

Fig. 3. Effect of the method of pretreatment on the daily synthesis of biogas (cattle manure and wheat straw-a and only wheat straw-b)

Table 3. Efficiency of biogas and methane synthesis

Substrate	Method of pretreatment	Utilization of VS (ΔVS), g/dm^3	Cumulative biogas yield (Q_Σ), ml/l working volume	Specific biogas yield (Q_{sp})*, ml/g ΔVS	Methane, %
Cattle manure+wheat straw	No pretreatment	14.7	1103	75.0	52
Cattle manure+wheat straw	Chemical	16.7	1027	61.5	57
Cattle manure+wheat straw	Biological	16.9	1388	82.1	58
Wheat straw	No pretreatment	3.5	833	238	48
Wheat straw	Chemical	3.6	863	239.7	51
Wheat straw	Biological	10.1	1195	118.3	49

*-$Q_{sp} = Q_\Sigma/\Delta$VS

433

The values of pH were followed during the whole process, and an increase from 5.5 to 7 was established, accompanied by an increase in methane yield, which is in accordance with the statement of Kheiredine and co-workers [15], who reported that the optimum pH for degradation in an anaerobic process is in the neutral range. This fact was also stated by Sánchez and co-workers [16].

The abundance of lignocellulosic substrates makes them a potential feedstock for biofuel production but their conversion is a major hurdle. They have to be pretreated physically, chemically, or biologically to be easily used by fermenting organisms for methane production. Alkaline pretreatment of lignocellulosic material aims to remove part of the lignin and hemicellulose by solubilization and to enhance the accessibility of the cellulosic part for cellulolytic enzymes [17], together with the effect of the amphyphilic substance polyethylene glycol which also helps in making the substrate highly water soluble [18] and favors the increase in the methane yield. In agreement with this are the results obtained after application of chemical preliminary treatment.

For most of the parameters followed in this study the biological pretreatment appeared to be the most effective. These results are due to the fact that many microorganisms in nature are able to attack and degrade lignin, thus making easy access to cellulose. Such organisms are abundantly found in the forest and include the wood decaying fungi [19]. They possess enzyme systems to attack, depolymerize and degrade the polymers in lignocellulosic substrates [20]. The application of fungi for delignification is an environmentally friendly technology that can be applied for lignocellulosic biofuel production, which was confirmed by our investigations and the results obtained.

CONCLUSIONS

Biotechnological exploitation of lignocellulosic wastes is promising for sustainable and environmentally-friendly energy production because of the abundant availability of these renewable sources.

Finding the most appropriate substrate and method of pretreatment could permit enhancement of biodegradation and increase in biomethane yield.

The biological method of pretreatment gave the highest cumulative biogas yield when wheat straw and its mixture with cattle manure were used as substrate. A ratio between the cattle manure and wheat straw (65:35) was the most appropriate one and together with application of biological treatment

of the straw improved the efficiency of biogas synthesis.

On the other hand, chemical pretreatment lead to higher specific biogas yield when only wheat straw was the substrate.

Most significant was the fact that both methods of pretreatment helped for obtaining an increased percentage of methane in the biogas released.

REFERENCES

1. C. Sawatdeenarunat, K.C. Surendra, D. Takara, H. Oechsner, S. K. Khanal, *Biores. Technol.* **178**, 178 (2015).
2. D. Deublein, A. Steinhauser, Wiley-VCH, Weinheim, 2008.
3. C. Shuo, M.A. Giovanna, *Biores. Technol.* **131**, 357 (2013).
4. H. Rodrиguez, S. Padmanabhan, G. Poon, J.M. Prausnitz, *Biores. Technol.* **102**, 7946 (2011).
5. T.D. Nguyen, K.-R. Kim, S. Han, H.Y. Cho, J.W. Kim, S.M. Park, J.C. Park, S.J. Sim, *Biores. Technol.* **101,** 7432 (2010).
6. D. Fu., G. Mazza, Y. Tamaki, *J. Agric. Food Chem.* **58**, 2915 (2010).
7. R. Chandra, H. Takeuchi, T. Hasegawa b, R. Kumar, *Energy* **43,** 273 (2012).
8. F. Monlau, A. Barakat, E. Trably, C. Dumas, J.-P. Steyer, H. Carrère, *Crit. Rev. Environ. Sci. Technol.*, **43**, 260 (2013).
9. Y.H. Jung, H.K. Kim, H.M. Park, Y.–C. Park, K. Park, J.-H. Seo, K.H. Kim, *Biores. Technol.* **179,** 467 (2015).
10. S.T. Thomsen, H. Spliid, H. Østergård, *Biores. Technol.* **154**, 80 (2014).
11. American Public Health Association, Standard methods for the examination of waste and wastewater. Washington, DC, 2005.
12. D. Updegraff, *Analyt. Biochem.* **32**, 420 (1969).
13. J. Cilerdzi, M. Staji, J. Vukojevi, *Int. Biodeter. & Biodegrad.* **114,** 39 (2016).
14. .M. Saritha, A. Arora, A. Lata, *Indian J Microbiol.* **52,** 122 (2012).
15. B. Kheiredine, K. Derbal, M. Bencheikh-Lehocine, *Chem. Eng. Transact.* **38**, 511 (2014).
16. E.Sánchez, R. Borja, P. Weiland, L. Travieso, A. Martín, *Biopro. Eng.* **22**, 247 (2000).
17. A.T.W.M Hendriks, G. Zeeman, *Biores. Technol.* **100**, 10 (2009).
18. D.J. Seo, H. Fujita, A. Sakoda, *Biores. Technol.,* **102,** 9605 (2011).
19. C. Wan, Y. Li, *Biotechnol. Adv.,* **30**, 1447 (2012).
20. A.D. Moreno, D. Ibarra, P. Alvira, E. Tomás-Pejó, M. Ballesteros, *Crit. Rev. Biotechnol.*, **35**, 342 (2015).

РАЗЛИЧНИ НАЧИНИ НА ПРЕДВАРИТЕЛНО ТРЕТИРАНЕ НА ЛИГНОЦЕЛУЛОЗНИ ОТПАДЪЦИ ЗА ПРОДУКЦИЯ НА МЕТАН

И. С. Симеонов, Д. Д. Денчев, Л. В. Кабаиванова*, Е. Ц. Крумова, Е. И. Чорукова, В. Н. Хубенов, С. Н. Михайлова

Институт по Микробиология „Стефан Ангелов" – Българска Академия на Науките, София 1113, ул. „Акад. Г. Бончев" 26

(Резюме)

Осъществени са биотехнологични процеси на анаеробна деградация на лигноцелулозни субстрати в лабораторен биореактор. Използваните биореактори работиха при 35°C и беше проследен процеса на продукция на метан. Оборски тор и пшенична слама се използват като субстрат в съотношение 65:35, както и само пшенична слама като единствен субстрат. Ние докладваме за прилагането на две техники на предварително третиране на субстратите – химическо с амониев хидроксид (NH$_4$OH) и полиетилен гликол (PEG) и биологическо – с участието на дървесина-разлагащи базидиомицети (*Trametes hirsuta*) преди стартиране на процеса в анаеробния реактор. Биологичният метод на претретиране доведе до най-висок кумулативен добив на биогаз при субстрат оборски тор и пшенична слама. При химическото претретиране се получи по – висок специфичен добив на биогаз, когато само пшенична слама се използва за субстрат. И двата метода са лесни за осъществяване и водят до увеличен добив на биометан в сравнение с този, получен с участие на нетретирани субстрати.

Study on the influence of devulcanization conditions on the reclaim-based vulcanizates operation characteristics

P.A. Malinova, N.T. Dishovsky*, A.Tz. Tzanev

University of Chemical Technology and Metallurgy, 8 KlimentOhridski Blvd., Sofia 1756, Bulgaria

The method of experimental design has been applied to study the dependences of the operational characteristics of reclaim-based vulcanizates on the devulcanization conditions of rubber crumbs from solid and superelastic tyres – temperature, treatment time and softener quantity. Mathematical models in the form of second order polynomials, representing the dependence of the most important operation characteristics of the reclaims and the vulcanizates based thereof vs. devulcanization conditions have been obtained. Optimizing a number of predetermined goal functions according to a chosen scan method allows determination of the optimum values of the working conditions. It has been established that there are no devulcanization conditions suitable to ensure the best values for all important operation characteristics studied. That is why the devulcanization process should be run under particular conditions, tailored according to obtaining of reclaim for specific technological purposes defined preliminary.

Keywords:reclaim characteristics, rubber crumb, experimental design, devulcanization conditions

INTRODUCTION

Although finely ground, disintegrated vulcanizates cause quality problems related to worsened operation characteristics of the final rubber products. From a theoretical point of view, the reason is in the thermodynamic incompatibility between the fresh rubber mesh matrix and the particles of the disintegrated vulcanizates, occurring mainly at their interface. That is why the studies on the reclaim of disintegrated worn and dispensed rubber particles aim first of allcreating ofeffective methods for improving their compatibility with the fresh rubber mesh matrix, as well as of possibilities for inter-diffusion or interaction at the phase boundary [1]. Reclaiming is one of the reliable methods for solving the problems mentioned, as more and more companies recognize rubber reclaim as an important source for rubber processing industry first of all because of the environmental and economic benefits of recycling [2].

The technological process of devulcanization consists of reclaiming worn tyres and dispensed or/and obsolete technical rubber particles and their turning into a product with prevailing plastic properties. It is also characterized by the opportunity to compound fresh rubber and ingredients, and then revulcanize the compound. The principle of the process is described in [3]: optimal destruction of the three-dimensional vulcanization net, rupture of the rubber-carbon black bonds and then transforming the elastic vulcanizate into a plastic recyclable product [4].

In comparison to the initial vulcanizate, the structural specifics of the reclaims are connected with the effect that a part of the rubber substance in the reclaim still keeps remnants of the non-destructed curing net, while the other part though lacking cross links differs from the crude rubber by its molecular chain structure resultant from devulcanizationside reactions. In fact, both features have negative effect on the reclaim quality.

During last years, many different reclaiming methods have been developed and successfully implemented [5-21]. One of them is devulcanization by thermal swelling in the presence of different agents, predominantly oil softeners [7,10]. Evidently, it is necessary to find optimal conditions for the devulcanization process, so that to achieve a maximum destruction rate of the curing net on one hand and on the other, to achieve minimization of the side reactions causing changes in the reclaim macromolecules.

This work aims at deriving polynomial mathematical models by planning a multifactor experiment via optimal experimental design and regression analysis. The models will describe the relationships between the process conditions for devulcanization *via* thermal swelling in oils and the basic rheological, vulcanization and mechanical properties of the obtained vulcanizates and reclaims.

EXPERIMENTAL

Initial vulcanizates

Initial vulcanizates for reclaims were obtained from protector crumbs based on: 70 % of stryrene-butadiene rubber (BULEX 1500, made in Bulgaria);

* To whom all correspondence should be sent:
E-mail:dishov@uctm.edu

20 % of isoprene rubber (SKI-3, made in Russia) and 10 % of butadiene rubber (SKD, made in Russia). The crumbs of waste vulcanizates from solid and superelastic tyres (made by Zebra Ltd., Bulgaria) were obtained on a 05-782/P3disk grinder with two disks having 800 mm outer diameter, at a rate of 900 rpm and power of 75 kW.

Some of the most important characteristics of the crumbs used for reclaiming are summarized in Table 1. As seen, the prevailing fraction size is about 250-500 μm, approximately.

The process of devulcanizing rubber crumbs by thermal swelling in highly aromatic oil (softener) as a swelling agent, was carried out in a horizontal autoclave of 6 m length with inner diameter of 1.6 m. The temperature conditions, duration of the treatment and the amount of softener (with regard to the amount of crumbs) were considered in the scope of the optimization parameters to be included in a model, obtained by industrial data.

Table 1. Characteristics of the raw protector rubber crumbs

Characteristics	Values
1.Particle size, mm	Share, %
>1.6 mm	2.2
1.25 mm – 1.6 mm	0.6
1.0 mm – 1.25 mm	4.3
0.63 mm – 1.0 mm	11.8
0.50 mm – 0.63 mm	10.4
0.25 mm – 0.50 mm	52.7
0.20 mm– 0.25 mm	7.2
0.16 mm – 0.20 mm	6.6
0.10 mm – 0.16 mm	3.7
0.09 mm – 0.10 mm	0.3
< 0.09 mm	0.2
2. Acetone extract, %	12
3. Ash content, %	6.5
4. Carbon black content, %	30.2
5. Rubber content, %	49
6. Loss on heating, %	0.49
7. Specific gravity, g/cm^3	1.15

The swelling agent was a highly aromatic oil type PN-6 (made in Russia), having the following characteristics: viscosity 35-40 CST (at 100 °C); density 0.96-0.98 g/cm^3; flash point 230 °C; solid point 36 °C; refractive index 1.53-1.54; sulphur content 2.71-3.08 %; aniline point 55-65 °C. The hydrocarbon composition of the oil was the following: paraffinic-naphthenic fraction 8-10 %, aromatic fraction (low, medium and heavy hydrocarbons) 82-90 %, resins 7.0-8.0 %.

Optimal experimental design

The experimental design was conducted using a B_m type optimal compositional plan [22, 23], containing 14 experiments for obtaining a second order mathematical model. The model factors (process variables), i.e. the devulcanization conditions of the experiment, as well as their levels in a normal and encoded form, were set up as follows:

X_1 - devulcanization temperature, °C
Low level – 185 °C, encoded as /-1/;
Main level – 200 °C, encoded as /0/;
High level - 215 °C, encoded as /+1/.
X_2 – time for treatment (devulcanization) of the crumbs, hours
Low level – 3 h, encoded as /-1/;
Main level – 5.5 h, encoded as /0/;
High level - 8 h, encoded as /+1/.
X_3 - amount of the softener with regard to the crumbs amount, %
Low level – 5 %, encoded as /-1/;
Main level – 10 %, encoded as /0/;
High level - 15 %, encoded as /+1/.

The following basic characteristics of the obtained reclaims and vulcanizates were chosen for goal functions (functions of desirability) of the performed experimental design:

Y_1– *Mooney* viscosity; Y_2 – devulcanization degree; Y_3 – crosslink density of the reclaim-based vulcanizates; Y_4 – tensile strength of the reclaim-based vulcanizates; Y_5 – heat aging resistance with regard to tensile strength of the reclaim-based vulcanizates.

The applied optimal compositional plan contained 14 experiments and is described by the following design matrix (Table 2):

Matrix of the experimental design in normal and encoded values

The reclaims obtained under the treatment conditions in each out of all 14 experiments (Table 2) were used for preparing identical rubber compounds according to the Bulgarian National Standard 5149-80, all having the following composition (in phr): reclaim - 100, zinc oxide – 2.5, dibenzothiazolyl disulfide – 0.9 and sulphur – 1.5.

The compounding was carried out on an open rubber two-roll mill with L/D 320×160 and friction rate of 1.27. Nominal speed of 25rpmon the slower roll was set.

The experimental samples (200×200×2mm) prepared from the examined compounds underwent vulcanization by electric heating on a hydraulic press at 143 °C, and pressure of 12MPa with time duration of 15 min.

Test treatment of the prepared compounds and vulcanizates

The following characteristics of the prepared compounds and the vulcanizates based thereof were further investigated:

- Vulcanization characteristics at 143 °C – according toISO 3417:2010;

- *Mooney* viscosity, ML (1+4) at 100°C of the reclaimsand the compounds based thereon (ISO 289-1:2002);

- *Shore A* hardness – according to ISO 7619:2001;

- Tensile stress-strain test properties of the vulcanizates ($M_{100}$and M_{300}-stress load at 100%and 300 % elongation, σ – tensile strength, $ε_{rel}$- relative elongation, $ε_{res}$- residual elongation (according to ISO 37:2008). The experimental tests were carried out at a stretching rate of 500 mm/min;

- Resistance to heat aging of the vulcanizates (at 70 °C for 72 hours) according to ISO 188:1998. The negative sign of the aging coefficient shows the worsening of the respective mechanical properties, in %;

- The equilibrium rate of swelling in xylene of the reclaims was determined by a particular laboratory method;

- The devulcanization rates of the modified crumbs (i.e. the reclaims) were evaluated as the ratio between the equilibrium swelling rate of the devulcanized samples under different conditions and the same index of the initial untreated sample.

RESULTS AND DISCUSSION

Table 3 presents the experimentally obtained *Moony* viscosity index of the reclaim samples devulcanized under different conditions, (according to the design matrix, Table 2). As seen, the conditions of the devulcanization process influence to a sufficiently high extent the *Mooney* viscosity values. So, this index varies under the prescribed test conditions in the range of 33÷52 units ML. The experimental results have good reproducibility, as shown by the parallel runs of experiment No. 9 (corresponding values: 36, 35,35). That issue allows assuming that by changing the devulcanization conditions, for particular needs one can obtain reclaims with preset *Mooney* viscosity levels.

Table 2. Matrix of the experimental design in normal and encoded values:

Experiment №	X_1 Devulcanization temperature		X_2 Devulcanization time		X_3 Amount of softener	
	normal	encoded	normal	encoded	normal	encoded
1	185	-1	3	-1	5	-1
2	215	+1	3	-1	5	-1
3	185	-1	8	+1	5	-1
4	215	+1	8	+1	5	-1
5	185	-1	3	-1	15	+1
6	215	+1	3	-1	15	+1
7	185	-1	8	+1	15	+1
8	215	+1	8	+1	15	+1
9	185	-1	5.5	0	10	0
10	215	+1	5.5	0	10	0
11	200	0	3	-1	10	0
12	200	0	8	+1	10	0
13	200	0	5.5	0	5	-1
14	200	0	5.5	0	15	+1

Table 3.*Mooney* viscosity index of the sampled reclaims according to the experimental design matrix

Experiment №	1	2	3	4	5	6	7	8	9	10	11	12	13	14
Mooney viscosity, units ML (1+4) 100 °C	42	52	33	47	40	48	33	36	35	42	44	34	38	34

Table4. Rate of equilibrium swelling (R of ES) in xylene and devulcanization rate (DR) of samples from modified reclaims obtained according to the experimental design matrix.

Experiment№	1	2	3	4	5	6	7	8	9	10	11	12	13	14
R of ES %	331	273	329	280	313	301	324	289	330	292	298	310	292	295
DR	1.96	1.83	2.21	1.87	2.09	2.01	2.20	1.93	2.19	1.95	1.99	2.07	1.95	1.97

3 parallel runs of experiment № 9: R of ES values-328,330,331; DR values: 2.19, 2.20, 2.19.
Untreated sample R of ES: 150

Table5. *Mooney* viscosity index of standard rubber compounds based on reclaims modified under different conditionsaccording to the experimental design matrix.

Experiment №	1	2	3	4	5	6	7	8	9	10	11	12	13	14
Mooney viscosity, units ML (1+4) 100 °C	34	30	27	29	33	30	26	29	29	35	37	28	32	30

The devulcanization rate of the reclaims obtained under different conditions has been determined with regard to their equilibrium swelling rate compared to the same index of an untreated sample. The investigations aim at establishing supervision and optimization of the devulcanization process, as well as the effect its conditions have on the obtained reclaim characteristics. The experimental results are given in Table 4. It is evident, that the reclaims resulting from experiments № 3 and №7 have the highest devulcanization rate. Also, their swelling equilibrium rate reaches the highest values, hence it is the closest to the index of a fresh elastomer. It is obvious, however, that the devulcanization is only fractional in all experimental cases. The process has been completed at the least extent in the case of experiments № 2 and № 4. Certain correlation between *Mooney* viscosity index and the devulcanization degree has also been observed. In brief, the lower the Mooney viscosity values, the higher devulcanization degree is obtained. Obviously, the devulcanization rate and the reclaim properties are strongly dependent on the process conditions. That is why the optimum devulcanization conditions should be specified in advance and first of all, the process should be run only under the prescribed controlled conditions to minimize the undesired side effects of worsening the qualities of the reclaims obtained.

Table 5 summarizes the values of *Mooney* viscosity index regarding the prepared standard rubber compounds based on reclaims devulcanized under different conditions. Obviously, *Mooney* viscosity values of the standard rubber compounds are generally lower than those of the respective reclaims. That meets the theoretical expectations as low-molecular ingredients (without reinforcing fillers) have been added to the reclaims and the system becomes less saturated in high molecular

products. Besides, an additional thermomechanical destruction of the rubber substance in the reclaims has taken place while being compounded with ingredients on the roller mill.

As seen from the table, *Mooney* viscosity values vary in the range of 26÷37 units. The highest values are obtained for compound № 11, and the lowest ones - for compound № 7. Having in mind that all other process conditions are fixed at the same levels, that means the variations observed are only due to the different reclaim properties, resulting from the devulcanization conditions. Reproducibility of the experimental results is good, as the parallel runs of experiment No. 9 show(corresponding values: 29, 30, 29).

The vulcanization characteristics of the prepared standard rubber compounds, based on reclaims, devulcanized under different conditions according to the experimental plan matrix are represented in Table 6. As shown, there is a significant difference in the vulcanization characteristics of the rubber compounds due to the devulcanization conditions.

The minimum torque (M_L), which correlates significantly with the effective viscosity of the compound prior to vulcanization, possesses values between 8 and 15 dNm, while the maximum torque(M_H), characterizing the vulcanizates hardness, varies in the range between 30-54 dNm.

The crosslink density of the curing net, which could be evaluated by ΔM values, varies between 32 and 40 dNm. Compound № 8 demonstrates the highest value, while compounds № 2 and 6 have the lowest ones.

The vulcanization scorch time is relatively uniform and for most of the compounds it is between 3.9 and 5.8 minutes. Compound № 2 has the longest scorch time, while compound № 4 - the shortest one.

Table 6. Vulcanization characteristics of standard rubber compounds obtained from reclaim devulcanized under different conditions.

Characteristic / Compound code	M_L dNm	M_H dNm	ΔM MH-ML dNm	t_s min	t_{90} min
1	12	46	34	5.8	12.0
2	15	54	39	4.4	11.1
3	9	41	32	5.0	11.1
4	11	49	38	3.9	12.1
5	10	48	38	4.4	10.9
6	13	53	40	4.3	10.8
7	9	43	34	4.8	12.0
8	8	30	22	4.4	8.9
9	9	44	35	4.8	12.0
10	11	46	35	4.4	10.3
11	12	47	36	4.6	10.9
12	9	44	35	4.6	11.6
13	10	46	36	4.4	10.9
14	9	47	38	4.0	10.1
3 parallel runs of experiment №9	9,9,9	44,44.5,45	35,35,36	4.8,4.7,4.8	11.8,12.0,11.9

Table 7. Mechanical properties of vulcanizates obtained from modified reclaims under different conditions

Experiment №	M_{100} MPa	M_{300} MPa	σ MPa	$\varepsilon_{rel.}$ %	$\varepsilon_{res.}$ %	*Shore A* hardness, rel. units	Aging coefficient $K\sigma$, %
1	1.64	-	5.66	238	7	56	-12.7
2	1.69	-	5.54	220	6	58	-8.1
3	1.68	-	4.85	237	8	55	4.3
4	1.47	-	4.81	228	8	56	10.2
5	1.69	-	5.73	227	8	57	-5.2
6	1.69	-	5.83	222	6	57	-7.7
7	1.51	-	4.21	216	4	55	5.5
8	1.57	-	5.27	220	7	56	-5.3
9	1.66	-	4.92	222	5	58	-6.7
10	1.58	-	5.69	235	7	55	-0.7
11	1.72	-	5.52	228	5	60	-15.0
12	1.50	-	4.60	229	5	55	-5.6
13	1.58	-	4.95	235	5	58	-10.9
14	1.52	-	4.33	241	8	57	0.5
3 parallel runs of experiment № 9	1.65; 1.66; 1.65	-	4.87; 4.95; 4.92	220; 225; 220	5; 5; 5	59; 58; 59	-6.7; -6.9; -6.7

The optimum vulcanization time (t_{90}) does not vary significantly. For most compounds it remains in the limits of 11-12 min, with an exception of that for compounds №№ 8, 10 and 14, which is about 9-10 min.The main mechanical properties of the vulcanizates obtained from reclaim devulcanization under different conditions according to the experimental design matrix are presented in Table 7. The values for M_{100} are close for all experimental cases investigated. The difference between the minimum and maximum values is about 10%. The

compounds based on reclaims №6, 5, 1 and 10possess the highest tensile strength values (in the range between 5.6-5.8 MPa), while compound № 7 reaches the lowest one (4.2 MPa). The highest tensile strength value for sample №6 correlates significantly with the highest crosslink density of the curing net (Table 6). The relative elongation of the particular compounds is almost the same. The residual elongation in all the cases considered is negligible. The values of *Shore A* hardness index for

each vulcanizate are also close, varying in the range of 55÷60 relative units.

The thermal aging resistance of the vulcanizates obtained from devulcanized reclaims under various conditions is different. The reason is in the various conditions under which the crude crumbs have been devulcanized: the different rate of devulcanization process and the side reactions, which worsen the reclaim quality, respectively. Best aging resistance properties with regard to all parameters studied (M_{100}, tensile strength and relative elongation) demonstrate compounds № 4 and № 10.

Having carried out the experimental plan in the design matrix, the results achieved allow deriving the following regression models in the form of second order polynomials, representing the existing dependences of the goal functions Y_1–Y_5 on the devulcanization conditions, including the factors:

X_1-devulcanization temperature, °C;

X_2-devulcanization time, h,

andX_3-softener quantity, %:

1)*Mooney* viscosity Y_1 for the reclaims obtained:

$Y_1 = 36.90 + 3.50[X_1] - 5.60[X_2] - 1.40[X_3] + 1.60[X_1]^2 + 2.10[X_2]^2 - 0.90[X_3]^2 - [X_1][X_2]$

2)Devulcanization rate Y_2:

$Y_2 = 2.00 - 0.12[X_1] + 0.07[X_1]^2 + 0.02[X_2]^2 - 0.05[X_3]^2 - 0.03[X_1][X_3] + 0.04[X_2][X_3]$

3)Crosslink density of the reclaims based vulcanizates Y_3:

$Y_3 = 38.20 + 3.00[X_1] + 2.20[X_3] - 3.25[X_1]^2 - 2.75[X_2]^2 - 1.25[X_3]^2 - 5.25[X_1][X_2] - -6.25[X_1][X_3] - 6.00[X_2][X_3]$

4)Tensile strength of the reclaims based vulcanizatesY_4

$Y_4 = 4.51 + 0.10[X_1]^2 + 0.54[X_2]^2 + 0.13[X_3]^2$

5)Aging coefficient with regard totensile strength of the reclaims based vulcanizates Y_5):

$Y_5 = -8.58 + 0.33[X_1] + 5.85[X_2] + 0.34[X_3] + 5.18[X_1]^2 - 1.72[X_2]^2 + 2.83[X_3]^2 - 0.79[X_1][X_2] - 3.06[X_1][X_3] - 2.86[X_2][X_3]$

Having tested the adequacy of the obtained mathematical models Y_1-Y_5 (optional goal functions) by the *Fisher* criterion (level of significance 0.02) and considering the affirmative results, the models have been subjected to an optimization procedure. The optimal coordinates of the global extrema to all goal functions have been determined implementing standard scan optimization methods. The values for the factors concerning devulcanization conditions have been obtained in the factorial space studied, respectively.

The final results obtained are the following:

1) For the relation *Mooney* viscosity *vs.* devulcanlation conditions - the lowest *Mooney* viscosity (Y_1^{MAX}=32 relative units) has been obtained under the following devulcanization conditions:

- devulcanization temperature 183°C;
- devulcanization time 8 h;
- softener quantity 5 % of the crumbs amount.

Comparing the results from Tables 2 and 3 and those derived by the optimization procedure one can consider that in the case of industrial experiment № 3 from the design matrix, the applied devulcanization conditions for waste vulcanizates are very close to the extremum coordinates, found by the numerical optimization software utility.

2) For the relation reclaim devulcanization rate Y_2 *vs.* devulcanization conditions – the highest devulcanization rate (Y_2=2.25) is obtained at the following factor values:

- devulcanization temperature 175 °C;
- devulcanization time 8 h;
- softener quantity 8.5 % of the crumbs amount.

Reclaims № 3и № 7 demonstrate the highest devulcanization rate achieved experimentally: 2.21 and 2.20, respectively (Table 4). These values deviate by about 2-3% from those predicted by the derived model.

3) For the relation ΔM (crosslink density of the reclaim-based vulcanizates) *vs.* reclaiming conditions in the form of highest vulcanizate crosslink density Y_3, Y_3=41 dNm has been obtained under the following devulcanization conditions:

- devulcanization temperature 215 °C;
- devulcanization time 21 min;
- softener quantity 5 % of the crumbs amount.

A practical experimental point with these coordinates does not exist in the generated experimental design matrix. The highest ΔM value, achieved experimentally for a compound based on reclaims № 6, isΔM=40 dNm (Table 6).

4) For the relation tensile strength of the reclaim-based vulcanizates *vs.* the reclaiming conditions Y_4, the highest value of the tensile strength of the reclaim-based vulcanizates Y_4=6.15 MPa has been measured at the following factor values:

- devulcanization temperature 215 °C;
- devulcanization time 3h;
- softener quantity 15 % of the crumbs amount.

A practical experimental point with these coordinates does really exist in the experimental design matrix as experiment № 6. The experimentally obtained highest tensile strength value is 5.83 MPa (Table **7**). It differs just by 5 % from the value predicted by the mathematical model.

5) For the relation aging coefficient (with regard to tensile strength of the reclaim-based vulcanizates) *vs.* reclaiming conditions Y_5, the highest value of the aging coefficient with regard to tensile strength of

the reclaim-based vulcanizates $Y_5=10.9$ % has been determined at the following factor values:

- devulcanization temperature 215 °C;
- devulcanization time 8 h;
- softener quantity 15 % of the crumbs amount.

There is such an experimental point in the experimental design matrix as experiment № 4. The aging coefficient value with regard to the tensile strength determined experimentally is 10.2 %. It differs just by 6 % from the one predicted by the derived mathematical model.

The analysis of the results obtained reveals that the optimal conditions for performing devulcanization of waste vulcanizates are considerably differing for each ofthe 5 goal functions, i.e. devulcanization conditions ensuring the most appropriate values for all important parameters simultaneously could not be found. That infers that the optimal devulcanization conditions should be chosen depending on the future reclaim application, keeping in mind the following issues:

- The lowest value of the *Mooney* viscosity index, the highest degree of devulcanization of the crumbs, respectively, is achieved at low temperature (175-185 °C) but for the longest treatment time (8 h) possible and at an average quantity of softener (8.5%). Evidently, the lower temperature and longer treatment time allow the softener to facilitate the highest rate of intermacromolecular diffusion and scission more bonds.

- In the case of longer treatment, undesired side destructive processes occur simultaneously with the devulcanization of waste vulcanizates. Therefore, if aiming at obtaining reclaim-based vulcanizates of maximum tensile strength, the reclaiming conditions should be intensified so that to minimize the undesired destructive processes yielding lower molecular mass and worsened mechanical parameters, respectively. The mathematical model prompts the same, namely: best mechanical properties have the vulcanizates based on reclaims devulcanized at higher temperature (215 °C) and maximum quantity of the softener – 15%. All these conditions lead to intensified vulcanization treatment since the conditions benefit the diffusion of the molecules of the softening agent. However, modification of the compound should proceed for the shortest time (3 h) in order to maximally eliminate the destruction processes. Assuming that first priority is to obtain reclaim-based vulcanizates with best mechanical properties, the reclaiming conditions should be set at the values shown above.

CONCLUSIONS

1) The dependences of the exploitation characteristics of obtaining reclaim-based vulcanizates on the conditions of reclaiming crumbs from solid and superelastic tyres – temperature, treatment time and softener quantity, have been studied by the method of experimental design.

2) Mathematical models in the form of second order polynomials representing the relations between the most important operation characteristics of the reclaims and the vulcanizates based thereof *vs.* devulcanization conditions have been derived. The extremum values of the processing conditions have been determined by optimization procedures implementing standard scan search routines.

3) It has been established that there are no practical devulcanization conditions ensuring the best values for all most important exploitation characteristics studied. That is why devulcanization should be conducted under conditions of compromise, tailored according to the specific future application of the reclaim obtained:

- the lowest *Mooney* viscosity value of the reclaims has been achieved at 183 °C for the longest treatment time (8 h) and at a minimum quantity of softener (5%);

- the highest devulcanization rate of the crumbs has been achieved at 175 °C for the longest treatment time (8 h) and at average quantity of softener (8.5%);

- best mechanical properties possess the vulcanizates based on reclaims devulcanized at 215 °C, for the shortest treatment time (3 h) and at a maximum quantity of the softener – 15%, in order to maximally eliminate the destruction processes;

- the highest aging resistance coefficient with regard to the tensile strength is obtained for the vulcanizates based on reclaims, devulcanized at 215 °C, for the longest treatment time and at a minimum quantity of the softener – 5%.

REFERENCES

1. H. Scholz, H. Michael, *Tire Technol. Int., Annual Review*, 150 (2002).
2. M. M. Antonio, *Tire Technol. Int., Annual Review*, 142 (2005).
3. I. Fanta (Ed.), Elastomers and Rubber Compounding Materials, Elsevier, New York, 1989.
4. C. Rader (Ed.), Plastic, Rubber and Paper Recycling, ACS, Washington D.C., 1995.

5. K. Baranwal, W. Klingensmith, *Rubber World*, **218**(3), 41(1998).

6. B. Adhikari, S. Maiti, *Prog.Polym. Sci.*, **25**, 909(2000).

7. J.R. White (Ed.), Rubber Technologist's Handbook, RAPRA, Shawbury, 2001.

8. J. Kim, S. Lee, *J. Appl.Polym. Sci.*, 78, 1573(2000).

9. B. Haggstrom, Rubber Handbook, Stockholm, SGE, 2000.

10. M. M. Antonio, *Tire Technol. Int., Annual Review*, 86 (2002).

11. J. Mark, B. Erman, F. Eirich, Science and Technology of Rubber, Elsevier Academic Press, Amsterdam, 2005.

12. J.S. Dick, Rubber Technology, Hanser Publishers, Munich, 2001.

13. V. L. Shulman, *Tire Technol. Int.*, 28 (2002).

14. P. Taylor, *Tire Technol. Int.*, 42(2002).

15. R. J. Farris, D. E. Williams, A. R. Tripathy, *Tire Technol. Int.*, 58(2003).

16. H. Gandhi, S. Kumar, *Tire Technol. Int., Annual Review*, 147 (2005).

17. E. Archer, *Tire Technol. Int.*, 58(2005).

18. D.N.Kolev, RB.Ljutzkanova,ST. Abadjiev,*Europ.Patent EP1879978 A1*(2008).

19. O.A. Al-Hartomy, A.A. Al-Ghamdi, S. A. Al-Said, N. Dishovsky, M.B.Ward, M. Mihaylov, M. Ivanov, *Materials Characterization,***101**, 90 (2015).

20. O.A. Al-Hartomy, A. A. Al-Ghamdi, S.A. Al-Said, N. Dishovsky, M. Mihaylov, M. Ivanov, P.Kolev, L. Ljutzkanov, *International Review of Chemical Engineering*, **6**, 160 (2014)

21. O.A Al-Hartomy, A.A. Al-Ghamdi, S.A.Al-Said, N.Dishovsky, M.Mihaylov, M. Ivanov, L. Ljutzkanov, *Progress in Rubber, Plastics and Recycling Technology*, **31**, 25 (2015)

22. I. Vuchkov, H. Yonchev, Experimental design in investigation of properties of blends and alloys, Technika, Sofia, 1979.

23. J.S. Dick (Ed.), Experimental Design and Compound Development in Rubber Technology, Hanser, Munich, 2001.

ИЗСЛЕДВАНЕ ВЛИЯНИЕТО НА УСЛОВИЯТА НА ДЕВУЛКАНИЗАЦИЯ ВЪРХУ ЕКСПЛОАТАЦИОННИТЕ ХАРАКТЕРИСТИКИ НА ВУЛКАНИЗАТИ НА БАЗАТА НА РЕГЕНЕРАТ

П.А. Малинова, Н.Т. Дишовски, А.Ц. Цанев

Химикотехнологичен и металургичен университет, бул.”Климент Охридски” 8, София 1756, България

(Резюме)

Чрез прилагане на метода на планирания експеримент бяха изследвани зависимостите на експлоатационните характеристики на вулканизати на базата на регенерат от условията на девулканизация на каучуково брашно от плътни и супереластични гуми - температура, време на третиране и количество на омекчителя. Получени бяха математични модели под формата на полиноми от втора степен, представящи зависимостта на най-важните експлоатационни характеристики на регенерата и базираните на него вулканизати от условията на девулканизация. Оптимизирайки значителен брой предвалително определени целеви функции по метода на сканирането бяха определени оптималните стойности на условията на девулканизация. Установено беше, че няма условия на девулканизация, които да осигуряват най-добрите стойности едновременно на всички изследвани важни експлоатационни характеристики. Ето защо процесът на девулканизация трябва да бъде провеждан при условия, дефинирани предварително с оглед получаването на регенерат за специфични технологични цели.

Corrosion study of ferrites prepared by hydrothermal method

S.U. Rather

Department of Chemical and Materials Engineering, King Abdulaziz University,
P.O. Box 80204, Jeddah 21589, Saudi Arabia

Zinc and nickel ferrite have been synthesized from metal nitrates using a hydrothermal method to study the structural, thermal, and corrosion properties. The XRD pattern of both zinc and nickel ferrite confirm face centered cubic (FCC) spinel structure with a very small impurity phase of hematite (α-Fe_2O_3). TGA and DSC shows two major weight losses, exothermic and endothermic, corresponding to moisture removal and decomposition of oxides to zinc/nickel ferrite. Sharp Auger electron peaks are visible throughout XPS spectrum of both ferrites. The corrosion protection of zinc ferrite is because of the unavailability of the metal for the redox pair reaction while cobalt ferrite corrosion protection is because of the passivation layer formed over time.

Keywords: Hydrothermal method, Ferrites, Potentiostat, Corrosion, Thermal decomposition, Working electrode

INTRODUCTION

Spinel ferrite MFe_2O_4, where M indicates Ni, Zn, Co, Mn, etc. is a close packed structure with two different crystallographic sites, namely tetrahedral and octahedral. These sites are also referred to as A and B-sites, respectively. Spinel structure contains two cation sites for metal cation occupancy. There are 8 A-sites in which the metal cations are tetrahedrally coordinated with oxygen atoms and 16 B-sites, which are octahedrally coordinated. Three kinds of spinel ferrites are formed by the occupancy of A and B-sites with M^{2+} and Fe^{3+} cations. Normal spinel ferrite is when A-sites are occupied by M^{2+} cations and the B-sites are occupied by Fe^{3+} cations. Inverse spinel ferrite is when A-sites are completely occupied by Fe^{3+} cations and B-sites are randomly occupied by M^{2+} and Fe^{3+} cations. In mixed spinel ferrite, both A and B-sites are occupied by M^{2+} and Fe^{3+} cations. Normal, inverse, and mixed spinel ferrite are shown in table 1.

Table 1. Normal, inverse and mixed spinel ferrite.

Site A	Site B	Ferrite Type
M^{2+}	Fe^{3+}	Normal spinel ferrite
Fe^{3+}	M^{2+}	Inverse spinel ferrite
M^{2+} or Fe^{3+}	M^{2+} or Fe^{3+}	Mixed spinel ferrite

Conventional size controlled co-precipitation [1], ultrasonic wave-assisted ball milling technology [2], co-precipitation [3], non-aqueous synthesis method [4], thermal treatment method [5-8], hydrothermal process [9], and polymerized complex method [10] were used to synthesize ferrite nanoparticles. Ferrites are nowadays quite often used as inductive components in various electronic circuits. High frequency applications such as telecommunication and radar systems make ferrites the most essential part of advanced technology. Furthermore, ferrites are also used in computers, TV, video systems, small and medium power related instruments. Other important application of ferrites is: electromagnetic interference (EMI) suppression related to notebooks, cameras, digital computers, scanners, etc. and biosciences related to magnetic materials present in the nanoparticles, specifically magnetite (Fe_2O_3), in various forms of living organisms [11]. Corrosion protection by coating of ferrites on steel alloy samples is performed to avoid surface damage in hostile environmental conditions. Furthermore, it was proved that doping of ferrites with Nd-Co increases the corrosion protection and resistance against aggressive environment as compared to pristine ferrites [12]. Morphology and chemical composition of ferrites are very crucial to improve their anticorrosion properties [13]. Keeping in mind above-mentioned applications, study of corrosion properties of ferrites such as zinc ferrites, cobalt ferrites, nickel ferrites, etc. may help to improve applications in a more advanced manner in near future.

In this paper, synthesis, characterization, and corrosion properties of zinc and cobalt ferrites are reported. Main aim of this report is to study the corrosion properties of ferrites at different time intervals.

EXPERIMENTAL

Materials and Preparation

Iron nitrate ($Fe(NO_3)_3 \cdot 9H_2O$), zinc nitrate ($Zn(NO_3)_3 \cdot 6H_2O$), and cobalt nitrate

---

* To whom all correspondence should be sent:
E-mail: rathersami@kau.edu.sa, rathersami@gmail.com

$(Co(NO_3)_3 \cdot 6H_2O)$, were purchased from Acros Organics with a purity exceeding 99%. Poly(vinyl pyrrolidone) (PVP) (MW = 30,000) was purchased from Sigma Aldrich and all the above chemicals were used without further purification. For the preparation of zinc and cobalt ferrites, an aqueous solution of PVP was prepared by dissolving 3 g of polymer in 100 mL of distilled water at 363 K. 0.2 mmol iron nitrate and 0.1 mmol zinc nitrate/cobalt nitrate were mixed into the above polymer solution and constantly stirred for 2 h using a magnetic stirrer. A litmus paper was used to determine the pH of the solution, which ranged from 4 to 5. The mixed solution was heated at 80°C for 24 h to evaporate moisture. The dried, orange, solid zinc/cobalt ferrite that remained was crushed and grounded in a mortar to form fine powder. The calcination of the powders was conducted at 600°C for 3 h for the decomposition of organic compounds and the crystallization of the nanocrystals.

Characterization

The structure of $ZnFe_2O_4$ and $CoFe_2O_4$ was characterized by XRD technique using an Inel X-Ray diffractometer model EQUINOX 1000 with CuKa radiation (k = 0.15406 nm) to generate diffraction patterns from powder crystalline samples at ambient temperature in the 2θ range of 15 to 70°. Thermal decomposition and examination of the absorptive surfaces were conducted at 950°C using thermogravimetric analysis (TGA) and differential scanning calorimetric analysis (DSC) on a model STA 449 F3 Jupiter. XPS was performed using XPS SPEC GmbH, Germany.

Measurement of Corrosion Properties

A three-electrode system is used to determine the Tafel curves for the ferrite powder in a 3.5% NaCl electrolyte solution. The working electrode is a compact ferrite powder in contact with a copper rod. Paraffin (C14) was used as a binder. The electrode is polarized to ±200 mV with respect to the open circuit potential. The Ir resistance is measured by zero run without the sample and is adjusted. The Tafel curves are then used to determine the corrosion rates. The potentiostat used to polarize the ferrite electrode is provided by AUTOLAB. The NOVA software is used to analyze the results.

RESULTS AND DISCUSSION

X-ray diffraction (XRD) was used to identify the structure of the zinc/cobalt ferrite samples. The patterns of zinc/cobalt ferrite as prepared and

calcined at 600°C are presented in Figs. 1 and 2. Peaks in the as prepared samples are not visible, but as calcination temperature increases to 600°C, sharp intense peaks appear. Both zinc and cobalt ferrite XRD patterns are characterized by several intense peaks between diffraction angle of 15 and 70°. The pattern shown in Fig. 1 is a form of cubic structure which is interpreted as cubic spinel zinc ferrite indexed by the peaks of (111), (220), (311), (222), (400), (331), (422), (511), and (440). Fig. 2 shows XRD pattern of as prepared and calcined cobalt ferrite samples. The peaks can be indexed to noticeable reflection from (111), (220), (311), (222), (400), (331), (422), (511), and (440) planes of cobalt ferrite. Both zinc and cobalt ferrite samples show very small impurity phase of α-Fe_2O_3 (H) and this impurity occurs naturally as hematite [14-16].
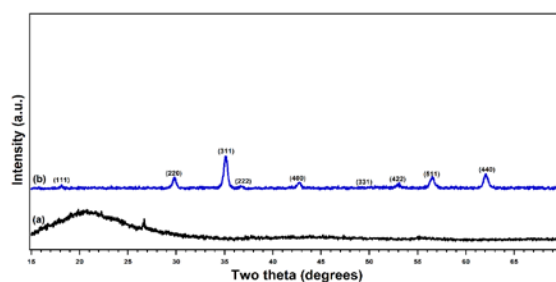
Fig. 1. X-ray diffraction (XRD) profile of zinc ferrite ($ZnFe_2O_4$) synthesized by hydrothermal method.
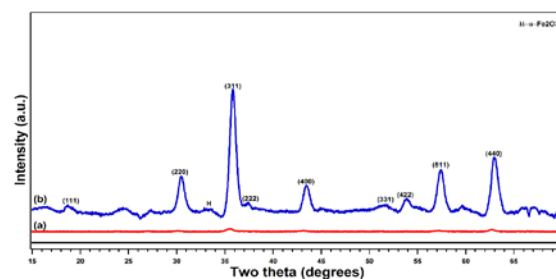
Fig. 2. X-ray diffraction (XRD) profile of cobalt ferrite ($CoFe_2O_4$) prepared by hydrothermal method.

Thermal decomposition of as prepared zinc/cobalt ferrite samples was studied by TGA and DSC, presented in Figs. 3 and 4, respectively. Two major weight loss curves for zinc ferrite, from 75 to 125°C are due to evaporation of moisture. From 400 to 500°C weight loss is due to decomposition of elemental oxides, zinc oxide, and hematite (Fe_2O_3) to the crystalline zinc ferrite. The extended curve after the last peak (>600°C) indicates sample stability and formation of crystalline zinc ferrite, as confirmed also by XRD. The corresponding DSC curve shows two major peaks, at 93°C, an endothermic peak indicates moisture removal and at 472°C, an exothermic peak confirms decomposition [17, 18]. Two major weight losses of cobalt ferrite were also observed, the first around

100ºC indicates moisture removal and the second at 400-500ºC, confirms decomposition of sample and formation of crystalline cobalt ferrite. The extended curve after the last peak (>600ºC) indicates sample stability and formation of crystalline cobalt ferrite, as confirmed by XRD, following the same trend as zinc ferrite. DSC curve also shows two major peaks, an endothermic peak indicates moisture removal and an exothermic peak at 473ºC confirms decomposition [19, 20].
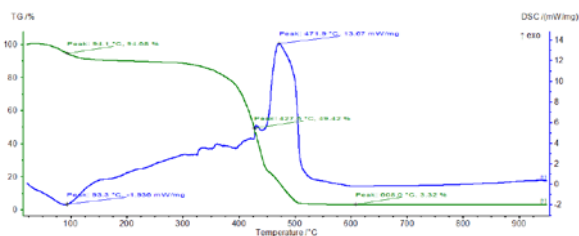
Fig. 3. Thermogravimetric analysis (TGA) and differential scanning calorimetry (DSC) data of zinc ferrite performed in an oxygen atmosphere. The heating ramp used is 10ºC/min.
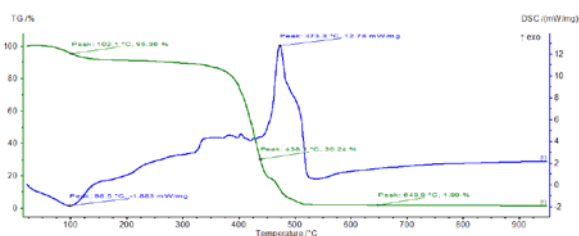
Fig. 4. Thermogravimetric analysis (TGA) and differential scanning calorimetry (DSC) data of cobalt ferrite performed in an oxygen atmosphere. The heating ramp used is 10ºC/min.

XPS results of zinc and cobalt ferrites are presented in Figs. 5 and 6, where binding energy (BE) ranges from 0 to 1100 eV. Sharp Auger electron peaks are visible throughout the XPS spectrum of zinc ferrite/cobalt ferrite. Core levels of Zn 2P, Co 2P, and Fe 2P are also visible. The presence of very low peaks of absorbed carbon on the spectra is due to PVP involved during the synthesis process [21].
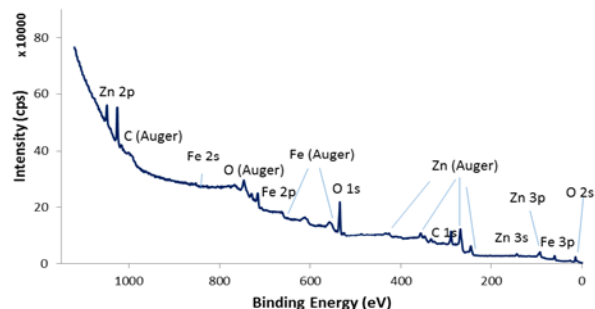
Fig. 5. Wide scan survey X-ray photoelectron spectra (XPS) of zinc ferrite (ZnFe$_2$O$_4$).
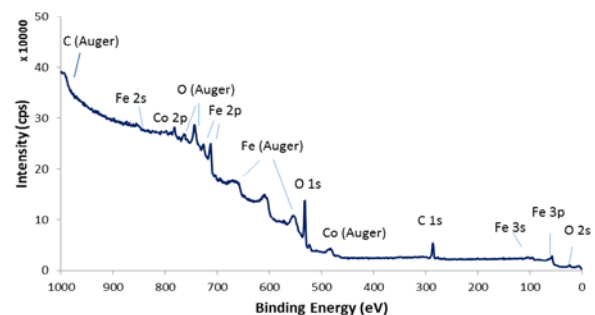
Fig. 6. Wide scan survey X-ray photoelectron spectra (XPS) of cobalt ferrite (CoFe$_2$O$_4$).

Full details of both zinc and cobalt ferrite are presented in Tables 2 and 3.

Table 2. Quantitative analysis of XPS data of ZnFe$_2$O$_4$

Sample Name	Name	Position	FWHM	Area / (T*MFP)	%At. Conc.	Mass	% Mass Conc.
Zn-Ferrite	Fe (Fe 2p3/2)	710.79	4.211	26355.1	11.79	55.8458	23.501
	O (O 1s)	529.99	3.609	44341.2	73.39	15.9994	41.911
	Zn (Zn 2p3/2)	1022.39	2.356	56527.1	14.82	65.3873	34.588
					100		100

Table 3. Quantitative analysis of XPS data of CoFe$_2$O$_4$.

Sample Name	Name	Position	FWHM	Area / (T*MFP)	%At. Conc.	Mass	% Mass Conc.
Co-Ferrite	Co (Co 2p)	780.04	4.533	34700.2	10.069	58.9332	21.779
	Fe (Fe 2p3/2)	710.34	3.844	32179.7	17.378	55.8458	35.618
	O (O 1s)	529.74	2.845	36520.7	72.553	15.9994	42.603
					100		100

The TAFEL curves for the zinc ferrite in saline solution are shown in Fig. 7. Zinc ferrite corrosion rates do not increase with time, essentially having constant anodic and cathodic surface reactions. This indicates that there is no change in the surface composition of zinc ferrite over time. Zinc ferrites anticorrosion pigments are embedded in various matrices of the paints/epoxy resins to enhance the anti-corrosion properties (22, 23). As the corrosion potential E_{cp} remains constant over the entire testing time period, therefore cathodic and anodic reactions and not the solid sample of the working electrode are the representation of the solution species (oxygen and water redox couple reactions). Thus, zinc ferrite does not show any metal dissolution into the solution. This is not true for the zinc nitrate and iron nitrate solid particles sintered below 600°C. Cobalt ferrite Tafel curves are shown in Fig. 8. Corrosion rate is almost constant over the entire testing period. However, the corrosion potential decreases over time. This indicates that there is some change on the surface of the cobalt ferrite that provides more resistance to polarization over the surface of the specimen. Cobalt is known to produce a passive layer if alloyed with steel under aggressive environment (24).
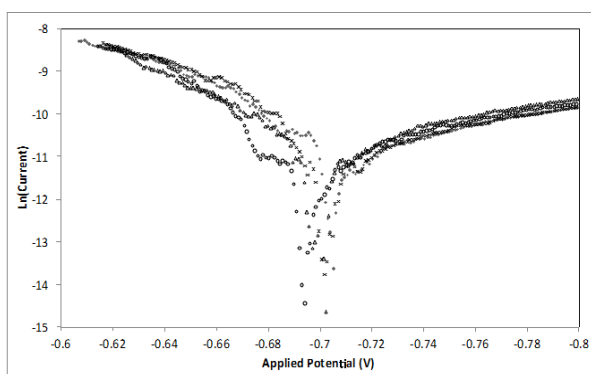
Fig. 7. Tafel curves of zinc ferrites over time, (Δ - 3 min), (O - 30 min), (× - 60 min), and (+ - 120 min).
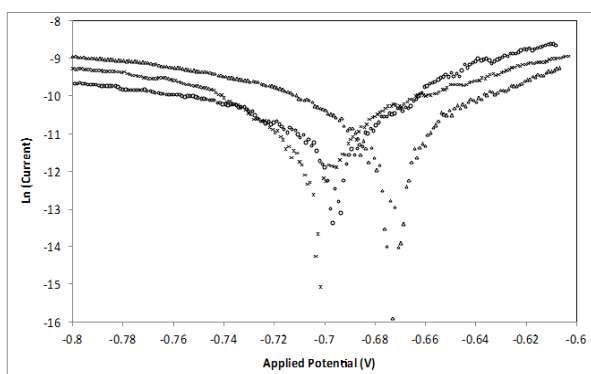
Fig. 8. Tafel curves of cobalt ferrite over time, (Δ - 3 min), (O - 60 min), and (× - 120 min).

CONCLUSIONS

The results of this investigation indicate that thermal treatment method can be used for synthesis of $ZnFe_2O_4$ and $CoFe_2O_4$ nanoparticles using poly(vinyl pyrrolidone) as a capping agent to stabilize the particles and prevent them from agglomerating. XRD patterns indicate the presence of face centered cubic spinel structure with natural impurities. TGA curves shows two major peaks related to the weight losses due to water evaporation and decomposition to crystalline phase. XPS results show the percentages of elements present on the surface of the metal ferrites. The corrosion protection of zinc ferrite is because of the unavailability of the metals for the redox pair reaction. While cobalt ferrite corrosion protection is because of the passivation layer formed over time.

REFERENCES

1. Y. Mattei, O. Pérez, O. Uwakweh, *J. Magn. Magn. Mater.,* **341**, 17 (2013).
2. D. Chenn, L. Li, J. Wang, *Ceram. Int.,* **39**, 4669 (2013).
3. M. El-Okr, M. Salem, M. Salem, M. Salim, *J. Magn. Magn. Mater.,* **323**, 920 (2009).
4. L. Ajroudi, S. Villain, V. Madigou, *J. Cryst. Growth*, **312**, 2465 (2010).
5. M.G. Naseri, E. B. Saion, H.A. Ahangar, A.H. Shaari, M. Hashim, *J. Nanomater.,* **1**, 1 (2010).
6. M.G. Naseri, E.B. Saion, H. A. Ahangar, A.H. Shaari, M. Hashim, *J. Powder Technol.,* **212**, 80 (2011).
7. M.G. Naseri, E.B. Saion, M. Hashim, A.H. Shaari, H.A. Ahangar, J. *Solid State Commun.,* **151**, 1031 (2011).
8. M. Stoia, P. Barvinschi, L. Tudoran, *J. Therm. Anal. Calorim.,* **108**, 1033 (2012).
9. M. Su, C. Hea, V. Sharma, *J. Hazard. Mater.,* **211**, 95 (2012).
10. S.M. Montemayor, L.A. Garcı´a-Cerda, J.R. Torres-Lubia´n, *Mater. Lett.,* **59**, 1056 (2005).
11. R. Valenzuela, *Phys. Res. Int.,* **2012**, 1 (2012).
12. C.A. Herme, G.P. Cicileo, P.G. Bercoff, S.E. Jacobo, *Pro. Mater. Sci.,* **9**, 150 (2015).
13. A. Kalendová, P. Rysánek, K. Nechvílová, *Prog. Org. Coat.,* **86**, 147 (2015).
14. J. Vidales, A. Lopez-Delgado, E. Vila, *J. Alloys Compd.*, **287**, 276 (1999).
15. M. Naseri, E. Saion, H. Ahangar, *J. Nanomater.*, **2010**, 1(2010).

447

16. Y. Qu, H. Yang, N. Yang, *J. Mater. Lett.,* **60**, 3548 (2006).
17. P. Aghav, V. Dhage, M. Mane, *J. Phys. B,* **406**, 4350 (2011).
18. P. Laokul, V. Amornkitbamrung, S. Seraphin, *J. Curr. Appl. Phys.,* **11**, 101 (2011).
19. B. Randhawa, M. Gupta, M. Kaur, *J. Ceram. Int.*, **35**, 3521 (2009).
20. S. Rana, J. Philip, B. Raj, *J. Mater. Chem. Phys.,* **124**, 264 (2010).
21. G. Fan, Z. Gu, L. Yang, F. Li, *J. Chem. Eng.,* **155**, 534 (2009).
22. Y.M.A. Ayana, S.M. El-Sawy, S.H. Salah, *Anticorr. Meth. Mater.* **44**, 381 (1997).
23. A.M. Musa, N.N. Shawal, H.U. dadum, M. Jibril, G. Abdurrahman, M.Z. Husna, *Appl. Mech. Mater.,* **695**, 110 (2015).
24. K.H. Kim, S.H. Lee, N.D. Nam, J.G. Kim, *Corr. Sci.,* **53**, 3576 (2011).

ИЗСЛЕДВАНЕ НА КОРОЗИЯТА НА ФЕРИТИ, ПРИГОТВЕНИ ПО ХИДРОТЕРМАЛЕН МЕТОД

С.У. Ратхер

Департамент по химично инженерство и материалознание, Университет „Крал Абдулазиз“, Джеда, Саудитска Арабия

(Резюме)

Цинковите и никеловите ферити се синтезират от метални нитрати по хидротермален метод, за да се изследват структурните, термичните и корозионните им свойства. Рентгено-структурните характеристики на двата ферита потвърждават челно-центрираната кубична (FCC) шпинелова структура с малки онечиствaн от хематит (α-Fe_2O_3). Термогравиметричният анализ и диференциално-сканиращата калориметрия показват две главни загуби на тегло (екзотермична и ендотермична), съответстващи на отстраняване на влага и разлагане на оксидите във феритите. Остри и Оже-електронни пикове се забелязват в рентгено-структурните спектри на двата ферита. Защитата от корозия на цинковия ферит се дължи на недостъпността на метала към редокс-реакции, докато корозионната защита при кобалтовия ферит се дължи на пасивиращия слой, формиран с времето.

Application of 1, 4-diaminoanthraquinone as a new selectophore material for construction of a potentiometric iron (III)-selective electrode

F. Kazemi[1], H. A. Zamani[1*], F. Joz-Yarmohammadi[1], M. Ebrahimi[1], M. R. Abedi[2]

[1]Department of Applied Chemistry, Mashhad Branch, Islamic Azad University, Mashhad, Iran
[2]Department of Applied Chemistry, Quchan Branch, Islamic Azad University, Quchan, Iran

A new Fe^{+3} selective electrode based on PVC membrane was prepared with a view to its application as an indicator electrode in the potentiometric cell. 1,4-Diaminoanthraquinone(DAQ) as a lipophilic selective element, sodium tetraphenylborate (NaTPB) as an anionic additive, nitrobenzene (NB) as a solvent mediator, and polyvinyl chloride (PVC) as a polymeric matrix were employed to form the membrane mixture. The best electrode response had a slope of 19.6 ± 0.2 mV per decade over a wide iron(III) concentration range (1.0×10^{-6} to 1.0×10^{-2} M) with a detection limit of 8.0×10^{-7}M. This electrode showed a fast response time (~12 s) over the whole concentration range in the pH range of 1.6-3.5. In order to study the selectivity of the electrode toward Fe^{+3}ions in presence of many common alkaline, alkaline earth, transition, lanthanide and heavy metal ions the matched potential method was applied. According to the obtained results the interference of all mentioned cations on the proposed iron(III) electrode was negligible. The sensor was successfully employed as an indicator electrode in the potentiometric titration of iron(III) with EDTA at pH 6.0. The applicability of the sensor was studied in determination of Fe^{3+} ions in mixtures with different ions.

Keywords: Sensor, Potentiometry, Ion-Selective Electrode, PVC Membrane

INTRODUCTION

Among different analytical methods, the potentiometric ion selective electrodes are mostly applied to determine the amount of various ions due to the wide linear range, low detection limit, good Nernstian slope, high sensitivity and selectivity, low cost, portability, easy maintenance, simplicity and speed of the usage, etc. [1-5].

Lately, a large number of PVC membrane electrodes for diverse ions such as iron were reported by us and other researchers [4-44].

Iron is a metal of the first transition series with atomic number 26. It is a mineral element which our body needs for numerous functions including complexation with oxygen in hemoglobin and myoglobin which are two prevalent proteins to transport oxygen in thebody. Moreover, the iron could be found in many other proteins and enzymes. The human body needs an appropriate amount of iron, otherwise the lack of iron causes iron-deficiency anemia. On the other hand, a high amount of iron in our body leads to iron poisoning [45].

In this paper the preparation of a new Fe^{+3} ion selective electrode was described, based on PVC membrane with DAQ as a selector element (Fig.1) with a special interaction between its heteroatoms such as nitrogen and iron(III) ion.
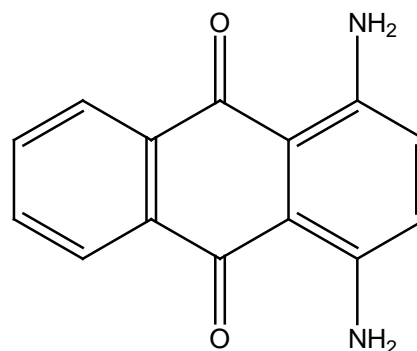
Fig. 1.1, 4-Diaminoanthraquinone (DAQ) structure

EXPERIMENTAL

Reagents

1, 4-Diaminoanthraquinone (DAQ) was purchased from Fluka. The nitrate and chloride salts of all used cations, reagent grade nitrobenzene (NB), acetophenone (AP), benzyl acetate (BA), dibutyl phthalate (DBP), sodium tetraphenyl borate (NaTPB), high molecular weight PVC,and tetrahydrofuran (THF) were purchasedfromMerck and Aldrich and used without modification or further treatments, except for the vacuum drying of the salts over P_2O_5. Doubly distilled deionized water was used in all experiments.

The EMF measurements

To potential measurement a Corning ion analyzer 250 pH/mV meter was used at 25.0 ℃. The activities were calculated by the Debye–Hückel procedure [46]. The electrochemical cell was assembled to

* To whom all correspondence should be sent:
E-mail:haszamani@yahoo.com

EMF measurements according to the following system:

Ag–AgCl | internal solution, $1.0×10^{-3}$ M Fe $(NO_3)_3$| PVC membrane | test solution | Hg–Hg$_2$Cl$_2$, KC1 (satd.)

PVC membrane electrode preparation

In order to prepare the membrane solution by the dipping method, specific amounts of PVC, ionophore (DAQ), plasticizer (NB), and anionic additive (NaTPB) were blended and dissolved in 3-5mL THF. AfterevaporatingTHF from the obtained solution an oily concentrated mixturewas formed. A pipet tip (3-5 mm o.d. on top) was dipped into the blend for about 5s in order to form a transparent membrane of about 0.3 mm thickness[47-55]. In the next stage the pipet tip was removed from the mixture and left at room temperature for about 12 h.At last the pipet tip was filled with $1.0×10^{-3}$ M Fe(NO$_3$)$_3$ solution as an internal filling solution and the pipet tip was soaked in the same solution for 24 has a pretreatment. A silver/silver chloride electrode was used as an internal reference electrode.

RESULTS AND DISCUSSION

Potential response of the electrode

In order to investigate the electrode response over a wide concentration range of various cationsnumerous polymeric liquid membrane sensors based on DAQ were fabricated. Due to the special structure of DAQ and its ability to form complexes with iron (III), the Fe^{+3} selective electrode showed the most sensitive response with a slope of 19.6±0.2 mV per decade (Fig. 2).

Effect of membrane composition

As the type and nature of membrane composition have a substantial impact on the ion selective electrodes response, to obtain the best Nernstian response with steady, noiseless and repeatable potentials, the membrane composition was optimized by employing various proportions of

additives, ionophore, plasticizer and PVC [56-61].
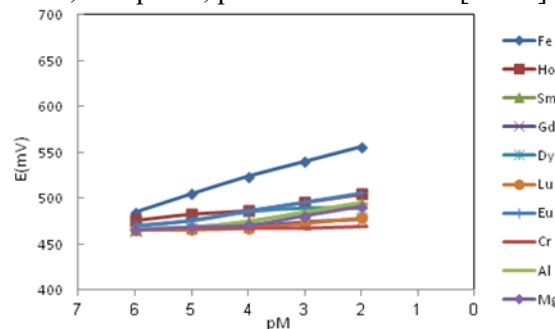
Fig. 2. Potential responses of various ion-selective electrodes based on DAQ.

According to the obtained results listed in Table 1, among four different plasticizers, NB showed the best sensitivity. Essentially the plasticizer acts as a solvent mediator to ameliorate the performance of the sensor via facilitating the movement of the ionophore in the polymeric membrane matrix. By changing the amount of NATPB the proper rate of ionic additives was achievedwhich could impress on the workability of the electrode by increasing the sensitivity of the membrane via reducing the ohmic resistance and speeding upthe process of ion extraction into the membrane [62-70]. Hence, the best Nernstian potential response was obtainedwith amembrane composition of (w/w):30% PVC, 5% DAQ, 2% NaTPB and 63% NB (electrode no.11).

Calibration curve

The potential response of the iron(III) selective electrode based on DAQ,which is demonstrated in terms of calibration curve (Fig. 3) shows the wide working range ($1.0×10^{-6}$ to $1.0×10^{-2}$ M) fortheoptimizedDAQ-based iron (III) ion selective electrode. The slope of the linear part of the calibration curve is 19.6±0.2 mV per decade with a detection limit of $8.0×10^{-7}$ M. According to the IUPAC recommendations, the detection limit is calculated bycrossing of two extrapolated segments of the calibration curve.

Table 1. Composition of membrane ingredients

Electrode No.	Composition of Carbon Paste (wt. %)							Slope (mV/ decade)	Dynamic Linear Range (M)
	PVC	NB	DBP	AP	BA	NaTPB	DAQ		
1	30	66	-	-	-	2	2	16.9±0.4	$1.0×10^{-6}$-$1.0×10^{-2}$
2	30	-	66	-	-	2	2	14.1±0.4	$1.0×10^{-5}$-$1.0×10^{-2}$
3	30	-	-	66	-	2	2	15.7±0.5	$1.0×10^{-5}$-$1.0×10^{-2}$
4	30	-	-	-	66	2	2	14.8±0.3	$1.0×10^{-5}$-$1.0×10^{-2}$
5	30	68	-	-	-	0	2	12.8±0.3	$1.0×10^{-4}$-$1.0×10^{-2}$
6	30	67	-	-	-	1	2	16.1±0.3	$1.0×10^{-6}$-$1.0×10^{-2}$
7	30	65	-	-	-	3	2	15.5±0.4	$1.0×10^{-6}$-$1.0×10^{-2}$
8	30	67	-	-	-	2	1	14.9±0.3	$1.0×10^{-6}$-$1.0×10^{-2}$
9	30	65	-	-	-	2	3	17.6±0.2	$1.0×10^{-6}$-$1.0×10^{-2}$
10	30	64	-	-	-	2	4	18.4±0.3	$1.0×10^{-6}$-$1.0×10^{-2}$
11	30	63	-	-	-	2	5	19.6±0.2	$1.0×10^{-6}$-$1.0×10^{-2}$
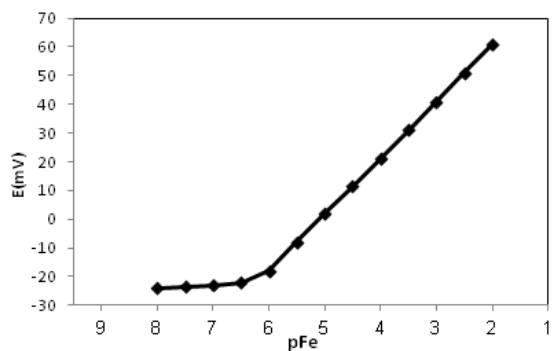
Fig. 3. Calibration curve of the DAQ-based Fe^{3+} sensor.

pH Effect

The profile of the designed electrode potential response versus the pH changes was investigated by employing 1.0×10^{-3} M Fe^{+3} solution and adding very small drops of HNO_3 or NaOH over the pH range 1.0-11.0. Pursuant to the obtained graph (Fig. 4) it is obvious that the working pH range of the electrode, where the potentials stay constant, is from 1.6 up to 3.5.
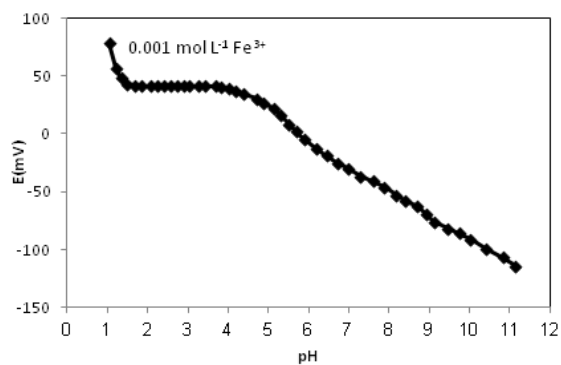
Fig. 4. The pH effect of the test solution on the potential response of the iron (III) sensor.

The potential drift at pH values lower than 1.6 could be attributed to the protonation of the heteroatoms of the ionophore, as a result of which DAQ loses the ability of forming complexes with the iron ions. On the other hand, the potential drift at higher pH values could be due to the formation of some hydroxyl complexes of Fe^{3+} ions in solution, which results in reduced amount of free iron (III) ions in the solution [71].

Dynamic response time

One of the most important factors in analytical applications is the response time of the ion selective electrode, which is defined as the average time needed to reach a stable potential value of the ion selective electrode after sequential submerging of electrodes in a series of primary ion solutions with ten-fold difference in concentration. In order to

measure the dynamic response time of the Fe^{+3} ion selective electrode, various concentrations of Fe^{+3} over the range from 1.0×10^{-6} to 1.0×10^{-2} M were employed. According to the obtained results illustrated in figure 5, the average response time required for the iron(III) electrode is about 12 s.
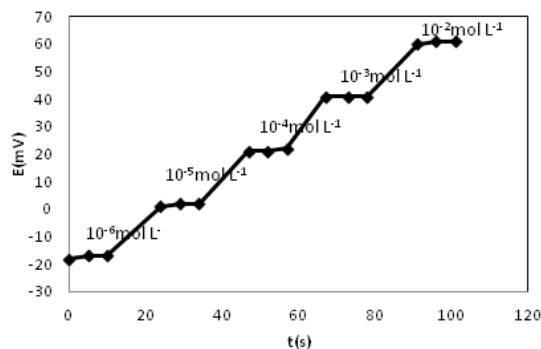
Fig. 5. Dynamic response time of Fe^{3+} sensor

Selectivity of the sensor

To assess the effect of interfering ions including lanthanides, alkali and alkaline earth elements, transition and heavy metals on the potential response of the proposed electrode, the selectivity coefficients were determined graphically by the match potential method (MPM). In order to determine the selectivity coefficients by MPM, the potential of adding the specific activity (concentration) of a Fe^{+3} solution to a reference solution was measured. On the other hand, in a separate experiment, a certain amount of various interfering ions was sequentially added to the same reference solution, as long as the obtained potential response matches the initial one. Eventually, by the ratio of primary ion (A) activity changes to the interfering ion (B) according to the following equation, the matched potential method selectivity coefficient (K_{MPM}) was determined for each cation [72]:

$$K_{ij}^{MPM} = \frac{\Delta a_A}{a_B}$$

Pursuant to the resulting values, which are summarized in table 2, the interference of other cations on the proposed electrode was negligible. This points to a very high performance of the designed electrode toward Fe^{+3} ions and special interaction between Fe^{+3} ions and DAQ.

Analytical applications

To verify the practical utility of the proposed electrode, it was applied as an indicator electrode in order to determine iron (III) in a potentiometric titration of 25 mL of 1.0×10^{-4} M Fe^{3+} solution with 1.0×10^{-2} M EDTA at pH=6 adjusted by acetate buffer. As figure 6 shows, by increasing the amount

Table 2. Selectivity coefficients ($K_{Fe^{3+}}^{MPM}$) of the proposed Fe^{3+} sensor.

Interfering Ion	$K_{Fe^{3+},B}^{MPM}$	Interfering Ion	$K_{Fe^{3+},B}^{MPM}$
Ho^{3+}	8.0×10^{-4}	Dy^{3+}	1.0×10^{-3}
La^{3+}	8.0×10^{-4}	Ca^{2+}	2.0×10^{-3}
Tm^{3+}	1.5×10^{-3}	Co^{2+}	1.0×10^{-3}
Nd^{3+}	1.0×10^{-3}	K^+	1.0×10^{-3}
Eu^{3+}	8.5×10^{-4}	Pb^{2+}	8.0×10^{-4}
Pr^{3+}	8.5×10^{-4}	Ni^{2+}	1.0×10^{-3}
Yb^{3+}	2.0×10^{-3}	Mg^{2+}	8.0×10^{-4}
Lu^{3+}	1.0×10^{-3}	Cd^{2+}	1.0×10^{-3}
Er^{3+}	8.0×10^{-4}	Na^+	8.0×10^{-4}
Tb^{3+}	1.5×10^{-3}	Cr^{3+}	2.5×10^{-3}
Sm^{3+}	8.5×10^{-4}		

Table 3. Determination of Fe^{3+} in presence of a mixture of metal ions.

Fe^{3+}(M)	Added cations (M)	Found[a](M)	Recovery (%)
1.0×10^{-6}	$(0.001)Eu(NO_3)_3$ & $(0.001)Er(NO_3)_3$	1.03×10^{-6}	103
1.0×10^{-6}	$(0.001)Gd(NO_3)_3$ & $(0.001)Pr(NO_3)_3$	1.03×10^{-6}	103
1.0×10^{-6}	$(0.001)La(NO_3)_3$ & $(0.001)Ho(NO_3)_3$	1.03×10^{-6}	103
1.0×10^{-6}	$(0.001)Dy(NO_3)_3$ & $(0.001)Yb(NO_3)_3$	1.00×10^{-6}	100
1.0×10^{-6}	$(0.001)Tb(NO_3)_3$ & $(0.001)Nd(NO_3)_3$	1.03×10^{-6}	103
1.0×10^{-6}	$(0.001)Pb(NO_3)_2$ & $(0.001)Ni(NO_3)_2$	1.00×10^{-6}	100
1.0×10^{-6}	$(0.001)Cr(NO_3)_3$ & $(0.001)Cd(NO_3)_3$	1.03×10^{-6}	103
1.0×10^{-6}	$(0.001)KNO_3$ & $(0.001)Mg(NO_3)_2$	1.00×10^{-6}	100
1.0×10^{-6}	$(0.001)NaNO_3$ & $(0.001)Ca(NO_3)_2$	1.03×10^{-6}	103
1.0×10^{-6}	$(0.001)Pb(NO_3)_2$ & $(0.001)Ca(NO_3)_2$ & $(0.001)KNO_3$	1.00×10^{-6}	100
1.0×10^{-6}	$(0.001)Cr(NO_3)_3$ & $(0.001)Na(NO_3)$ & $(0.001)Ca(NO_3)_2$	1.03×10^{-6}	103

[a]Results are based on three measurements

of EDTA, a reduction in the potential values is seen, which is attributed to a decrease in free iron(III) concentration due to complexation with EDTA. As a result, the sharp end point in the titration curve reflects the fact that this electrode could successfully play the role of an indicator electrode. Furthermore, the designed Fe^{+3} electrode was employed to determine Fe^{+3} ions in presence of binary mixtures containing various cations, the result of which, listed in table 3, demonstrates the acceptable recovery for Fe^{+3} ion in all mixtures.
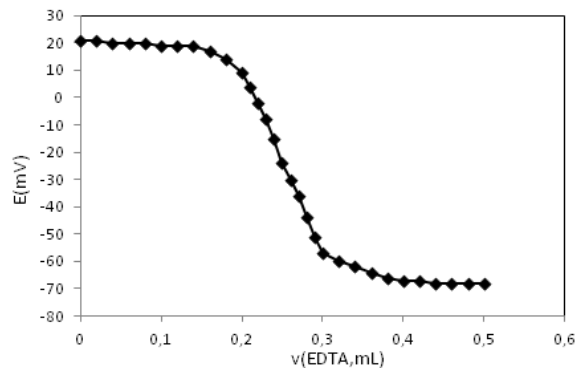
Fig. 6. Potential titration curves of 25 mL of 1.0×10^{-4} M Fe^{3+} solution with 1.0×10^{-2} M of EDTA.

CONCLUSION

In the present work, a new iron-selective PVC membrane electrode based on DAQ as a carrier ion and NB as a solvent mediator was developed. The best membrane composition (5% DAQ, 2% NaTPB, 30% PVC, 63% NB) showed a slope of 19.6±0.2 mV decade⁻¹ in the linear range of 1.0×10^{-6} -1.0×10^{-2} M and a limit of detection of 8.0×10^{-7}M. This electrode is independent of pH changes in the range of 1.6-3.5. It was successfully employed in titration and direct potentiometric methods.

REFERENCES

1. H. A. Zamani, M. T. Hamed-Mosavian, E. Hamidfar, M. R. Ganjali, P. Norouzi, *Mater. Sci. Eng. C,* **28**, 1551 (2008).
2. M. Pooyamanesh, H.A. Zamani, G. Rajabzadeh, M.R. Ganjali, and P. Norouzi, *Anal. Lett.*, **40,** 1596 (2007).
3. H.A. Zamani, M.R. Ganjali, H. Behmadi, M.A. Behnajady, *Mater. Sci. Eng. C,* **29**, 1535 (2009).
4. H.A. Zamani, M. Shoshtari, B. Feizyzadeh, *Int. J. Electrochem. Sci.,* **10**, 8644 (2015).
5. H.A. Zamani, M.R. Ganjali, F. Faridbod, M. Salavati-Niasari, *Mater. Sci. Eng. C,* **32,** 564 (2012).
6. K. Alizadeh, R. Parooi, P. Hashemi, B. Rezaei, and M. R. Ganjali „*J. Hazard Mater,* **186**, 1794 (2011).

7. H.A. Zamani, A. Imani, A. Arvinfar, F. Rahimi, M.R. Ganjali, F. Faridbod, and S. Meghdadi, *Mater. Sci. Eng. C*, **31**, 588 (2011).

8. M. R. Ganjali, N. Motakef-Kazami, F. Faridbod, S. Khoee, P. Norouzi, *J Hazard Mater*, **173**, 415 (2010).

9. H.A. Zamani, M.R. Ganjali, F. Faridbod, and M. Salavati-Niasari, *Mater. Sci. Eng. C*, **32**, 564 (2012).

10. R. Zare-Dorabei, P. Norouzi, M.R. Ganjali, *J Hazard Mater*, **171**, 601 (2009).

11. H. A. Zamani, B. Feizyzadeh, F. Faridbod, M. R. Ganjali, *Sensor Lett.*, **9**, 1767 (2011).

12. M. Masrournia, H.A. Zamani, H.A. Mirrashid, M.R. Ganjali, F. Faridbod, *Mater. Sci. Eng. C,* **31**, 574 (2011).

13. H.A. Zamani, M. Mohammadhossieni, Saeed Haji-Mohammadrezazadeh, F. Faridbod, M. R. Ganjali, S. Meghdadi, A. Davoodnia, *Mater. Sci. Eng. C,* **32**, 12 (2012).

14. A. S. Dezfuli, M. R. Ganjali, P. Norouzi, *Mater. Sci. Eng. C*, **42**, 774 (2014).

15. M. R. Ganjali, M. Hosseini, A. Ghafarloo, M. Khoobi, F. Faridbod, A. Shafiee, P. Norouzi, *Mater. Sci. Eng. C*, **33**, 4140 (2013).

16. H. A. Zamani, B. Feizyzadeh, F. Faridbod, and M.R. Ganjali, *Mater. Sci. Eng. C,* **31**, 1379 (2011).

17. H.A. Zamani, B. Feizyzadeh, F. Faridbod, M.R. Ganjali, *Sensor Lett.,* **9**, 1767 (2011).

18. H. Ilkhani, M. R. Ganjali, M. Arvand,; F. Faridbod, P. Norouzi, *Mater. Sci. Eng. C*, **32**, 653 (2012).

19. H. A. Zamani, R. Kamjoo, M. Mohammadhossieni, M. Zaferoni, Z. Rafati, M. R. Ganjali, F.Faridbod, S. Meghdadi, *Mater. Sci. Eng. C,* **32**, 447 (2012).

20. A. Shirdel, H.A. Zamani, F. Joz-Yarmohammadi, S.A. Beyramabadi, M.R. Abedi, *J. Incl. Phenom. Macrocycl. Chem.,* **86**, 351 (2016).

21. H.A. Zamani, F. Joz-Yarmohammadi, M.R. Abedi, *J. Indian Chem. Soc.,* **93**, 1035 (2016).

22. H. A. Zamani, A. Imani, A. Arvinfar, F. Rahimi, M. R. Ganjali, F. Faridbod, S. Meghdadi, *Mater. Sci. Eng. C,* **31**, 588 (2011).

23. H.A. Zamani, Fatemeh Naghavi-Reyabbi, M. Mohammadhossieni, Babak Feizyzadeh, M.R. Abedi, F. Faridbod, M. R. Ganjali, *Sensor Lett.,* **10**, 112 (2012).

24. H.A. Zamani, S. Langroodi, S. Meghdadi, *E-J. Chem.* **8**, S237 (2011).

25. H.A. Zamani, B. Feizyzadeh, F. Faridbod, M.R. Ganjali, *Mater. Sci. Eng. C*, **31**, 137 (2011).

26. M.R. Abedi, H.A. Zamani, *E-J. Chem.,* **8**, S467 (2011).

27. Y. Umezawa, K. Umezawa, H. Sato, *Pure Appl. Chem.*, **67**, 507 (1995).

28. S. Moshirian Farahi, H.A. Zamani, F. Joz-Yarmohammadi, M.R. Abedi, H. Behmadi, *J. Indian Chem. Soc.,* **93**, 1139 (2016).

29. H.A. Zamani, M.S. Zabihi, M. Rohani, A. Zangeneh-Asadabadi, M.R. Ganjali, F. Faridbod, S. Meghdadi, *Mater. Sci. Eng. C*, **31**, 409 (2011).

30. V. K. Gupta, R. N. Goyal, R.A. Sharma, *Int. J. Electrochem. Sci.*, **4**, 156 (2009).

31. F. Ghasediana, H.A. Zamani, F. Joz-Yarmohammadi, S.A. Beyramabadi, M.R. Abedi, *Russ. J. Appl. Chem.,* **89**, 2001 (2016).

32. H. A.Zamani, M. Rohani, M. Mohammadhosseini, M. R. Ganjali, F. Faridbod, S. Meghdadi, *Sensor Lett.*, **9**, 1745 (2011).

33. H. A. Zamani, M. R. Ganjali, F. Faridbod, *J. Serb. Chem. Soc.,* **76**, 1295 (2011).

34. M. Ebrahimi, H.A. Zamani, M.R. Abedi, *J. Indian Chem. Soc.,* **91**, 431 (2014).

35. H.A. Zamani, F. Naghavi-Reyabbi, F. Faridbod, M. Mohammadhosseini, M.R. Ganjali, A. Tadjarodi, M. Rad, *Mater. Sci. Eng. C*, **33**, 870 (2013).

36. H.A. Zamani, F. Faridbod, M.R. Ganjali, *Mater. Sci. Eng. C* , **43**, 488 (2014).

37. H.A. Zamani M. Zaferoni, S. Meghdadi, *E-J. Chem.,* **9**, 1941 (2012).

38. H.A. Zamani, *E-J. Chem.*, **9**, 83 (2012).

39. F. Joz-Yarmohammadi, H.A. Zamani, F. Mohammadabadi, *Int. J. Electrochem. Sci.*, **10**, 8124 (2015).

40. F. Mohammadabadi, H.A. Zamani, F. Joz-Yarmohammadi, M.R. Abedi, *Int. J. Electrochem. Sci.*, **10**, 2791 (2015).

41. H.A. Zamani, M. Ranjkesh, and M.R. Abedi, *Int. J. Electrochem. Sci.,* **9**, 8435 (2014).

42. H.A. Zamani, and Faridbod, *J. Anal. Chem.,* **69**, 1073 (2014).

43. H.A. Zamani, A. Zanganeh-Asadabadi, M. Rohani, M. S. Zabihi, J. Fadaee, M. R. Ganjali, F. Faridbod, and S. Meghdadi, *Mater. Sci. Eng. C*, **3**, 984 (2013).

44. H. A. Zamani, F. Faridbod, M.R. Ganjali, *Mater. Sci. Eng. C*, **33**, 608 (2013).

45. O.R. Kirk, F.D. Othmer, *Encyclopedia of Chemical Technology,* Wiley, New York, 1982.

46. S. Kamata, A. Bhale, Y. Fukunaga, A. Murata, Anal. Chem., **60**, 2464 (1998).

47. H.A. Zamani, M.R. Ganjali, P. Norouzi,M.Adib, *Sensor Lett.,* **5**, 522 (2007).

48. E. Naddaf, H. A. Zamani, *Anal. Lett.*,**42**, 2838 (2009).

49. H. A. Zamani, M. R. Ganjali, P. Norouzi, S. Meghdadi, *Anal. Lett.,* **41**, 902 (2008).

50. H. A. Zamani, M. R. Ganjali, M. Adib, *Sensor Lett, .***4**, 345 (2006).

51. H. A. Zamani, M. R. Ganjali, H. Behmadi, M. A. Behnajady, *Mater. Sci. Eng. C*, **29**, 1535 (2009).

52. H.A. Zamani, M. Rohani, A. Zangeneh-Asadabadi, M.S. Zabihi, M.R. Ganjali, M. Salavati-Niasari, *Mater. Sci. Eng. C*, **30**,917 (2010).

53. H. A. Zamani, M. Mohammadhosseini, M. Nekoei, and M. R. Ganjali, *SensorLett.,* **8,** 303 (2010).

54. M. R. Abedi, H. A. Zamani, *Anal. Lett.,* **41**, 2251 (2008).

55. H.A. Zamani, M.R. Ganjali, P. Norouzi, A. Tadjarodi, and E. Shahsavani, *Mater. Sci. Eng. C*, **28**, 1489 (2008).

56. H.A. Zamani, M. Masrournia, H. Mohamadzadeh, M. R. Ganjali, M. Rahimizadeh, P. Ziaei, *Mater. Sci. Eng. C*, **29**, 976 (2009).

57. H. A. Zamani, M. Nekoei, M. Mohammadhosseini, M. R. Ganjali, *Mater. Sci. Eng. C,* **30,** 480 (2010).

58. M. Mohammadhossieni, H.A. Zamani, M. Nekoei ,*Anal. Lett.,* **42**, 298 (2009).
59. H.A. Zamani, M. Masrournia, S. Sahebnasagh, M. R. Ganjali, *Anal. Lett.,* **42**, 555 (2009).
60. H. A. Zamani, M. Masrournia, M. Rostame-Faroge, M. R. Ganjali, H. Behmadi, *Sensor Lett.,* **6**, 759 (2008).
61. E. Ammann, E. Pretsch, W. Simon, E. Lindner, A. Bezegh, and E. Pungor, *Anal Chim. Acta.,* **171**, 119 (1985).
62. G.J. Moody, B.B. Saad, J.D.R. Thomas, *Sel. Electrode Rev.,* **10**, 71 (1988).
63. N. Zaheiritousi, H. A. Zamani, M. R. Abedi, S. Meghdadi, *Int. J. Electrochem. Sci.,* **12**, 2647 (2017).
64. H.A. Zamani, M.R. Ganjali, H. Behmadi, and M.A. Behnajady, *Mater. Sci. Eng. C,* **29**, 1535 (2009).
65. H.A. Zamani, G. Rajabzadeh, M.R. Ganjali, *Sensor Lett.,* **7**, 114 (2009).
66. M. Pooyamanesh, H.A. Zamani, G. Rajabzadeh, M.R. Ganjali, and P. Norouzi, *Anal. Lett.,* **40**, 1596 (2007).
67. H. A. Zamani, M. T. Hamed-Mosavian, E. Hamidfar, M. R. Ganjali, P. Norouzi, *Mater. Sci. Eng. C,* **28**, 1551 (2008).
68. H. A. Zamani, M. Ranjkesh, M. R. Abedi, M. Salavati-Niasari, *Int. J. Electrochem. Sci.,* **9**, 6475 (2014).
69. M. R. Ganjali, P. Norouzi, F. Faridbod, S. Riahi, J. Ravanshad, J. Tashkhourian, M. Salavati-Niasari, M. Javaheri, *IeeeSens J*, **7**, 544 (2007).
70. H. A. Zamani, M. Ranjkesh, M. R. Abedi, S. Meghdadi, *Int. J. Electrochem. Sci.,* **9**, 6485 (2014).
71. H.A. Zamani M. Zaferoni, S. Meghdadi, *E-J. Chem.,* **9**, 1941 (2012).
72. S. K. Mittal, P. Kumar, A. Kumar S K, L. F Lindoy, *Int. J. Electrochem. Sci.,* **5**, 1984 (2010).

ПРИЛОЖЕНИЕ НА 1, 4-ДИАМИНОАНТРАХИНОН КАТО НОВ СЕЛЕКТОФОРЕН МАТЕРИАЛ ЗА ПРОИЗВОДСТВОТО НА ПОТЕНЦИОМЕТРИЧЕН Fe(III)-СЕЛЕКТИВЕН ЕЛЕКТРОД

Ф. Каземи[1], Х.А. Замани[1], Ф. Джоз-Ярмохамади[1], М. Ебрахими[1], М.Р. Абеди[2]

[1]*Департамент по приложна химия, Ислямски университет „Азад“, Клон Машхад, Машхад, Иран*
[2] *Департамент по приложна химия, Ислямски университет „Азад“, Клон Кучан, Кучан, Иран*

(Резюме)

Приготвен е нов, йон-селективен електрод за определянето на Fe^{+3} , базиран на PVC-мембрана. Индикаторният електрод е предназначен за потенциометрични определяния. Използват се 1,4-диаминоантрахинон (DAQ) като липолитичен селективен агент, натриев тетрафенилборат (NaTPB) като анионна добавка, нитробензен (NB) като разтворител-медиатор и поливинилхлорид (PVC) като полимерна матрица. Най-добър отговор на електрода се при наклон 19.6 ± 0.2 mV за декада за широк интервал на концентрации на желязо (III) от 1.0×10^{-6} до 1.0×10^{-2} М при чувствителност от 8.0×10^{-7} М. Този електрод показва бърз отговор (~12 s) за широк интервал от концентрации на Fe^{+3} (1.0×10^{-6} М до 1.0×10^{-2} М) за pH в обхвата 1.6-3.5. Селективността на електрода спрямо Fe^{+3} е изследвана в присъствие на много метални йони (алкални, алкалоземни, тежки метали, преходни елементи и лантаниди). Според получените резултати смущенията от страна на изследваните метали са пренебрежими. Така направеният сензор е използван успешно при потенциометричното титруване на разтвори на желязо (III) с EDTA при pH 6.0. Приложимостта на сензора е потвърдена и в присъствие на смеси от различни йони.

Evaluating the performance of decision-making units using hybrid neural network model for predicting the performance and data envelopment analysis approach Case study: Khuzestan steel company treatment plant

K.Rahbari[1], A.H. Hassani[2*], M.R. Mehrgan[3], A.H. Javid[4]

[1-]*Department of Environmental Science, Faculty of Environment and Energy, Tehran Science and Research Branch, Islamic Azad University, Tehran, Iran*
[2-]*Department of Environmental Engineering, Faculty of Environment and Energy, Tehran Science and Research Branch, Islamic Azad University, Tehran, Iran*
[3-]*Department of Management, University of Tehran, Iran*
[4-]*Department of Environmental Science, Faculty of Marine Science and Technology, Tehran Science and Research Branch, Islamic Azad University, Tehran, Iran*

One of the main problems with using Data Envelopment Analysis (DEA) is the weak separability of the decision-making units. This is mainly due to the low number of units compared to the number of inputs and outputs of the model [1]. This problem is evident in evaluation of the performance of 144 decision-making units (2007-2014) of Khuzestan Steel Company industrial wastewater treatment plant due to the large number of inputs and outputs of the treatment system. Thus, in the present research, in order to evaluate the performance of the treatment plant in removal of environmental pollutants, first input-based CCR model was used to rank efficient units in the form of DEA models and weaknesses of the models in terms of calculation and separability of efficiency of the treatment plant. Then, in order to analyze and evaluate the efficiency of the treatment plant, neural networks for predicting the performance in the form of hybrid models of data envelopment analysis and artificial neural networks (Neuro/DEA) were used. The result of the analysis of the calculated efficiency of the units using these models suggested the strength of the network in calculation and separability of the treatment plant performance in terms of efficiency over the studied years.

Keywords: treatment plant, efficiency, data envelopment analysis, artificial neural networks (ANN), neuro-DEA

INTRODUCTION

Measurement of efficiency, due to its importance in evaluation of the performance of a system, has always been considered by researchers. In 1957, Farrel used a method similar to engineering efficiency measurement to evaluate the efficiency of a production unit. In his study, Farrel considered one input and one output. His study consisted of evaluating the technical efficiency and allocation and the efficient production function derivative. Farrel used his model to estimate the efficiency of USA agriculture section in comparison to other countries. However, he was not successful in presenting a model containing multiple inputs and outputs [2]. Charnes, Cooper and Rohdes developed Farrel's model and presented a model which had the ability to evaluate the efficiency using multiple inputs and outputs. This model was called Data Envelopment Analysis. Since this model was presented by Charnes, Cooper, and Rudez, it became known as CCR model, which stood for the initials of the names of these three researchers. The aim of this model is to evaluate and compare the relative efficiency of organizational units with multiple inputs and outputs similar to each other [3]. Evidently, creating an efficient system and optimal use of the resources will prevent from wasting substantial amounts of material and moral resources, that is, a small percentage of increase in efficiency can save a large amount of resources. Therefore, studying the level of efficiency in industrial treatment systems is essential. Although choosing the best process for the treatment of industrial waste is important, some quantitative studies have been conducted in this regard using numerous scientific and mathematical techniques and have had a good feedback [4].

To reach this goal, it is necessary to, first, evaluate and analyze the performance of the treatment systems and then identify the units that are not efficient, determine the causes of their inefficiency and try to remove them. Many methods for measuring efficiency have been proposed in the research literature, but in comparison to other models, DEA is a better method for organizing and analyzing the data, because it allows for changes in efficiency over time and requires no assumptions about efficiency limit [5]. Therefore, DEA has been

---

used more than any other method for evaluating the performance and is a suitable technique for comparing the units in terms of efficiency. However, the efficiency limit obtained from DEA is sensitive to statistical turbulence and outlying data caused by measurement errors or any external factor and statistical turbulence or outlying data may shift the efficiency limit and deviate the analysis results [6]. Therefore, caution should be taken in using DEA to evaluate the performance of other decision-making units (DMU). Thus, recently Artificial Neural Networks have been used as a suitable alternative for estimation of efficiency limits for decision-making, because due to their learning ability and generalizability, the performance of neural networks is such that they are more resistant to outlying data and turbulence caused by inaccurate measurement [7].

In 2011, Salgado *et al.,* in a research entitled Evaluation of Efficiency of Wastewater Treatment Plants using Data Envelopment Analysis (DEA) Method, studied modern technologies for comparing the efficiency of wastewater treatment technologies. In order to calculate technological economic efficiency and Technological Gap Ratios (TGRs) of WasteWater Treatment Plants (WWTPs), a heterogeneous technological factor was used. This model included four alternative technologies: activated sludge, aerated lagoon, trickling filter and biological rotation. The results showed that the mean efficiency was relatively high and uniform across various technologies. Furthermore, analysis of the calculation of technological economic efficiency and technological gap ratios (TGRs) indicates that optimal technological economic efficiency for WWTPs is using activated sludge and basically, it could be stated that activated sludge is more efficient compared to other technologies [8].

Nasr (2012) used an artificial neural networks method to study the reduction of efficiency costs in a treatment plant in Egypt. In this study, the data including input Total Suspended Solids (TSS), Chemical Oxygen Demand (COD) and Biological Oxygen Demand (BOD), environmental temperature, pH, Mixed Liquor Suspended Solids (MLSS) concentration in aerated lagoon, nitrogen and phosphorus were used in the network for a year. The results showed that Feed Forward Back Propagation (FFBP) Neural Network with a correlation coefficient of 0.9 can estimate the return sludge in this treatment plant [9].

Neelakantan *et al.* (2014) used artificial neural networks to predict the qualitative factors of output wastewater of industrial/urban treatment plants in

the United States. In this study, multilayer perceptron (MLP-7) artificial neural network, which is the most common neural network structure, was employed. They used the characteristics of sewage pH, COD and BOD in the neural network input in order to predict pH, COD and BOD in the wastewater. Their results showed good efficiency of the used neural network with minimum absolute percentage errors (MAPEs) of 4, 11 and 7 for pH, COD and BOD, respectively [10].

Steel industry is one of the main consumers of water and Khuzestan Steel Plant, due to its geographical location, has diverse and abundant water consumptions. In a process where sewage is collected and reused in the best way possible, efficiency has a special role in all the stages and can play a significant role in sustainable development of the country. This research develops and presents a new approach based on DEA models to evaluate the performance of wastewater treatment plant of Khuzestan Steel Company by which in addition to evaluating the current efficiency of the performance of treatment plant in removal of the pollutants, predictions can be made of the quality of the output wastewater in the future. In this research, it is tried to use neural networks, DEA and a combination of the two (Neuro/DEA) to measure the technical efficiency of the industrial treatment plant of Khuzestan Steel Company (2009-2014). After calculation of efficiency, the obtained results are compared with the conventional DEA results, because given the number of inputs and outputs, basic DEA models cannot rank the units. The rest of the article is arranged as follows. Section two contains an overview of the principles of DEA and section three briefly introduces neural networks. Section four describes the used method and structure of Neuro/DEA, and in section five the data are analyzed. Finally, section six includes conclusion and recommendations for future research.

RESEARCH METHOD

Studied area

Khuzestan Steel Company treatment plant

With an area of 3.8 square kilometers, Khuzestan Steel Company is located on the 10th kilometer of Ahwaz-Imam Khomeini Port road. Khuzestan Steel Company wastewater treatment plant was established in 2006 and began operation in 2008. Wastewater treatment plant was constructed next to the south wing of the factory. The current capacity of the wastewater treatment plant is 3000 m³/h and in the future, it can be increased to 5715 m³/h. The wastewater produced

by various units of Khuzestan Steel Complex enters the main canal through two (eastern-southern) canals.

This treatment plant uses physical/chemical treatment methods in several stages during the operation (such as increasing polyelectrolyte and alum and directing the wastewater to settling basins in order to reduce suspended materials, etc.). The effluent is discharged directly to Maleh River by considering environmental standards and eventually, enters Shadegan international wetland and some of it is employed to irrigate the company's green area. (Khuzestan Steel Company Public Relations Department, 2012)

Due to the high volume of this wastewater, discharging it to the environment without observance of control measures can cause considerable damage to the environment. In recent decades, many legal regulations and restrictions on the methods of treatment and disposal of industrial wastewater to the environment have been established. Therefore, to solve the problem of wastewater, environmental experts have proposed two general ideas: reuse and final disposal.

The treatment process of this plant is shown in Figure 1.

Sampling and Analysis methods

In this research, the data from raw sewage and output wastewater of Khuzestan Steel Company industrial wastewater treatment plant were studied.

Since for modeling data with a high degree of accuracy and richness in the studied period are required, parameters and quality indicators were used that create an output for an input (2009-2014). Thus, Oil, COD, TSS and pH factors were selected. Raw sewage and output wastewater were sampled to measure and monitor the above-mentioned parameters and based on the book *Standard Methods for the Examination of Water and Wastewater,* input sewage samples were kept in polyethylene and glass containers on which the date, time and place of sampling, as well as the water temperature at the time of sampling had been written and these containers were immediately transferred to the laboratory of Khuzestan Steel Company where tests were performed on the parameters (Table 1). To analyze the output wastewater, online monitoring systems were used, the specifications of which are given in the equipment and devices section.

Equipment and devices:

To analyze the output wastewater, online monitoring devices were used, the specifications of which are given in the following: HACH-LANGE FP 360 sc was used to measure Oil and G, HACH-LANGE UVAS Plus was adopted to measure COD, HACH-LANGE SOLITAX sc was employed to measure TSS and HACH-LANGE 1200-S/sc100 was used to measure pH.
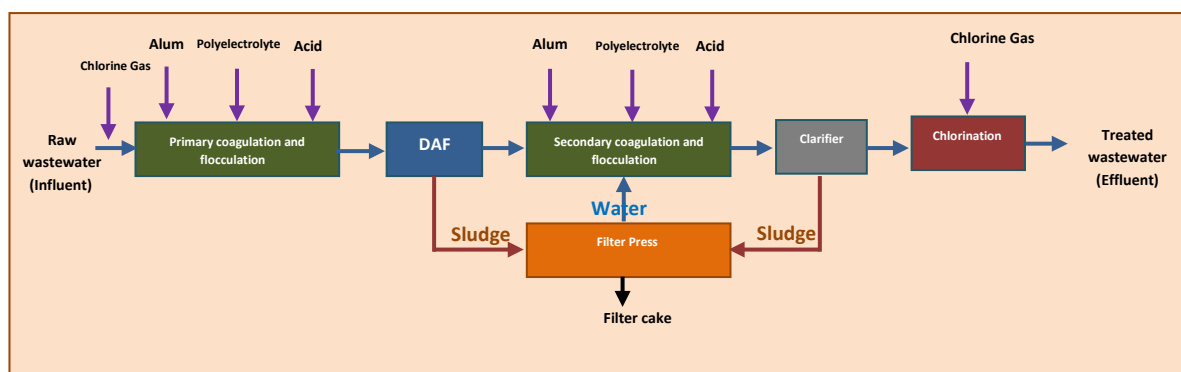
Fig. 1. Schematic of the process of Khuzestan Steel Company industrial wastewater treatment plant

Table 1. Methods of conducting the examinations (Standard methods for the examination of water and wastewater)

	Method number	Used method	Parameter	Number
4500 - M. B.	Section 4- p. 86	Electrometric method	pH[*1]	1
2540 D.	Section 2- p. 57	Total suspended solids dried at 10^3-10^5 CC [*4]	Total suspended solids[*2]	2
5220 .B.	Section 5- p. 13	Reading COD	Chemical oxygen demand[*3]	3
5220 .B.	Section 5- p. 35	Ben Marie– Oil&G	Oil	4

[*1-] Method of calculating pH: using pH Meter Metrohm type made in Switzerland.

[*2-] Method of calculating TSS: using vacuum pump.

[*3-] Method of calculating COD: kept for 2 h at a temperature of 150ºC in a DRB200 reactor (HACH Company) and read by DR5000 (HACH Company).

[*4-] Cubic centimeter

Table 2. Inputs and outputs of the model

Parameter	Output	Parameter	Input
Oil	O_1	Oil	I_1
COD	O_2	COD	I_2
TSS	O_3	TSS	I_3
pH	O_4	pH	I_4

Other devices that were used in the examinations were Memmert oven and incubator, Sartorius GM 502 digital scale with an accuracy of 0.00001. The chemicals used were products of Merck Company, Germany. It should be noted that all laboratory operations were carried out in the environmental laboratory of Khuzestan Steel Company and all the used devices belonged to this center.

Stages of the research

This research is conducted in four stages:
Stage one: Data collection;
Stage two: Reviewing, selecting and collecting data on wastewater and effluent quality index, according to the past years' statistics;
Stage three: Sampling and testing parameters and quality indices in the input wastewater and effluent from the treatment plant;
Stage four: Data analysis and modeling.

Steps in the analysis of performance and determining the efficiency of the treatment system:

First step: Collecting the data related to Decision Making Units (DMUs) input/output:

In the study of real systems, to calculate the efficiency, the first step is to determine the inputs and outputs of each DMU so that they reflect the efficiency. In analyzing the efficiency of treatment plants, determining inputs and outputs is particularly important, because each DMU or time period has numerous inputs and outputs and considering a lot of them or ignoring them will cause some problems. After determining the inputs and outputs of each DMU, to compare and measure the efficiency of DMUs, the data related to each DMU were collected.

Each year, 24 samples (2 samples per month) are taken for the 4 input and output parameters (Oil, COD, TSS, pH) and it could be stated that each year we had 24 DMUs and over a six-year research period, a total of 144 DMUs are calculated (Table 2).

Second step: After collecting the data, the efficiency of all DMUs is calculated using the CCR model. In this research, the data related to all DMUs from 2009 to 2014 (each year includes 24 DMUs, where DMU-1 represents August and DMU-24 represents July) are used for the input (Oil, COD, TSS, pH) and output (Oil, COD, TSS, pH) parameters. (Similar input and output parameters)

Third step: The data required for training the artificial neural network are obtained from the results of the DEA-CCR model.

Fourth step: In this stage, the artificial neural network (ANN) is trained using the data selected in the previous step.

Fifth step: The efficiency of the performance of the industrial wastewater treatment plant of Khuzestan Steel Company is predicted using artificial neural networks (ANNs).

Data Envelopment Analysis (DEA)-(DEA-CCR model):

Data Envelopment Analysis (DEA) is a method adopted to measure the relative efficiency of decision making units (DMUs). In DEA, the criteria are not weighed by the decision maker and this is done by the model in a way that each DMU achieves its highest level of efficiency. A DMU is an institution which turns the data into outputs. DMUs are units that perform similar types of tasks and share the same goals and ideals. DMUs which are used in DEA must be homogeneous and have the same kind of data and outputs [11].

Efficiency is defined as the ratio of the output to input. When there are multiple inputs and outputs, efficiency is defined as the ratio of weighed total outputs to weighed total inputs. If the values of the inputs and outputs are known, efficiency is simply calculated as follows (Equation 1):

$$TE_i = \frac{u_1 y_{1i} + ... + u_s y_{si}}{v_1 x_{1i} + ... + v_m x_{mi}} \qquad (Eq.1)$$

where v is the input value and u is the output value of the ith unit. But the difficulty is in determining the value of inputs and outputs. If the units under evaluation are manufacturing units, evaluating or pricing the inputs and outputs is not difficult but if they are not manufacturing units, determining the real value of the inputs and outputs is difficult and perhaps impossible. Therefore, in the DEA method the value of the inputs and outputs is assumed variable and in order to calculate efficiency, the following fractional model was

presented by Charnes, Cooper and Rhodes in 1978, which is known as CCR model. (Equation 2):

$$\max \quad \frac{\sum\limits_{r} u_r y_{rp}}{\sum\limits_{i} v_i x_{ip}}$$

$$\frac{\sum\limits_{r} u_r y_{rj}}{\sum\limits_{i} v_i x_{ij}} \leq c$$

$$st \quad u_r, v_i \geq 0 \qquad\qquad (\text{Eq.2})$$

where c is an arbitrary constant which is usually assumed to be 1. In fact, the above model considers all possible weights for the inputs and outputs of the pth unit and finds weights for which the objective function will be maximized. Due to the constraints of the problem, maximum objective function value can be c. If the pth unit is inefficient compared to other units, in the process of maximizing the objective function, constraints related to efficient units in the set of constraints first reach the value of c and force the pth unit to reach a level lower than c. However, if the pth unit is efficient, the objective function reaches the value of c is without destroying the feasibility of the constraints. [12]

It should be noted that the CCR model described above is fractional and in practice, its linear type is used. In the following, some of the most widely used models of DEA are described. (Equation 3)

Above models are all input models; that is, they determine the efficiency frontier in a way that the input is minimized to the extent that the output is not reduced. A similar model with an output nature can also be written. Output models determine the efficiency frontier in a way that the output is maximized to the extent that the input is not increased. [12]

Artificial neural networks (ANNs)

Artificial neural networks are mathematical models that imitate human brain's function and are capable of extracting patterns from the observed data without the need for assumptions about the relationships among the variables. In neural networks, a neuron is the smallest processing unit and is the basis of a neural network. In Figure 2 a neuron with one input is shown. This simple neuron is composed of two simple elements: weight (w) and transfer function (f).

Input (p) is applied to the neuron and is weighed by multiplying it by weight (w). The result is applied to transfer function (f) as an input and the final output is obtained. By adding bias to the

Multiplier form of BCC (Banker, Charnes and Cooper) model [18]

$$Max \quad \sum_{r=1}^{s} u_r y_{rp} + u_0$$

$$st \quad \sum_{i=1}^{m} v_i x_{ip} = 1,$$

$$\sum_{r=1}^{s} u_r y_{rj} - \sum_{i=1}^{m} v_i x_{ij} + u_0 \leq 0, \quad j=1,...,n$$

$$u_r \geq \varepsilon, \qquad r = 1,...,s$$

$$v_i \geq \varepsilon, \qquad i = 1,...,m$$

$$u_0 \text{ free in sign}$$

Multiplier form of CCR model

$$Max \quad \sum_{r=1}^{s} u_r y_{rp}$$

$$st \quad \sum_{i=1}^{m} v_i x_{ip} = 1,$$

$$\sum_{r=1}^{s} u_r y_{rj} - \sum_{i=1}^{m} v_i x_{ij} \leq 0, \quad j=1,...,n$$

$$u_r \geq \varepsilon, \qquad r = 1,...,s$$

$$v_i \geq \varepsilon, \qquad i = 1,...,m \qquad (\text{Eq.3})$$
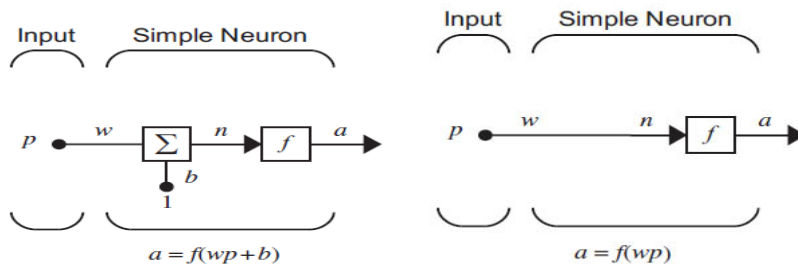
Fig. 2. Simple biased neuron (left) and nonbiased neuron (right) [13]

structure of the neuron in the previous figure, a biased neuron (on the left) is created. b and w are two regulating parameters in the neurons [14]. The main idea of neural networks is that by changing the values of w and b, the network makes a decision. In the used tool in MATLAB, bias has been considered but using it is optional. Neural networks can have more than one layer. They are called multilayer networks. Generally, neural networks can be divided into two types of feedforward and recursive networks. In feedforward networks, no feedback is given to the network input from the network output. But in recursive networks, at least one recursive signal is sent from one neuron to the same neuron or neurons in the previous layer(s). Also, neural networks can be divided into fully connected networks and partially connected networks. In partially connected networks, some of the synaptic connections have been removed [15].

Learning in neural networks:

Simply put, learning in neural networks means that synoptic weights (w, b) change in a way that the neuron input/output relation is adjusted to a specific goal. Learning in neural networks is often done in two ways: supervised learning and unsupervised learning. In supervised learning, a set of data pairs, known as learning data, are applied. A learning pair {(xi ,ti),i,1,2,...m} in which xi is network input and ti is the desirable output for xi. After applying xi input to the network, in the network output, Oi is compared with ti and then learning error is calculated and used to adjust the network factors. In unsupervised learning (self-organizing learning), neural network factors are only modified and adjusted by system's response. In other words, the input merely comprises the data received by the network from the environment and optimal vector is not applied to the network [16]. One of the most common and most widely used neural networks are multilayered perceptron neural networks with backpropagation algorithm. In backpropagation algorithm, frequent input data are given to the network and the output is compared with optimal output and error is calculated in each repetition. This error is propagated across the network and synoptic weights are adjusted in a way that reduces the error in each repetition [17].

Hybrid model of neural networks and data envelopment analysis (Neuro/DEA):

In the present research, a combination of neural networks and data envelopment analysis is used to evaluate the performance of Khuzestan Steel

Company wastewater treatment plant. The potential of neural networks for identifying patterns, estimating functions, prediction and clustering makes it possible to combine them with DEA in order to evaluate the efficiency of the units. Hybrid models of neural networks and DEA used in this research include two approaches (scenarios) which will be discussed in detail in the following section.

In the following, to implement the Neuro/DEA model, first the data are collected. Then, the collected data are saved in the form of EXCELL files in MATLAB software. The networks used in this research include multilayer, feedforward networks and self-organizing networks, which were discussed in the previous section.

Modeling the defined scenarios:

In the present research, two main approaches have been adopted to model the scenario. Before describing these two approaches, to model the scenario, the data must be normalized. In leading neural networks with backpropagation learning algorithm, activation functions errors in the input and latent layers are tangent sigmoid and in the last layer, linear activation function is used. Since sigmoid functions are saturated for values larger than 1 and smaller than -1, input and output values must be scaled to prevent saturation. In addition, the output must also be scaled to be proportionate to the sizes obtained from the neural network. Radial neural network is also composed of a middle layer and an external layer. Activation function of the main layer is a Gaussian radial function, which varies between 0 and 1 and its external layer is a linear activation function. Both neural networks need scaling inputs and outputs. There are various methods for normalization of the data. In this project, mapstd was used to normalize the data in a way that the mean of the data was zero and their standard deviation was one. After scaling and normalization of the input and output data, the following two approaches (scenarios) were considered and the normalized data were entered into the model.

First approach: performance prediction network:

In the first approach in hybrid Neuro/DEA-1 models, a multilayer perceptron network was used to predict the performance of the decision-making units, which as a simulator can simulate the performance of the units in the coming years and analyze the sensitivity of the units. 8 data including Oil_i ،COD_i ،TSS_i ،pH_i ،Oil_o ،COD_o ، TSS_o ،pH_o as well as the efficiency calculated by DEA (input-based multiple CCR model) are

taught to the network. The network learns the efficiency pattern of the units based on network topology and Scaled Conjugate Gradient (SCG) and Levenberg–Marquardt (LM) learning algorithms and establishes a nonlinear mapping between inputs and outputs. The calculated output is actually the efficiency of the data in the new year, that is, 2014. Therefore, we call the first network "performance prediction network". Our goal is to be able to predict the outputs based on these inputs. To do so, we will consider the first five years data as training data and the sixth year data as test data.

Second approach: efficiency calculation network:

In the second approach in hybrid Neuro/DEA-2 models, also a multilayer perceptron network was used. At this stage, the aforementioned neural network calculates the efficiency of the units. 5 data including Oil_i ‹COD_i ‹TSS_i ‹pH_i ‹DEA-CCR are considered as inputs and 4 data including Oil_o ‹ COD_o ‹TSS_o ‹pH_o as outputs. The available data for the units from 2009 to 2014 are divided into learning data and test data. Test data are selected randomly from units' data and are entered into the network along with their efficiency which is calculated by DEA (input-based CCR model). The network learns the pattern of efficiency between inputs and outputs and then, calculates the efficiency of the new data which have been kept as test data. This network is referred to as efficiency calculation network. Our aim is to be able to predict the outputs based on these inputs. To this end, we will consider the first five years data as training data and the sixth year data as test data.

The method employed in hybrid Neuro/DEA models (first and second approach) to evaluate the units:

In the present research, to evaluate the performance of Khuzestan Steel Company industrial wastewater treatment plant during 2009-2014, DMUs of inputs and outputs are determined

and efficiency is measured using DEA (input-based CCR model).

To measure efficiency, the data related to the inputs and outputs of the treatment plant during the mentioned years were used as Fig. 3.

For measuring the technical efficiency of each industrial treatment plant in terms of reducing wastewater parameters to the standard environmental level, COD, pH, TSS and Oil can be considered as model inputs and the treatment plant outputs corresponding to the mentioned parameters can be considered as model outputs. Nevertheless, there are numerous parameters that are considered while evaluating technical efficiency of a treatment plant and it could be stated that efficiency of each industrial treatment plant can be a function of the abovementioned variables and changes in each of them affects the performance of the company. Under such conditions, the assumption of linearity of the relationship between the variables can be ignored and based on the law of diminishing returns and by considering the interactions between the variables, efficiency function of the ith unit, that is, fi=(x1,x2,x3,x4,y1,y2,y3,y4), can be a nonlinear function. The aim of Neuro/DEA model is to minimize the number of inputs required to achieve the desired output. To measure the efficiency of the treatment plant using Neuro/DEA model, first based on the mentioned approaches, 5 scenarios are introduced as shown in Table 3. In this table, the inputs and outputs corresponding to each scenario are described. Then, a suitable neural network model is simulated and after that, using the data for initial processing as well as preprocessing data, the network is trained using a suitable output calculated by DEA so that the network can learn the reference model and based on it, calculate the efficiency of the units. Then, the observed results are studied using DEA/CCR and Neuro/DEA models.

Fig. 3. Khuzestan Steel Company industrial treatment plant inputs and outputs.

Table 3. Inputs and outputs corresponding to each scenario.

Scenario No.	Model inputs	Model output
1	Oil_i, COD_i, TSS_i, pH_i, Oil_o, COD_o, TSS_o, pH_o + DEA-CCR	DEA-CCR sixth year (2014)
2	Oil_i, COD_i, TSS_i, pH_i, DEA-CCR	pH_o
3	Oil_i, COD_i, TSS_i, pH_i, DEA-CCR	TSS_o
4	Oil_i, COD_i, TSS_i, pH_i, DEA-CCR	COD_o
5	Oil_i, COD_i, TSS_i, pH_i, DEA-CCR	Oil_o

Table 4. Inputs and outputs of decision making units (DMUs)*.

Year		Input (Oil)	Input (COD)	Input (TSS)	Input (pH)	Output (Oil)	Output (COD)	Output (TSS)	Output (pH)
2009	Mean	9.733	85.817	58.092	7.938	4.242	43.929	14.000	7.700
	Std. Dev.	8.470	59.619	53.557	0.186	4.311	23.760	7.945	0.232
	Min	1.3	26	9	7.5	0.3	11	3	7.2
	Max	37	254	271	8.3	20	115	35	8.1
2010	Mean	4.317	69.333	45.775	8.075	1.883	25.458	12.896	7.850
	Std. Dev.	4.473	53.921	35.277	0.217	2.676	10.371	4.191	0.159
	Min	0.6	25	14	7.8	0.2	3	6	7.6
	Max	22	261	150	8.6	11	40	22	8.2
2011	Mean	4.279	55.133	55.825	7.942	2.333	38.500	21.750	7.725
	Std. Dev.	2.960	9.644	26.411	0.289	1.001	6.711	8.774	0.285
	Min	1.2	40	26	7.1	0.6	25	6	6.9
	Max	15	81	129	8.5	4.5	53	48	8.2
2012	Mean	7.435	62.058	71.446	7.982	2.863	33.083	13.917	7.663
	Std. Dev.	8.430	20.317	38.274	0.261	0.283	13.897	5.770	0.300
	Min	2.9	22	17	7.5	2.4	6	4	7
	Max	40	103	162	8.6	3.5	62	32	8.5
2013	Mean	4.571	65.221	74.168	8.079	3.596	20.747	15.333	7.854
	Std. Dev.	1.926	23.135	39.179	0.257	1.434	10.448	11.126	0.195
	Min	2.9	33.8	20	7.6	2.6	13	9	7.5
	Max	11.3	111	210	8.6	10.1	64	66	8.2
2014	Mean	3.617	46.625	61.583	8.004	2.775	23.417	20.833	7.800
	Std. Dev.	0.725	14.832	33.628	0.146	0.182	6.928	17.264	0.147
	Min	2.8	29	23	7.7	2.2	12	11	7.4
	Max	5.1	98	143	8.3	3.1	40	99	8

* According to the table, the measurement unit of Oil, COD and TSS parameters in the input and output of the treatment plant is mg/L.

RESULTS AND FINDINGS OF THE RESEARCH

The present research was conducted based on the data gathered over the period of six years from 2009 to 2014.

The results of the analyses conducted on Oil, COD, TSS and pH parameters of the raw sewage entering the treatment plant and the output wastewater, are presented in Table 4 in the form of decision making units (DMUs).

As can be seen, the range of annual mean of Oil in the raw input sewage varies from 3.62 mg/L in 2014 to 9.73 in 2009 and in the output wastewater from 1.88 mg/L in 2010 to 4.24 in 2009. The total mean in the raw input sewage and in the output wastewater was estimated to be 5.66 and 2.95 mg/L respectively.

Also regarding TSS, BOD and pH parameters, according to Table 4, the range of annual mean of COD in the raw input sewage varies from 46.63 mg/L in 2014 to 85.82 in 2009 and in the output wastewater from 20.75 mg/L in 2013 to 43.93 mg/L in 2009. The total mean in the raw input sewage

and output wastewater was estimated to be 63.84 and 30.86 mg/L, respectively. The range of annual mean of TSS in the raw input sewage varies from 45.78 mg/L in 2010 to 74.17 in 2013 and in the output wastewater from 12.92 mg/L in 2010 to 21.75 in 2011. The total mean in the raw input sewage and the output wastewater was estimated to be 61.15 and 16.45 mg/L, respectively. Finally, the annual mean of pH in the range of the raw input sewage varies from 7.93 in 2009 to 8.08 in 2013 and in the output wastewater varies from 7.66 mg/L in 2012 to 7.86 in 2013. The total mean in the raw input sewage and the output wastewater is estimated to be 8 and 7.77, respectively.

Results of process performance evaluation using DEA

In this section, the real application of the proposed model in water and wastewater industry is explained. As noted above, our study includes 144 homogeneous decision making units, each of which has four input variables and four similar output variables. As explained above, in order to measure

efficiency and compare the units, the data from 2009 till 2014 were used. Decision making units (DMUs), which are the years studied in this research, are presented in Table 4. Efficiency of the treatment system during these years was calculated based on inputs and outputs using DEA-RCC, the results of which are shown in Table 5. According to the results, the number of efficient units in 2014, 2013, 2012, 2011, 2010 and 2009 was 7, 7, 9, 8, 12 and 10, respectively, and the number of inefficient units in 2014, 2013, 2012, 2011, 2010 and 2009 was 17, 17, 15, 16, 12 and 14, respectively (Table 5).

Results of Neuro/DEA section:

First scenario: DEA/CCR prediction of the performance in the sixth year (2014)

The results of the first scenario are presented in Table 6 and Figure 4. Figure 4 shows the outputs simulated by the neural network and the output already existing, corresponding to the learning data. The color blue stands for the existing outputs and red stands for simulated outputs. Ideally, the two

graphs should match each other. Following the implementation of the program, we observe that the same thing occurs and the two graphs approximately match each other, which shows that our network has been properly trained for learning data. In this graph, the x axis shows the number of the used test data and the y axis shows the DEA/CCR value.
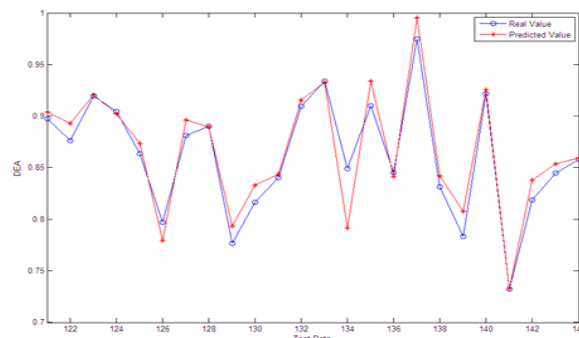
Fig. 4. Comparison of the output of the neural network with the real values of the first scenario.

Table 5. The results obtained from the DEA-RCC model.

	2009	2010	2011	2012	2013	2014
DMU01	0.7725	1	1	1	0.9133	1
DMU02	0.7844	0.9083	1	1	1	0.9727
DMU03	0.7958	0.8589	1	0.9398	0.8331	1
DMU04	0.8638	0.88	0.8658	0.9674	0.9204	0.9443
DMU05	0.785	0.8967	0.9551	0.9917	1	0.9429
DMU06	0.7956	1	0.8404	1	1	0.8661
DMU07	0.8907	0.8626	0.7691	0.9257	0.8966	1
DMU08	0.7252	1	1	1	0.9217	1
DMU09	0.8779	0.9269	0.9039	0.8701	0.7732	0.9047
DMU10	0.6869	0.9609	1	0.9368	1	0.9326
DMU11	1	1	0.9813	0.9499	0.8907	0.9573
DMU12	0.9331	0.9707	1	1	0.9405	0.9769
DMU13	1	0.9487	0.9815	0.8352	1	1
DMU14	0.8512	0.8611	1	0.9688	1	1
DMU15	1	1	0.955	0.967	0.8197	1
DMU16	0.8149	0.9298	0.89	0.9318	0.9185	0.9612
DMU17	0.9565	0.9084	1	1	1	1
DMU18	0.9006	0.9076	0.8591	0.9336	0.8992	0.9194
DMU19	1	0.8569	0.9433	0.9255	1	0.8817
DMU20	1	0.7996	0.9183	0.9683	1	1
DMU21	1	0.9231	0.7956	0.8819	0.8172	0.839
DMU22	0.8895	1	0.9532	0.8811	1	0.9161
DMU23	0.8362	1	0.8483	1	1	0.9657
DMU24	1	0.8827	1	1	1	1
# of efficient units	7	7	9	8	12	10
# of inefficient units	17	17	15	16	12	14

Real values- First scenario:

The results of the second through fifth scenarios:

To better compare the value predicted by the neural network to the expected values in the test data, in the second through fifth scenarios, the following graphs are used. In these graphs, the x axis is the number of the used test data and the y axis shows the value of the predicted output parameter. The (predicted) neural network output values are shown in red and the real values of the test data in blue.

DISCUSSION AND CONCLUSION

Selection of the superior model or approach to evaluate the performance and rank the decision-making units (during the studied years)

Data Envelopment Analysis model

In Data Envelopment Analysis models, only input-based multiple CCR approach (model) has been used and evaluation of the performance of Khuzestan Steel Company treatment plant during the studied years has been done using the mean of the data, which, given the final conclusion in Table 5, reveals that in 2009 and 2010 most of the units have been inefficient and some of the units have had almost equal efficiency. Therefore, it suggests poor separation of the performance of the units using the aforementioned model in 2009 and 2010.

This problem in evaluation of the performance of the units is also evident in 2011 and 2012, because in 2011, 9 DMUs had efficiency of 1 and some of the units had almost equal efficiency, and in 2012, 8 DMUs were considered efficient. In 2013, 12 DMUs had the highest level of efficiency (1) and in 2014, 10 DMUs were considered efficient and the rest of the DMUs had equal efficiency. Evaluation of the performance of the units using the mean of the data during the studied years (2009-2014) may have a better evaluation logic in comparing the efficiency of the units during the studied years (2009-2014), but evaluation of the performance using multiple input-based CCR model indicates poor separability of this model in analyzing efficiency. Because according to Table 5, it is shown that in this evaluation, 53 DMUs have had the highest efficiency (1) during 6 years (2009-2014) and some other have had similar performance. Also, based on the obtained results, the most important parameter affecting the efficiency of the treatment plant system is pH. In other words, by removing or changing pH, changes will occur in the performance of the treatment plant, which can be due to the significant impacts of this parameter on different phases of wastewater

treatment including the process of removal of dissolved metals and wastewater chlorination. In the event that wastewater with acidic or basic pH enters receiving waters, depending on the conditions, it can have severe environmental consequences for the water ecosystem.
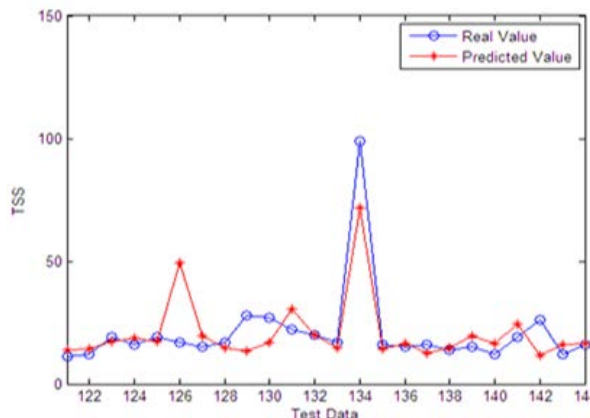
Fig. 5. Comparison of the output of the neural network with the real values of the second scenario.

As we know about the Data Envelopment Analysis method, this method is a nonparametric method and the efficiencies calculated by this method have relative values. In this method, unlike the parametric method, the function has no predetermined shape and the efficiency limit is determined based on the location of the data. Thus, it is natural to speak of the contribution of each unit or index in forming the limit.
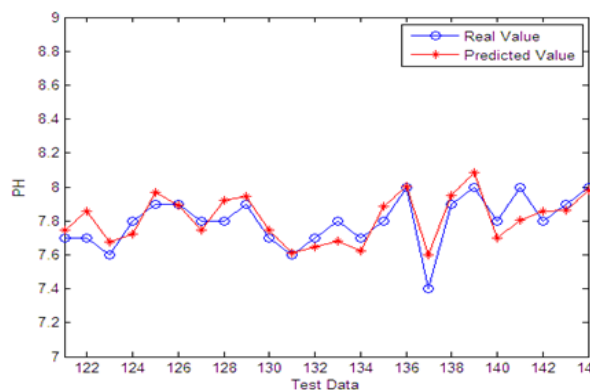
Fig. 6. Comparison of the output of the neural network with the real values of the third scenario.

Because any change in the data shifts the production function and particularly the efficiency of each unit, this will be discussed while analyzing sensitivity. In this section by removing each of the indices, we study the change in efficiency of the units. It should be noted that there is a direct correlation between the input and output indices and removing each of the input indices will lead to the removal of its corresponding output index. In general, it could be said that considering the used

models and conducted analyses in each section, it is evident that in none of the results obtained from the models employed in this research, except for few of the units, there has been a remarkable difference between the performances of the units. Regardless of the individual performance of the units, it could be stated that there is a perceptible balance in the system.

Therefore, considering the conducted analysis, it seems that Data Envelopment Analysis models are not a suitable approach to analyze and evaluate the units in a comprehensive and complete way. Thus, hybrid Neuro/DEA models were adopted to evaluate the performance of the treatment plant during the studied years.
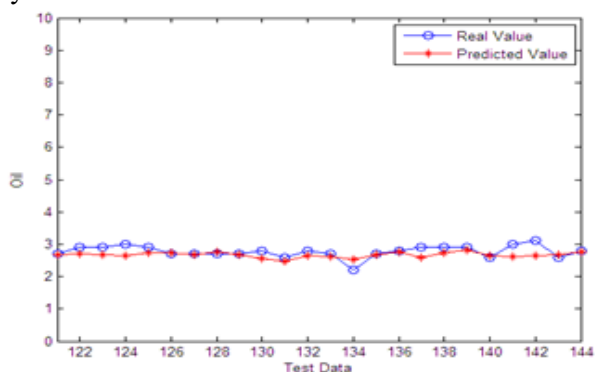
Fig. 7. Comparison of the output of the neural network with the real values of the fourth scenario.
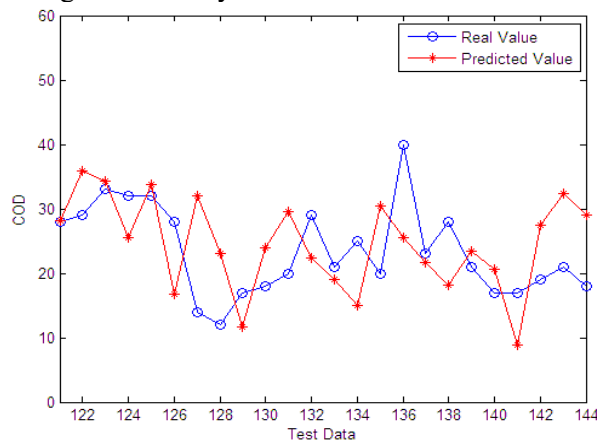
Fig. 8. Comparison of the output of the neural network with the real values of the fifth scenario.

Table 6. Results obtained from scenario one

Scenario	Year	name	Input								Output	Output
			Oil_i	COD_i	TSS_i	pH_i	Oil_o	COD_o	TSS_o	pH_o	DEA-CCR	Neuro-DEA
First	2014.07.23	DMU-121	3.1	35	60	8	2.7	28	11	7.7	0.8972	0.9039704
	2014.08.13	DMU-122	3.1	40	55	8.1	2.9	29	12	7.7	0.8762	0.8926328
	2014.08.27	DMU-123	3.9	54	25	7.9	2.9	33	19	7.6	0.9196	0.9203327
	2014.09.10	DMU-124	3.1	35	50	7.9	3	32	16	7.8	0.9047	0.902035
	2014.09.24	DMU-125	3.9	46	32	8.1	2.9	32	19	7.9	0.8636	0.8733432
	2014.10.15	DMU-126	5.1	32	136	8.3	2.7	28	17	7.9	0.7974	0.7795509
	2014.11.05	DMU-127	4.5	45	43	7.9	2.7	14	15	7.8	0.8812	0.8961407
	2014.11.11	DMU-128	3.2	61	23	8.2	2.7	12	17	7.8	0.8904	0.8895371
	2014.11.25	DMU-129	4.5	58	85	8.1	2.7	17	28	7.9	0.7765	0.7931143
	2014.12.09	DMU-130	3.1	63	78	7.9	2.8	18	27	7.7	0.8167	0.83287
	2014.12.24	DMU-131	3.2	49	114	7.7	2.6	20	22	7.6	0.8402	0.8434945
	2015.01.06	DMU-132	3.2	37	56	7.8	2.8	29	20	7.7	0.9093	0.9157205
	2015.01.21	DMU-133	2.8	29	49	7.9	2.7	21	17	7.8	0.9338	0.9327067
	2015.02.03	DMU-134	2.9	36	143	7.8	2.2	25	99	7.7	0.8489	0.7917352
	2015.02.25	DMU-135	3.1	35	32	8.1	2.7	20	16	7.8	0.9101	0.9336293
	2015.03.11	DMU-136	3.5	50	34	8.1	2.8	40	15	8	0.8454	0.8413867
	2015.04.08	DMU-137	3.1	36	32	7.9	2.9	23	16	7.4	0.9748	0.9952334
	2015.04.15	DMU-138	3.1	45	61	8.1	2.9	28	14	7.9	0.8315	0.8420976
	2015.04.29	DMU-139	3.4	57	59	8.2	2.9	21	15	8	0.7833	0.8076925
	2015.05.13	DMU-140	3	31	50	7.9	2.6	17	12	7.8	0.9217	0.9257734
	2015.05.22	DMU-141	5.1	98	104	8.1	3	17	19	8	0.7326	0.7329739
	2015.06.05	DMU-142	4.9	51	70	8	3.1	19	26	7.8	0.8185	0.8379982
	2015.06.22	DMU-143	3.9	42	62	8	2.6	21	12	7.9	0.8446	0.8538165
	2015.07.06	DMU-144	4.1	54	25	8.1	2.8	18	16	8	0.8579	0.859641

Evaluating the approaches (scenarios) in the form of hybrid Neuro/DEA models

In the first approach (scenario) in hybrid Neuro/DEA models, a multilayer perceptron network was used to predict the performance of the decision-making units during the studied years, which as a simulator can simulate the performance of the units in the coming years and analyze the sensitivity of the units. 8 data including Oil_i، COD_i ،TSS_i ،pH_i ،Oil_o ،COD_o ،TSS_o ، pH_o, as well as the efficiency calculated by DEA (input-based multiple CCR model) are taught to the network. The network learns the efficiency pattern of the units based on network topology and SCG and LM learning algorithms and establishes a nonlinear mapping between inputs and outputs. The calculated output is actually the efficiency of the data in the new year, that is, 2014. Therefore, we call the first network "performance prediction network". As shown in Table 6, all the units that have high efficiency have been separated, which indicates high separability of this model. Therefore, this approach (neural networks for predicting the performance) can be considered a suitable approach for evaluating DMUs of Khuzestan Steel Company treatment plant. In the second through fifth approaches (the first through fifth scenarios), the performance of 144 decision-making units (2007-2014) of Khuzestan Steel Company wastewater treatment plant has been calculated using the neural network for calculation of performance. Our goal is to be able to predict the outputs based on these inputs. To do so, we will consider the first five years data as training data and the sixth year data as test data. In this approach also a perceptron network is used which calculates the efficiency of the units. Test data are selected randomly from units' data and are entered into the network along with their efficiency which is calculated by DEA (input-based CCR model). The network learns the pattern of efficiency between inputs and outputs and then, calculates the efficiency of the new data which

have been kept as test data. This network is referred to as efficiency calculation network. Our aim is to be able to predict the outputs based on these inputs. Analysis of the results obtained from this approach indicates high separation power of the scores of efficiency of the units in this network. The obtained results show that this model has high power in separation and calculation of the scores of efficiency of the units. Furthermore, in calculation of efficiency by DEA, as the results indicate, efficiency scores are equal, which shows that this model cannot separate the units from each other in terms of efficiency. Whereas, the neural network eliminates this weakness of the DEA model, through separation and calculation of efficiency. Based on the results of several tests, we came to the conclusion that it is better to use four single-output neural networks instead of one four-output neural network. In this way we will be able to use a neural network with a specific structure for each output and produce minimum error in predicting each of the outputs. In the following, both networks have been evaluated and compared based on the efficiencies calculated by DEA/CCR and Neuro/DEA models.

Evaluation of the modelings:

To evaluate the modelings, the following parameters are used (Equation 4):

$$RMSE = \sqrt{\frac{\sum_{i=1}^{n}(T_{actual} - T_{forecast})^2}{n}}$$

$$NRMSE = \frac{RMSE}{T_{average}}$$

$$R^2 = 1 - \frac{\sum_{i=1}^{n}(T_{actual} - T_{forecast})^2}{\sum_{i=1}^{n}(T_{actual} - T_{average})^2}$$

$$MAE = \frac{\sum_{i=1}^{n}|T_{actual} - T_{forecast}|}{n}$$

$$NMAE = \frac{MAE}{T_{average}}$$

(Eq.4)

Table 7. Summarization of the results of simulations.

Item	Scenario No	MODELING	RMSE	NRMSE	R	MAE	NMAE
1	1	DEA-CCR	0.0423	0.8344	0.8267	0.0683	1.3494
2	1	Neuro-DEA	0.0032	40.6721	0.9902	0.0330	59.1425
3	2	DEA-CCR	0.0349	0.6345	0.7967	0.04321	1.0056
4	2	Neuro-DEA	0.0186	101.8391	0.8418	0.1132	203.1523
5	3	DEA-CCR	0.0349	0.6345	0.7489	0.04321	1.0056
6	3	Neuro-DEA	0.036	110.8391	0.8618	0.0932	188.1167
7	4	DEA-CCR	0.0987	52.6382	0.4588	0.1753	64.8007
8	4	Neuro-DEA	0.0564	37.479	0.5388	0.08301	52.5800
9	5	DEA-CCR	0.0887	47.6382	0.5488	0.1523	71.7695
10	5	Neuro-DEA	0.0564	0.7902	0.6788	0.04321	1.0056
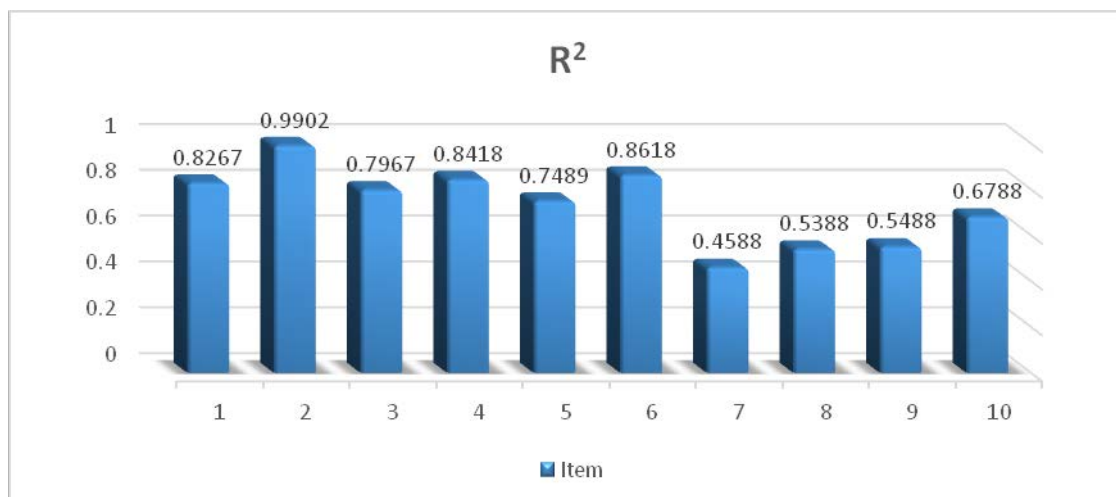
Fig. 9. Comparison of the correlation coefficients in various scenarios

In Figure 9, a comparison of the correlation coefficients in various scenarios is presented.

As shown in Table 7 and Figure 9, in all the defined scenarios, the best correlation coefficients are observed in Neuro/DEA models. In other words, hybrid models (including leading neural and artificial networks using error backpropagation model and DEA) have the best performance and are capable of predicting the data with minimum error (in most cases since the value of R is close to 1, there is a good linear relationship between the observed and modeled values) and real results are within a suitable range, because the ups and downs of the graphs simulated for various scenarios in order of priority include: the first scenario with 0.99, the third scenario with 0.86, the fifth scenario with 0.67 and the fourth scenario with 0.53 in the specific intervals in the model are consistent with reality. Also in most time points, the values obtained from simulation are very close to the real values. On the whole, the most accurate modeling for evaluation of the performance of Khuzestan Steel Company treatment plant during the studied years (2009-2014) is that of Neuro/DEA rather than DEA. On the other hand, the hybrid Neuro/DEA model not only evaluates the performance but also predicts the performance of the treatment plant in the coming years and this is one of the unique features of this model.

RECOMMENDATIONS FOR FUTURE RESEARCH

The results of the research showed that neural networks have a high capability to learn efficiency patterns, yet it is noteworthy that the network should be properly trained. A combination of DEA and neural networks can be employed in cases where basic models cannot separate and identify the units.

Given the fact that Neuro/DEA hybrid model has not been implemented in the treatment plants of the country, by using the findings of this research and modeling Khuzestan Steel Company treatment plant in terms of efficiency, other industrial treatment plants in the country can be studied to determine whether or not they are efficient and also strategies for improving efficiency can be presented. In this regard, other input and output criteria of the industrial treatment plants of the country can be extracted, the efficiency of the units can be evaluated and the units can be ranked using Neuro/DEA model.

Using Neuro/Fuzzy model and entering external factors as the inputs of the neural network and determining the efficient units in the future based on the changes in these factors can also be an area for future research. In subsequent studies, basic DEA models can be used to conduct more extensive research on this subject. Efficiency calculation networks and self-organizing networks can be used to create a network that analyzes efficiency independently of DEA. Since in DEA, the calculated weights are the most suitable weights for maximizing the efficiency of the units, it is expected that the efficiency of all units will be equal to one.

REFERENCES

1. M. Mehregan, A. Farasat, A.K. Moghadas, *Human and Social Science journal*, **6**, 23 (2006).
2. M. Mehregan, Quantitative models in evaluating organizations performance (DEA), Published by Faculty, **National Iranian Gas Company**, 2004.
3. F.J. Delgado, *Economics Bulletin*, **3**(15), 1 (2005).
4. J.-L. Hu, S.-C. Wang, F.-Y. Yeh, *Resources Policy,* **31**, 217 (2006).

5. D. Wu, Z. Yang, L. Liang, *Expert System with Application*, 1 (2005).
6. P.W. Bauer, *Journal of Econometrics*, **46**, 39 (1990).
7. S. Wang, *Computers and Operation Research*, **30**, 279 (2003).
8. R. Sala-Garrido, M. Molinos-Senante, F. Hernández-Sancho, *Chemical Engineering Journal.*, **173**(3) 766 (2011).
9. M. Nasr, S. Medhat, A.E. Hamdy, G.G. El Kobrosy, *Alexandria Engineering*, **48**(10), **p.27-32,** (2012).
10. T.R. Neelakantan, T.R. Brion, S. Lingireddy, *Water Science and Technology*, **43**, 125 (2014).
11. L. Castelli, R. Pesenti, W. Ukovich, *European Journal of Operational Research*, **154**, 465 (2004).
12. L. Liang F. Yang, W.D. J.C. Zhu, *Annals of Operations Research*, **145**, 35 (2006).
13. F. S. Mjalli, S. Al-Asheh, H.E. Alfadala, *Journal of Environmental Management*, 83(3)., 329 (2007).
14. G.R. Shalkef, Artifical Neural Networks, Publishied by Chamran Ahwaz University, 1st Edition, Ahwaz, 2003.
15. A.Vellido, P.J.G. Liboa, Vaughan, J., *Expert Systems with Application*, **17,** 51 (1999).
16. N.D. Gupta, A.S. Kate, *Computers & Operations Research*, **27** , 1023 (2000).
17. M.D. Troutt, A. Rail, A. Zhang, *Computers and Operation research*, **4**, 405 (1995).
18. R.D. Banker, A. Charnes, W.W. Cooper, *Management Science*, **30**, 1078 (1984).

ХИБРИДЕН ПОДХОД НА НЕВРОННА МРЕЖА И АНАЛИЗ НА ОБХВАТА НА ДАННИТЕ ЗА ОЦЕНКА И ПРЕДСКАЗВАНЕ НА ЕФЕКТИВНОСТТА НА ЕДИНИЦИ ЗА ВЗЕМАНЕ НА РЕШЕНИЕ НА ПРИМЕР НА СИСТЕМА ЗА ПРЕЧИСТВАНЕ НА ИНДУСТРИАЛНИ ОТПАДЪЧНИ ВОДИ НА КОМПАНИЯ ЗА ПРЕРАБОТКА НА СТОМАНА В ХУЗЕСТАН

К. Рахбани[1], А.Х. Хасани[2*], М.Р. Мерган[3], А.Х. Джавид[4]

[1-] *Департамент по екологични науки, Факултет по екология и енергетика, Научно-изследователски клон в Техеран, Ислямски университет „Азад“, Техеран, Иран*
[2-] *Департамент по екологично инженерство, Факултет по екология и енергетика, Научно-изследователски клон в Техеран, Ислямски университет „Азад“, Техеран, Иран*
[3-] *Департамент по управление, Университет в Техеран, Иран*
[4-] *Департамент по екологични науки, Факултет по науки и технологии за морето, Ислямски университет „Азад“, Техеран, Иран*

(Резюме)

Един от основните проблеми, свързани с подхода за анализ на обхвата на данните (Data Envelopment Analysis, DEA)) е липсата на чувствителност при оценка на ефективността на отделните единици за вземане на решение, които представляват резултати от анализа на параметрите на входящите и изходящи потоци на системата за пречистване на отпадъчни води. Този проблем се дължи на малкия брой единици в сравнение с броя на входовете и изходите на модела. Доказателство за това е разглеждането на пример за оценка на ефективността на 144 единици за вземане на решение за периода (2007-2014) на система за пречистване на отпадъчни води на Khuzestan компания за преработка на стомана с голям брой входове и изходи. За да се изчисли ефективността на пречиствателната система за преработка на замърсителите, първоначално е използван CCR подход за моделиране, основаващ се на анализ на данните за входовете на системата, който служи за подреждане на ефективните единици чрез прилагане на DEA модели. Показани са основните недостатъци на този подход, а именно наличието на трудности при отделянето на резултатите за ефективността на разглежданите единици за вземане на решение. С цел постигане на по-висока чувствителност модела за анализ на обхвата на данните е комбиниран с модел на изкуствена невронна мрежа за предсказване на ефективността на единиците за взимане на решения чрез създаване на т.н. хибриден Neuro/DEA модел. Резултатите от проведения анализ на ефективността на единиците за вземане на решение показват по-високата чувствителност на изкуствените невронни мрежи при изчисляване на ефективността на разглежданите единици за вземане на решения за определен период от време.

An inverse approach in designing a humidifier for humidification-dehumidification desalination process

F. Abdel-Hady[1], A.K. Mazher[2], A. Alzahrani[1], M. Hamed[3]

[1] Chemical and Materials Engineering Department, King Abdulaziz University, Jeddah, KSA
[2]Nuclear Engineering Department, King Abdul-Aziz University, Jeddah, KSA
[3]Mechanical Engineering Department, King Abdulaziz University, Jeddah, KSA

The need of small amounts of water daily in desert areas motivates the design of a humidifier-dehumidifier desalination portable unit using solar energy. The objective of this paper is to calculate the humidifier performance parameter (KaV) for various values of its exit temperature. KaV includes the mass transfer coefficient of the water K, the surface area of the packing a, and the volume V of the humidifier. A numerical method is employed to calculate the KaV of the humidifier; and NTU method to calculate the distilled water and exit temperatures of the dehumidifier. The usual approach in analyzing the HDH is to select KaV and solve the mathematical model of HDH to find the exit temperatures and amount of distilled water. In this paper, instead of calculating the exit temperature of the water from the HD, we reverse this process. The KaV is calculated given the exit temperature of the HD, and the amount of the distilled water. The results of KaV variations for a range of 25-40ºC of exit temperature; and the corresponding amounts of the distilled water are presented for four cases of operating conditions of humidifier and dehumidifier: water mass rate, air flow rate; and inlet water temperature to the humidifier. The calculated value of KaV, for a given region and amount of water required, will be used to design the evaporator.

Keywords: desalination, humidification, dehumidification, numerical method, design

INTRODUCTION

Humidification-Dehumidification (HD-DHD) process is an efficient method for desalination in remote areas to produce a small amount of water [2-23].The work presented in this paper is the result of a project that aims to design a HD-DHD desalination unit in the Saudi Arabia weather. The goal of the research project is to manufacture a portable unit suitable to the gulf area weather to produce a small amount of fresh water daily. In the gulf region, the solar energy is abundant and it will be employed to power the HD-DHH unit. The research project consists of two parts; the first part concerns the design a parabolic thermal solar collector with control unit to heat the seawater to a specified temperature to produce at least 500 Lit/day of desalinated water. The first part of the project completed the analysis and the design of the solar collector to heat the seawater to a controllable temperature; and the model of the solar irradiance available at Jeddah Saudi Arabia was published [1]. In that paper, the parameters concerning the gulf region, the solar power, ambient temperature were reported. The second part of the research focuses on the sizing and material selection parameter of the HD-DH to produce a small amount of water based on a given inlet water temperature, mass flow rate, air flow rate, and cooling water mass flow rate for a range of HD exit temperature. Our specific goal is to study the effect of HD exit temperature on the performance characteristic parameter KaV. This parameter is composed of the mass transfer coefficient K of water (kg/m^2 s), the surface area of the packing a, and the volume V of the humidifier (m^3). The objective of the calculation is to relate the brine exit temperature of the evaporator (HD) to the amount of water produced during the day and the KaV.

The research results will help to design a portable HD using the KaV value to produce the distilled water required per day in the desert environment. In present paper, the result of the research concerning the procedure to calculate KaV to produce a small amount of distilled water is reported under the assumption that the exit temperature of the seawater equals the ambient temperature of the region.

A MATLAB code uses a numerical iterative method was employed to calculate the produced clean water for different exit temperatures of the humidifier; and for different values of airflow and seawater flow rates. The calculation is repeated for the inlet temperature range of 85 – 45 ºC of a humidifier during the day. The amount of the produced water is calculated for 10 hours daily from 9:00 am to 7:00 pm. To produce a minimum of 500 liters/10 hours daily, the designer have different options by selecting the mass flow rate of air; and seawater rates to the HD and the DHD. The main result from the above calculations, are a set of curves that relate the exit temperature of the humidifier

versus the *KaV* and the produced distilled water. The calculated results show the effect of exit temperature variation for a given mass flow rates of air and seawater on the amount of distilled water and *KaV*. These results can be used to size and select the packing material of the HD-DHD unit.

A brief review of the methods of analyzing the working of HD-DHD

Researchers used theoretical, computational, and experimental methods to analyze the performance of HD-DHD unit. They studied the effect of different parameters on the amount of distilled water produced. The researchers in references [2, 3] analyzed the HD-DHD hybrid desalination process using solar still. Modeling and experimental validation for the unit is analyzed for different cases in [4]-[7]. Entropy and thermodynamic analysis are used to analyze the performance of the desalination unit [8]-[11]. Experimental researchers [15, 17] used a pilot plant and measured the temperature, humidity and the produced water for different water inlet temperature for units that use solar power. Other researchers[13, 15] used numerical methods and designed experiments to validate the computational results.

The research reported here belongs to the modeling and numerical methods that used to study the HD-DHD process. In papers[16]-[23] numerical methods are used to solve the energy and mass conservation equations for the HD and DHD in addition to enthalpy balance for the humidifier and the LMTD equation for the dehumidifier. For the humidifier the mathematical model is a set of three equations with three unknowns. The humidifier unknowns are the exit water temperature, the mass flow rate, and the exit temperature of the hot humid air. Given a value of *KaV*, an iterative method is used to solve these three equations for the three the unknowns. The results of the published numerical research, used a different empirical formula for *KaV* borrowed from the empirical cooling tower research[20-23].

For the dehumidifier the mathematical model is a set of three equations with three unknowns too. The dehumidifier unknowns are the exit cooling water temperature, the mass flow rate of the distilled water, and the exit temperature of the cooled air. Given a value of *UA*, an iterative method is used to solve the three equations for the three unknowns of the dehumidifier.

The objective of the present study is to solve numerically only the mass and energy conservation

equations of the HD to calculate the distilled water as a function of the exit temperature of hot water from the HD. From the solution, the enthalpy balance equation is used to calculate the performance parameter *KaV* needed to produce the amount of distilled water during 10 hours in a desert environment for a given mass flow rates of air and seawater; and for various values of inlet and exit temperatures of HD of the desalination unit. For the dehumidifier, the NTU method [24] is used to solve the dehumidifier equations.

HD-DHD desalination unit

Figure 1 shows the HD-DHD unit for a desalination process using a parabolic trough collector (PTC) as a heat source to produce a minimum of 500 liters of water per 10 hours in Jeddah weather condition [1].Also, figure 2 shows a schematic diagram of the HD-DHD process for desalination.

HD-DHD desalination process

In the HDH unit, a hot seawater is sprayed into the evaporator compartment of the unit (humidifier); and the air passed to the evaporator is humidified and then moved to the condenser (dehumidifier) where water in the humidified air condenses releasing its enthalpy of condensation. In the cooling process of the dehumidifier the heat is recovered, and used to preheat the inlet seawater to the HD; but this amount of heat is not enough and the seawater is heated more by a solar PTC heat source before entering again to the evaporator.

The seawater, with mass flow rate of m_{HD-in}, is heated using the solar energy and flows to the HD at temperature T_{HD-in}. It exits the HD at temperature T_{HD-out} with mass flow rate m_{HD-out}. The air enters the HD at temperature T_1 with a specific humidity ω_1 and mass flow rate m_{air}. It exits the HD at temperature T_2 with saturated air with specific humidity ω_2. In the dehumidifier, the saturated air enters at temperature T_2 with a specific humidity ω_2 and air mass flow rate m_{air}. A cooling seawater, that is used to cool the hot humid air, enters the DHD at temperature T_{SW-in} and mass flow rate m_{sw}. It exits the DHD with the same mass flow rate at temperature T_{SW-out}. The hot air is cooled and exits the DHD with the same air mass flow rate, specific humidity ω_1 and temperature T_1. The condensed water is produced with the rate of m_d at temperature T_d. In this process the condensation temperature T_d is set equal to T_1. It is assumed that the air is saturated at the exit and inlet of the DHD.
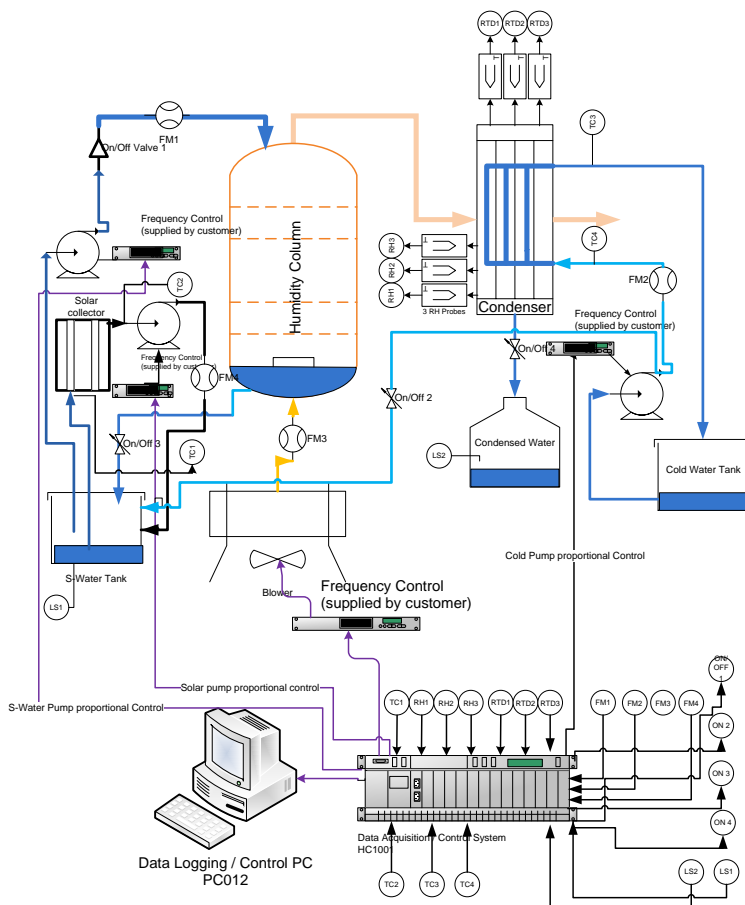
Fig. 1. Complete solar HD-DHD desalinationunit.
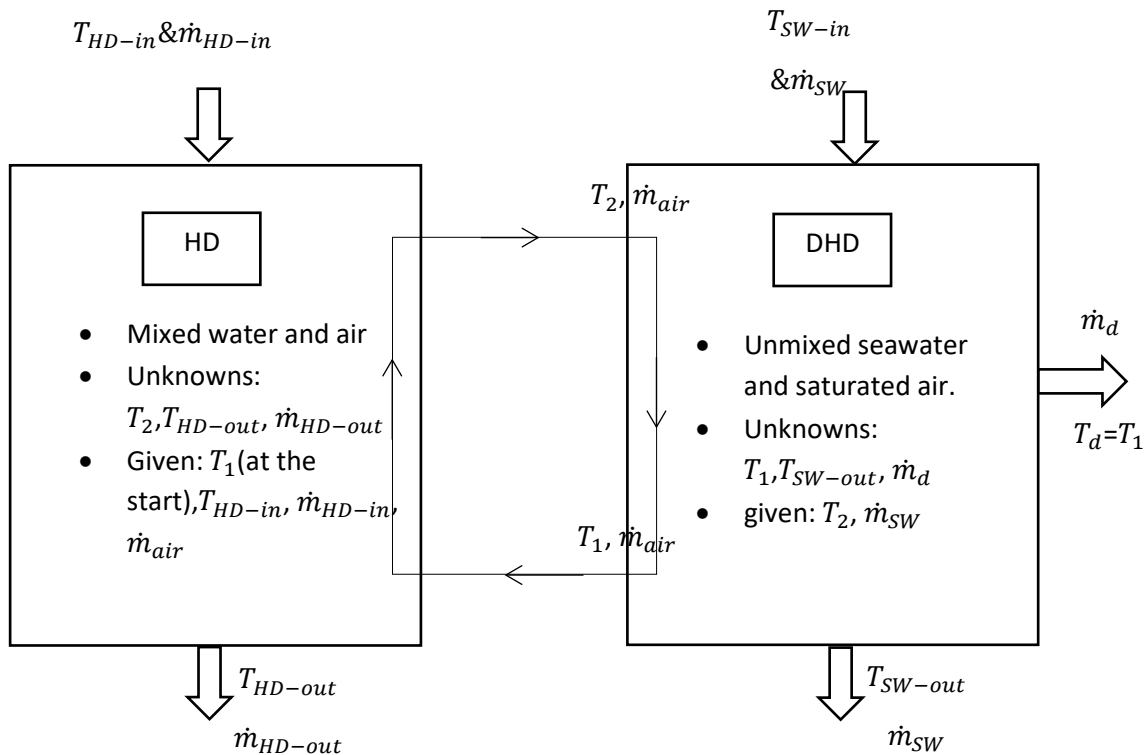
Fig .2. The schematic diagram of the HD-DHD unit.

Sizing the HD depends on the amount of water produced, rate of air and seawater flows, and the exit temperatures of HD and DHD. The objective of this paper is to study the effect of exit temperatures on the amount of water produced during a day for various values of mass flow rates of air and seawater; and compute the corresponding design parameter *KaV*.

Mathematical model

The mathematical model for the HD-DHD unit is derived from the conservation of mass and energy principles. Since the number of unknowns are greater than number of equations, in HD and DHD, the researchers in the references[16-23] used additional equations to close the system.

I. Mathematical model of the humidifier

The solar energy source heats the inlet water to the humidifier to a temperature $T_{HD\text{-}in}$. In the HD, the unknowns are T_2, $T_{HD\text{-}out}$, and $m_{HD\text{-}out}$. The HD parameters are: 1) the mass flow rate of the hot water to the humidifier m $_{HD\text{-}in}$, 2) the mass flow rate of the air to the humidifier m_{air}, and 3) the inlet seawater temperature to the humidifier $T_{HD\text{-}in}$. Since we have three unknowns, three equations are needed. The researchers in references [16-23]used the energy and mass conservation and added an enthalpy balance equation. Hence, the mathematical model of the HD is given by the following equations:

Mass balance:

$$\dot{m}_{HD-in} + \dot{m}_{air}w1 = \dot{m}_{HD-out} + \dot{m}_{air}\dot{w2} \qquad (1)$$

Energy balance:

$$\dot{m}_{HD-in}h_{HD-in} + \dot{m}_{air}h_1 = \dot{m}_{HD-out}h_{HD-out} + \dot{m}_{air}h_2 \qquad (2)$$

Enthalpy balance analogy equation:

$$\dot{m}_{air}(h_2-h_1) = KaV \left[\frac{(h_{HD-in}-h_2)-(h_{HD-out}-h_1)}{\ln\left(\frac{h_{HD-in}-h_2}{h_{HD-out}-h_1}\right)}\right] \qquad (3)$$

KaV in equation (3) is used in sizing and selecting material properties of the evaporator. Different values of *KaV* are given in references [20-23]. The selected value of *KaV* affects the exit temperature of the seawater $T_{HD\text{-}out}$. The *KaV* parameter consists of *K,* which represents the mass transfer coefficient, the surface area of the packing *a* ; and *V* which is the volume of the humidifier. To solve the above equations, the following thermodynamic relations are used:

h = Cp T + ω hg
hg = 2500 + 1.8 T - 1.9 x 10⁻⁵T²- 9.3 x 10⁻⁶T³

ω= 0.662Pg/(P- φ Pg)
Pg = 0.61 + 0.044 T + 0.0014 T² + 2.7 x 10⁻⁵ T³ + 2.8 x 10⁻⁷ T⁴ + 2.7 x 10⁻⁹ T⁵

For the saturated air, the specific humidity is given by the formula:

ω = 0.002 + 0.00071 T - 1.95 x 10⁻⁵ T² + 7.7 x 10⁻⁷ T³

II. Mathematical model of the dehumidifier

The unknowns of the DHD, are T_1, $T_{SW\text{-}out}$, and m_d.To solve for these unknowns three equations are required. The researchers in references [16-20] used the energy and mass conservation and added heat transfer equation employed in the analysis of heat exchangers. The mathematical model of the DHD is given by the following equations:

Mass balance:

$$\dot{m}_{air}w_2 = \dot{m}_{air}w_1 + \dot{m}_d \qquad (4)$$

Energy balance:

$$\dot{m}_{air}h_2 + \dot{m}_{SW}h_{SW-in} = \dot{m}_{air}h_1 + \dot{m}_{SW}h_{SW-out} + \dot{m}_dh_d \qquad (5)$$

Heat transfer balance equation (LMTD):

$$\dot{m}_{SW}CP_w(T_{SW-out}-T_{SW-in}) = UA \left[\frac{(T_2-T_{SW-out})-(T_1-T_{SW-in})}{\ln\left(\frac{T_2-T_{SW-out}}{T_1-T_{SW-in}}\right)}\right] \qquad (6)$$

Equations (4)- (6) are solved for the unknowns of the DHD, which are T_1, $T_{SW\text{-}out}$, and m_d. For the given inlet temperature to the DHD, T_2, the temperatures T_1& $T_{SW\text{-}out}$ and m_d are obtained. The solution will vary for different values of the DHD parameters which are: 1) themass flow rate of the cooling seawater to the dehumidifier m_{SW}, 2) the mass flow rate of the air to the dehumidifier m_{air}, and 3) the inlet seawater temperature $T_{SW\text{-}in}$ to the dehumidifier.*UA* parameter in equation (6) affects the solution too.

A new approach

In the published method of solution; the unknowns are calculated using iteration to solve equations (1) - (6) for the exit air temperaturesT_2, $T_{HD\text{-}out}$, $T_{SW\text{-}out}$, and the distilled mass flow rate m_d. In the present research, a numerical method is employed to solve equations (1) & (2) for the HD to compute T_2 and $m_{HD\text{-}out;}$ and for the DHD, the NTU method [23] is used to calculate T_1 and $T_{SW\text{-}out}$. In solving the evaporator equations an inverse approach is used. Instead of selecting *KaV* and solving equations (1)-(3) for the T_2, $T_{HD\text{-}out}$, and $m_{HD\text{-}out}$, the exit temperature of the HD selected that match the ambient temperature and *KaV* is calculated from equation (3).This calculated value will be used to size and select the material of the HD.

472

To the knowledge of the authors no one used this approach before. This approach is suitable for the design of evaporator for a portable unit to produce a small amount of water for gulf area. Using this method, the designer can manufacture a customized small units for different areas by changing the size and the material of the HD.

The numerical algorithm

The following are the steps used to calculate the *KaV* and the distilled water for the given specified parameters:

Humidifier

1) Select the inlet temperature of the hot seawater T_{HD-in}, and the mass flow rates m_{HD-in} & m_{air} to the humidifier.

2) Select the required temperature of the exit water T_{HD-out}.

3) Select the air inlet temperature to the humidifier T_1

4) Solve equations (1) & (2) iteratively to calculate the unknowns T_2 and m_{HD-out}.

Dehumidifier

5) Use the calculated value T_2 from the humidifier to calculate the air exit temperature of the dehumidifier T_1 and the exit temperature of the cooling seawater of the dehumidifier T_{SW-out}. Given the mass flow rate m_{sw} and the inlet temperature of the cooling seawater T_{SW-in} to the dehumidifier, the NTU method[24] is used to calculate T_1 and T_{SW-out}

6) If the computed T_1 in this step is different from the T_1 selected in step 3), the steps 3) - 5) are repeated until convergence.

7) From the converged solution for T_1, T_2, T_{SW-out}, equation(4) is used to calculate the amount of distilled water in the condenser m_d for ten hours. The *KaV* is calculated from equation (3).

8) Steps (2) -(7) are repeated for another values of T_{HD-out}, and the *KaV* and m_d are plotted

8) The procedure (1) - (7) is repeated for different values of m_{HD-in}, m_{air}, and T_{HD-in}

The above algorithm of HD-DHD can be repeated for different values of m_{HD-in}, m_{air}, T_1, m_{SW}, and T_{SW-in}.

RESULTS AND DISCUSSION

The main objective of this paper is to produce a code to calculate the amount of distilled water per day for HD-DHD unit for any mass low rates of air and seawater. The numerical results of the code is used to analyze the effect of exit temperature on the amount of produced water. Also, the result showed that the *KaV* parameter of equation (3) depends on the exit temperature of the humidifier as expected.

The following results are obtained for two values of the inlet temperature to the HD: T_{HD-in} = 45 ºC and 85ºC. The amount of water in kg based on the assumption the humidifier works 10 hours/day at the given T_{HD-in} is plotted for all cases considered. For analyzing the humidifier, a range of the T_{HD-out} is selected to vary from the maximum T_{HD-in} - 5 to a minimum of 20 ºC, and the iteration is conducted for each 5 degrees Celsius.

Case I

Figures 3 -6 show the results for T_1, T_2, m_d, *KaV* variation versus T_{HD-out} for the following values of the parameters : m_{HD-in} = .1 kg/s, m_{air} =.2 kg/s, m_{SW} = .1 kg/s, and T_{HD-in} = 45 ºC. Figure 3 shows the variation of the exit air temperatures T_1 & T_2 as a function of T_{HD-out}. It is observed that the T_2 decreases as the exit water temperature increases. This is physically logical since decreasing the exit temperature allow more water goes to the air. Also, T_1 stabilizes to a fixed temperature 21 ºC.
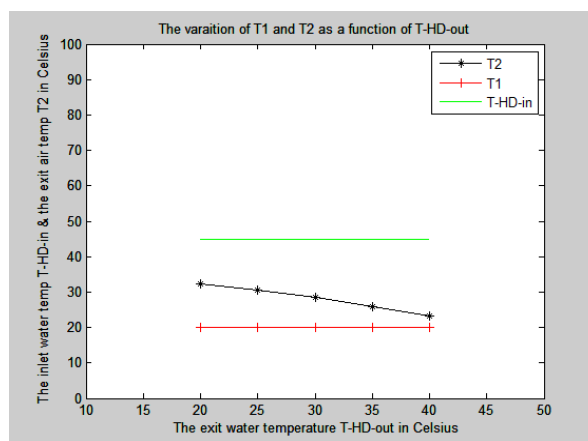
Fig. 3. The variation of T_1 and T_2 as a function of T_{HD-out}
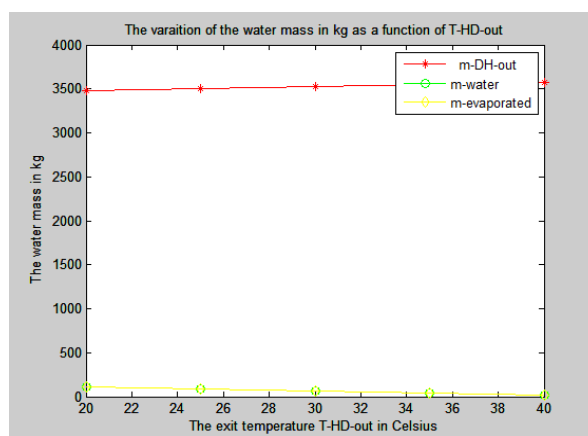
Fig. 4. The variation of the water mass in kg as a function of T_{HD-out}

Figure 4 shows the variation of the mass flow rate of the seawater exiting the HD, and the evaporated air mass flow rate exiting the HD. The figure shows

that the water going to the air in HD increases with decreasing the T_{HD-out}, and m_{HD-out} decreases too.

Figure 5 shows the variation of the total distilled water produced in kg in 10 hours. The curve shows the increase of distilled water with decreasing T_{HD-out}. The maximum occurs when the exit temperature of the water from the HD is minimum.
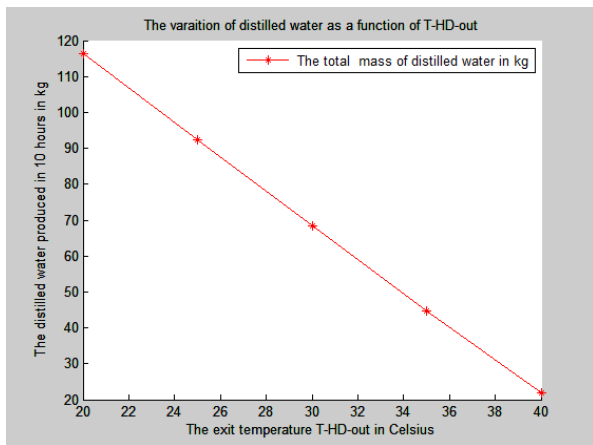
Fig. 5. The variation of distilled water as a function of T_{HD-out}

Figure 6 shows the variation of the exit cooling seawater temperature of the DHD as a function of the exit seawater temperature of the HD. The figure shows that the T_{sw-out} decreases as T_{HD-out} increases, which reflect the conservation of heat for the unit.
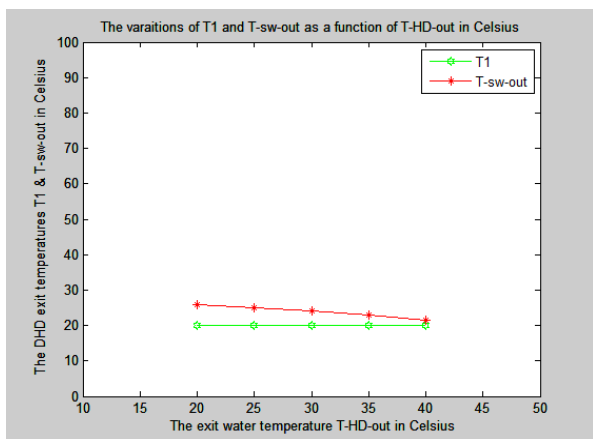
Fig. 6. The variations of T_1 and T_{SW-out} as a function of T_{HD-out}

Figure 7 shows the variation of the performance characteristic parameter *KaV* of the humidifier as a function of the exit temperature. The calculated results are employed in equation (3) to compute *KaV*. Also, the figure shows that *KaV* decreases as the exit temperature increases; and this trend is the same for the other cases presented in this paper. This result for *KaV* means that, for the same mass transfer coefficient *K* and material packing parameter *a*, the

volume *V* should decrease as the exit temperature T_{HD-out} increases.

Case II

Figures 8 shows the produced water variations as a function of T_{HD-out}, while figure 9 shows the variation of *KaV* with the exit temperature of the humidifier. This curve is calculated for the following values of the parameters: m_{HD-in}= .1 kg/s, m_{air}=0.2 kg/s, m_{SW}= .1 kg/s, and T_{HD-in} = 85 ºC. The behavior of m_d and *KaV* are similar qualitatively to case I but quantitatively are different. The only difference of this case, compared to case I, is the value of the inlet hot seawater to the HD. This reflects an increasing the amount of the distilled water in Fig 8; and an increasing the values of *KaV* in Fig. 9.
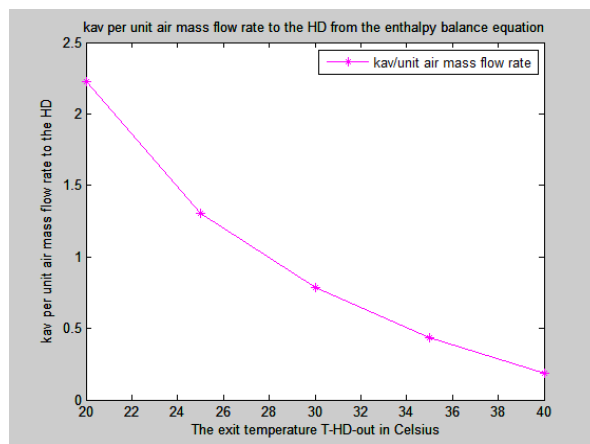
Fig. 7. *KaV*/m_{air} to the HD from the enthalpy balance equation
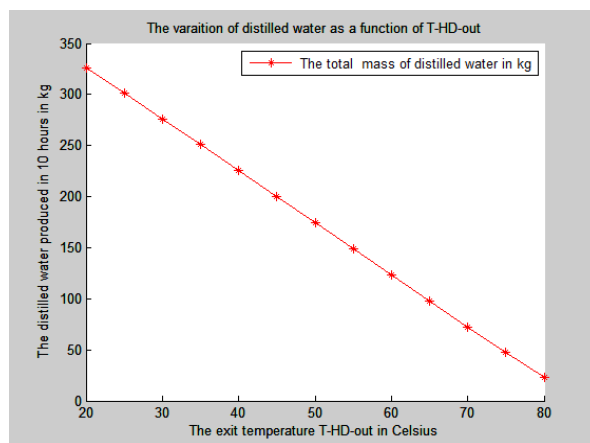
Fig. 8. The variation of distilled water as a function of T_{HD-out}

Fig. 9. *KaV* /m$_{air}$ to the HD from the enthalpy balance equation.
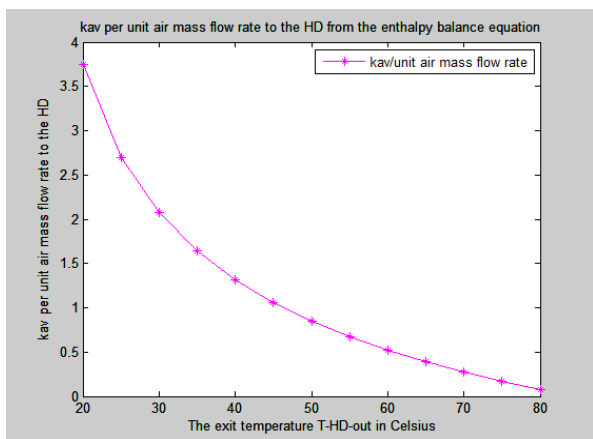
Fig. 11. *KaV*/m$_{air}$ to the HD from the enthalpy balance equation

Case III

Figure10   shows the variation of the amount of the produced water with T$_{HD-out}$,while figure 11 shows the   variation of *KaV* with T$_{HD-out}$ for the following values of the parameters: m$_{HD-in}$= .5 kg/s , m$_{air}$= 1.0 kg/s , m$_{SW}$= .1 kg/s, T$_{HD-in}$ = 45 ºC. Case III shows the same trend of variations qualitatively as cases I and II; but it is quantitatively different. The only difference between this case and case I are the values of m$_{HD-in}$ and m$_{air}$. But the ratio of these mass rates is the same and equals 0.5. Figure 10 shows a rise of the m$_d$ vs. T$_{HD\_out}$ curve; while Fig 11 shows an increase in the value of *Kav* as T$_{HD-out}$ increases. In this case, the ratio m$_{HD-in}$/m$_{air}$ and the T$_{HD-in\ are}$ the same as in cases I and III. The only difference between cases I and III is the amount of hot seawater and air mass flow rate. Here the water rate is increased which reflect the increase in the amount of distilled water.

Fig. 10. The variation of distilled water as a function of T$_{HD-out}$

Case IV

Figures 12shows the variation of the amount of the produced water with THD-out. Figure 13shows the variation of *KaV* with T$_{HD-out}$ for the following values of the parameters: m$_{HD-in}$= .5 kg/s, m$_{air}$= 1.0 kg/s, m$_{SW}$= .1 kg/s, and T$_{HD-in}$ = 85 ºC.

This case has the same trend as cases I, II, and II qualitatively, but   the values of m$_d$ and *KaV* are different quantitatively. These differences are due to the different values of the seawater, air mass flow rates and the T$_{HD-in}$. Comparing this case to case III the only difference is the inlet T$_{HD-in}$, which equals to 85ºC. Figure 12 shows an increase in the total distilled water produced in 10 hours; while Fig. 13 shows an increase in the value of *KaV* as T$_{HD-out}$ increases. In this case and case II, the ratio m$_{HD-in}$/m$_{air}$ and the T$_{HD-in}$ are the same, but the only difference between cases I and III is the amount of hot seawater and air mass flow rates. In case IV, the water rate is increased which reflect the increase in the amount of distilled water.
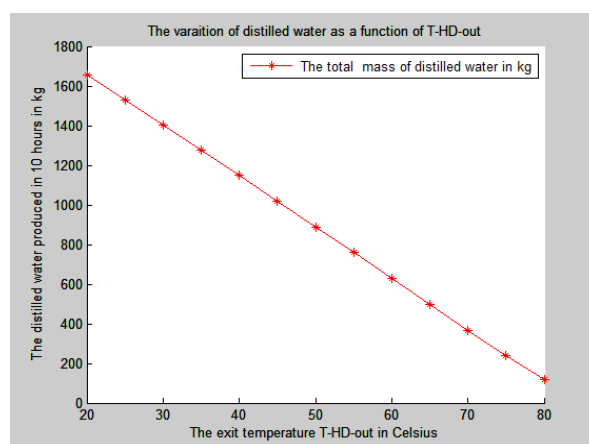
Fig. 12. The variation of distilled water as a function of T$_{HD-out}$
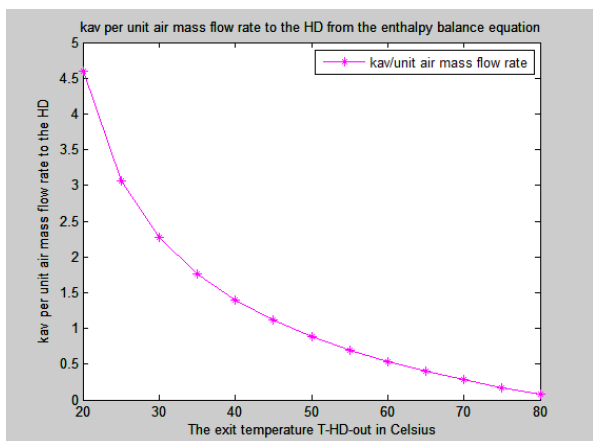
Fig.13. KaV/m_{air} to the HD from the enthalpy balance equation.

From the above result, to design a humidifier for a specific amount of distilled water, the designer have many options to select KaV to cool the seawater of the humidifier. From this selection follows the selection of the packing area, the material, and the humidifier volume.

CONCLUSIONS

The main objective of the research in this paper is to design a portable HD-DHD unit to produce a minimum amount of 5000 lit/ day in gulf weather using solar energy. To design a portable unit to produce a small amount of water a computational procedure is introduced to calculate KaV for a range of the exit temperature of the seawater from the humidifier consistent with the range of the ambient temperature variation of the different areas of the region. This KaV will be used to calculate the size and the select the material of the evaporator for any value of the controllable inlet temperature of the seawater to the humidifier. In a remote areas in the gulf regions the ambient temperature varies, so the calculation procedure to design a humidifier take the exit temperature of the HD as input and calculate the performance characteristic parameter KaV consequently. The amount of produced water depends also on the inlet temperature of hot seawater to the HD. This temperature is controlled by the design of the solar source and can be selected to control the amount of distilled water.

A computer program using MATLAB was developed to calculate the amount of distilled water in a HD-DHD unit at any hour during the day. The program solves numerically the standard conservation equations of mass and energy. The calculation depends of the given values of the exit temperature of the seawater from the HD. The employed algorithm that solves the mathematical model of the desalination unit can be used

extensively to simulate the working of the HD-DHD unit for different ranges of the mass flow rates of air and water as well as inlet temperature to the HD; and seawater cooling temperature. The designer can select the amount of water needed per 10 hours daily based on his selection of T_{HD-in} and T_{HD-out}; and the best choice, in the above calculations, occurs when the T_{HD-out} is 20 ºC. The results for four cases are represented to show the usage of the code to generate the designed amount of water. Based on the amount of water needed per day the designer can select the mass flow rate of air and seawater, and the exit temperatures to size the unit. The main result from the above calculations is a bank of data that can be used to design the DH of the unit. To produce the maximum amount of water the exit temperature of the humidifier T_{HD-out} should be minimum.

Recommendation: Design the solar energy PTC system to produce a constant highest possible temperature, and design the evaporator to cool the water (brine) to a temperature close to the ambient temperature of the region.

Nomenclature

A - surface area of the packing (m²)
C_{pair} - specific heat of dry air (kJ/kg ºC)
C_{pw} - specific heat of seawater (kJ/kg ºC)
h - enthalpy (kJ/kg)
h_g - enthalpy of the saturated water vapor(kJ/kg)
K - masstransfer coefficient of the water in the humidifier (kg/ m² s)
m_{air} - air mass flow rate to the humidifier (kg/s)
m_{sw} - cooling sweater mass flow rate to the dehumidifier (kg/s)
m_d - rate of distilled water in the dehumidifier (kg/s)
m_{HD-in} - water mass flow rate to the humidifier (kg/s)
P - atmospheric pressure (kPa)
P_g - saturation pressure
T_{HD-out} - outlet temperature from the humidifier (ºC)
T_{HD-in} - inlet temperature from the humidifier (ºC)
T_1 - inlet air temperature to the humidifier (ºC)
T_2 - exit air temperature from the humidifier (ºC)
T_{sw-in} inlet seawater temperature to the dehumidifier(ºC)
T_{sw-out} - exit seawater temperature to the dehumidifier (ºC)
UA - heat transfer coefficient of the dehumidifier

V - volume of the humidifier (m^3)
of the water vapor

Greek symbols
ω -specific humidity
φ - relative humidity

REFERENCES

1. F. Abdelhady, H. Bamufleh, M.M. El-Halwagi,·J.M. Ponce-Ortega, *Chemical Engineering Science*, **136**, 158 (2015).
2. A. Ghobeity, A. Mitsos, *Current Opinion in Chemical Engineering*, **6**, 61 (2014).
3. S. Hou, H. Zhang, *Desalination*, **220**(1–3), 552 (2008).
4. Z.M. Omara, M.A. Eltawil, E.A. ElNashar, *Desalination*, **325**, 56 (2013).
5. H.B. Bacha, *Desalination*, **322**, 182 (2013).
6. K.H. Mistry, A. Mitsos, J.H. Lienhard V, *International Journal of Thermal Sciences*, **50**(5), 779 (2011).
7. E.H. Amer, H. Kotb, G.H. Mostafa, A.R. El-Ghalban, *Desalination*, **249**, 949 (2009).
8. Karan H. Mistry, John H. Lienhard V, Syed M. Zubair, *International Journal of Thermal Sciences*, **49**, 1837 (2010).
9. G.P. Narayan, J.H. Lienhard V, S.M. Zubair, *International Journal of Thermal Sciences*, **49**, 2057 (2010).
10. K.M. Chehayeb, G.P. Narayan, S.M. Zubair, J.H. Lienhard V, *International Journal of Heat and Mass Transfer*, **68**, 422 (2014).
11. J. Wang, N. Gao, Y. Deng, Y. Li, *Desalination*, **305**, 17(2012).
12. A.M.I. Mohamed, N.A. El-Minshawy, *Energy Conversion and Management*, **52**, 3112 (2011).
13. C. Yamalı, İ. Solmuş, *Desalination*, **205**, 163 (2007).
14. C. Yıldırım, İ. Solmuş, *Energy Conversion and Management*, **86**, 568 (2014).
15. J. Moumouh, M. Tahiri, M. Salouhi, *International Journal of Hydrogen Energy*, **39**, 15232 (2014).
16. N.Kh. Nawayseh, M.M. Farid, A. Aziz Omar, A. Sabirin, *Conversion and Management*, **40**, 1441 (1999).
17. H. Ettouney, *Desalination*, **183**(1–3), 341 (2005).
18. G. Al-Enezi, H. Ettouney, N. Fawzy, *Energy Conversion and Management*, **47**, 470 (2006)..
19. J.-J. Hermosillo, C.A. Arancibia-Bulnes, C.A. Estrada, *Solar Energy*, **86**(4), 1070 (2012).
20. N.Kh. Nawayseh, M.M. Farid, A.Aziz Omar, A. Sabirin, *Energy Conversion and Management*, **40**, 1423 (1999).
21. G. Franchini, A. Perdichizzi, *Energy Procedia*, **45**, 588 (2014).
22. S. Farsad, A. Behzadmehr, *Desalination*, **278**, 70 (2011).
23. M.M. Farid, S. Parekh, J.R. Selman, S. Al-Hallaj, *Desalination*, **151**(2), 153 (2002).
24. Y.A. Cengel, A.J. Ghajar, "Heat and Mass transfer", 4th edition, McGraw-Hill, USA, 2011, p. 651.

ОБРАТЕН ПОДХОД ЗА КОНСТРУИРАНЕ НА ОВЛАЖНИТЕЛ ЗА ПРОЦЕСИ НА ОБЕЗСОЛЯВАНЕ С ОВЛАЖНЯВАНЕ/ИЗСУШАВАНЕ

Ф. Абдел-Хади[1], А.К. Мазхер[2], А. Алзахрани[1], М. Хамед[3]

[1] *Департамент по химично инженерство и материалознание, Университет „Крал Абдулазиз“, Джеда, Саудитска Арабия*
[2]*Департамент по ядрено инженерство, Университет „Крал Абдулазиз“, Джеда, Саудитска Арабия*
[3]*Департамент по машинно инженерство, Университет „Крал Абдулазиз“, Джеда, Саудитска Арабия*

(Резюме)

Ежедневната нужда от малки количества питейна вода особено в сухи пустинни области ни мотивира да разработим и проектираме овлажнител (DHD), който да произвежда обезсолена питейна вода с помощта на слънчева енергия. Целта на тази статия е да определи ефективния коефициент на овлажняване (*KaV*) за различни изходни температури. *KaV* включва в себе си коефициента на масообмена на водата, повърхността на пълнежа а и обема *V* на овлажнителя. За определяне на *KaV* е използван числен метод както и NTU метод за изчисляване на обема на дестилираната вода и изходящата температура от овлажнителя. Традиционния подход използван за описание на (DHD) е да се избере *KaV* и да се реши математическия модел (DHD) за да се намерят количеството и изходната температура на водата. В настоящата работа вместо да изчисляваме изходната температура на водата от HD, ние обръщаме този процес. *KaV* е изчислен за предварително зададени температура и количество на получената вода. *KaV* е определен за температури в интервала от 25 до 40 ºC за три случая на работни условия: масов дебит на водата, дебит на въздуха, входна температура на водата в овлажнителя. Получените стойности на (*KaV* са използвани за проектиране на овлажнителя.

Mg(ClO₄)₂-catalyzed one-pot synthesis of 2-amino-4H-chromenes and dihydropyrano[c]chromenes

H. Emtiazi, M.A. Amrollahi*

Department of Chemistry, Yazd University, P.O.Box 89195-741, Yazd, Iran

This report provides a description of an efficient and simple procedure for the synthesis of 2-amino-4H-chromenes and dihydropyrano[c]chromenes *via* one-pot three-component reaction of aldehydes, active methylene compounds and resorcinol or 4-hydroxycoumarin catalysed by magnesium perchlorate. The remarkable advantages are simplicity of the experimental procedure, high yields, short reaction times, and reusability of the catalyst.

INTRODUCTION

Coumarin derivatives like 2-amino-4H-chromenes and dihydropyrano[c]chromenes have received considerable attention because they possess several pharmacological properties [1]. These compounds can be prepared by one-pot three-component condensation of aldehydes, active methylene compounds and resorcinol or 4-hydroxycoumarin in the presence of a variety of acids or bases [2-11]. Some of these procedures suffer from the use of toxic, highly acidic and expensive catalysts and require organic solvents. Therefore, cleaning processes have been in permanent focus. Magnesium perchlorate as a solid acid is a moisture-stable, non-toxic, cheap, and commercially available material which can be handled easily and removed from the reaction mixtures. In continuation of our research on the applications of solid acids in organic synthesis [12,13], we have investigated the one-pot three-component synthesis of 2-amino-4H-chromenes and dihydropyrano[c]chromene derivatives in the presence of Mg(ClO₄)₂.

RESULTS AND DISCUSSION

Initially, we explored the catalytic efficiency of Mg(ClO₄)₂ and other salts with various cations and anions such as MgSO₄, MgBr₂, MgCl₂ and LiClO₄. However, MgSO₄ and MgBr₂ did not exhibit any significant catalytic activity; only 60% and 70% yield was obtained in the presence of MgCl₂ and LiClO₄, respectively, establishing that amongst the various salts used, Mg(ClO₄)₂ was the most effective catalyst for the synthesis of 2-amino-4H-chromenes and dihydropyrano[c]chromenes. For optimizing the experimental conditions, the reaction between malononitrile, benzaldehyde and 4-hydroxycoumarin in the presence of Mg(ClO₄)₂ was considered as a model reaction. This condensation reaction was studied in various solvents at different temperatures and with different amounts of catalysts. The best conditions were found to be 0.035 g catalyst at 60 ºC in H₂O (Table 1).

After completion of the reaction, the mixture was filtered and the aqueous filtrate extracted by 5 mL of ethyl acetate to remove any starting materials. The aqueous phase containing magnesium perchlorate was separated and reused for three times although a gradual decline was observed in its activity (Table 1, entries 18, 19). Apparently, the reaction of various aldehydes, active methylene compounds and 4-hydroxycoumarine in the presence of an optimized amount of Mg(ClO₄)₂ in H₂O at 60 ºC resulted in the formation of dihydropyrano[c]chromene derivatives (Table 2).

Aromatic aldehydes containing electron-withdrawing groups have reacted very well at a faster rate in a shorter time than aromatic aldehydes with electron-donating groups (Table 2, entries 2, 3). Also, in this reaction with ethyl cyanoacetate as a substrate instead of malononitrile, the corresponding products have been produced in high yields but in a longer reaction time (Table 2, entries 11,12). This may be due to the lower activity of ethyl cyanoacetate than malononitrile. Also, the reactions of active methylene compounds, pyridine carbaldehydes and 4-hydroxycoumarine were examined and the corresponding products were found to be yielded highly and within short times (Table 2, entries 13-16). Although the mechanism

---

* To whom all correspondence should be sent:
E-mail: mamrollahi@yazd.ac.ir

of the reaction has not yet been experimentally established, the formation of the product can be rationalized as outlined in the Scheme 1.

The reaction of malononitrile, resorcinol and aldehydes was carried out in the above-mentioned optimized reaction conditions and various 2-amino-4H-chromenes were obtained (Table 3). This reaction produces 2-amino-7-hydroxy-4H-chromene derivatives instead of the expected 2-amino-5-hydroxy-4H-chromene derivatives, that is probably due to the steric hindrance between the two hydroxyl groups in resorcinol.
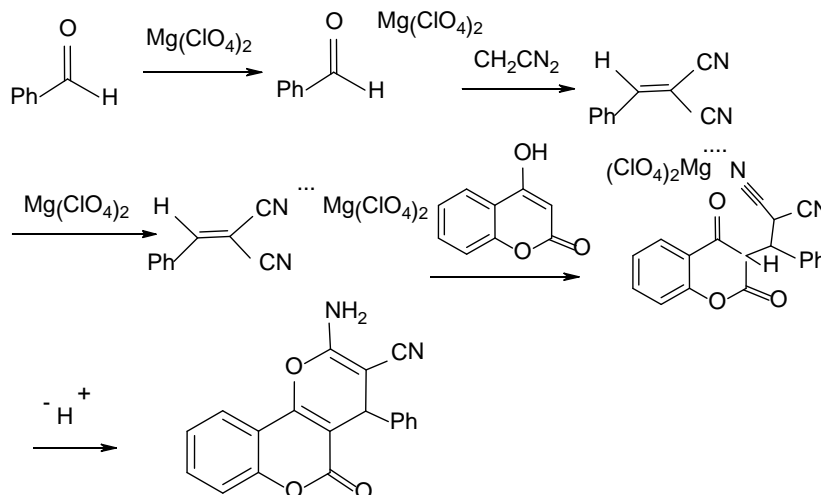
Scheme 1. A possible mechanism for the synthesis of dihydropyrano[c]chromenes

Table 1. Optimization of the reaction conditions for one-pot synthesis of dihydropyrano[c]chromenes [a]
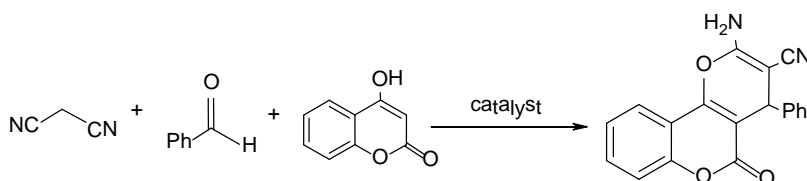
Entry	Catalyst (g)	Temp. (°C)	Solvent	Time (min)	Yield (%) [b]
1	-	70	EtOH	120	30
2	MgCl₂.xH₂O (0.020)	70	EtOH	60	60
3	MgBr₂ (0.030)	70	EtOH	60	45
4	MgSO₄ (0.025)	70	EtOH	60	40
5	LiClO₄ (0.020)	70	EtOH	60	70
6	Mg(ClO₄)₂.xH₂O (0.030)	70	EtOH	50	84
7	Mg(ClO₄)₂.xH₂O (0.020)	70	EtOH	50	60
8	Mg(ClO₄)₂.xH₂O (0.035)	70	EtOH	50	90
9	Mg(ClO₄)₂.xH₂O (0.045)	70	EtOH	50	87
10	Mg(ClO₄)₂.xH₂O (0.035)	70	EtOH/H₂O	50	85
11	Mg(ClO₄)₂.xH₂O (0.035)	70	H₂O	50	90
12	Mg(ClO₄)₂.xH₂O (0.035)	70	MeCN	50	50
13	Mg(ClO₄)₂.xH₂O (0.035)	70	CHCl₃	50	-
14	Mg(ClO₄)₂.xH₂O (0.035)	r.t	H₂O	50	60
15	Mg(ClO₄)₂.xH₂O (0.035)	40	H₂O	50	72
16	Mg(ClO₄)₂.xH₂O (0.035)	50	H₂O	50	83
17	Mg(ClO₄)₂.xH₂O (0.035)	60	H₂O	50	90
18	Mg(ClO₄)₂.xH₂O (0.035) (2th run)	60	H₂O	50	82
19	Mg(ClO₄)₂.xH₂O (0.035) (3th run)	60	H₂O	50	75
20	Mg(ClO₄)₂.xH₂O (0.035)	u.s.[c]	H₂O	15	50

[a] Reaction conditions: malononitrile (1 mmol) benzaldehyde (1 mmol), 4-hydroxycoumarin (1 mmol). [b] Isolated yields. [c] Reaction under ultrasonic waves (60 W).

Table 2. Synthesis of dihydropyrano[c]chromenes in the presence of $Mg(ClO_4)_2$ [a]
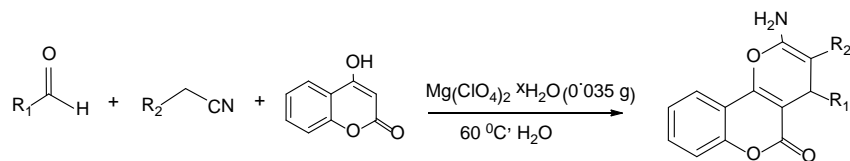
Entry	R_1	R_2	Time(min/h)	Yield (%) [b]	M.p. (°C) Observed	M.p. (°C) Reported	Ref.
1	C_6H_5	CN	50 min	89	256-258	256-258	[3]
2	$3\text{-}NO_2\text{-}C_6H_4$	CN	45 min	95	260-261	256-259	[11]
3	$3\text{-}OH\text{-}C_6H_4$	CN	70 min	75	272-273	-	-
4	$4\text{-}F\text{-}C_6H_4$	CN	50 min	88	265-267	262-263	[3]
5	$4\text{-}OMe\text{-}C_6H_4$	CN	48 min	86	258-260	248-250	[3]
6	$4\text{-}Me\text{-}C_6H_4$	CN	55 min	88	254-256	253-255	[3]
7	$2,6\text{-}Cl_2\text{-}C_6H_3$	CN	52 min	89	299-300	274-277	[11]
8	$4\text{-}Cl\text{-}C_6H_4$	CN	45 min	92	260-262	260-262	[3]
9	$C_6H_5CH_2CH_2$	CN	60 min	74	190-192	187-188	[6]
10	2-furyl	CN	55 min	78	253-255	250-252	[4]
11	$3\text{-}Br\text{-}C_6H_4$	CO_2Et	14 h	78	220-222	-	-
12	$3\text{-}NO_2\text{-}C_6H_4$	CO_2Et	15 h	75	245-247	247-250	[12]
13	3-pyridiyl	CN	12 min	90	251-253	-	-
14	3-pyridiyl	CO_2Et	20 min	85	227-229	-	-
15	4-pyridiyl	CN	10 min	94	186-188	182-184	[5]
16	4-pyridiyl	CO_2Et	15 min	87	220-222	-	-

[a] Reaction conditions: aldehyde (1 mmol), malononitrile (1 mmol), 4-hydroxycoumarin (1 mmol). [b] Isolated yields

Table 3. Synthesis of 2-amino-4H-chromenes in the presence of $Mg(ClO_4)_2$ [a]
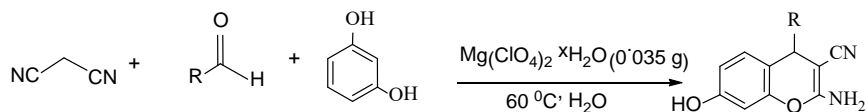
Entry	R	Yield (%) [b]	Time (min)	M. p. (°C) Observed	M. p. (°C) Reported	Ref.
1	C_6H_5	83	80	237-238	235-236	[7]
2	$4\text{-}Me\text{-}C_6H_4$	82	85	190-191	182-184	[7]
3	$4\text{-}F\text{-}C_6H_4$	90	70	188-190	187-189	[7]
4	$3\text{-}NO_2\text{-}C_6H_4$	92	70	210-212	215-217	[13]
5	$4\text{-}Cl\text{-}C_6H_4$	88	75	165-167	163-164	[7]

[a] Reaction conditions: malononitrile (1 mmol) aldehyde(1 mmol), resorcinol (1 mmol). [b] Isolated yields

EXPERIMENTAL

The products were characterized by IR, ^{1}H-NMR, ^{13}C-NMR spectra and by comparing their physical properties with those reported in the literature. IR spectra were run on a Bruker Eqinox 55 spectrometer. ^{1}H- and ^{13}C-NMR spectra were obtained using a Bruker Avance 500 MHz spectrometer (DRX). Melting points were determined by a Buchi melting point B-540 B.V.CHI apparatus. Purity determination of the substrates and reaction monitoring were accompanied by TLC using pre-coated plastic sheets of silica gel G/UV-254 of 0.2 mm thickness.

General procedure for the synthesis of dihydropyrano[c]chromenes and 2-amino-4H-chromenes

4-Hydroxycoumarin or resorcinol (1 mmol) was added to a stirred mixture of aldehyde (1 mmol), active methylene compound (1 mmol), $Mg(ClO_4)_2.xH_2O$ (0.035 g), and water (3 mL). The mixture was stirred at 60 °C for the appropriate period of time until the initial materials were no longer detectable (TLC). The mixture was filtered and recrystallized in ethanol to obtain pure products. The aqueous filtrate containing magnesium perchlorate was used to investigate the reusability of the catalyst.

Selected spectra data

2-Amino-4-(3-hydroxyphenyl)-5-oxo-4,5-dihydropyrano[3,2-c]chromene-3-carbonitrile (Table 2, entry 3). IR (KBr) ($\bar{\upsilon}_{max}$): 3314, 3186, 2209, 1707, 1668, 1604, 1587, 1484 cm^{-1}. ^{1}H-NMR (500 MHz, DMSO-d$_6$): δ = 4.35 (s, 1H), 6.62 (d, 1H, J = 7.1 Hz), 6.63 (s, 1H), 6.67 (d, 1H, J = 8.0 Hz), 7.10 (t, 1H, J = 7.5 Hz), 7.39 (brs, 2H), 7.47 (d, 1H, J = 8.5 Hz), 7.50 (t, 1H, J = 7.5 Hz), 7.72 (t, 1H, J = 8.1 Hz), 7.90 (dd, 1H, J = 7.9 Hz, J = 1.5 Hz), 9.36 (s, 1H).^{13}C-NMR (125 MHz, DMSO-d$_6$): δ = 32.45, 60.45, 106.34, 114.64, 120.45, 124.89, 127.89, 129.35, 130.23, 133.23, 133.56, 134.23, 139.45, 142.12, 148.12, 155.46, 157.89, 164.12, 167.23. Anal. calc. for C$_{19}$H$_{12}$N$_2$O$_4$: C 68.67, H 3.64, N 8.43. found: C 68.4, H 3.8, N 8.9.

2-Amino-5-oxo-4-(2-phenylethyl)-4,5-dihydropyrano[3,2-c]chromene-3-carbonitrile (Table 2, entry 9). IR (KBr) ($\bar{\upsilon}_{max}$): 3368, 3167, 2202, 1703, 1639, 1612, 1601, 1376, 1171 cm^{-1}. ^{1}H-NMR (500 MHz, DMSO-d$_6$): δ = 1.80 (m, 1H), 2.10 (m, 1H), 2.50 (m, 1H), 2.54 (m, 1H), 3.54 (t, 1H, J = 4.0 Hz), 7.03 (t, 1H, J = 7.1 Hz), 7.12 (d, 2H, J = 7.4 Hz), 7.16 (t, 2H, J = 7.3 Hz), 7.36 (s, 2H), 7.45 (m, 2H), 7.69 (t, 1H, J = 7.8 Hz), 7.80 (d, 1H, J = 7.8 Hz).^{13}C-NMR (125 MHz, DMSO-d$_6$): δ = 30.31, 30.75, 34.67, 54.60, 103.76, 112.92, 116.42, 119.60, 122.09, 124.47, 126.64, 128.14, 132.67, 141.30, 152.04, 154.04, 159.44, 159.91.

2-Amino-4-(furan-2-yl)-5-oxo-4,5-dihydropyrano[3,2-c]chromene-3-carbonitrile (Table 2, entry 10): IR (KBr) ($\bar{\upsilon}_{max}$): 3364, 3164, 2201, 1702, 1670, 1639, 1604, 1374, 1257 cm^{-1}.^{1}H-NMR (500 MHz, DMSO-d$_6$): δ = δ4.63 (s, 1H), 6.27 (d, 1H, J = 3.1 Hz), 6.38 (dd, 1H, J = 3.0, 1.8 Hz), 7.47 (d, 1H, J = 3.3 Hz), 7.48 (s, 2H), 7.50 (t, 1H, J = 8.0 Hz), 7.53 (d, 1H, J = 6.0 Hz), 7.69 (t, 1H, J = 8.0 Hz), 7.79 (d, 1H, J = 7.0 Hz). ^{13}C-NMR (125 MHz, DMSO-d$_6$): δ = 29.23, 58.99, 105.23, 106.78, 111.88, 116.78, 117.67, 124.23, 125.67, 126.67, 141.67, 143.45, 152.56, 153.98, 159.47, 160.98, 161.90.

Ethyl-2-amino-4-(3-bromophenyl)-5-oxo-4,5-dihydropyrano[3,2-c]chromene-3-carboxylate (Table 2, entry 11). IR (KBr) ($\bar{\upsilon}_{max}$): 3432, 3311, 1708, 1684, 1655, 1608, 1536, 1517, 1492, 1455 cm^{-1}. ^{1}H-NMR (500 MHz, DMSO-d$_6$): δ = 1.09 (t, 3H, J = 7.5 Hz), 3.99 (q, 2H, J = 7.0 Hz), 4.82 (s, 1H), 7.45 (d, 1H, J = 8.3 Hz), 7.51 (t, 1H, J = 7.4 Hz), 7.55 (t, 1H, J = 7.9 Hz), 7.7 (d, 1H, J = 8.4 Hz), 7.72 (t, 1H, J = 7.5 Hz), 7.96 (s, 2H), 8.00 (d, 1H, J = 8.0 Hz), 8.04 (d, 1H, J = 8.0 Hz), 8.06 (s, 1H). ^{13}C-NMR (125 MHz, DMSO-d$_6$): **δ** = 14.90,

36.36, 60.03, 106.32, 108.12, 113.91, 122.42, 123.49, 123.71, 125.53, 130.41, 133.77, 135.76, 148.02, 148.23, 153.12, 154.43, 159.36, 160.77, 168.12. Anal. calc. for C$_{21}$H$_{16}$BrNO$_5$: C 57.03, H 3.65, N 3.17. found: C 57.3, H 3.4, N 2.9.

2-Amino-5-oxo-4-(pyridin-3-yl)-4,5-dihydropyrano[3,2-c]chromene-3-carbonitrile (Table 2, entry 13). IR (KBr) ($\bar{\upsilon}_{max}$): 3376, 3190, 2194, 1713, 1674, 1639, 1603, 1506, 1460, 1377 cm^{-1}.^{1}H-NMR (500 MHz, DMSO-d$_6$): δ = 4.56 (s, 1H), 7.35 (t, 1H, J = 7.2 Hz), 7.46-7.53 (m, 4H), 7.71-7.75 (m, 2H), 7.90 (d, 1H, J = 6.8 Hz), 7.46 (d, 1H, J = 4.0 Hz), 8.55 (s, 1H). ^{13}C-NMR (125 MHz, DMSO-d$_6$): δ = 34.45, 56.96, 102.92, 113.95, 116.57, 119.03, 122.54, 123.79, 124.66, 132.02, 135.45, 138.75, 148.23, 149.03, 152.21, 153.79, 158.02, 159.56. Anal. calc. for C$_{18}$H$_{11}$N$_3$O$_3$: C 68.14, H 3.49, N 13.24. found: C 68.3, H 3.4, N 12.9.

Ethyl-2-amino-5-oxo-4-(pyridin-3-yl)-4,5-dihydropyrano[3,2-c]chromene-3-carboxylate (Table 2, entry 14). IR (KBr) ($\bar{\upsilon}_{max}$): 3376, 3190, 2194, 1713, 1674, 1639, 1603, 1506, 1460, 1377 cm^{-1}. ^{1}H-NMR (500 MHz, DMSO-d$_6$): δ = 1.07 (t, 3H, J = 7.2 Hz), 4.00 (d, 2H, J = 6.8 Hz), 4.73 (s, 1H), 7.38 (d, 1H, J = 8.0 Hz), 7.49-7.54 (m, 2H), 7.70 (t, 1H, J = 8.0 Hz), 7.78 (d, 1H, J = 8.0 Hz), 7.96-7.99 (m, 3H), 8.43 (d, 1H, J = 4.0 HZ), 8.58 (s, 1H).^{13}C-NMR (125 MHz, DMSO-d$_6$): δ = 14.10, 33.35, 59.10, 62.55, 105.27, 113.05, 116.56, 122.60, 124.65, 132.88, 136.43, 137.38, 141.13, 146.10, 148.13, 152.24, 153.16, 158.49, 159.90, 167.20. Anal. calc. for C$_{20}$H$_{16}$N$_2$O$_5$: C 65.93, H 4.43, N 7.69. found: C 66.1, H 4.2, N 8.0.

Ethyl-2-amino-5-oxo-4-(pyridin-4-yl)-4,5-dihydropyrano[3,2-c]chromene-3-carboxylate (Table 2 entry 16). IR (KBr) ($\bar{\upsilon}_{max}$): 3358, 3182, 1715, 1688, 1658, 1594, 1549, 1492, 1373 cm^{-1}. ^{1}H-NMR (500 MHz, DMSO-d$_6$): δ = 1.10 (t, 3H, J = 7.2 Hz), 4.00 (d, 2H, J = 6.8 Hz), 4.74 (s, 1H), 7.42 (d, 2H, J = 6.2 Hz), 7.48 (d, 1H, J = 8.2 Hz), 7.51 (t, 1H, J = 8.0 Hz), 7.72 (t, 1H, J = 8.0 Hz), 7.76 (d, 1H, J = 8.0 Hz), 8.00 (s, 2H), 8.51 (d, 2H, J = 6.2 Hz).^{13}C-NMR (125 MHz, DMSO-d$_6$): δ = 14.11, 35.34, 59.17, 62.13, 104.89, 112.98, 115.76, 116.58, 122.62, 124.15, 130.76, 133.02, 145.18, 147.66, 152.21, 155.59, 158.57, 159.86, 167.14. Anal. calc. for C$_{20}$H$_{16}$N$_2$O$_5$: C 65.93, H 4.43, N 7.69. found: C 65.9, H 4.4, N 7.8.

2-Amino-7-hydroxy-4-phenyl-4H-chromene-3-carbonitrile (Table 3, entry 1). IR (KBr) ($\bar{\upsilon}_{max}$): 3500, 3428, 3331, 2193, 1650, 1619, 1588, 1506, 1453, 1403, 1325 cm^{-1}. ^{1}H-NMR (500 MHz,

DMSO-d₆): δ = 4.62 (s, 1H), 6.41 (d, 1H, *J* = 2.0 Hz), 6.48 (dd, 1H, *J* = 8.43, 2.0 Hz), 6.8 (d, 1H, *J* = 8.4 Hz), 6.84 (brs, 2H), 7.16 (d, 2H, *J* = 8.0 Hz), 7.20 (t, 1H, *J* = 7.0 Hz), 7.30 (t, 2H, *J* = 7.5 Hz).¹³C-NMR (125 MHz, DMSO-d₆): δ = 56.14, 102.11, 112.32, 113.70, 120.65, 126.60, 127.34, 128.55, 129.89, 146.35, 148.80, 157.02, 160.02.

***2-Amino-7-hydroxy-4-(p-tolyl)-4H-chromene-3-carbonitrile* (Table 3, entry 2)**. IR (KBr) (v̄$_{max}$): 3441, 3339, 3207, 2190, 1643, 1588, 1508, 1464, 1406, 1155 cm⁻¹. ¹H-NMR (500 MHz, DMSO-d₆): δ = 2.25 (s, 3 H), 4.56 (s, 1H), 6.39 (d, 1H, *J* = 2.5 Hz), 6.47 (dd, 1H, *J* = 8.2, 2.3 Hz), 6.77 (d, 1H, *J* = 8.4 Hz), 6.81 (brs, 2H), 7.04 (d, 1H, *J* = 7.9 Hz), 7.10 (d, 1H, *J* = 7.9 Hz).¹³C-NMR (125 MHz, DMSO-d₆): δ = 15.87, 55.23, 104.21, 110.30, 117.87, 125.65, 126.32, 127.78, 128.54, 141.86, 143.56, 146.45, 159.10, 161.34.

In summary, this paper reports a facile and efficient method for the synthesis of 2-amino-4H-chromenes and dihydropyrano[c]chromenes in the presence of magnesium perchlorate. This method offers significant advantages such as high conversions, easy handling, clean and mild reaction profile, and a straightforward work-up which make it a useful and attractive process for the rapid synthesis of substituted 2-amino-4H-chromenes and dihydropyrano[c]chromenes.

REFERENCES

1. (a) B. Karmakar, J. Banerji, *Tetrahedron Lett.*, **52**, 6584 (2011). (b) G.K. Verma, K. Raghuvanshi, R. Kumar, M. Singh, *Tetrahedron Lett.*, **53**, 399 (2012).
2. (a) L.L. Andreani, E. Lapi, *Bull. Chim. Farm.*, **99**, 583 (1960). (b) L. Bonsignore, G. Loy, D. Secci, A. Calignano, Eur. *J. Med. Chem.*, **28**, 517 (1993). (c) A. Martinez-Grau, J.L. Marco, *Bioorg. Med. Chem. Lett.*, **7**, 3165 (1997). (d) M.M. Khafagy, A.H.F. Abd El-Wahab, F.A. Eid, A.M. El-Agody, *Farmaco.*, **57**, 715 (2002). (e) K. Hiramoto, A. Nasuhara, K. Michiloshi, T. Kato, K. Kikugawa, *Mutat Res.*, **395**, 47 (2002). (f) D.R. Anderson, S. Hegde, E. Reinhard, L. Gomez, W.F. Vernier, L. Lee, S. Liu, A.S. Sambandam, P.A. Nider, L. Masih, *Bioorg. Med. Chem. Lett.*, **15**, 1587 (2005). (g) S.J. Mohr, M.A. Chirigos, F.S. Fuhrman, J.W. Pryor, *Cancer Res.*, **35**, 3750 (1975).
3. H. Mehrabi, M. Kazemi-Mireki, *Chinese Chem. Lett.*, **22**, 1419 (2011).
4. J.M. Khurana, B. Nand, P. Saluja, *Tetrahedron*, **66**, 5637 (2010).
5. H. Nagabhushana, S. Sandeep Saundalkar, L. Muralidhar, B.M. Nagabhushana, C.R. Girija, D. Nagaraja, M.A. Pasha, V.P. Jayashankara, *Chinese Chem. Lett.*, **22**, 143 (2011).
6. H.R. Shaterian, A.R. Oveisi, *J. Iran. Chem. Soc.*, **8,** 545 (2011).
7. S. Makarem, A. Mohammadi, A.R. Fakhari, *Tetrahedron Lett.*, **49**, 7194 (2008).
8. D.S. Raghuvanshi, K.N. Singh, *Arkivoc*, 305 (2010).
9. R. Ghorbani-Vaghei, Z. Toghraei-Semiromi, R. Karimi-Nami, *J. Braz. Chem. Soc.*, **22**, 905, (2011).
10. M.M. Heravi, B. Alimadadi Jani, F. Derikvand, F.F. Bamoharram, H.A. Oskooie, *Catal. Commun.*, **10**, 272, (2008).
11. D. Hui, G. Siyi, F. Zhaolong, L. Shizhong, *Chin. J. Org. Chem.*, **31**, 1056 (2011).
12. B.B.F. Mirjalili, A.H. Bamoniri, M.A. Amrollahi, H. Emtiazi, *Digest. J. Nanomater. Biostruct.*, **5,** 897 (2010).
13. M.A. Amrollahi, B.B.F. Mirjalili, H. Emtiazi, *J. Chem. Sci.* 125, 1 (2013).

ЕДНОСТАДИЙНА СИНТЕЗА НА 2-АМИНО-4Н-ХРОМЕНИ И ДИХИДРОПИРАНО [с] ХРОМЕНИ, КАТАЛИЗИРАНА ОТ Mg(ClO₄)₂

Х. Емтиази, М.А. Амролахи *

Департамент по химия, Университет в Язд, П.К. 89195-741, Иран

(Резюме)

Тази статия дава описание на ефикасна и проста процедура за синтезата на 2-амино-4Н-хромени и дихидропирано [с] хромени чрез едностадийна три-компонентна реакция на алдехиди, активни метиленови съединения и резорцинол или 4-хидроксикумарин, катализирана от магнезиев перхлорат. Забележителни предимства са простотата на експерименталната процедура, високите добиви, кратките времена за реакцията и многократната употреба на катализатора.

An efficient ultrasound-promoted method for the synthesis of xanthene derivatives

S. Bagherpoor, M.A. Amrollahi*

Department of Chemistry, Yazd University, Yazd, Iran P.O. Box 89195-741

Zirconium (IV) chloride was used as an efficient, stable, inexpensive, environmentally friendly, and convenient catalyst for preparation of xanthene derivatives *via* one-pot three-component condensation of aldehydes with 2-naphthol and 5,5-dimethyl-1,3-cyclohexanedione under ultrasonic irradiation conditions. EtOH was found as an effective solvent for this transformation. This method offers several advantages such as high yields, simple procedure, low cost and short reaction times.

INTRODUCTION

Ultrasound irradiation is a very effective method and can be widely used in organic synthesis. Higher reaction rates, simple experimental procedure, and high yields are the notable features of the ultrasound approach as compared to established methods [1–3]. In recent times, xanthenes have attracted attention of medicinal chemists, as well as organic chemists due to their wide range of biological and pharmacological activities such as antiviral [4], antibacterial [5], and anti-inflammatory properties [6]. A variety of reagents and catalysts has been reported for the preparation of these compounds such as $Fe(HSO_4)_3$ [7], PVPP-BF_3 [8], $NaHSO_4.SiO_2$ [9], $Sr(OTf)_2$ [10], $Zr(HSO_4)_4$ [11], $RuCl_3 \cdot nH_2O$ [12], P_2O_5/Al_2O_3 [13], $BF_3.SiO_2$ [14], $C_2H_2O_4$ [15], $P(4-VPH)HSO_4$ [16], H_3NSO_3 [17], $BiCl_3$ [18], ZnO-NPs [19], SUSA [20], $Sc[N(SO_2C_8F_{17})_2]_3$ [21], Pd [22], $InCl_3$ [23], $BF_3.OEt_2$ [24], $AcOH/H^+$ [25], p-TSA [26]. The use of each of these materials has its own advantages, but it also suffers from one or more disadvantages such as prolonged reaction time, low yields, use of toxic and costly catalysts, harsh reaction conditions, and complex work-up procedures. Zirconium (IV) chloride ($ZrCl_4$) is generally considered to be a green, inexpensive, non-toxic (LD50: 1688 mg/kg) and commercially available zirconium salt [27]. Its application as a Lewis acid catalyst in various organic transformations has been reported [28–32]. In continuation of our studies towards the development of novel methodologies for the synthesis of biologically active heterocyclic compounds [33], herein we report a improved and convenient method for the synthesis of xanthene derivatives through the condensation of various aromatic aldehydes, 2-naphthol, and 5,5-dimethyl-1,3-cyclohexanedione (dimedone) in the presence of $ZrCl_4$ as an efficient catalyst under silent and ultrasonic irradiation conditions.

EXPERIMENTAL

^{1}H- and ^{13}C-NMR spectra were recorded on Bruker Avance-400 MHz spectrometers. IR spectra were run on a Bruker Eqinox 55 spectrometer. Ultrasonic irradiation was run on Bandelin Sonopuls HD 3200 with an output power of 60 W. Purity determination of the substrates and reaction monitoring were accompanied by TLC using pre-coated plastic sheets of silica gel G/UV-254 of 0.2 mm thickness.

General experimental procedure

Silent conditions. A mixture of aldehyde (1 mmol), 2-naphthol (1 mmol), dimedone (1.2 mmol) and $ZrCl_4$ (8 mol%) was stirred for appropriate time in EtOH at reflux temperature. The completion of the reaction was monitored by TLC ($CHCl_3$:MeOH 9:1). After cooling, the reaction mixture was poured onto crushed ice (20 g). The resulting precipitate was filtered under suction, and then recrystallized from EtOH to afford the pure product with yield of 70-82%. The results are summarized in Table 2.

Ultrasound irradiation. A mixture of aldehyde (1 mmol), 2-naphthol (1 mmol), dimedone (1.2 mmol) and $ZrCl_4$ (8 mol%) was irradiated with ultrasound at reflux temperature for appropriate time. After cooling, the reaction mixture was poured onto crushed ice (20 g). The resulting precipitate was filtered under suction, and then recrystallized from EtOH to afford the pure product with yield of 75-95%. The results are summarized in Table 2.

Selected spectra data

9,9-dimethyl-12-phenyl-9,10-dihydro-8H-benzo[a]xanthen-11(12H)-one Yield: 85%, White solid, m.p. 158-160 °C; IR (KBr): 2913, 1647, 1620, 1596, 1469, 1452, 1372. ^{1}H-NMR (400 MHz,

* To whom all correspondence should be sent:
E-mail: mamrollahi@yazd.ac.ir

CDCl3): δ 0.97 (s, 3H), 1.13 (s, 3H), 2.25 (d, 1H), 2.32 (d, 1H), 2.58 (s, 2H), 5.71 (s, 1H), 7.06 (t, 1H), 7.18 (t, 2H), 7.32-7.46 (m, 5H), 7.77 (d, 1H), 7.79 (d, 1H), 8.00 (d, 1H). ^{13}C-NMR (100 MHz, CDCl3): δ 27.5, 29.7, 32.6, 35.3, 41.8, 51.2, 114.71, 117.4, 118.1, 124.1, 125.3, 126.6, 127.4, 128.6, 128.8, 128.8, 129.2, 131.8, 131.9, 145.1, 148.2, 165.3, 197.2.

9,9-dimethyl-12-(p-tolyl)-9,10-dihydro-8H-benzo[a]xanthen-11(12H)-one Yeild: 85%, White solid, m.p. 172-174 °C; IR (KBr): 2957, 1646, 1620, 1597, 1511, 1466, 1369. ^{1}H-NMR (400 MHz, CDCl3): δ 1.00 (s, 3H), 1.14 (s, 3H), 2.23 (s, 3H), 2.35 (m, 2H), 2.6 (s, 2H), 5.7 (s, 1H), 6.99 (d, 2H), 7.24 (d, 2H), 7.32-7.43 (m, 2H), 7.46 (t, 1H), 7.78 (t, 2H), 8.03 (d, 1H). ^{13}C-NMR (100 MHz, CDCl3): δ 20.9, 27.3, 29.2, 32.3, 34.3, 41.4, 50.9, 114.4, 117.0, 117.9, 123.7, 124.8, 126.9, 128.2, 128.3, 128.7, 128.9, 131.4, 131.5, 135.6, 141.8, 147.7, 163.7, 196.9.

12-(2-fluorophenyl)-9,9-dimethyl-9,10-dihydro-8H-benzo[a]xanthen-11(12H)-one Yeild: 87%, White solid, m.p. 175-177 °C; IR (KBr): 2948, 1649, 1620, 1595, 1515, 1485 (-CH$_2$ bend.), 1371. ^{1}H-NMR (400 MHz, CDCl$_3$): δ 1.03 (s, 3H), 1.16 (s, 3H), 2.23-2.42 (m, 2H), 2.63 (s, 2H), 5.9 (s, 1H), 6.96-6.99 (m, 2H), 7.38-7.41 (m, 2H), 7.42-7.48 (m, 2H), 7.52 (t, 1H), 7.75-7.80 (m, 2H), 8.12

(d,1H).^{13}C-NMR (100 MHz, CDCl$_3$): 27.1, 27.2, 29.4, 32.2, 41.4, 50.8, 115.7, 116.5, 117.1, 118.8, 121.5, 123.2, 123.4, 124.0, 124.3, 124.9, 125.2, 127.1, 128.2, 128.4, 128.7, 128.9, 130.9, 165.2, 196.6.
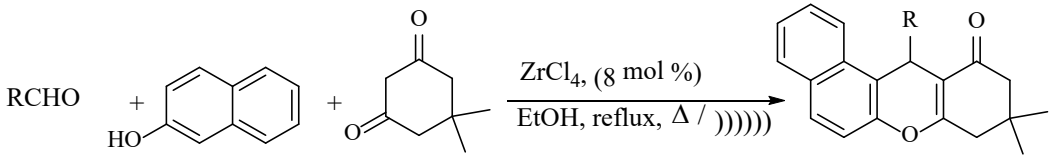
RESULTS AND DISCUSSION

In our initial study, the reaction of benzaldehyde, 2-naphthol, and dimedone was considered as a model reaction to optimize the conditions. The reaction was first carried out in H$_2$O in the absence of ZrCl$_4$ and at reflux temperature. No reaction occurred under silent and ultrasound irradiation conditions (Table 1, entry 1). The reaction was then attempted in the presence of 8 mol % of ZrCl$_4$. The result in Table 1, entry 2 shows a trace amount of product prepared under both silent and ultrasound irradiation conditions. To find the best solvent, several solvents such as CH$_2$Cl$_2$, AcOEt, MeCN, EtOH and solvent-free conditions were employed as media. It was noticed that the highest yield was achieved with EtOH, when the reaction was performed under silent conditions (Table 1, entry 6), while the formation of the product was more facile and proceeded in shorter time and with high yield under ultrasonic irradiation conditions.

Table 1. Optimization of the reaction conditions for one-pot synthesis of 9,9-dimethyl-12-phenyl-9,10-dihydro-8H-benzo[a]xanthen-11(12H)-one under various conditions [a)]

Entry	Catalyst (mol%)	Solvent	Yield (%) [b)]
1	-	H$_2$O	-
2	ZrCl$_4$ (8)	H$_2$O	trace
3	ZrCl$_4$ (8)	CH$_2$Cl$_2$	-
4	ZrCl$_4$ (8)	AcOEt	-
5	ZrCl$_4$ (8)	MeCN	-
6	ZrCl$_4$ (8)	EtOH	75
7	ZrCl$_4$ (8)	solvent-free	trace
8 [c)]	ZrCl$_4$ (8)	EtOH	65
9 [d)]	ZrCl$_4$ (8)	EtOH	40
10	ZrCl$_4$ (4)	EtOH	55
11	ZrCl$_4$ (6)	EtOH	60
12	ZrCl$_4$ (10)	EtOH	71
13	ZrOCl$_2$.8H$_2$O (9)	EtOH	20
14	ZnBr$_2$ (8)	EtOH	70
15	CoCl$_2$ (8)	EtOH	40
16	CuCl$_2$ (8)	EtOH	35
17	Ni(NO$_3$)$_2$ (10)	EtOH	65

[a)] Reaction conditions: benzaldehyde (1 mmol), 2-naphthol (1 mmol), dimedone (1.2 mmol), EtOH (5 mL), [b)] Isolated yields under normal conditions. [c)] 60 °C, [d)] room temp.

Table 2. Synthesis of benzo[a]xanthenone derivatives under silent and ultrasonic conditions [a)]

Entry	R	Time (min) Sonication/Silent	Yield (%) [b)] Sonication [c)]/Silent	Melting points (°C)		
				Found	Reported	Ref.
1	C$_6$H$_5$	20/120	85/75	158-160	151-153	[23]
2	3-NO$_2$C$_6$H$_4$	15/65	92/80	162-164	168-170	[23]
3	4-NO$_2$C$_6$H$_4$	15/60	95/82	181-182	178-180	[23]
4	2-FC$_6$H$_4$	17/70	87/80	175-177	-	
5	4-ClC$_6$H$_4$	18/70	85/78	185–187	180–182	[23]
6	2-ClC$_6$H$_4$	18/75	87/80	184-186	179-180	[23]
7	4-OMeC$_6$H$_4$	30/140	80/72	202-204	204-205	[23]
8	2-OMeC$_6$H$_4$	28/150	82/70	166-168	163-165	[23]
9	4-MeC$_6$H$_4$	25/130	84/75	172-174	176-178	[23]
10	4-C$_3$H$_7$C$_6$H$_4$	30/125	83/73	155-157	150-152	[20]
11	3,4-(OMe)$_2$C$_6$H$_3$	40/150	77/70	208-210	201–204	[12]
12	2-naphtyl	20/115	87/79	210-212	215-217	[20]
13	3,4(Me)$_2$C$_6$H$_3$	25/125	82/77	176–178	181–182	[10]
14	4-OHC$_6$H$_4$	40/145	75/70	155–156	151–153	[12]
15	2,4-Cl$_2$C$_6$H$_3$	17/65	90/80	182–184	178–181	[12]

[a)] Reaction conditions: aldehyde (1 mmol), 2-naphthol (1 mmol), dimedone (1.2 mmol), EtOH (4 mL), [b)] Isolated yields. [c)] Constant frequency: 60 W.

Table 3. Comparison of the efficiency of ZrCl$_4$ with that of the reported catalysts for the synthesis of benzo[a]xanthenones.

Entry	Catalyst	Yield (%)	Ref.
1	Sr(OTf)$_2$ (10 mol%)	70-88%	[10]
2	Zr(HSO$_4$)$_4$ (2 mol%)	69-90%	[11]
3	RuCl$_3$·xH$_2$O (5 mol%)	75-92%	[12]
4	ZrCl$_4$ (8 mol%)	75-95%	This work

The effect of temperature on the reaction was also studied. We found that the best results were obtained in EtOH at reflux temperature under silent conditions (Table 1, entries 6, 8, 9). Similar reactions were then attempted in the presence of 4, 6, and 10, mol% of ZrCl$_4$. The results in Table 1, entries 6, 10-12 show that the use of 8 mol% of ZrCl$_4$ is sufficient to push the reaction forward. Higher loading of the catalyst had no significant influence on the reaction yield. Thus, 8 mol% of ZrCl$_4$ and a reaction temperature at reflux were the optimal conditions. When ZrOCl$_2$.8H$_2$O, ZnBr$_2$, CoCl$_2$, CuCl$_2$, and Ni(NO$_3$)$_2$ were used as catalysts, benzo[a]xanthenone was formed in lower yields (Table 1, entries 13-17).

Under the optimized conditions, xanthene derivatives were synthesized in high yields under silent and ultrasound irradiation conditions. Ultrasound irradiation accelerated such reactions. The results are summarized in Table 2. It can be observed that the process tolerates both electron-

donating and electron–withdrawing substituents in the benzaldehydes.
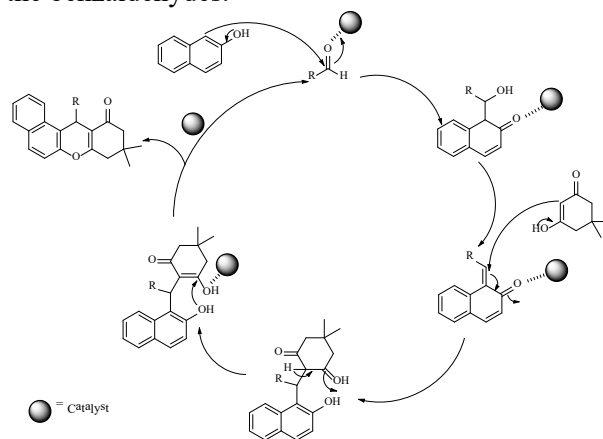
Scheme 1. The proposed mechanism of synthesizing benzo[a]xanthenones catalyzed by ZrCl$_4$

In all cases, the reactions proceeded efficiently at reflux under mild conditions to afford the corresponding products in high yields. All the products were characterized by ^{1}H- and ^{13}C-NMR, and IR spectroscopy.

Finally, in order to assess the efficiency and generality of this methodology, we compared the method with some reported results in the literature (Table 3). It was found that $ZrCl_4$ is the most efficient catalyst with respect to reaction time, temperature, yield of the product, and catalyst nature.

Although the mechanism of the reaction has not yet been established experimentally, the formation of the product can be rationalized as outlined in Scheme 1.

In conclusion, we have developed an improved and convenient procedure for the synthesis of xanthene derivatives under ultrasonic irradiation in the presence of $ZrCl_4$ as a catalyst in EtOH at reflux temperature. The remarkable advantages of this method are: simple experimental procedure, short reaction times, high yields, and ease of product isolation.

REFERENCES

1. T.J. Mason, J.P. Lorimer, Sonochemistry: Theory, Application and Uses of Ultrasound in Chemistry, John Wiley & Sons, New York, 1988.
2. K.S. Suslick, Ultrasound, its Chemical, Physical and Biological Effects, VCH, Weinheim, 1988.
3. T.S. Saleh, N.M.A. El-Rahman, A.A. Elkateb, N.O. Shaker, N.A. Mahmoud, S.A. Gabal, *Ultrason. Sonochem*, **19**, 491 (2012).
4. R.W. Lambert, J.A. Martin. J.H. Merrett, K.E.B. Parkes, G. Thomas, *Chem. Abstr.,* **126**, p212377y (1997).
5. T. Jpn. Hideo, *Chem. Abstr.*, **95**, 80922b (1981).
6. J.P. Poupelin, G. Saint-Ruf, O. Foussard-Blanpin, G. Narcisse, G. Uehida-Ernouf, R. Lacroix, *Eur. J. Med. Chem.,* 13, 67 (1978).
7. H.R. Shaterian, A. Hosseinian, M. Ghashang, *Turk. J. Chem.*, **33**, 233 (2009).
8. M. Mokhtary, S. Refahati, *Dyes Pigments*, **99**, 378 (2013).
9. B. Das, K. Laxminarayana, M. Krishnaiah, Y. Srinivas, *Synlett*, 3107 (2007).
10. J. Li, W. Tang, L. Lu, W. Su, *Tetrahedron Lett*., **49**, 7117 (2008).
11. N. Foroughifar, A. Mobinikhaledi, H. Moghanian, *Int. J. Green Nanotechnology: Phys. Chem.*, **1**, 57 (2009).
12. K. Tabatabaeian, A. Khorshidi, M. Mamaghani, A. Dadashi, M.K. Jalali, *Can .J .Chem.*, **89**, 623 (2011).
13. A. Zarei, A.R. Hajipour, L. Khazdooz, *Dyes Pigments,* **85**, 133, (2010).
14. B.B.F. Mirjalili, A. Bamoniri, A. Akbari, *Tetrahedron Lett*., **49**, 6454 (2008).
15. N.D. Kokare, J.N. Sangshetti, D.B. Shinde, *Chin. Chem. Lett*., 19, 1186 (2008).
16. N. GhaffariKhaligh, *Ultrason. Sonochem.,* **19**, 736 (2012).
17. B. Rajitha, B.S. Kumar, Y.T. Reddy, *Tetrahedron Lett.,* **46**, 8691 (2005).
18. E. Soleimani, M.M. Khodaei, *Chin. Chem. Lett*., **22**, 927 (2011).
19. G.B.D. Rao, M.P. Kaushik, A.K. Halve, *Tetrahedron Lett*., **53**, 2741 (2012).
20. F. Shirini, N.G. Khaligh, *Dyes Pigments*, **95**, 789 (2012).
21. M. Hong, C. Cai, *J. Fluorine Chem.,* **130**, 989 (2009).
22. J.G. Wang, R. Harvey, *Tetrahedron*, **58**, 5927 (2002).
23. G.C. Nandi, S. Samai, R. Kumar, M.S. Singh, *Tetrahedron*, **65**, 7129 (2009).
24. W. Yuan, M. Shi, *Tetrahedron*, **66**, 7104 (2010).
25. A. Jha, J. Beal, *Tetrahedron Lett.,* **45**, 8999 (2004).
26. A. Bazgir, Z.N. Tisseh, P. Mirzaei, *Tetrahedron Lett.,* **49**, 5165 (2008).
27. X. Fan, X. Hu, X. Zhang, J. Wang, *Can. J. Chem.*, **83**, 16 (2005).
28. G. Song, B. Wang, H. Luo, L. Yang, *Catal. Commun*. **8**, 673 (2007).
29. B. Das, P. Thirupathi, I. Mahender, K.R. Reddy, B. Ravikanth, L. Nagarapu, *Catal. Commun*., **8**, 535 (2007).
30. B. Das, P. Thirupathi, I. Mahender, V.S. Reddy, Y.K. Rao, *J. Mol. Catal. A: Chem.*, **247**, 233 (2006).
31. R. Kumar, G.C. Nandi, R.K. Verma, M.S. Singh, *Tetrahedron Lett*, **51**, 442 (2010).
32. M. Dabiri, S.C. Azimi, A. Bazgir, *Chem. Pap.,* **62**, 522 (2005).
33. H. Emtiazi, M.A. Amrollahi, *Helv. Chim. Acta*, **96**, 2196 (2013).

ЕФИКАСЕН УЛТРАЗВУКОВ МЕТОД ЗА СИНТЕЗ НА КСАНТЕНОВИ ПРОИЗВОДНИ

С. Багерпур, М.А. Амролахи*

Департамент по химия, Университет в Язд, Язд, Иран

(Резюме)

Използван е циркониев (IV) хлорид като ефикасен, стабилен, евтин, екологично съвместим и удобен катализатор за приготвянето на ксантенови производни чрез едно-стадийна три-компонентна кондензация на алдехиди с 2-нафтол и 5,5-диметил-1,3-циклохександион при ултразвуково облъчване. Етанолът е най-подходящия разтворител за случая. Този метод предлага няколко предимства, като висок добив, проста процедура, ниска цена и кратки реакционни времена.

Magnetohydrodynamic stability of self-gravitating compressible resistive rotating streaming fluid medium

A.A. Hasan

Basic and Applied Sciences Department, College of Engineering and Technology, Arab Academy for Science, Technology and Maritime Transport (AASTMT), Sadat road - P.O. Box 11Aswan, Egypt

Magnetohydrodynamic stability of a gravitational medium with streams of variable velocity distribution for a general wave propagation in the presence of the rotation forces has been studied. The magnetic field has strong stabilizing influence but the streaming is a destabilizing. The rotating forces have a stabilizing influence under certain restrictions. It is proved that the gravitational Jean's instability criterion is not influenced by the electromagnetic force or the rotation force or even by the combined effect of them whether the fluid medium is streaming or not and whether the rotation in one or more dimension.

INTRODUCTION

The self-gravitational instability of a homogeneous fluid medium at rest has been investigated since long time ago, for its practical application in astrophysics see Jeans [1]. It is founded that the model is unstable under the restriction

$$k^2 C_S^2 - 4\pi G \rho_o < 0$$

called after Jeans by Jeans' criterion, where k is the net wave number of the propagated wave, C_S^2 is a sound speed in the fluid, of density ρ_o, and G is the self-gravitational constant. Chandrasekhar and Fermi [2], and later on Chandrasekhar [3] made several extensions. The Jeans' model of self-gravitating medium has been elaborated with streams of variable velocity distribution by Sengar [4]. Recently Radwan et. al. [5], developed the magnetogravitational stability of variable streams pervaded by the constant magnetic field $(H_o, 0, 0)$. The stability of different cylindrical models under the action of self-gravitating force in addition to other forces has been elaborated by Radwan and Hasan [6], [7]. Hasan [8] has investigated the stability of an oscillating streaming fluid cylinder subject to the combined effect of the capillary, selfgravitating and electrodynamic forces in all axisymmetric and non-axisymmetric perturbation modes. He [9] has investigated the stability of oscillating
streaming self-gravitating dielectric incompressible

fluid cylinder surrounded by tenuous medium of negligible motion pervaded by transverse varying electric field for all the axisymmetric and non-axisymmetric perturbation modes. He [10] has studied the instability of a full fluid cylinder surrounded by self-gravitating tenuous medium pervaded by transverse varying electric field under the combined effect of the capillary, self-gravitating, and electric forces for all the modes of perturbations. He [11] the magnetodynamic stability of a fluid jet pervaded by transverse varying magnetic field while its surrounding tenuous medium is penetrated by uniform magnetic field.

Here in the present work we study the magnetodynamic stability of a self-gravitating rotating streaming viscous fluid medium pervaded by general magnetic field. Such studies have a correlation with the formation of sunspots. Also they have relevance in describing the condensation within astronomical bodies cf. Chandrasekhar and Fermi [2], and also Chandrasekhar [3].

BASIC STATE

We consider an infinite self-gravitating fluid medium. The fluid is assumed to be homogeneous and viscous. The model is acting upon the following forces
(*i*) the pressure gradient force, (*ii*) electromagnetic force, (*iii*) self-gravitating force, (*iv*) the forces due to rotating factors and (*v*) the forces due to resistivity.

We shall utilize the cartesian coordinates (*x*, *y*, *z*) for investigating such problem. The required equations for the present problem

---

* To whom all correspondence should be sent:
E-mail: alfaisal772001@gmail.com

$$\rho\left(\frac{\partial \underline{u}}{\partial t}+(\underline{u}\cdot\nabla)\underline{u}\right)=-\nabla P+\mu(\nabla\wedge\underline{H})\wedge\underline{H}+\rho\nabla V$$

$$-2\rho(\underline{u}\wedge\underline{\Omega})+\frac{1}{2}\rho(\underline{\Omega}\wedge\underline{r})^2 \qquad (1)$$

$$\frac{\partial\rho}{\partial t}+(\underline{u}\cdot\nabla)\rho=-\rho(\nabla\cdot\underline{u}) \qquad (2)$$

$$\frac{\partial\underline{H}}{\partial t}=\nabla\wedge(\underline{u}\wedge\underline{H})-\nabla\wedge(\eta\nabla\wedge\underline{H}) \qquad (3)$$

$$\nabla\cdot\underline{H}=0 \qquad (4)$$

$$\nabla^2 V=-4\pi G\rho \qquad (5)$$

$$P=K\rho^{\Gamma} \qquad (6)$$

Here ρ, $\underline{u}$, and P are the fluid density, velocity vector and kinetic pressure, μ and $\underline{H}$ are the magnetic field permeability and intensity, V and G are the self-gravitating potential and constant, η is the coefficient of resistivity, $\underline{\Omega}$ is the angular velocity of rotation, K and Γ are constants where Γ is the polytropic exponent.

We assume that the medium: (i) rotates with the general uniform angular velocity

$$\underline{\Omega}=(\Omega_x,\Omega_y,\Omega_z) \qquad (7)$$

(ii) be pervaded by the two dimensions homogeneous magnetic field

$$\underline{H}_o=(0,H_{oy},H_{oz}) \qquad (8)$$

and (iii) posses streams moving in the x_direction with velocity

$$\underline{u}_o=(U(z),0,0) \qquad (9)$$

varying along the z-direction of the Cartesian coordinates (x, y, z).

PERTURBATION ANALYSIS

For small departures from the initial state, every variable quantity Q may be expressed as

$$Q=Q_o+Q_1 \qquad , \qquad |Q_1|\ll Q_o \qquad (10)$$

where Q stands for each $\rho, \underline{H}, P, \underline{u}$ and V. Based on the expansion (10), the perturbation equations could be obtained from (1)--(6) in the form:

$$\rho_o\left(\frac{\partial\underline{u}_1}{\partial t}+(\underline{u}_o\cdot\nabla)\underline{u}_1+(\underline{u}_1\cdot\nabla)\underline{u}_o\right)=-\nabla P_1+\mu(\nabla\wedge\underline{H}_1)\wedge\underline{H}_o$$

$$+\mu(\nabla\wedge\underline{H}_o)\wedge\underline{H}_1+\rho\nabla V_1-2\rho_o(\underline{u}_1\wedge\underline{\Omega}) \qquad (11)$$

$$\frac{\partial\underline{H}_1}{\partial t}=\nabla\wedge(\underline{u}_1\wedge\underline{H}_o)+\nabla\wedge(\underline{u}_o\wedge\underline{H}_1)-\nabla\wedge(\eta\nabla\wedge\underline{H}_1) \qquad (12)$$

$$\frac{\partial\rho_1}{\partial t}+(\underline{u}_o\cdot\nabla)\rho_1+(\underline{u}_1\cdot\nabla)\rho_o+\rho_o(\nabla\cdot\underline{u}_1)+\rho_1(\nabla\cdot\underline{u}_o)=0 \qquad (13)$$

$$\nabla\cdot\underline{H}_1=0 \qquad (14)$$

$$\nabla^2 V_1=-4\pi G\rho_1 \qquad (15)$$

$$\frac{dP_1}{dt}=C_S^2\frac{d\rho_1}{dt} \qquad (16)$$

where $C_S\left(=\sqrt{\dfrac{\Gamma P_o}{\rho_o}}\right)$ is the sound speed in the fluid.

By the use of the components of $\underline{u}_1$ and $\underline{H}_1$, viz.

$$\underline{u}_1=(u,v,w) \qquad (17)$$

$$\underline{H}_1=(h_x,h_y,h_z) \qquad (18)$$

together with the assumptions (7)--(9), the system of equations (11)--(16) may be rewritten as

$$\rho_o\left[\frac{\partial u}{\partial t}+U_o\frac{\partial u}{\partial x}+w\frac{dU_o}{dz}\right]=-\frac{\partial P_1}{\partial x}-\mu\frac{\partial}{\partial x}\left(H_{oy}h_y+H_{oz}h_z\right)$$

$$-\mu\left(H_{oy}\frac{\partial}{\partial y}+H_{oz}\frac{\partial}{\partial z}\right)h_x+\rho_o\frac{\partial V_1}{\partial x}+2\rho_o\Omega_y w-2\rho_o\Omega_z v \qquad (19)$$

$$\rho_o\left[\frac{\partial v}{\partial t}+U_o\frac{\partial v}{\partial x}\right]=-\frac{\partial P_1}{\partial y}-\mu\frac{\partial}{\partial y}\left(H_{oy}h_y+H_{oz}h_z\right)$$

$$-\mu\left(H_{oy}\frac{\partial}{\partial y}+H_{oz}\frac{\partial}{\partial z}\right)h_y+\rho_o\frac{\partial V_1}{\partial y}+2\rho_o\Omega_z u-2\rho_o\Omega_x w \qquad (20)$$

$$\rho_o\left[\frac{\partial w}{\partial t}+U_o\frac{\partial w}{\partial x}\right]=-\frac{\partial P_1}{\partial z}-\mu\frac{\partial}{\partial z}\left(H_{oy}h_y+H_{oz}h_z\right)$$

$$-\mu\left(H_{oy}\frac{\partial}{\partial y}+H_{oz}\frac{\partial}{\partial z}\right)h_z+\rho_o\frac{\partial V_1}{\partial z}+2\rho_o\Omega_x u-2\rho_o\Omega_x v \qquad (21)$$

$$\frac{\partial h_x}{\partial t}+U_o\frac{\partial h_x}{\partial x}=\left(H_{oy}\frac{\partial}{\partial y}+H_{oz}\frac{\partial}{\partial z}\right)u+h_z\frac{dU_o}{dz}$$

$$-\left(\frac{\partial}{\partial y}\left(\frac{\partial}{\partial x}h_y-\frac{\partial}{\partial y}h_x\right)-\frac{\partial}{\partial z}\left(\frac{\partial}{\partial z}h_x-\frac{\partial}{\partial x}h_z\right)\right) \qquad (22)$$

$$\frac{\partial h_y}{\partial t}+U_o\frac{\partial h_y}{\partial x}=\left(H_{oy}\frac{\partial}{\partial y}+H_{oz}\frac{\partial}{\partial z}\right)v+H_{oy}\left(\frac{\partial u}{\partial x}+\frac{\partial v}{\partial y}+\frac{\partial w}{\partial z}\right)$$

$$+\left(\frac{\partial}{\partial x}\left(\frac{\partial}{\partial x}h_y-\frac{\partial}{\partial y}h_x\right)-\frac{\partial}{\partial z}\left(\frac{\partial}{\partial y}h_z-\frac{\partial}{\partial z}h_y\right)\right) \qquad (23)$$

$$\frac{\partial h_z}{\partial t}+U_o\frac{\partial h_z}{\partial x}=\left(H_{oy}\frac{\partial}{\partial y}+H_{oz}\frac{\partial}{\partial z}\right)w+H_{oz}\left(\frac{\partial u}{\partial x}+\frac{\partial v}{\partial y}+\frac{\partial w}{\partial z}\right)$$

$$-\left(\frac{\partial}{\partial x}\left(\frac{\partial}{\partial z}h_x-\frac{\partial}{\partial x}h_z\right)-\frac{\partial}{\partial y}\left(\frac{\partial}{\partial y}h_z-\frac{\partial}{\partial z}h_y\right)\right) \qquad (24)$$

$$\frac{\partial\rho_1}{\partial t}+U_o\frac{\partial\rho_1}{\partial x}=-\rho_o\left(\frac{\partial u}{\partial x}+\frac{\partial v}{\partial y}+\frac{\partial w}{\partial z}\right) \qquad (25)$$

$$\frac{\partial h_x}{\partial x}+\frac{\partial h_y}{\partial y}+\frac{\partial h_z}{\partial z}=0 \qquad (26)$$

$$\frac{\partial^2 V_1}{\partial x^2}+\frac{\partial^2 V_1}{\partial y^2}+\frac{\partial^2 V_1}{\partial z^2}=-4\pi G\rho_1 \qquad (27)$$

$$\frac{\partial P_1}{\partial t}+U_o\frac{\partial P_1}{\partial x}=C_S^2\left(\frac{\partial\rho_1}{\partial t}+U_o\frac{\partial\rho_1}{\partial x}\right) \qquad (28)$$

EIGENVALUE RELATION

Apply sinusoidal wave along the fluid interface. Consequently, from the viewpoint of the stability approaches given by Chandrasekhar [3], we assume that the space-time dependence of the wave propagation of the form

$$Q_1\sim\exp\left[i\left(k_x x+k_y y+k_z z+\sigma t\right)\right] \qquad (29)$$

Here σ is gyration frequency of the assuming wave. k_x, k_y and k_z are (any real values) the wave numbers in the (x, y, z) directions. By an appeal to the time-space dependence (29), the relevant perturbation equations (19)-(28) are given by

$$n\rho_o u+\rho_o wDU_o=-ik_x C_S^2\rho_1-i\mu\left(k_y H_{oy}+k_z H_{oz}\right)h_x$$

$$+ik_x\mu\left(H_{oy}h_y+H_{oz}h_z\right)+ik_x\rho_o V_1+2\rho_o\Omega_y w-2\rho_o\Omega_z v \qquad (30)$$

$$n\rho_o v=-ik_y C_S^2\rho_1-i\mu\left(k_y H_{oy}+k_z H_{oz}\right)h_y$$

$$+ik_y\mu\left(H_{oy}h_y+H_{oz}h_z\right)+ik_y\rho_o V_1-2\rho_o\Omega_x w+2\rho_o\Omega_z u \qquad (31)$$

$$n\rho_o w=-ik_z C_S^2\rho_1-i\mu\left(k_y H_{oy}+k_z H_{oz}\right)h_z$$

$$+ik_z\mu\left(H_{oy}h_y+H_{oz}h_z\right)+ik_z\rho_o V_1+2\rho_o\Omega_y u-2\rho_o\Omega_x v \qquad (32)$$

$$nh_x=i\left(H_{oy}k_y+H_{oz}k_z\right)u+h_z DU_o+i\eta\left(-\left(k_y^2+k_z^2\right)h_x+k_x k_y h_y+k_x k_z h_z\right) \qquad (33)$$

$$nh_y=i\left(H_{oy}k_y+H_{oz}k_z\right)v-iH_{oy}\left(k_x u+k_y v+k_z w\right)$$

$$+i\eta\left(k_x k_y h_x-\left(k_x^2+k_z^2\right)h_y+k_y k_z h_z\right) \qquad (34)$$

$$nh_z=i\left(H_{oy}k_y+H_{oz}k_z\right)w-iH_{oz}\left(k_x u+k_y v+k_z w\right)$$

$$+i\eta\left(k_x k_z h_x+k_y k_z h_y-\left(k_x^2+k_y^2\right)h_z\right) \qquad (35)$$

$$n\rho_1=-i\rho_o\left(k_x u+k_y v+k_z w\right) \qquad (36)$$

$$ik_x h_x+ik_y h_y+ik_z h_z=0 \qquad (37)$$

$$k^2 V_1=-4\pi G\rho_1 \qquad (38)$$

where

$$k^2 = k_x^2 + k_y^2 + k_z^2 \quad , D = \frac{d}{dz} \tag{39}$$

$$n = i(\sigma + k_x U_o) \tag{40}$$

The foregoing system equations (30)-(38) could be rewritten in the matrix form

$$[a_{ij}][b_j] = 0 \tag{41}$$

where the elements $[a_{ij}]$ of the matrix are given in the appendix I while the elements of the column matrix $[b_j]$ are being $u, v, w, h_x, h_y, h_z, \rho_1$ and V_1. One has to mention here that equation (37) is identically satisfied.

For non-trivial solution of the equations (41), setting the determinant of the matrix $[a_{ij}]$ equal to zero (see Appendix I), we get the general eigenvalue relation of seven order in n in the form

$$A_7 n^7 + A_6 n^6 + A_5 n^5 + A_4 n^4 + A_3 n^3 + A_2 n^2 + A_1 n + A_0 = 0 \tag{42}$$

where the compound coefficients $A_i \ (i = 0,1,2,3,4,5,6,7)$ are calculated.

DISCUSSIONS AND RESULTS

Equation (42) is a general MHD eigenvalue relation of a rotating self-gravitating fluid medium pervaded by magnetic field of two dimensions. Some previously publishing results may be obtained as limiting cases here. That confirms the present analysis.

In absence of the rotating, electromagnetic forces and for inviscid fluid i.e. $\underline{\Omega} = 0$, $\underline{H}_o = 0$ and $\eta = 0$, equation (42) yields

$$k^2 n^3 + k^2 \left(k^2 C_S^2 - 4\pi G \rho_o\right) n - k_x k_z \left(k^2 C_S^2 - 4\pi G \rho_o\right) D U_o = 0 \tag{43}$$

This relation coincides with the dispersion relation, of a pure self-gravitating fluid medium streams with variable streams $(U_o(z),0,0)$ derived by Sengar [1]. For more details concerning stability of this case we may refer to Sengar (1981).

If
$$\underline{\Omega} = 0, \ \underline{H}_o = 0, \ \eta = 0 \ \text{and} \ U_o = 0,$$
equation (42) reduces to
$$n^2 = k^2 C_S^2 - 4\pi G \rho_o \tag{44}$$
This gives the same results given by Jean's (1902). For more details concerning the instability of this case we may refer to the discussions of Jean's (1902).

In absence of the magnetic field and we assume that the fluid medium is stationary i.e. $H_o = 0, \eta = 0$ and $U_o = 0$, equation (42) gives another relation. The purpose of the present part is to determine the influence of rotation on the Jean's

criterion (44) of a uniform streaming fluid. So in order to carry out and to facilate the present situation we may choose $\Omega_x = 0$, $\underline{H}_o = 0$, $\eta = 0, k_x = 0$ and $k_y = 0$, equation (42), gives

$$n^4 + \left(4\pi G \rho_o - C_S^2 k_z^2 - 4\Omega^2\right) n^2 + 4\Omega_z^2 \left(C_S^2 k_z^2 - 4\pi G \rho_o\right) = 0 \tag{45}$$

with

$$\Omega^2 = \Omega_y^2 + \Omega_z^2 \tag{46}$$

Equation (45) indicates that there must be two modes in which a wave can be propagated in the medium. If the roots of (45) are being n_1^2 and n_2^2, then we have

$$n_1^2 + n_2^2 = C_S^2 k_z^2 + 4\Omega^2 - 4\pi G \rho_o \tag{47}$$

$$n_1^2 n_2^2 = 4\Omega_z^2 \left(C_S^2 k_z^2 - 4\pi G \rho_o\right) \tag{48}$$

and so we see that both the roots n_1^2 and n_2^2 are real. The discussions of (45) indicate that if the Jean's restriction

$$C_S^2 k_z^2 - 4\pi G \rho_o < 0 \tag{49}$$

is valid, then one of the two roots n_1^2 or n_2^2 must be negative and consequently the model will be unstable. This means that under the Jean's restriction (49), the self-gravitating rotating fluid medium is unstable. This shows that the Jean's criterion for a self-gravitating medium is unaffected by the influence of the uniform rotation.

In order to examine the influence of the electromagnetic force on the instability of the present model we use the relation (42) with the assumptions $\underline{\Omega} = 0, \eta = 0, k_x = 0$ and $k_y = 0$. Then, equation (42)

$$n^4 + An^2 + B = 0 \tag{50}$$

with

$$A = 4\pi G \rho_o - C_S^2 k_z^2 - \frac{\mu H_o^2 k_z^2}{\rho_o} \tag{51}$$

$$B = \frac{\mu H_o^2 k_z^2}{\rho_o}\left(C_S^2 k_z^2 - 4\pi G \rho_o\right) \tag{52}$$

where

$$H_o^2 = H_{oz}^2 + H_{oy}^2 \tag{53}$$

Again as in the previous case of rotation, we have here also two modes of wave propagation, and therefore, we obtain

$$n_1^2 + n_2^2 = C_S^2 k_z^2 - 4\pi G \rho_o + \frac{\mu H_o^2 k_z^2}{\rho_o} \tag{54}$$

$$n_1^2 n_2^2 = \frac{\mu H_o^2 k_z^2}{\rho_o}\left(C_S^2 k_z^2 - 4\pi G \rho_o\right) \tag{55}$$

By comparing (47) & (48) with (54) & (55) we may say that $4\Omega^2$ is replaced by $\dfrac{\mu H_o^2 k_z^2}{\rho_o}$. Following the same analysis of the rotating case we finally find out that Jean's self-gravitating instability restriction of a streaming fluid medium is not influenced by the effect of the electromagnetic force.

In order to determined the combined effect of the rotation and the electromagnetic force we may put $k_x = 0$ and $k_y = 0$ for simplicity but $\underline{\Omega}$ and $\underline{H}_o$ are still as they are given in their general forms given by equations (7) and (8). In such a case the relation (42) reduces to

$$n^6 - E_1 n^4 + E_2 n^2 - E_3 = 0 \tag{56}$$

with

$$E_1 = 4\Omega^2 + \frac{2\mu H_{oz}^2 k_z^2}{\rho_o} + \frac{2\mu H_{oy}^2 k_z^2}{\rho_o} + C_s^2 k^2 - 4\pi G \rho_o \tag{57}$$

$$E_2 = 4\left[\Omega_y \left(\frac{\mu H_{oz}^2 k_z^2}{\rho_o} \right)^{\frac{1}{2}} - \Omega_z \left(\frac{\mu H_{oy}^2 k_z^2}{\rho_o} \right)^{\frac{1}{2}} \right]^2$$

$$+ \frac{\mu H_{oz}^2 k_z^2}{\rho_o} \left[4\Omega_x^2 + \frac{\mu H_{oy}^2 k_z^2}{\rho_o} + \frac{\mu H_{oz}^2 k_z^2}{\rho_o} + C_s^2 k^2 - 4\pi G \rho_o \right]$$

$$+ \left(C_s^2 k^2 - 4\pi G \rho_o \right) \left[4\Omega_x^2 + \frac{\mu H_{oz}^2 k_z^2}{\rho_o} \right] \tag{58}$$

$$E_3 = \left(\frac{\mu H_{oz}^2 k_z^2}{\rho_o} \right)^2 \left(C_s^2 k^2 - 4\pi G \rho_o \right) \tag{59}$$

where

$$\Omega^2 = \Omega_x^2 + \Omega_y^2 + \Omega_z^2 \tag{60}$$

The relation (56) is of sixth order algebraic equation in *n*, so there will be three modes for which the proposing sinusoidal wave may be propagated in the medium. If we assume that the oscillation frequencies i.e. the roots of (56) are n_1 , n_2 and n_3, then using the theory of equations we get

$$n_1^2 + n_2^2 + n_3^2 = E_1 \tag{61}$$

$$n_1^2 n_2^2 n_3^2 = E_3$$
$$= \left(\frac{\mu H_{oz}^2 k_z^2}{\rho_o} \right)^2 \left(C_s^2 k^2 - 4\pi G \rho_o \right) \tag{62}$$

By the use of equation of multiple roots n_1 , n_2 and n_3 we see that if Jeans's criterion (cf. equation 49) is satisfied then one of the three roots is negative and consequently the model will be unstable with respect to one of the three modes.

We conclude that the Jeans's self-gravitating restriction of a streaming medium is not affected by the combined influence of the electromagnetic and rotational forces.

If $G = 0, \underline{\Omega} = 0, \underline{H}_o = 0$ and $\eta \neq 0,$ equation (42) degenerates to a somewhat complicated relation. The purpose of the present part is to determine the effect of the viscosity of fluid. So in order to carry out and to facilate the present situation we may choose $k_x = 0$ and $k_y = 0$ so equation (42), at once, yields

$$\left(\sigma + k^2 \eta \right)^2 \left(\sigma^5 k^2 + k^4 \sigma C_s^2 \right) = 0 \tag{63}$$

Equation (63) indicates that resistivity has a destabilizing influence under certain restrictions.

CONCLUSION

The gravitational Jeans instability criterion is not influenced by the electromagnetic force or the rotation forces or even by the combined effect of them whether the fluid medium is streaming or not and whether the rotation in one dimension or more. The resistivity has destabilizing influence under certain restrictions.

REFERENCES

1. J. Jeans, H. Philos, *Trans. R. Soc. London*, **199,** 1 (1902).
2. S. Chandrasekhar, E. Fermi, *Astrophys J.,* **118**, 116 (1953).
3. S. Chandrasekhar, Hydrodynamic and hydromagnetic stability, Dover, New York, 1981.
4. R. S. Sengar, Gravitational instability of streams, Proc. Acad. Sci., India, **51A**, 39 (1981).
5. A.E. Radwan, H.A. Radwan, M. Hendi, *Chaos, Solitons and Fractals*, **12,** 1729 (2001).
6. A.E. Radwan, A.A. Hasan, *Int J Appl Math.* **38**(3), 113 (2008).
7. A.E. Radwan, A.A. Hasan, *Appl Math Model.*, **33**(4), 2121 (2009).
8. A.A. Hasan, *Physica B.*, **406**(2), 234 (2011).
9. A.A. Hasan, *Boundary Value Problems*, **31**, 1 (2011).
10. A.A. Hasan, *J Appl Mech ASME*, **79**(2), 1 (2012).
11. A.A. Hasan, *Mathematical Problems in Engineering*, 1 (2012).

Appendix I

The elements $a_{ij} \left(i = 1, 2, ..., 8 \text{ and } j = 1, 2, ..., 8 \right)$ of the matrix $\left[a_{ij} \right]$ in equation (41) of the linear algebraic equations (30)-(38) are being

$$a_{11} = \left(n\rho_o \right),$$

$$a_{12} = \left(2\rho_o \Omega_z \right),$$

$$a_{13} = \left(\rho_o DU_o - 2\rho_o \Omega_y \right)$$

$$a_{14} = i\mu \left(k_y H_{oy} + k_z H_{oz} \right),$$

$$a_{15} = ik_x \mu H_{oy} ,$$

$$a_{16} = ik_x \mu H_{oz} ,$$

$$a_{17} = ik_x C^2 ,$$

$$a_{18} = -i\rho_o k_x$$

$$a_{21} = \left(-2\rho_o \Omega_z \right),$$

$$a_{22} = \left(n\rho_o \right),$$

$a_{23} = \left(2\rho_o \Omega_x \right),$

$a_{24} = 0$

$a_{25} = i\mu \left(2k_y H_{oy} + k_z H_{oz} \right),$

$a_{26} = ik_y \mu H_{oz},$

$a_{27} = ik_y C^2,$

$a_{28} = -i\rho_o k_y$

$a_{31} = \left(-2\rho_o \Omega_y \right),$

$a_{32} = \left(2\rho_o \Omega_x \right),$

$a_{33} = \left(n\rho_o \right),$

$a_{34} = 0$

$a_{35} = ik_z \mu H_{oy},$

$a_{36} = i\mu \left(k_y H_{oy} + 2k_z H_{oz} \right),$

$a_{37} = ik_z C^2, \quad a_{38} = -i\rho_o k_z$

$a_{41} = i\left(k_y H_{oy} + k_z H_{oz} \right),$

$a_{42} = 0,$

$a_{43} = 0,$

$a_{44} = -\left(n + i\left(k_x^2 + k_y^2 \right) \right),$

$a_{45} = ik_x k_y,$

$a_{46} = DU_o + ik_x k_z,$

$a_{47} = 0,$

$a_{48} = 0$

$a_{51} = -ik_x H_{oy},$

$a_{52} = ik_z H_{oz},$

$a_{53} = -ik_z H_{oy},$

$a_{54} = ik_x k_y,$

$a_{55} = -\left(n + i\left(k_x^2 + k_z^2 \right) \right),$

$a_{56} = ik_y k_z,$

$a_{57} = 0, a_{58} = 0$

$a_{61} = -ik_x H_{oz},$

$a_{62} = -ik_y H_{oz},$

$a_{63} = -ik_y H_{oy},$

$a_{64} = ik_x k_z,$

$a_{65} = ik_y k_z,$

$a_{66} = -\left(n + i\left(k_x^2 + k_y^2 \right) \right),$

$a_{67} = 0,$

$a_{68} = 0$

$a_{71} = i\rho_o k_x,$

$a_{72} = i\rho_o k_y,$

$a_{73} = i\rho_o k_z,$

$a_{74} = 0,$

$a_{75} = 0,$

$a_{76} = 0,$

$a_{77} = n,$

$a_{78} = 0$

$a_{81} = 0,$

$a_{82} = 0,$

$a_{83} = 0,$

$a_{84} = 0,$

$a_{85} = 0,$

$a_{86} = 0,$

$a_{87} = -4\pi G,$

$a_{88} = k^2$

МАГНИТОХИДРОДИНАМИЧНА СТАБИЛНОСТ НА САМОГРАВИТИРАЩА, СВИВАЕМА, РЕЗИСТИВНА, ВЪРТЯЩА СЕ ПОТОЧНА СРЕДА

А.А. Хасан

Катедра "Базови и приложни науки", Колеж по инженерство и технологии, Арабска академия за наука, технологии и морски транспорт (AASTMT), Садат роуд - П. К. 11, Асуан, Египет

(Резюме)

Изследвана е магнитохидродинамичната стабилност на гравитационна среда с потоци с променливо скоростно разпределение за общо разпространение на вълните в присъствие на ротационни сили. Магнитното поле има силно стабилизиращо влияние, но стриймингът е дестабилизиращ. Ротационните сили имат стабилизиращо влияние при определени ограничения. Доказва се, че гравитационният критерий за нестабилност на Jean не е повлиян от електромагнитната сила или от въртящата сила или дори от комбинираното въздействие на това дали течната среда тече или не и дали въртенето е в едно или повече измерения.

Sunflower and soybean oil stabilized with natural extracts of turnip's peel

S. Rehman[1], S. Rasheed[1], M. Imran[1*], A. Kanwal[1], F. Kanwal[1], I. Begum[1], L. Mitu[2*]

[1]*Institute of Chemistry, University of the Punjab, Lahore-54890, Pakistan*
[2]*Department of Chemistry, University of Pitesti, Pitesti-110040, Romania*

Turnip (*Brassica rapa*) is considered to be one of the oldest cultivated vegetable since prehistoric times. Antioxidant activity of methanolic extracts from turnip's peel (TP) at variable concentrations (250 ppm, 500 ppm, 1000 ppm) was determined by total phenolic contents, total flavonoid contents, ferric reducing antioxidant power assay, 2,2'-azinobis-3-ethylbenzothiazoline-6-sulphonic acid (ABTS) radical cation scavenging activity and β-carotene linoleic acid emulsion system. The highest antioxidant activity of turnip's peel was observed at 1000 ppm. Stabilization of two edible oils *i.e.* sunflower and soybean using these extracts was evaluated under ambient conditions. Butyl-hydroxyanisole (BHA) and butyl-hydroxytoluene (BHT) at 200 ppm were used as synthetic reference antioxidants. Parameters like peroxide values (PV), free fatty acid values (FFA) and iodine values (IV) demonstrated that antioxidant potential of turnip's peel extract is relatively more than BHA and slightly less than BHT.

Keywords: *Brassica rapa*, Antioxidant activity, Sunflower oil, Soybean oil.

INTRODUCTION

Antioxidants are the substances that terminate oxidation, the absence of which effectuates membrane lipids, deoxyribonucleic acid (DNA), proteins and carbohydrates damage and in some cases even lead to cell death. In order to cope this, synthetic antioxidants such as butyl-hydroxyanisole (BHA) and butyl-hydroxytoluene (BHT) are widely utilized as food additives to stop such oxidative deterioration. However, they are quite toxic as well expensive. In this context, there is a rapid need to replace synthetic antioxidants with natural antioxidants for safety concerns. Natural antioxidants have opened a floor of great applications in nutraceuticals for disease prevention [1]. It is well established in the literature that several fruits, vegetables, plants, nuts, oilseeds and many other materials containing natural antioxidants have scavenging abilities [2] and can hence be employed for stabilization of vegetable oils.

Turnip (*Brassica rapa*) belongs to family *Cruciferae* or *Brassicaceae* and usually cultivated in different regions particularly possessing temperate climates [3]. It contains vitamin C, E, phenolic compounds, β-carotene and flavonoids and therefore can scavenge free radicals production and oxidative reactions. Search through accessible literature reveal that not so much work with reference to antioxidant potential of turnip has been reported except; chemical and antioxidative

assessment of dietary turnip [4], phenolic compounds in brassica vegetables [5], growth and antioxidant response of *Brassica rapa* (turnip) irrigated with different compositions of paper and board mill (PBM) effluent [6], nutritional facts and antioxidant activity of turnip by 2,2-Diphenyl-1-picrylhydrazyl radical (DPPH) method [7]. These studies demonstrated that turnip have good antioxidant properties. However, it was surprising to be noted in the accessible literature that no work describing the stabilization of sunflower and soybean oil with natural antioxidants extracted from turnip's peel has been yet reported. Therefore in this paper we describe antioxidant potential of turnip's peel extract (turnip collected from local market) as well as its efficiency to stabilize the sunflower and soybean oil.

EXPERIMENTAL

Materials

Refined, bleached and deodorized (RBD) sunflower and soybean oil were obtained from local refinery located in Layyah, Pakistan. Turnips were purchased from local market of Lahore, Pakistan. All the chemicals and reagents were of analytical grade and were used as received. Synthetic antioxidants butyl-hydroxytoluene (BHT) and butyl-hydroxyanisole (BHA) were procured from Fluka.

Preparation of extract

Turnip (*Brassica rapa*) was peeled off, thoroughly washed with deionized water and finally dried at room temperature for one week. The dried

---

peel was then pulverized to fine powder. 5 g of peel was soaked in 150 mL of methanol and then stirred well on shaker at room temperature and then filtered. Methanol has been recommended to be best solvent for extraction of antioxidants [8]. The resulting filtrate was evaporated at room temperature to yield semi solid extract which was used for further analysis.

Evaluation of antioxidant activity of extract

Following different assays were performed to determine the antioxidant activity of turnip's peel.

Determination of total phenolic content

The total phenolic content of turnip's peel extract were determined by an already reported method [9]. Absorbance at 765 nm was measured and the total phenolic contents in turnip's peel were calculated from the standard curve of gallic acid. The results are reported in GAE (mg/100 g) of dry weight.

Determination of total flavonoids

Total flavonoids were measured spectrophotometrically using the method described by [10]. Absorbance of the mixture was determined at 510 nm and calibration curve was prepared by using catechin at concentrations of 0.2 to 1 mg/mL in methanol. The results were reported as catechin equivalent (CE) as mg/100g of dry extract.

Ferric-reducing antioxidant power assay (FRAP)

FRAP assay was performed according to well documented reported method [10]. 10 μl of extract, 300 μl of FRAP reagent was added in 30 μl of distilled water and its absorbance was measured at 593 nm. $FeSO_4.7H_2O$ at different concentrations (0.2 mM/L to 1 mM/L) was used to develop the standard curve and the antioxidant activity was expressed as concentration of antioxidants having ferric reducing ability equivalent to mM/L of $FeSO_4.7H_2O$.

Determination of ABTS radical cation scavenging activity

The ABTS (2,2'-azinobis-3-ethylbenzo-thiazoline-6-sulphonic acid) radical cation assay was carried out by the procedure reported in the literature [11]. The absorbance of sample at 734 nm was measured against control and the results were expressed by the following formula.

$ABTS^{•+}$ radical scavenging (%)=((Ac-At)/Ac) x 100 where, Ac is the absorbance of only $ABTS^{•+}$ solution and At is the absorbance of the sample which reacted with $ABTS^{•+}$ solution.

β-carotene linoleic acid emulsion system

Antioxidant activity of extract was determined by the β-carotene linoleic acid emulsion system by an already reported method [12]. Absorbance was recorded at 470 nm after every 15 minutes for 1 hour.

STABILIZATION STUDIES

Sample preparation

Methanolic extracts of turnip's peel (250, 500 and 1000 ppm concentrations) were added to RBD sunflower and soybean oil. Synthetic antioxidants, BHT and BHA (200 ppm) were also added in both oils for comparative study [13]. Parallel control sample of both oils *i.e.* without any antioxidants were also prepared. All the samples were stored at room temperature for 45 days. On first day, after 15 days, 30 days, 45 days analysis was carried out to check the stabilization of oils by antioxidants.

Determination of free fatty acid value (FFA), peroxide value (PV) and iodine value (IV)

Antioxidant potential of turnip's peel extract for stabilization of sunflower and soybean oil was evaluated for free fatty acid, peroxide and iodine values. Each prepared oil sample was tested for antioxidant activity after regular interval of 15 days till 45 days by following the AOAC official methods [14].

Statistical analysis

All the samples were set in triplicate and results were reported as mean ± standard deviation. Significant differences of data ($P < 0.05$) were tested by using one way ANOVA.

RESULTS AND DISCUSSION

Measurement of antioxidant activity of extract

Total phenolic and total flavonoid contents of methanolic extract of turnip's peel are 54.6 and 25.4 mg/100g, respectively.

The presence of such phenolic and flavanoid compounds in turnip's peel may impart antioxidant potential to it. It is reported that antioxidant activity of phenolic compounds is mainly due to redox properties, hydrogen donors, singlet oxygen quenches and metal chelators [15].

In FRAP assay, the reduction of methanolic extract of turnip's peel was measured. The FRAP assay showed the reducing ability of extract 0.359 ± 0.01 mM/L of $FeSO_4$ which indicates that there is a presence of antioxidative potential in turnip's peel. $ABTS^{•+}$ method shows free radical scavenging

activity of turnip's peel methanolic extract with the decolorization of its blue color. Literature reveals that reactions of phenols with ABTS radical cations are rapid, hence more will be the presence of phenolic content in extract more will be the free radical scavenging ability of extract [16]. Antioxidant activity of turnip's peel extract determined by this method was compared with synthetic antioxidants (BHA and BHT) at different concentration such as 0.2, 0.4 and 0.6 mg/mL Fig.1. This figure depicts that by increasing concentration of turnip's peel extract (0.6 mg/mL), radical scavenging activity increases and becomes almost equal to that of BHA. However it is still lower than BHT.
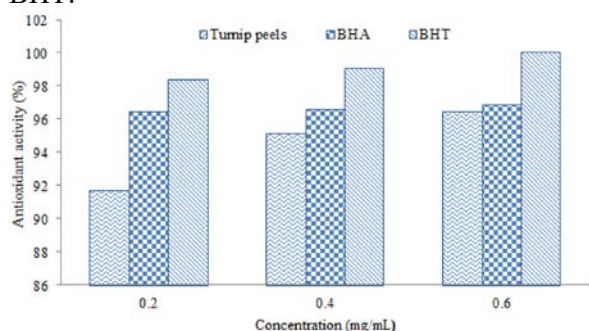
Fig. 1. Comparison of antioxidant activity (%) of turnip's peel extract with BHA and BHT.

β-Carotene linoleic acid emulsion system is also a useful method to assay the antioxidant potential [17]. It is observed and reported that the presence of antioxidants increases with the reduction of decolorization rate of β-carotene. Fig. 2 show the graph plotted between absorbance of samples at 470 nm and time required by the sample to decolorize β-carotene.
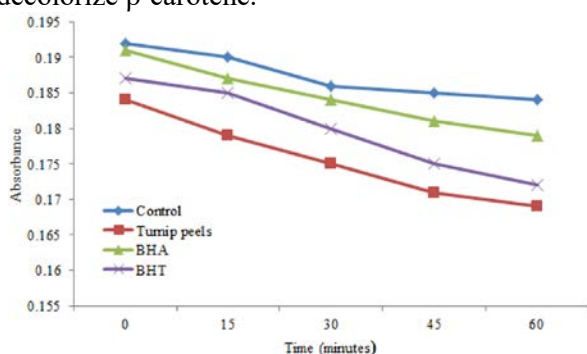
Fig. 2. Graph between absorbance of samples at 470 nm and time (minutes) required by the sample to decolorize β-carotene.

It can be concluded from these results that with increase of time, turnip's peel extract has maximum antioxidants as observed by the reduction of decolorization rate of β-carotene (absorbance 0.184 to 0.169). Similar trend for synthetic antioxidants was found to be BHA (0.191 to 0.179) and BHT (0.187 to 0.172). Least reduction was observed in

control sample i.e. only linoleic acid (0.192 to 0.184). Thus β-carotene linoleic acid emulsion system proved that the turnip's peel extract have enough potential to be used as natural antioxidant.

Stabilization of sunflower oil (SFO) and soybean oil (SBO)

RBD sunflower and soybean oil were used as oxidative substrates. Stabilization of these oils was done using turnip's peel extracts. Comparison was made with synthetic antioxidants (BHA and BHT).

Peroxide value (PV)

PV determines the initial oxidation of fats and oils which occurred due to the formation of peroxides [8]. Fig .3 and Fig. 4 exhibit the gradual increase in PV during storage period at room temperature of treated sunflower and soybean oil samples. On 45th day, maximum enhancement in peroxide value was observed for all samples in both oils. Initially, PV of control sunflower oil sample was 9.85 ± 0.21 meqO$_2$/kg which reaches to 43.6 ± 0.28 meqO$_2$/kg of oil on 45th day, whereas PV of control soybean sample was observed as 2.1 ± 0.14 meqO$_2$/kg of oil which reaches to maximum value of 7.03 ± 0.23 meqO$_2$/kg on 45th day. Control sample showed maximum oil deterioration with increase of storage period as it was without antioxidants. Turnip's peel extract (1000 ppm) showed minimum PV value in both oils; initially in sunflower oil sample it was 9.85 ± 0.21 meqO$_2$/kg which raised to 19.9 ± 0.42 meqO$_2$/kg of oil on 45th day. Similarly in soybean sample it was 2.1 ± 0.14 meqO$_2$/kg on 0 day and 2.99 ± 0.01 meqO$_2$/kg of oil on 45th day which shows the antioxidant presence in methanolic turnip's peel extract preventing oil from deterioration. Our results are consistent with the findings of other workers who reported that lipid peroxides were significantly reduced by the addition of natural antioxidants in oils [18, 19]. PV for other concentrations of turnip's peel extract (250 ppm and 500 ppm) and BHA, BHT (200 ppm) were also measured and has been graphically represented in Fig. 3 and Fig. 4 for sunflower and soybean oil respectively. From these figures following trend has been concluded; for sunflower oil, the trend is: TP 1000 ppm > BHT 200 ppm > TP 500 ppm > TP 250 ppm > BHA 200 ppm > Control; For soybean oil, the trend is as follow: TP 1000 ppm > BHT 200 ppm > BHA 200 ppm > TP 500 ppm > TP 250 ppm > Control. Comparable results of TP extract at 1000 ppm with synthetic antioxidants BHA and BHT were observed in both oils.
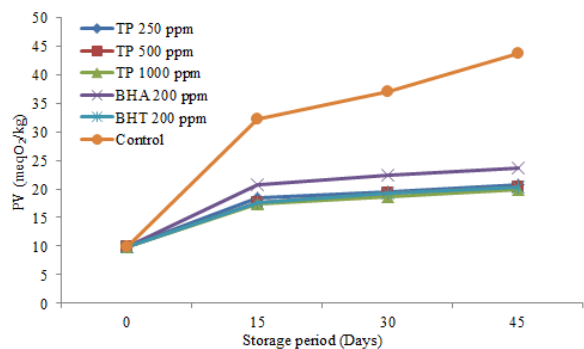
Fig. 3. Increase in PV (meqO$_2$/kg) during storage period of treated sunflower oil samples.
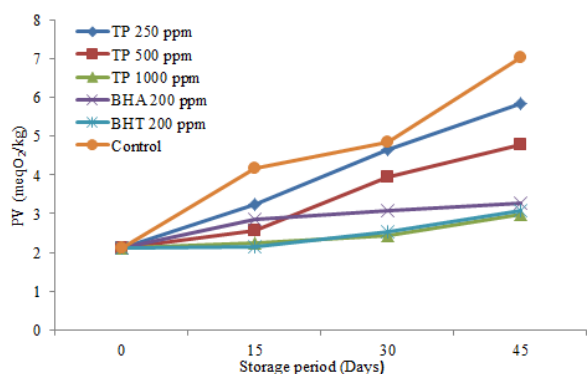
Fig. 4. Increase in PV (meqO$_2$/kg) during storage period of treated soybean oil samples.

Free fatty acid value (FFA)

When oils come in contact with moisture, hydrolysis of triglycerides may lead to the formation of free fatty acids [20]. Fig. 5 and Fig. 6 shows that FFA value goes on increasing during storage period at room temperature of treated sunflower and soybean oil samples respectively. Control exhibits highest FFA value in both oils. For instance; FFA of control sunflower oil sample from zero to 45th day was; 1.91 ± 0.08 % to 4.60 ± 0.07 %, whereas FFA of control soybean sample was 1.42 ± 0.01 % to 4.42 ± 0.07 %. Turnip's peel extract (1000 ppm) in sunflower oil exhibited FFA value 2.57 ± 0.05 % and in soybean it was 2.14 ± 0.05 %. Similar pattern of increase in FFA value during storage period due to decomposition products of hydroperoxides was reported by [21].

The FFA value for other concentrations of turnip's peel extract (250 ppm and 500 ppm) and for BHA, BHT (200 ppm) were also determined and are graphically represented in Fig. 5 and Fig. 6 for sunflower and soybean oil samples respectively. The comparison revealed following trend in sunflower oil samples: TP 1000 ppm > BHT 200 ppm > TP 500 ppm > TP 250 ppm > BHA 200 ppm > Control. In case of soybean oil samples, the trend is as follow: TP 1000 ppm > BHT 200 ppm > TP 500 ppm > TP 250 ppm > BHA 200 ppm > Control.

496
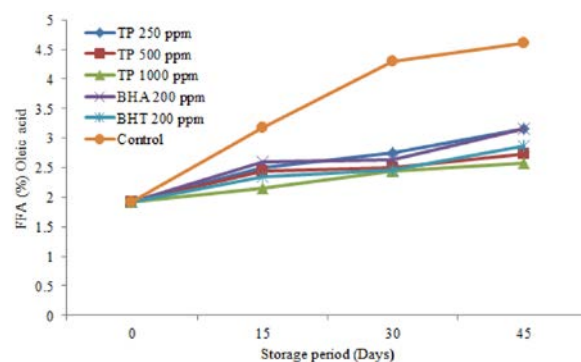
Fig. 5. Increase in FFA (%) value of treated sunflower oil samples during storage period.
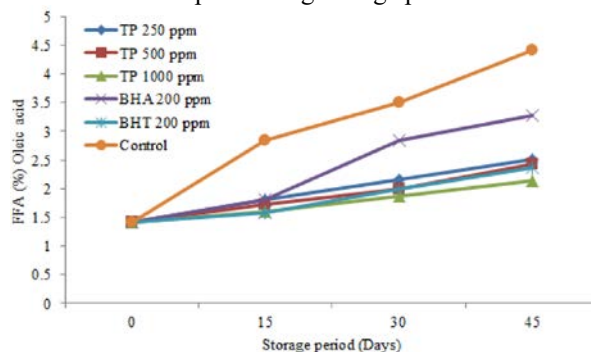
Fig. 6. Increase in FFA (%) value of treated soybean oil samples during storage period.

Iodine value (IV)

Degree of unsaturation of given oil can be determined by iodine value. Greater iodine value gives information about better quality of oil [22]. Fig. 7 and Fig. 8 show the relative decrease of iodine value in sunflower and soybean oil respectively as storage period increases. IV (gI$_2$/100g of oil) for TP extract (1000 ppm) in sunflower oil was 153.17 ± 1.26 gI$_2$/100g to 64.73 ± 1.81 gI$_2$/100g which is higher than BHT (153.17 ± 1.26 gI$_2$/100g to 56.38 ± 1.02 gI$_2$/100g) and BHA (153.17 ± 1.26 gI$_2$/100g to 53.02 ± 1.40 gI$_2$/100g); while IV of TP 1000 ppm in soybean oil was 169.82 ± 1.48 gI$_2$/100g to 88.34 ± 1.11 gI$_2$/100g which is also higher than BHT (169.82 ± 1.48 gI$_2$/100g to 79.83 ± 1.64 gI$_2$/100g) and BHA (169.82 ± 1.48 gI$_2$/100g to 61.63 ± 1.02 gI$_2$/100g), respectively. Generally, control exhibited the lowest content of IV followed by TP 250 ppm, TP 500 ppm, BHA 200 ppm, BHT 200 ppm and TP 1000 ppm in sunflower oil while samples in soybean oil followed this pattern: control < TP 250 ppm < BHA 200 ppm < TP 500 ppm < BHT 200 ppm < TP 1000 ppm, respectively. Iodine value of all stabilized samples is higher than control of both oils indicating good antioxidant potential of turnip's peel extract under investigation.
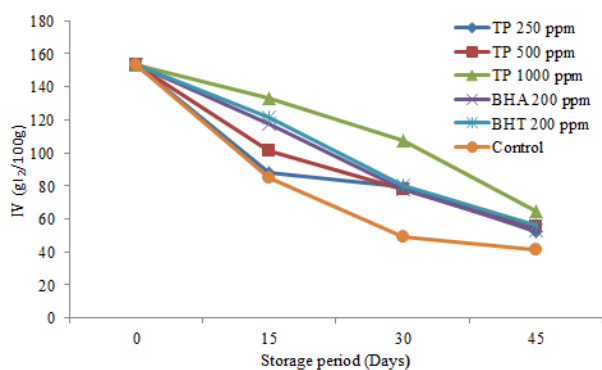
Fig. 7. Decrease in IV (gI$_2$/100g) of treated sunflower oil samples during storage period.
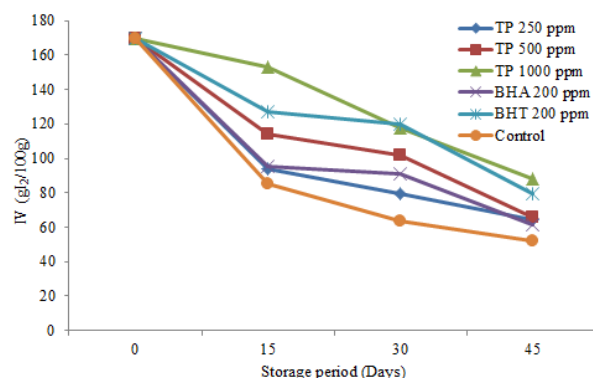
Fig. 8. Decrease in IV (gI$_2$/100g) of treated soybean oil samples during storage period.

CONCLUSIONS

The study for stabilization of sunflower and soybean oil revealed that turnip's peel extract having antioxidative potential can be safely employed as a better natural antioxidant when compared with synthetic antioxidants (BHT and BHA). Generally it was observed that turnip's peel extract has better stabilized oil samples than BHA, however its stabilization efficiency was slightly lower than BHT. It inhibits oxidative deterioration of both oils thus play role in preventing against diseases and can be utilized as food additive.

REFERENCES

1. L. Das, E. Bhaumik, U. Raychaudhuri, R. Chakraborty, *J .Food Sci. Technol.,* **49**, 173 (2012).
2. D.E. Pratt, B.J. Hudson, *In Food antioxidants*, Springer, Netherlands, 1990, p.171.
3. M.K. Saeed, S. Anjum, I. Ahmad, A. Nisa, S. Ali, A. Zia and S. Ali, *World Appl. Sci. J.,* **19**, 370 (2012).
4. F. Fernandes, P. Valentão, C. Sousa, J.A. Pereira, R.M. Seabra, P.B. Andrade, *Food Chem.*, **105**, 1003 (2007).
5. M.E. Cartea, M. Francisco, P. Soengas and P. Velasco, *Molecules,* **16**, 251 (2010).
6. S. Iqbal, U. Younas, K.W. Chan, Z. Saeed, M.A. Shaheen, N. Akhtar, A. Majeed, *Chemosphere,* **91**, 1196 (2013).
7. M.K. Saeed, S. Anjum, I. Ahmad, A. Nisa, A. Zia S. Ali, *World Appl. Sci. J.,* **19**, 370 (2012).
8. S. Iqbal, S. Haleem, M. Akhtar, M. Zia-ul-Haq and J. Akbar, *Food Res Int.,* **41**, 194 (2008).
9. D.O. Kim, O.K. Chun, Y.J. Kim, H.Y. Moon and C.Y. Lee, *J. Agric. Food Chem,* **51**, 6509 (2003).
10. I.F. Benzie, J. Strain, *Anal. Biochem.,* **239**, 70 (1996).
11. E.A. Shalaby, S.M. Shanab, *Indian J. Geo-Mar. Sci.,* **42**, 556 (2013).
12. P. Terpinc, M. Bezjak, H. Abramovič, *Food Chem.,* **115**, 740 (2009).
13. P.D. Duh, G.C. Yen *J. Am. Oil Chem. Soc.,* **74**, 745 (1997).
14. AOAC, Official method of analysis (15th ed.), Association of Official Analytical Chemists, Washington DC, 1990.
15. J. Jurenka, *Altern Med Rev.,* **13**, 128 (2008).
16. V. Katalinic, M. Milos, T. Kulisic, M. Jukic, *Food Chem.,* **94**, 550 (2006).
17. A.A. Mohdaly, M.A. Sarhan, I. Smetanska and A. Mahmoud, *J. Sci. Food Agr.,* **90**, 218 (2010).
18. K. Kiyomi, S. Yasuko, *Kassigeku Kenkyu,* **41**, 91 (1995).
19. W. Yanping, Z. Mourning, Z. Yuhang and P. Zhying, *Zhongguo Youzhi,* **24**, 37(1999).
N. Frega, M. Mozzon and G. Lercker, *J. Am. Oil Chem. Soc.,* **76**, 325 (1999).
20. H. Wang, F. Liu, L. Yang, Y. Zu, H. Wang, S. Qu and Y. Zhang, *Food Chem.,* **128**, 93 (2011).
21. A.L. Kerrihard, K. Nagy, B.D. Craft, M. Beggio and R.B. Pegg, *J. Am. Oil Chem. Soc.,* **92**, 1153 (2015).

СЛЪНЧОГЛЕДОВИ И СОЕВИ МАСЛА, СТАБИЛИЗИРАНИ С ЕСТЕСТВЕНИ ЕКСТРАКТИ ОТ КОРИ НА РЯПА

С. Рехман[1], С. Рашийд[1], М. Имран[1*], А. Кануал[1], Ф. Кануал[1], И. Бегун[1], Л. Миту[2*]

[1]*Институт по химия, Университет в Пунджаб, Лахор -54890, Пакистан*
[2] *Институт по химия, Университет в Питещ, Питещ-110040, Румъния*

(Резюме)

Ряпата (*Brassica rapa*) се смята за един от най-ранните култивирани зеленчуци още от пра-исторически времена. Антиоксидантните свойства на метаноловите екстракти от кората (TP) при различни концентрации (250 ppm, 500 ppm, 1000 ppm) са определени като общо съдържание на феноли, на флавоноиди, редукционна способност на тривалентно желязо, радикало-отстраняваща способност (ABTS) и β-каротин/линолова киселина емулсия. Най-висока антиоксидантна активност на корите от ряпа при 1000 ppm. Стабилизирането на две едливи масла (т.е. слънчогледово и соево масло), с помоща на тези екстракти е оценено при обикновени условия. BHA и BHT (200 ppm) са използвани като синтетични референтни антиоксиданти. Параметри, като пероксидно число (PV), свободни мастни киселини (FFA) и йодно число (IV) демонстрират, че антиоксидантният потенциал на екстрактите от кори от ряпа е относително по-висок отколкото на BHA и малко по-малко от този на BHT.

Reaction mechanisms between acrylamide and mercaptan in high temperature system with different humidity

Z. Xiong[1,2], B. Li[1,3,*], L. Li[1,3,4,*], X. Peng[1], Y. Yin[1], L. Weng[1]

[1]School of Food Sciences and Engineering, South China University of Technology, Guangzhou, China, 510640

[2]School of Chemical Engineering and Materials Science, Beijing Institute of Technology Zhuhai, Zhuhai, China, 519088

[3]Guangdong Province Key Laboratory for Green Processing of Natural Products and Product Safety, Guangzhou, China, 510640

[4]School of Chemical Engineering and Energy Technology, Dongguan University of Technology, Dongguan, 523808, China

The reactions between acrylamide and food aroma mercaptans including 1,2-ehanedithiol, butyl mercaptan, 2-methyl-1-butyl mercaptan and 2-methyl-3-furanthiol under both high temperature and high humidity(HTHH) and high temperature and low humidity(HTLH) were determined in the present study. The results showed that the acrylamide elimination capability of 2-methyl-3-furanthiol was stronger, compared with butyl mercaptan and 2-methyl-1-butyl mercaptan, in the HTHH system, while that was the lowest in the HTLH system. Besides, pH could significantly affect the acrylamide content in HTHH system, but the effection of pH was not so obvious in HTLH system. With the addition of antioxidants, the elimination of acrylamide was decreased significantly. In conclusion, the reaction experienced different mechanisms under the high temperature.The nucleophilic addition and radical addition take the dominant role in HTHH system and HTLH system, respectively.

Key words: food, acrylamide, mercaptans, antioxidants.

INTRODUCTION

The acrylamide is a kind of hazardous substance appearing during the food heat processing in starch-based food[1]. Considering the toxicity damage of acrylamide in liver, neuro and reproduction confirmed by the previous researches, the acrylamide has been denominated as a "potential cancerogen" by the IARC in 1994[2]. Besides, the acrylamide might react with some food substances due to its active C=C[3, 4].

Mercaptan is a kind of flavor compound widely spread in the plant kingdom, such as the garlic, onion, coffee and food undergoing the heat processing. The mercaptan could attach admirable smell, such as sesame oil, green onion, garlic and barbecue smells, to food with a trace amount. Moreover, over 100 mercaptans are already enrolled as a safe food additives. Recently, the FEMA(Flavour Extact Manufacturers's Association) has newly published a list of GRAS(Generally Recognized as Safe) additives, which contains lots of mercaptans[5].

Compared with amino and hydroxyl groups, sulphur owns superior alkene nucleophilic addition ability. The "click" reaction between sulphur and alkene has drawn numerous attention[6]. Thus, the reaction between acrylamide and mercaptan might occur theoretically and some previous study had been done aiming to figure out the reaction kinetics[7, 8]. As far as we know, due to the supreme polarizability of thiol sulfur atoms, both nucleophilic addition and free radical type reaction might be triggered when the sulphur is enrolled with alkene. The complexity of food heat processing procedure results in the complexity of reaction of acrylamide and mercaptan. Therefore, the present study is carried out to illuminate the transformation of acrylamide and mercaptan under different heat process including high temperature and high humidity(HTHH) and high temperature and low humidity(HTLH).

EXPERIMENTAL

Materials and methods

Materials

Acrylamide(>99.9%), butyl mercaptan (≥98%) and DMSO(≥99.9%) were all purchased form Sigma-Aldrich company; [1,2,3,-^{13}C3] Acrylamide isotope internal standard was obtained from the Cambridge Isotope Laboratories Inc; 2-methyl-3-furanthiol(≥98%)and dithioglycol were acquired from Shanghai Aladdin Inc. Ultrapure water was purchased from Watsons. All other reagent were of analytic purity.

* To whom all correspondence should be sent:
E-mail: bli@scut.edu.cn, felinli@scut.edu.cn

Methods

The establishment of high temperature high humidity model

The HTHH model was established according to Cai[9] with slight modification. The acrylamide (0.1 μmol), different concentration of mercaptan(0~10μmol) and buffer(0.2 mol/L, 2 mL, sodium citrate pH 3-6, phosphate pH 7-8)were added into 20 mL custom-made stainless steel reaction tube which was lined with teflon. Then, screw the stainless steel cap tightly to ensure the air impermeability and totally mixed on vortex mixture for 5 min. Next, stainless tubes were exposed to the oil bath pan (DF-101S, HengYan, Zhengzhou, China) with temperature ranging from 80~180 °C for 0~30 min. After that, the tubes were cooled immediately in 0 °C water for 20 min. Then 10μL [1,2,3,-^{13}C3] acrylamide isotope internal standard(1mg/mL) was introduced into the tube and the ultrapure water was added to the reaction system to a content volume 10 mL.

The establishment of high temperature low humidity model

The HTLH model was built following the experiment of Francisco[10] and Cai[9] with minor modification. The acrylamide (0.1 μmol), different concentrations of mercaptan(0~10μmol)and 300 mg of silica gel were added into 20 mL custom-made stainless steel reaction tube which was lined with teflon. Next, 50 μL buffer(0.2 mol/L, 2 mL, sodium citrate pH 3-6, phosphate pH 7-8) to assure Aw 0.95 and screw the stainless steel cap tightly to ensure the air impermeability and totally mixed on vortex for 5 min. Then, stainless tubes were exposed to the oil bath pan with temperature ranging from 80~180 °C for 0~30 min. After that, the tubes were cooled immediately in 0 °C water for 20 min. Then 10 μL [1,2,3,-^{13}C3] acrylamide isotope internal standard(1 mg/mL)was introduced into the tube and the 10 mL ultrapure water water was added to the reaction system. Then the system was votexed for 5 min. After standing, remove the supernatant as sample.

GC-MS determination of acrylamide

The pretreatment and analysis of samples were carried out by Francisco[7] and Zhang[11], respectively, with slight modification. 300μL10%(v/v)H_2SO_4, 400 mL 0.1 mol/LKBrO$_3$ and 0.5 g KBr was introduced to 2 mL sample in sequence. Then, the system was mixed on the vortex for 3 min and stood for 1 h in 4 °C. After that, 0.1 mL0.1 mol/L sodium thiosulfate was added to terminate the derivatization reaction. Then, the mixture was introduced to 2 ml ethyl acetate/hexane (4:1, v:v) for three times and the extract liquor was exposed to anhydrous sodium sulfate for 30 min. Then the pre-dried mixture was totally dried by blowing nitrogen. The dried sample was dissolved in 50 mu L ethyl acetate solution, then 10 mL triethylamine was added into the solution, which was then transferred to 100 μL gas sampling bottle.

GC-MS conditions are as follows: Agilent HP 6890 gas chromatography-HP 5975 UPLC-MS-MS (J and W Scientific, Agilent, Santa Clara, CA, USA); HP5-MS polysiloxane capillary column (polysiloxane polymers, 30 m × Ø 0.25 mm, 0.25 m, J and W Scientific, Agilent, Santa Clara, CA, USA) , injection volume: 1 μL splitless. The nitrogen gas flow was 1 mL/min. The temperature of injection port and inspection port were 250 °C and 280 °C, respectively. Mass spectrometer conditions: EI ionization; Ion source temperature was 230 °C and electron energy was 70 ev under the SIM mode. Ion determined: 2-propanamide($[C_3H_4NO]^+$=70, $[C_3H_{479}BrNO]^+$=149, $[C_3H_{481}BrNO]^+$=151, m/z 149 was considered as quantitative ion)and 2- bromine (^{13}C3)propionamide($[^{13}C_2H_{38}1Br]^+$ = 110, $[^{13}C_3H_{481}BrNO]^+$ =154, m/z 154 was considered as quantitative ion).
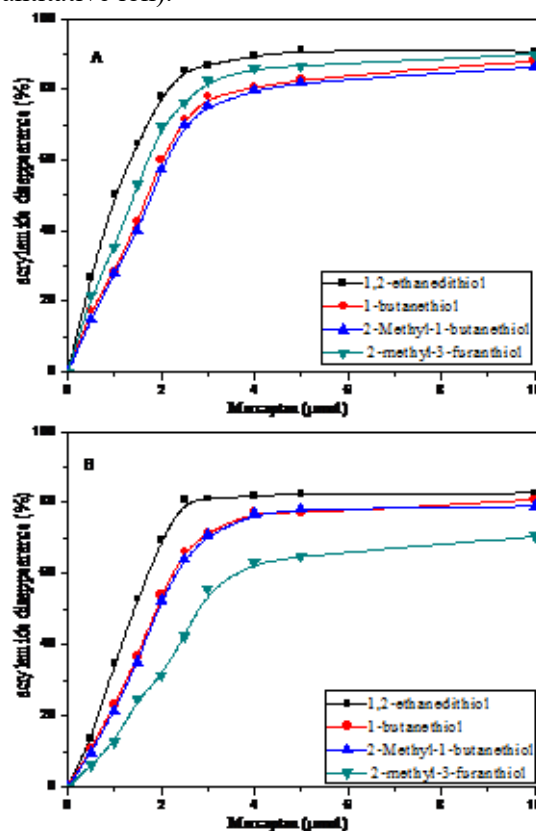
Fig. 1. The different concentrations of mercaptans in acrylamide elimination in (A)HTHH system and (B)HTLH system(acrylamide 0.1μmol, 160 °C, pH7, reaction time 30 min)

RESULTS

Mercaptan contents in reaction

The elimination of acrylamide exhibited a positive correlation with the increasing concentration of mercaptan in both HTHH and HTLH system. The reaction achieved a balance with 5 μmol mercaptan enrolled in the system. As shown in Fig.1, the 1,2-dithioglycol presented the best eliminating acrylamide capability(91%) in HTHH system. The eliminating ability of mercaptan was superior in HTHH system to in HTLH system, which maybe result from the fully reaction between the substrates. Whereas, the reaction was hindered due to the solid substrate adsorption of reactants. Besides, the 2-methyl-3-furanthiol presented the best eliminating ability in HTHH system, while the lowest in HTLH system.
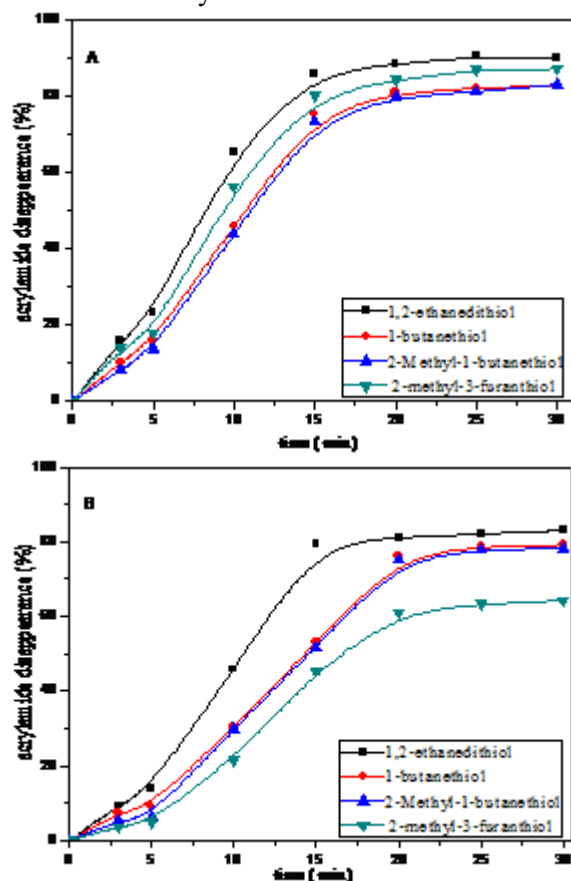
Fig. 2. The different reaction times in the eliminating of acrylamide in (A)HTHH system and (B)HTLH system (acrylamide 0.1 μmol, mercaptan 4 μmol, 160 º C, pH7)

Reaction time in the acrylamide elimination

As shown in Fig. 2, the elimination of acrylamide was increased with the lengthening of reaction time. The elimination of acrylamide reached the mount (90%) after 25 min reaction. The

acrylamide content decreased with a linear correlation during the first 10 min. The slope of the simulated line could imply the reaction activities between acrylamide and mercaptans. The eliminating ability of 3-methyl-2-furan mercaptan was superior than butyl mercaptan in HTHH system and the result reversed when the reaction was carried out in HTLH system.

Temperature on the eliminating of acrylamide

The eliminating of acrylamide increased with the increasing of heating temperature from 80~160 º C. The elimination achieved a balance in 160 º C. The temperature under 100 º C shows no significant effect in the HTLH system due to the different matrix which hindered the fully contact between the substrates. The temperature over 100 º C shows good inhibition ability on acrylamide.
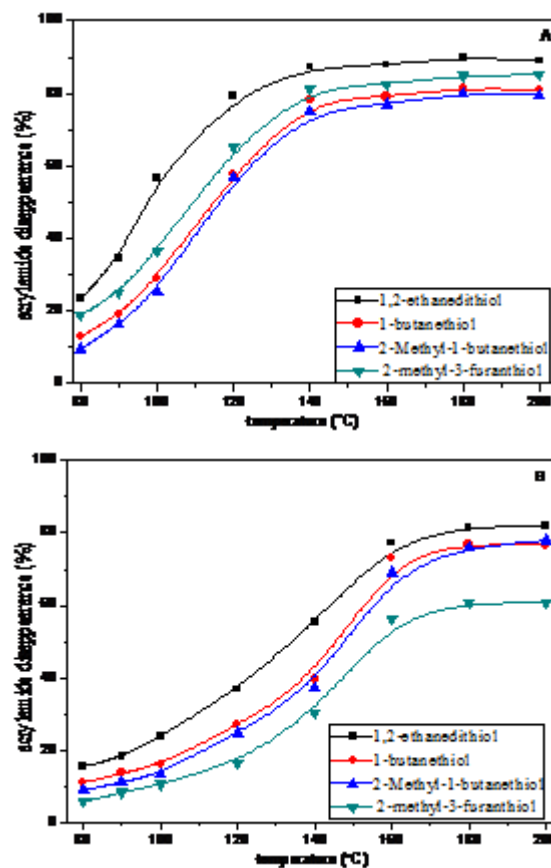
Fig. 3. Different temperatures in eliminating of acrylamide in (A)HTHH system and (B)HTLH system (acrylamide 0.1 μmol, mercaptan 4 μmol, pH7, reaction time 30 min)

pH in eliminating of acrylamide

The effect of pH in elimination reaction of acrylamide varies in different system. Considering the HTHH system, low pH under value pH 6 resulted in the low elimination ability, while under higher pH the eliminations were promoted

dramatically. There was a trace amount of acrylamide left with pH 8. However, compared with HTHH system, the elimination was less sensitive to the pH in HTLH system in which the pH shows less effective in removing the acrylamide(Fig. 4).
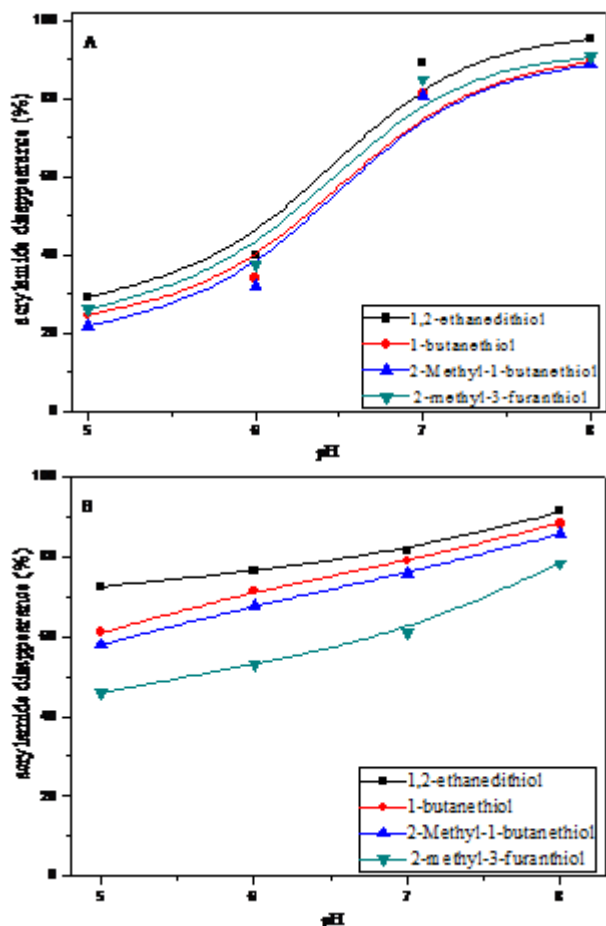
Fig. 4. Different pH in eliminating of acrylamide in (A)HTHH system and (B)HTLH system (acrylamide 0.1μmol, mercaptan 4 μmol, 160 °C, reaction time 30 min)

Oxygen and antioxidants in elimination of acrylamide

Exposed to different antioxidants including Vc and gallic acid, the elimination capabilities of different mercaptans are presented in Fig. 5. The air and nitrogen atmosphere showed no significant effect in HTHH system and when the antioxidants were applied the acrylamide slightly reduced. Whereas, a nitrogen atmosphere showed its negative effect in HTLH system acrylamide elimination. Furthermore, addition of Vc and gallic acid both turned out better elimination and less acrylamide remaining.

The mercaptans which own outstanding reducibility could be oversensitive to the oxygen exposed to alkali. In the present study, the LC-MS was applied to determine the transformation of

mercaptans. The result confirmed the formation of disulphide, which could not be considered as an effective factor related to the elimination reaction because no significant influence between air and nitrogen atmosphere was observed in HTHH system.
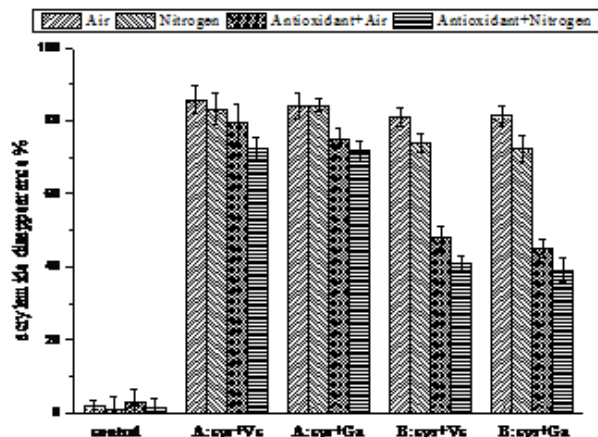
Fig. 5. Oxygen and antioxidants in the eliminating of acrylamide in (A)HTHH system and (B)HTLH system (acrylamide 0.1μmol, mercaptan 4 μmol, antioxidants 2 μmol, 160 °C, reaction time 30 min)

DISCUSSION

Up to now, there is no significant evidence about acrylamide could lead to cancer[12], while its wide spread in foods, especially fried food which contains high acrylamide, has aroused the public concern and numerous researches focused on its carcinogenic potency. The acrylamide could react with some nucleophiles. The mercaptan is a kind of nucleophilic aromas which usually coexist with acrylamide in food[7]. In the present study, the mercaptans, temperature, time, pH, oxygen and antioxidants in the elimination of acrylamide were measured. 3-methyl-2-furan mercaptan shows superior eliminating ability than butyl mercaptan 2-methyl-1-butyl mercaptan in HTHH system, whereas in the HTLH 3-methyl-2-furan mercaptan turned out the lowest, which implied the different mechanism took place between acrylamide and mercaptans. In the HTHH system, the nucleophilic addition might take place and the sulfur might loss the hydrogen and turn into sulfion. Compared with sulfion of the butyl mercaptan, that of the 3-methyl-2-furan mercaptan is more steady, which could lead to higher eliminating activity. However, it is hard for mercaptans to loss the hydrogen in HTLH system. Thus, the radical addition is the dominant reaction in HTLH, which could explain the better activity of butyl mercaptan due to its less steady radical.

The pH assay shows similar results. The increase in pH could favor the formation of sulfur anion which could improve its nucleophilic ability, thus the elimination was promoted in HTHH system. Whereas in HTLH system, the elimination has not been improved, which could also hint the radical reaction occurred.

In conclusion, the reaction between acrylamide and mercaptans follows different mechanisms. The nucleophilic addition and radical addition take the dominant role in HTHH system and HTLH system, respectively.

REFERENCES

1. A. Zinedine, J. Soriano, J. Manes, *Food Chem Toxicol.,* **45**, 1 (2007).
2. P. Fohgelberg, J. Rosén, K.E. Hellenäs, *Food Chem. Toxicol.,* **43**, 6 (2005).
3. W.L. Claeys, ,V.K. De, M.E. Hendrickx, *Biotechnol Progr.,* **21**, 5 (2005).
4. V. Gökmen, H.Z. Şenyuva, *Food Addit. Contam.,* **23**, 4 (2006).
5. S. Cohen, S. Flikushima, N. Gooderham, S. Hecht, L. Marnett, I. Rietjens, R. Smith, M. Bastaki, M. Mcgowen, C. Harman, *J. Agric. Food Chem.* **36**, 220, (2015).
6. N.S. Krishnaveni, K. Surendra, K.R. Rao, *Cheminform,* 36, 22 (2005).
7. H. Franciscoj, , D. Rosam, Z. Rosario, *Food Chem,* **122**, 3 (2010).
8. R. Zamora, R. M. Delgado, F.J. Hidalgo, *J. Agric. Food Chem.,* **58**, 3 (2010).
9. Y. Cai, Z. Zhang, S. Jiang, M. Yu, C. Huang, R. Qiu, Y. Zou, Q. Zhang, S. Ou, H. Zhou, *J. Hazard Mater,* **268C**, 6 (2014).
10. F.J. Hidalgo, R.M. Delgado, R. Zamora, *Food Res. Int.,* **44**, 4 (2011).
11. Y. Zhang, Y. Dong, Y. Ren and Y. Zhang, *J. Chromatogr. A,* **1116**, 1 (2006).
12. L. A. Mucci, P.G. Dickman, H.O. Adami and K. Augustsson, *Brit. J. Cancer,* **88**, 1, (2003).

РЕАКЦИОННИ МЕХАНИЗМИ МЕЖДУ АКРИЛАМИД И МЕРКАПТАН ПРИ ВИСОКОТЕМПЕРАТУРНА СИСТЕМА С РАЗЛИЧНА ВЛАЖНОСТ

З. Сюн[1,2], Б. Ли[1,3,*], Л. Ли[1,3,4,*], С. Пън[1], И. Ин[1], Л. Вън[1]

[1]*Училище по хранителни науки и инженерство, Южен Китайски технологичен университет, Гуанджоу, Китай, 510640*

[2]*Училище по химично инженерство и наука за материалите, Пекински институт по технологии, Жихай, Жихай, Китай, 519088*

[3]*Лаборатория за зелена обработка на природни продукти и безопасност на продуктите, провинция Гуандун , Гуанджоу, Китай, 510640*

[4]*Училище по химическо инженерство и енергийни технологии, Технологичен университет в Донгуан, Донгуан, 523808, Китай*

(Резюме)

В настоящото изследване са изследвани реакциите между акриламид и хранителни ароматни меркаптани, включващи 1,2-енандитиол, бутил меркаптан, 2-метил-1-бутил меркаптан и 2-метил-3-фурантиол при висока температура и висока влажност (HTHH) и при висока температура и ниска влажност (HTLH). Резултатите показват, че способността за елиминиране на акриламид на 2-метил-3-фурантиол е по-силна в сравнение с тази на бутил меркаптана и 2-метил-1-бутил меркаптана в HTHH системата, докато в системата HTLH е най-ниска. Освен това, pH може значително да повлияе на съдържанието на акриламид в HTHH системата, но ефекта на pH не е толкова очевиден в системата HTLH. С добавянето на антиоксиданти елиминирането на акриламида е значително намалено. В заключение, реакцията се характеризира с различни механизми при висока температура. Нуклеофилното присъединяване и радикалното присъединяване заемат доминиращата роля съответно в HTHH и HTLH системите.

Bio-oil production from fast pyrolysis of *Cladophora glomerata* in a fluidized bed reactor

A.G. Ebadi*, H. Hisoriev

Institute of Botany, Plant Physiology and Genetics, Tajik Academy of Sciences, P.O. Box: 734017, 27th Karamov Street, Dushanbe- 17, Republic of Tajikistan

Algae proved that are very good oil resource in recent years. Southern coast of Caspian Sea has good potential for reservoir of filamentous Macro-algae bearing oils such as, *Cladophora glomerata.* Among various auto thermal conversion routines for production of energy from biomass, fast pyrolysis (conversion of a solid/liquid carbon-based fuel into a large number of energetic components (gaseous component and small quantities of liquid) and solid residue (char and ash) in the absence of a fluidizing medium) is one of the methods that are receiving more attention from researchers. In this work, several experiments were carried out to evaluate the qualities of product yields especially bio-oil in *Cladophora glomerata* by a fluidized bed reactor. The data obtained showed that an increase in the Reaction time (RT) leads to significant increases in the gas yield and a considerable decrease in both bio-oil and char yield. The experimental runs also showed that the reaction temperature (T_p) has an effective role in the quality of the product yields; higher temperature is favorable for higher gas yield and lower char yield production from *Cladophora glomerata.*

Keywords: Algae, *Cladophora glomerata*, Fast pyrolysis, Bio-oil, Char, Fluidized bed, Farahabad Region, Iran

INTRODUCTION

In recent years Algae showed third generation of biodiesel and biofuel reservoir that economically has more yields than crops. For example proved that lipid content in algae (% of lipid content by dry weight), is as good as in other oil crops. In recent years, interest is growing in the production of bio-oil and bio-gas from autothermal conversion of biomass because it is renewable, CO_2 neutral, and abundantly available. Another reason is the present energy crisis due to dependency on fossil fuels and economic problems. Algae biofuels are important sources of renewable energy for production clean energy through auto thermal or biological conversion [1].

Among various autothermal conversion routines for production of energy from biomass, fast pyrolysis (conversion of a solid/liquid carbon-based fuel into a large number of energetic components (gaseous component and small quantities of liquid) and solid residue (char and ash) in the absence of a fluidizing medium) is one of the methods that are receiving more attention from researchers. The main purpose of fast pyrolysis is to convert solid feedstocks into a liquid fuel which contains water, organic acids, non-polar hydrocarbons and other oxygenated components [2]. In this process, feedstock rapidly heated to high temperature in the range of 500-700 ℃ to yield: solid residue, 10-15%;

liquids, 70-80%; and light gaseous components, 10-15% [3].

The advantages of fast pyrolysis of biomass materials include availability and simplicity, and it has been studied by numerous authors using various kinds of reactors like bubbling fluidized beds (BFBs), circulating fluidized beds (CFBs), and fixed beds (FBs). For instance, Ali et al. [4] investigated the influence of working conditions (particle size, 1.0-2.0 mm and reaction temperature, 360-540 ℃) on the yield of bio-oil from fast pyrolysis of biomass and concluded that the maximum yield of bio-oil obtains with a carrier gas flow rate of 11.0 m³/h. Pattiya and Suttibak studied the effects of reaction temperatures and hot vapor filter on pyrolysis product yields and concluded that the optimum pyrolysis temperature for production of maximum bio-oil is about 475 ℃ [5]. The use of hot vapor also led to a decrease of 6.0-7.0 wt% of bio-oil yield. An experimental study for enhancing the yield of produced bio-oil from fast pyrolysis of microalgae biomass was carried out by Miao and Wu. The authors found that the yield of bio-oil produced from *Chorella protothecoides* is much higher than from autotrophic cells during the process [6].

Most of the studies reported above have been focused on biomass gasification at different working conditions and have not considered the influence of fuel particle size and reaction time, both having a major influence in the in kinetics of the fast pyrolysis process and thus on the yield of bio-oil. Thus, this work aims to study the effects of hydrodynamic characteristics on the yield of bio-oil. Given the

---

* To whom all correspondence should be sent:
E-mail: dr_ebadi2000@mail.ru

relatively low emphasis on hydrodynamic parameters, the purposes are to achieve a better understanding of the fast pyrolysis under different hydrodynamic conditions, as well as to help establish the maximum yield of bio-oil from *Cladophora glomerata* grown in southern coast of Caspian Sea.

EXPERIMENTAL

Experiments

The experimental runs have been performed at the pyrolysis equipment shown in Figure 1. The pilot plant consists of a feeding system (K-Tron) which enables to control the algal biomass feeding ratio, a fluidized bed system (equipped with 150 μm gas distributor), and a hot gas filtering system. The reactor was indirectly heated by two electric heaters which enable to keep the pyrolysis temperature constant. Two K-type thermocouples have been installed at the outer wall to measure and control the process temperature.
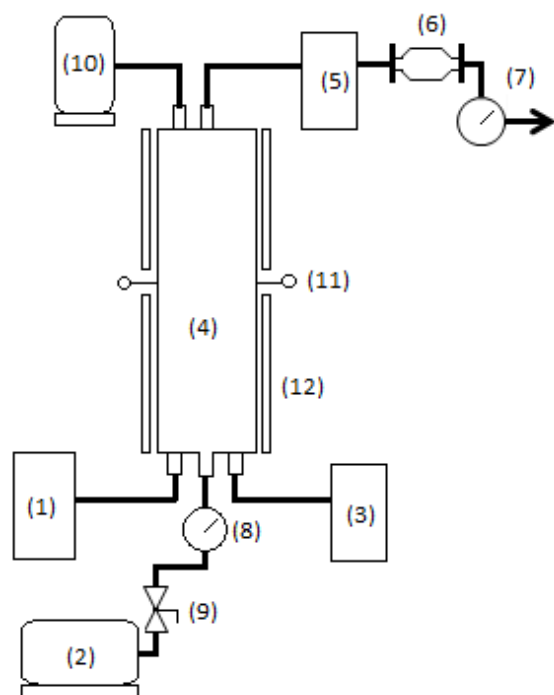
Fig. 1. A schematic diagram of fluidized bed; (1) bio-oil storage tank; (2) Nitrogen gas feeding system; (3) solid hopper; (4) fluidized bed reactor; (5) filtering system (6) pressure transducer; (7) gas meter; (8) nitrogen flow meter system (9) valve (10) feedstock feeding system (11) thermocouple (12) electric heater.

An solid hopper located at the bottom of the fluidized bed allows to collect the solid residues of the pyrolysis process including ash and char. The nitrogen (inert gas) and biomass feeding rates were about 20 L/min and 300 kg/h, respectively. The gas

and liquid products were analyzed by a gas chromatograph (Model Agilent 428A) and a Py-GC/MS (Model TH-411), respectively.

Raw material

The feedstock used in this work is *Cladophora glomerata* which collected from Farahabad Region (Sari city of Mazandaran, 2016) located in Caspian Sea, Iran, according to standard method [7-8]. The *Cladophora glomerata* belong to filamentous Ulvophyceae (Chlorophyta-green algae) is the main and dominant macro algae in the southern coast of Caspian Sea that has extensive distribution in all seasons in this region (Figure 2). It mainly grown on the big stones (usually near to 80-90% covering) and near sea coast walls. Its appearance is tolerating permanent change so that it will depend directly on age, habitat and also environmental conditions. Prior to the pyrolysis experimental tests, the algae biomass has been dried under atmospheric conditions for 36 h and then crushed to a particle size below 7.0 mm. The properties of the algae biomass, such as the proximate and elemental analysis, and also feedstock caloric value are listed in Table 1.

Table 1. Detailed Properties of *Cladophora glomerata*.

Proximate analysis (wt %)	
Moisture	05.01
Volatile matter	77.71
Fixed carbon	16.94
Ash	0.34
HHV (MJ/kg)	19.97
Ultimate analysis (wt %), daf[a]	
C	50.26
H	06.72
O	42.66
N	00.16
S	00.20

[a] Dry and free ash

RESULTS AND DISCUSSION

In the first test series, the influence of process temperature (T_p) on product yields and higher heating value (HHV) was analyzed, where the particle size (PS) and reaction time (RT) were kept constant. Metrics can be expressed as follows [9]:

$$HHV\,(MJ/kg) = 0.3491C + 1.1783H + 0.1005S - 0.1034O - 0.0151N - 0.0211A \quad (1)$$
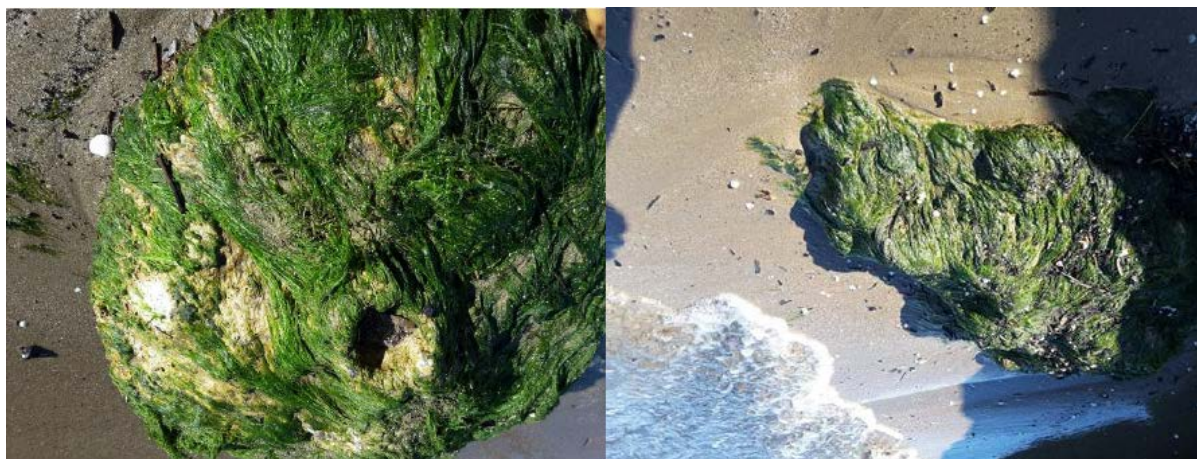
Fig. 2. *Cladophora glomerata* obtained from Farahabad region of Caspian Sea (November 2016).

$$Y(\%) = \frac{\text{Mass of fraction } i}{\text{Total mass in the feed}} \times 100 \qquad (2)$$

Here Y is the product yield (gas, solid, and oil) in %. C, H, S, O, N, and A also are the mass of carbon, hydrogen, sulfur, oxygen, nitrogen, and ash in the dry biomass. Summarized in Table 2 are the results of the experimental tests based on various working conditions during the fast pyrolysis of *Cladophora glomerata*. Major changes in the results occurred with changes made in the reaction temperature. The highest and lowest bio-oil yields were around 45.5 and 24.2 % which achieved at T_p of 360 and 520 ℃. For the gas yield, the highest (24%) and lowest (7.0%) value are obtained at around 520 ℃ and 380 ℃, respectively (Table 2).

Table 2. Effect of Tp on product yields (PS= 7.0 mm, RT = 10 min)

Run	T_p	Yields (%)			HHV (MJ/kg)
		Bio-oil	Char	Gas	
1	360	26	65.0	9.0	15.28
2	380	59.2	52.2	7.0	14.73
3	400	57.0	47.5	9.5	14.07
4	420	47.5	39.8	12.7	13.52
5	440	54.5	30.1	15.4	12.88
6	460	55.0	26.7	18.3	12.16
7	480	59.1	20.8	20.1	11.72
8	500	62.1	15.4	22.5	11.24
9	520	65.5	10.5	24.0	10.87

Finally, process temperatures of 360 and 520 ℃ correspondingly attained the highest (65%) and lowest (10.5%) char yield. Although the yield of bio-oil obtained in this work is found to be slightly lower than those derived from agricultural residue (60-78%), the result is still higher than those of other

works (26-43%) which used algae biomass as fuel for bio-oil production [10]. The results show that the present process is a promising method as a sustainable and clean way for the production of bio-oil; however, there is a relatively high quantities of char residue which leads to a reduction in the total efficiency. With increase of reaction temperature from 360 to 520 ℃, the bio-oil production decreased due to the endothermic reactions occurring along the fluidized bed.

Table 3. Effect of PS on product yields (Tp = 520 ℃, RT = 10 min)

Run	T_p (℃)	PS (mm)	Yields (%)		
			Bio-oil	Char	Gas
1	520	7.0	65.5	10.5	24.0
2	520	6.5	65.4	10.3	24.3
3	520	6.0	65.5	10.1	24.4
4	520	5.5	65.5	10.0	24.5
5	520	5.0	65.8	09.5	24.7
6	520	4.5	66.0	08.9	25.1
7	520	4.0	66.3	08.4	25.3
8	520	3.5	66.8	07.6	25.6
9	520	3.0	67.0	07.2	25.8

Table 3 shows the product yields as a function of PS. As far as the PS is concerned, this hydrodynamic parameter has influence upon the product yields and emissions of the process. As can be seen, PS has a slight influence on the product yields (which is associated with a slight decrease in the heat and mass transfer restrictions); however, the use of small size particles as a feedstock entails environmental and socioeconomic benefits. Clearly, between 5.0 and 7.0 mm, the char yield (and thus the char conversion ratio) suffers a significant decrease, which shows that for fuel particles above 5.0 mm not only are

thermal decomposition enhanced, but also are the char conversion ones, hence increasing gas production. Note that the effect of PS on the yield of bio-oil depends on the heating rate of the process; higher heating rates (smaller particles) favorable more bio-oil and gas production [11]. Among the different methods for improving economic aspects of the process, a reduction in the PS is more economical than those of other methods because it allows the reduction of reactor length.

In fact, a reduction in the particle size leads to an increase in the produced gas quality and a decrease in the residence time of particles to achieve a higher conversion of char. Wei et al [12] investigated the influence of the PS in the pyrolysis process in a free fall reactor, and they found that pyrolysis of smaller particles leads to a decrease in the solid residues and an increase in the yield of product gas.

Table 4. Effect of RT on product yields (PS = 3.0 mm, RT = 10 min)

Run	T_p (^{0}C)	RT (min)	Yields (%)		
			Bio-oil	Char	Gas
1	520	10	67.0	07.2	25.8
2	520	12	68.8	05.1	26.1
3	520	14	69.5	03.2	27.3
4	520	16	67.5	03.0	29.5
5	520	18	66.8	02.8	30.4
6	520	20	66.4	02.7	30.9
7	520	22	64.8	02.5	32.7
8	520	24	64.6	02.3	33.1
9	520	26	64.5	02.0	33.5
10	520	28	64.0	01.8	34.2
11	520	30	63.7	01.5	34.8

Table 4 shows the product yields as a function of reaction time in the range of 10-30 min. Reaction time is another important variable which affects the gas composition, bio-oil quality and quantity, and char yield. As observed, with increasing the reaction time (RT), the yield of bio-oil increases and then decreases while the syngas yield continuously increases due to a significant improvement in the rate of endothermic reactions with increasing RT. Another reason is the expansion of char conversion and tar cracking reactions, as the RT improves. In this sense, Fonts et al. [13] suggested that biomass pyrolysis rates strongly depend on the reaction time, and that reactivity of a biomass fuel was related to the long of reaction time and heating rates.

CONCLUSION

The production of bio-oil from *Cladophora glomerata* biomass using fast pyrolysis in a fluidized bed reactor was studied. Effects of some important variables such as reaction temperature (T_p), Algae particle size (PS) and reaction time (RT) on product yields were evaluated by experimental and analyses. The data obtained show that an increase in the RT leads to a significant increases in the gas yield and a considerable decrease in both bio-oil and char yield. The experimental runs also showed that the PS has a slight influence on the product yields; however, it plays a major role in the economic aspects of the process.

REFERENCES

1. C.A. Mullen, A.A. Boateng, N.M. Goldberg, I.M. Lima, D.A. Laird, K.B. Hicks, *Biomass Bioenerg.*, **34**, 67 (2010)   .
2. X. Xu, C. Zhang, Y. Liu, Y. Zhai, R. Zhang, *Chemosphere*, **93**, 652 (2013)   .
3. M.F. Demirbas, M. Balat, *J. Sci. Ind. Res.*, **66**, 797 (2007)   .
4. N. Ali, M. Saleem, K. Shahzad, S. Hussain, A. Chughtai, *Polish J. Chem. Technol.*, **18**, 88 (2016).
5. A. Pattiya, S. Suttibak, *J. Anal. Appl. Pyro.*, **95**, 227 (2012).
6. X. Miao, Q. Wu, *J. Biotechnol.*, **110**, 85 (2004).
7. H. Hisoriev, P. Korbanova, I. Kodirova, Erfan Publication, Dushanbe, Republic of Tajikistan, 2015,. 116.
8. A.G. Ebadi, H.H. Hisoriev, *Toxicol. Environ. Chem.*, DOI 10.1080/02772248.2017.1323894 (2017).
9. S.A. Channiwala, P.P. Parikh, *Fuel*, **81**, 1567 (2002).
10. M.A.F. Mazlan, Y. Uemura, N.B. Osman, S. Yusup, *J. Physics: Conference Series*, **622**, 012054 (2015).
11. F. Yan, S.Y. Luo, Z.Q. Hu, B. Xiao, G. Cheng, *Bioresour. Technol.*, **101**, 5633 (2010).
12. L. Wei, S. Xu, L. Zhang, H. Zhang, C. Liu, H. Zhu, S. Liu, *Fuel Process Technol.*, **87**, 863 (2006).
13. I. Fonts, A. Juan, G. Gea, M.B. Murillo, J.L. Sanchez, *Ind. Eng. Chem. Res.*, **47**, 5376 (2008).

ПРОИЗВОДСТВО НА БИО-МАСЛО ЧРЕЗ БЪРЗА ПИРОЛИЗА НА *Cladophora Glomerata* В РЕАКТОР С КИПЯЩ СЛОЙ

А. Г. Ебади *, Х. Хисориев

Институт по ботаника, фитология и генетика на растенията, Таджикска академия на науките, П. К. 734017, улица Карамов №27, Душанбе-17, Република Таджикистан

(Резюме)

През последните години водораслите са доказали, че са много добрър източник на масла. Южното крайбрежие на Каспийско море има добър потенциал като резервоар на филаментозни макро-водорасли, съдържащи масла като *Cladophora glomerata*. Сред различните начини за автотермична преработка за производство на енергия от биомаса, бързата пиролиза (преобразуване на твърдо/течно въглеродно гориво в голям брой енергийни компоненти (газообразен компонент и малки количества течност и твърди остатъци (въглен и пепел) в отсъствието на флуидизираща среда) е един от методите, които получават повече внимание от изследователите. В тази работа бяха проведени няколко експеримента за оценка на качествата на продукта, особено био-масло в *Cladophora glomerata* чрез реактор с кипящ слой. Получените данни показват, че увеличаването на реакционното време (RT) води до значително увеличение на добива на газ и до значителен спад както в добива на био-масло, така и на въглен. Експерименталните тестове също показват, че реакционната температура (T_p) има ефективна роля в качеството на продукта; По-високата температура е благоприятна за по-висок добив на газ и по-ниска производителност на добив на въглен от *Cladophora glomerata*

Limitations of measurements of supercritical CO_2 sorption isotherms on coals with manometric equipment－A theoretical description

R. Jiang, H. Yu[*], L. Wang

School of Chemical and Environmental Engineering, Shandong University of Science and Technology

CO_2 adsorption isotherms on coals are important for estimating the CO_2 sequestration potential of coal beds and enhanced coalbed methane recovery using CO_2 injection into coal seams. This paper provides the characteristic of CO_2 compressibility factor and density change of CO_2 based CO_2 Equation of State. The paper investigates the effect of experimental pressure and its error, adsorption/desorption hysteresis, and coal swelling on measurements of supercritical CO_2 adsorption isotherms on coals with manometric equipment at high pressure. The results show that the characteristic density-change of CO_2 in proper pressure range determines great influence of experimental parameters, coal swelling and adsorption/desorption hysteresis on CO_2 adsorption on coal at high pressure. The effect of the hysteresis on sorption at high-pressure may leads to negative observed-adsorption. And coal swelling at high pressure has obvious effect on the precision and reproducibility of CO_2 adsorption. There are potential pitfalls of measurements of supercritical CO_2 adsorption isotherms on coals with manometric equipment at high pressure.

Keywords: Adsorption, CO_2, coal, uncertainty, CO_2 sequestration.

INTRODUCTION

CO_2 injection into coal bed has received increased attention as a potential option to reduce greenhouse gas CO_2 emissions to the atmosphere and to enhance the coalbed methane recovery (ECBM) [1]. Accurate measurements of CO_2 sorption isotherms on coals are vital for the optimum techniques of CO_2 sequestration and ECBM. For a given coal seam, sorption isotherm measurements provide information about the storage capacity, the overall economics of the process, and the types of operating conditions [2].

Much work has been carried out on the sorption capacity of coal with respect to CO_2 at low- and moderate pressure with manometric, volumetric, or gravimetric apparatus [3-10]. However, there have been very few high-pressure studies of CO_2-coal sorption isotherms under in-seams conditions [11-20].

Unusual adsorption isotherms of CO_2 on coals at high pressure have been reported in the available literatures. Krooss et al. [11] performed CO_2-sorption experiments on coals with manometric apparatus between 40 and 80 °C and pressures up to 20 MPa. The results of Kross et al. [11] showed that all high-pressure CO_2 adsorption isotherms for moist samples were bimodal with distinct minima and even negative excess sorption values in the 8-10 MPa

range and beyond this range CO_2 adsorption capacity increased with increasing pressure. The strong bimodal character of the CO_2 excess isotherms on moist coals is interpreted as the result of a swelling effect caused by supercritical CO_2 and enhanced by water. Fitzgerald et al. [12] performed pure CO_2 adsorption on wet Tiffany mixed coal sample with volumetric apparatus at 327.6 K and pressures up to 14 MPa. The result of Fitzgerald et al. [12] showed that at high pressure (>7 MPa) the CO_2 Gibbs sorption capacity decreases with increasing pressure.

Coal swelling due to gas adsorption is a well-known phenomenon, and is used to correct adsorption isotherms for coal swelling [20-23]. Many researchers investigated the coal swelling with various ranks and experimental technique, and gave different conclusions. Reucroft et al. [24, 25] measured the swelling of various ranks of Kentucky coal by directly observing directional changes and found that the volume increase was between 0.36 and 4.18% at pressure from 0 to 1.5 MPa. Walker et al. [26] measured the expansion of powered coals and macerals induced by CO_2 and found that expansion to an equilibrium value was fast and concluded that most of the CO_2 uptake was in open and closed (to He) micropores. Chikatamarla et al. [27, 28] measured CO_2 induced swelling on four coal samples with pressures up to 5.0 MPa and found that the volumetric strain at 0.6 MPa was from 0.26% to 0.66% for CO_2 and the volumetric strain and pressure can be described using a Langmuir like

---

* To whom all correspondence should be sent:
E-mail: yuhongguan65@163.com

equation and the volumetric strain was approximately linearly proportional to the amount of gas adsorbed. St. George and Barakat [29] measured volumetric strains for adsorption at 4.0 MPa for CO_2 on a coal sample from New Zealand and found that the volumetric strain was 2.1% for CO_2.

Pan and Connell [30] presented a theoretical model to describe adsorption-induced coal swelling. The developed model combines the two processes affecting coal volumetric changes, namely, swelling due to gas adsorption and matrix compression due to gas pressure. They found that the model was able to describe coal swelling behavior for the whole pressure range, including at very high gas pressure, where the coal swelling ratio may decrease after reaching a swelling maximum.

In order to better understand the variation in measured Gibbs-sorption of CO_2 with manometric technique at high pressure, this paper investigates the effect of the experimental parameters (including pressure and volume of two cells), adsorption/desorption hystersis and volume swelling of coal on CO_2 adsorption. This main purpose of this paper is only to provide the general interpretations which the low repeatability and inter-laboratory reproducibility of CO_2 adsorption isotherm measurements, negative adsorption, unimodal isotherm is unavoidable due to the limitation of manometric measurement caused by the characteristic change of CO_2 compressibility factor or density at high pressure.

MATERIALS AND METHODS

Mass balance equation for co₂ adsorption isotherm measurement

The increased Gibbs-sorption at equilibrium step i is calculated with mass balance of the amount of CO_2 transferred from the reference cell to the sample cell and the equilibrium amount of CO_2 in the sample cell. The increased Gibbs-adsorption (Δn_i^{ex} in mmol/g) at the end of ith step is calculated by the real gas law shown in Eq. (1)

$$\Delta n_i^{\text{ex}} = \left(\frac{1}{RTm}\right)\left(V_R\left(\frac{P_{R,I}^i}{Z_{R,I}^i} - \frac{P_{R,F}^i}{Z_{R,F}^i}\right) - V_0\left(\frac{P_{S,Eq}^i}{Z_{S,Eq}^i} - \frac{P_{S,Eq}^{i-1}}{Z_{S,Eq}^{i-1}}\right)\right) \quad (1)$$

where the subscripts, "I","F" and "Eq", refer to the conditions in the cell before, final the gas expansion and adsorption equilibrium, the subscripts, "R" and "S" represent the reference and sample cell, the superscripts, i and $(i-1)$ represent the ith and $(i-1)^{\text{th}}$ step, respectively, P is the pressure, Z is the compressibility factor of CO_2, T is the temperature, R is the molar gas constant, m is the

mass of the coal sample, V_R and V_0 is the volume of sample cell and the void volume in the sample cell, respectively.

The total Gibbs sorption in the sample cell at step j is the total amount exchanged with the reference cell for step 1 to j. The estimate of the total amount of excess adsorption (n_j^{ex}) at the end of the jth step is determined from Eq. (2)

$$n_j^{\text{ex}} = \Delta n_1^{\text{ex}} + \Delta n_2^{\text{ex}} + \cdots\cdots + \Delta n_i^{\text{ex}} + \cdots\cdots + \Delta n_j \quad (2)$$

So, the Eq. (2) can be written from Eq. (3)

$$n_j^{\text{ex}} = \left(\frac{1}{RTm}\right)\left(V_R\sum_{i=1}^{j}\left(\frac{P_{R,I}^i}{Z_{R,I}^i} - \frac{P_{R,F}^i}{Z_{R,F}^i}\right) - V_0\frac{P_{S,Eq}^j}{Z_{S,Eq}^j}\right) \quad (3)$$

The bulk density of CO_2 is a function of pressure and temperature, the amount of CO_2 exchanged is calculated from the difference in density in the reference cell between the charging and equilibrium phase. If $V_{Rm} = \frac{V_R}{m}$, $V_{0m} = \frac{V_0}{m}$, $\Delta\rho_R^i = \left(\frac{P_{R,I}^i}{Z_{R,I}^i} - \frac{P_{R,F}^i}{Z_{R,F}^i}\right)\Big/RT$, $\Delta\rho_S^i = \left(\frac{P_{R,I}^i}{Z_{R,I}^i} - \frac{P_{R,F}^i}{Z_{R,F}^i}\right)\Big/RT$, $\rho_S^j = \frac{P_{S,Eq}^j}{RTZ_{S,Eq}^j}$, the Eq.s (1) and (3) can be written as shown in Eq.s (4) and (5),

$$\Delta n_i^{\text{ex}} = V_{Rm}\Delta\rho_R^i - V_{0m}\Delta\rho_S^i, \quad (4)$$

$$n_j^{\text{ex}} = V_{Rm}\left(\sum_{i=1}^{j}\Delta\rho_R^i - x\rho_S^j\right). \quad (5)$$

where V_{Rm} and V_{0m} is specific volume of reference cell and void volume of sample cell, respectively, $\triangle\rho_R$ is density change of CO_2 in reference cell, ρ_S and $\triangle\rho_S$ is density of CO_2 and its change in sample cell.

The equilibrium amount of CO_2 in the sample cell is the density at the equilibrium pressure and temperature multiplied by x, a volume ratio of void of sample cell and reference cell (V_0/V_R). The Eqs. (4) and (5) can be written as the following,

$$\Delta n_i^{\text{ex}} = V_{Rm}\left(\Delta\rho_R - x\Delta\rho_S\right), \quad (6)$$

$$n_j^{\text{ex}} = V_{Rm}\left(\sum_{i=1}^{j}\Delta\rho_R^i - x\rho_S^j\right). \quad (7)$$

The compressibility factor and density

The change of compressibility factor and density with pressure. The independent variables for the excess adsorption are the initial and finial pressure in the reference and sample cell, the empty and void volume of the reference and sample cell, the sample weight, and temperature. Also, the compressibility factor is another variable, whose value is dependent on the temperature and pressure. Although there is so many variables affecting the measured value of

CO_2 Gibbs adsorption, the compressibility factor (Z) or density of CO_2 is the root of the effect at high pressure. The change of Z-factor and density of CO_2 are used to explain the limitation of measurements of supercritical CO_2 sorption with manometric apparatus at high pressure, the effect of other factors is investigated based on the change.
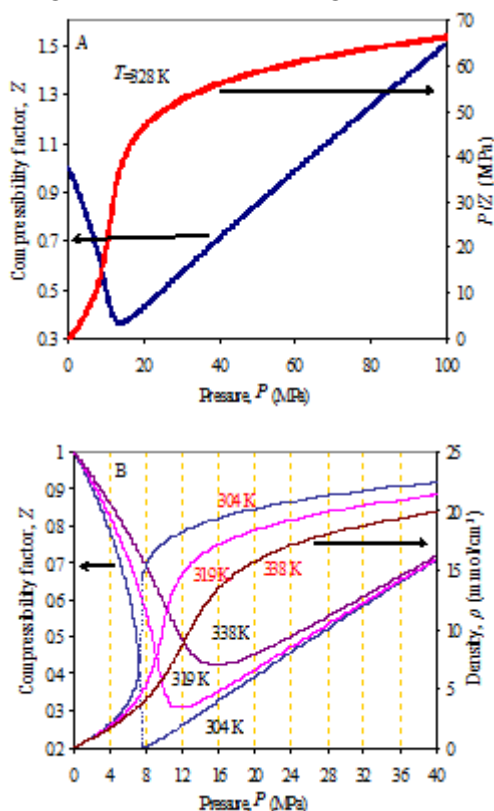
Fig. 1. The compressibility factor of CO_2 (Z) and density of CO_2, obtained from the Span and Wagner-EOS [31

The compressibility factor (Z) and the density (ρ) of CO_2 were calculated at temperature from 31 ℃ to 65 ℃ and pressure up to 100 MPa based on the Span and Wagner Equation of State [31]. The Z- and P/Z-value at 55 ℃ and pressure up to 100 MPa (A) and the Z- and ρ-value at temperature of 31, 46, 65 ℃ and up to 40 MPa (B) is shown in Fig. (1).

Just as shown in Fig. (1A), the Z-values decrease to 0.3647 from 1 at a pressure of 13.62 MPa, and increase from 0.3647 to 1.504 at 100 MPa and 55 ℃. It is known that CO_2 at pressures up to 100 MPa have increasing P/Z-value with the pressure increase (Fig. 1A).

It can be seen from Fig. (1B) that all Z-factors of CO_2 are unimodal with distinct minima in the 8-16 MPa range, which is dependent on the temperature. There is the range of a pressure (P_{min}-P_{max}) corresponding the minimum of Z-factor (Z_{min})

because the limit of error for calculated Z-factor based on the Span and Wagner Equation of State is 0.0001. The Z_{min} and its corresponding pressure (P_{min} or P_{max}) increase with the increase of temperature. Table 1 gives the minimum Z-factor and its corresponding pressure range at from 31 to 65 ℃.
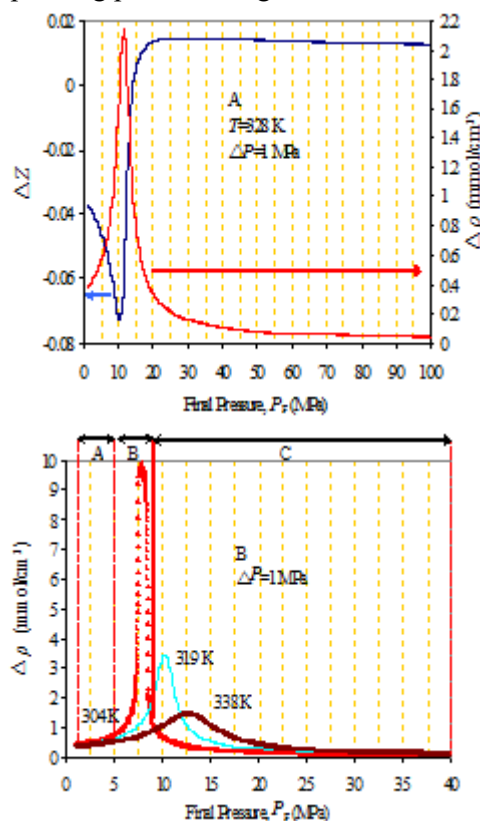
Fig. 2. The CO2 compressibility factor and density change at 328 K and pressure up to 100 MPa (A) and comparison of density change at 304, 319 and 338 K and pressure up to 40 MPa (B), with pressure change of 1.0 MPa.

The unimodality and minimum of CO_2 Z-factor determine the shape of CO_2 density isotherms as shown in Fig. (1B). The density-values increase sharply with the increasing pressure and decreasing Z-factor as pressure below "valley" pressure (P_{min}) corresponding minimum Z-factor (Z_{min}), and increase smoothly with the increasing Z-factor and pressure at pressure of more than the P_{min}. For example, the density of CO_2 increases sharply at pressure of less than 13.62 MPa and 55 ℃, and increases smoothly at pressure of more than 13.62 MPa. Table 1 gives also the density range of CO_2 corresponding P_{min} and P_{max} at the temperature of from 31 to 65 ℃.

The density change with pressure at a constant temperature. The change of bulk density of CO_2 is used to calculate the Gibbs sorption based Eq. (5) or (7). The Fig. (2) shows the change of density of CO_2,

511

$\triangle\rho$, with pressure-change ($\triangle P$), of which Fig. (2A) gives the $\triangle\rho$ with $\triangle P$ of 1.0 MPa at 55 ℃ and pressure of up to 100 MPa, Fig. (2B) gives it with $\triangle P$ of 1.0 MPa at temperature of 31, 46 and 65 ℃ and up to 40 MPa. The $\triangle\rho$ with $\triangle P$ of 0.5, 1.0, 1.5 and 2.0 MPa at temperature of 31 ℃ (A) and 55 ℃ (B) is shown in Fig. (3).

It can be seen from Fig. (2) that the density changes exhibit a three-stage tendency with the pressure increase. Although the change increases at low pressure and decreases at high pressure with the pressure increases, the change is comparatively small compared with that at medium pressure. The density change ($\triangle\rho$) increase first and then decrease with pressure increase at medium pressure, and the maximum $\triangle\rho$ is achieved at a pressure. The maximum $\triangle\rho$ and its corresponding pressure is expressed as $\Delta\rho_{max}$ and P_{max}, respectively. The $\Delta\rho_{max}$ decreases and P_{max} increases with the temperature increase.

The change of bulk density of CO_2 is used to calculate the Gibbs sorption based Eq. (5) or (7). The Fig. (3) shows the change of density of CO_2, $\triangle\rho$, with various pressure-change ($\triangle P$= 0.5, 1.0, 1.5 and 2.0 MPa) at temperature of 31 ℃ (A) and 55 ℃ (B).

The density-change curve can be divided into three regions (i.e. A, B and C) based on its value and corresponding final-pressure as seen in Fig. (3). Because of $\rho_{R,I}^{i} > \rho_{R,F}^{i}, \rho_{S,Eq}^{i} > \rho_{S,Eq}^{i-1}$, it should be noted that the final pressure (P_F) in Fig (3) means the initial pressure of reference cell ($P_{R,I}^{i}$) or equilibrium pressure of sample cell ($P_{S,Eq}^{i}$). The region A at relatively low pressure and region C at relatively high pressure are of small $\triangle\rho$ values with the pressure change, and the region B at high pressure are great $\triangle\rho$-values. The pressure ranges of region B increase with increase of temperature and $\triangle P$, as shown in Fig. (3). The highest $\triangle\rho$-value and its corresponding pressure in region B at temperature of from 31 ℃ to 65 ℃ is given in Table 1.
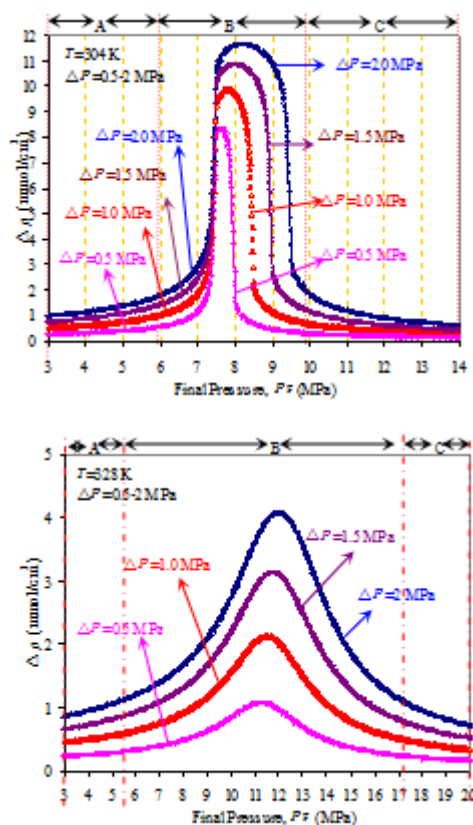
Fig. 3. The change density of CO_2 and dividing region with change of pressure 0.5, 1.0, 1.5 and 2.0 MPa at temperature of 304 K (A) and 328 K (B).

The density change with temperature at a constant pressure: A CO_2 Excess-sorption isotherm describes the CO_2 amount on coal at the equilibrium pressure at constant temperature. So, the CO_2 density change with temperature at a constant pressure ($[\partial\rho/\partial T]_P$) is expressed with that the pressure as the *x*-axis and the density-change as the *y*-axis under different temperatures, as shown in Fig. (4).

It can be seen from Fig. (4) that the density changes still exhibits a three-stage tendency with the pressure increase, and CO_2 density decreases with temperature increase. The effect of temperature on density-change decreases with temperature increase. Although the change increases at low pressure and decreases at high pressure with the pressure increases, the decrease of density change is comparatively small compared with that at medium pressure. The decrease of density change increases first and then decreases with pressure increase at medium pressure, and the maximum -$[\partial\rho/\partial T]_P$ is achieved at a pressure.

Table 1. The minimum Z-factor (Z_{min}) and its corresponding pressure (P_{min}, P_{max}) and density range (ρ_{min}, ρ_{max}), and maximum change of CO_2 density ($\triangle\rho_{max}$) with different pressure change ($\triangle P$) and its corresponding final-pressure (P_F') at temperature of from 31 ℃ to 65 ℃.

T (℃)	Z-factor minimum, its pressure and density					Density change and its final pressure with different pressure change							
	Z_{min}	Pressure range (MPa)		Density range (mmol/cm³)		$\triangle P$=0.5 MPa		$\triangle P$=1.0 MPa		$\triangle P$=1.5 MPa		$\triangle P$=2.0 MPa	
		P_{min}	P_{max}	ρ_{min}	ρ_{max}	$\triangle\rho_{max}$	P_F'	$\triangle\rho_{max}$	P_F'	$\triangle\rho_{max}$	P_F'	$\triangle\rho_{max}$	P_F'
31	0.2047	7.9	7.95	15.269	15.365	8.357	7.60	9.864	7.81	10.880	8.01	11.668	8.18
32	0.2120	8.14	8.25	15.141	15.346	7.649	7.77	9.333	9.97	10.430	8.20	11.271	8.39
33	0.2192	8.41	8.51	15.080	15.259	6.921	7.96	8.795	8.18	9.980	8.37	10.871	8.56
34	0.2264	8.65	8.80	14.968	15.228	6.207	8.12	8.252	8.33	9.523	8.55	10.464	8.79
35	0.2335	8.91	9.05	14.901	15.135	5.523	8.29	7.713	8.51	9.061	8.74	10.060	8.91
36	0.2405	9.21	9.26	14.906	14.987	4.887	8.46	7.181	8.68	8.607	8.88	9.654	9.11
37	0.2476	9.40	9.58	14.729	15.011	4.323	8.62	6.671	8.84	8.157	9.06	9.250	9.26
38	0.2545	9.69	9.79	14.724	14.876	3.832	8.79	6.181	9.00	7.717	9.22	8.849	9.47
39	0.2614	9.95	10.03	14.673	14.791	3.410	8.94	5.719	9.19	7.289	9.38	8.455	9.58
40	0.2683	10.17	10.31	14.565	14.766	3.057	9.10	5.293	9.32	6.877	9.56	8.073	9.79
41	0.2751	10.42	10.55	14.508	14.689	2.758	9.24	4.902	9.49	6.482	9.72	7.700	9.94
42	0.2819	10.63	10.82	14.398	14.655	2.503	9.41	4.546	9.66	6.114	9.88	7.338	10.10
43	0.2886	10.87	11.06	14.335	14.586	2.289	9.56	4.225	9.81	5.764	10.04	6.991	10.26
44	0.2952	11.15	11.26	14.331	14.472	2.102	9.81	3.935	9.95	5.439	10.17	6.662	10.40
45	0.3018	11.38	11.51	14.261	14.424	1.942	9.85	3.675	10.11	5.136	10.33	6.349	10.55
46	0.3084	11.56	11.79	14.132	14.414	1.805	10.00	3.442	10.25	4.856	10.49	6.050	10.69
47	0.3148	11.87	11.95	14.172	14.267	1.684	10.16	3.233	10.40	4.596	10.65	5.770	10.84
48	0.3213	12.02	12.25	14.017	14.285	1.576	10.27	3.045	10.55	4.359	10.76	5.507	10.99
49	0.3276	12.32	12.41	14.047	14.149	1.481	10.45	2.875	10.66	4.139	10.93	5.259	11.17
50	0.3340	12.46	12.72	13.891	14.181	1.396	10.55	2.721	10.80	3.937	11.05	5.029	11.27
51	0.3402	12.73	12.89	13.890	14.065	1.321	10.73	2.582	10.97	3.750	11.22	4.812	11.44
52	0.3464	12.96	13.10	13.845	13.995	1.252	10.86	2.454	11.10	3.579	11.35	4.609	11.60
53	0.3526	13.13	13.37	13.738	13.989	1.190	10.01	2.339	11.22	3.421	11.50	4.420	11.75
54	0.3587	13.35	13.58	13.689	13.925	1.133	11.23	2.233	11.35	3.275	11.62	4.245	11.85
55	0.3647	13.62	13.73	13.694	13.805	1.082	11.26	2.135	11.53	3.138	11.76	4.081	11.98
56	0.3707	13.83	13.94	13.639	13.747	1.034	11.44	2.044	11.64	3.013	11.88	3.926	12.14
57	0.3767	13.97	14.22	13.516	13.758	0.991	11.56	1.961	11.74	2.895	12.03	3.781	12.27
58	0.3826	14.18	14.43	13.467	13.704	0.952	11.66	1.884	11.84	2.786	12.17	3.646	12.38
59	0.3884	14.45	14.56	13.478	13.580	0.915	11.80	1.813	12.06	2.684	12.30	3.519	12.51
60	0.3942	14.66	14.76	13.432	13.523	0.881	11.84	1.747	12.22	2.590	12.39	3.400	12.62
61	0.4000	14.78	15.04	13.306	13.540	0.849	11.99	1.685	12.33	2.501	12.49	3.288	12.77
62	0.4057	14.98	15.24	13.256	13.486	0.819	12.19	1.629	12.40	2.418	12.63	3.182	12.90
63	0.4113	15.30	15.31	13.315	13.324	0.792	12.33	1.574	12.53	2.340	12.72	3.082	13.06
64	0.4170	15.33	15.67	13.120	13.411	0.766	12.47	1.523	12.69	2.267	12.87	2.988	13.18
65	0.4225	15.58	15.79	13.122	13.298	0.742	12.58	1.476	12.79	2.197	13.40	2.900	13.30

DISCUSSION

In order to construct an adsorption isotherm of CO_2 on coal, the increasing pressure is repeated for incrementally increasing the pressure of CO_2 in sample cell, $P_{S,Eq}^i > P_{S,Eq}^{i-1}$. A portion of CO_2 is transferred from the reference cell to the sample cell,

at this point, $P_{R,I}^i > P_{R,F}^i$. In case of positive adsorption, $P_{S,Eq}^i > P_{S,Eq}^{i-1}$ and $P_{R,I}^i > P_{R,F}^i$ do hold. Consequently, the CO_2 ρ-values in two cells increase with equilibrium pressure increasing in the sample cell, just as shown in Fig. (1), $\rho_{R,I}^i > \rho_{R,F}^i, \rho_{S,Eq}^i > \rho_{S,Eq}^{i-1}$. We regard the initial pressure in reference cell ($P_{R,I}^i$) and

equilibrium pressure in sample cell ($P_{S,Eq}^i$) as the final pressure (P_F) of pressure change ($\triangle P$). The P_F is used for the pressures of two cells in the regions (A, B and C), as shown in Fig. (3).

Theoretically, the excess sorption of CO_2 can be calculated from Eqs. (1) and (2). The incremental Gibbs-adsorption (Δn_i^{ex}) is zero or positive if no adsorbed CO_2 is desorbed during CO_2 expansion from reference cell into sample cell. However, the change characteristic of CO_2 density as shown in Fig. (2), may be result in the negative incremental Gibbs-adsorption, just discussed in the following text.

From Eq. (4), the relation between the CO_2 density change ratio in the two cells ($\Delta\rho_S^i/\Delta\rho_R^i$) and the void volume ratio of two cells (V_R/V_S), involves three case, i.e. (1) $\Delta\rho_S^i/\Delta\rho_R^i = V_R/V_S$ for zero adsorption increment (Δn_i^{ex}), (2) $\Delta\rho_S^i/\Delta\rho_R^i < V_R/V_S$ for positive Δn_i^{ex} and (3) $\Delta\rho_S^i/\Delta\rho_R^i > V_R/V_S$ for negative Δn_i^{ex}. The V_R/V_S value is constant for a manometric setup, known coal and its mass, and the changed volume caused by coal swelling. The V_R/V_S values are between 0.2 and 2 from the published references. A smaller volume of reference cell or lower V_R/V_S value is not favorable to raise the pressure in the sample cell.
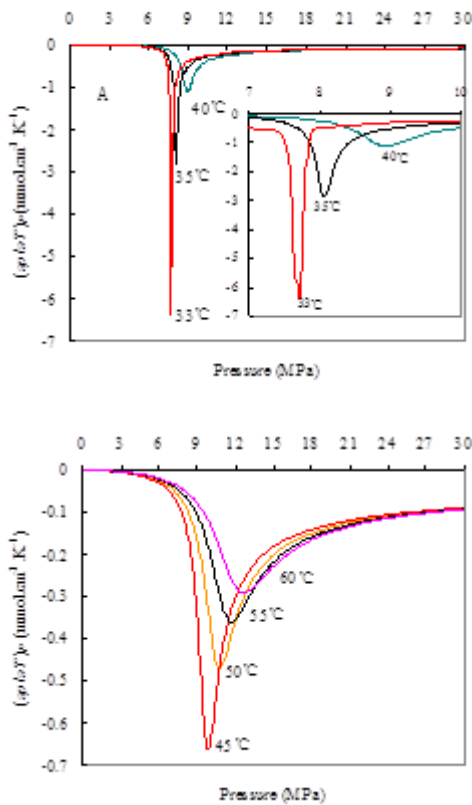
Fig. 4. The comparison of CO_2 density change with temperature at constant pressure

Effect of pressure on CO₂ Gibbs sorption isotherm

(1) In case that both the final pressures of two cells are in region A as shown in Fig. (3), $P_{R,I}^i$ and $P_{S,Eq}^i$ are obviously less than the final pressure ($P_F^/$) with the maximum density-change ($\triangle\rho_{max}$) as shown in Table 1. In this case, the adsorption isotherm of CO_2 can be obtained at low and moderate pressure, which is dependent on the temperature. We must take into account two cases in case of region A. (I) The adsorption of CO_2 on coal in sample cell at low pressure determine $V_{Rm}\triangle\rho_R > V_{0m}\triangle\rho_S$ from Eq. (4), and is described with Langmuir. The small $\triangle\rho_R$ and $\triangle\rho_S$ in region A decide hold of $V_{Rm}\triangle\rho_R > V_{0m}\triangle\rho_S$ in case of $V_{Rm} > V_{0m}$. The adsorption of CO_2 on coal lead to $\triangle P_R > \triangle P_S$ and $\triangle\rho_R > \triangle\rho_S$ in case of $V_{Rm} < V_{0m}$, which make $V_{Rm}\triangle\rho_R > V_{0m}\triangle\rho_S$ hold. (II) As CO_2 adsorption reaches approximately maximum (saturation), the $\triangle P_R$-value is not obvious greater than $\triangle P_S$ as the CO_2 adsorption increment is smaller. Although there is $P_{R,I}^i > P_{S,Eq}^i$ in this case, the adsorption is constant with the pressure as $V_{Rm}\triangle\rho_R \approx V_{0m}\triangle\rho_S$.

Currently, most investigators carried out studies of CO_2 sorption on coal adsorption, which focused on the experimental pressure in region A. This also explains why the sorption isotherm reported by Goodman et al. [32] had good reproducibility for different independent laboratories at temperatures of either 22 °C or 55 °C and pressures up to 7 MP.

(2) In case $P_{R,I}^i$ is in region B and $P_{S,Eq}^i$ is in region A, in which the adsorption isotherm of CO_2 can be obtained at moderate and high pressure. In this case, the density change in reference cell is obviously higher than that in sample cell, i.e. $\triangle\rho_R > \triangle\rho_S$. The measured CO_2-adsorption like the saturation sorption in the case of (1), but the measuring error of CO_2 sorption caused by measurement error of volume and pressure in reference cell is great. The reproducibility of CO_2 Gibbs sorption is mainly dependent on the measurement error of pressure and volume as the great density change in this case. As there is a saturation-adsorption, the expansion CO_2 from reference cell mainly increases the density of bulk CO_2 in sample cell, and the equilibrium pressure of

sample cell should increase to the pressure in region B.

(3) In case that both the final pressure of reference and sample cell are in region B, in which the sorption isotherm of CO_2 can be obtained at high pressure. The measured adsorption like that of case (2) except that the measurement error of adsorption is great with the pressure errors of two cells. The negative sorption increment and bad reproducibility of CO_2 Gibbs sorption may be obtained with the pressure and volume errors of two cells as the greater $\triangle\rho_R$ and $\triangle\rho_S$ with the same $\triangle P$ in this case.

(4) In case that the final pressure of reference cell is in region C and the final pressure of sample cell is in region B, in which the adsorption isotherm of CO_2 can be obtained at high pressure. The obvious negative sorption increment may be obtained with the pressure and volume errors of sample cell and great $\triangle\rho_S$ with the same $\triangle P$ in this case.

(5) In case both the final pressure of reference and sample cell is in region C, in which the adsorption isotherm of CO_2 can be obtained at high pressure. In this case, the increased-adsorption is not distinct as $\triangle\rho_R \approx \triangle\rho_S$ with the same $\triangle P$.

No distinct difference in density change of CO_2 with pressure at low and moderate pressure determine better repeatability and small error for CO_2 sorption isotherms with manometric equipment. The distinct CO_2 density change in sample or reference cell with pressure at high pressure determine that it is difficult to measure CO_2 sorption isotherms with better repeatability and small error, which will discussed in the following text.

To minimize the effect of the measurement error of pressure on CO_2 adsorption, the pressure range in reference cell should be controlled in region A or C, rather than B region. The initial pressure in the reference cell is controlled by the charged amount with syringe pump, and the finial pressure is controlled by the transferred portion of CO_2. That is, the experimental procedures involve the cases (1), (4) or (5) described above, which is used to construct the adsorption in low, moderate and high pressure, respectively.

Effect of the measurement error of pressure

The estimation of the error with respect to each independent variable about CO_2 adsorption measurement is not the scope of this paper. The adsorption error caused by measurement error of pressure in region B is investigated as the density change is greater than that in region A and C with the same $\triangle P$. This main purpose of the analysis about the measurement error of pressure is only to

provide an explanation for the negative incremental Gibbs-adsorption and less repeatability, which may be caused by the error of pressure at appropriate pressure range.

Although the pressure transducers have accuracy from ±0.001 to ± 0.01 MPa, the reading is generally accurate to ± 0.01 MPa. The reading error of 0.01 MPa and 0.02 MPa are employed to estimate its effect on CO_2 density.

The Fig. (4) shows the density change of CO_2 ($\triangle\rho$) for the pressure change ($\triangle P$) of 0.01 and 0.02 MPa at temperature 31, 32 and 55 ℃. The temperature obviously affect on $\triangle\rho$ for the same $\triangle P$ at proper pressure, in which the changed-density maximum is 1.21, 0.63 and 0.045 mmol/cm³ for 0.02 MPa increased-pressure at 31, 32 and 55 ℃, respectively, and it is 0.63, 0.53 and 0.02 mmol/cm³ for $\triangle P$ of 0.01 MPa at 31, 32 and 55 ℃, respectively. The maximum error caused by the pressure error mainly takes place in region B.
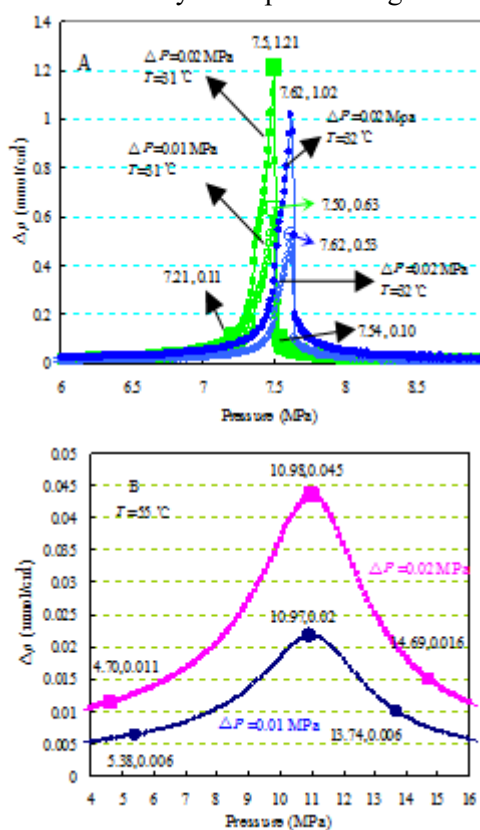
Fig. 5. The change density of CO_2 with change of pressure 0.01 MPa and 0.02 MPa at 31, 32 °C (A) and 55 °C (B) obtained from the Span and Wagner-EOS. Positions on the curves are identified as (*a*, *b*) where *a* and *b* are the pressure and its density change with the pressure change

The density change due to the error of pressure reading causes the bad accuracy of excess adsorption

and exceptional Gibbs sorption of CO_2 at proper pressure, such as negative adsorption. As a portion of CO_2, $\triangle n_R$ mmol, is transferred from the reference cell to the sample cell and both cells are allowed to equilibrate. The density error is 1.21 mmol/cm³ and 0.63 mmol/cm³ for the error of pressure reading of 0.02 and 0.01 MPa at equilibrium pressure of 7.5 MPa and 31 ℃. If the specific volume of sample cell or void volume of sample cell is 1 cm³/g-coal, the negative adsorption of 1.21 mmol/cm³ and 0.63 mmol/cm³ at 31 ℃ will be obtained due to pressure reading-error of 0.02 and 0.01 MPa in reference cell at $P_{Eq,I}^i$ of 7.5 MPa or in -0.02 and -0.01 MPa in sample cell at $P_{R,I}^i$ of 7.5 MPa. However, when the $P_{Eq,I}^i$ or $P_{R,I}^i$ is 7.21 MPa at 31 ℃, the pressure error of 0.02 MPa in sample cell or -0.02 MPa in reference cell will result in negative adsorption of 0.11 mmol/g. When the $P_{Eq,I}^i$ or $P_{R,I}^i$ increases from 7.5 MPa to 7.54 MPa at 31 ℃, the negative adsorption error caused by pressure error of 0.02 MPa decreases from 1.21 mmol/g to 0.10 mmol/g. So, the influence range of the pressure error on adsorption is narrow. The effect of pressure error on adsorption decrease with temperature increase, and the influence range of the error get wide.

Adsorption/desorption hysteresis

The clear negative effect of temperature on the adsorption capacity [11] made the CO_2 desorption from coal as increase of temperature. The adsorption/desorption hysteresis isotherm was observed for pure CO_2 [7, 8, 19, 21, 33-37]. The desorption isotherm generally lies to the upside of the adsorption one, which mean at the same equilibrium pressure the CO_2 adsorption obtained in the process of pressure increase is lower than it obtained in the course of pressure decrease.

Construction of the adsorption isotherms of CO_2 on coal requires the expansion of gas from reference cell into sample cell. During the gas expansion procedure, the temperature was increased or decreased in the two cells as a result of the Joule-Thompson effect [31]. During the gas expansion, the temperature was decreased in the reference cell as CO_2 is expanded in this cell, while it was increased in sample cell as CO_2 is compressed in this cell. However, at equilibrium, both temperatures were reached the temperature of the water bath. 5 minutes was satisfactory for reaching the thermal equilibrium [9].

The portion CO_2-adsorption on coal may desorbed from coal as the temperature of sample cell

increase in the course of CO_2 expansion from the reference cell to sample cell. The Adsorption/desorption hysteresis determines the portion of desorbed CO_2 can not be adsorbed when the temperature of sample cell decrease with reaching the thermal equilibrium. The CO_2 adsorption is so great that the desorbed CO_2 caused by the adsorption/desorption hysteresis can not be observed at low and moderate pressure, however, the hysteresis may result in the negative adsorption because of no or less sorption increment at high pressure.

Coal Volume Swelling

According to Ozdemir et al. [21], the uncertainties in volume estimations include nascent volume created by the swelling or shrinkage of solid adsorbent (ΔV_C), the over- or underestimation of the void volume due to adsorption of He and/or the extra volume due to the sieving effect (ΔV_0), the volume change due to the dissolution of the adsorbing gas (ΔV_d), and so forth. So, the change in the void volume in the sample cell (ΔV_x) is $\Delta V_x = \Delta V_c \mp \Delta V_0 \mp \Delta V_d$.

In case of the void volume correction term in step i (ΔV_x^i), the realistic adsorption increment ($\Delta n_{i,R}^{ex}$) can be obtained from Eq.s (8) and (9) based on Eq.s (1) and (4),

$$\Delta n_{i,R}^{ex} = \left(\frac{1}{RTm}\right)\left(V_R\left(\frac{P_{R,I}^i}{Z_{R,I}^i} - \frac{P_{R,F}^i}{Z_{R,F}^i}\right) - \left(V_0 - \Delta V_x^i\right)\left(\frac{P_{S,Eq}^i}{Z_{S,Eq}^i} - \frac{P_{S,Eq}^{i-1}}{Z_{S,Eq}^{i-1}}\right) \right), \qquad (8)$$

$$\Delta n_{i,R}^{ex} = V_{Rm}\Delta \rho_R^i - \left(V_{0m} - \Delta V_x^i\right)\Delta \rho_S^i. \qquad (9)$$

The measured adsorption increment (ΔV_x^i) is lower than the realistic adsorption increment ($\Delta n_{i,R}^{ex}$) based on Eq.s (4) and (9). If a volume ratio of void of sample cell and reference cell in case of volume correction ($x_i^{/} = \left(V_0 - \Delta V_x^i\right)/V_R$), the Eq. (6) can be written to

$$\Delta n_{i,R}^{ex} = V_{Rm}\left(\Delta \rho_R - x_i^{/}\Delta \rho_S\right). \qquad (10)$$

Coal swelling of 2-3% has been observed at CO_2 pressures of 1 MPa [25]. Although the degree of coal swelling was measured in low pressure, coal swelling is dependent on CO_2 pressure. At moderate to high pressure, coal swelling may result in significant errors in measurements of CO_2 adsorption on coals using gas adsorption techniques that work well with rigid solids. With a manometric apparatus, the coal swelling will change the ratio of container volume to sample volume [20]. St. George

and Barakat [29] had been observed that an initial contraction occurred due to the hydrostatic pressure before expansion due to CO_2 adsorption.

We do not investigate the effect of coal swelling on CO_2 adsorption at low pressure. Volume change due to coal swelling is only investigated at moderate and high pressure in this paper. As the equilibrium pressure of sample is in region B as shown in Fig. (3), the density change is much large that the effect of coal swelling on measured-adsorption is great and the adsorption obvious decrease. The negative CO_2-adsorption will be obtained in this case.

Based on Eq. (9), the realistic CO_2-sorption increment is dependent on the correction volume (ΔV_x^i), specific volume of two cells (V_R, V_0) and the density change of bulk CO_2 in two cells ($\Delta \rho_R$, $\Delta \rho_S$). The effect of volume change (ΔV_x) will get small in case of $\Delta V_x^i \ll \Delta V_{0m}$ based on Eq. (9), which means great volume of sample cell in comparison with coal volume (i.e. small mass of coal sample). $\Delta V_x^i \ll \Delta V_{0m}$ can be obtained with control the experimental parameters. The coal swelling of 2-3% and small $\Delta \rho_S$ at low and moderate pressure (in region A) slightly affect the CO_2 adsorption in case of $\Delta V_x^i \ll \Delta V_{0m}$, but the great $\Delta \rho_S$ in region B still make great error of CO_2 adsorption, especially negative adsorption.
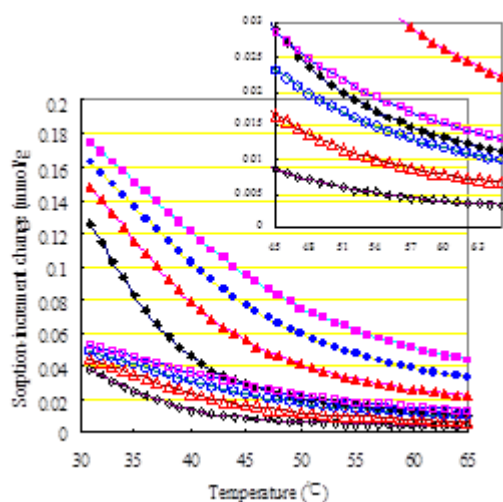
Fig. 6. Gibbs adsorption change of CO_2 for specific void-volume decrease of 0.015 cm³/g-coal (open symbols) and 0.05 cm³/g-coal (closed symbols) and the pressure-change of 0.5 MPa (◇, ◆), 1.0 MPa (△, ▲), 1.5 MPa (○, ●) and 2.0 MPa (□, ■) at a pressure corresponding the maximum density-change and temperature from 31 to 65 °C

The coal swelling of 0.25-10% is equivalent to the volume increase of 1.67×10^{-3}-6.67×10^{-2} cm³/g-

coal in case of the coal density of 1.5 g/cm³. The specific void-volume increase of 0.015 and 0.05 cm³/g-coal (the coal swelling of 2.25 and 7.75%) and the pressure change (ΔP) of 0.5, 1.0, 1.5 and 2.0 MPa in sample cell are used to investigate the effect of coal swelling on adsorption change maximum. $\Delta \rho_S \Delta V_x$ is calculated with ΔV_x of 0.015 and 0.05 cm³/g-coal and $\Delta \rho_S$-value at temperature from 31 to 65 °C and ΔP of 0.5, 1.0, 1.5 and 2.0 MPa as shown in Table 1, which expresses the maximum of CO_2 adsorption increase caused by coal swelling of 2.25 and 7.75%. Fig. (6) shows the maximum of CO_2 adsorption increase as a function of temperature and coal swelling of 2.25 and 7.75%.

The effect of coal swell on sorption increment reduces with experimental temperature increase. As the coal swelling of 2.25%, the sorption-increment change is 0.01-0.05 mmol/g-coal at equilibrium-pressure increment of 2.0 MPa, and 0.003-0.04 mmol/g-coal at the increment of 0.5 MPa at the temperature from 31 to 65 °C. As the coal swelling of 7.75%, the change is 0.01-0.13 and 0.04-0.18 mmol/g-coal at pressure increment from 0.5-2.0 MPa and the temperature from 31 to 65 °C. Although the decreasing value of sorption increment due to coal swell of 2-3% is small, the effort of this on sorption isotherm is noticeable as error propagation of each step of sorption.

In case of without regard to coal swelling, which is adopted with rigid solid, the CO_2 adsorption on coal get small in comparison with realistic value and the decrease is dependent on temperature, pressure, swelling amount and specific void-volume of sample cell. The decrease of CO_2 adsorption may lead to the negative adsorption under proper conditions, such as equilibrium pressure in region B and small specific void-volume in sample cell. As shown in Fig. (6), the coal swelling effect on the adsorption decrease with the increase of experimental temperature.

The Gibbs adsorption change of CO_2 on coal is the function of temperature, the coal swelling amount, the pressure change amount in sample and equilibrium pressure of CO_2. It is noted that with the coal swelling amount obtained at low pressure, the large correction is underestimated at the high pressures because the coal swelling decrease as the CO_2 pressure dropped [20]. The effect of coal swelling on adsorption mainly takes place in the larger density change, which is dependent on temperature and equilibrium pressure of CO_2.

CONCLUSIONS

This study provides the idea about limitation of measurements of supercritical CO_2 adsorption isotherms on coals with manometric equipment at high pressure. The characteristic density-change of CO_2 in proper pressure range determines great influence of experimental parameters on measured adsorption of CO_2 on coal at high pressure. Unusual adsorption isotherms of CO_2 on coals may be obtained with manometric technique at proper pressure range (high pressure), which is from 8 to 16 MPa and is dependent on the temperature. The experimental parameters include volume of two cells, coal mass, error of pressure and volume and coal swelling. The error of pressure and volume in two cells may result in the less reproducibility and repeatability of CO_2 adsorption on coals at high pressure because of great change of CO_2 density. The experimental parameters and their errors may result in negative sorption increment and even negative adsorption. The coal swelling may result in negative adsorption. Without consideration of measurement error of pressure and volume, the influence of experimental parameters and coal swelling, the adsorption isotherm of CO_2 on coal obtained with manometric equipment at high pressure can not express accurately the CO_2 sorption capacity on coal.

REFERENCES

1. H. Yu, L. Zhou, W. Guo, J. Cheng, Q. Hu, *J. Coal Geol.*, **73**, 115 (2008).
2. C. M. White, D. H. Smith, K. L. Jones, A. L. Goodman, S. A. Jikich, R. B. LaCount, S. B. DuBose, E. Ozdemir, B. I. Morsi, K. T. Schroeder, *Energ. Fuel.*, **19**, 659 (2005).
3. A. Nodzeński, *Fuel*, **77**, 1243 (1998).
4. C. R. Clarkson, R. M. Bustin, *Fuel*, **78**, 1333 (1999).
5. C. R. Clarkson, R. M. Bustin, *Int. J. Coal Geol.*, **42**, 241 (2000).
6. A. Busch, B. M. Krooss, Y. Gensterblum, F. van Bergen, H. J. M. Pagnier, *J. Geochem. Explor.*, **78-79**, 671 (2003).
7. A. Busch, Y. Gensterblum, B. M. Krooss, *Int. J. Coal Geol.*, 55, 205(2003).
8. A. L. Goodman, A. Busch, G. J. Duffy, J. E. Fitzgerald, K. A. M. Gasem, Y. Gensterblum, B. M. Krooss, J. Levy, E. Ozdemir, Z. Pan, R. L. Robinson, K. Schroeder, M. Sudibandriyo, C. M. White, *Energ. Fuel.*, **18**, 1175 (2004).
9. E. Ozdemir, PhD Thesis, University of Pittsburgh, 2004.
10. S. Tang, D. Hao, D. Tang, D. Liu, *Chinese Sci. Bull.*, **50(S1)**, 72 (2005).
11. B. M. Krooss, F. van Bergen, Y. Gensterblum, N. Siemons, H. J. M. Pagnier, P. David, *Int. J. Coal Geol.*, **51**, 69 (2002).
12. J. E. Fitzgerald, Z. Pan, M. Sudibandriyo, J. R. L. Robinson, K. A. M. Gasem, S. Reeves, *Fuel*, **84**, 2351 (2005).
13. A. L. Goodman, A. Busch, R. M. Bustin, L. Chikatamarla, S. Day, G. J. Duffy, J. E. Fitzgerald, K. A. M. Gasem, Y. Gensterblum, C. Hartman, C. Jing, B. M. Krooss, S. Mohammed, T. Pratt, R. L. Robinson Jr., V. Romanov, R. Sakurovs, K. Schroeder, C. M. White, *Int. J. Coal Geol.*, **72**, 153 (2007).
14. Y. Gensterblum, P. van Hemert, P. Billemont, E. Battistutta, A. Busch, B. M. Krooss, G. De Weireld, K. H. A. A. Wolf, *Int. J. Coal Geol.*, 84, **115** (2010).
15. D. Li, Q. Liu, P. Weniger, Y. Gensterblum, A. Busch, B. M. Krooss, *Fuel*, **89**, 569 (2010).
16. E. Battistutta, A. A. Eftekhari, H. Bruining, K. Wolf, *Energ. Fuel.*, **26**, 746 (2012).
17. P. Weniger, J. Franců, P. Hemza, B. M. Krooss, *Int. J. Coal Geol.*, **93**, 23 (2012).
18. N. Siemons, A. Busch, *Int. J. Coal Geol.*, **69**, 229 (2007).
19. E. Ozdemir, B. I. Morsi, K. Schroeder, *Fuel*, **83**, 1085 (2004).
20. V. N. Romanov, A. L. Goodman, J. W. Larsen, *Energ. Fuel.*, **20**, 415 (2006).
21. E. Ozdemir, B. I. Morsi, K. Schroeder, *Langmuir*, **19**, 9764 (2003).
22. S. Day, R. Fry, R. Sakurovs, *Int. J. Coal Geol.*, **93**, 40 (2012).
23. P. Chareonsuppanimit, S. A. Mohammad, R. L. Jr. Robinson, K. A. M. Gasem, *Int. J. Coal Geol.*, **12**1, 98 (2014).
24. P. J. Reucroft, H. Patel, *Fuel*, **65**, 816 (1986).
25. P. J. Reucroft, A. R. Sethuraman, *Energ. Fuel.*, **1**, 72 (1987).
26. P. L. Walker, S. K. Verma, J. Rivera-Utrilla, M. R. A. Khan, *Fuel*, **67,** 719 (1988).
27. L. Chikatamarla, X. Cui, R. M. Bustin, in: Proc. of 2004 Int. CBM Symposium, Tuscaloosa, Alabama, USA, 2004, paper 0435.
28. K. Wang, G. Wang, T. Ren, Y. Cheng, *Int. J. Coal Geol.*, **13**2, 60 (2014).
29. J. D. St. George, M. A. Barakat, *Int. J. Coal Geol.*, **45**, 105 (2001).
30. Z. Pan, L. D. Connell, *Int. J. Coal Geol.*, **69**, 243 (2007).
31. R. Span, W. Wagner, *J. Phys. Chem. Ref. Data*, **25**, 1509 (1996).
32. A. L. Goodman, A. Busch, G. J. Duffy, J. E. Fitzgerald, K. A. M. Gasem, Y. Gensterblum, B. M. Krooss, J. Levy, E. Ozdemir, Z. Pan, R. L. Robinson, K. Schroeder, M. Sudibandriyo, C. M. White, *Energ. Fuel.*, **18**, 1175 (2004).
33. E. Ozdemir, K. Schroeder, *Energ. Fuel.*, **23**, 2821 (2009).
34. E. Battistutta, P. van Hemert, M. Lutynski, H.

Bruining, K. Wolf, *Int. J. Coal Geol.*, **84**, 39 (2010).

35. J. He, Y. Shi, S. Ahn, J. W. Kang, C. Lee, *J. Phys. Chem. B*, **114**, 4854 (2010).

36. P. Dutta, S. Bhowmik, S. Das, *Int. J. Coal Geol.*, **85**,

289 (2011).

37. K. Wang, G. Wang, T. Ren, Y. Cheng, *Int. J. Coal Geol.*, **13**2 ,60 (2014).

ОГРАНИЧЕНИЯ НА ИЗМЕРВАНИЯТА НА СВРЪХКРИТИЧНИТЕ ИЗОТЕРМИ ЗА СОРБЦИЯ НА CO₂ ВЪРХУ ВЪГЛИЩА С МАНОМЕТРИЧНО ОБОРУДВАНЕ - ТЕОРЕТИЧНО ОПИСАНИЕ

Р Дзян, Х. Ю *, Л. Уан

Училище по химическо и екологично инженерство, Университет за наука и технологии Шандонг

(Резюме)

Изотермите на адсорбция на CO₂ върху въглищата са важни за оценката на потенциала за улавяне на CO₂ на въглищните пластове и подобрената регенерация на метан от въглища чрез впръскване на CO₂ във въглищните пластовеове. Тази статия представя характеристиката на коефициента на свиваемост на CO₂ и изменението на плътността на CO₂, базирано на CO₂ уравнението на състоянието. Статията изследва ефекта на експерименталното налягане и неговата грешка, хистерезис на адсорбция / десорбция и набъбване на въглищата върху измерванията на изотермите на суперкритична CO₂ адсорбция върху въглища с манометрично оборудване при високо налягане. Резултатите показват, че характерната промяна на плътността на CO₂ в подходящия диапазон на налягането определя голямо влияние на експерименталните параметри, набъбване на въглищата и хистерезис на адсорбция / десорбция върху адсорбцията на CO₂ върху въглища при високо налягане. Ефектът на хистерезиса върху сорбцията при високо налягане може да доведе до отрицателна наблюдавана адсорбция. Набъбването на въглищата при високо налягане има очевиден ефект върху точността и възпроизводимостта на адсорбцията на CO₂. Съществуват потенциални клопки за измерване на изотермите на свръхкритична CO₂ адсорбция върху въглища с манометрично оборудване при високо налягане.

The performance test and evaluation of rock asphalt modified asphalt and mixture

K. Zhong[1,2], J. Tian[3*], X. Wei[3], X. Ma[4]

[1] Research Institute of Highway Ministry Transport, Beijing 100088, China
[2] School of Transportation Science and Engineering, Beijing University of Aeronautics and Astronautics, Beijing 100191, China
[3] School of transportation, Southeast University, Nanjing 210096, China
[4] Zhonglugaoke (Beijing) Highway Technology CO LTD, Beijing100088, China

In order to study rules of property variation of modified asphalt with rock asphalt and its mixture, Binzhou 90[#] base bitumen and Maoming 70[#] base bitumen are modified respectively with Xinjiang rock asphalt of 5, 10, 15 and 20%. Property variation of modified asphalt is studied through conventional indexes of grading index penetration system and DSR, BBR as well as quantities of experiments on modified asphalt graded as AC-13 in properties of high temperature, water stability, low-temperature crack resistance and fatigue. The results show that the modifier of rock asphalt is helpful to improve the performance of asphalt at high temperature, but it may also affect the performance at low temperature. The optimum content range of rock asphalt should be controlled in 5 ~ 15%. The improvement in performance of modified asphalt is helpful to the high -temperature performance, water stability and fatigue property of its mixture, but the low-temperature performance may get worse in a small range.

Key words: rock asphalt; modified asphalt; asphalt mixture; test and evaluation

INTRODUCTION

With the rapid development of transportation industry, the road performance of asphalt pavement should meet higher requirements for heavy and canalized traffic. The wide use of modified asphalt in high-grade pavement greatly improves asphalt mixture's road performance. Currently, effective and widely used modifiers are mainly SBS, PE, SBR, etc. However, with the rise in prices of SBS and other modifiers, it is becoming a hotspot in transportation domain to find a modifier of low price and good effect.

Rock asphalt is a stable kind of natural asphalt and Overseas studies have shown that the modifier of rock asphalt will improve mixture's road performance, especially in its high-temperature stability, water stability and fatigue resistance. However, the engineering application of rock asphalt, especially the natural storage in Kalamayiwuerhe, Xinjiang and Qingchuan, Sichuan, etc, is limited for a lack of detailed and clear methods and standards but principle technical requirements by the current specification. The objective of this study is evaluating rules of property variation of modified asphalt with rock asphalt of Kalamayi, Xinjiang and its mixture through experiments, providing reference to our country's rock asphalt's engineering application.

MATERIALS AND METHODS

Materials

Bitumen

Considering effects of different base bitumen to experiments, Binzhou 90[#] and Maoming 70[#] base bitumen were used respectively.

Rock asphalt used in this study is Xinjiang Wuerhe rock asphalt.

Aggregate

As for the modified asphalt mixture's tests, if without special explanations, the coarse aggregate was Chengde, Hebei graded basalt material, the fine aggregate was limestone sand and the filler was limestone filler.

Gradation

The use of AC-13 as asphalt mixture's gradation is given by stipulation in the current specification to insure that testing results are stable and reliable.

Material Preparation

Base bitumen and rock asphalt

According to related experiment stipulation, Binzhou 90[#] and Maoming 70[#]base bitumen have been tested with conventional indexes and testing results meet requirements, which is listed in Table.1 and those of Wuerherock asphalt are indicated in Table.2

Table 1. Technical index of base bitumen

Pilot projects		Types of base bitumen	
		Binzhou AH-90	Maoming AH-70
Penetration(100g，5s，25°C) 0.1mm		87	67
Ductility(5cm/min，15°C） cm		>150	>100
Softening point(ring and ball method)°C		45.3	48.3
RTFOT（160°C 5h）	Loss of mass %	0.29	0.41
	penetration ratio %	58.6	59.7
	Ductility (25°C) cm	>150	>100
	Ductility (15°C) cm	>150	54

Table 2. Technical index of rock asphalt

Pilot projects	Unit	Test results
Asphalt content	％	99.4
Ash content	％	0.54
Specific gravity	g/cm³	1.06
Flash point	°C	＞230°C
Loss of mass	％	0.632
Moisture content	％	0.1%
Maximum particle size of mineral	mm	4.75

Gradation

To ensure the accuracy of grading, the target gradation of AC-13 is compounded by aggregates of single size sieving from qualified coarse aggregates by standard sifter, blended with fine aggregates.

Modified asphalt and asphalt mixture

Binzhou 90[#] and maoming 70[#] base bitumen were preheated to 150°C and rock asphalt was blended in with predetermined proportion of 5, 10, 15 and 20%. Heat and stir them to disperse rock asphalt gradually in base bitumen, then continue at 175°C for 30 min and preserve it in an oven for 1h and then blend it at 175°C for 15 min for later use of pouring an asphalt model. In addition, the method of high-speed shearing can also be used to prepare samples.

The match ratio design of asphalt mixture was determined by Marshall mix design method according to the current specification. In the experiment, the heating temperature of the asphalt mixture was 185°C, the mixing temperature was 175°C, and the compaction temperature was 160°C, according to the viscosity curve of the rock asphalt.The match ratio design of asphalt mixture was determined by Marshall mix design method according to the current specification. In the experiment, asphalt mixture's testing temperature of aggregate, mixing and compaction were at 185,175 and 160°C according to the modified viscosity temperature curve. According to the

preparation method, the modified asphalt was prepared in advance, and then the rock bitumen modified asphalt was added into the mineralizer for 90s to obtain the rock asphalt modified mixture. Finally, the mineral powder was added and then mixed for 90s.

According to the tests, the results of the match ratio design of Binzhou 90[#] base bitumen were shown in fig.3 to fig.8 and its OAC was 4.9%. Note that the optimum amount of asphalt with different content of rock asphalt may change as a result of blending modifier and changes in viscosity and other indexes of itself. In this paper, the same optimum amount of asphalt is taken with different content of modifier, which emphasizes the comparison of how different quality of asphalt may affect the properties of mixtures.

Tests of bitumen

Penetration, ductility and softening point tests

Penetration reflects asphalt's deformation capacity under loading. Ductility reflects asphalt's ability to resist cracks. As for the softening point, it can reflect asphalt's high-temperature performance and is closely connected with asphalt mixture's rut resistance. This study modifies Binzhou 90[#] or Maoming 70[#] base bitumen with Xinjiang rock asphalt of 5, 10, 15 and 20% respectively for penetration test at 5, 15, 25 °C, for ductility, softening point and toughness test at 5, 15°C before and after aging according to the test procedure.

Tests of asphalt mixture

Marshall tests, rutting tests and water stability tests

The Marshall Test method is used for the HMA proportion design, according to the current technical specification. This study modified Binzhou 90# base bitumen and Maoming 70# base bitumen with rock asphalt of 5, 10, 15 and 20% graded as AC-13. The test specimen adopts the same asphalt-aggregate ration according to relevant test procedures. The number of a single group of specimen is not less than 4 to test asphalt mixture's stability and flow value. The residual stability of immersion Marshall test and freeze thawing split test's residual strength are two main indexes to evaluate asphalt mixture's resistance to water damage.

Tests of low-temperature performance

According to current specification, low-temperature bending test is used to evaluate asphalt mixture's low-temperature crack resistance. Binzhou 90# base bitumen and Maoming 70# base bitumen were modified with rock asphalt of 5, 10, 15 and 20% respectively by wheel roller. The track board was compacted by wheel grinding and was cut into beams of 250×30×25mm at -10°C and the loading rate was 50mm/min. Asphalt mixture's

low-temperature crack resistance is evaluated by failure strain at low temperature.

ANALYSIS

Asphalt

Ductility test results

Penetration test results As is shown in Fig.1 and Fig.2, modified Binzhou 90# and Maoming 70# base bitumen show similar rules:

① At the same temperature, modified asphalt's penetration is obviously lower than that of base bitumen and the penetration reduces with the increase of the proportion of rock asphalt. This means that modified asphalt is stiffer and stronger in deformation resistance.

② Equivalent softening point T800 is significantly lower after modification. With the increase of the proportion of rock asphalt, there is an increasing trend in the equivalent softening point, which means rock asphalt can improve asphalt's high-temperature stability.

③ A limited increase in the equivalent brittle point is observed with rock asphalt's modification, which means the addition of rock asphalt will slightly worsen asphalt's low-temperature stability.
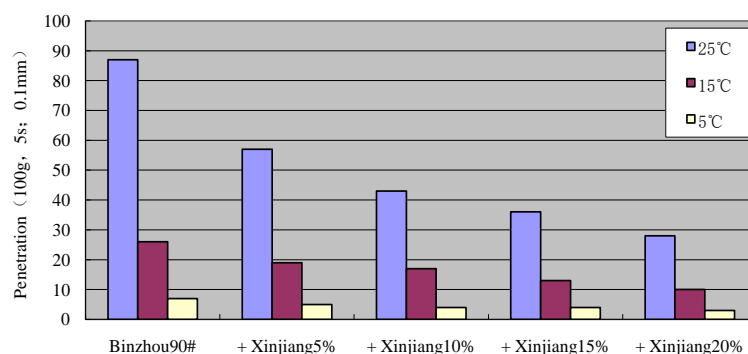
Fig. 1. Penetration variation of Binzhou 90# modified with rock asphalt
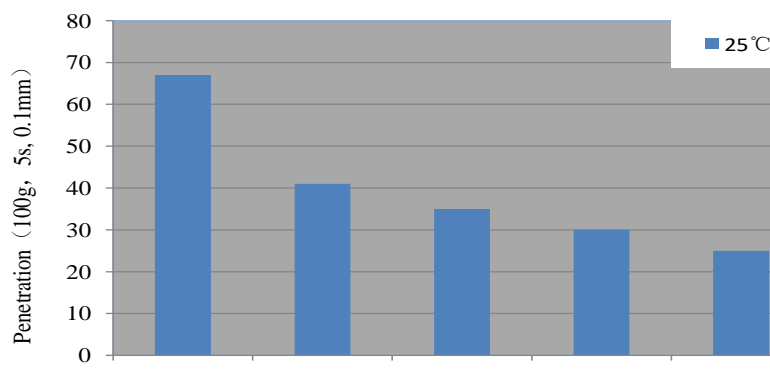
Fig. 2. Penetration variation of Maoming 70# modified by rock asphalt

From Fig.3~Fig.5, It can be seen from fig.14 to 17 that rock asphalt can remarkably reduce base bitumen's ductility before and after aging, and with the increase of rock asphalt, the asphalt's ductility reduced remarkably.

Softening point

As can be seen in Fig.6 and Fig.7:

① Rock asphalt can obviously elevate asphalt's softening point, so it's helpful to asphalt mixture's high-temperature stability and rut resistance.

② Asphalt's softening point elevates with the increase of rock asphalt content, but the increasing range reduces gradually. As 5% rock asphalt was added to Binzhou 90# bitumen asphalt for three times constantly, the increasing ranges of softening point were 5, 3 and 2°C.

Before and after asphalt's aging, the variation rule of the softening point changes with the rock asphalt's proportion as follows:

$$T_{R\&B} = 45.5 + 0.924p - 0.0160p^2 \qquad R^2 = 0.995$$

$$T_{R\&B} = 50.4 + 0.893p - 0.0114p^2 \qquad R^2 = 0.996$$

where **p** means the amount of rock asphalt (%).
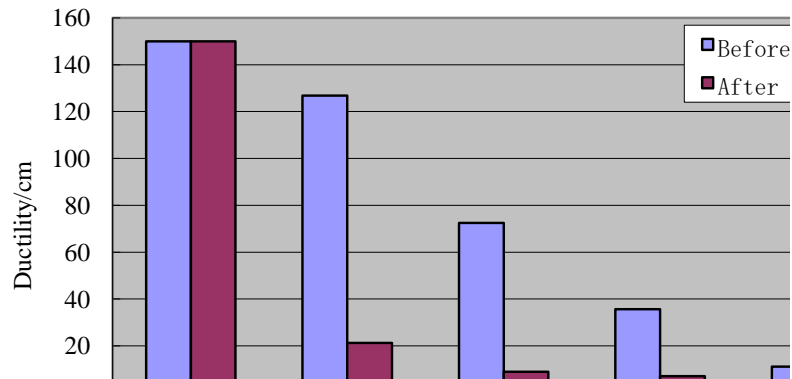
Fig. 3. The ductility of Binzhou 90# with different proportion of rock asphalt at 15°C
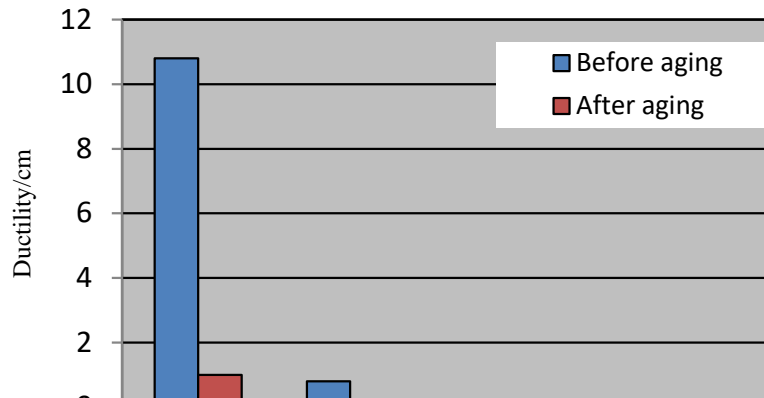
Fig. 4. The ductility of Binzhou 90# with different proportion of rock asphalt at 5°C
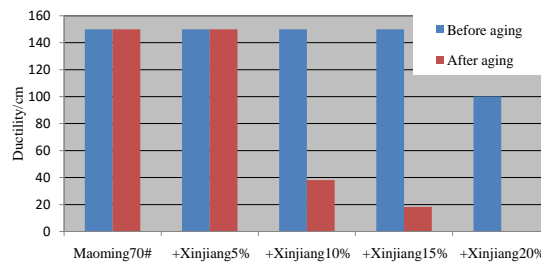
Fig. 5. The ductility of Maoming 70# with different proportion of rock asphalt at 25°C
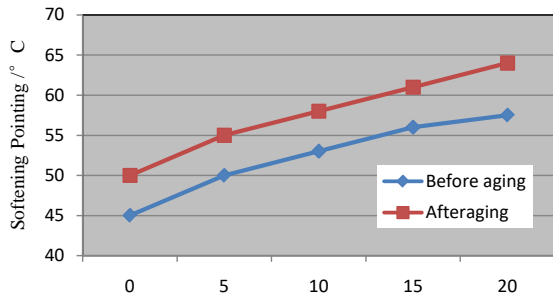
Fig. 6. Binzhou 90# with different proportion of rock asphalt's variation of softening point before and after aging
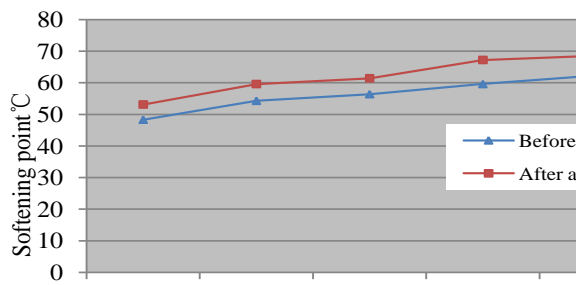
Fig. 7. Maoming 70# with different proportion of rock asphalt's variation of softening point before and after aging.

Asphalt mixture

Analysis of Marshall test results

As can be seen in Fig.8 and Fig.9:

①   The modified asphalt mixture's stability is higher than that of base bitumen mixture and its Marshall Stability increased gradually with the increase of rock asphalt's proportion.

②   The stability of Binzhou 90# asphalt mixture modified with 20% rock asphalt is the highest, but the stability's change doesn't show a linear relationship with the change of rock asphalt's blending ratio. The stability increased to the maximum amplitude, 13.4% when 5% Xinjiang rock asphalt was blended.

③   Respect to rock asphalt's changing content, the change rule of flow value is not obvious.
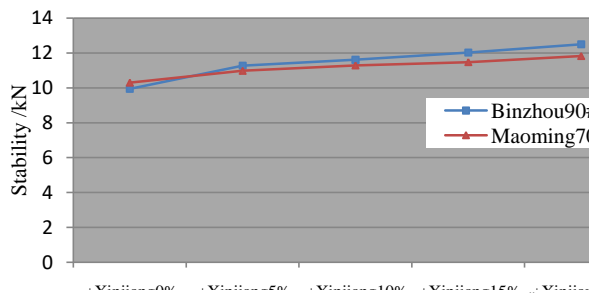
Fig. 8. Marshall Stability of Maoming 70# base bitumen with different proportion of rock stability.
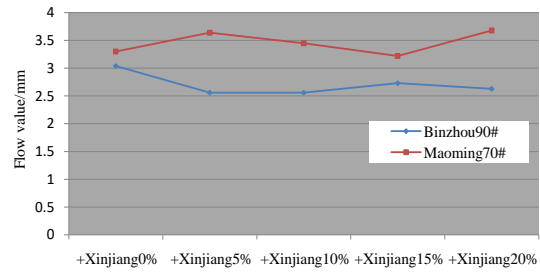
Fig. 9. Flow value of Maoming 70# base bitumen with different proportion of rock asphalt.

Rutting tests

As can be seen from fig.10:

①   Modified with rock asphalt, Binzhou 90# base bitumen's dynamic stability and high-temperature rut resistance were improved obviously. For the maximum amount of rock asphalt (20%), asphalt's dynamic stability was increased to5.8 times the previous value and for the minimum (5%),to 2.1 times.

②   Modified with rock asphalt, Maoming 70# and Binzhou 90# asphalt show the same rules, but with the increase of rock asphalt's content, the later increasing rangeof dynamic stability degree of Maoming 70# asphalt has reduces gradually. Thereforeit is not sure that Maoming 70# base bitumen's dynamic stability is higher than that of Binzhou 90# base bitumen when they are modified with the same amount of rock asphalt.
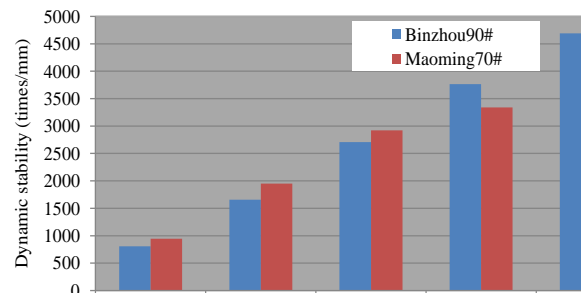
Fig. 10. Dynamic Stability of Asphalt Mixtures with Different Rock Asphalt Content.
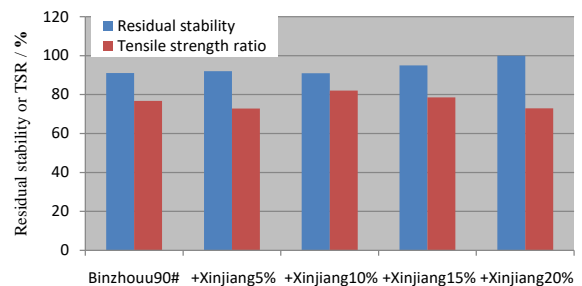
Fig. 11. Residual stability and freeze - thaw splitting intensity strength ratio of Binzhou 90# mixed with different contents of rock asphalt.
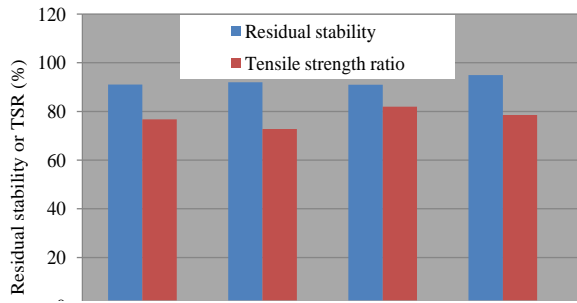
Fig. 12. Residual stability and freeze - thaw splitting intensity ratio of MaoMing 70# mixed with different contents of rock asphalt.

Water stability

From Fig.11 and Fig.12, it can be seen that Binzhou 90# and Maoming 70# base bitumen show similar rules when they are mixed with different proportions of rock asphalt:

① The residual stability and tensile strength ratio TSR of Binzhou 90# modified asphalt mixture are apparently higher than those of base bitumen, and the mixture's water stability increases with rock asphalt's addition. Modified with 5% Xinjiang rock asphalt, the residual stability of the mixture increased 3.9%, the tensile strength ratio increased 8.3%, and the increase extent can be bigger with more rock asphalt.

② After the water damage occurs, the residual strength of the Binzhou 90# asphalt modified with rock asphalt is significantly improved compared to that of base bitumen. For example, after freeze-thaw cycle, the residual tensile strength of base bitumen was 0.9MPa, while modified with10% rock asphalt, it could reach1.4MPa. It's the same with Maoming 70# asphalt modified with rock asphalt but with a certain fluctuation.

Analysis of low-temperature performance

Low-temperature test results of failure strength, failure strain and failure stiffness modulus of Binzhou 90# and Maoming 70# base bitumen mixture modified with Xinjiang rock asphaltare shown in Fig.13~Fig15.
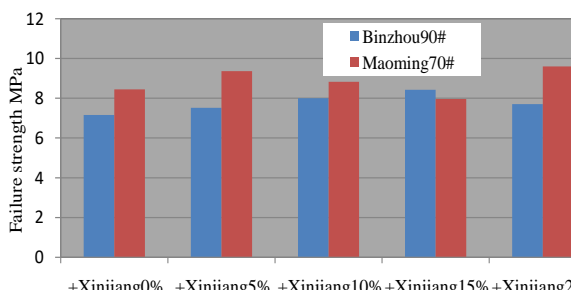
Fig. 13. Change of low temperature failure strength of modified asphalt
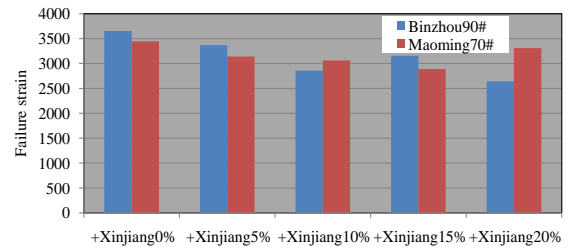
Fig. 14. Change of low temperature failure strain of modified asphalt
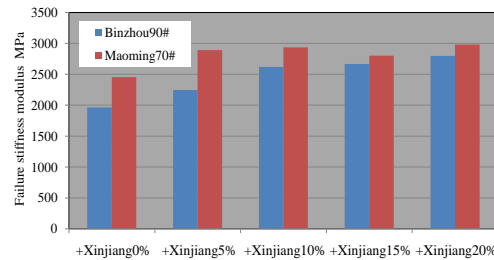
Fig. 15. Change of low temperature failure stiffness modulus of modified asphalt

① When the failure strain was used as the evaluation index, that of Binzhou 90# and Maoming 70# asphalt mixture was the largest, but after the modification of rock asphalt, it showed a decreasing trend, indicating that asphalt mixture's low-temperature performance became worse. With the increase of the amount of rock asphalt, the low-temperature damage strain decreased gradually.

② In terms of failure strength index, after rock asphalt's addition, Binzhou 90# asphalt mixture's ultimate bending strength at low temperature became higher.

CONCLUSION

1. After rock asphalt's modifying, base bitumen's penetration decreases and its softening point, rutting factor $G^*/\sin\delta$ and elastic component increase , contributing to improving asphalt's high-temperature deformation resistance and fatigue performance.

2. Modified with rock asphalt, asphalt's low-temperature ductility decreases. It is shown that the addition of rock asphalt will improve the high temperature performance, but at the same time will reduce the low temperature crack resistance of asphalt. The optimum amount of rock asphalt is 5% to 15%.

3. Modified asphalt mixture with rock asphalt has higher Marshall Stability, and the greater the amount of rock asphalt content is, the better asphalt's high-temperature rut resistance becomes.

4. The residual stability and split strength

ratio of modified asphalt mixture are both obviously higher than those of base bitumen, and increases with the addition of rock asphalt content, that is, the modification can improve mixture's water resistance.

5.   Rock asphalt's modification can obviously improve asphalt mixture's mechanical strength and fatigue resistance and those will increase with the addition of rock asphalt content.

6.   Modified asphalt's softening point has good correlations with modified mixture's dynamic stability, indicating that the improvement in asphalt mixture performance comes from the modification ock asphalt.

7.   With addition of rock asphalt mixture's low-temperature damage strain may decrease slightly.

REFERENCES

1. D.S. Harmelink, Gilsonite, An Asphalt Modifier, Colorado Department of Transportation, 1992, 3.
2. G.A. Huber, D.S. Decker, Evaluation of Aging Characteristics of Modified Asphalt Mixtures, American Society for Testing and Materials, Philadelphia, 1995.
3. Asphalt Concrete with Gilsonite, State of Ohio Department of Transportation Supplemental Specification 857, 7, 2002.
4. M.G. Bouldin, Gilsonite Modifier Hard Pen Binder Study, American Gilsonite Company, 2002, 5.
5. Rl. Gaughan, *Darwin*, **15**(2), 41 (1990).
6. F.A. Hossein, P. Afshin. *Bulgarian Chemical Communications,* ,**47**(D), 56 (2015).
7. H. Gou, C. Lai, *Journal of China&Foreign Highway*, **23**(5), (2003).
8. A. Morsali, Z. Alavi, S.A. Beyramabadi, *Bulgarian Chemical Communications,* **47**(1), 89 (2015).
9. F. He, J. Wang, *Highway*, **12**, 2005.
10. H. Burrell, Gilsonite Information Bulletin, Polymer Handbook, 2nd. Wiler-InterScience, New York, 1975.
11. Rl. Gaughan, *Development of High Strength Asphalt Mixes*, 15th ARRB Conference, Darwin, **15**(2), 41 (1990).
12. C. Wong, Mk. Ho, The Effect of Gilsonite-Modified Asphalt On Hot Mix Asphaltic Concrete Mixes Used in Distirct 12, Houston, Texas. Texas State Department of Highways & Public, 1990.

ЗА ЕФЕКТИВНОСТ И ОЦЕНКАТА НА ШИСТОАСФАЛТ, МОДИФИЦИРАН АСФАЛТ И СМЕСИ

К. Джун[1,2], Дз. Тиан[3] *, С. Уей[3], С. Ма[4]

[1] *Изследователски институт на Министерството на транспорта, Пекин 100088, Китай*
[2] *Училище по транспорт и инженерство, Пекински университет по аеронавтика и астронавтика, Пекин 100191, Китай*
[3] *Училище по транспорт, Югоизточен университет, Нанджин 210096, Китай*
[4] *Жонглуаоке магистрални технологии СО ООД, Пекин 100088, Китай*

(Резюме)

За да се изучат правилата за изменение на свойствата на модифициран асфалт с шистоасфалт и техните смеси, Binzhou 90[#] асфалтов битум и Maoming 70[#] асфалтов битум са модифицирани съответно с 5, 10, 15 и 20% асфалтови шисти от Синцзян. Промяната на свойствата на модифицирания асфалт се изследва чрез конвенционалните показатели на системата за градуиране на индекса за класификация и DSR, BBR, както и експерименти върху модифициран асфалт, класифициран като AC-13, свойства при висока температура, устойчивост на вода, нискотемпературна устойчивост на пукнатини и умора. Резултатите показват, че модификаторът на шистоасфалта е полезен за подобряване на работата на асфалта при висока температура, но може да повлияе и на работата при ниска температура. Оптималният обхват на съдържанието на шистоасфалт трябва да се контролира от 5 ~ 15%. Подобряването на характеристиките на модифицирания асфалт е полезно за високотемпературните характеристики, устойчивостта на вода и умората на неговата смес, но ниско температурните характеристики могат да се влошат в тесен диапазон.

Rheological properties of RHMOD-INVERT™—A Study on a novel oil-based drilling fluid with high thixotropy

Y. G. Liu[1,2], Y. Zhang[2], J. Yan[2], Y. J. Xu[1*]

1 Harbin Institute of Technology, Harbin, Heilongjiang, China 150001*
2 Drilling Engineering Technology Research Institute, Daqing Oilfield Drilling Engineering Company, Daqing，Heilongjiang, China 163413

Using conventional oil-based drilling fluids typically involves the disadvantages of low borehole cleaning efficiency, easy cuttings bed formation and drill pipe sticking. In order to address these problems, we developed the gemini surfactant SRHJ-1, after which we manufactured the oil-based drilling fluid RHMOD-INVERT™. This new drilling fluid demonstrates excellent rheological properties, including low viscosity and high shear. The microscopic structure of the drilling fluid was observed through freeze-fracture electron microscopy. Then, combining high-temperature, high-pressure rheometry with optical microscopy, the RHMOD-INVERT™ drilling fluid was analyzed both macroscopically and microscopically. The observation data showed strong van der Waals forces active between emulsion droplets, organic clay, and other solid-phase particles, resulting in close interactions and the formation of network-like aggregates. Due to these forces, the new drilling fluid exhibits a "cake batter" structure. Emulsion droplets, organic clay, and other solid-phase particles, when at rest, form a complex, three-dimensional piling structure in space, which has a higher suspending power. When flowing, the reticular formation can be destroyed even under extremely low shear stress, facilitating the flow of the drilling fluid. This is manifested as low viscosity and high shear on the microscopic level. The new drilling fluid was applied in field tests to several deep horizontal wells, including WS1-H2, GS3, and XS1-H8, where it demonstrated stable performance. The rheological properties of low viscosity and high shear make it easier to overcome challenges in the cuttings, carrying, and sticking phenomena in deep horizontal wells in tight gas reservoirs, while simultaneously improving the drilling efficiency.

Keywords: Emulsion, high thixotropy, low viscosity and high shear, oil-based drilling fluid, rheology.

INTRODUCTION

Oil-based drilling fluids (OBDFs) possess excellent capacities for inhibitive activity, lubrication, and pollution reduction. In drilling projects, these fluids can be used to inhibit the hydration swelling of shale, prevent the collapse of borehole walls, and reduce hole shrinkage [1]. When applied to high-temperature deep wells and wells with large displacement or complex structures, OBDFs can prevent borehole instability in complex strata, thereby ensuring safe and rapid drilling [2-3].OBDFs have undergone rapid changes through research conducted in foreign countries. In fact, the application rate of OBDFs has reached over 80% in North America and Mexico. Baroid and M-I Corporation have developed high-performance, OBDF systems such as INNOVERT and INTOL™, based on FACTANT and VETSAMUL, respectively [4-6]. High-performance emulsifiers are important for developing desirable OBDFs; however, the development of emulsifiers has fallen far behind in China compared with other regions of the world. At present, single-chain and single-functional-group surfactants are extensively used in China. These surfactants are low in both emulsification efficiency and resistance to high temperature; therefore, they are added in large amounts to OBDFs, leading to unstable performance, poor shear thinning ability, high viscosity, and low shear. As a result, these OBDFs may present problems of low borehole cleaning efficiency and easy cuttings bed formation, such that they are unsatisfactory for horizontal wells and wells with complex structures [7-9].To address these defects, we developed a high thixotropy OBDF called RHMOD-INVERT™ that incorporates the SRHJ-1 emulsifier. This new drilling fluid achieves low viscosity and high shear, and it was applied successfully to several horizontal wells in deep tight gas reservoirs in the Daqing oilfield (horizontal wells WS1-H2 and XS1-H8). RHMOD-INVERT™ also resolves the frequent phenomena of low borehole cleaning efficiency, cuttings bed formation, low drilling speed, and drill pipe sticking in complex structure wells.

EXPERIMENTAL

Development of new emulsifier and high thixotropy OBDF

Working mechanism of new emulsifier, SRHJ-1

---

* To whom all correspondence should be sent:
E-mail: xuyongjun@hit.edu.cn

We prepared the new emulsifier using the organic acids N-Vinylpyrrolidone and epichlorohydrin as raw materials, in an attempt to address the problems of instability and hydrolysis under certain temperatures and in alkaline environments. The gemini emulsifier SRHJ-1 was synthesized through a three-step method. Fig. 1 shows the molecular structure of the SRHJ-1 emulsifier, which is a dimer with two head groups introduced to enhance the adsorption capacity on the oil-water interface. The two alkyl chains of the emulsifier molecule display strong intramolecular interactions, increasing the strength of the interfacial film between oil and water and thereby promoting the emulsification capacity. On the oil-water interface, both intramolecular interaction in the alkyl chains and intermolecular interaction based on hydrogen bonding occur, greatly improving the formation and stability of a water-in-oil emulsion[10]. The bi-layer structure of the gemini emulsifier SRHJ-1 enables a tighter molecule arrangement on the oil-water interface. In solutions, the emulsifier exists as a suspension of micelles with low curvature. In low-concentration liquids, the emulsifier exists as wormlike or linear micelles, which intertwine to form a network structure. This unique feature provides high viscoelasticity [11-16] and the shear properties of non-Newtonian fluids [17] to the solution into which the emulsifier is added.

In rheological terms, a stress must act on the fluid in order for the fluid to flow. Gel strength is defined as the maximum elastic deformation of the fluid before it is made to flow. When added to fluid, SRHJ-1 can increase the elastic deformation and gel strength of the emulsion. When left standing, the emulsion will increase in elasticity as well as in gel strength and suspending ability. Because the SRHJ-1 emulsifier is easily dissolved in the dispersed phase, it will not increase friction within the continuous phase. While increasing the yield point-plastic viscosity ratio, the SRHJ-1 emulsifier does not increase plastic viscosity itself [18].
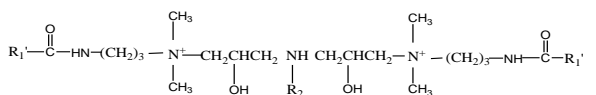
注: R_1: $C_{15}H_{31}$□$C_{17}H_{32}OH$ R_1'□$(C_{17}H_{33}O(C_6H_9NO)m)n$ R_2: $C_{18}H_{29}$, $m \geq$ □$_1$□ $n \geq$ □$_2$

Fig. 1. Molecular structure of SRHJ-1 emulsifier

Performance evaluation of SRHJ-1

Using a DSX500 opto-digital microscope, we evaluated the morphology of an emulsion formed by adding SRHJ-1 emulsifier and assessed the suspending performance of the emulsifier. We then determined the capacity of the organic clay-containing emulsion to improve shear strength. The base fluids used were inverse emulsions with an oil-to-water ratio of 80:20.

Microscopy of emulsion formed by SRHJ-1

Under the microscope, we observed changes in emulsion droplet size and morphology after hot aging at a high temperature, and we compared these results with an emulsion formed by Span-80. Figs. 2 and 3 show the differences in droplet size using the two emulsifiers. Compared with Span-80, SRJH-1 produced a smaller droplet size and a more uniform size distribution after hot aging [19], indicating its higher emulsification capacity.
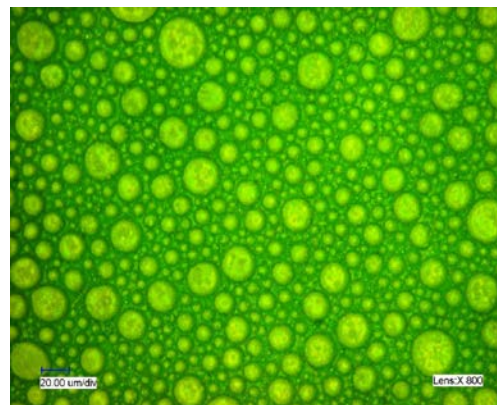
Fig. 2. Emulsion droplets formed by Span-80
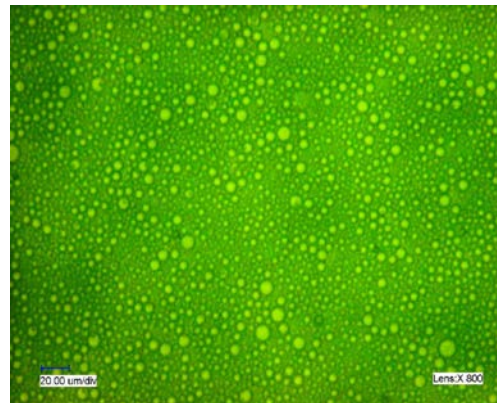
Fig. 3. Emulsion droplets formed by SRHJ-1

(Note on emulsion formulation: a) oil-to-water ratio 80:20, $CaCl_2$ concentration 20%+4.0% Span-80+3.0% oleic acid+3.0% naphthenamide; b) oil-to-water ratio 80:20, $CaCl_2$ concentration 20%+3.0% SRHJ-1+1.0% naphthenamide; conditions of hot aging at a high temperature 260°C/16 h in both a and b)

Suspending performance

Loss factors of emulsions formed with different emulsifiers in static states were determined using Rheolaser^TM (Fig. 4). The loss factor is a

measurement of suspending performance, defined as the ratio of the loss modulus to the modulus of elasticity. The smaller the value, the higher the suspending performance, and the lower the possibility of static settlement of the solid phase under the action of weight [20]. As Fig. 4 shows, the loss factor of the emulsion formed by SRHJ-1 decreased fastest compared with several other emulsifiers developed by foreign researchers, and it stabilized after about 7 min. In actual applications, the new emulsifier's macroscopic performance corresponded well with its microscopic performance. This emulsifier improved the rheological properties, thixotropy, and suspending performance of the OBDFs, thereby promoting borehole cleaning efficiency.
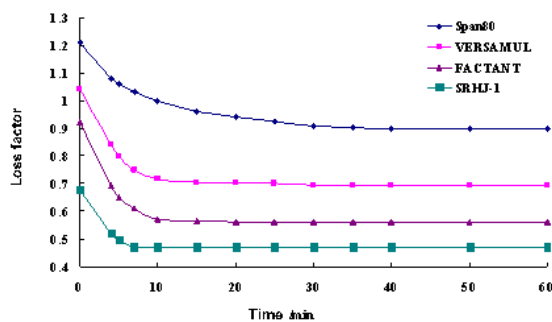
Fig. 4. Loss factors of emulsions formed with different emulsifiers

Capacity of organic clay-containing emulsions to improve shear strength

Separate water-in-oil emulsions were prepared with Span-80 and SRHJ-1, with different amounts of organic clay added. The corresponding changes in yield point were then determined (Fig. 5). The results indicate that SRHJ-1 demonstrated a better capacity for improving shear strength. Even at a small addition amount of 0.3%, SRHJ-1 worked synergistically with the organic clay to improve emulsification efficiency. The mixture of SRJH-1 and the organic clay enhanced the overall performance of the OBDF.
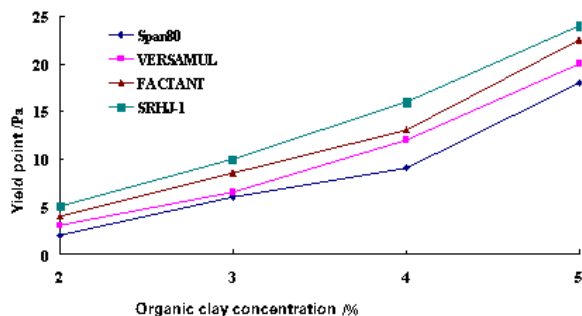
Fig. 5. Effect of SRHJ-1 on the yield point of organic clay-containing emulsions

Establishment of high thixotropy OBDF system

Gemini emulsifiers, when used synergistically with conventional emulsifiers, can greatly enhance emulsification performance[21-22]. We combined SRHJ-1 with naphthenamide, a conventional emulsifier, as well as a filtrate reducer, organic clay, and wetting agent. We then prepared a high thixotropy OBDF system, RHMOD-INVERT^{TM}, which demonstrated resistance to temperatures as high as 260°C. Its performance properties are shown in Table 1. The formula of the drilling fluid system consists of biodiesel, 20% CaCl$_2$ water solution (oil-to-water ratio 80:20), 3.0-3.5% SRHJ-1, 1.0-1.2% naphthenamide, 4% organic clay, 1.5% calcium oxide, 3-5% filtrate reducer, 2-4% wetting agent, 4% ultrafine calcium carbonate (1250 mesh), and barite powder. The performance of the new drilling fluid system was verified by field tests in several deep horizontal wells (WS1-H2, GS3, and XS1-H8). Its rheological features of low viscosity and high shear are effective in resolving common problems with OBDFs, such as difficulty in cuttings carrying, pipe sticking, and the instability of deep wells in tight gas reservoirs. The horizontal completion length of the WS1-H2 well was 1704.35 m, and the mechanical drilling speed was as high as 1.8 m/h; both of these values set new records in the field.

Table 1. Performance parameters of RHMOD-INVERT^{TM}

Experimental conditions	AV/ mPa·s	PV/ mPa·s	YP/ Pa	Gel/ Pa/ Pa	YP/PV	ES/ V	FL$_{HTHP}$/ mL
Before aging	26	18	8	3.5/5.0	0.44	1653	/
260°C/16 h	27	19	8	4.0/6.5	0.42	1644	8.2
260°C/48 h	29	20	9	4.0/6.5	0.45	1613	8.4
260°C/72 h	30	21	9	3.5/6.0	0.43	1548	8.4

RESULTS AND DISCUSSION

Hypothesis of the microscopic structure of high thixotropy OBDF

The low viscosity and high shear properties of RHMOD-INVERT^{TM} can be explained on the basis of microscopic factors. These rheological features may be caused by the intertwining of wormlike or linear micelles, which form a stereoscopic cake batter structure through interactions with quaternary ammonium clay. The hypothesized forms of interactions between emulsion droplets and solid-phase particles are illustrated in Fig. 6. When left standing, the elasticity of the emulsion droplets

formed by SRHJ-1 continues to increase, giving the emulsion high gel strength and suspending performance. Moreover, strong van der Waals forces are created between the emulsion droplets and the organic clay, forming a cake batter structure that correlates to the interactions between emulsion droplets, organic clay, and other solid-phase particles. This system is associated with higher gel strength and suspending performance. The drilling fluid system's shear stress τ_y was only 2.71 Pa as the fluid flowed. This suggests that the reticular formation can easily be destroyed even under an extremely small shear stress, facilitating the flow of the drilling fluid.
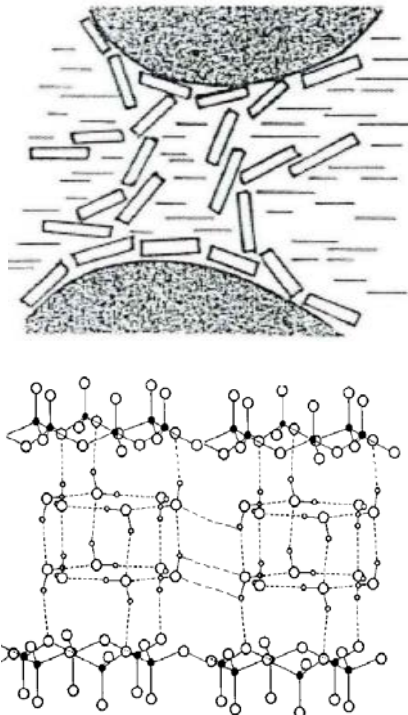
a. Stereo view of the cake batter structure
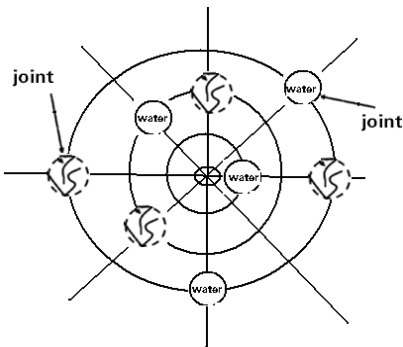
b. Planar view of the cake batter structure

Fig. 6. Hypothetical microscopic structure of the high thixotropy OBDF

Verification of the rheological properties of high thixotropy OBDF

In order to determine its rheological properties,

samples of the drilling fluid were cryopreserved in liquid nitrogen, which helped preserve its flow characteristics. Then, Cryo-scanning electron microscopy (Cryo-SEM) was used to investigate the drilling fluid's microstructure development. Moreover, a HTHP rheometer was used to test the new fluid's unique rheological properties.

Microscopic analysis

We used a DSX500 opto-digital microscope combined with Cryo-SEM to observe the microscopic structure of RHMOD-INVERT^{TM}. First, the moving fluid was flast frozen in -173°C liquid nitrogen, and images were taken using a transmission electron microscope with 100 KV accelerating voltage. Figs. 7 and 8 are the high-magnification images and Cryo-SEM images, respectively. As indicated in Figs. 7 and 8, the water-in-oil emulsion formed by SRHJ-1 enjoyed high stability and was resistant to the breaking of the emulsion. Moreover, there were more emulsion droplets formed, with smaller droplet sizes and a more uniform size distribution. Aggregates formed between the emulsion droplets and organic clay particles through hydrogen bonding. Based on these factors, a cake batter structure was observed as the form of interaction between emulsion droplets, organic clay, and other solid-phase particles; this structure provides higher gel strength and yield point. The emulsion droplets, organic clay, and other solid-phase particles interact by van der Waals forces, which are easily broken by high shear rate, leading to "shear thinning."
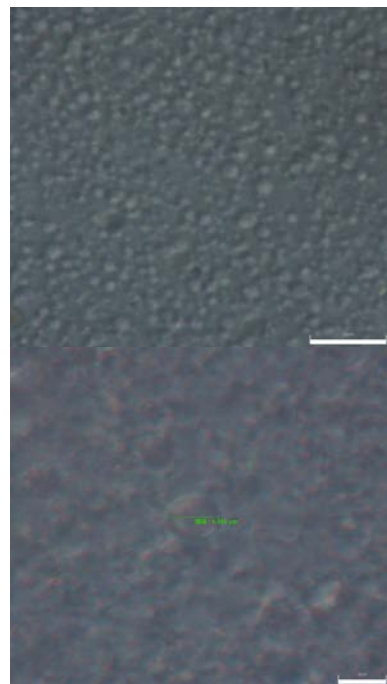
Fig. 7. SEM images of high thixotropy OBDF
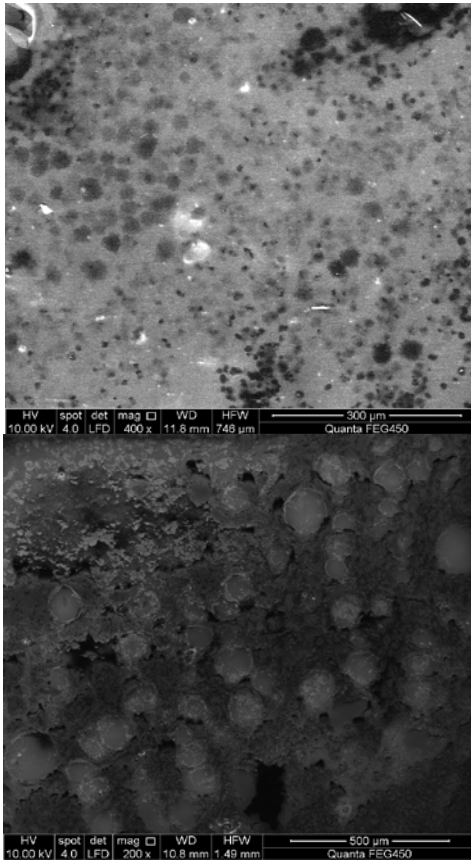
Fig. 8. Freeze-fracture electron microscopy images of high thixotropy OBDF

Macroscopic analysis

To characterize the macroscopic properties, a DHR-2 rheometer was applied to both conventional drilling fluid and RHMOD-INVERT^{TM} at 50°C. The rheological curves at high temperature and high pressure were then plotted so as to compare the rheological differences between the two. Figs. 9 and 10 show the changes to viscosity and shear stress, respectively, with shear rate. According to Fig. 9, the viscosities of both drilling fluids declined sharply at a shear rate of 0-100s^{-1}, which is typical of non-Newtonian fluids. With the shear rate fixed, the viscosity of RHMOD-INVERT^{TM} was obviously lower than that of the conventional drilling fluid, indicating a stronger shear thinning effect. This is conducive not only to increasing the drilling speed, but also to carrying cuttings in a circular space.

However, neither the Bingham model nor the power law model can accurately depict the rheological properties of these OBDFs. As Fig. 10 illustrates, the conventional OBDF more closely resembles a dilatant fluid at a shear rate of 0-1000 s^{-1}. As the shear rate increases, some particles intertwine together to form a reticular structure, which causes the flow resistance to increase,

resulting in the rheological features of high viscosity and low shear during the drilling operation. This is not favorable for borehole stability or the carrying of cuttings. In contrast, RHMOD-INVERT^{TM} conforms to the Herschel-Bulkely equation[23], expressed as $\tau = \tau_y + K\gamma^n$, which provides a more accurate model. The emulsion droplets formed by SRHJ-1 show a constant increase in elasticity in a static state, providing the emulsion with higher gel strength and suspending performance, also known as high shear. The initial shear stress τ_y of the flowing drilling fluid is only 2.71 Pa, which means both that the fluid can flow under minimal shear stress and that the drilling fluid is superior in thixotropy.
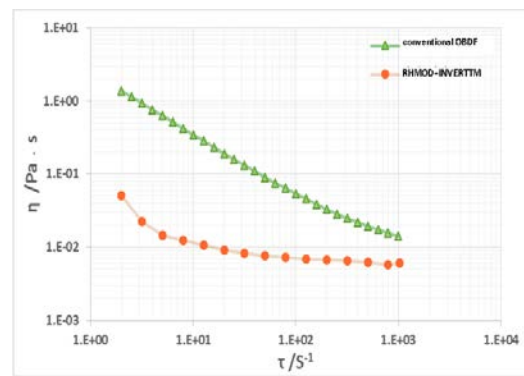
Fig.9. Viscosity-shear rate curves for different OBDFs
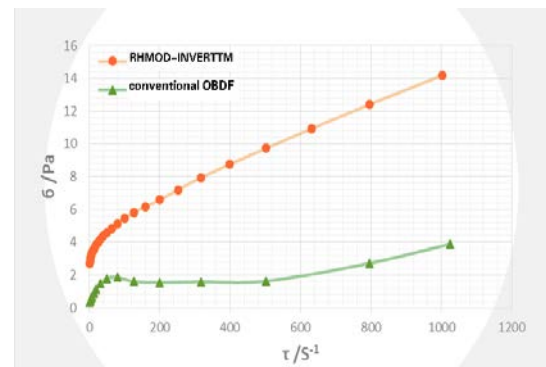
Fig.10. Shear stress-shear rate curves for different OBDFs

CONCLUSIONS

We developed a gemini emulsifier, SRHJ-1, for use in OBDFs. This emulsifier demonstrated excellent performance and compatibility with conventional emulsifiers. This emulsifier can increase the yield point of emulsion droplets, enhancing the strength of the interfacial film between oil and water. When added to a high thixotropy OBDF, SRHJ-1 can provide high shearing force and suspending ability. Based on

531

SRHJ-1, we then prepared a high thixotropy OBDF, RHMOD-INVERT^{TM}, which can resist high temperatures (260°C). Field tests proved the low viscosity and high shear of RHMOD-INVERT^{TM}, which has a unique cake batter structure. This three-dimensional piling structure, which is helpful in enhancing suspending performance, is formed by the interactions between emulsion droplets, organic clay, and other solid-phase particles.

Microscopic and macroscopic analyses of RHMOD-INVERT^{TM} indicate the formation of reticular aggregates comprised of emulsion droplets, organic clay, and other solid-phase particles. This drilling fluid system conforms to the Herschel-Bulkely equation and shows a good correspondence between its microscopic and macroscopic features.

REFERENCES

1. J.M. Davison, M. Jones, Oil-based muds for reservoir drilling: Their performance and clean-up characteristic [R]. SPE 72063, 2001.

2. P.V. Fossum, T.K., Moum, E.Sletfjerding, , et al. Design and utilization of low solids OBM for Aasgard reservoir drilling and completion [R]. SPE 107754, 2007.

3. F.C. Shu, Q.S.Yue, H.X.Huang, et al. *Fault-Block Oil & Gas Field*, **15**(3), 103 (2008).

4. B.F. Services, INNOVERT High Performance Paraffin/Mineral Oil-Based Fluids from Baroid [P]. US: 6887832, 2008-05-20.

5. M. Mas, T. Tapin, , SPE, Márquez, R., SPE, Gabay, R., Negrín, Z. PDVSA Intevep, etc. A New High-Temperature Oil-Based Drilling Fluid. SPE 53941, 1999.

6. M.W. Alberty, M.S.Aston, M.R. Mclean, Drilling method [P]. US: 7431106, 2008-10-07.

7. K.W. Oyler, K.J. Burrows, G.C. West, Diesel oil-based invert emulsion drilling fluids and methods of drilling boreholes: US, 7696131 [P].

8. F.T.G. Dias, R.R. Souza, E.F. Lucas, *Fuel*, 711 (2014).

9. Z.H. Wang, *Petroleum Drilling Techniques*, **39**(2), 1 (2011).

10. J. Liu, NMR studies on physicochemical behaviours of geminic surfactants in aqueous solution [D]. Wuhan: Wuhan Institute of Physics and Mathematics, Chinese Academy of Sciences, 2014, 20.

11. D. Danino, Y. Talmon, R. Zana, *Langmuir*, **11**(5): 1448 (1995).

12. R. Zana, M. In, H. Levy, et al., *Langmuir,* **13**(21): 5552 (1997).

13. D.P. Acharya, H. Kunieda, Y. Shiba, et al. *The Journal of Physical Chemistry B*, **108**(5), 1790 (2004).

14. A. Bemheim-Groswasser, R. Zana, Y. Talmon, *The Journal of Physical Chemistry B*, **104**(17): 4005 (2000).

15. R. Oda, P. Panizza, M. Schmutz, et al., *Langmuir*, **13**(24), 6407 (1997).

16. D. Wu, Y. Feng, G. Xu, et al. *Colloids and Surfaces A: Physicochemical and Engineering Aspects*, **299**(1), 117 (2007).

17. L.M. Walker, *Current Opinion in Colloid & Interface Science*, **6**(5-6), 451 (2001).

18. G.C. Jiang, Y.B. He, H.B. Huang, et al. *Petroleum Exploration and Development*, , **2**(43), 131 (2016).

19. L.X. Xia, A study on the relationship of interfacial film between oil and water and emulsion stability [D]. Dalian: Dalian Institute of Chemical Physics, Chinese Academy of Sciences, 2003, 2.

20. A., Saasen, D. Liu, C.D. Marken, Prediction of barite sag potential of drilling fluids from rheological measurements [R]. SPE 29410, 1995.

21. R. Zana, H. Levy, K. Kwetkat, *J Colloid Interface Sci*, **197**(2), 370 (1998).

22. J. Zhao, S.D. Christian, B.M. Fung, *J Phys Chem B,* **102**(39), 7613 (1998).

23. J.N. Yan, Drilling Fluids Technology [M]. Shandong: China University of Petroleum Press, 2006, 77.

РЕОЛОГИЧНИ СВОЙСТВА НА RHMOD-INVERT[TM] - ИЗСЛЕДВАНЕ НА НОВА СОНДАЖНА ТЕЧНОСТ НА ОСНОВАТА НА МАСЛО С ВИСОКА ТИКСОТРОПИЯ

И. Г. Лиу[1,2], И. Джан[2], Дз. Ян[2], И. Дж. Сю[1]*

[1] *Технически институт Харбин, Харбин, Хейлонджианг, Китай 150001,*

[2] *Инженерно-изследователски институт за сондажно инженерство, Нефтено-сондажна инженерна компания в Дацин, Дацин, Хейлонджианг, Китай 163413*

(Резюме)

Използването на конвенционални сондажни флуиди на основата на масло обикновено включва недостатъците на ниска ефективност на почистване на сондажа, лесно образуване на коритото и слепване на сондажните тръби. За да се справим с тези проблеми, ние разработихме повърхностно-активния агент SRHJ-1, след което произведохме сондажната течност RHMOD-INVERT[TM], базирана на нефт. Тази нова сондажна течност показва отлични реологични свойства, включително нисък вискозитет и висока степен на срязване. Микроскопската структура на сондажния флуид се наблюдава чрез електронно микроскопия с фрагментиране чрез замразяване. След това, съчетавайки високотемпературна реометрия с високо налягане с оптична микроскопия, сондажният флуид RHMOD-INVERT[TM] беше анализиран както макроскопски, така и микроскопски. Данните от наблюденията показват силни сили на ван дер Ваалс, които са активни между емулсионни капчици, органична глина и други частици в твърда фаза, което води до близки взаимодействия и образуване на мрежови агрегати. Поради тези сили новата течност за пробиване показва структура на " тесто за торта". Емулсионните капчици, органичната глина и другите частици в твърда фаза, когато са в покой, образуват сложна, триизмерна пространствена структура на, която има по-висока задържаща сила. Когато тече, ретикуларното образуване може да бъде унищожено дори при изключително ниско срязване, улесняващо протичането на сондажната течност. Това се проявява като нисък вискозитет и висока степен на срязване на микроскопично ниво. Новият пробивен флуид беше приложен при полеви тестове в няколко дълбоки хоризонтални кладенци, включително WS1-H2, GS3 и XS1-H8, където показа стабилна производителност. Реологичните свойства като нисък вискозитет и висока степен на срязване улесняват преодоляването на недостатъците при сондирането в дълбоки хоризонтални кладенци, в тесни газови резервоари, като същевременно се подобрява ефективността на пробиване.

Core-flooding experimental study of oil displacement by using sulfate-reducing bacteria

W. Song[*], D. Ma, K. Wu, Y. Zhu, J. Wu, B. Yu

[1]*State Key Laboratory of Enhanced Oil Recovery, Research Institute of Petroleum Exploration and Development, CNPC, Beijing 100083, China*

Sulfate reducing bacteria (SRB) are anaerobic microorganisms which are widely distributed in global oil reservoirs. They have been reported to play an important role in enhancing oil recovery (EOR). In this study, a *Desulfobacteriaceae* spp. isolated from Daqing oilfield (China), was used as a candidate for microbial oil displacement in a core flooding experiment that two important experimental parameters were optimized, including numbers of injection slugs and bio-retention time. To find out the EOR mechanism, the produced liquid and recovered oil were analyzed. By the results, SRB showed a best distribution in porous medium when they were injected as two slugs. The oil recovery efficiency was proportional to bio-retention time. By optimizing these two parameters (injection slug and bio-retention time), the oil recovery efficiency could be increased to 11.48%. The viscosity of recovered oil was significantly reduced based on bio-degradation of NSO compounds. Therefore, SRB could be a good candidate in use of microbial enhanced oil recovery.

Keywords: SRB, EOR, TPH, injection slug, core-flooding experiment

INTRODUCTION

Sulfate-reducing bacteria (SRB) are genetically anaerobic organisms that were firstly discovered by Hamilton [1]. SRB could use a very wide spectrum of different low molecular organic compounds for growth, including lactate, acetate, proprionate, succinate, pyruvate, ethanol, sugars, etc. Moreover, SRB use Sulfate (SO_4^{2-}) as electron receptor instead of oxygen for their respiration with SO_4^{2-} being reduced to hydrogen sulfide (H_2S) [2-4]. However, SRB is well known as harmful bacteria in the productive process of oilfields. They might cause serious problems (e.g. corrosion of iron in anaerobic conditions and reduction of the property of injection of water injection wells by precipitation of amorphous ferrous sulfide, etc.) in oilfield water systems [5].

Some recent study indicated that SRB might play an important role in microbial enhanced oil recovery (MEOR) [6-7]. For example, SRB could diminish oil viscosity, replenish the declining pressure of reservoir, and change heavy oil to light oil through yields of bio-generated acids, gas (H_2S) and degradation of hydrocarbons (Aliphatic and Aromatic). Also, different types of SRB are widely distributed in global oil reservoirs. Therefore, SRB could be a great target that used for enhancing oil recovery (EOR).

This study were mainly focused on evaluating the oil displacement efficiency by using SRB. To do this,

the entire research was divided into two parts. In the first part, the experimental parameters were optimized, including injection slug (fresh SRB culture) and retention periods (SRB cells interact with crude oil inside of the experimental core after injection). Injection slug is one of important factors for diffusion of microbial cells in porous medium (experimental cores), thus affecting EOR efficiency. Single-slug injection will exhibit a highest local concentration in porous medium, but may limit further diffusion efficiency. In contrast, multi-slug injection could obviously improve microbial diffusion efficiency, whereas the local cell concentration might lose remarkably (decrease in bio-reaction intensity). In this research, the total injection volume is chosen as 0.5 PV of pore volume (experimental core) [8]. To optimize the injection slug, three different injection slugs were tested based on EOR efficiency, including single-slug (1×0.5 PV), two-slugs (2×0.25 PV) and three-slugs (3×0.17 PV).

Once the microbes contact with residual oil, they might use their natural carbon sources for metabolism, including growth, reproduction and respiration, etc. During the metabolic processes, byproducts (bio-mass, bio-gases, organic acids, alcohols and even functional enzymes) are released to the environment [9], thereby resulting in the physical and chemical changes in crude oil. All those bio-physical and bio-chemical reactions require sufficient time to take place. Therefore, three different retention periods (3, 5 and 7 days) was optimized in this study depending on their EOR efficiency. These three experimental retention times

* To whom all correspondence should be sent:
E-mail: songwf@petrochina.com.cn

were commonly used in other microbe-related laboratory researches [10].

In the second part, the produced liquid and recovered oil during subsequent water-flooding (after SRB flooding) were analyzed. The produced liquid were analyzed by cell count to compare the diffusion efficiency among different injection slugs. For recovered oil, its viscosity and composition changes of total petroleum hydrocarbons were evaluated in order to find out the EOR mechanism in core experiment. This is the first time to use SRB for evaluating oil displacement efficiency in experimental core study.

MATERIALS AND METHODS

All reagents (media and buffers) used were prepared gravimetrically using a Sartorius A200S analytical balance, and made up to volume with room temperature sterile distilled water (dH$_2$O). All chemicals used in this paper were reached the analytical standard, and have been autoclaved at 121 °C for 20 min for sterilizing before use.

The SRB was isolated from pipe line of water injection well in Daqing Oilfield, China. The isolation was carried out in Postgate medium C (sPGC) [11]. The medium consists of the following: NaCl (0.12 M), MgCl$_2$·6H$_2$O (5.9×10^{-3} M), KH$_2$PO$_4$ (3.6×10^{-3} M), NH$_4$Cl (0.019 M), Na$_2$SO$_4$ (0.032 M), CaCl$_2$·2H$_2$O (2.8×10^{-4} M), MgSO$_4$·7H$_2$O (1.2×10^{-4} M), FeSO$_4$·7H$_2$O (1.4×10^{-5} M), trisodium citrate (1.1×10^{-3} M), sodium lactate (70% w/v, 0.077 M), yeast extract (1 g L^{-1}) and agar (20 g L^{-1}). The pH was finally adjusted to 7.2.

The plates were incubated at 45 ºC for 20 days under anaerobic conditions in a 3.5 L anaerobic jar (Traditional system; Oxoid Company) filled with carbon dioxide and hydrogen which was produced by using anaerogen sachets according to the instructions of the manufacturer. Preparation and inoculation of plates were carried out inside an environmental chamber which contained a mixture of gases (Nitrogen 87%, carbon dioxide 10%, and hydrogen 3%) in oxygen free environment. After

incubating for a week, several colonies of SRB were observed. The different bacteria were isolated and allowed to grow on separate plates and were found to be of the same type belonging to *Desulfobacteriaceae* family.

The cell culture was carried out in ATCC medium 1249 type III [12]. Cell culture was prepared by inoculating a single colony from the agar plate into 80 mL of broth in a 120 mL headspace vial. The headspace vial was covered by septa, and subsequently sealed with aluminum cap by capping clamp. Preparation and inoculation were carried out inside an environmental chamber which contained a mixture of gases (Nitrogen 87%, carbon dioxide 10%, and hydrogen 3%) in oxygen free environment. Headspace vials were then grown anaerobically on an orbital shaker (150 rpm) at 45 °C for 20 days (The cell concentration was grown to A600 nm to 1.5 (stationary phase) and stored at 4 °C until required, but no longer than 8 hours.

The crude oil samples were collected from Daqing oilfield with density of 0.851 g cm^{-3}. The permeability of target reservoir is 180.7×10^{-3} μm^2. Reservoir temperature is 45 °C and salinity of formation water is 14,139 mg L^{-1}. Synthetic cores were chosen based on reservoir conditions (Table 1).

The oil displacement experiments were conducted by using the standard core flooding system [13] (Figure 1). Core flooding experiment is composed of a series of steps including, vacuumization of core followed by saturation with formation water, water-phase permeability measurements, determination of crude oil saturation level, aging interaction between crude oil and the core (7 days), water flooding until 98% water cut, chemical flooding slug injection, and subsequent water flooding until 99% water cut. The experiment was conducted at reservoir pressure (9.95 MPa) and temperature (45 °C) with fluid injection rate of 0.2 mL min^{-1}. During the experiments, the pressure differential, oil production, water production and total fluid production were recorded timely to make sure the oil recovery were calculated precisely.

Table1. Physical properties of experimental cores

Core ID	Length [mm]	Diameter [mm]	Pore Volume [ml]	Porosity φ [%]	Air permeability K$_g$ [10^{-3} μm^2]	Water permeability K$_w$ [10^{-3} μm^2]
ZF-04	200	24.25	13.14	27.07	300	185.90
ZF-05	200	24.80	11.74	24.03	300	196.49
ZF-06	200	24.28	14.14	28.77	300	172.68
ZF-07	200	24.36	12.56	25.69	300	169.27
ZF-09	200	24.37	13.07	26.51	300	190.32
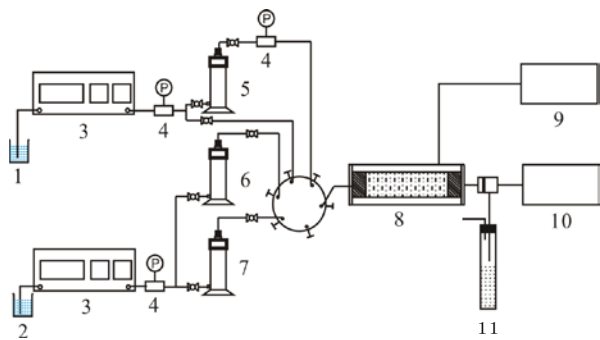
Fig. 1. Schematic of the core flooding setup. 1. Brine; 2. Water; 3. Injection pump; 4. Pressure gauge; 5. Microbial culture tank; 7. Oil tank; 8. Core holder; 9. Confining pump; 10. Back-pressure pump; 11. Produced liquid collector.

During the subsequent water flooding, the produced liquid was collected every 0.1 PV. 100 µL of produced water with appropriate dilutions were pipet out and spread onto a Postgate medium C agar plate. The plates were incubated at 30 ºC for 14 days under anaerobic conditions in a 3.5 L anaerobic jar (Traditional system; Oxoid Company) filled with carbon dioxide and hydrogen which was produced by using anaerogen sachets according to the instructions of the manufacturer. Preparation and inoculation of plates were carried out inside an environmental chamber which contained a mixture of gases (Nitrogen 87%, carbon dioxide 10%, and hydrogen 3%) in oxygen free environment. The number of colony forming units (CFU) mL^{-1} were then calculated.

Viscosity of recovered oil sample was measured by using a NDJ-8S digital viscometer (Nirun Intelligent Technology, China) at 45°C.

30 mg of recovered oil were consecutively extracted with hexane, dichloromethane, and chloroform (100 mL each). All three extracts were pooled and dried at room temperature by evaporation of solvents under a gentle nitrogen stream in a fume hood. After solvent evaporation, the amount of residual TPH was then determined gravimetrically. After gravimetric quantification, the residual TPH was fractionated into alkane, aromatic, asphaltene, and NSO (nitrogen, sulfur, and oxygen-containing compounds) on a silica gel column. To do this, samples were dissolved in hexane and separated into soluble and insoluble fractions (asphaltene). The soluble fraction was located on a silica gel column and eluted with different solvents. The alkane fraction was eluted with 100 mL of toluene. Finally, the NSO fraction was eluted with methanol and chloroform (100 mL each) [14]. The alkane and aromatic fractions were then analyzed by GC-MS.

RESULTS AND DISCUSSION

To optimize the number of injection slugs, three injection plans were designed, including sing-slug, two-slug and three-slug injection. Three days bio-reaction period was used as retention time in this experiment.

Two-slug assay showed the best oil displacement efficiency among the three assays, in which the EOR was improved by 6.69% after subsequent water flooding (Figure 3). In contrast, single-slug (Figure 2) and three-slug assays (Figure 4) only could improve EOR by 4.71% and 4.05%, respectively. Of the three, three-slug assay showed the lowest EOR efficiency. The results indicated that the optimal injection plan is two-slug injection.
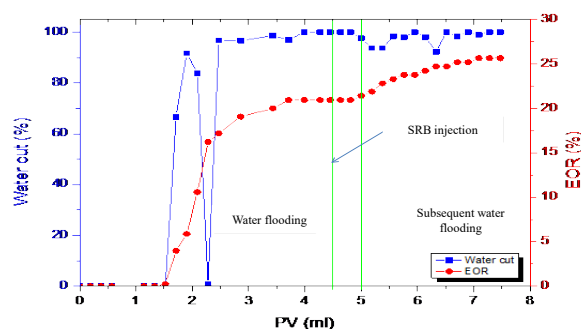
Fig. 2. SRB EOR efficiencies of 3-day retention assay with single-slug injection.
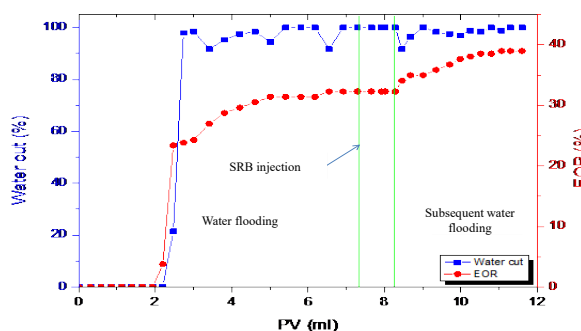
Fig. 3. SRB EOR efficiencies of 3-day retention assay with two-slug injection.
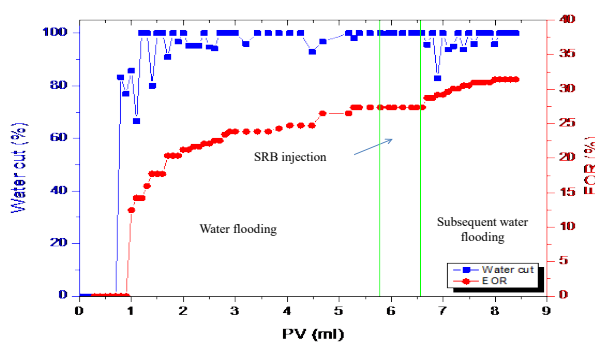
Fig. 4. SRB EOR efficiencies of 3-day retention assay with three-slug injection.

The reason that two-slug assay showed the best EOR result is unclear. However, the highest EOR efficiency might be caused by the best diffusion of SRB cells inside of the core. There were four contact areas between SRB culture and the residual oil in the cross-section of the experimental core in two-slug assay, whereas there was only two in single-slug assay. In contrast, small multi-slugs might lose more cell concentrations during they went through the porous medium, even if they created more contact areas (six contact areas in cross-section in three-slug assay). Moreover, small slugs (low in total cell numbers) might limit the diffusion of microbial cells.

To optimize the retention period, the other two bio-reaction times (5 and 7 days) were tested by their following EOR efficiency. Two-slug injection was used in this experiment. As shown in results, SRB could improve EOR by 9.34% and 11.48% after bio-reacting with residual oil in 5 (Figure 5) and 7 (Figure 6) days, respectively. This might indicated that the EOR efficiency was proportional to the bio-reaction period.
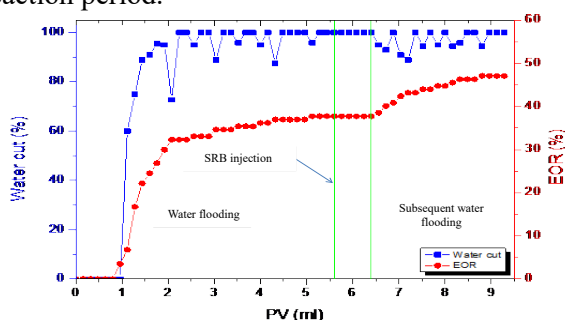
Fig. 5. SRB EOR efficiency of 5-day bio-retention assay with two-slug injection.
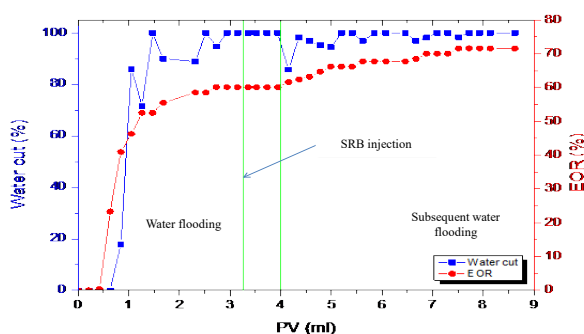
Fig. 6. SRB EOR efficiency of 7-day bio-retention assay with two-slug injection.

This results could be understand by the previous studies. For example, microbial metabolites are amphiphilic molecules which contain both hydrophilic and hydrophobic groups [9]. These metabolites are known as bio-surfactants (e.g. bio-mass, organic acids, and organic alcohols, etc.), which could bind both water and oil molecules, thereby forming a stable emulsification system between oil and liquid, and also decreasing oil/liquid

interfacial tension. This will result in a decrease in oil viscosity, thus increasing oil fluidity [15]. Furthermore, SRB has been reported to degrade oil compounds such as alkane and methylbenzene [16, 17]. Degradation of heavy hydrocarbons would also increase oil fluidity. Therefore, the longer the retention period is, the more functional metabolites produced and the greater intense of bio-reaction took place.

In a previous study, *Pseudomonas* spp. has been reported to use for oil displacement experiment [18]. It could improve EOR efficiency by about 5% - 13% with more than 3.5 PV of microbial injection. In contrast, SRB could improve EOR by about 10% with 0.5 PV of injection. This represents that SRB is a good candidate for MEOR. Recently, most of MEOR-related studies are focused on basic mechanisms (e.g. microbial communities in target reservoir, oil degradation mechanism, production of bio-surfactants, and changes of wettability, etc.) [19-22]. However, there is still require more core-flooding studies to compare.

To best understand the influence of microbial injection slugs in porous medium, produced liquid was collected every 0.1 PV to indirectly evaluate cell diffusion efficiency by counting cell numbers. The results were shown in Figure 7. In single-slug assay (blue bars), SRB showed a "mountain-shape" graph. The highest cell number occurred in the middle of experimental cores with concentration of 10^7 cell mL^{-1}. There was no SRB found in the first 0.1 PV of produced liquid, which was similar with three slug assay. Of the three, three-slug assay exhibited the lowest diffusion efficiency in average (green bars). In contrast to those two, SRB cells were found in every collection of produced liquid (red bars). This indicated that microbes were well distributed inside of the entire core. The result might give the evidence why tow-slug injection of SRB showed the highest EOR efficiency.
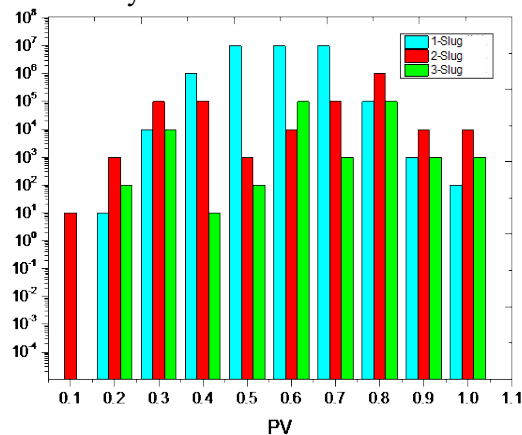
Fig. 7. Cell number count of produced liquid with different SRB slug-injection assays.

To find out the SRB-EOR mechanism during core-flooding experiment, the viscosity of recovered oil was tested (7-day bio-retention). The viscosity of crude oil was also analyzed as control. In comparison with crude oil, the viscosity of recovered oil was significantly reduced by 15% (Figure 8). The reason of decrease in recovered oil viscosity need to be further studied.
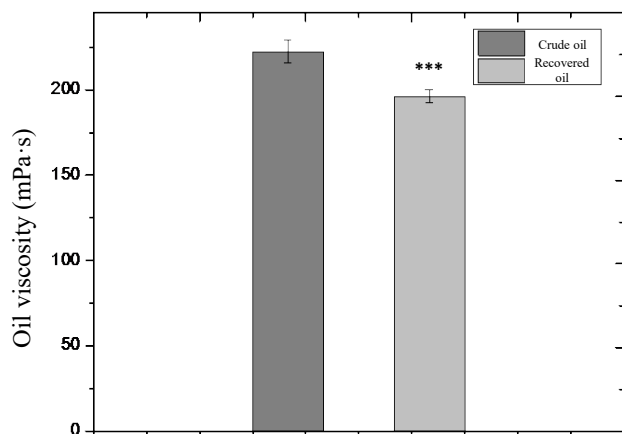
Fig. 8. Viscosity comparison between crude and recovered oil samples. *: significant difference from crude oil assay. The number of stars (*) indicates the significance level. *: P<0.05; **: P<0.01; ***: P<0.005; ****: P<0.001.The significant difference was determined in paired test. n=4, error bars are standard error.

To better understand the relationship between oil composition changes and viscosity declination during core-flooding experiment, the TPH ratios of recovered oil were analyzed. The TPH composition of crude oil was also studied as the control. After SRB flooding, three fraction ratios of TPH were slightly increased (alkane, aromatic and asphaltene) compared to crude oil samples (Table 2). However, those variations were remained in estimated errors. Of the four fractions, only NSO was significantly reduced when compared with their control counterpart. The reason is unclear. It might be that the compounds in NSO are more readily to be used by SRB. This result indicated that an increase in EOR efficiency was based on the reduction of oil viscosity by bio-consumption of NSO compounds.

Table 2. Fraction changes of TPH between crude and recovered oil samples

Fraction	Contents (Mean ± SD) (%)	
	Crude oil	Recovered oil
Alkane	55.71 ± 0.24	56.38 ± 0.31
Aromatic	11.25 ± 0.28	12.12 ± 0.28
Asphaltene	1.96 ± 0.03	1.99 ± 0.02
NSO	30.97 ± 0.26	27.41 ± 0.18*

*: significant difference from crude oil assay. The number of stars (*) indicates the significance level. *: P<0.05.

Both oil samples were then analyzed by GS-MS to compare with the changes of alkanes and aromatics. However, no statistically significant difference was found in both assays (data not shown). It has been reported that SRB could degrade oil hydrocarbons (e.g. alkane and methylbenzene, etc.) [16, 17]. This might be caused that SRB bio-activity could not be sufficiently exhibited in 7-day retention period. It is believed that SRB flooding efficiency could be further improved by extending retention time.

CONCLUSION

In this study, SRB was the first time to be used as a candidate in core experimental oil displacement. By optimize the experimental factors (microbial injection slugs and bio-retention time), SRB could increase EOR by more than 11% after subsequent water flooding. By analysis of produced liquid (cell number count), two-slug injection showed the best distribution efficiency of SRB cells in porous medium. By analysis of recovered oil (evaluation of oil viscosity and changes of TPH), the oil viscosity was significantly reduced by bio-degradation of NSO compounds. Therefore, SRB can be a good candidate in use of MEOR.

REFERENCES
1. E.A. Ghazy, M.G. Mahmound, M.S. Asker, M.N. Mahmound, M.M. Abo Elsoud, M.E.A. Sami, *J. Am. Sci.*, **7**, 604 (2011).
2. S. Al-Zuhair, M.H. El-Naas and H. Al-Hassani, *J. Biochem. Technol.*, **1**, 39 (2008).
3. N. Benaroudj, D.H. Lee, A.L. Goldberg, *J. Biol. Chem.*, **276**, 24261 (2001).
4. A. Brioukhanov, L. Pieulle, A. Dolla, *Technology and Education Topics in Applied Microbiology and Microbial Biotechnology*, **148** (2010).
5. H.P. Castro, R. Kirby, *J. Appl. Microbiol.*, **82**, 87 (1997).
6. A. Suarez-Suarez, A. Lopez-Lopez, A. Tovar-Sanchez, P. Yarza, A. Orfila, J. Terrados, J. Amds, S. Marques, H. Niemann, P. Schmitt-Kopplin, R. Amann, R. Rosello-Mora, *Environmental Microbiology*, **13**, 1488 (2011).
7. C.P. Champagne, F. Mondou, Y. Raymond, D. Roy, *Food Research International*, **29,** 555 (1996).
8. R.P. Cao, Han and G. Sun, *Oil Drilling & Production Technology*, **33**, 88 (2011).
9. H. Al-Sulaimani, S. Joshi, Y. Al-Wahaibi, S.N. Al-Bahry, A. Elshafie, *Bioinformatics and Bioengineering*, **1**, 147 (2011).
10. R.T. Armstrong, and D. Wildenschild, *J. Petrol. Sci. Eng.*, **94-95**, 155 (2012).

11. J.R. Postgate, The Sulfate-reducing bacteria. 2nd ed. Cambridgeshire, Cambridge University Press , 1984.
12. D. Shao, Y. Kang, S. Wu, M.H. Wong, *Science of the Total Environment*, **424**, 331 (2012).
13. L. Yang, Z. Yang, *Chinese Oil and Gas* Industry Standards: Analytical method of alkali-surfactant-polymer flooding system (SY/T 6424-2000), Petroleum Industry Press, Beijing , 2012.
14. T. Hadibarata, S. Tachibana, *Interdisciplinary Studies on Environmental Chemistry - Environmental Research in Asia*, 317 (2009).
15. R.K. Singh, *J. Mol. Biol*., **376,** 950 (2008).
16. A.V. Callaghan, B.E.L. Morris, I.A.C. Pereira, M.J. McInerney, R.N. Austin, J.T. Groves, J.J. Kulor, J.M. Suflita, L.Y. Young, G.J. Zylstra, B. Wawrik, *Environmental Microbiology*, **14**, 101 (2011).
17. L. Wohlbrand, J.H. Jacob, M. Kube, M. Mussmann, R. Jarling, A. Beck, R. Amann, H. Wilkes, R. Reinhardt, R. Rabus, *Environmental Microbiology*, **15**, 1334 (2013).
18. K.M. Kaster, A. Hiorth, G. Kjeilen-Eilertsen, K. Boccadoro, A. Lohne, H. Berlan, A. Stavland, O.G. Brakstad, *Transport Porous Med*., **91**, 59 (2012).
19. J. Li, J. Liu, M.G. Trefry, K. Liu, J. Park, B. Haq, C.D. Johnston, M.B. Clennell, H. Volk, *Transport Porous Med*., **92**, 373 (2012).
20. S. Liu, S. Liang, *Applied Informatics and Communication*, **224**, 143 (2011).
21. F.Y. She, H. Li, X. Zhang, F. Shu, Z. Wang, L. Yu, D. Hou, *Appl. Microbiol. Biot*., **95**, 811 (2012).
22. N. Zhang and C. Xue, *Adv. Mater. Res*., **345**, 233 (2012).

ЕКСПЕРИМЕНТАЛНО ИЗСЛЕДВАНЕ НА ИЗМЕСТВАНЕТО НА НЕФТ С ПОМОЩТА НА СУЛФАТ-РЕДУЦИРАЩИ БАКТЕРИИ ПРИ ИЗПИТАНИЕ СЪС ЗАЛИВАНЕ НА СКАЛНА ЯДКА

У. Сун*, Д. Ма, К. У, И. Джу, Дж. У, Б. Ю

Държавна лаборатория за повишаване на нефтодобива, Изследователски институт за проучване и развитие на петрола, CNPC, Пекин 100083, Китай

(Резюме)

Сулфат-редуциращите бактерии (SRB) са анаеробни микроорганизми, които са широко разпространени в глобалните петролни резервоари. Те играят важна роля за подобряването на добива на петрол (EOR). В това проучване, щам *Desulfobacteriaceae* spp. изолиран от петролното находище Дацин (Китай), е използван като кандидат за микробиологично изместване на петрол в експеримент за заливаневане на ядрото, при който са оптимизирани два важни експериментални параметри, включително броя на инжектиране и време за биозадържане. За да се установи механизмът на EOR, бяха анализирани получените течности и петрол. Чрез резултатите SRB показа най-доброто разпределение в порестата среда, когато са двукратно инжектирани. Ефективността на оползотворяването на петрола е пропорционална на времето за биозадържане. Чрез оптимизирането на тези два параметъра (инжектиране на шлака и време на биозадържане), ефективността на добива на петрол може да се увеличи до 11,48%. Вискозитетът на петрола е значително намален чрез биоразграждане на NSO съединенията. Следователно SRB могат да бъдат добър кандидат за използване на микробиално подобрение на добива на петрол.

Measurement of some chemical and Biochemical parameters in *Cladophora glomerata* L. from Farahabad Region of Iran

A. G. Ebadi*, H. Hisoriev, K. Aliev

Institute of Botany, Plant Physiology and Genetics, Tajik Academy of Sciences, P.O. Box: 734017, 27th Karamov Street, Dushanbe- 17, Republic of Tajikistan

Algae has many different applications such as food, agricultural (fertilizer making), pharmaceutical, and medical industries. *Cladophora glomerata* is one the abundant filamentous green algae in the southern coast of Caspian. Algae samples obtained from 4 sampling points in Farahabad region of Iran (late 2016-early 2017). Selection of stations was for touristic importance, discharge of pollutions, and oil residues, hence study of some chemical and biochemical indexes of *Cladophora glomerata* as indicator algae can be important in this region. In this paper, some chemical and biochemical characterizations such as, dry weight, chlorophyll a, b, total Chlorophyll, Carotenoids, Total protein, Proline content, and Antioxidant activity) measured based on standard methods. Results showed that station 3 had lowest amount of dry weight, chlorophyll a, b, total Chlorophyll, Carotenoids, and Total protein ($p < 0.05$) and there were significant different between stations but proline content and Antioxidant activity were high amount in station 3 ($p < 0.05$). Results showed and proved high stress conditions in this point for higher content of heavy metals based on before studies.

Keywords: *Cladophora glomerata*, chemical and biochemical parameters, Farhabad region, Iran

INTRODUCTION

In recent years, algae from marine ecology viewpoints, considered as first producers and supply chain for receiving energy from the sun that can guarantee the energy for aquatic life. In the global division of plants, algae have about 1,800 genera and 21,000 species. Due to the extensive presence of algae in the air and groundwater, occupied wider area in comparison with other plants. An alga has many applications and uses such as food industries, making different fertilizers, pharmaceutical and medical industries [1-3].

Cladophora glomerata L. is green filamentous alga that has almost highly distribution in the southern coast of Caspian Sea. It has mostly grown on big stones, wood residues and also beside walls in southern coast part of Caspian Sea as long filaments such as Farahabad region. This region is the pleasant location for local and international tourists in Mazandaran Province, for enjoy from seaside and monitoring of this place is very important for human health. Some researchers showed, Marine organisms such as *Cladophora glomerata*, can be a useful biomarker or bio indicator for highly absorbable heavy metals. Hence, it is very more reliable than chemical analysis of water and sediment for environmental researchers [4].

In former research by Ebadi and Hisoriev [4], content of three heavy metals chromium (Cr), lead (Pb), and cadmium (Cd) in four sampling sites, measured for one year (2016) in *Cladophora glomerata* samples. Results of this study showed that the range of Cr, Pb and Cd in various algal samples was 29–55, 2 to 8, and 1.5 to 8.2 ppm/g dry weight respectively. Although amount of metals are not very serious but can be environmental alarm for human health and ecological risks. With increasing of pollutions in the Caspian Sea that mostly related to petroleum products, pesticides, agricultural fertilizers, heavy metals and domestic sewage, can effect on growth and physiology of this organism. This finally leads to environmental problems such as reducing oxygen to marine plants and animals and death of them [1,4-5]. The goal of this study was to examine some chemical and biochemical characterizations mainly in *Cladophora glomerata* for show effects of measured pollutions in different studies on factors such as, Dry weight, Chlorophyll a, b, Total Chlorophyll, Carotenoids, Total protein, Proline content, and Antioxidant activity. This study also shows the response of this alga to environmental pollutions as an ecological stress.

EXPERIMENTAL

Algae sampling and preparation

Samples obtained from 4 sampling points of Farahabad region (Mazandaran Province of Iran). Sampling, Preparation and drying procedures performed based on standard methods. All samples collected in same conditions from weather in the late of 2016 and early 2017 (Table 1 & Figure 1).

---

* To whom all correspondence should be sent:
E-mail: dr_ebadi2000@mail.ru
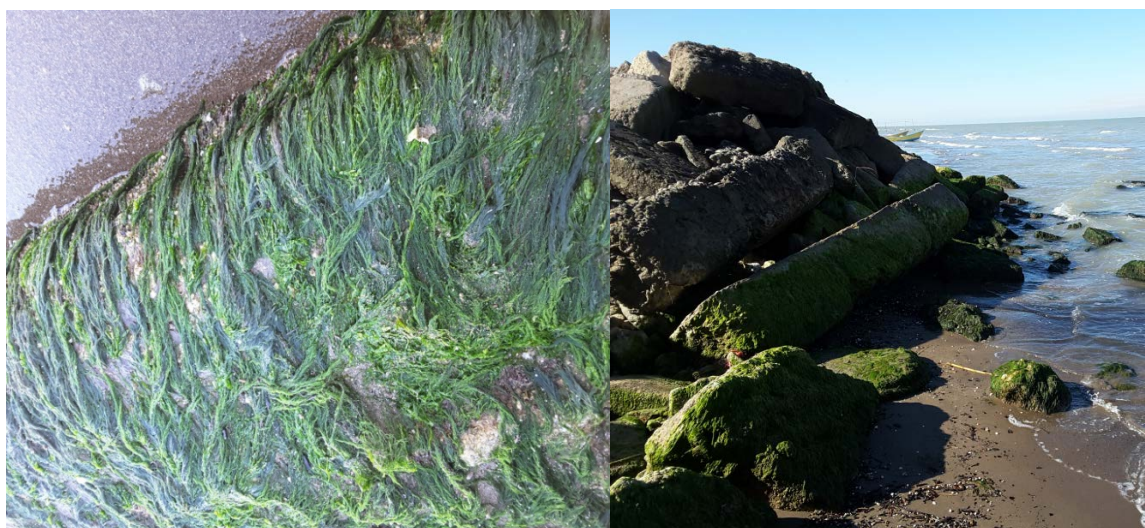
Fig. 1. *Cladophora glomerata* obtained from Farahabad region of Caspian Sea (2016-2017).

Table1. Coordinates of sampling points in Farahabad region (2016-2017).

Farahabad Region sampling points	Geographical characteristics
Point 1	36°48'41.59" N ; 53°06'24.38" E
Point 2	36°48'48.40" N ; 53°06'55.33" E
Point 3	36°48'46.94" N ; 53°06'39.84" E
Point 4	36°48'37.70" N ; 53°06'09.86" E

Dry weight detection, Chlorophyll a, b, Total Chlorophyll and Carotenoids

Dry weight measured based on standard method [5]. Chlorophyll a, b, Total Chlorophyll and Carotenoids measured based on below formula and shown based on mg/g wet weight [6].

Chlorophyll a $= (19.3 * A663 - 0.86 * A645) \, V/100W$ (1)

Chlorophyll b $= (19.3 * A645 - 3.6 * A663) \, V/100W$ (2)

Total Chlorophyll = Chlorophyll a + Chlorophyll b (3)

Carotenoids $= 100(A470) - 3.27(\text{mg chl. a}) - 104(\text{mg chl. b})/227$ (4)

Where, V: volume of supernatant liquid; A: light absorbance in different wavelengths (663, 645, and 470 nm); W: sample wet weight based on gram.

Total protein, Proline content and Antioxidant activity

Total protein, Proline content and antioxidant activity measured based on standard methods [7-9]. Total protein shown based on mg/g wet weight. Proline amount shown based on µmol/ g wet weight based on below formula and in wavelength of 520 nm:

µmol in each gram = µgram Proline in each ml * amount of consumed Toluene (ml) / 115.17 µgram in mol (5)

Antioxidant activity measured in wavelength of 517 nm and based on capacity of damage of active radicals [5] based on below formula:

% of damage of active radicals = [absorb in control sample – absorb in test sample / absorb in control sample] * 100 (6)

Statistical analysis

Statistical analysis performed by SPSS program version 9. Mean comparison done based on Duncan test in $p < 0.05$ level. All diagrams prepared with excel program.

RESULTS AND DISCUSSION

Chlorophyll a content

Amount of Chlorophyll a in four sampling points showed in Figure 2. Based on this figure, order of Chl a was S1> S4> S2> S3. Highest amount was for point 1 (8.65 mg/g wet weight) and lowest for point 3 with 6.5 mg/g wet weight.
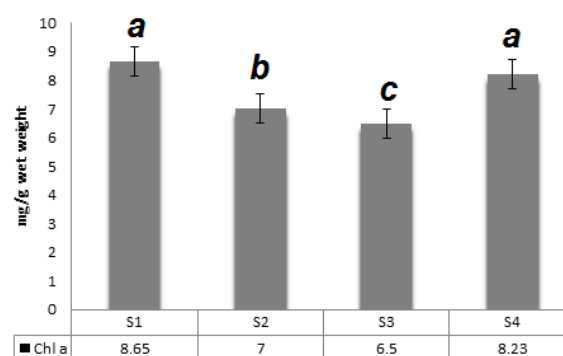
Fig. 2. Measurement of Chlorophyll a content in *Cladophora glomerata* samples from stations in 2016-2017 (Mean ± SE, $p < 0.05$).

Duncan test showed that treatment divided in three groups and also significant different between sampling points ($p < 0.05$).

Chlorophyll b content

Amount of Chlorophyll b in four sampling points showed in Figure 3. Based on this figure, order of Chl b was as S1> S4> S2> S3. Highest amount was for point 1 (9.53 mg/g wet weight) and lowest for point 3 with 6.63 mg/g wet weight.
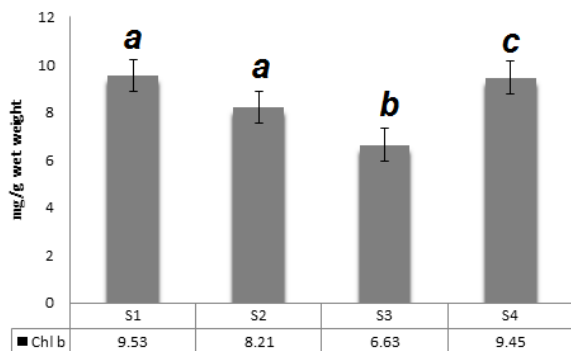
Fig. 3. Measurement of Chlorophyll b content in *Cladophora glomerata* samples from stations in 2016-2017 (Mean ± SE, $p < 0.05$).

Duncan test showed that treatment divided in three groups and also different between points was significant ($p < 0.05$).

Total Chlorophyll

Total Chlorophyll amount (a+b) in four sampling points showed in Figure 4. Based on this figure, order of total Chl is S1> S4> S2> S3. Highest amount was for point 1 (9 mg/g wet weight) and lowest for point 3 with 7.35 mg/g wet weight. Duncan test also showed that treatment divided in three groups and significant different between points ($p < 0.05$).
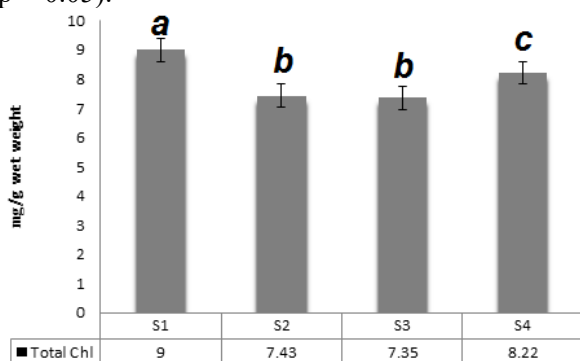
Fig. 4. Measurement of Total Chlorophyll (a+b) content in *Cladophora glomerata* samples from different stations in 2016-2017 (Mean ± SE, $p < 0.05$).

Carotenoids content

Carotenoids content in four sampling points showed in Figure 5. Based on this figure, order of Carotenoids content was S1> S4> S2> S3. Highest

amount was for point 1 (1.41 mg/g wet weight) and lowest for point 3 with 1 mg/g wet weight. Duncan test also showed that treatment divided in three groups and also significant different between points ($p < 0.05$).
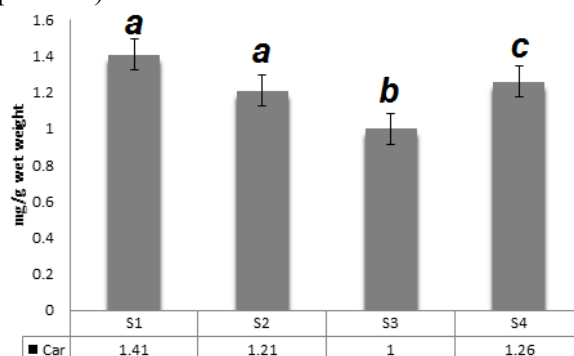
Fig. 5. Measurement of Carotenoids content in *Cladophora glomerata* samples from different stations in 2016-2017 (Mean ± SE, $p < 0.05$).

Total Proteins

Total protein content in four sampling points showed in Figure 6. Based on this figure, order of total protein is S1> S4> S2> S3. Highest amount was for point 1 (3.7 mg/g wet weight) and lowest for point 3 with 2 mg/g wet weight. Duncan test also showed that treatment divided in two groups and significant different between points ($p < 0.05$).
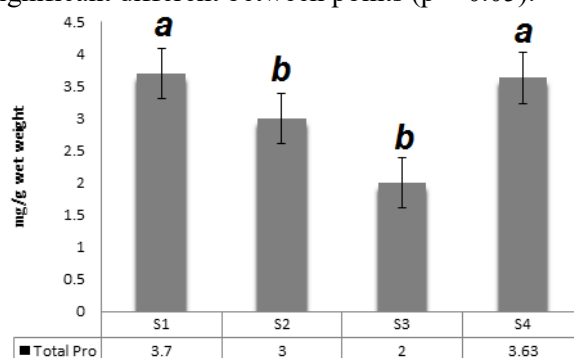
Fig. 6. Measurement of Total Proteins in *Cladophora glomerata* samples from different stations in 2016-2017 (Mean ± SE, $p < 0.05$).

Proline content

Proline content in four sampling points showed in Figure 7. Based on this figure, order of proline content is S3> S2> S4> S1. Highest amount was for point 3 (0.65 mg/g wet weight) and lowest for point 1 with 0.25 mg/g wet weight. Duncan test also showed that treatment divided in three groups and significant different between points ($p < 0.05$).

Antioxidant activity

Antioxidant activity in four sampling points showed in Figure 8. Based on this figure, order of activity is S3> S2> S4> S1. Highest amount was for point 3 (67 μmol/g wet weight) and lowest for point

1 with 25 µmol/g wet weight. Duncan test also showed that treatment divided in three groups and significant different between points (p < 0.05).
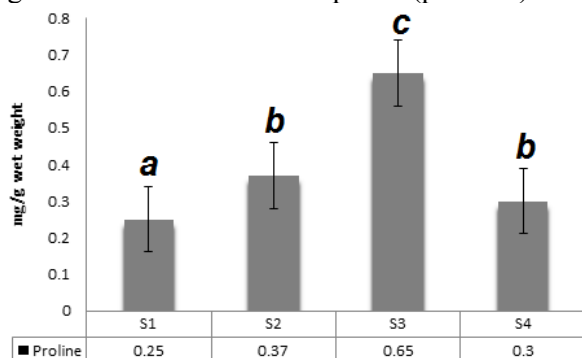
Fig. 7. Measurement of Proline content in *Cladophora glomerata* samples from different stations in 2016-2017 (Mean ± SE, p < 0.05).
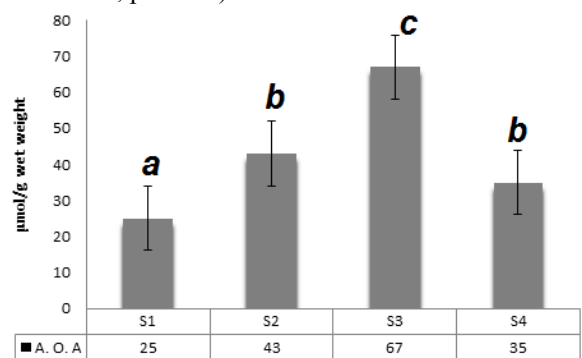
Fig. 8. Measurement of Antioxidant activity in *Cladophora glomerata* samples from different stations in 2016-2017 (Mean ± SE, p < 0.05).

Dry weight

Dry weight amount in four sampling points showed in Figure 9. Based on this figure, order of dry weight is S1> S4> S2> S3. Highest amount was for point 1 (16%) and lowest for point 3 with 8.45%. Duncan test also showed that treatment divided in three groups and significant different between points (p < 0.05).
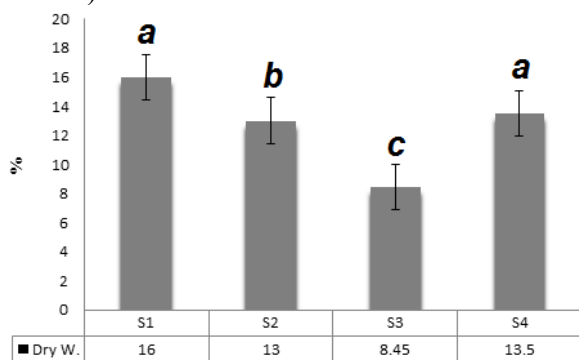
Fig. 9. Measurement of Dry weight in *Cladophora glomerata* samples from different stations in 2016-2017 (Mean ± SE, p < 0.05).

Based on results and former researches of current authors, accumulation of heavy metals and also agricultural and industrial pollutants can make high stress conditions specially in sampling point of 3. Content of Chl a, b, total Chl and also Carotenoids presented lower synthesis in stress point (point 3) and also higher content was for points with lower stress effects. Many studies proved this reality means in stress condition, amount of Chl can be as a physiologic assessment in *Cladophora glomerata*. Chlorophyll content has direct relation with stress condition for example, salty, drought, and also heavy metal pollution. Some researchers proved that decrease in Chl content under stress can increase amount of Chlorophyllase activity [9-10].

Statistical analysis about proline content showed that created stress due to heavy metal accumulation based on former researches in this region and on this algae [4], was significant in sampling point of 3. Increase of proline can have many reasons for increase of resistance against of stress such as prevent of proline oxidation and prevent of its contribution in protein synthesis [11].

Increase of Antioxidant activity based on results, showed also direct relationship with increase of stress. Entrance, absorption, and accumulation of heavy metals in plants and algae can increase free radicals in the cells hence antioxidant system activates for decrease of destruction effects. Results of this study proved that in sampling point of 3, increase in antioxidant activity can exit oxygen free radicals and more protection of cellular lipids, proteins and even nucleic acids and finally increase of algae tolerance [11]. Finally many studies proved that stress can decrease dry weight and protein synthesis. This relates to decrease in Chlorophyll making for increase of plant economy for more tolerance in stress condition. There is also balanced division of photosynthetic materials in Algae [12].

CONCLUSION

The southern shores of the Caspian Sea, especially Farahabad region, host many tourists from inside and outside of Iran every year. Unfortunately, due to poor management about control on agricultural-industrial and human pollutants, it has become a potential environment for the growth of harmful algae. Since *Cladophora glomerata* is the dominant algae in this region, this study showed a relative cognition of chemical and biochemical properties. Antioxidant activity and also proline content showed higher amount in Station of 3. This resulted in higher stress conditions in this point. This increase can be for heavy metal accumulation and also oil residues in this region. The results of this

study are crucial for solving some environmental and economic problems, and finally introduction of an industrial method for the use of these algae and its application for remediation researches are highly necessary.

REFERENCES

1. N. Abdel-Raouf, A.A. Al-Homaidan,I.B.M. Ibraheem, *Afr. J. Biotechnol.*, **11**, 11648 (2012)
2. R.E. Cameron, *J. Arizona Acad. Sci.*, **1**, 85 (1960).
3. D. Tang, S. Shi, D. Li, C. Hu, Y. Liu, *J. Arid Environ.*, **71**, 312 (2007).
4. A. G. Ebadi, H. Hisoriev, *Tox. Environ. Chem.*, DOI 10.1080/02772248.2017.132389451(2017).
5. N. Abe, T. Murata, A. Hirota, *Biosci. Biotechnol. Biochemi*, 62, 661 (1998).
6. A.N. Arnon, *Agron. J.*, **23**, 112 (1967).
7. R.M. Auge, X. Duan, J.L. Croker, W.T. Witter, C.D. Green, *J. Experim. Bot.*, **32**, 753 (1998).
8. D. H. Ngo, T. Vo, D. N. Ngo, I. Wijesekara, S. Kim, *Int. J. Biol. Macromol.*, **51**, 378 (2012).
9. L. S. Bates, R.P. Waldran, I.D. Teare, *J. Plant Soil,* **39**, 205 (1973).
10. M. Bertrand, B. Schoefs, In: M. Pessarakli (ed.), PP: 527-543 (1999).
11. N. Pedrol, P. Ramos, M.J. Riegosa, *Plant Physiol.*,**157**, 383 (2000).
12. B. Huang, R. R. Duncan, R. N. Carrow, *Crop Sci.,* **37**, 1863 (1997).

ИЗМЕРВАНЕ НА НЯКОИ ХИМИЧНИ И БИОХИМИЧНИ ПАРАМЕТРИ В *Cladophora glomerata* L. ОТ РЕГИОНА НА ФАРАХАБАД В ИРАН

А. Г. Ебади *, Х. Хисориев, К. Алиев

Институт по ботаника, фитология и генетика на растенията, Таджикска академия на науките, П. К. 734017, улица Карамов №27, Душанбе-17, Република Таджикистан

(Резюме)

Водораслите имат много различни приложения като храни, в селскостопанската (торове), фармацевтичната и медицинската промишленост. *Cladophora glomerata* е от изобилните филаментозни зелени водорасли в южния бряг на Каспийско море. Проби от водорасли, бяха получени от 4 пункта за вземане на проби в района на Фарахабад в Иран (края на 2016 г. - началото на 2017 г.). Изборът на станции е от значение за туризма, изхвърлянето на замърсявания и остатъчни масла, поради което проучването на някои химични и биохимични показатели на *Cladophora glomerata* като индикаторни водорасли може да бъде важно за този регион. В тази статия са определени някои химични и биохимични характеристики като сухо тегло, хлорофил *a* и *b*, общ хлорофил, каротеноиди, общ протеин, съдържание на пролин и антиоксидантна активност, измерени на базата на стандартни методи. Резултатите показват, че станция 3 има най-малко количество сухо тегло, хлорофил *a* и *b*, общ хлорофил, каротеноиди и общ белтък (p <0,05) и има значителни разлики между станциите, но съдържанието на пролин и антиоксидантна активност са високи в станция 3 (p <0.05). Резултатите показаха и доказаха високи стресови условия от гледна точка на тежки метали в тази точка (основани на предишни проучвания).

BULGARIAN CHEMICAL COMMUNICATIONS

Instructions about Preparation of Manuscripts

General remarks: Manuscripts are submitted in English by e-mail or by mail (in duplicate). The text must be typed double-spaced, on A4 format paper using Times New Roman font size 12, normal character spacing. The manuscript should not exceed 15 pages (about 3500 words), including photographs, tables, drawings, formulae, etc. Authors are requested to use margins of 3 cm on all sides. For mail submission hard copies, made by a clearly legible duplication process, are requested. Manuscripts should be subdivided into labelled sections, e.g. **Introduction, Experimental, Results and Discussion**, *etc*.

The title page comprises headline, author's names and affiliations, abstract and key words.

Attention is drawn to the following:

a) **The title** of the manuscript should reflect concisely the purpose and findings of the work. Abbreviations, symbols, chemical formulas, references and footnotes should be avoided. If indispensable, abbreviations and formulas should be given in parentheses immediately after the respective full form.

b) **The author**'s first and middle name initials, and family name in full should be given, followed by the address (or addresses) of the contributing laboratory (laboratories). **The affiliation** of the author(s) should be listed in detail (no abbreviations!). The author to whom correspondence and/or inquiries should be sent should be indicated by asterisk (*).

The abstract should be self-explanatory and intelligible without any references to the text and containing not more than 250 words. It should be followed by key words (not more than six).

References should be numbered sequentially in the order, in which they are cited in the text. The numbers in the text should be enclosed in brackets [2], [5, 6], [9–12], etc., set on the text line. References, typed with double spacing, are to be listed in numerical order on a separate sheet. All references are to be given in Latin letters. The names of the authors are given without inversion. Titles of journals must be abbreviated according to Chemical Abstracts and given in italics, the volume is typed in bold, the initial page is given and the year in parentheses. Attention is drawn to the following conventions:

a) The names of all authors of a certain publications should be given. The use of "*et al.*" in the list of references is not acceptable.

b) Only the initials of the first and middle names should be given.

In the manuscripts, the reference to author(s) of cited works should be made without giving initials, e.g. "Bush and Smith [7] pioneered...". If the reference carries the names of three or more authors it should be quoted as "Bush *et al*. [7]", if Bush is the first author, or as "Bush and co-workers [7]", if Bush is the senior author.

Footnotes should be reduced to a minimum. Each footnote should be typed double-spaced at the bottom of the page, on which its subject is first mentioned.

Tables are numbered with Arabic numerals on the left-hand top. Each table should be referred to in the text. Column headings should be as short as possible but they must define units unambiguously. The units are to be separated from the preceding symbols by a comma or brackets.

Note: The following format should be used when figures, equations, *etc*. are referred to the text (followed by the respective numbers): Fig., Eqns., Table, Scheme.

Schemes and figures. Each manuscript (hard copy) should contain or be accompanied by the respective illustrative material as well as by the respective figure captions in a separate file (sheet). As far as presentation of units is concerned, SI units are to be used. However, some non-SI units are also acceptable, such as °C, ml, l, etc.

The author(s) name(s), the title of the manuscript, the number of drawings, photographs, diagrams, etc., should be written in black pencil on the back of the illustrative material (hard copies) in accordance with the list enclosed. Avoid using more than 6 (12 for reviews, respectively) figures in the manuscript. Since most of the illustrative materials are to be presented as 8-cm wide pictures, attention should be paid that all axis titles, numerals, legend(s) and texts are legible.

The authors are asked to submit **the final text** (after the manuscript has been accepted for publication) in electronic form either by e-mail or mail on a 3.5'' diskette (CD) using a PC Word-processor. The main text, list of references, tables and figure captions should be saved in separate files (as *.rtf or *.doc) with clearly identifiable file names. It is essential that the name and version of

the word-processing program and the format of the text files is clearly indicated. It is recommended that the pictures are presented in *.tif, *.jpg, *.cdr or *.bmp format, the equations are written using "Equation Editor" and chemical reaction schemes are written using ISIS Draw or ChemDraw programme.

The authors are required to submit the final text with a list of three individuals and their e-mail addresses that can be considered by the Editors as potential reviewers. Please, note that the reviewers should be outside the authors' own institution or organization. The Editorial Board of the journal is not obliged to accept these proposals.

EXAMPLES FOR PRESENTATION OF REFERENCES

REFERENCES

1. D. S. Newsome, *Catal. Rev.–Sci. Eng.*, **21**, 275 (1980).
2. C.-H. Lin, C.-Y. Hsu, *J. Chem. Soc. Chem. Commun.*, 1479 (1992).
3. R. G. Parr, W. Yang, Density Functional Theory of Atoms and Molecules, Oxford Univ. Press, New York, 1989.
4. V. Ponec, G. C. Bond, Catalysis by Metals and Alloys (Stud. Surf. Sci. Catal., vol. 95), Elsevier, Amsterdam, 1995.
5. G. Kadinov, S. Todorova, A. Palazov, in: New Frontiers in Catalysis (Proc. 10th Int. Congr. Catal., Budapest, 1992), L. Guczi, F. Solymosi, P. Tetenyi (eds.), Akademiai Kiado, Budapest, 1993, Part C, p. 2817.
6. G. L. C. Maire, F. Garin, in: Catalysis. Science and Technology, J. R. Anderson, M. Boudart (eds), vol. 6, Springer-Verlag, Berlin, 1984, p. 161.
7. D. Pocknell, *GB Patent* 2 207 355 (1949).
8. G. Angelov, PhD Thesis, UCTM, Sofia, 2001.
9. JCPDS International Center for Diffraction Data, Power Diffraction File, Swarthmore, PA, 1991.
10. CA **127**, 184 762q (1998).
11. P. Hou, H. Wise, *J. Catal.*, in press.
12. M. Sinev, private communication.
13. http://www.chemweb.com/alchem/articles/1051611477211.html.

CONTENTS

СЪДЪРЖАНИЕ

549